
The Kinematics of Turbulent Boundary Layer Structure

Stephen Kern Robinson



DO NOT DESTROY
RETURN TO LIBRARY
DEPT. 422A

April 1991



National Aeronautics and
Space Administration



LM166867E

BRN 83934

The Kinematics of Turbulent Boundary Layer Structure

Stephen Kern Robinson, Ames Research Center, Moffett Field, California

April 1991



National Aeronautics and
Space Administration

Ames Research Center

Moffett Field, California 94035-1000

TABLE OF CONTENTS

Table of Contents	iii
Nomenclature	ix
Summary	1
1. INTRODUCTION	3
1.1 Motivation	3
1.2 Background	3
1.3 Objectives	4
1.4 Approach	5
1.5 Nomenclature and Usages	5
1.6 General Description of Coherent Motions	6
1.7 Outline of Dissertation	8
1.8 Reader's Guide	8
2. HISTORY OF TURBULENCE STRUCTURE EXPERIMENTS	15
2.1 Background	15
2.2 The Discovery Era (1932-1957)	15
2.3 The Flow Visualization Era (1958-1971)	17
2.3.1 Near-Wall Region	18
2.3.2 Outer Flow, Large Eddies, and Entrainment	20
2.3.3 Inner/Outer Interaction	20
2.3.4 Conceptual Models	21
2.4 The Conditional Sampling Era (1972-1983)	22
2.4.1 Near-Wall Region	22
2.4.2 Outer Flow, Large Eddies, and Entrainment	23
2.4.3 Inner/Outer Interaction	24
2.4.4 Vortical Structures and Models	27
2.4.5 Wall-Pressure Studies	29
2.4.6 Conditional Sampling Studies	31
2.4.7 Summary of 1972-1983 Era	32
2.5 The Computer Simulation Era (1984 -Present)	34
2.5.1 Near-Wall Region	34
2.5.2 Outer Flow, Large Eddies, and Entrainment	35
2.5.3 Inner/Outer Interaction	36
2.5.4 Vortical Structures and Models	37
2.5.5 Wall-Pressure Studies	40
2.5.6 Conditional Sampling Studies	41
2.6 Summary of Experimental History	42
3. HISTORY OF STRUCTURE IN NUMERICAL SIMULATIONS	45

3.1 Background	45
3.2 Structure in Large-Eddy Simulations	45
3.3 Structure in Direct Simulations	49
3.4 Summary of Simulation History	52
4. DISCUSSION, OBJECTIVES, AND STRATEGY	55
4.1 Comments on Historical Review	55
4.1.1 Measurement and Analysis Limitations	55
4.1.2 Research Focus	56
4.1.3 Communication of Results	57
4.1.4 Discussion Summary	57
4.2 Recap of Objectives	58
4.3 Analysis Strategy	59
5. TAXONOMY OF STRUCTURES	63
5.1 Wall Low-Speed Streaks	64
5.2 Ejections	64
5.3 Sweeps	65
5.4 Vortical Structures	65
5.5 Near-Wall Shear Layers	66
5.6 Pockets	67
5.7 Large-Scale Motions and Bulges	67
5.8 Backs of Large-Scale Motions	67
5.9 Summary	68
6. NUMERICAL SIMULATION	73
6.1 Numerical Method	73
6.2 Simulation Parameters	76
6.3 Statistical Results	77
6.4 Boundary Layer Database	78
7. ANALYSIS TECHNIQUES AND SOFTWARE TOOLS	91
7.1 Scientific Visualization	91
7.2 Data Flow and Hardware	91
7.3 Graphical Analysis: Software	93
7.3.1 Types of Data Display	93
7.3.2 Data Preparation	94
7.3.3 EDDY	94
7.3.4 GAS	97
7.4 Animations	97
7.5 Stereo Imagery	98
7.5.1 Stereopsis	99
7.5.2 Stereoscopic Display Systems	99

7.5.3 Depth Cues	100
7.5.4 Stereoscopic Techniques	101
7.5.5 Effects of Varying Stereo Parameters	105
7.5.6 Stereo Summary	106
7.6 Listing of Analysis Sets	106
8. CHARACTER OF TURBULENCE IN 2-D PLANES	117
8.1 $x - z$ Planes	117
8.1.1 Same Quantity at Several y^+ Values	117
8.1.2 Various Quantities at Same y^+ Values	123
8.2 $x - y$ Planes	124
8.2.1 u', v , and w in $x - y$ Planes	124
8.2.2 ω'_x, ω_y , and ω_z in $x - y$ Planes	126
8.2.3 $u'v'$, Ejections, and Sweeps in $x - y$ Planes	127
8.2.4 Pressure, Dissipation, and TKE in $x - y$ Planes	128
8.3 $y - z$ Planes	128
8.3.1 u', v , and w in $y - z$ Planes	129
8.3.2 ω'_x, ω_y , and ω_z in $y - z$ Planes	129
8.3.3 $u'v'$, Ejections, and Sweeps in $y - z$ Planes	130
8.3.4 Pressure, Dissipation, and TKE in $y - z$ Planes	130
8.4 Summary of Observations from 2-D Planes	131
9. VORTICES AND THEIR IDENTIFICATION	199
9.1 Vortex Definition Issues	199
9.1.1 Vortices in the $y - z$ Plane	200
9.1.2 Vortices in the $x - y$ Plane	200
9.1.3 Vortex Propagation Velocities	200
9.1.4 Definitions	201
9.2 Detection Methods	201
9.2.1 Vorticity	202
9.2.2 Vorticity Lines	203
9.2.3 Dissipation	204
9.2.4 Second Invariant	205
9.2.5 Low Pressure	205
9.3 Comparisons in Two Dimensions	208
9.3.1 $y - z$ Planes	209
9.3.2 $x - y$ Planes	210
9.4 Comparisons in Three Dimensions	211
9.5 Summary of Vortex Detection Methods	213
10. SPATIAL/TEMPORAL STRUCTURE RELATIONSHIPS	253
10.1 Instantaneous Streamwise Velocity Profiles	254
10.2 Sublayer Streaky Structure	254

10.3 Ejections and Sweeps	255
10.4 Low-Speed Streaks with Ejections and Sweeps	257
10.5 Vortical Elements and Structures	257
10.6 Vortical Structures with Streaks, etc.	260
10.7 Near-Wall Shear Layers	265
10.8 NWSLs with Vortices, Ejections, High-Pressure	266
10.9 Vortical Structures with High-Pressure	268
10.10 Wall-Pressure Fluctuations	269
10.11 P_{wall} with Vortices, Ejections, Sweeps	269
10.12 Pockets	271
10.13 Pockets with Sweeps and Wall-Pressure	271
10.14 Bulges and Large-Scale Motions	272
10.15 Vortical Structures and Dissipation	273
10.16 Vortical Structures and Entrainment	273
10.17 Backs	274
10.18 Backs with Vortical Structures	275
10.19 Wall-Shear Fluctuations	276
10.20 τ_{wall} with Vortical Structures	276
10.21 Summary	277
11. VORTICAL ELEMENTS AND STRUCTURES	401
11.1 Quasi-Streamwise Vortices	401
11.2 Spanwise Vortices	404
11.3 Hairpin/Horseshoe Vortex Models	406
11.4 Literature Summary	409
11.5 Vortices in the Simulated Boundary Layer	409
10.5.1 Quasi-Streamwise Vortex Results	410
10.5.2 Spanwise Vortex Results	411
11.6 Summary	412
12. CONCLUSIONS	433
12.1 Conclusions Regarding the Key Controversies	434
12.1.1 The Bursting Process	434
12.1.2 Wall Streak Formation	436
12.1.3 Outward Interactions	436
12.1.4 Inward Interactions	437
12.1.5 Hairpin, Horseshoe, and Ring Vortices	437
12.2 Kinematic Relationships	438
12.2.1 Inner Vortices and Low-Speed Streaks	438
12.2.2 Inner Vortices and Ejections/Sweeps	439
12.2.3 Inner Vortices and Near-Wall Shear Layers	439
12.2.4 Inner Vortices and Wall-Pressure	439

12.2.5 Inner Vortices and Pockets	439
12.2.6 Inner Vortices and Dissipation	439
12.2.7 Outer Vortices and Ejections/Sweeps	439
12.2.8 Outer Vortices and LSMs	440
12.2.9 Outer Vortices and Entrainment	440
12.2.10 Outer Vortices and Pressure	440
12.2.11 Outer Vortices and Dissipation	440
12.3 Kinematic Characterization of TBL	440
12.3.1 Buffer Region	441
12.3.2 Logarithmic Region	441
12.3.3 Wake Region	441
12.4 Vortical Structure Formation and Evolution	441
12.4.1 Near-Wall Arch Formation	442
12.4.2 Near-Wall Q-S Vortex Formation	442
12.4.3 Outward Growth of Arches	443
12.4.4 Outer Region Transverse Vortex Formation	443
12.4.5 Vortex Regeneration Patterns	443
12.4.6 Summary: Vortex Evolution	444
12.5 Future Research Issues	445
12.6 Final Discussion	446
 REFERENCES	 469

NOMENCLATURE

C_f	coefficient of skin-friction, $\tau_w/(0.5\rho U_e^2)$
k	turbulent kinetic energy per unit mass, $(\overline{u'^2} + \overline{v'^2} + \overline{w'^2})/2$
p	static pressure
Re_θ	momentum-thickness Reynolds number, $(U_e \theta)/\nu$
u, v, w	instantaneous velocity components in the x, y , and z -directions
u_τ	friction velocity, $\sqrt{\tau_w/\rho}$
$-\overline{u'v'}$	Reynolds shear stress per unit mass
$(u'v')_1$	outward interaction: motion in the first quadrant of the $u'v'$ plane
$(u'v')_2$	ejection: motion in the second quadrant of the $u'v'$ plane
$(u'v')_3$	inward interaction: motion in the third quadrant of the $u'v'$ plane
$(u'v')_4$	sweep: motion in the fourth quadrant of the $u'v'$ plane
U_e	free-stream velocity
U_c	streamwise convection velocity
VITA	Variable-Interval Time-Average
x, y, z	cartesian coordinates: streamwise, wall-normal, spanwise directions
δ	mean boundary-layer thickness, defined where $\bar{u} = 0.99U_e$
δ^*	displacement thickness, $\int_0^\delta (1 - \bar{u}/U_e) dy$
ϵ	rate of dissipation of turbulent kinetic energy per unit mass
Γ	vortex circulation
λ^+	mean spanwise spacing between sublayer low-speed streaks ($\approx 100\nu/u_\tau$)
μ	dynamic viscosity
ν	kinematic viscosity, μ/ρ

$\omega_x, \omega_y, \omega_z$ instantaneous vorticity components in the x, y , and z -directions

ρ density

τ_w wall shear-stress

θ momentum thickness, $= \int_0^\delta (\bar{u}/U_e)(1 - \bar{u}/U_e)dy$

Superscripts

$\overline{(\quad)}$ mean value (temporal or spatial average)

$+$ non-dimensionalization by “wall” parameters, u_τ and ν

$'$ fluctuating value ($=$ instantaneous value $-$ mean value)

Subscripts

$(\quad)_e$ conditions at edge of boundary layer

$(\quad)_x$ x direction

$(\quad)_y$ y direction

$(\quad)_z$ z direction

SUMMARY

The long history of research into the internal structure of turbulent boundary layers has not provided a unified picture of the physics responsible for turbulence production and dissipation. The goals of the present research are to: 1) Define the current state of boundary layer structure knowledge; and 2) Utilize direct numerical simulation results to help close the unresolved issues identified in Part A and to unify the fragmented knowledge of the various coherent motions into a consistent kinematic model of boundary layer structure.

The results of the current study show that all classes of coherent motion in the low Reynolds number turbulent boundary layer may be related to vortical structures, but that no single form of vortex is representative of the wide variety of vortical structures observed. In particular, ejection and sweep motions, as well as entrainment from the free-stream are shown to have strong spatial and temporal relationships with vortical structures. Distributions of vortex size, location, and intensity show that quasi-streamwise vortices dominate the buffer region, while transverse vortices and vortical arches dominate the wake region. Both types of vortical structure are common in the log region.

The inter-relationships between the various structures and the population distributions of vortices are combined into a conceptual kinematic model for the boundary layer. Aspects of vortical structure dynamics are also postulated, based on time-sequence animations of the numerically simulated flow.

CHAPTER 1 - INTRODUCTION

1.1 Motivation

In a turbulent boundary layer, kinetic energy from the mean flow is converted into turbulent fluctuations and then dissipated into internal energy by viscous action. This process is continual, such that the turbulent boundary layer is self-sustaining in the absence of strong stabilizing effects.

For as long as these facts have been known, researchers have sought to understand just how turbulence is generated at the expense of the mean motion, and just how it is dissipated. This is the topic of the present effort. The specific aim is to collect, organize, verify, and extend by numerical simulation a large portion of the knowledge concerning the physics of boundary-layer turbulence. The focus is on the kinematics of coherent motions embedded within the boundary layer; dynamical issues will be raised, but the techniques utilized here are not capable of providing direct answers to dynamic questions. The final objective is a conceptual kinematic model of turbulence physics - one that unifies the known aspects of boundary layer structure.

From a practical standpoint, the motivation for turbulent boundary layer research is obvious and of major importance: most mechanical devices that involve the movement of gas or liquid are affected by turbulent fluid flow that is constrained by a solid boundary. Many geophysical and biological flows also involve turbulent boundary layers. The simplest (and therefore the most important to understand first) of wall-bounded turbulent flows is the flat-plate, zero-pressure gradient boundary layer, in which the layer is allowed to grow through natural entrainment at the outer edge. Physical understanding of this generic, “canonical” case (Fig. 1.1) is prerequisite to successful study of more complex (and more practically important) flows.

1.2 Background

Since boundary layer flows are the technical driver for so many engineering applications, immense human and financial resources have been brought to bear on the problem in 80 years of study. The progress made, however, has not been commensurate with the effort expended, reflecting the fundamental complexity of turbulence phenomena.

The field of turbulent boundary layer study has evolved into three distinct areas. 1) Predictive modelling of the gross statistics of turbulent flows; 2) Alteration and control of turbulence by mechanical or chemical means; 3) Physical understanding of the internal workings of turbulence through study of its “coherent” features. Currently, these three motivations for turbulence investigation function as essentially separate disciplines, with minimal crosstalk between them. The widest gap is between the statistical modeling community and the turbulence structure com-

munity, neither of which has benefited consistently by knowledge gained by the other.

The difference between turbulence modelling and turbulence understanding is fundamental. Modellers ask “what” are the statistical characteristics that must be reproduced by a mathematical model, whereas “eddy-chasers” ask “how” the statistics came to be the way they are. Turbulence modellers generally disregard detailed kinematical information and employ statistical techniques which neither utilize nor provide detailed structural information. On a more basic level, understanding of turbulence dynamics has never been complete enough to allow the formulation of an alternative to the Reynolds-averaged statistical approach to prediction.

The usefulness of turbulent boundary layer structure information is currently limited by three major problems. First, the state of the knowledge concerning turbulence structure is diffuse and ill-defined. There are too many unconnected pieces of information, at disparate levels of detail. A conceptual model that combines all known structural aspects has not yet emerged, and controversies about even the fundamentals abound.

Second, several classes of coherent motions have been identified experimentally in boundary layers, but the kinematic and dynamic associations between them are unclear. This has prevented the assimilation of structure information into a consistent picture that might eventually be used to guide the formation of predictive models.

Finally, the contributions that structural features make to terms in the Reynolds-averaged modelling equations are poorly understood.

In summary, we are unable to accurately predict many turbulent flows of engineering value, due partly to a lack of physical insight into the nature of turbulence. Yet the large quantity of detailed structural information generated over the last thirty years has attracted few customers and has thus served little practical purpose. There is an immediate need for an overarching project to gather the structure information together, fill the gaps in the knowledge, and create a unified picture of how turbulence is generated and dissipated in boundary layers.

1.3 Objectives

The overall objectives of the current effort are dictated by the needs identified above: A) Define the state of the turbulence structure knowledge and clarify the major unresolved issues; B) Develop a conceptual model of the physics of boundary layer turbulence that accounts for the known structural features and describes the kinematics of turbulence production and dissipation.

The pursuit of these two objectives has been divided into two projects, the second of which (Part B) is described in this report.

1.4 Approach

To meet objective A, the author and S.J. Kline have organized a community-wide survey and evaluation of what is known about coherent motions in turbulent boundary layers. This effort has included personal interviews with researchers, development of a standard nomenclature list, and a comprehensive literature survey. The process and results of this cooperative evaluation effort are described in Kline and Robinson (1989a, 1989b).

Objective B, the creation of an improved conceptual (non-predictive) model of boundary layer structure, has utilized direct Navier-Stokes simulation results as a tool with which to verify and extend experimental results. There are four key (and somewhat nonstandard) aspects to the approach taken to analyze the simulated turbulent boundary layer: 1) No hypothesis concerning the dominant forms of coherent motion is made a priori - all possibilities are considered; 2) All identifiable coherent motions are considered, rather than a predetermined subset; 3) A primarily qualitative overall kinematic picture is developed, rather than a statistical characterization of a particular extracted detail; 4) Where possible, key features of the kinematic picture are backed by time-sequences, event counting, and distributions of measured properties. The philosophy behind these ideas is that meaningful progress in the field now requires a global approach - one that bonds together the many parts and brings the remaining unknowns into sharper focus.

Objective B requires investigating in detail: 1) the spatial character of each class of coherent motion; 2) the spatial relationship between different structural features; 3) the generation mechanisms and time-evolution of structures; and 4) the statistical relevance of each class of structure. The strategy employed in analyzing the simulated boundary layer is detailed in Chapter 4.

The current effort will be limited to the simple “canonical” flat-plate boundary layer with zero mean pressure gradient (Fig. 1.1). The DNS simulation of a boundary layer with these characteristics by Spalart (1988) has been used. The results obtained from the numerical simulation are necessarily limited to low ($Re_\theta = 670$) Reynolds number, although implications for boundary layers at more practical Reynolds numbers are discussed.

1.5 Nomenclature and Usages

During the portion of the current project described as Part A above, a turbulence structure nomenclature list was compiled by the author and edited by the research community as a cooperative project. This list is available from the author, and its definitions will be adhered to within this paper. To simplify reading, a few of the most commonly-used terms are briefly described below.

To the detriment of the field, no generally-accepted definition of “coherent motion” for turbulent flows has emerged. For the present work, a coherent motion is defined as: *a three-dimensional region of the flow over which at least one fun-*

damental flow variable (velocity component, density, temperature, etc.) exhibits significant correlation with itself or with another variable over a range of space and/or time that is significantly larger than the smallest local scales of the flow. A number of different definitions for “coherent motion” or “coherent structure” are available in the literature (e.g. Hussain 1986, Fiedler 1986, Blackwelder 1988). For the purposes of this report, the above definition is preferred (and may indeed be criticized) for its generality. Specific examples of boundary-layer coherent motions are discussed in Chapter 5. The term “coherent motion” is used interchangeably with “turbulent structure” in this report.

Names, symbols, and terminology related to the Cartesian coordinate system are shown in Fig. 1.2. The terms “up” and “out” are occasionally used to describe the wall-normal, or $+y$ -direction. Wall or “plus” units refer to normalization by the viscous length and velocity scales, ν/u_τ and u_τ , respectively. The region $y^+ \leq 100$ is usually considered the “wall region;” this includes the sublayer, buffer region, and at least part of the logarithmic region. The rest of the layer is the “outer region.”

“Vortex” has no rigorous definition for use in turbulent flows, but a useful working definition is proposed in Section 9.1. The term “quasi-streamwise vortex” will be applied to any vortical element with a predominantly streamwise (x) orientation, although it may be curved as well as tilted at a significant angle to the x -axis. “Transverse” and “spanwise” will be used interchangeably to refer to vortices (or anything else) with an orientation primarily in the z -direction.

“Sweeps” and “ejections” are defined here as $(u'v')_4$ and $(u'v')_2$ motions, respectively, in accordance with the $u'v'$ quadrant-splitting scheme introduced by Wallace et al (1972) and by Willmarth and Lu (1972) (see Figure 2). There are other interpretations of these terms, especially for sweeps, but the present usage is the most common, and has been chosen for its strong association with the Reynolds shear stress.

“Low-speed” and “high-speed” are used as relative terms, referring to perturbations from the mean value at that y -location. These terms are generally used to describe velocities in the streamwise direction, so low-speed implies $-u'$, and high-speed implies $+u'$.

The simplest possible turbulent boundary layer is referred to here as the “canonical” case, which describes a flat-plate, smooth-wall boundary layer with a two-dimensional mean flow, in the absence of pressure gradient, large free-stream fluctuations, wall-heating, force fields, or compressibility effects (Fig. 1.1). An analogous canonical channel flow is also implied, but with the necessary mean streamwise pressure gradient. This work will restrict itself solely to canonical cases.

1.6 General Description of Coherent Motions in the Turbulent Boundary Layer

An overview of what is known concerning turbulent boundary layer coherent

motions is appropriate as a preface for surveying the history of the field. Specific and referenced facts are cited in Chapters 2 and 3.

The streamwise velocity field in the sublayer and buffer regions is organized into alternating narrow streaks of high and low-speed fluid which are persistent and relatively quiescent most of the time. The majority of the turbulence production in the entire boundary layer occurs in the buffer region during intermittent, violent outward ejections of low-speed fluid, and during intrushes of high-speed fluid at a shallow angle toward the wall. This near-wall turbulence production process is considered to be an intermittent, quasi-cyclic sequence (usually referred to as “bursting”), but there is not a consensus as to which observed features of near-wall activity are essential to the continuity of the cycle (see Sec. 12.1.1). A complicating factor is the observation that several of the structural elements apparently arise in more than one way. This is well-documented in Chapters 10 and 12.

In the outer region, three-dimensional bulges on the scale of the boundary layer thickness form in the turbulent/non-turbulent interface. Deep irrotational valleys occur on the edges of the bulges, through which free-stream fluid is entrained into the turbulent region. Large, weakly rotational eddies are commonly observed beneath the bulges. Relatively high-speed fluid impacts the upstream sides of these large-scale motions, forming sloping, delta-scale shear layers which are easily detected experimentally.

Although the inner region production cycle appears to be largely self-sustaining, it is believed that the outer structure has at least a modulating influence on the near-wall events, and that this influence is Reynolds number dependent. The dynamical relationships between the inner region of intense turbulence production and the larger-scale, less-active outer layers are poorly understood. As a result, the correct scaling parameters for the near-wall production time and length-scales remain a topic of controversy.

Embedded tornado-like vortices with a variety of strengths are known to exist in the boundary layer, and they are thought by many to be the central elements in the turbulence production cycle and also in the transport of momentum between the inner and outer layers. Inclined horseshoes or hairpins are the commonly proposed shapes for the vortex structures. However, three-dimensional vortices are extremely difficult to characterize in the laboratory. Numerical simulations show vortices in the shape of complete loops or horseshoes to be rare, although elements of these vortical structures are common. At this point (1990), the question of vortex geometry in the boundary layer (especially over a significant Reynolds number range) remains open.

Shear-layer structures are also common in the boundary layer, especially near the wall, and local shear-layer instability arguments are usually invoked to explain the birth of vortices. The details of vortex generation, evolution, interaction, and

demise remain under active discussion.

To summarize, the most controversial issues in the field of boundary layer structure can be grouped as follows:

- Near-wall streak formation
- The bursting process
- Mass and momentum transfer from the inner to the outer layers
- Mass and momentum transfer from the outer to the inner layers
- Reynolds number effects and appropriate scaling variables for near-wall turbulence production events
- The existence and role of hairpin/horseshoe/ring vortices

Of these phenomena, the near-wall bursting process of turbulence production (see Section 12.1.1) has received the most scrutiny. There is now considerable consensus concerning several of the kinematical issues of coherent motions, but the dynamics (including issues of “importance” and relative cause and effect) remain largely unsettled. Although the kinematics of coherent structures was necessarily the focus of the current work, hypotheses for some of the dynamical issues are offered in Chapter 12.

1.7 Outline of Dissertation

The remainder of this report follows the following plan: First, the history of turbulence structure research is outlined (Chapters 2 and 3), followed by a detailed formulation of the project’s objectives and strategies (Chapter 4), and an introduction to the known structural features (Chapter 5). A description of the direct numerical simulation is given in Chapter 6, followed by a discussion of the techniques employed to analyze the numerical database (Chapter 7). The instantaneous spatial character of the turbulent boundary layer is presented in Chapter 8, and the topic of vortex structures in turbulent boundary layers is taken up in Chapter 9. Spatial relationships between many of the different classes of coherent motion are examined in Chapters 10 and 11, leading to a set of general conclusions on the nature of turbulent structure, and a proposed conceptual model of boundary-layer turbulence kinematics (Chapter 12).

1.8 Reader’s Guide

Assimilation of the volume of information included in this report may be as daunting for the reader as it was for the author. Thus, some guidance concerning the best way to approach this work may be useful.

For those concerned with new conclusions in the field of turbulence structure, the most efficient reading would be to proceed directly to Chapters 10 and 12 after Chapter 1. Chapter 10 focusses on three-dimensional space-time relationships between various coherent structures found in the numerically-simulated boundary

layer, and Chapter 12 summarizes the unified kinematic picture drawn from those observations. For a deeper appreciation of the findings discussed in these chapters, a background for the analysis strategy as well as a taxonomy of the structures investigated is available in Chapters 4 and 5.

The history of the field of turbulent boundary layer structure is thoroughly reviewed in Chapters 2 and 3. Since progress in this field has been so strongly dependent on technology development, the background is presented as a chronological recounting, rather than as the traditional literature review organized by category.

Spalart's (1988) direct numerical simulation and the methods employed during the current investigation to analyze it are discussed in Chapters 6 and 7. Chapter 8 is for the specialist in turbulence structure. This chapter considers the structure of boundary-layer turbulence as derived from two-dimensional instantaneous slices through the simulation data. These 2-D findings lay the groundwork for the three-dimensional approach taken in Chapter 10. Chapter 8 also serves to remind the reader that two-dimensional data are rich in information, but are extremely difficult to assimilate into a consistent three-dimensional conceptual picture of turbulence production processes.

Vortices play the central role in this report as well as in the turbulent boundary layer. The definition, identification, and kinematic/dynamic role of vortices in turbulence production and dissipation are discussed in Chapters 9 and 11.

CANONICAL BOUNDARY LAYER

- Flat, smooth, solid, stationary wall; undisturbed since transition
- Fully turbulent boundary layer
- Zero pressure gradient
- 2-D mean flow
- Steady outer flow with low free-stream turbulence
- Constant density
- Newtonian fluid
- Single-phase fluid
- No force fields

Fig. 1.1 Defining attributes of the canonical boundary layer. An analogous canonical channel flow is implied, but without the zero pressure-gradient restriction.

tensor subscript	axis	axis name	view name
1	x	streamwise (axial) (longitudinal)	end
2	y	wall-normal	plan
3	z	spanwise (transverse) (lateral)	side

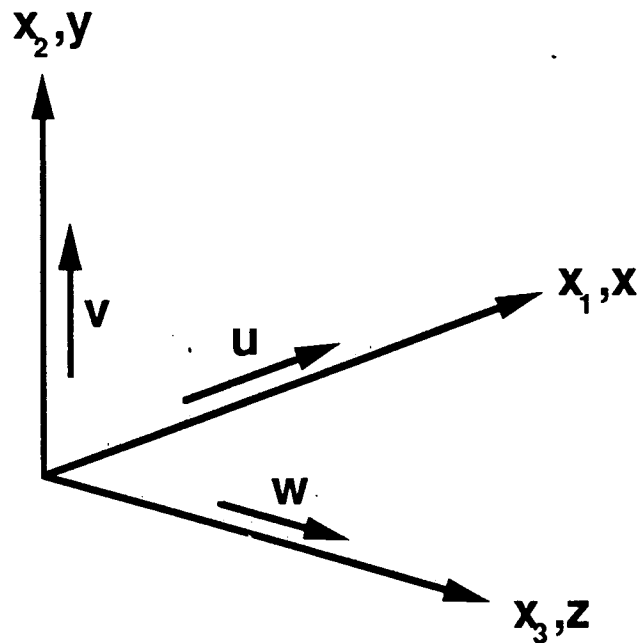


Fig. 1.2 Coordinate system and geometrical terminology.

CHAPTER 2 - HISTORY OF TURBULENCE

STRUCTURE EXPERIMENTS

Since the current study represents a broad approach to the topic of coherent motions in turbulent boundary layers, a thorough historical perspective is appropriate. The discussion is divided into separate reviews of the experimental (Chapter 2) and computational (Chapter 3) literature. Due to the large number of papers in the literature, only selected works are mentioned here.

2.1 BACKGROUND

The decomposition of a time-varying quantity in turbulent flow into its mean and fluctuating components (Reynolds, 1894) is a concept that forms the basis for most of the turbulence research ever done. Implicit in the Reynolds decomposition is the notion that the fluctuating component is random, and thus is representable by statistical theories.

Turbulence researchers in the early 1900's noticed, however, that repeating sequences of events intermittently appeared in the midst of otherwise random fluctuations. These discoveries raised the question of whether average statistical representations of the turbulent fluctuations were adequate to predict turbulent flows of engineering interest.

Today, most predictive methodologies still ignore the presence of "coherent structures" in turbulence, partly because Reynolds-averaged turbulence modeling approaches do not allow for the explicit inclusion of intermittent three-dimensional motions, but also because it has never been proven that a model based on "structures" would necessarily improve the predictive accuracy. However, the persistent inability of Reynolds-averaged turbulence models to accurately predict many turbulent flows, and the desire for a deeper understanding of the underlying physics have constituted strong motivations for the study of coherent motions for at least 50 years.

Over the years, the study of turbulent boundary layer coherent motions has progressed along several intricately-connected paths. This, combined with the massive body of literature associated with the subject, makes a simple organization of the evolution of knowledge in the field nearly hopeless. It is useful and appropriate, however, to divide the experimental history of the field into four eras (1932-1957, 1958-1971, 1972-1983, 1984-present). Each era has been referred to here according to an appropriate enabling technology or focus.

2.2 THE DISCOVERY ERA (1932-1957)

The first quantitative evidence that turbulence is not a continuously random field of velocity fluctuations was apparently hot-wire traces that showed drop-outs,

or intermittently turbulent/non-turbulent behavior in the signal when the probe was placed near the edge of the turbulent layer. Corrsin (1943) was the first to report on the intermittent behavior of turbulence in a jet, and Townsend (1947) investigated intermittency in a cylinder wake in some detail. The implication of intermittent processes in turbulent flows was that the general behavior of shear flows cannot be fully inferred on a homogeneous shear flow basis but must involve boundary phenomena of some sort. This realization was the motivation for in-depth studies of intermittency in the turbulent boundary layer by Sandborn (1959), and by Corrsin and Kistler (1954). The latter paper is a tour de force on the turbulent/non-turbulent interface in turbulent flows, including the spatial and statistical character of the interface and its propagation properties.

Flow-visualizations, mixing-length hypothesis ideas, and speculation as to the cause of the intermittency phenomenon gave rise to a the concept of large, coherent motions, or “eddies” (note the implied vortical motion) within turbulent flows. Two-point correlation studies were conducted in several laboratories to map the average shape and size of these eddies. Favre, Gaviglio, and Dumas (1957) provide a summary of extensive spectra and space-time correlations of u' in a turbulent boundary layer. This paper is notable for its detailed measurements but the discussion of results is minimal. Most impressive of the early correlation studies is Grant (1958) (a student of Townsend) who combined two-point correlation techniques with profound insight to grid turbulence, cylinder wakes, and boundary layers. For the boundary layer, these investigations revealed that the average large-eddy character had a downstream slope and a slow rotation in the direction of the mean shear.

During this time period, attention was drawn to the near-wall region of wall-bounded turbulent pipe flows by Laufer (1953), who demonstrated that both the production and dissipation of turbulence kinetic energy peak dramatically in the zone just outside the “laminar” sublayer. Klebanoff (1954) corroborated Laufer’s results in a turbulent boundary layer, and showed that more than a third of the production and dissipation of turbulent energy occurs within the inner two percent of the boundary layer at $Re_\theta \approx 7500$. These results made it clear that the thin wall region plays a dominant role in maintaining turbulence in the entire boundary layer, and marked the beginning of the concentrated scrutiny the near-wall region has received ever since.

Although the sublayer was still called “laminar” in the mid-fifties, experimentalists had long observed and reported distinctly non-laminar, coherent motions in the buffer region. Fage and Townend (1932) studied the motion of flow in the sublayer and reported continual and significant departures from rectilinear flow for $y^+ < 4$. Einstein and Li (1956) published photographs of dyed fluid in the sublayer spreading through the outer turbulent fluid through localized outward eruptions. Grant (1958) provided two-point correlations of u' and v' near the wall that he

interpreted (almost prophetically) as localized outward “jets” of fluid originating at the outer edge of the sublayer and functioning as “stress-relieving motions” in the high shear region very near the wall. Grant also found that the near-wall motions and in particular the “erupted” fluid, were highly elongated in the streamwise direction, but narrow in the spanwise direction.

The elongated, or streaky nature of the flow near the wall had apparently been observed by researchers in flow-visualization studies for many years, but was not investigated as an interesting phenomena in its own right until the mid-fifties. Up until then, streaky “residue” of marked fluid near the wall of water channels was regarded either as an artifact of the facility or technique, or else a phenomena with limited probable importance to the turbulence in the rest of the boundary layer away from the wall. Near-wall streaky structure was also noted in transitional boundary layers by Ruetenik (1954) and by Hama (in Corrsin, 1957). These passive observations formed the foundation for the large subsequent body of work done on the coherent structure of near-wall turbulent shear flow.

As the evidence for coherent motions within the boundary layer became more convincing, simplified models consistent with the experimentally observed features were formulated.

Townsend (1951) proposed a model of the large-eddy structure consisting of large inclined vortices with their plane of rotation normal to the principal axis of strain. Townsend (1970, 1976) later modified this concept into a double roller eddy model.

In a landmark paper, Theodorsen (1952) proposed the first structural model for near-wall turbulence production. The model was developed by reference to the vorticity transport form of the Navier-Stokes equations and consisted of vortex lines bent into an inclined horseshoe shape. This vortical model was proposed as the fundamental structure of both transitional and fully turbulent boundary layers, and is the ancestor of most coherent structure models to follow in the ensuing 35 years. Theodorsen’s model is discussed in more detail in Chapter 11.

2.3 THE FLOW VISUALIZATION ERA (1958-1971)

As researchers worked to gain a better physical understanding of the types and variety of coherent motions in boundary layers, the dominant experimental technique was flow-visualization, both qualitative and quantitative. Hot-wire anemometry, and dynamic wall-pressure sensors, sometimes with simultaneous flow-visualization, also saw extensive use.

By 1957 it was clear that turbulent boundary layers possessed interesting “coherent” features in the outer turbulent/non-turbulent interface, in the large-eddy nature of the internal turbulence, and in the elongated, erupting motions very near the wall. In 1959, a paper by Kline and Runstadler on the coherent structure

of the near-wall region gained wide attention, and set off a considerable wave of controversy and new research into boundary layer turbulence structure.

During the early 1950's, the Stanford group had noticed that streaky marker residue appeared at the walls of diffuser flows **only** when the flow was turbulent and **always** when the flow was turbulent. This prompted a series of in-depth studies of near-wall coherent structure. The first results were published by Kline and Runstadler (1959), who showed that the streaky pattern near the wall was due to the sublayer being composed entirely of spanwise-alternating elongated regions of high- and low-speed fluid. This and the earlier evidence that motion in the sublayer was unsteady and three-dimensional eventually killed the notion that the sublayer was actually laminar.

2.3.1 Near-Wall Region

Following the 1959 paper, Stanford issued a series of reports and motion pictures (e.g. Kline et al, 1967; Kim et al, 1971) based on extensive investigations with dye injection, hydrogen bubble techniques, and hot-film probes. These works described a repeating sequence of intermittent events in the near-wall region that accounts for the majority of the turbulence production in boundary layers on smooth surfaces. The sequence begins with the lift-up of streamwise-elongated streaks of low-speed fluid from the sublayer into the buffer region, creating a locally inflectional streamwise velocity profile. The markers caught in the lifted low-speed streaks evolved into a wavy configuration, after which the markers were suddenly and rapidly ejected outward and then scattered in the ensuing fine-scale turbulence. This three-stage sequence of lift-up, oscillation, and ejection/breakup of the marked low-speed streak was named the “bursting process” to emphasize its intermittent character.

These early Stanford investigations showed that virtually all of the near-wall Reynolds stress ($-\overline{u'v'}$) was produced during bursting, and that the mean spanwise spacing between low-speed streaks was approximately 100 viscous length units. Kim et al also noted that apparent streamwise vortical motion commonly accompanied the oscillation stage of bursting, with transverse rotation or a “wavy” motion less common.

Laufer's (1953) and Klebanoff's (1954) results had identified the region just outside the sublayer as the birthplace of most of the boundary layer's turbulent fluctuations. The significance of the Stanford work was that it established a conceptual description of the mechanism that bears primary responsibility for the near-wall turbulence kinetic energy production.

Parallel to the Stanford work, Corino and Brodkey (1969) published one of the most influential papers of this era, in which they described detailed flow-visualization studies of the near-wall region. In the sublayer ($y^+ \leq 5$), Corino and Brodkey found distinctly non-laminar fluctuations that were strongly related

to disturbances in the generation (or buffer) region, and which included occasional penetrations to the wall from the outer flow. In the region adjacent to the sublayer ($5 \leq y^+ \leq 15$), small elements of locally decelerated (low-speed) fluid were ejected outward, apparently without triggering by outer-region motions. The ejected fluid commonly interacted with a region of intense shear which formed at the upstream interface of the ejection. The interaction resulted in intense, chaotic velocity fluctuations, which were considered to represent a major source of turbulence production. The ejection phase ended with the entry from upstream of a large-scale “sweep” of fluid, with velocity nearly parallel to the wall. The sweep motion moved at approximately the mean velocity ($u' \approx 0$), and thus could not be a major contributor to the Reynolds shear stress. This attribute constitutes an important distinction from the “inrushes” observed by Grass (1971), which made high contributions to $-\overline{u'v'}$.

In contrast to the Stanford studies, Corino and Brodkey’s observations did not include any significant oscillatory or vortical motion in relation to the turbulence production processes. This may be attributable to the limited and nearly two-dimensional segment of the flow that was visualized.

Clark and Markland (1971) reported on visualization experiments similar to those at Stanford, employing hydrogen bubble studies in a water channel. The results included observations of streak formation, ejection, and breakup, but special attention was paid to the appearance of vortices in the flow. Observations were recorded for occasional counter-rotating streamwise vortices, short transverse vortices, and some U-shaped (or horseshoe) vortices.

Grass (1971) helped complete the early visual picture of near-wall turbulence with a study of coherent motion in smooth- and rough-wall boundary layers. Grass observed intermittent wallward “inrushes” of high-speed fluid as well as the outward ejections of low-speed fluid, irregardless of wall roughness. Since both inrushes and ejections made high contributions to the Reynolds stress, Grass concluded that turbulence production is dominated by joint contribution from inrush and ejection events.

Additional important near-wall investigations explored the nature of fluctuations of the wall-pressure and wall-shear stress beneath turbulent boundary layers. Willmarth and Woolridge (1962), building on work by Corcos (1962; see also Corcos, 1964), found that the scale of the pressure fluctuations beneath a turbulent boundary layer were of the order of the displacement thickness, much larger than the near-wall scales. They also found that the fluctuating wall-pressure footprints were not elongated or streaky, but were approximately round. Reiss and Hanratty (1963) used mass-transfer probes to make an early attempt at measuring fluctuating wall shear stress and found that the longitudinal length scale was an order of magnitude greater than the transverse, corresponding with the streaky nature of the sublayer.

2.3.2 Outer Flow, Large Eddies, and Entrainment

Although most of the attention during this era was focussed upon newly-discovered near-wall phenomena, several groups continued to investigate the outer-layer intermittency and the associated large-scale structure. The early work of Corrsin and Kistler (1954) and others had made it clear that the intermittent nature of turbulence in free turbulent flows was closely associated with the entrainment process. Townsend (1970) summarized his own and others' work on entrainment and the large-eddy structure of free turbulent flows in general, proposing a simple visco-elastic model of the turbulent/ non-turbulent interface. Townsend observed that the slow rate of entrainment in boundary layers is due to the lack of an active instability of the interface, such as is present in a plane wake.

Gartshore (1966) experimentally confirmed Townsend's (1956) large-eddy equilibrium hypothesis in a boundary layer, which states that the largest eddies of a turbulent shear flow are in approximate energy equilibrium throughout most of their lives. Fiedler and Head (1966) provided intermittency measurements in boundary layers with various pressure gradients.

In 1970, Kovasznay, Kibens, and Blackwelder reported extensive intermittency and two-point correlation measurements in the outer region of the boundary layer to relate the form and motion of the turbulent/non-turbulent interface with the underlying large-eddy motions. Extensive use was made of the emerging techniques of conditional sampling and ensemble-averaging of hot-wire data. The authors proposed a model for the outer interface consisting of three-dimensional, δ -scale bulges of turbulent fluid with the outer, faster irrotational flow riding over and around the bulges. Entrainment occurs in relatively narrow valleys of potential fluid that form at the upstream and downstream boundaries of the bulges. A schematic picture of the process can be found only in a review paper by Kovasznay (1970). (The Kovasznay et al paper also contains a quote which serves to remind us of progress in laboratory resources: "... wind tunnel time was inexpensive in comparison to available digital computers.")

2.3.3 Inner/Outer Interaction

The interaction of coherent motions in the near-wall region with those in the outer region of the boundary layer received relatively sparse attention during the period 1958-1971. The Stanford group speculated that the direction of influence was generally from the inner to the outer regions, in the form of fluid from the buffer zone being ejected into the outer flow. Grass (1971) agreed that the ejection process may be the dominant mode of momentum transport for the entire boundary layer outside the sublayer. Corino and Brodkey (1969) observed that the large-scale outer flow had little influence on the near-wall turbulence production events except to "sweep" the area after the major interactions had occurred.

Narahari Rao et al (1971) approached the question of coupling between the

inner and outer layers and fired the first salvo of a battle which has yet to be resolved; that of the proper scaling parameters for the “burst frequency.” These authors used the conditionally sampled signal from a single hot-wire to derive a passage frequency for “bursts.” Unfortunately, the connection between the educed bursts and the liftup/oscillation/breakup process was presumed, rather than demonstrated. The results for several Reynolds numbers showed a mixed inner/outer scaling for the “burst” frequency, in opposition to the inner scaling found for visually-identified events by Kline et al (1967) over a limited Reynolds number range. The mixed scaling was taken to be evidence for a strong coupling between the inner and outer coherent motions. Narahari Rao et al were perhaps the first to grapple with the difficult and still significant problem of matching signals from a single probe with the occurrence of specific three-dimensional events in the flow.

2.3.4 Conceptual Models

As knowledge of the mechanisms for near-wall turbulence production rapidly expanded, a number of conceptual models of the near-wall structure were put forth to explain the observed behavior. Willmarth and Tu (1967) used space-time correlations between the wall pressure and all three velocity components near the wall to devise a model for the average eddy structure of the near-wall region. The model proposes three-dimensional vortex lines in a hairpin shape (similar to Theodorsen, 1952), with the dominant element being vortices with a streamwise component.

Bakewell and Lumley (1967) combined an eigenfunction decomposition of near-wall u' measurements with a mixing length approximation to extract a dominant average near-wall eddy structure in the form of counter-rotating vortices with purely streamwise orientation. This result was consistent with Kline et al’s conclusion that streamwise vorticity was necessary for the formation and outward migration of low-speed streaks.

A concept by Lighthill (1963) was invoked by Kline et al (1967) to explain the formation of the sublayer streaky structure. In this idea, any fluctuating velocity normal to the wall stretches (for wallward movement) or buckles (for outward movement) the near-wall spanwise vorticity lines. Since the spanwise vorticity is due mainly to $\partial u / \partial y$, this stretching and compressing would lead to spanwise variation in the near-wall value of u . Kline et al also drew on Stuart’s (1965) vortex-stretching concepts from transition work to explain the formation of intense local shear layers above lifted low-speed elements, which are a precursor to the oscillation and breakdown phases of bursting. A diagram of an initially spanwise vortex line being lifted and stretched into a loop concludes the paper. In contrast to most other vortex-line models, which reflected an average eddy structure, Kline et al’s concepts were intended to apply to the instantaneous flow field, and to show evolution of the structure.

Tritton’s (1967) two-point correlation measurements in a boundary layer ex-

tended the work of Grant (1958) and challenged any then-existing model of the large-eddy structure. Tritton went against the grain of contemporary research by concluding that the inner and outer region eddies do not require separate description and that coherent eruptions from the wall region are unlikely.

2.4 THE CONDITIONAL SAMPLING ERA (1972-1983)

Although conditional sampling of hot-wire signals had been employed by Kovaszny et al, Narahari Rao et al, and others, the availability in the early 1970's of inexpensive digital laboratory computers completely changed the nature of turbulence structure research. 1972 is arbitrarily chosen for the beginning of this era because, although analog techniques still prevailed, it was the year that quadrant-splitting of the $u'v'$ signal came into use, triggering a community-wide concentration (and perhaps preoccupation with) conditional sampling methods.

During this time period, the literature grew first to impressive, then to overwhelming proportions, giving rise to a number of reviews of the issues involved with coherent structures in turbulent boundary layers. The most significant are Willmarth (1975a), Laufer (1975), Hinze (1975), Saffman (1978), Cantwell (1981), and Laufer (1983).

In addition, proceedings from workshops at Lehigh University (Smith and Abbott, 1978) and at Ohio State (The Delta Conferences; Brodkey, Wallace, and Lewalle, 1984) recorded the state of the knowledge, the controversies, and the needs at their respective moments in history.

2.4.1 Near-Wall Region

Wallace, Eckelmann, and Brodkey (1972) introduced the quadrant-splitting technique, which allowed the motions responsible for the Reynolds shear stress, $-\overline{u'v'}$, to be sorted into categories that reflect their physical character. The four quadrants of the instantaneous $u'v'$ hodograph plane were labeled outward interaction, ejection, inward interaction, and sweep, as shown in Fig. 5.1. The ejection and sweep classifications were meant to correspond to the near-wall turbulence-producing events observed visually by Kline et al, Corino and Brodkey, and Grass. Wallace et al found that ejection and sweeps motions dominated throughout the boundary layer (as they must, for $\overline{u'v'}$ to be negative.) For $y^+ < 15$, the Reynolds shear stress was due mostly to sweep motions, while for $y^+ > 15$, ejections dominated. The first and third quadrants contribute negatively to the Reynolds stress, but were found to be scarcer, weaker, and smaller relative to sweeps and ejections.

At about the same time, Willmarth and Lu (1972), extended by Lu and Willmarth (1973), utilized an improved quadrant technique with an amplitude threshold to make a detailed assesment of the Reynolds stress-producing motions in boundary layers up to $Re_\theta = 38000$. The results confirmed Wallace et al's finding that quadrant 2 (ejection) motions are the largest contributors to $\overline{u'v'}$ outside the edge

of the sublayer, and supported Kim et al's (1971) conclusion that virtually all of the net Reynolds stress in the near-wall region was produced during bursting. Although most violent in the buffer zone, ejection motions were observed throughout the boundary layer, suggesting that ejected fluid from the near-wall region travels to the outer edge of the layer, as speculated by Kim et al, Kovasznay et al, and Grass.

Willmarth and Lu found ejections to be intermittent, intense, small-scale, and containing appreciable streamwise vorticity. These characteristics are consistent with the passage of a propagating coherent disturbance, such as the hairpin vorticity line model proposed by Willmarth and Tu (1967). Willmarth and Lu suggested that near-wall hairpin vortices may evolve to a larger scale, producing the intermittent bulges in the outer edge of the boundary layer and providing an outward interaction mechanism between the inner and outer regions.

Smith and Metzler (1983) examined the statistical characteristics of low-speed streaks in boundary layers for Re_θ between 740 and 5830. They concluded that the mean spanwise spacing of $\lambda^+ = 100$ in the sublayer is essentially Reynolds number invariant. A streamwise-elongated hairpin vortex structure with counter-rotating legs was proposed as the cause of streak formation and persistence, in support of many other vortex-loop models.

2.4.2 Outer Flow, Large Eddies, and Entrainment

In an extension of the Kovasznay et al (1970) work, Blackwelder and Kovasznay (1972) employed conditional sampling and space-time correlations of $u'v'$ hot-wire probes to further map the character of the large-scale motions (LSMs) associated with bulges in the outer turbulent/non-turbulent interface of the boundary layer. Their results show that there is a large-scale rotation in the direction of the mean shear within a conditionally averaged bulge, and that the large eddies have long lifetimes and carry nearly all of the turbulence energy and Reynolds stress in the outer (intermittent) region. Blackwelder and Kovasznay's basic picture of the outer large-scale motion was successively refined in complementary studies by Falco (1977), Brown and Thomas (1977), and Chen and Blackwelder (1978).

Hedley and Keffer (1974) compared the upstream and downstream edges of the outer region turbulent bulges in a boundary layer with hot-wires and conditional sampling techniques. They found that the upstream interface (back) of the large-scale motion is well-defined, with sharp velocity gradients, but the downstream side is diffuse and poorly-defined. These results were interpreted as high-speed, non-turbulent fluid sweeping over the back of the bulge, straining the interface and creating sharp interfacial gradients. The faster fluid sees the slower bulge as an obstacle which leaves a diffuse wake on the downstream side of the bulge.

Large-scale outer motions in the boundary layer were further investigated by Falco (1977), who used simultaneous flow visualization and hot-wire studies to in-

fer a two-dimensional (x-y plane) structural picture for the large-scale motions and their upstream boundaries (“backs”). The backs of the LSM’s were shown to possess a quasi-stagnation point when viewed from a downstream-convecting reference frame. Falco also described smaller, Reynolds number-dependent ring-shaped vortices which formed on the backs of the large-scale motions.

Bevilaqua and Lykoudis (1977) proposed a physical explanation of entrainment in free turbulent flows, in which enfolding of nonturbulent fluid by the rotational motion of the large eddies within the interface bulges draws new fluid into the turbulent region. Townsend (1979) found experimental evidence for his inclined “attached roller eddy” model for boundary layers (see Townsend, 1976), though the conditionally-sampled data were insufficient to distinguish whether the eddies should occur singly or in pairs.

Concern that most turbulence structure investigations were being performed at low Reynolds numbers led Murlis, Tsai, and Bradshaw (1982) to examine the behavior of boundary layers over a range of Reynolds numbers. They concluded that at Reynolds numbers above $Re_\theta = 5000$, the overall shape of the turbulent/non-turbulent interface is determined by the large-scale eddies of the outer region, and not by viscosity-dependent superlayer eddies.

2.4.3 Inner/Outer Interaction

During this era, a strong interest developed in the relationships, if any, between the outer region coherent motions characterized by Kovasznay et al, and the near-wall production processes described by Kline et al, Corino and Brodkey, and Grass. The Ohio State group blazed the trail with detailed descriptions of flow-visualization studies in 2-D (Nychas, Hershey, and Brodkey, 1973), and later in 3-D (Praturi and Brodkey, 1978).

Nychas et al (1973) described large-scale transverse vortices (of both rotational signs) that appeared to roll up at the shear-layer interface of high and low-speed fluid in the outer boundary layer. These vortices were suggested to be the cause of the outer interface bulges described by Blackwelder and Kovasznay, and others. In addition, a close spatial association was observed between the passage of transverse vortices and the occurrence of near-wall ejections of low-speed fluid. Outer-region transverse vortices were therefore suggested to be the key structural element which connects the near-wall activity with the outer-flow large eddies.

These views were basically confirmed and greatly extended in stereo visualizations of the three-dimensional boundary layer structure by Praturi and Brodkey (1978). These results showed inflows of free-stream potential fluid (entrainment) in the vicinity of the large outer-flow transverse vortices. Contrary to the earlier speculations of several groups, it was stated by Praturi and Brodkey that outer-interface bulges are not caused by “super-ejections” of fluid from the near-wall region, but instead by the transverse vortical motions. Near-wall streamwise vortex

motions were also observed, which were suggested to be formed in an interaction between high-speed outer fluid and low-speed ejections from the wall zone. This idea was in contrast to the popular concept of near-wall ejections arising from pre-existing streamwise vortices. Although the components of hairpin or horseshoe vortical structures were present, no complete vortical structure was observed (or could have been expected to be observed given the experimental technique.) Praturi and Brodkey summarized the Ohio State observations in a cyclic conceptual picture of boundary layer turbulence and the inner/outer region interaction mechanisms.

Wallward motions of various types (sweeps, intrushes, inflows) had been observed and/or quantified by Corino and Brodkey, Grass, Wallace et al, and Willmarth and Lu in the late 1960's and early 1970's. Since the earlier Stanford techniques did not show the wallward motions, Offen and Kline (1974) used improved visualization methods to investigate the relationships between the bursting process and the outer-flow motions. The results suggested that ejections from the near-wall region are triggered by wallward disturbances from the outer flow, but that the fluid is actually drawn away from the wall by near-wall vortices, rather than ejected by forcing from other motions. This picture was similar to that of the Ohio State group, in that vortices are involved with ejections, which in turn are responsible for the majority of Reynolds stress production. However, the Stanford vortices were generally streamwise and were observed in the near-wall region while Ohio State vortices were transverse and found in the outer flow. Both groups suggested that the vortices arise as the result of a local shear-layer instability at a low/high-speed fluid interface. Offen and Kline further suggested that a pairing interaction of vortices sometimes leads to new wallward flow (thus restarting the cycle) and also to the creation of large-scale motions in the outer region.

By the mid-seventies, two camps had developed on the question of inner/outer region interaction. One felt that the near-wall bursting process and associated vortices self-generated subsequent near-wall activity and gave birth to the motions that eventually were convected to the outer region. The other camp believed that large-scale outer region motions triggered the violent near-wall turbulence production events. Repik and Sosedko (1980), in a little-known paper, attempted to settle the argument by two-point space-time correlations of filtered u' hot-wire signals. The results supported Offen and Kline's (1974) conclusion that near-wall events are primarily associated with previous near-wall events, rather than with large-scale outer-flow motions, as was proposed by Praturi and Brodkey (1978).

Brown and Thomas (1977) addressed the issue of inner/outer causality quantitatively, although through two-dimensional measurements, with a y-rake of u' hot-wires and a wall-mounted shear-stress gage. The results gave a picture of the large-scale motion in the boundary layer, which included bulges in the outer interface, large-scale rotational motion in the x-y plane, and a sloping "back" of the large

structure which was formed by the high/low-speed fluid interface at the upstream side of the large eddy. This picture of the outer-motion structure was in essential agreement with those of Blackwelder and Kovasznay (1972) and Falco (1977). Brown and Thomas found that the passage of these large-scale outer eddies were in phase with intermittent periods of large, high-frequency fluctuations in the wall shear which, in turn, were presumed to reflect the occurrence of bursting. A model of the outer/near-wall interaction and streamwise vortex formation based upon a local Görtler instability was proposed, similar to the Görtler model proposed by Cantwell, Coles, and Demotakis (1978) for turbulent spots.

Using heat-tagging conditional sampling techniques, Chen and Blackwelder (1978) provided further details concerning the backs of the large-scale outer eddies as a possible dynamical link between the outer and inner coherent motions. The backs were confirmed to be shear-layer interfaces of low-speed fluid followed by high-speed fluid, and were commonly found to extend from the outer region into the near-wall region, where their passage was related to the occurrence of “bursting.” However, bursting in this study was assumed to be detected by the VITA criterion, which was later shown to have a non-unique association with near-wall regions of high turbulence production. (See discussion of Bogard and Tiederman’s results in Sec. 2.5.1.)

Rajagopalan and Antonia’s (1979) two-point correlations between a wall-shear probe and a traversing u' hot-wire supported the concept of a large (spanning much of the boundary layer) coherent structure at an angle to the wall. The angle was found to be 13° in the outer flow, and much smaller near the wall. This compares reasonably for the outer-region angle of 18° by Brown and Thomas (1977). The convection speed of the wall-shear stress fluctuations was $0.62U_e$ for duct Reynolds numbers above $R_d = 35000$.

Until the late seventies, most investigations of the instantaneous character of the outer large-scale motions had been confined to the x-y plane of view. Falco (1980a) extended the knowledge to include the x-z plane, employing simultaneous side and plan-view visualizations of the large-scale motions. He reported that the LSM’s exhibit a highly three-dimensional character, with inflows of free-stream fluid passing over and around the slower bulges, creating high-speed wallward motions at the side of the LSM’s. Since the “lateral inflows” were seen to reach deep into the boundary layer, Falco’s observations of the three-dimensionality of entrainment served to expand Nychas et al’s 2-D picture of the possible influence on the near-wall structure by outer motions.

The technique of simultaneous flow visualization and hot-wire anemometry was further refined by the Michigan State group and was used to study the near-wall region (Falco, 1980b), as well as the interactions between the near-wall and the LSM’s (Falco, 1983). The results suggested that the large-scale outer motions affect,

but do not govern the near-wall production processes. A comprehensive conceptual model of the boundary layer turbulence production cycle was outlined in Falco (1983), which involved ring-like vortices that scale on the wall variables, ejections, sweeps, “pockets” of sublayer fluid free of marker, near-wall streamwise vortices, hairpin vortices, and streaky structures. Most of these features were theorized to be associated with the movement of the ring-like vortices and the pocket wall region disturbances.

Nakagawa and Nezu (1981) employed $u'v'$ quadrant-splitting and space-time correlation techniques to the data from two $u'v'$ hot-film probes to examine length and timescales of sweeps (quadrant 4 motions) and ejections (quadrant 2 motions) in open channel flow. The most significant conclusion of the work was that the bursting motion (sweep following ejection with a sloping interface between) retains its coherence for several boundary-layer thicknesses as it convects downstream. This view of the bursting processes as quasi-frozen turbulence was in sharp contrast to the generally-accepted view that the turbulence production processes resemble localized explosions, which are highly intermittent in both space and time. Nakagawa and Nezu summarized their observations and inferences in a qualitative model which is essentially similar to that of Praturi and Brodkey (1978), except for inclusion of spanwise scales and interactions. The Nakagawa and Nezu model is a schematic of the spatial relationships between the various components of the bursting process, rather than a dynamic model explaining causes and effects.

2.4.4 Vortical Structures and Models

By the mid-1970's the belief that vortical motion was at the heart of turbulence production events was nearly consensual, and the loop-like or horseshoe vortex model, with both streamwise and spanwise components, was the most popular concept. For example, Offen and Kline (1975) attempted to synthesize most of the known visual features of near-wall boundary layer structure with a lifted and stretched vortex which was basically the same as the models of Theodorsen (1952), Willmarth and Tu (1967), Kline et al (1967), and Black (1968).

In a review of boundary layer structure concepts, Hinze (1975) also attempted to relate the known coherent elements of near-wall turbulence production to the dynamics of horseshoe-shaped vortices. In his scenario, Hinze suggests that fluid lifted between the legs of the vortex loop undergoes a local shear-layer instability, which then violently breaks down (bursts) into a “blob of fluid of high turbulence intensity,” apparently destroying the parent vortex structure in the process. Wall-ward inrush motions were suggested to be initiated by the tip of the vortex loop on its downstream side, and later aided by pressure waves created during the sudden vortex/shear-layer breakdown.

A common element of the vortex loop models was the existence of counter-rotating vortices along the legs, with their principal axes in the streamwise direc-

tion. A relationship between low-speed streak/ejection structures near the wall and vortices with a major streamwise component had been discussed early on by several investigators, including Kline et al (1967), Bakewell and Lumley (1967), and Willmarth and Lu (1972). These results spawned a number of experimental studies of streamwise rotation in the near-wall region.

Utilizing conditionally averaged streamwise vorticity measurements near the wall of an oil channel, Kastrinakis et al (1978) found evidence of small, intense streamwise vortices alongside ejections of low-speed fluid. This work was extended by Blackwelder and Eckelmann (1979), who summarized their measurements in a model of the ensemble averaged near-wall structure. The model consisted of an elongated side-by-side pair of counter-rotating streamwise vortices, which pump low-speed fluid away from the wall, forming a low-speed streak and an instantaneously inflectional streamwise velocity profile.

Kreplin and Eckelmann (1979) interpreted their near-wall two-point correlation measurements as evidence for sloping discontinuities in u' . These “fronts” were hypothesized to be associated with sloping streamwise vortices with centers at $y^+ > 30$. The fronts, or near-wall shear layers reached from the wall to at least $y^+ = 50$. At the wall, they formed an angle with the wall of about 4.7° , which increased to about 10° at $y^+ = 50$. The existence of a sloping structure near the wall echoed similar findings in the outer region by Brown and Thomas (1977), Chen and Blackwelder (1978), and others.

Direct visual evidence of instantaneous streamwise vortical motion in the near-wall region was provided by Smith and Schwartz (1983). In end-views of spanwise bubble-lines, rotational motion was observed, frequently in counter-rotating pairs, and generally beside upwellings of low-speed fluid. The centers of these vortices occurred in the buffer region. Though not full confirmation, these results supported the hypothesis that low-speed streaks were caused by streamwise vortices in the near-wall region.

One of the most extensive and influential publications on the existence of loop-shaped vortical structures in turbulent boundary layers was that of Head and Bandyopadhyay (1981). These authors’ flow-visualization results in boundary layers over a broad Reynolds number range ($500 < Re_\theta < 17500$) provided images of hairpin-shaped structures virtually filling the boundary layer. Head and Bandyopadhyay interpreted the looped shapes visible in the smoke as evidence of vortical structures. At high Reynolds numbers, the loops were elongated and hairpin-shaped, forming a characteristic angle of 45° with the wall. Large-scale structures were observed to consist of agglomerations of hairpins. At low Re_θ , the loops were observed to be less elongated, and more horseshoe-like, and the large-scale features were composed of just one or two horseshoes. Although quantitative evidence of the dominance of hairpin/horseshoe vortices is still lacking, Head and Bandyopadhyay’s work has

motivated a number of attempts at "structural" models for canonical boundary layers.

Head and Bandopadhyay's work helped to inspire Perry and Chong's (1982) analysis of a model for the mechanism of wall-bounded turbulence. In this model, the boundary layer is represented by a forest of potential-flow Λ -shaped vortices, which were introduced as a candidate form for Townsend's (1976) "attached-eddy" hypothesis. Biot-Savart calculations of a geometrical hierarchy of such vortices gave promising reproductions of the mean profile, Reynolds shear-stress, turbulence intensities, and spectra for a turbulent boundary layer, lending further credibility to the idea of vortical loops as the dynamically dominant boundary layer structure.

Wallace (1982; updated in 1985) reviewed and collected the quantitative experimental evidence for hairpin vortices in boundary layers. To explain the birth of the vortex loops, Wallace invokes the Navier-Stokes equations at the wall, which show that local wall-pressure gradients are equivalent to an outward diffusion of vorticity from the wall. Although the equations predict the generation of strongly kinked vorticity lines near the wall, the concept is not necessarily applicable to the formation of true vortices, which can be quite distinct from vorticity lines. This issue will be taken up at length in Section 9.2.2.

2.4.5 Wall-Pressure Studies

Because of the importance of aircraft cabin noise and undersea vehicle sound generation, fluctuating wall-pressure studies during this era remained the aspect of turbulence structure investigation with the closest link to practical application.

A large body of wall-pressure measurements were taken even before 1972, and the significant results published up until 1974 were reviewed by one of the key contributors in Willmarth (1975b). In brief, the data at that time indicated that wall-pressure fluctuations were fairly intermittent, roughly circular in shape (more so for the smaller scales), and possessed a mean propagation velocity of $0.56U_e$ to $0.83U_e$, with large-scale disturbances extending further from the wall, and hence travelling faster than small scale ones. (In most of the studies, transducer size limitations affected the ability to measure the contribution of small-scale, high-amplitude pressure fluctuations.) Bradshaw (1967) proposed that "active" (Reynolds stress-producing) motions in the near-wall region were responsible for the small-scale (or high-frequency to a wall-mounted transducer) wall-pressure fluctuations, and large-scale wall-pressure pulses were due to inactive motions in the outer regions.

In a spectacular wind tunnel experiment, Emmerling et al (1973) (see also Dinkelacker et al, 1977) hand-reduced optical fringe patterns obtained from an interferometry technique applied to a slightly flexible wall membrane beneath a turbulent boundary layer. The results gave the instantaneous wall pressure at 650 simultaneous points, for many frames of a high-speed movie. These data confirmed the roundish, non-elongated shape of the pressure pulses, and provided propagation

velocities and downstream travel distances for a variety of wall-pressure disturbance scales.

Burton (1974) employed simultaneous measurements of fluctuating wall pressure, wall-shear stress, and streamwise velocity at $y^+ = 15$ or 30 , all at the same x -location. The results indicated that most large wall-pressure fluctuations originate outside the sublayer, that neither ejections nor sweeps are well-correlated with wall-pressure pulses, but that local retardations of sublayer fluid (and its subsequent ejection) are associated with large instantaneous adverse pressure gradients.

Schewe (1983) demonstrated that transducer diameters of $d^+ < 20$ are necessary to accurately detect the high-amplitude, small-scale peaks in the wall-pressure signal. Schewe's results showed the wall-pressure signal to be intermittent and significantly non-Gaussian, with events of $p' \geq 3p_{rms}$ contributing 40% of the r.m.s. pressure in 1% of the time. High-amplitude pressure events were observed to grow and decay much more rapidly than those with lower amplitudes. The high-amplitude events resembled high-frequency wave-trains, with a mean streamwise peak-to-peak distance of 145 viscous units and a mean convection velocity of $11.9u_\tau (= 0.53U_e)$. This velocity corresponds to the mean velocity in the buffer region, leading to speculation by Schewe and others that the high-amplitude wall-pressure events are related to the intermittent production of turbulence at the edge of the sublayer.

Thomas and Bull (1983), in a combined extension of previous efforts (Brown and Thomas, 1977; Bull, 1967), studied the relationships between wall-pressure fluctuations, wall-shear fluctuations, near-wall shear layers, and the "burst-sweep" cycle in the buffer region. (Note that the bursting process by this time was widely believed to include a slightly wallward, high-speed "sweep" following a low-speed ejection. This view had evolved largely from the combined conclusions of the early Stanford and Ohio State studies.) Thomas and Bull show that characteristic high-pressure regions associated with the burst-sweep cycle are due to the passage of inclined shear layers which occur on the upstream side of the bursting process and which may traverse most of the boundary layer. In direct disagreement with Burton's (1974) conclusions, Thomas and Bull find that fluid lifting from a low-speed wall streak is subjected to a **favorable** instantaneous streamwise pressure gradient. However, the authors conclude that streamwise pressure gradients of either sign do not play an active role in the near-wall turbulence production process. Side-view diagrams are included to describe the phase relationships between large-scale outer-motions and their inclined backs, near-wall bursting activity, and fluctuations in wall-shear stress and wall pressure.

Despite the many studies preceding and during this era that provided statistical and instantaneous information concerning wall-pressure fluctuations, the Thomas and Bull results provided the only extensive and quantitative evidence concerning a

kinematical relationship between the turbulence generation processes and the wall-pressure fluctuations.

2.4.6 Conditional Sampling Studies

Conditional sampling techniques became an almost universal analysis tool during this era of turbulence structure research (see Antonia's 1981 review). In addition to the many interpretive results based upon conditionally sampled probe data, a new breed of papers surfaced in which the character of the sampling schemes themselves took precedence over the education of turbulence physics. Much of this work was fueled by the controversy of the unknown scaling parameters for the frequency of "bursts" detected by a stationary probe. This question was in turn motivated by the unresolved issue of whether near-wall events dominated a self-regenerative cycle of near-wall turbulence generation, or if the production processes were instead triggered by the passage of outer-flow motions.

One of the seeds for this new breed of studies was a paper by Blackwelder and Kaplan (1976). In this work, a conditional sampling scheme previously introduced by Gupta, Laufer, and Kaplan (1971) was employed to detect the passage of especially energetic flow events with z - and y -rakes of u' hot-wires. The VITA (Variable-Interval Time-Average) method was shown to detect sloping near-wall structures that consisted of a low/high-speed discontinuity in the streamwise velocity, similar to the near-wall shear layers observed by Kim et al (1967) and by Corino and Brodkey (1969). This structure was found to be associated with occurrence of sharp spikes in $u'v'$ at $y^+ = 15$, and was thus hypothesized to be related to the bursting process. The frequency of occurrence of the VITA event scaled with outer variables (δ and U_e).

Many other conditional sampling techniques emerged with the proliferation of affordable laboratory digital computers during this era. An example is a modification of the already-discussed $u'v'$ quadrant-splitting technique. Wallace, Brodkey, and Eckelmann (1977) defined quadrant motions using a streamwise perturbation velocity relative to a local, or "floating" average. Pattern recognition of the resulting fluctuating velocity signals provided the criteria for detection of the near-wall turbulence-producing events. Though applied extensively by its authors, the additional free variables introduced into the detection process by the pattern recognition apparently discouraged its widespread use.

Following the Blackwelder and Kaplan paper, the VITA technique was employed in numerous investigations, of which Johansson and Alfredsson (1982) and Blackwelder and Haritonidis (1983) may be considered representative. All of the results shared to some degree the problem of an unclear and/or inconsistent meaning of the term "bursting." As defined by Kim et al (1971), bursting refers to a process which consists of three visually-identified and not easily separable flow characteristics. Thus, attempts to detect the occurrence of this complex, evolving, multi-stage

process in 1-D or 2-D data from a stationary probe naturally tend to produce inconclusive results, if the objective is to learn about the specific processes of near-wall turbulence production. Many papers make a crucial and often undiscussed assumption that the detection criteria employed has a strong association with some aspect of the dynamics of turbulence generation. Undoubtedly one major factor in the confusion over the meaning of “bursting” is that it is defined differently in Kline et al (1967) from the process definition in Kim et al (1971) (see Sec. 12.1.1).

Although conditional sampling studies have provided a mass of detailed statistics, the gross three-dimensional and temporal features of the responsible flow modules and events are in most cases unknown. As a result, the question of “burst-frequency” scaling, as well as that of the inner/outer causal direction, remains essentially unresolved, especially over a significant Reynolds number range.

A review of conditional sampling and ensemble-averaging techniques for turbulent flows is provided by Antonia (1981).

2.4.7 Summary of 1972-1983 Era

Most of what is known today (1989) about the structure of turbulent boundary layers had already been established by the end of 1983. The key points of qualitative consensus at the end of this era can be summarized as follows:

- The sublayer is not laminar, and the buffer region is not transitional in the laminar-to-turbulent sense.
- The sublayer, buffer region, and outer region (log and wake) each have coherent motions with different structural characteristics.
- The sublayer consists of elongated, unsteady regions of high- and low-speed streamwise velocity.
- The thin, near-wall buffer region is the most important zone of the boundary layer in terms of turbulence energy production and dissipation. Buffer region activity is characterized by a bursting process, during which low-speed fluid (provided in the form of streaks) is flung outward from the wall, generating most of the turbulence production in the boundary layer. A “burst” was pictured as a sweep of high-speed fluid upstream of a low-speed ejection, with a sloping shear-layer interface between.
- Both outward ejections of low-speed fluid and slightly wallward sweeps of high-speed fluid occur intermittently in the wall region ($y^+ < 100$) and are the major contributors to the Reynolds shear stress.
- Thin shear layers (with $\partial u'/\partial x$ and $\partial u'/\partial y$) exist throughout the boundary layer at interfaces between upstream high-speed fluid and downstream low-speed fluid. These shear layers are highly sloped with the outer portion downstream ($12 - 18^\circ$), with a shallower slope near the wall ($2 - 4^\circ$).
- The intermittent region of the boundary layer is dominated by large-scale motions (also called entrainment eddies) which exist beneath bulges in the outer

interface. These bulges are three-dimensional (δ -scale in both x and z), and are accompanied by well-defined upstream “backs,” slow rotational motion in the direction of the mean strain, and deep crevasses of high-speed potential fluid around the edges.

- Entrainment of potential fluid occurs in valleys in the turbulent/non-turbulent interface that exist at the edges of bulges.
- Transverse vortices exist in the outer (log and wake) region.
- Streamwise vortices with a slight upward tilt exist in the wall region ($y^+ < 100$).
- Instantaneous wall-pressure patterns are rounded, not elongated, and contain regions of high-amplitude, high-frequency fluctuations. Internal near-wall shear layers are associated with high-pressure regions on the wall beneath them.
- Loop-shaped vortical structures (horseshoes, hairpins, Λ -eddies) probably exist and play some role in the dynamics of turbulence production, but spatial and evolutionary details as well as statistical relevance is unclear.

Despite the progress made in thirty years, many major issues remained unsatisfactorily resolved at the end of 1983, including:

- Dynamical role and importance of loop-shaped vortices in boundary layer turbulence.
- Dominant orientation and topological form of vortices (loops, rings, streamwise, transverse).
- Cause of large-scale bulges in the outer interface.
- Causal direction of inner/outer interactions. This is the issue that drives the questions of Reynolds number effects and scaling laws for the bursting process.
- Dynamical details of the interactions between the near-wall bursting process and the outer-region large-scale motions.
- Role, evolution, and formation mechanisms for internal shear layers. (Should they be considered as active elements of structure, or as passive neighbors to the active zones?).
- Transverse relationships between structural elements. (Most information obtained in two-dimensional experiments).
- Origin, dynamical role, and spatial character of $(u'v')_4$ motions.
- Cause/effect relationship between the bursting process and wall-pressure fluctuations.
- Streamwise extent of streamwise vortices and their dynamical relationship to the near-wall streaky structure.
- Existence and statistical relevance of counter-rotating pairs of streamwise vortices.
- Formation and persistence mechanisms for low-speed wall streaks.

- **Instantaneous** three-dimensional spatio-temporal relationships between the structural elements. (Compare instantaneous mechanisms to ensemble-averaged measurements).

2.5 THE COMPUTER SIMULATION ERA (1984-present)

The development of computer-generated turbulence has had a gradual, yet irreversible impact on the field of turbulence structure experimentation. Although large-eddy simulations (LES) had been available throughout the 1970's, it wasn't until almost 1980 that numerically-simulated turbulence began to be probed in depth for answers to the questions that had eluded the experimentalists for several decades. As structural features of the 3-D pressure, vorticity, and velocity fields emerged from the numerical databases, the experimental community found its focus shifting away from ad-hoc digital conditional sampling schemes to pursuit of deeper physical understanding of the three-dimensional coherent motions. Today, the simulations function as both complement and competition to experiments and are inexorably moving the laboratory community beyond the low Reynolds number flat-plate boundary layer.

The year 1984 was chosen (somewhat arbitrarily) as the mid-point of the period over which experimental emphasis shifted from conditional-sampling studies to more complex investigations that were either directly inspired by or subtly influenced by the presence of numerically-simulated turbulence.

2.5.1 Near-Wall Region

One of the experimental approaches to return to vogue during this era is combined flow-visualization and anemometry. Although the methods have been employed over the years by several groups (notably Michigan State, Lehigh, and Stanford), its recent new popularity has led to a number of significant advances in the state of the knowledge.

Talmon, Kunen, and Ooms (1986) utilized simultaneous flow visualization and two-component laser-Doppler anemometry to investigate the contributions of visually-identified near-wall events to the Reynolds shear stress, $-\overline{u'v'}$. High correlation was achieved between observed ejections and measured second-quadrant $u'v'$ events. In addition, visual analysis allowed Talmon et al to group clustered quadrant 2 detections into single bursts, thus quantitatively differentiating between ejection events and bursts. Note, however, that this grouping of ejections into bursts introduces yet another definition of the term "bursting," altering its meaning from a three-stage process to a cluster of ejections. (The evolution of the term and its various interpretations are further discussed in Chapter 12.)

In similar, more extensive work, the Purdue group used combined visualization and hot-film anemometry to study the spatial and temporal characteristics of near-wall ejections, as well as to evaluate the performance of many single-point "burst-

detection” conditional sampling techniques. (The conditional-sampling papers are discussed in Section 2.5.6). Bogard and Tiederman (1987) employed phase-aligned ensemble-averages and found that bursts (defined as grouped ejections) are responsible for 80% of the quadrant 2 contribution to $-\overline{u'v'}$ in the buffer region. Ejections were confirmed to be packets of low-speed fluid with concentrated regions of outward ($+v'$) velocity, and consequently $(u'v')_2$, near their downstream edges. For multiple-ejection bursts, the farthest downstream ejection of the group tended to be the strongest. Bogard and Tiederman’s results confirmed, clarified, and added quantitative information to the early visual descriptions bursting by Kline et al (1967) and Kim et al (1971).

After the initial flurry of use of the VITA conditional-sampling technique to detect “bursts,” it was generally accepted that VITA (as usually applied) actually triggers on steep local streamwise gradients in the instantaneous streamwise velocity, which is what Blackwelder and Kaplan (1976) had shown in their original paper. Thereafter, VITA was used profitably to study the nature of sloping internal shear layers near the wall, the existence of which had been noted by nearly every research group that has investigated near-wall turbulence structure.

Johansson, Alfredsson, and Eckelmann (1987a) used VITA with two-probe measurements in the buffer region of a channel flow to confirm that near-wall shear layers form at the upstream boundary of a lifting low-speed streak. The shear layers were found to extend approximately $100\Delta x^+$, and to travel at least $500\Delta x^+$ at a speed of $13u_\tau$. Randolph, Eckelmann, and Nychas (1987) studied the same near-wall shear layer structures in the same facility, but renamed them sweeps, following Corino and Brodkey’s (1969) description of a relatively high-speed “front” moving in from upstream to sweep the viewing area of turbulence production events. Randolph et al’s results show that instantaneous values of $\partial u / \partial y$ in the buffer region can reach -0.7 to 1.7 times the mean velocity gradient at the wall.

2.5.2 Outer Flow, Large Eddies, and Entrainment

Antonia, Browne, and Bisset (1989) summarized and extended several of their own investigations of the large-scale motion in the boundary layer, and its Reynolds number dependence (e.g. Antonia, 1972; Antonia et al, 1982). Using space-time correlations of the data from an 8-sensor y-rake of $u'v'$ hot-wires, Antonia et al concluded that the large-scale, outer-region motions display Reynolds number effects only for $Re_\theta < 5000$. The large-scale motions were suggested to contribute from one quarter to one third of the Reynolds shear stress, but only a small fraction of v'_{rms} in the outer region for $Re_\theta < 10000$. Quasi-instantaneous and conditional streamlines, spanwise vorticity contours, and strain-rate contours in the $x - y$ plane show large-scale roller-eddies (or agglomerations of them) with sloping backs, separated by about 2.5δ in the streamwise direction. Although two-dimensional, the results are consistent with the concept of hairpin vortices extending to a wide range

of distances from the wall.

To extend the question of outer-region turbulence structure universality to compressible boundary layers at high Reynolds numbers, Robinson (1986) and Spina and Smits (1987) employed multi-sensor hot-wire probes in Mach 3 turbulent boundary layers. Using two-point space-time correlations as well as VITA detections, Robinson found large, sloping disturbances spanning most of the supersonic boundary layer, at similar angles to those found in low-speed experiments (e.g. Chen and Blackwelder, 1978; Brown and Thomas, 1977). Robinson also found that the y -extent of the intermittent region is apparently Mach number dependent, occupying less of the boundary layer for higher Mach numbers. Spina and Smits also concluded that the large, sloping structures are relatively unaffected by compressibility, but the slope of the disturbances was found (using different techniques from Robinson's) to be approximately 45° for most of the boundary layer. Spina and Smits related the sloping disturbances to Head and Bandyopadhyay-like hairpin vortices, rather than to high/low-speed streamwise interfaces, as did Robinson.

2.5.3 Inner/Outer Interaction

Most turbulence structure experiments have been performed at very low (< 5000) momentum-thickness Reynolds numbers. Since transport fuselage Reynolds numbers (for example) can reach $Re_\theta = 80000$, practical-minded critics have repeatedly raised the question of whether low-Reynolds number laboratory results are representative of the physics at higher, more practical Reynolds numbers. Accordingly, increasing attention has been paid to the effects of Reynolds number on structure measurements. (Although many of the papers in this section address the issue of "burst", or VITA-event scaling, the present study will not attempt to resolve the Reynolds number question, so related discussion is minimal).

Andreopoulos et al (1984) found that ensemble averages of VITA detections (rapid u' accelerations) in a near-wall ($y^+ < 50$) hot-wire signal were essentially similar over a range $3000 \leq Re_\theta \leq 15000$. Robinson (1986) extended this finding to $Re_\theta = 35000$, and Narasimha and Kailas (1987) reached similar conclusions outside the wall region of an atmospheric boundary layer ($Re_\theta \approx 1.3 \times 10^8$). Antonia et al (1989) investigated the character of the large-scale outer motions for $1300 \leq Re_\theta \leq 9600$, as discussed above. Wei and Willmarth (1987) obtained high spatial resolution Laser Doppler Anemometer (LDA) measurements in the near-wall region of fully developed channel flows for $3000 \leq Re_{d/2} \leq 40000$, or approximately $420 \leq Re_\theta \leq 5600$. Wei and Willmarth's profiles of u' and v' statistics in the near-wall region did not scale with inner variables (u_τ and ν), apparently due to streamwise stretching of the near-wall vorticity field and to cross-contamination by eddies from the opposite wall of the channel. The Wei and Willmarth paper includes an excellent review of the inner-region scaling controversy, which will not be expanded upon here. The issue of Reynolds number dependence of coherent motions is by no means closed,

and progress in this direction will be exclusively experimental for some time to come.

In any study of Reynolds number effects on turbulence structure and statistics, Spalart's (1988) advice is well-considered: "... one must differentiate between Reynolds number effects and low-Reynolds number effects."

2.5.4 Vortical Structures and Models

VORTEX LOOPS

By 1984, many forms of vortex models had been proposed, and, although most were based on loop-shaped structures, there remained significant controversy concerning their role, dynamical evolution, and contribution to turbulence production and dissipation. In particular, the role of hairpin vortices in the near-wall bursting sequence and in low-speed streak generation remained unclear. The issue has resisted resolution mainly because actual hairpin or horseshoe vortices are very difficult to detect as a structure either by visual means or with fixed Eulerian probes. Head and Bandyopadhyay's (1981) results provided the clearest evidence as to the existence of hairpin vortices in a boundary layer, but the details of formation, growth, destruction, and dynamical contribution remained obscure.

Working from the many vortex models in the literature as well as from his own extensive visualization studies, Smith (1984) described the broadest conceptual model yet proposed for hairpin-shaped vortices in the wall region ($y^+ < 100$). The model describes the kinematics and dynamics of hairpin vortices and their relations to low-speed streaks, the bursting process, near-wall shear layers, ejections, and sweeps. Smith proposes that the "bursting" of a low-speed streak is the visual and probe signature of vortex roll-up (one or a packet) in the unstable shear layer formed on the top and sides of the streak. Once formed, a vortex loop moves outward by self-induction and downstream due to the streamwise velocity gradient. The trailing legs of the loop remain in the near-wall region but are stretched, forming counter-rotating quasi-streamwise vortices which serve to pump fluid away from the wall (ejection) and to accumulate low-speed fluid between the legs, thus perpetuating the low-speed streak. (The implication is that streamwise vortices are not required to have length-scales as long as the streaks.) The streamwise array of vortices which comprises a burst then grows outward and may agglomerate into large-scale rotational outer-region bulges.

Although the elements of Smith's model can be traced to the previous literature, (especially Theodorsen, Willmarth and Tu, Offen and Kline, Wallace, and Hinze), his model is the most complete in its relationship to the stages of the bursting process and in its explanation for streak length and longevity. (The conceptual models of Smith as well as others are considered further in Section 11.3).

Acarlar and Smith (1987a,b) continued their investigation of hairpin vortex dynamics with a pair of papers in which vortices were generated in a laminar bound-

ary layer by shedding from a wall-mounted hemisphere or by rollup on an artificial low-speed streak at the wall. The results support the concept of three-dimensional vortex formation through the rollup of an unstable shear layer wrapped over the top and sides of a low-speed streak. Low-speed regions were observed to lift, oscillate, and break into small-scale motions during the passage of a hairpin vortex.

Perry, Henbest, and Chong (1986) extended both the attached-eddy hypothesis of Townsend (1976) and the Λ -vortex model of Perry and Chong (1982) to include the entire turbulent boundary layer rather than just the wall (log) region. The updated Perry et al model for wall turbulence is based upon the existence of hierarchies of attached coherent eddies. The first hierarchy of attached eddies forms at the outer edge of the sublayer, then stretch and grow with a fixed orientation to the wall (e.g. 45° for hairpin vortices). Eddies that do not die through viscous diffusion or vorticity cancellation merge to form eddies of a larger length scale, which comprise the second hierarchy. This continual process creates a "hierarchy of geometrically similar hierarchies" of attached eddies, which are responsible for the mean vorticity, Reynolds shear stress, and most of the energy-containing motions.

Perry et al propose that the attached eddies are immersed in a soup of detached isotropic small-scale motions which are responsible for the Kolmogoroff spectral region and most of the turbulent energy dissipation. Thus, in the model, energy is extracted from the mean flow by coherent motions and dissipated into heat by incoherent, small-scale motions. The model involves energy flow to low wave numbers through eddy-merging, and energy flow to high wave numbers through the unattached, dissipative motions. Interestingly, the assumptions involved in Perry et al's model lead to a logarithmic law of the wall, a constant Reynolds shear stress region, and an inverse power law u' spectrum near the wall for a variety of attached eddy shapes and distributions. This indifference of the statistics to the topology of the eddy structure tends to de-focus the attention being paid to the exact form of coherent eddy structure dominant in the boundary layer.

An example of the advantages of modern digital image-processing techniques as applied to coherent structure research is the work of Utami and Ueno (1987). These authors used successive pictures of particles in $x-z$ cross-sections at several y -values to obtain instantaneous distributions in the $x-z$ plane of the three components of velocity and vorticity, and of various associated spatial statistics. (This work has probably come the closest to producing experimental data approaching the detail provided by direct numerical simulations.) The results were interpreted by the authors with vortical structures in mind, and a Smith-like horseshoe vortex model is proposed which exhibits causal relationships to low- and high-speed streaks, ejections and sweeps (quadrant 2 and 4 $u'v'$ motions, respectively), longitudinal vortices, and internal shear layers.

STREAMWISE VORTICES

In the region near the wall where the production and dissipation of turbulence kinetic energy peak ($y^+ \approx 15$), flow-visualization studies (e.g. Smith and Schwartz, 1983) had shown that vortical motions are common, and are generally streamwise, or quasi-streamwise (ie, with an upward tilt of 5 to 20 degrees). This fact motivated several additional investigations of streamwise vortices in the near-wall region during this era. Though many of the papers are based on theory rather than directly upon experimental data, laboratory observations of streamwise vortices were the basis for all of the studies.

Pearson and Abernathy (1984) modelled an idealized infinite streamwise vortex embedded in a linear, unbounded shear flow, and showed that even a weak streamwise vortex can generate strongly inflectional streamwise velocity profiles. This result raises the question of spanwise shear-flow instabilities in the vicinity of streamwise vortices, which is further explored with the numerically-simulated boundary layer in the present study.

Ersoy and Walker (1986) considered the influence of a symmetric pair of counter-rotating streamwise vortices on the viscous flow near a wall. In their numerical results, the vortex pair induces an adverse pressure gradient near the wall which gives rise to rapidly-growing local recirculating flow regions. This effect was suggested to be related to the near-wall bursting process and to a Görtler instability process.

Jang, Benney, and Gran (1986) proposed a mechanism for the formation of streamwise vortices in the near-wall region with a spanwise wavelength of 90 viscous lengths, similar to the known mean spanwise streak spacing of $\lambda^+ = 100$. Jang et al found that a “direct resonance” (in which a three-dimensional disturbance initially arising from an algebraic instability) is intrinsically associated with the mean velocity profile of a turbulent boundary layer. Integral to this resonance is a mean secondary flow in the form of side-by-side streamwise vortices. Jang et al’s approach does not assume a Görtler-like instability as the cause of the vortex structures.

Further insight into the statistical contributions and mean spatial character of quasi-streamwise vortices in the wall region was provided by Herzog’s (1986) proper orthogonal decomposition of his two-point space-time correlation tensor measurements for $1.25 \leq y^+ \leq 40$ in a turbulent pipe flow. Similar to Bakewell and Lumley’s (1967) results, but using a more extensive experimental dataset, Herzog found that the dominant eigenmode of the decomposed correlation tensor took the mean form of a pair of counter-rotating vortices 60 viscous lengths apart, 40 viscous lengths from the wall on average, tilted 5° up from the wall, and which were responsible for 50% to 90% of the Reynolds stress and kinetic energy near the wall. Herzog pointed out that the centerlines of the slightly tilted streamwise vortices are not vorticity

lines. Instead, if the mean velocity profile is superimposed on the streamwise vortex, the resulting vorticity lines resemble horseshoe shapes when viewed from upstream.

In a experiment reminiscent of Smith and Schwartz (1983), Kasagi, Hirata, and Nishino (1986) used downstream end-views of hydrogen bubble tracers released at $5 \leq y^+ \leq 75$ to observe streamwise rotations. The mean diameter of the streamwise vortical motions was about 40 viscous lengths, and their centers occurred at $25 \leq y^+ \leq 30$. These results were used to create a simple model of streamwise vortex motions, which was able to reproduce the known velocity and Reynolds shear stress statistics in the near-wall ($y^+ < 30$) region.

Swearingen and Blackwelder (1987) studied the growth and breakdown of counter-rotating streamwise Görtler vortices on a concave wall, as a model for similar vortices in the near-wall region of flat-plate turbulent boundary layers. The results confirm that streamwise vortices in a wall-bounded shear layer generates inflectional velocity profiles in both the normal and spanwise directions, as well as elongated low-speed streaks. The significant conclusion of Swearingen and Blackwelder was that the local shear layers set up by streamwise vortices were most unstable along the sides, rather than on the top of the low-speed streak.

A more complete review of vortical structures in turbulent boundary layers is given in Chapter 11.

2.5.5 Wall-Pressure Studies

Most of the wall-pressure experiments since 1984 have involved ensemble averages of fluctuating wall-pressure conditioned on velocity-event detections in the buffer region, for the purpose of relating wall pressure patterns to the near-wall turbulence production process. The relationship is not expected to be straightforward, since the pressure is related through a Poisson equation to the volume integral of the entire velocity field. However, since the pressure field is a spatially-integrated quantity, it may serve to connect events in the buffer region to those at the wall.

Experiments preceding 1984 had established the approximate spatial shape of wall pressure fluctuations (e.g. Willmarth, 1975b; Emmerling, 1973) and their scale-dependent propagation velocities (e.g. Willmarth and Woolridge, 1962; Bull, 1967). In addition, an association between positive wall-pressure peaks and near-wall interfaces between high and low-speed regions had been identified by Burton (1974), Thomas and Bull (1983), Dinkelacker and Langeheineken (1983), and others. This latter relationship received still more attention during this era, since the passage of the high/low streamwise velocity interface is what triggers the VITA detection technique (Alfredsson and Alfredsson, 1984).

Kobashi and Ichijo (1986) measured u' and v' at several y -locations above a 2-D array of wall-mounted dynamic pressure transducers. These authors found that VITA detections in the u' signal at $y^+ = 25$ corresponded to a distinctive ensemble-averaged pressure footprint at the wall, with a high pressure region directly be-

low the detection point extending approximately 50 viscous lengths to either side. Kobashi and Ichijo interpreted their correlation and conditional sampling results as evidence for a completely unique vortex ring model of the coherent motions in a turbulent boundary layer.

Using a similar experimental setup as Kobashi and Ichijo, the team of Johansson, Her, and Haritonidis (1987c) also investigated the relationship between buffer layer VITA detections and wall-pressure fluctuations in both a turbulent boundary layer and a turbulent spot in transitional flow. In both cases, Johansson et al found a bi-directional relationship between high wall-pressure peaks and buffer-layer VITA detections (which correspond to internal shear layers), meaning the two events are not just associated, but uniquely related to each other. A weaker association between large negative wall-pressure peaks and local high-speed (sweep-like) motions in the buffer region was found.

In another study similar to those just mentioned, Dinkelacker and Sieber (1987) confirmed and extended the previous work of Dinkelacker and Langeheineken (1983) with a traversing hot-wire and a wall-mounted pressure transducer in turbulent pipe flow. Results indicated that the large-scale flow structures related to VITA detections in the outer layer (and thus to positive wall-pressure peaks) persist for at least 13 pipe diameters downstream.

2.5.6 Conditional Sampling Studies

Since 1984, the VITA and $u'v'$ quadrant techniques have remained the favorite techniques for detecting the occurrence (or passage) of coherent structures with fixed probes. Fortunately, much of the research emphasis during this era has been on relating conditional averages to physical processes of known existence and importance, such as the near-wall bursting sequence and its associated ejections, sweeps, and near-wall shear layers. Considerable attention has also been paid to the still controversial question of scaling for detected near-wall events (often called, sometimes accurately, the “bursting frequency”).

Alfredsson and Johansson (1984) compared the VITA and $u'v'$ quadrant techniques and discovered a close correspondence between VITA detections and $(u'v')_2$ (ejection) motions in the buffer region of a turbulent channel flow. These authors proposed mixed inner/outer scaling for the rate of VITA detections near the wall, implying an interaction between outer and near-wall coherent motions. Alfredsson and Johansson did not discuss the possibility that VITA events ($+/-u'$ interfaces) may occur in conjunction with a variety of types of coherent motion that need not be related.

In the mid-1980's, the issue of detection techniques and their relationships to physical events in the boundary layer was investigated with welcome thoroughness by the Purdue research group. Bogard and Tiederman (1986) compared the VITA, $u'v'$ quadrant, TPAV, U -level, and Positive slope algorithms with simultaneous

flow visualizations to evaluate the effectiveness of single-probe methods for detecting turbulence-producing events near the wall. All of the methods were found to be strongly dependent upon their respective free parameters, resulting in a wide variation in the mean frequency of event detection. After all of the techniques had been “tuned up” to minimize false detections, the $u'v'$ quadrant technique of Wallace et al (1972) was found to have the greatest reliability for detecting visually-identifiable ejections from the buffer region. Bogard and Tiederman also redefined a burst as one or more ejections from a single low-speed streak. Ejections were grouped into bursts by Barlow and Johnston’s (1985) method, using the probability distribution of time between ejections. (Grouped ejections were also defined as bursts by Talmon et al, 1986.) Luchik and Tiederman (1987) followed up on Bogard’s work, using the various “tuned” detection algorithms to measure the average time between ejections and bursts.

2.6 SUMMARY OF EXPERIMENTAL HISTORY

Coherent motions in turbulent boundary layers have turned out to be quite easy (in fact almost unavoidable) to detect, but nearly impossible to satisfactorily characterize by experimental means. This is not surprising. If we define coherent motions as those which possess significant correlation in three-dimensional space for a time span longer than that of the smallest eddies, it is unlikely that one (or even several) fixed probes could accurately educe the essence of any complex three-dimensional structure. The result has been a dependence upon statistical detection techniques with poorly understood behavior. These “structure” detection algorithms provide ensemble averages and correlations which can sometimes be as misleading as they are enlightening.

Flow visualization methods offer much higher information density for a given area or volume, but are susceptible to varying degrees of embedded history in the marker patterns, making visual conclusions at least partially ambiguous. Although flow-visualization techniques can be made quantitative (e.g. image-processing of particle or bubble displacements), this has been successful so far only in two-dimensional planes of turbulent flows.

Probe resolution problems and wind tunnel economics have limited nearly all turbulence structure experiments to low Reynolds numbers. As a result, the nature of coherent motions at “flight” Reynolds numbers, and the role structures play in turbulence energy transport dynamics remains poorly understood.

These experimental limitations are the reasons why, despite nearly universal agreement on the dominant importance of coherent vortex structures, so little solid information on the shape, strength, and dynamical behavior of vortices in boundary layers is available. Instead, we have a considerable number of both qualitative and quantitative bits of information concerning low-speed streaks, ejections, sweeps,

wall-pressure patterns, and outer-flow large eddies, but connections between these items are in most cases obscure. In particular, the magnitude and even the direction of influence between the inner and outer regions is still unclear.

After 50 years of experimental research, the overwhelming need for vastly more detailed information at many space points in turbulent flows has finally been met (at least for low Reynolds numbers) by the development of supercomputers and numerically simulated turbulence. The relatively brief history of coherent structure research via numerical simulations is covered in the next chapter.

CHAPTER 3 - HISTORY OF TURBULENCE STRUCTURE IN NUMERICAL SIMULATIONS

3.1 BACKGROUND

Computer simulation of wall-bounded turbulent flows has been underway for twenty years, and the cumulative results from the relatively few numerical investigations has created a modern renaissance in turbulence knowledge. Two approaches to turbulent simulation have been utilized in the investigation of turbulent structure: Large-Eddy Simulation and Direct Numerical Simulation.

In Large-Eddy Simulation (LES), the small scales of the flow are modelled while the remaining scales are computed directly with the three-dimensional, time-dependent Navier-Stokes equations, which are averaged over the small scales. This approach is based upon the observation that the small scales in turbulent flows are nearly universal, while the turbulent behavior at larger scales is a strong function of the flow geometry and gross flow parameters.

Direct Numerical Simulation (DNS) dispenses with the subgrid-scale model at the expense of greatly increased computational cost in order to accurately resolve the turbulent motions at **all** relevant scales.

Both simulation methods require state-of-the-art supercomputers for reasonable runtimes. Computational resource requirements for turbulence simulations are given in Reynolds (1989). Current equipment is now enabling course-grid LES solutions for simplified engineering applications, but DNS solutions are still limited to low Reynolds number research flows with simple geometries.

The LES technique for wall-bounded flows was pioneered by Deardorff (1970), who computed a fully-developed turbulent channel flow at high Reynolds number by modeling the entire near-wall (sublayer, buffer, and logarithmic) region. This approach was extended for the channel flow case by Schumann (1975) and Grotzbach (1978).

The methods, results, and key references for Large-Eddy Simulation of wall-bounded turbulence are discussed in a review by Rogallo and Moin (1984).

3.2 STRUCTURE IN LARGE-EDDY SIMULATIONS

Early LES researchers were initially concerned with accurate reproduction of the mean and turbulence statistical profiles. As the method matured and the results showed good agreement with experiments, interest in the nature of instantaneous fields grew. The first look at the instantaneous flow-field of a numerically-simulated channel flow was by Grotzbach (1978), who produced a movie of the instantaneous wall pressure fluctuations from his LES solution. The LES wall pressure field was found to strongly resemble experimental results (Willmarth and Woolridge, 1975;

Emmerling, 1973), both in the rounded, non-elongated shapes of the pressure contours and in the size-dependent convection velocities of the disturbances. In the first large-eddy simulation that extended to the wall, Moin et al (1978) found the well-known streaky pattern in the near-wall u' -field of their simulated channel flow.

Kim and Moin (1979) published the first extensive investigation into the structural features of simulated wall-layer turbulence, using an LES channel flow solution. Kim and Moin demonstrated the streaky nature of the near-wall streamwise velocity field, the spatially intermittent character of the $u'v'$ regions, and near-wall transfer of energy from the vertical to the transverse velocity components through “splatting” of wallward fluid against the wall. All of these features were in good qualitative agreement with established experimental results, demonstrating the value of numerical simulations as a tool for turbulence physics research. Of particular importance was Kim and Moin’s observation that the contours of streamwise vorticity did not exhibit a streamwise elongation as did the contours of streamwise velocity. This result brought into question the notion of a one-to-one correspondence between near-wall low-speed streaks and streamwise vortices, as proposed in, for example, Blackwelder and Eckelmann (1979).

The NASA/Stanford LES channel flow simulations were summarized in Moin and Kim (1982), and utilized extensively during the following three years for various structural investigations. Although the grid resolution of this simulation was inadequate to resolve the near-wall features at their correct scales, the overall qualitative results showed good agreement with most confirmed experimental findings.

Moin and Kim (1982) pointed out that instantaneously high wall-pressure regions in the LES solution often occurred in regions of wallward, high-speed flow. This correlation was described by the authors as evidence for “quasi-stagnation” regions (possibly identical to the “pockets” of Falco, 1983) which form upon the impact of high-speed fluid on a portion of the low-speed wall layer. This hypothesis was consistent with the experimental findings of Burton (1974), Dinkelacker and Langeheineken (1982) and others, which showed high wall-pressure beneath the interface formed between high- and low-speed elements of near-wall fluid. In the same paper, Moin and Kim included stills from a computer-generated movie which simulated flow-visualization experiments with hydrogen bubble time-lines. The resulting images are strikingly similar to the experiments of H.T Kim et al (1971), displaying low-speed streaks, ejections, inflectional velocity profiles, and streamwise vortices.

Kim (1983) was the first to apply conditional sampling/ensemble-averaging techniques to Large-Eddy Simulation results. Kim employed a variant of Blackwelder and Kaplan’s (1976) VITA detection scheme to obtain conditional averages of the velocity, pressure, shear-stress, and vorticity fields in the near-wall region of the LES channel flow. In agreement with experiments, Kim found that near-wall

VITA events consist of sloping interfaces of high-speed “sweeping” fluid following low-speed fluid, with a high-pressure peak (which is nearly vertical rather than inclined) accompanying the interface. Near the wall, the pressure peak precedes the velocity interface, imposing a local adverse pressure gradient on the near-wall fluid, which Kim (as well as Offen and Kline, 1975 and Nychas et al, 1973) postulated as the cause of outward ejection of near-wall fluid. Using the conditionally-averaged vorticity fields, Kim suggested that the streamwise vorticity born of the “splat” of a wallward sweep on the wall becomes a pair of tilted streamwise vortices with considerably shorter streamwise extent than the low-speed streaks. This scenario is largely consistent with Falco’s (1982) description of near-wall formation of “pockets” and their associated streamwise vortices.

Kim (1985) extended his conditional-sampling study of the LES channel flow with streamlines and velocity vectors plotted in the average flow-fields surrounding a VITA event detection in the buffer region. These results showed the high-speed fluid flowing both overtop (creating the sloping interface or shear layer) and around the sides of a narrow low-speed region.

It should be noted that the spanwise-symmetrical character of Kim’s and all other conditional averages from single-point detections are an unavoidable artifact of the spanwise homogeneity of the flow and of the averaging method. Thus, such ensemble averages are not able to prove or disprove the simultaneous, side-by-side occurrence of streamwise vortices or other structures.

In further exploitation of the LES channel flow database, Moin (1984) reported on the structure of the vorticity field and also on the application of a proper orthogonal decomposition analysis to the simulated turbulence. With histograms of the vorticity vector inclination angle ($\alpha = \tan^{-1}(\omega_y/\omega_x)$) and instantaneous planar plots of the vorticity vectors, Moin showed that vorticity lines are most likely to be inclined at 45 degrees to the wall in the outer region of the flow. This implies the existence of organized vortical structures in the flow which are able to take advantage of the 45 degree orientation of the principal axes of the mean strain-rate tensor. It is along these 45 degree axes that vorticity production due to mean-gradient stretching is maximized in the channel flow.

Moin’s (1984) application of Lumley’s (1981) “characteristic eddy” decomposition in $y - z$ cross-flow planes of the LES data identified idealized organized structures that made significant contributions to the turbulence energy and production. The two-dimensional LES eddy pattern was similar to that of Bakewell and Lumley’s (1967) eigenfunction decomposition of experimental pipe-flow data.

The most influential structural investigation of the Ames LES channel flow was reported in a pair of papers by Moin and Kim. Beginning with Theodorsen (1952), many theoretical and conceptual models promoting hairpin vortices as the fundamental element of turbulence had been proposed, but experimental evidence

was sparse and mostly circumstantial. Thus, the objective of Moin and Kim's research was to locate, identify, and characterize hairpin vortices in the simulated turbulent channel flow.

In the first of the two papers, Moin and Kim (1985) analyzed the vorticity field, employing vorticity vector angle histograms (as in Moin, 1984), two-point vorticity correlations, and vorticity line tracing in individual flow-fields. A hairpin vortex was defined as "an agglomeration of vortex lines in a compact region (with higher vorticity than the neighboring points) that has a hairpin or horseshoe shape." (A definition of this form can be utilized only by numerical simulation researchers, who have complete access to the three-dimensional vorticity vector field.)

In their results, Moin and Kim showed that for the outer region of the flow, the vorticity vectors tend to be inclined at about 45 degrees to the wall. Two-point velocity and vorticity correlations in the 45 and 135 degree planes also provided evidence for 45 degree vortical structures. These data provided evidence only for single, inclined vortical structures, with unknown connection to hairpins themselves. To investigate the three-dimensional nature of the vortical structures, instantaneous vorticity lines (everywhere parallel to the vorticity vector) were traced through the flow, and were commonly found in horseshoe shapes, though usually asymmetric in shape. The horseshoe-shaped vorticity lines appeared to coalesce from deformed vortex sheets, and generally did not exhibit elongated streamwise legs. From these results, Moin and Kim concluded that 45 degree, hairpin-shaped **vortices** are statistically relevant features of turbulent channel flow structure.

In the follow-on paper, Kim and Moin (1986) applied variants of the VITA and $u'v'$ quadrant-splitting technique to detect turbulence-producing events in the LES channel flow. Although the objective was to isolate the structures associated with the near-wall bursting process, the detection points were placed in the outer regions of the flow to avoid triggering by near-wall sweep motions. Detection heights were varied ($y^+ = 100, 200, 300$) to investigate the effect of detection-point location on the ensemble-averaged structures. The resulting conditionally-averaged fields were then visualized by vorticity line tracing. The results exhibited horseshoe-shaped vortex lines in both the conditionally averaged and selected instantaneous fields. The bunched instantaneous vorticity line structures were taken to be true vortices (with pronounced circular motion about the axis). Upright horseshoe-shaped vorticity lines were found to be associated with ejection ($u'v'_2$) motions, while inverted horseshoes were found in conjunction with sweep ($u'v'_4$) motions. Since the horseshoe vortex structures were detected well away from the wall, it was argued that horseshoe vortices are a result of only vortex stretching, and thus may be characteristic of all turbulent shear flows, whether or not there is a wall. Streamwise vortices were rarely found, and were generally of limited ($\Delta x^+ < 100$) streamwise extent, in agreement with Kim's (1983) earlier conclusions from the

same data. The major results of this paper were also confirmed in a new direct simulation without a subgrid model.

The two Moin and Kim papers (1985 and 1986) provide the first quantitative evidence for the existence of 45 degree vortical structures, and for the existence of hairpin-shaped vorticity lines. At the same time, the papers also raised a provocative issue: when do vorticity lines equal vortices? Although some streamwise vorticity line agglomerations were demonstrated to be true vortices in an appendix to Kim and Moin (1986), a distinction between the shapes of vortex lines and the existence of actual vortices is difficult to make consistently. This is due mainly to lack of a rigorous, unambiguous definition for a vortex, in contrast to the clear, mathematical definition of a vorticity line.

Vorticity line tracing must be employed carefully, as the results can be misleading in a variety of ways. For instance, as shown by Kim and Moin (1986), an inclined hairpin vorticity line is a kinematic necessity for a region of fluid with limited spanwise extent moving across the gradient in a shear layer. A parcel of low-speed fluid moving outward into higher-speed fluid (ejection) necessarily produces an upright hairpin vorticity line with the tip inclined downstream. A high-speed region moving downward into low-speed flow (sweep) must produce an inverted hairpin vorticity line. In neither case is a true vortex necessarily present, nor can causality for the motion be assigned to the vorticity line. Furthermore, a streamwise or quasi-streamwise vortex in a shear flow gives rise to both upright and inverted hairpin vorticity lines which do not coincide with the driving vortex (see Figs. 9.5 and 9.6). These issues are examples of problems which have gained increased importance with the availability of numerical simulations, and will be taken up in depth in Chapter 9.

3.3 STRUCTURE IN DIRECT SIMULATIONS

In order to observe the temporal evolution of an ejection and its associated vorticity field in a cleaner environment than full turbulence, Kim (1987) simulated a laminar boundary layer with a single embedded vortical structure as the initial condition. The initial disturbance field was that of an ensemble averaged $u'v'$ second-quadrant (ejection) motion obtained from a detection point at $y^+ = 100$ in a DNS channel flow. Being a single-point conditional average, the initial field was necessarily symmetrical about its centerline x - y plane. By definition (see Chapter 9), the vorticity lines of the initial disturbance formed upright horseshoe shapes, but did not constitute an actual vortex in the sense of circular instantaneous streamlines (see vortex definition in Section 9.1).

Kim described the evolution of the initial disturbance in the simulated laminar boundary layer in terms of self-induction and stretching of the vorticity lines. As the disturbance moved downstream, the vorticity line loops lifted outward due to self

induction effects and the legs were stretched into a nearly streamwise orientation by the ambient velocity gradient. (Note that the lifting of the disturbance could also be thought of as the continuing outward velocity of the initial ejection disturbance field.) The resulting disturbance was visualized as a hairpin-shaped bundle of vorticity lines with an upright head and elongated legs. Significantly, this structure exhibited the character of a true vortex, as evidenced by a core of low pressure and concentrated vorticity in the head and neck regions. Thus, Kim's result suggest that vorticity production by vorticity line stretching is sufficient in this case to create a vortex through agglomeration of vorticity lines, apparently without requiring a shear-layer instability. Maximum contribution to $-u'v'$ occurred just below and upstream of the head, with somewhat lesser contributions on the upward-rotating sides of the necks and legs.

Also evident in Kim's results was the formation of a secondary concentration of spanwise vorticity upstream of the head of the mature vortex loop, above the legs. This structure was consistent with Smith's (1984) concept of hairpin vortex regeneration, although Smith described the process as the rollup of a local instability whereas Kim attributed the secondary structure to vorticity line stretching alone.

Although hairpin/horseshoe vortices dominate the conceptual models available for turbulent boundary layer coherent motions, Falco's (1977, 1982) vortex ring concept provides an alternative view of the eddy structures. Although the process has not been observed in turbulence, Falco postulates that rings may be formed by "pinch-off" of hairpin vortices. In fact, the mature vortical structures in the simulations of Moin and Kim (1985) and of Kim (1987) commonly exhibit a Ω shape in the tip region of the hairpin, suggesting subsequent possible pinch-off into a ring. Moin, Leonard, and Kim (1986) (following early analysis by Hama, 1962) investigated mechanisms for vortex ring formation using direct numerical simulation. The results showed that a perturbed vortex sheet in shear evolves into a hairpin-shaped structure of concentrated vorticity. The hairpin vortex in Moin et al's results suggested eventual pinch-off into a vortex ring, although the computation was not carried that far.

An overview of the contemporary state of the art in numerical turbulence structure research was given by Moin (1987). For the DNS channel flow, Moin observed that, unlike the u' field near the wall, the v' and w' contours do not show significant streamwise elongation and that the regions of large v' tend to occur in side-by-side inward/outward pairs, suggesting streamwise vortices. These vortices were found to occur most commonly singly, not in pairs, in contrast to conditionally averaged results from both experiments (e.g. Guezennec, 1985; Herzog, 1986) and simulations (Kim, 1983; Moin, 1984). The streamwise vortices were only 100 to 200 viscous units long, but retained their coherence while travelling several channel half-widths downstream. Moin reported regions of high $u'v'$ adjacent to every observed stream-

wise vortex in the wall region, and concluded that relatively short, single vortices are the fundamental structures associated with regions of high turbulence production.

Moin also demonstrated the horseshoe shape of vorticity lines in the vicinity of ejections (upright horseshoes) and sweeps (inverted horseshoes). It bears repeating that horseshoe-shaped vorticity lines are a kinematic consequence of any local region with wall-normal velocity occurring in a shear flow. Moin noted that some of the hairpin vortices in the channel flow possessed only one leg, which is consistent with the observation of isolated streamwise vortices in the wall region.

The first direct Navier-Stokes simulations of turbulent boundary layers were performed by Spalart and Leonard (1985), and improved by Spalart (1986). Spalart (1986) provided extensive analysis of the statistical character of simulated boundary layers at momentum-thickness Reynolds numbers of 300, 670, and 1410. Although “structural” analysis of the simulated flow was limited, Spalart included instantaneous 2-D contours of vorticity magnitude in several planes for $Re_\theta = 300$ and 1410. In qualitative agreement with experimental visualizations, these plots exhibited large-scale bulges in the outer turbulent/non-turbulent interface, punctuated by deep irrotational valleys. Spalart’s simulation database forms the basis of the research discussed in this report, and will be described further in Chapter 6.

The long-standing controversy over the “bursting frequency” was taken up by Kim and Spalart (1987), who utilized Spalart’s (1986) boundary layer simulation at $Re_\theta = 300, 670$, and 1410. Following Luchik and Tiederman (1987), Kim and Spalart defined a burst as a regional group of ejection ($u'v'_2$) motions in the $y^+ = 12$ plane. The results showed that both the number of bursts per unit area in the x - z plane and the mean distance between bursts scaled best with inner units (ν, u_τ) over the range of very low Reynolds numbers available in the simulation.

Kim, Moin, and Moser (1987) published an extensive compilation of turbulence statistics in a DNS channel flow at a half-width Reynolds number of 3300. To confirm the physical realism of the simulation, several structural features were shown to compare well with experimental findings. For instance, two-point correlations of streamwise velocity were consistent with a near-wall streaky structure possessing a mean spanwise spacing of approximately 100 viscous lengths. Spanwise correlations of v' suggested the existence of streamwise vortex structures with diameters of approximately 25 viscous lengths. Particle visualization simulations also resembled experimental results, exhibiting vortical motions and near-wall pockets (Falco, 1980b) of swept-out fluid.

Moin, Adrian, and Kim (1987) employed a single-point linear stochastic estimation technique to characterize the flow structures associated with large contributions to the Reynolds shear stress in the DNS channel flow. The results revealed counter-rotating streamwise vortices with an upward tilt. The flow angles of the conditional events were found to increase significantly in the buffer region, implying

a transition from nearly streamwise vortex “legs” to more upright vortex “necks” as y^+ increases (see Chap. 9, Fig. 9.4).

In an effort to make the simulation databases available to turbulence structure experimentalists, the NASA/Stanford Center for Turbulence Research conducted month-long summer programs in 1987 and 1988. During these short time periods, a number of significant advances in turbulence structure knowledge were made by the visiting researchers conducting “experiments” in the “numerical wind tunnels” created on the Ames supercomputers. Although the results are too numerous to cite here, many will be referred to within the body of this report (see Kim, 1987; Alfredsson et al, 1988 for references).

As part of a comprehensive review of turbulence structure knowledge, Robinson, Kline, and Spalart (1989) analyzed Spalart’s (1986) $Re_\theta = 670$ boundary layer simulation to identify all known coherent structures in the simulation and to describe their spatial relationships with each other. Vortices were identified by their low-pressure cores, and were found to be involved with almost all significant coherent motions in the boundary layer. These results will all be described in detail within the current paper.

3.4 SUMMARY OF SIMULATION HISTORY

Turbulence simulations are the most computer-intensive (and therefore costly) of CFD applications. However, the return on investment has been good, considering that all of the NASA Ames work described above has derived from just one series of large-eddy simulation and two series of direct Navier-Stokes simulations.

Most of the experimentally-known aspects of turbulent wall-layer structure have been confirmed in the numerical simulations. In addition, simulations have enabled a number of clarifications of key structural features. For instance, the notion of the sublayer consisting of a bed of extremely long streamwise vortices with interlying low and high-speed streaks has now been replaced with the more probable view of relatively short streamwise vortices being “dragged” through the near-wall flow, leaving streaks behind. This concept has led to new interpretations of the bursting process, in which relatively long-lived near-wall vortices, rather than violent instabilities, cause eruptions of near-wall fluid. Also, it is now clear that spanwise-symmetric structures such as counter-rotating vortices are as likely to be an artifact of single-point conditional averaging procedures as of the turbulence. The simulations show that the common mode is for near-wall streamwise vortices to occur singly, not in pairs (although pairs do occur); single near-wall quasi-streamwise vortices are responsible for much of the momentum transfer in the near-wall region of the low Reynolds number boundary layer. All of these points are investigated in Chapters 9, 10, and 12.

New difficulties with analysis techniques have also surfaced with the arrival of numerical turbulence. In particular, vorticity line tracing has proved both useful

and misleading for identifying vortices in the turbulence. This issue will be discussed in depth in Section 9.2.

Many of the largest mysteries regarding coherent structures in turbulent boundary layers remain unanswered (see Sections 2.4.7 and 4.2), and so we must consider the potential of the simulations as far from fully exploited. It is rather surprising that even with turbulence databases that must contain the answers to virtually all of our low Reynolds number structure questions, we still have so much to learn about our subject. One reason for our apparently slow progress is the almost overwhelming volume and complexity of information represented by a database of instantaneous velocity vectors at several million grid points. Since complete quantitative access to turbulent flow-fields has not been available before the advent of numerical simulation, the tools that have been applied to analyzing their coherent structures have generally been extensions of established experimental approaches, such as single-point conditional sampling and two-point correlations. Now that turbulence can be considered “captive,” new ways to interrogate the four-dimensional database may be developed and utilized to further our understanding. A significant fraction of the current work focuses upon the development and application of such tools.

CHAPTER 4 - DISCUSSION, OBJECTIVES, AND STRATEGY

The purpose of this Chapter is to summarize the historical background presented in Chapters 2 and 3, and to recapitulate the objectives of the current study from the perspective of the many years of preceding work. This Chapter will also discuss the strategy developed for the detailed analysis of the numerically simulated turbulent boundary layer.

4.1 Comments on Historical Review

The complexity of turbulence is well illustrated by the fact that so many important issues remain unresolved after such a long and active history of research into boundary layer physics. Causes for the lack of understanding may be grouped for clarity into three areas: (1) measurement and analysis limitations; (2) research focus; (3) communication of results. These problems are well-known to workers in the field, but are listed here to clarify the motivations for mounting yet another research project (the current one).

4.1.1 Measurement and Analysis Limitations

Experimental measurement techniques have provided only limited information about three-dimensional vortex structures, which are now generally considered the most important of the turbulent boundary layer coherent motions.

As every experimentalist knows, flow visualization techniques can be susceptible to “history” effects in the visualized flow-patterns. That is, patterns discernible in the fluid marker may be due to events which occurred some time previous, but are no longer active. The problem is highly non-linear, in that the amount of history in a given image is dependent upon the history of activity in the particular mass of fluid being visualized. Some visual methods (such as the combined time-streak hydrogen bubble method of Schraub et al, 1966) avoid this qualitative problem by utilizing only the spatial displacement between images obtained at slightly different times to estimate the instantaneous velocity.

Probe measurements, though quantitative, rarely provide multi-component data with a sufficient spatial density to educe a clear picture of complex three-dimensional structures. This is particularly true where velocity derivatives are required, as for the vorticity field. In the case of vortex structures, detection is difficult even given the complete velocity fields from numerical simulations.

The use of conditional sampling has quantified the nature of certain repeating events in turbulence, but the results are often difficult to relate to causal physics for several reasons. All probe-based detection methods involve independent variables which must be chosen by the researcher. In most cases, the detection results are dependent upon the values of these parameters, resulting in some ambiguity in the meaning of the data.

The u' VITA detection scheme has been used by many researchers as a detector for turbulence-producing “bursts,” but VITA actually triggers on a rapid acceleration in the streamwise velocity, which occurs with the convection of an internal shear layer structure (with locally high $\partial u/\partial x$) past the fixed probe. While the bursting process originates in the buffer region (by definition), VITA detections occur throughout the boundary layer. VITA detections in the outer region have occasionally led to conclusions that the bursting process either occurs everywhere, or that ejected fluid from the near-wall region commonly traverses the layer. Interpretation of VITA-detected shear-layer passage as “bursts” has also led to a significant amount of confusion over the correct scaling for the “bursting frequency.” Most of these points are now common knowledge, but the burst scaling controversy is still not universally settled.

The use of averaged statistics is necessary to produce a description of turbulence which is less complex than turbulence itself. However, the details that are discarded during the averaging process carry an unknown amount of information which may be important for physical understanding. For example, in two-point correlation curves, it is often forgotten that the only useful information is gained from non-zero correlation, or from well-defined zero-crossings of the correlation coefficient line. A low correlation coefficient value between two variables may reflect phase or position jitter just as well as a true lack of interdependence between the variables. This point is also true for conditional averages, where nearly zero values do not necessarily denote the limit of the extent of the responsible structure in space or time, but instead simply a dominating variation in individual realizations (jitter).

The resemblance of conditional averages to instantaneous realizations depend upon the detection criteria, the averaging method, and the case-to-case variation in realizations. Event-centering techniques have been successfully employed in several studies to minimize this problem (e.g. Alfredsson et al, 1988). A common example is the appearance of spanwise-symmetric, counter-rotating streamwise vortices in conditionally-averaged near-wall data. The symmetry is a necessary result of single-point detection techniques in a spanwise-homogeneous flow. Instantaneous visualizations show that single vortices are at least as common as pairs.

4.1.2 Research Focus

As mentioned in Section 1.2, one of the motivations for the “big picture” approach taken in the current project is to integrate the many discrete bits of boundary-layer structure knowledge into a comprehensive model.

The underlying reason for the current fragmented state of the knowledge is clearly the fundamental complexity of the subject itself. The problem is too large for any one effort to tackle whole, so research projects must be focussed upon specific sub-issues. This necessity sometimes generates false controversy between results that seem inconsistent only because of differences in their approach and focus. An

example is the difference in published views concerning vortex elements between the Ohio State and Stanford groups in the early 1970's. Praturi and Brodkey (1978) focussed upon the outer region and observed mainly transverse vortices as the dominant vortical structure in the production of Reynolds stresses. Kim et al (1971) cited streamwise vortices as the dominant visible vortical motion, but they employed techniques which emphasized the near-wall region. It is now clear that these two views are not inconsistent, but rather both correct. This particular case of an apparent difference between observations helped fuel the still controversial question of outer/inner region dominance in turbulent boundary layers.

The realization that narrow focus tends to divide the research community is not new, but the tools for avoiding the problem are. Numerical simulations, used in the context of the rich history of experimental structure knowledge, provides an environment in which **all** relevant issues may be considered, at least within the confines of the flows that may currently be simulated. This opportunity has been the driver for the simulation structure research reviewed in Chapter 3, as well as for the present project.

4.1.3 Communication of Results

The accumulation of knowledge in the field of turbulence structure has not progressed linearly due partly to a lack of efficient and comprehensive communications between research groups. The rapid growth of the field has made it difficult for any one scientist to even read, let alone assimilate all of the information available in the literature. (The references in Chapters 2 and 3 comprise about one third of the boundary layer structure literature.) Long publication lead times and short discussions at conferences further hinder communication. Moreover, no common set of nomenclature for the field has evolved, despite its 40 year heritage, contributing confusion in both communications and concepts.

As a result of incomplete communications, most researchers are not fully aware of the extent of other groups' findings. The significant effect is to diffuse the overall goals of structure research, and ultimately to retard the rate of useful return on the energy expended by the community. The goal of the first phase of the current project (Part A: Community-Wide Evaluation) has been to improve communications between research groups through personal interviews, cooperative generation of a nomenclature list, and creation of an annotated and sorted bibliography. This work is reported upon separately (e.g. Kline and Robinson, 1989a,b).

4.1.4 Discussion Summary

The pervasiveness and persistence of the limiting factors cited above has prevented the research community from achieving the ultimate objective of the field: a consensus description, based on true understanding, of the physics of boundary-layer turbulence. The current project is certainly not immune to these same problems,

but the realization of their importance has helped shape the strategy of our approach. The use of numerically-simulated data effectively avoids single-probe or flow-visualization limitations. The focus is as broad as possible (within the limitations of the low Reynolds number simulation), including every experimentally-confirmed structure in both the inner and outer regions, and the spatio/temporal relationships between them. Finally, an attempt to optimize information transfer from the rest of the community to the current project has been made, through on-site interviews and extensive literature reviews.

4.2 Recap of Objectives

As stated in Section 1.3, the overall objective of the present study is to develop a conceptual model of the physics of turbulent boundary layer turbulence that unifies the known structural features and describes their relationships in kinematic terms. To achieve this goal, a number of crucial unresolved issues regarding coherent structures in turbulent boundary layers must be addressed. These include:

Kinematic Issues:

- What is the three-dimensional spatial character of each of the known boundary-layer structural features?
- How are the various structural features related to each other in space and in time?
- What range of vortical structure topologies exist in the flow? How are they distributed in space?
- What is the range of strengths (circulation) of the vortex structures?
- To what extent do vortical structures play a role in determining the average production and dissipation of turbulence kinetic energy and Reynolds shear stress?
- How are the coherent motions in the field related to the wall-pressure fluctuations?

Although only kinematic issues may be resolved with certainty through post-processing of the simulation results, dynamical issues will also be probed and hypotheses proposed where possible. These include:

Dynamic Issues:

- How do vortical structures form, evolve, regenerate, and die?
- What is the role of the outer layer in determining the details of near-wall turbulence production?
- What is the repeating sequence of events that is responsible for the maintenance of turbulence, including the role of all known structures?

Investigation of each of the above issues comprises the specific objectives of the research described in this report.

4.3 Analysis Strategy

The analysis strategy for the simulated boundary-layer database was formulated to investigate all known types of turbulent structure, rather than focus on a pre-determined subset. The availability of the complete velocity and pressure field in the simulation allowed a somewhat non-standard approach to the pursuit of structural understanding in the simulated boundary layer: First, graphical means were employed to gain a conceptual understanding of the various structural features, and then statistical methods were used to determine the statistical relevance of the concepts suggested by the computer-generated images.

This strategy is the reverse of most traditional approaches, in which statistics are computed with available (and often sparse) data, and then dominant structural features and kinematics are reconstructed from the statistical results. The traditional, statistical approach requires a-priori decisions about which types of structural features are important. The averaging and filtering inherent in most statistical techniques can discard phase information, disguise true characteristics of individual realizations, create false symmetries, and contaminate ensemble averages by the inadvertent inclusion of more than one type of flow element. The current availability of numerical turbulence marks the first time in history that a significant sample of each structure can be inspected prior to the compiling of statistics for the significant features.

Spalart's numerical boundary layer simulation offers access to over 31 gigabytes of flow-field data. The extensive computational and graphical power available to study the simulation results makes possible the pursuit of hundreds of "interesting" questions. Effective progress toward an understanding of turbulence production therefore required a well thought-out strategy in order to set work priorities.

The following six-phase strategy was adopted for the study of the simulation databases (Fig. 4.1) :

- Ia. Identify all structures in the numerical boundary layer that are known to exist in laboratory boundary layers. These can be grouped into eight classes, which are delineated in Chapter 5.
- Ib. Once examples of these structures have been identified in the simulation results, obtain detailed descriptions of their spatial character by studying individual time-steps.
- II. Determine the spatial relationships between the various structures by visualizing them together in individual "frozen" time steps.
- III. Study the spatio-temporal relationships between structures by using many stored time-steps and, where necessary, computing intermediate solutions at very small time increments ($\Delta t^+ = 0.3$) between the stored time-steps.
- IV. Determine the statistical significance of the various structures, their apparent generation mechanisms and any interaction events. Populations, frequencies in

space and time, and statistics of occurrence will be computed. Contributions to future statistical/structural models will be made at this stage by computing probability distributions of events and structures, and their contributions to specific terms in the Reynolds-averaged model equations.

- V. Combine the results of stages I through V to develop a phenomenological model of the maintenance of turbulence in flat-plate boundary layers. This should include a description of the important sequences of events, and should describe the roles of all classes of experimentally observed structure. The flow of cause and effect within these sequences should be modeled, as well as any significant interactions between structural features.

Phases I through IV involve only the kinematics and statistics of turbulence structure. Dynamical information does not result directly from passive observation of phenomena. Some kind of model must be proposed which explains the observed sequential events through causative mechanisms. Thus, only Phase V addresses the problem of dynamics in the turbulent boundary layer.

In the context of this strategy, most quantitative experimental results have addressed Phases I, II, and IV, while most flow-visualization studies could be categorized as Phase III. A number of authors have proposed structural models which include dynamical hypotheses and so belong in Phase V.

This five-phase analysis strategy allows us to build up knowledge in a logical order, and facilitates prioritization of the large number of possible queries that might otherwise become disorderly and overwhelming. In the current study, the phases of the strategy represent an iterative, rather than a one-pass, sequential process.

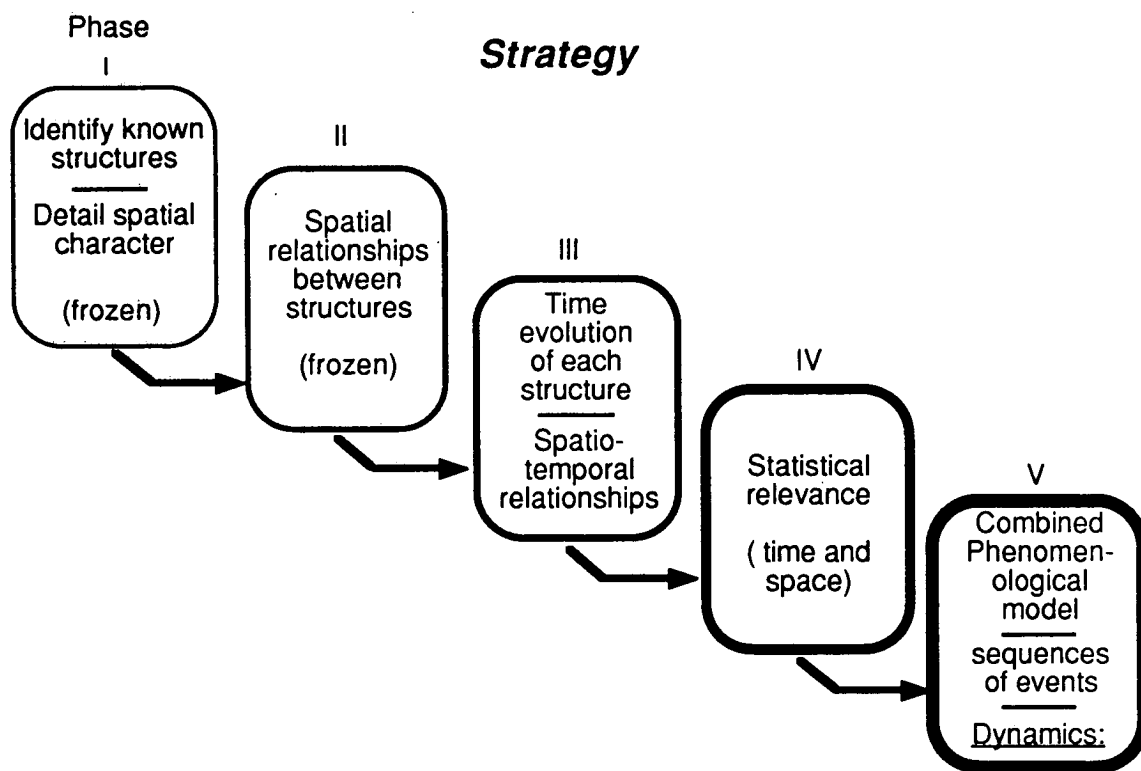


Fig. 4.1 Phased strategy for analysis of the numerical simulation database.

CHAPTER 5 - TAXONOMY OF STRUCTURES

A consistent and accepted definition of “structure” (in the turbulence sense) has not yet surfaced. Thus, it may be viewed as a hopeless task to categorize the many flavors of turbulence structure to be found in the literature. However, a taxonomy, even though somewhat arbitrary, can help focus thinking and inject organization into the somewhat tangled information on the subject.

The various structures, events, flow modules, and organized motions found in the literature may be divided into eight classes. The intent is to include all types of non-random events that have been singled out for study by the researchers in the field, rather than utilize a definition that would necessarily exclude some of the data. This classification is only one of several possibilities, and the following list is not a conclusion of the current work, but rather a starting point for it.

A Classification of Boundary Layer Turbulence Structures:

- (1) Wall low-speed streaks
- (2) Ejections of low-speed fluid outward from the wall, including lifting low-speed streaks
- (3) Sweeps of high-speed fluid inward toward the wall, including intrushes from the outer region
- (4) Vortical structures of various forms
- (5) Near-wall shear layers, exhibiting local concentrations of spanwise vorticity and $\partial u'/\partial x$.
- (6) Near-wall “pockets”, seen as regions swept clean of near-wall marked fluid in experiments.
- (7) Large (δ -scale) motions capped by bulges in the outer turbulent/potential interface.
- (8) “Backs” of large-scale outer-region motions, consisting of (δ -scale) discontinuities in the streamwise velocity.

This classification is meant to provide a skeleton of organization on which the current study of the numerical simulations can build. Reflected in the broad coverage of the list is the objective of including in the current study all of the known structural features of turbulence, rather than just a few.

A brief description of each of the above structural features will be included here, although more complete information is given by Kline and Robinson (1989a), as well as in the final document for Part A of this project, the community-wide evaluation. A well-organized collection of known attributes of these structural features is also included in Cantwell (1981).

5.1 Wall Low-Speed Streaks

So far as is known, the viscous sublayer of every turbulent boundary layer is composed of elongated regions of high- and low-speed fluid. In fact, this streaky structure is useful as a diagnostic to determine whether a wall-bounded flow is turbulent or simply unsteady but laminar. These discrete elongated regions in the sublayer are referred to here as “wall” streaks to differentiate from low-speed streaks that are lifted into the buffer region and beyond.

In the sublayer, the streaky structure exhibits a mean spanwise length-scale of approximately 100 viscous lengths, with a mode of 80, and a log-normal distribution (Kim et al, 1971). These streak characteristics are apparently independent of Reynolds number (Smith and Metzler, 1983), but the spanwise spacing increases with distance from the wall outside the sublayer. For $y^+ > 40$, the streaky structure of the streamwise velocity field is barely noticeable (Smith and Metzler, 1983).

In the canonical flat-plate boundary layer, the streamwise velocity of the sublayer low-speed streaks is typically $1/2$ the local mean, while the velocity of the high-speed streaks is roughly $3/2$ the local mean speed (Kline et al, 1967). Low-speed streaks are from 20 to 60 viscous lengths wide (spanwise), and extend up to a thousand or more viscous lengths in the streamwise direction (Hirata and Kasagi, 1979). The wall low-speed streaks meander spanwise in time over approximately 30 to 50 viscous lengths, and exhibit a sinuous character, commonly branching and reconnecting (Kline et al, 1967).

5.2 Ejections

The quadrant technique (Wallace et al, 1972; Fig. 5.1) will be used to define and identify ejections and sweeps, which are the contributors to the positive Reynolds shear stress, $-\rho \overline{u'v'}$.

In the current paper, any motion which instantaneously occupies the second quadrant $(-u', +v')$ of the u', v' plane will be described as an ejection. This definition may be criticized on the grounds that an instantaneous $(u'v')_2$ motion at a point need not necessarily correspond to a “coherent” motion, that is, a significant volume of fluid moving essentially as one. For instance, Wallace et al (1977) use a short-time averaged streamwise velocity to detect “ejections” from a reference frame moving with a larger, enveloping mass of fluid. However, the current definition is the most common, and is used here to avoid the arbitrariness of floating averages, and to maintain a strong connection to the Reynolds shear stress.

Quadrant 2 $u'v'$ motions occur throughout the boundary layer, so ejections as defined here are not confined to the near-wall region. However, “lifted low-speed streaks” occur in the buffer region and are by definition (low-speed fluid moving outward) ejection motions. Thus “lifted low-speed streaks” are considered a subset of “ejections.”

Ejection motions are at the heart of the bursting process, as described by Kim

et al (1971), and are known to be the major contributor to $-\overline{u'v'}$ in the region beyond $y^+ \approx 12$ (Willmarth and Lu, 1972; Kim, Moin, Moser, 1987). Ejections are known to occur intermittently when observed from a stationary frame of reference, but the literature has been unclear about whether ejections are intermittent in both space and time. In fact, few authors have called attention to such a distinction. This dynamically important issue is taken up again in Chapter 12.

5.3 Sweeps

Continuity requires a net wallward flow to balance the fluid mass pumped outward during ejections. Because of the mean shear in the boundary layer, wallward flow generally takes the form of high-speed fluid descending into lower-speed fluid. For the current work, a sweep is defined as any instantaneous motion which occupies the fourth $(+u', -v')$ quadrant of the u', v' plane.

Since near-wall fluid markers accumulate in low-speed regions, leaving the high-speed fluid relatively invisible, the character of low-speed ejections is better known than that of high-speed sweeps. The earliest description of a sweep as a coherent motion is found in Corino and Brodkey (1969), who observed a relatively large-scale, front-like motion which “swept” away near-wall ejection activity. The fluid of the sweep was observed to move downstream at approximately the local mean streamwise velocity ($u' \approx 0$), and thus Corino and Brodkey’s sweep motions were not direct contributors to the Reynolds shear stress.

Grass (1971), however, described “inrushes” of wallward-moving fluid which made high contributions to $-\overline{u'v'}$ in the near-wall region. The inrushes of Grass were described as being of smaller scale and possessing stronger $-v'$ than Corino and Brodkey’s sweeps.

In keeping with the general spirit of the terms employed by Corino and by Grass, the term “inrush” will be reserved for quadrant 4 motions with a significant wallward ($-v'$) component. Thus “inrushes” will be considered a subset of “sweeps.” The distinction between the two motions is arbitrary, but nevertheless qualitatively useful for understanding the interactions between inner and outer layers.

Sweep motions are the dominant contributor to $-\overline{u'v'}$ in the region $y^+ < 12$ (Willmarth and Lu, 1972; Kim, Moin, Moser, 1987), even though the vertical velocity component is severely constrained by the presence of the wall. Thus, near the wall, the Reynolds shear stress is due largely to locally high-speed regions with a slight wallward component.

At $y^+ \approx 12$, ejections and sweeps together account for about 120% of $-\overline{u'v'}$, while quadrants 1 and 3 are responsible for -20% (Kim, Moin, Moser, 1987).

5.4 Vortical Structures

A vortical structure is defined for the present purposes as an instantaneous vortex, generally forming a complex three-dimensional shape. This is in contrast to

the occasional usage of “vortical structure” in the literature to describe any region with locally concentrated vorticity. The difference between the two usages of the term arises from the need to distinguish between vortices and vorticity. A vortical element is defined (in Section 9.1.4) as a vortex with a single dominant orientation.

Although there is a virtual consensus that vortical structures play a key, and possibly central role in the production of boundary layer turbulence, several different forms of vortical structures have been postulated in the literature (hairpins, horseshoes, streamwise vortices, rings), and limited quantitative evidence exists to support any one of the concepts. A major objective of the present project is to significantly increase the level of knowledge concerning vortical structures in turbulent boundary layers by first developing identification techniques and then examining a large sample of instantaneous three-dimensional vortical structures in the DNS database.

An in-depth discussion of the character of vortical structures, along with a definition of vortex and a review of the literature on the subject is included in Chapters 9 and 11.

5.5 Near-Wall Shear Layers

The existence of sloping $+\partial u/\partial y$ shear layers near the wall ($y^+ < 80$) in turbulent channels and boundary layers has long been established both by flow-visualization studies (e.g. Kline et al, 1967; Corino and Brodkey, 1969) and by probe-based investigations (e.g. Burton, 1974; Brown and Thomas, 1977; Kreplin and Eckelmann, 1979; Dinkelacker and Langeheineken, 1982; Johansson et al. 1987a). The VITA technique in particular has been commonly employed to detect the rapid changes in the streamwise velocity associated with the passage of a near-wall shear layer. Bogard and Tiederman (1987) have shown that such shear layers can occur on the upstream face of ejections from the buffer region, at the interface between the lifting low-speed fluid and the higher-speed fluid overtaking it from behind. However, the limited ability of the VITA technique to detect ejections left open the question of whether near-wall shear layers also occur in other locations.

Although their existence was experimentally established, it remained for numerical simulations to show just how pervasive NWSL's are in wall-bounded flows. In a recent investigation of numerically simulated channel flows, Jimenez et al (1987) proposed a mechanism for the generation and maintenance of the shear layers which is essentially equivalent to that responsible for the instability of two-dimensional Tollmien-Schlichting waves. Additional recent work on near-wall shear layers in numerically simulated turbulent flows has been reported by Johansson et al (1987b) and by Alfredsson et al (1988). These authors found that shear layers in the near-wall region propagate with a velocity of about $10.6u_\tau$, retain their coherence over streamwise distances of up to 1000 viscous lengths, and commonly occur on the

upstream side of a spanwise kink in a low-speed streak.

5.6 Pockets

When distributed markers are introduced into the sublayer of a turbulent boundary layer or channel, roughly circular regions devoid of marked fluid appear in the plan view. These have been called pockets (Falco 1980), and they give the visual impression of being a “footprint” of some outer structure that induces fluid toward the wall. The most extensive description of the “pocket flow module” is given by Falco (1982), who attributes pocket formation to the impingement of a ring-shaped eddy upon the viscous sublayer. Falco describes the temporal evolution of such an interaction, and relates most of the observed features of near-wall turbulence structure to the pocket, including ejections, sweeps, near-wall shear layers, and hairpin vortices.

Although the existence of pockets and their proximity to regions of turbulence production in the buffer region are well-documented by experiment, the question of whether pockets are primarily a cause or an effect of turbulence activity remains controversial. Further light will be shed on this issue in Chapter 10.

5.7 Large-Scale Motions and Bulges

The instantaneous interface between the turbulent boundary layer and the irrotational free stream consists of large-scale bulges, separated by deep, narrow incursions of free-stream flow into the layer (e.g. Kovasznay et al, 1970; Bevilaqua and Lykoudis, 1977). The interfacial bulges exhibit streamwise and spanwise length scales on the order of the boundary layer thickness. The large-scale motions (LSMs) beneath bulges in the boundary layer show a weak rotation in the direction of the mean shear, when observed from a frame of reference moving with the LSM (Blackwelder and Kovasznay, 1972; Falco, 1977; Thomas and Bull, 1983).

The large-scale motions in the boundary layer and their associated interfacial bulges have been attributed both to near-wall ejections of fluid into the outer region (Kim et al, 1971; Blackwelder and Kovasznay, 1972), and to the presence of large-scale, outer-region vortical structures around which the free-stream fluid flows (Willmarth and Lu, 1972; Nychas et al, 1973; Praturi and Brodkey, 1978). The latter view is more prevalent today, especially for high Reynolds number flows, and will also be explored in the present study.

5.8 Backs of Large-Scale Motions

The most evident and well-documented of the outer-region structural features of the turbulent boundary layer is the upstream side, or “back” of the large-scale motions. Flow visualization and multi-point hot-wire anemometry have established that backs span most of the boundary layer, travel downstream at a 12 to 30 degree angle from the wall, and consist of a sharp spatial discontinuity in the streamwise velocity (e.g. Kovasznay et al, 1970; Falco, 1977; Brown and Thomas, 1977; Chen

and Blackwelder, 1982;). The back is effectively a shear layer formed where high-speed fluid impinges upon the relatively slower fluid on the upstream face of the LSM. When viewed from a reference frame travelling with the back (at about $0.8 U_e$), the back exhibits a quasi-stagnation point, in accordance with the notion of the LSM as an obstacle around which the faster surrounding fluid must flow (Hedley and Keffer, 1974; Falco, 1977).

The relationship between the commonly-measured 12 to 30 degree angle of the δ -scale backs and the assumed 45 degree orientation of vortical structures has remained unresolved, with a number of concepts in circulation. This issue will be addressed in detail in Chapter 10.

In the current work, a distinction is drawn between backs and near-wall shear layers. Backs are defined as large-scale structures with spacing in the streamwise direction of the order of the boundary layer thickness, and which presumably scale with outer variables (U_e and δ). Near-wall shear layers exist generally below $y^+ = 80$, with dimensions and spacing that would be expected to scale with wall variables (u_τ and ν). It is not clear from the literature whether the size and spacing of these shear-layer structures are distributed smoothly from small to large, or if there is a bimodal distribution, suggesting two different types of structure. Recent statistical analyses of simulated turbulence by Adrian et al (1987) has shown some evidence of a “two-layer” structural makeup of a low Reynolds number channel.

In cases where backs extend all the way to the wall (e.g. Brown and Thomas, 1977), the distinction between backs and near-wall shear layers is unnecessary, but such cases do not appear to be the rule, so separate consideration of the two structures still seems appropriate. Certainly more near-wall shear layers exist than backs in a given large volume of flow at any given instant. Also, near-wall shear layers are known to occur in fully-developed channel flows (e.g. Alfredsson et al, 1988) but backs and large-scale motions in fully-developed channels may differ from those in boundary layers due to the lack of a potential free-stream in the channel case.

Experimental ensemble averages have not generally separated the data into two structures (backs and near-wall shear layers) possibly because the commonly-used VITA technique will trigger on either structure, independent of its vertical extent. Also, the scale separation between the two structures, if such a separation exists, would be most pronounced at high Reynolds numbers, where sensor lengths are usually too long to isolate the small-scale structures near the wall.

5.9 Summary

This brief (and necessarily incomplete) summary of the major known boundary layer structural features illuminates the wide variety of coherent motions that have been studied in order to better understand turbulence physics. The quantitative data and qualitative observations of the character of these structural features are extensive and surprisingly non-controversial (see Kline and Robinson, 1989a).

However, major unknowns remain in four categories:

- (1) Time-evolution of each structural feature, including origin and demise.
- (2) Spatio-temporal relationships between the various structures.
- (3) Population and three-dimensional character of vortical structures.
- (4) Statistical relevance of the various structures in terms of contribution to turbulence kinetic energy production and dissipation.

These questions are the focus of the results reported in the remaining chapters.

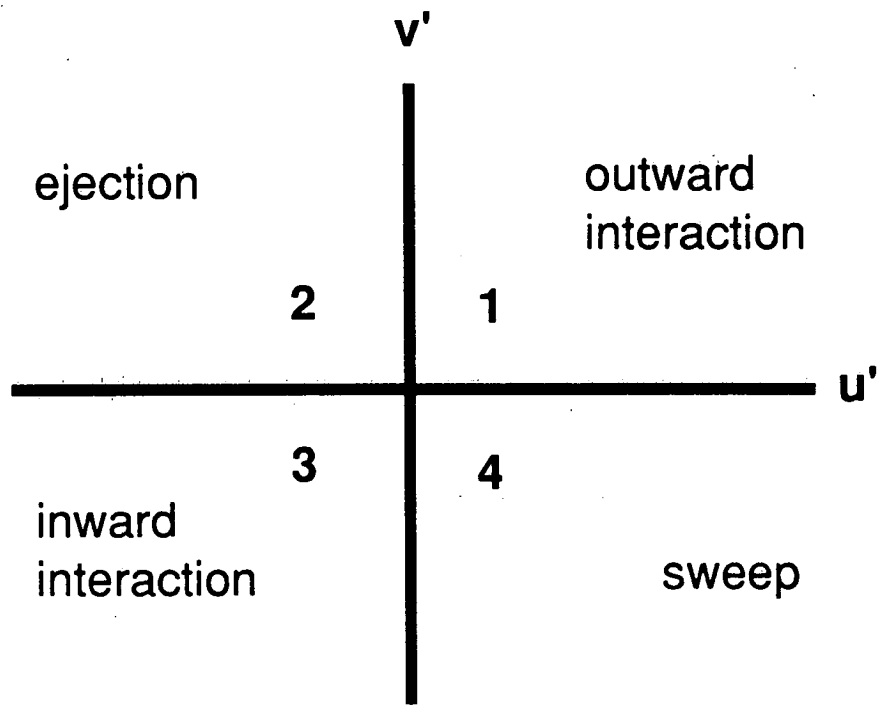


Fig. 5.1 Quadrants of the instantaneous $u'v'$ plane. Quadrants 2 and 4 contribute to the Reynolds shear stress, $-\overline{u'v'}$.

CHAPTER 6 - NUMERICAL SIMULATION

The recent availability of direct numerical simulations of turbulent flows has relegated experiments to a secondary role, at least for the low Reynolds Number canonical flows. Accordingly, a numerically-simulated boundary layer was employed in the present study as a numerical wind tunnel, providing “captive” turbulence in which the open questions delineated in the previous chapters could be pursued.

Spalart’s (1988) direct Navier-Stokes numerical simulation of a flat-plate turbulent boundary layer was the source of turbulence data for the present study. The code has been run to statistical equilibrium for four Reynolds numbers: $Re_\theta = 225$, 300, 670, and 1410. The analysis reported herein has concentrated on the $Re_\theta = 670$ case due to the high computational cost and longer turnaround times for the $Re_\theta = 1410$ case. At $Re_\theta = 670$, each time-step is computed on a $384 \times 288 \times 85$ grid, comprising 9.4 million nodes. At each node, for each time-step, pressure and all three components of velocity (and thus vorticity) are available. Grid resolution is approximately 12.8 viscous lengths in the streamwise (x) direction, and 4.3 viscous lengths in the spanwise (z) direction. Resolution in the wall-normal (y) direction varies from 0.03 to 16.0 viscous lengths, with 14 grid points between the wall and $y^+ = 10$. The grid spacing for the $Re_\theta = 670$ case gives a computational domain with streamwise, spanwise, and wall-normal dimensions of 4900, 1225, and 1100 viscous units, respectively (Fig. 6.1). The boundary layer is approximately 300 viscous units thick at this Reynolds number.

6.1 Numerical Method

The numerical method used to compute the boundary layer simulation will be only briefly reviewed here. More complete discussions are available in Spalart (1986 and 1988).

Spectral methods were used in all three spatial directions to maximize the numerical accuracy. Fourier series were used for the periodic (x and z) directions, and exponential mapping with Jacobi polynomials was used in the wall-normal (y) direction. Time integration was accomplished with hybrid second order methods.

The key element of Spalart’s numerical approach is to expand the computational grid with the spatially growing boundary layer so that periodic boundary conditions in the streamwise direction are justifiable. The equations solved on the grid are the full, three-dimensional, time-dependent Navier-Stokes equations for incompressible flow, with a set of small “growth terms” added to account for the gradual downstream growth of the boundary layer thickness and energy level.

To allow the periodic computational domain to grow with the boundary layer, a new coordinate η is chosen, which replaces y as the wall-normal coordinate. Then the governing equations are transformed from the Cartesian (x, y, z) coordinate system to the non-Cartesian (x, η, z), and the streamwise periodic boundary conditions

are applied along lines of constant η . The form of η is chosen so that the boundary layer thickness, δ , and the viscous sublayer thickness are independent of x . Spalart used a weighted average of y^+ and y/δ :

$$\eta \equiv \frac{y_2^p(10^{-3}y^+) + y^p(y/\delta)}{y_2^p + y^p}, \quad (6.1)$$

where $y_1^+ \equiv 15$, $y_3/\delta \equiv 0.3$, $y_2 \equiv (y_1 y_3)^{1/2}$, and $p \equiv 5/\log_{10}(y_3/y_1)$. This choice forces η to follow y^+ lines near the wall, and y/δ lines away from the wall, thus allowing η to grow with the natural coordinates of the boundary layer. This minimizes the boundary layer variation along constant- η lines which in turn minimizes the growth terms that must be added to the Navier-Stokes equations. The slope of the η -lines as measured from the Cartesian coordinate system is $S \equiv \partial y / \partial x$. Note that η -lines are not straight, so S is not a constant for each η -line.

The metric coefficients of the general coordinate transformation from (x, y, z) to (x, η, z) are S and T , defined by

$$\begin{pmatrix} dx \\ dy \end{pmatrix} \equiv \begin{pmatrix} 1 & 0 \\ S & T \end{pmatrix} \begin{pmatrix} dx \\ d\eta \end{pmatrix}. \quad (6.2)$$

The transformation may be simplified by allowing y and η to coincide at a given x -station, giving $T = 1$.

The transformation of the Cartesian velocity field (u^*, v^*, w^*) to the non-Cartesian field $(\tilde{u}, \tilde{v}, \tilde{w})$ is given by:

$$\tilde{u} = u^* \quad (6.3a)$$

$$\tilde{v} = v^* - S u^* \quad (6.3b)$$

$$\tilde{w} = w^* \quad (6.3c)$$

The Navier-Stokes equations in the non-Cartesian coordinate system (x, η, z) are then:

$$\tilde{u}_x + \tilde{v}_y + \tilde{w}_z + S_y \tilde{u} = 0 \quad (6.4a)$$

$$\begin{aligned} \tilde{u}_t + \tilde{u}\tilde{u}_x + \tilde{v}\tilde{u}_y + \tilde{w}\tilde{u}_z = & -p_x + S p_y + \nu(\tilde{u}_{xx} + (1 + S^2)\tilde{u}_{yy} \\ & - 2S\tilde{u}_{xy} + (2SS_y - S_x)\tilde{u}_y + \tilde{u}_{zz}) \end{aligned} \quad (6.4b)$$

Before the transformed Navier-Stokes equations may be solved using periodic boundary conditions, the behavior of the velocity along instantaneous η -lines must be considered. For given values of η, z , and t , the mean and RMS values of each

velocity component varies with x (see Fig. 6.2). This makes periodic boundary conditions inappropriate for the velocity field. To resolve this, each velocity component may be written (using u as an example) as:

$$u = U + Au_p \quad (6.5)$$

where

$$u = u(x, \eta, z, t),$$

$$U = U(x, \eta) = \text{mean over } z \text{ and } t,$$

$$A = A(x, \eta) = \text{amplitude function which is proportional to the RMS value of } u \text{ at } x \text{ and } \eta,$$

$$u_p = u_p(x, \eta, z, t) = \text{“periodic” velocity component.}$$

With this formulation, the periodic boundary conditions may be applied to u_p , which has zero mean and an RMS value independent of x . The streamwise variation of U and A are dealt with in growth terms, as discussed below.

The streamwise gradient of each velocity component is now given by differentiating equation (6.5) with x :

$$\frac{\partial u}{\partial x} = \frac{\partial U}{\partial x} + A \frac{\partial u_p}{\partial x} + \frac{\partial A}{\partial x} u_p. \quad (6.6)$$

Spalart re-names the terms in (6.6) as

$$U_X \equiv \frac{\partial U}{\partial x} \quad (6.7a)$$

$$u_X \equiv \frac{\partial A}{\partial x} u_p \quad (6.7b)$$

$$u_x \equiv A \frac{\partial u_p}{\partial x}. \quad (6.7c)$$

so that

$$\frac{\partial u}{\partial x} = u_x + [U_X + u_X] \quad (6.7d)$$

The variation of U and A with x is presumed small relative to the local streamwise gradient of u_p . Thus, U_X and u_X are referred to as “slow” derivatives; these refer to the global downstream variation of U and A . The term u_x is called a “fast” derivative, and is the local spatial derivative of the instantaneous velocity.

Now the Navier-Stokes equations may be rewritten in terms of the “periodic” velocity field u_p . The steps taken are as follows:

- 1) Apply the Reynolds decomposition to the dependent variables, e.g. $\tilde{u} = U + u$.
- 2) Apply the fast and slow derivatives defined by (6.6) and (6.7) to the Navier-Stokes formulation (6.4).

- 3) Develop the Taylor expansion of the resulting Navier-Stokes equations, up to order ϵ^2 , where ϵ is defined as the order of u_τ/U_∞ . ($u_\tau/U_\infty \approx 0.05$ for the $Re_\theta = 670$ case) (see Spalart, 1988).

The resulting equations are the usual instantaneous Navier-Stokes equations with the addition of growth terms (in square brackets) that involve the slow derivatives and the slope of the η -lines, S :

$$V_y + [U_X + S_y U] = 0 \quad (6.8a)$$

$$u_x + v_y + w_z + [u_X + S_y u] = 0 \quad (6.8b)$$

$$\begin{aligned} U_t + u_t + (U + u)u_x + v(U + u)_y + wu_z + [UU_X + VU_y + Uu_X + U_Xu + Vu_y] \\ = -p_x - [P_X] + \nu(U_{yy} + \nabla^2 u) \end{aligned} \quad (6.8c)$$

$$v_t + (U + u)v_x + vv_y + wv_z + [Uv_X + (V_y + 2US_y)v + Vv_y] = -p_y + \nu \nabla^2 v \quad (6.8d)$$

$$w_t + (U + u)w_x + vw_y + ww_z + [Uw_X + Vw_y] = -p_z + \nu \nabla^2 w \quad (6.8e)$$

For each streamwise station of the boundary layer, equations (6.8) are integrated in time to produce a simulated turbulent boundary layer that is periodic in x and z .

The slow derivatives (S, u_X, v_X, w_X , and U_X) that dominate the growth terms in (6.8) are estimated simply by performing simulations at two different X -stations of the boundary layer, and differencing the profiles of y, u, v, w , and U . For example,

$$S \equiv \frac{\partial y}{\partial X} \approx \frac{y(X_2, \eta) - y(X_1, \eta)}{X_2 - X_1}, \quad (6.9a)$$

and

$$U_X \approx \frac{U(X_2, \eta) - U(X_1, \eta)}{X_2 - X_1}. \quad (6.9b)$$

The only information needed from the upstream (X_1) station is U, u_{rms}, v_{rms} , and w_{rms} as a function of y .

6.2 Simulation Parameters

The spatial wavelengths for the periodic computational domain are $\Lambda_x = 100\delta^*$ and $\Lambda_z = 25\delta^*$. These choices provide low two-point correlations at $\frac{1}{2}\Lambda$, which ensures statistical freedom from “feedback” in the simulation.

For the present case of $Re_{\delta^*} = 1000$ ($Re_\theta = 670$), the code was run for approximately 1400 time-steps, with a non-dimensional time-step of $\Delta t u_\tau^2 / \nu \approx 0.32$. Code convergence was judged by monitoring accumulated turbulence statistics.

Spalart (1988) has performed simulations at a number of different grid resolutions. The mean and turbulence profiles for statistical quantities up to third order

(skewness) were found to be satisfactorily independent of grid for the resolutions chosen, except for a very coarse case. Fourth-order velocity statistics (flatness), especially for v' , exhibited a pronounced sensitivity to grid resolution in the near-wall region. Overall, however, the grid resolution appears satisfactory for a large majority of the statistics, including those near the wall, and was therefore presumed sufficient to accurately capture the important structural features. Note that the grid utilized for the present study (384 x 288 x 85) is significantly finer than that described in Spalart (1988) (256 x 192 x 64).

6.3 Statistical Results

The simulation and boundary layer parameters for the $Re_\theta = 670$ case used in the present study are listed in Table 6.1. At each y -value, the various statistical profiles are calculated using averages in the x - z plane of the computational domain, accumulated over many computational time-steps of the simulation. Figures 6.2 through 6.5 are reproduced from Spalart (1988). Note that the boundary layer thickness δ used in the outer-layer normalizations has been defined in a non-standard but more reliable way by Spalart as follows:

$$\delta \equiv 1.85 \int_0^\infty \tau^+(y) dy \quad (6.10)$$

where

$$\begin{aligned} \tau(y) &= \text{total shear stress} = \mu \partial \bar{U} / \partial y - \overline{\rho u' v'} \\ \tau^+(y) &= \tau(y) / \tau(0) \end{aligned}$$

The mean velocity profile is plotted in wall variables in Fig. 6.3. The $Re_\theta = 670$ profile exhibits a small but noticeable logarithmic region, which is fit well by $U^+ = \log(y^+) / 0.41 + 5.0$ in the region $30 < y^+ < 75$.

Turbulence intensities for u' , v' , and w' are plotted against y/δ in Fig. 6.4a and against y^+ in Fig. 6.4b. The simulation results show reasonably good agreement with Klebanoff's (1954) $Re_\theta \approx 7500$ experimental data in the outer region, where Reynolds number effects are negligible. In the near-wall region (Fig. 6.4b), the simulation agrees well with recent LDV measurements at $Re_\theta = 600$ by Karlsson and Johansson (1987) (not shown).

Outer-layer distributions of total shear stress, $\mu \partial \bar{U} / \partial y - \overline{\rho u' v'}$, and Reynolds shear stress, $-\overline{u' v'}$ (Fig. 6.5a), normalized by u_τ , agree well with Klebanoff's (1954) results. Near-wall profiles of shear stresses and turbulence kinetic energy production, $\overline{u' v' \partial \bar{U} / \partial y}$, also normalized by u_τ , are shown in Fig. 6.5b. The production peak occurs at $y^+ \approx 10$, and the distributions of both production and shear stress match the experimental data of Kim, Kline, and Reynolds (1971) well. It is notable that of all the near-wall turbulence quantities examined by Spalart (1988), the production profiles show the least effect of Reynolds number, over the range simulated ($Re_\theta \leq 1410$).

A number of additional statistical checks of the simulated boundary layer have been performed by Spalart (1988), including turbulence intensities, skewnesses, flatness factors, Reynolds stress and turbulence kinetic energy budgets, and spectra. The most significant known discrepancy is a 5% overprediction of the friction coefficient for the highest Reynolds number ($Re_\theta = 1410$) case. In addition, as noted above, near-wall fourth-order statistics, especially for v' , show a dependence on grid resolution. It is unclear how significant these may be in terms of the structural behavior of the turbulence. However, the overall excellent agreement between the simulated turbulence and the best of the experimental data strongly suggest that the simulation is structurally equivalent to a physical low Reynolds number boundary layer.

6.4 Boundary Layer Database

The simulated turbulent boundary layer provides a turbulent region of flow approximately 25 wall-streak spacings wide (z) and 14 boundary layer thicknesses long (x). The velocity, vorticity, and pressure fields of the computational domain (Fig. 6.1) have been saved on tape for 104 time steps, each three viscous time-units apart and computed after the simulation reached statistical equilibrium. Thus, for each time-step, 7 words of information ($u, v, w, p, \omega_x, \omega_y, \omega_z$) are stored for each node of the $384 \times 288 \times 85$ grid, giving 6.58×10^7 words per time step, or a total of 6.84×10^9 words. For the computers used to analyze these datasets, 32-bit words were standard, so the total database represents 27.37 Gbytes of turbulence information.

To minimize the amount of random searching through this massive database, the analysis strategy described in Section 4.2 (Fig. 4.1) was developed. A large portion of the early stages of study was spent researching and developing graphical and statistical software with which to efficiently extract information from the simulation database. The software tools employed for the structural and statistical analysis of the simulated turbulence are described in Chapter 7.

To compare various instantaneous structural aspects of the numerically-simulated turbulence, a specific subvolume of the computational domain was chosen to illustrate typical results (Fig. 6.6). The same subvolume of data (referred to as "subvolume S") will be used repeatedly to illustrate several structural features. Many other subvolumes have been included in the overall analysis, however, so the figures presented in subsequent chapters should be considered examples, and not necessarily representative of all realizations. In the wall-normal (y) direction, the subvolume reaches from $y^+ = 3$ to $y^+ = 254$, which is approximately 85% of the mean boundary layer thickness. Over 1500 subvolumes of this size are available in the stored turbulence database. It is worth noting that examples of each class of structural feature listed in Chapter 5 are detectable in nearly every subvolume studied (approximately 200).

TABLE 6.1 - Simulation and Boundary Layer Parameters

Simulation:

Grid: 384(x) by 288(y) by 85(z)

$$\Delta x^+ \approx 12.8$$

$$\Delta z^+ \approx 4.3$$

$$\Delta y^+ \approx 0.03 \text{ to } 9.0 \text{ for } y^+ < \delta$$

$$\Lambda_x^+ \approx 4900$$

$$\Lambda_z^+ \approx 1225$$

$$\Delta t^+ \approx 0.32$$

Boundary Layer:

$$R_{\delta^*} = 1000$$

$$R_\theta \approx 670$$

$$\delta^+ \approx 300$$

$$u_\tau/U_\infty \approx 0.05$$

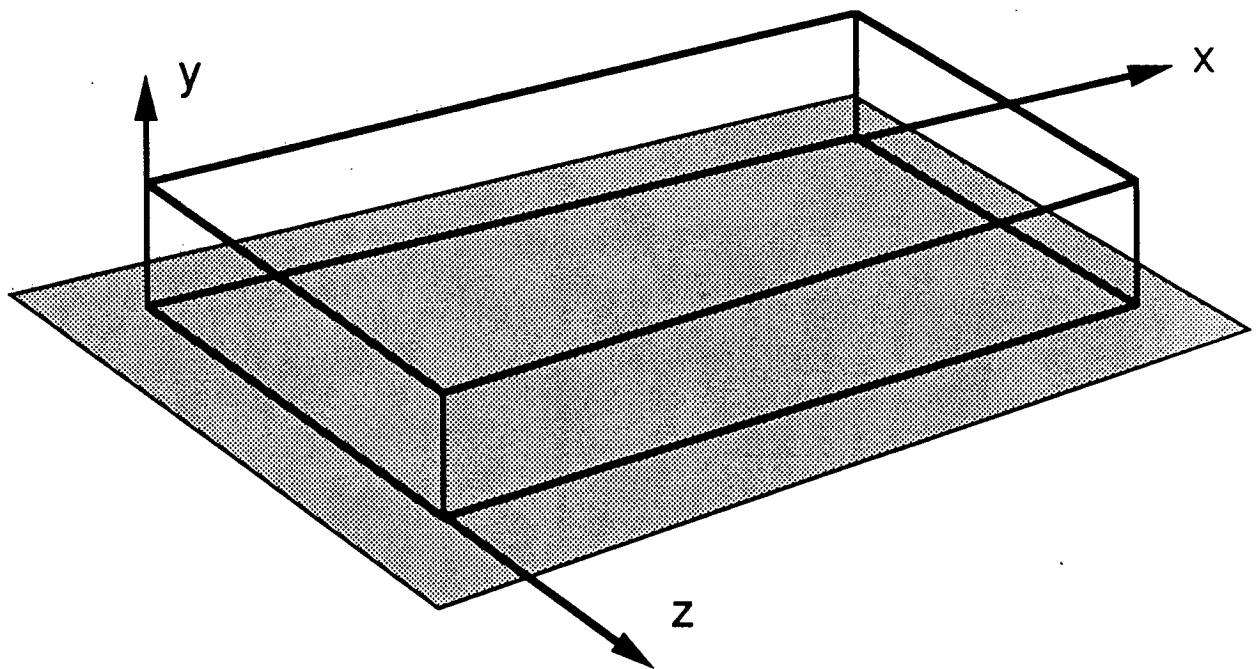
$$C_f \approx 0.0048$$

Computational Domain

$$\Delta x^+ = 12.8$$

$$\Delta z^+ = 4.3$$

$$\Delta y^+ = 0.3 \text{ to } 17.0$$



	x	z	y
grid points:	384	x 288	x 85
viscous lengths:	4900	x 1225	x 1100

Fig. 6.1 Computational domain.

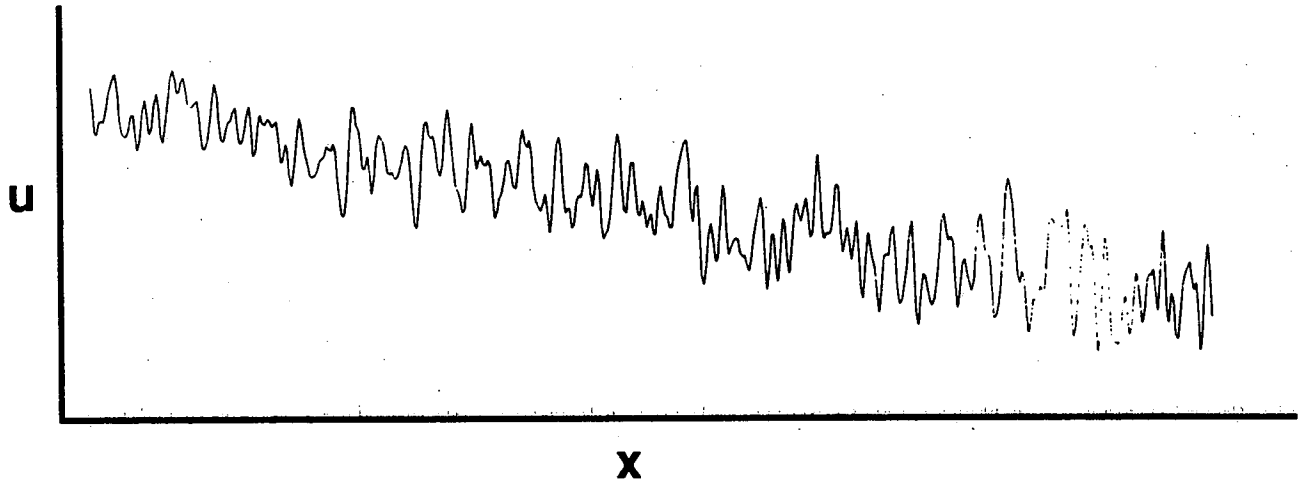


Fig. 6.2 Example of an instantaneous turbulent signal in a spatially-developing boundary layer, (from Spalart, 1988).

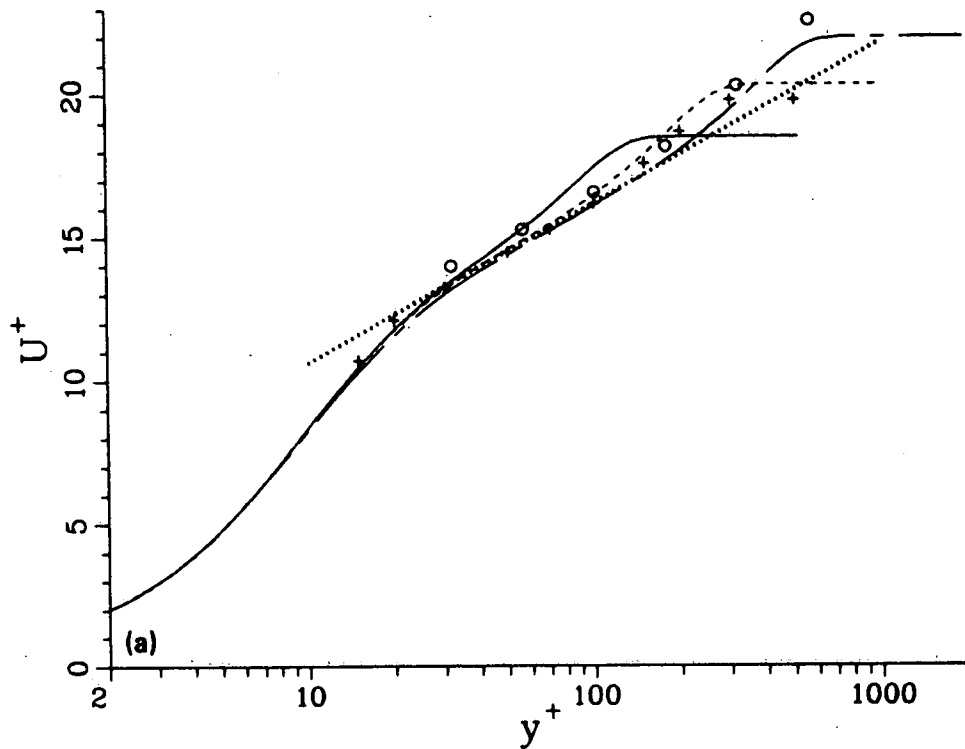


Fig. 6.3 Mean velocity profile for the numerically-simulated boundary layer at three Reynolds numbers. - - - $Re_\theta = 670$, (from Spalart, 1988).

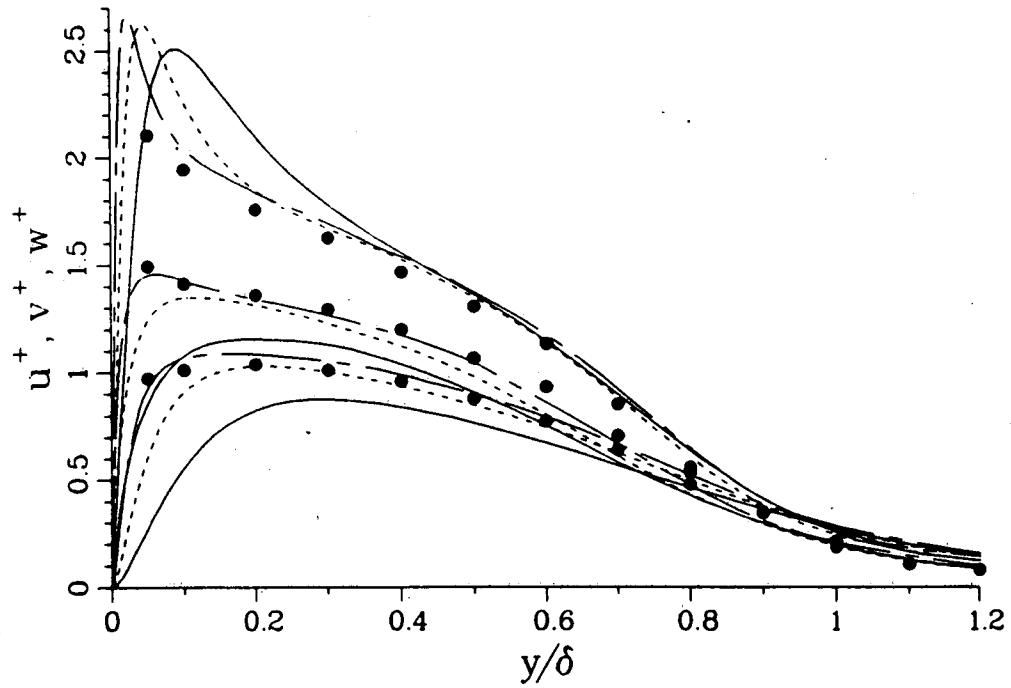


Fig. 6.4a Turbulence intensities for the numerically-simulated boundary layer at three Reynolds numbers. - - - $Re_\theta = 670$. Upper curve is u'_{rms}/u_τ , middle curve is w'_{rms}/u_τ , lower curve is v'_{rms}/u_τ . • experiment at $Re_\theta \approx 7500$ (Klebanoff, 1954), (from Spalart, 1988).

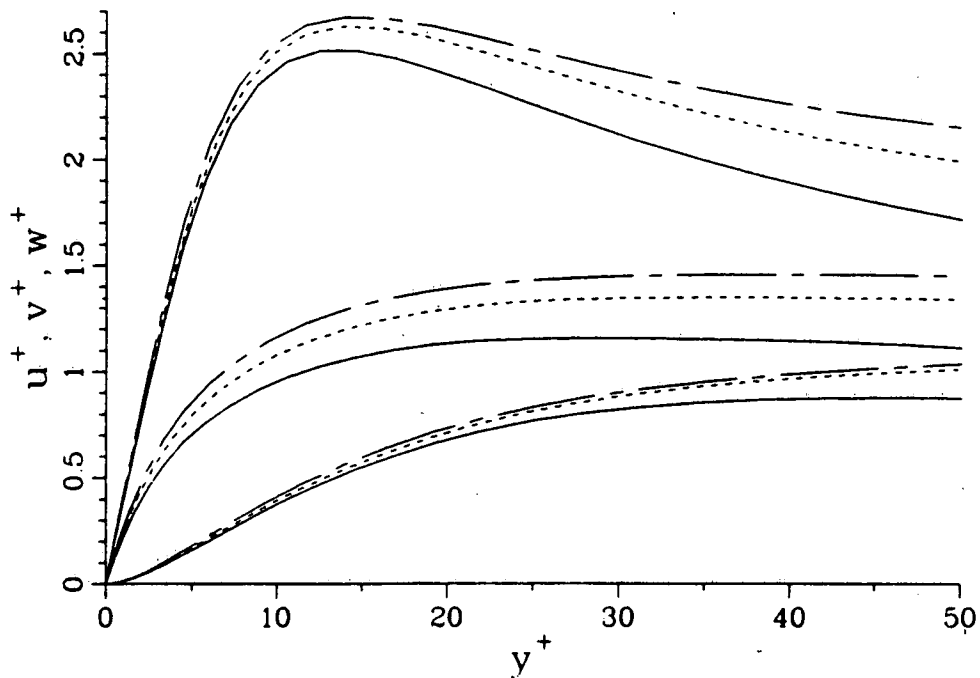


Fig. 6.4b Near-wall turbulence intensities for the numerically-simulated boundary layer at three Reynolds numbers. - - - $Re_\theta = 670$. Upper curve is u'_{rms}/u_τ , middle curve is w'_{rms}/u_τ , lower curve is v'_{rms}/u_τ , (from Spalart, 1988).

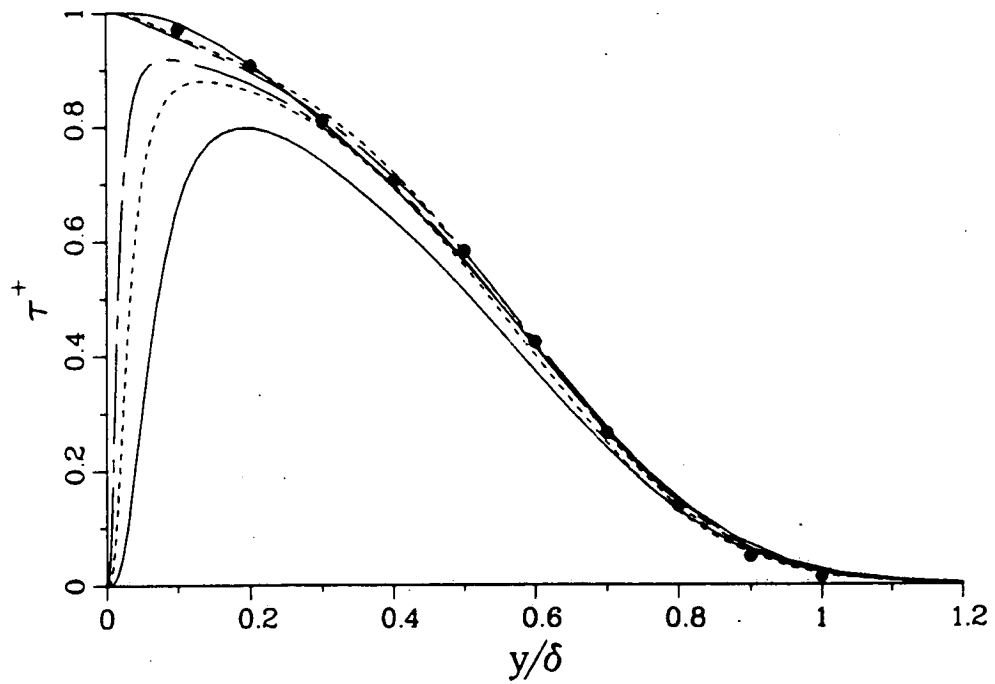


Fig. 6.5a Shear stress distribution for the numerically-simulated boundary layer at three Reynolds numbers. - - - $Re_\theta = 670$. Upper curve is total shear stress, lower curve is Reynolds shear stress, (from Spalart, 1988).

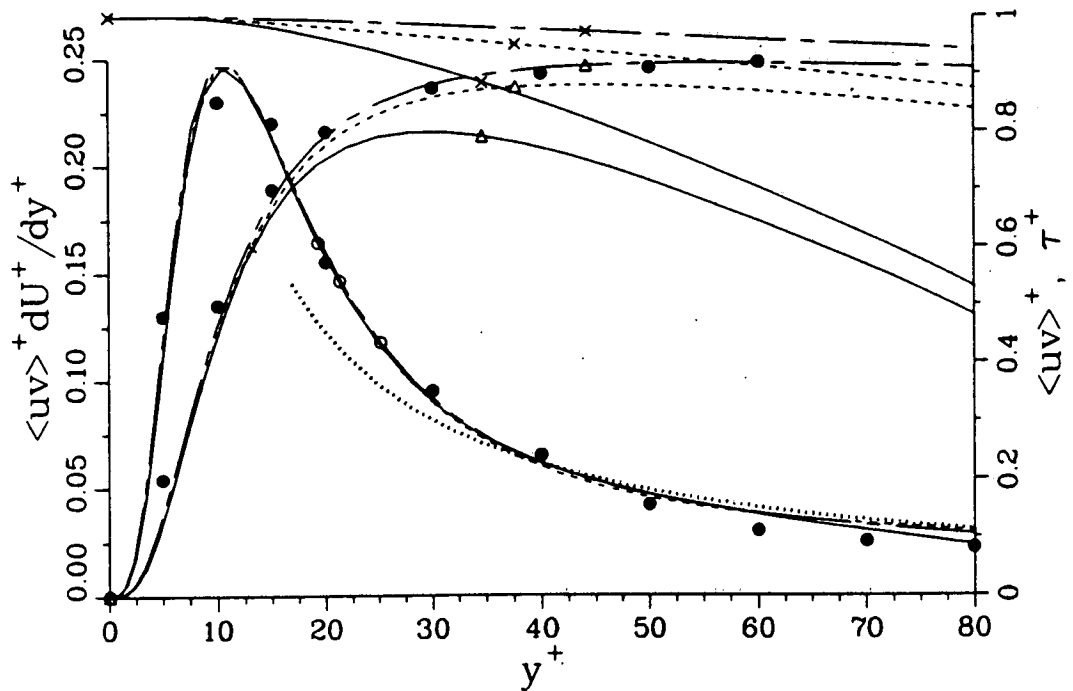


Fig. 6.5b Stresses and production near the wall for the numerically-simulated boundary layer at three Reynolds numbers. - - - $Re_\theta = 670$. Δ Reynolds stress; \times total stress; \circ production; \bullet experiment (Kim et al, 1968), (from Spalart, 1988).

Computational Subvolume

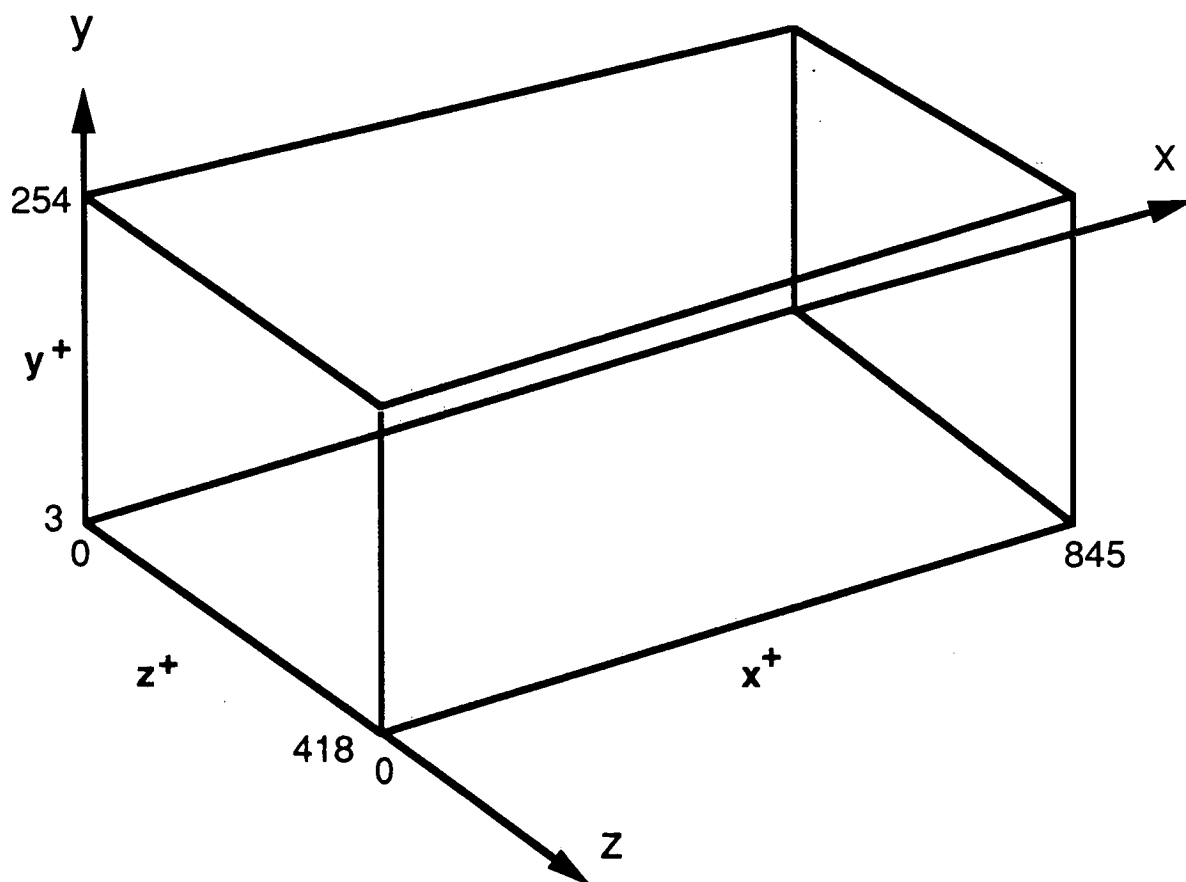


Fig. 6.6 Computational subvolume.

CHAPTER 7 - ANALYSIS TECHNIQUES AND SOFTWARE TOOLS

This Chapter will describe some of the techniques employed for the graphical/statistical analysis of Spalart's simulated boundary layer, which was performed following the strategies described in Chapter 4.

7.1 Scientific Visualization

In the present investigation, computer-generated imagery of the complex turbulent flow-field was employed as a compliment to traditional statistical analyses. Since the human vision system can rapidly acquire information in at least seven dimensions (three spatial dimensions, time, color, intensity, texture) while simultaneously acting as a dynamic filter against noise or uncorrelated information, visualization techniques were effective for developing structural hypotheses which could then be substantiated with targeted statistics. In several cases, three-dimensional images provided key concepts which were distorted or passed over by the more traditional statistical techniques. The concentrated use of graphical techniques in the current investigation is more closely comparable to an "experimental" study than to the heavily statistical analyses of numerical turbulence undertaken in previous work (Chapter 3).

However, graphical analysis of numerical turbulence is also fundamentally different from experimental flow visualization for several reason. Images derived from the numerical database are precise quantitative representations of flow variables with known significance, while many laboratory flow-visualization techniques illuminate motions chosen by the fluid marker for their transport properties alone. The simulation images are free of the inactive history and other ambiguous influences that affect laboratory visualizations. In addition, the simulation database allows mapping regions of any desired quantity, both independently and in combination with others. Finally, the simulated turbulence is exactly repeatable, and events may be repeatedly traced both forward and backward in time.

For turbulence, the challenge of visualization is to extract only the information necessary for understanding, and to display the information in a form which conveys the essential physics, but is less complex than the turbulence itself. Some of the techniques developed during the present study are described further in Robinson and Hu (1989).

7.2 Data Flow and Hardware

All of the analysis reported herein was performed on computers at NASA Ames Research Center. To access the results of Spalart's simulation at a particular time-step, the simulation code was run for one iteration from an instantaneous flow-field at an existing time-step. The results of each time step are stored permanently in a condensed form which consists of the spectral expansion coefficients for the velocity field. The code requires about 6 Cray XMP CPU minutes to step through

$\Delta t^+ = 3$, and then to transform the flow-field into velocity, pressure, and vorticity field in real space. A single "restart" generally required from one to 20 hours of real time. 104 temporally sequential restart files (with $\Delta t^+ = 3$) are saved on Cray tape. Approximately 300 restart runs of the code were executed during the course of the present investigation.

Once reconstituted in real space, the turbulence data could be stored for processing on the Cray XMP, a DEC Vax 785 or a Silicon Graphics IRIS 3030 workstation. In all cases, this required selecting a subset of the database, which consisted of 6.58×10^7 words per time-step. For instance, the IRIS could handle only 1.4×10^6 words per file. To avoid long waits in the Cray XMP queue, real-space data was transferred over Ethernet lines to a Vax 785, and then written to Vax tapes. Approximately 60 Vax tapes of approximately 7 million words each were created. For graphical analysis, data was transferred via Ethernet from the Vax to the IRIS workstation. Various forms of data on the IRIS was stored on tape cartridges to free up disk space. Approximately 150 IRIS tapes of about 10 million words each were written. Statistical analyses were performed on the Cray, Vax, and IRIS, two-dimensional plotting was done on the Vax, and color graphics were done on the IRIS.

A flowchart for the creation of a single image of the numerical turbulence is shown in Fig. 7.1. Each image produced in the current project required from 2 to 45 minutes of computer time in addition to the time required to run the simulation code on the Cray. Approximately 2000 images were created.

The Silicon Graphics 3030 IRIS workstation used for the graphical analyses and image generation utilizes the Motorola 68020 32-bit processor, with many graphics routines (hidden surface removal, polygon shading, vector rendering) resident in hardware. The screen has 1024 x 780 resolution, 16.7 million colors and eight bit-planes. Eight Mbytes of dynamic RAM are available, and two custom 380 Mbyte hard disks were installed for this project. Images created on the IRIS were generally stored in RGB format, which is a bit-map of the screen image, compressed with a simple run-length encoding scheme. Hardcopy output of the images was generated with Dunn 360, Focus 4566, and Dunn 632 film recorders (for Polaroid, 35 mm, 8x10, and 16mm movie formats), as well as Seiko CH5312 and Tektronix 4693DX color printers.

In addition to the IRIS, a Stellar GS1000 graphics workstation was used to create volume-rendered images of the numerical turbulence. This machine is of a new class of "graphics supercomputer," with 100 Mbytes of dynamic RAM, 2.5 Gbytes of disk storage, and vastly improved graphics performance over the IRIS 3030.

7.3 Graphical Analysis: Software Techniques and Tools

7.3.1 Types of Data Display

Each variable in the numerical turbulence database is strongly four-dimensional, with fluctuations in three spatial dimensions and time. Accordingly, a wide variety of graphical techniques were employed to illuminate various aspects of the turbulence structure. These were applied to several types of data configuration:

2-D: Single or multiple slices of the computational volume along Cartesian planes.

2-D plus time: Slices at several time-steps combined in an animation.

3-D: Subvolumes of the computational domain.

3-D plus time: Subvolumes of the computational domain at several time-steps, either as a stationary (Eulerian) control volume, or as a volume moving with the flow at some specified convection velocity.

Scalar fields (such as pressure and energy) and vector fields (such as velocity and vorticity) in the turbulence database require different display techniques (Fig. 7.2). In two dimensions, scalars are generally represented by contour lines or color fills in slices through the computational volume. Two-dimensional scalar data may also be displayed as a “carpet plot,” in which the third spatial dimension is used to represent the local magnitude of the scalar. The height (and usually color) of the sheet-like surface in a carpet plot corresponds to the scalar magnitude. Three-dimensional scalar data can be displayed as stacked two-dimensional contour lines or sheets, as iso-value three-dimensional surfaces, or as volume-rendered “clouds.”

An iso-value surface is the three-dimensional extension of a contour line, in that the value of the scalar is constant at each point on the surface. The surface is rendered as a construction of rectangular or triangular tiles that are shaded according to light-source location, viewer location, and a reflectance model. For the current work, the large size of the datasets to be rendered (up to 150,000 polygons per scene) dictated the use of very rudimentary rendering algorithms. Thus, single light-sources were used, which were co-located with the viewpoint, and flat-surface shading was employed. Gouraud or Phong shading, which produces a smooth-shaded surface by interpolating the light intensity between neighboring polygons, was not used extensively due to the excessive computation time required to sort the polygons. On the other hand, the fine spatial resolution of the simulation provides fairly smooth surfaces for most scalar quantities, so the flat-shading of the polygons does not reduce the information available to the viewer.

Vector quantities (e.g. velocity, vorticity, gradients of scalars) may be represented in two dimensions as projections of vectors (arrows), which may be enhanced by coloring according to the magnitude of any scalar quantity. Also, lines everywhere parallel to the two-dimensional projection of a vector field (streamlines for the velocity field, vorticity lines for the vorticity field) may be displayed, also with

the option of coloring with a scalar. Simulated passive, massless particles may also be released in the two-dimensional projection of a three-dimensional vector field to investigate temporal mass transfer characteristics and to compare with experimental flow visualizations. In three dimensions, all of these techniques may be used, although scene complexity generally requires some compromise such as viewing three-dimensional vectors in a two-dimensional data plane, or restricting the length of the integration path for streamlines. For inherently three-dimensional data such as the numerical turbulence, stereo techniques (Sec. 7.5) greatly increase the volume-density of information that may be transferred to the viewer.

7.3.2 Data Preparation

For use on the IRIS workstation, the simulation results for a given time-step were written in a four-dimensional array by the Cray and then transferred through the Vax to the IRIS. The data array was configured $Q(I, J, K, N)$, where I, J, K are the x, z, y indices, respectively, and N specifies one of the seven stored flow variables, $u, v, w, p, \omega_x, \omega_y$, and ω_z . The spatial location of each node in the computational grid was written in three arrays, $X(I, J, K)$, $Y(I, J, K)$, and $Z(I, J, K)$.

Mean values of the seven basic variables were averaged over the x - z plane for each y -value, using many time-steps, and then stored in a permanent file.

The graphical software (EDDY) used on the IRIS workstation could handle data for 200,000 grid points of the turbulence simulation, which is only about 2% of the computational domain. This limitation required studying the simulation database in many subsections, and either averaging the results from each, or piecing together images into a mosaic. Three basic subset types were chosen for most analyses: (1) x - z slice of the computational domain, 384×288 ; (2) x - y slice of the computational domain, 384×85 ; (3) 3-D subvolume of the computational domain, $67 \times 55 \times 50$. For some of the subvolumes, workstation memory limitations required averaging every two data points in the z -direction for graphical analysis (but not for the simulation), resulting in a graphical resolution in the spanwise direction of $\Delta z^+ \approx 8.5$.

7.3.3 EDDY

The main software tool utilized for the present study was an interactive graphics program on the IRIS, called EDDY. This program evolved during the course of the project, and is essentially a modification of PLOT3D, which was written for the graphical analysis of CFD output files by P. Buning at Ames. Another modification of PLOT3D called TURB3D was developed by P. Spalart and Buning, and this was also used in the development of EDDY.

EDDY reads the data and grid files described in Sec. 7.3.2 and enables the user to plot contour lines, contour surfaces, vectors, streamlines, or vorticity lines in two or three virtual dimensions. The resulting image may be displayed on the

screen or written to a file as a display list of polygons and/or vectors for later use by GAS (Sec. 7.3.4). When displayed on the screen, the object may be manipulated in screen space with a mouse, which allows separate control of orientation, lateral and vertical placement, and size. The specialized graphics hardware of the IRIS permits manipulation of displayed objects fast enough to be considered real-time, at least for relatively small sets of data. For surfaces requiring several thousand polygons, the rotation rate was too slow to be useful, and so animations were made on film or video. The ability to interactively rotate the complex 3-D shapes of various turbulence structures has proven to be one of the key advantages of graphical analysis of turbulence data.

In EDDY, the user may specify the color and transparency of surfaces, and the color, thickness, and line type (solid, dash, etc.) of vectors. In addition, the vector functions (vectors, streamlines, and vorticity lines) may be colored according to the local magnitude of any scalar.

Features of EDDY include:

- Use of global (averaged over many time-steps) mean quantities for the computation of fluctuating quantities.
- 104 various scalar and vector functions to choose from.
- Run-time specification of convection velocity of reference frame.
- Calculation of circulation Γ in all three Cartesian planes.

The scalar functions available for plotting in EDDY are as follows:

- Instantaneous velocities u, v, w .
- Fluctuating velocities u', v', w' .
- Instantaneous vorticities $\omega_x, \omega_y, \omega_z$.
- Fluctuating vorticities $\omega'_x, \omega'_y, \omega'_z$.
- Instantaneous and fluctuating pressure, p and p' .
- Instantaneous and fluctuating velocity magnitude, $(u^2 + v^2 + w^2)^{1/2}$.
- Instantaneous and fluctuating vorticity magnitude, $(\omega_x^2 + \omega_y^2 + \omega_z^2)^{1/2}$.
- Fluctuating velocity magnitude in the $x - y$ plane, $(u'^2 + v'^2)^{1/2}$.
- Fluctuating velocity magnitude in the $x - z$ plane, $(u'^2 + w'^2)^{1/2}$.
- Fluctuating velocity magnitude in the $y - z$ plane, $(v'^2 + w'^2)^{1/2}$.
- Fluctuating velocity products, u'^2, v'^2, w'^2 .
- Shear products, $u'v', u'w', v'w'$.
- $u'v' \frac{\partial \bar{U}}{\partial y}$.
- Quadrant-split $u'v'$.
- Quadrant-split $u'w'$.
- Quadrant-split $v'w'$.
- Streamwise VITA kernel function for u' (normalized short-space variance), with run-time input of integration distance.

- Streamwise VITA kernel function for v' (normalized short-space variance), with run-time input of integration distance.
- Streamwise VITA kernel function for w' (normalized short-space variance), with run-time input of integration distance.
- Streamwise VITA kernel function for p' (normalized short-space variance), with run-time input of integration distance.
- $u'p', v'p', w'p', \omega_x p', \omega_y p', \omega_z p'$.
- All elements of the instantaneous deformation tensor, $\partial u_i / \partial x_j$.
- All elements of the fluctuating deformation tensor, $\partial u'_i / \partial x_j$.
- Streamwise pressure gradient, $\partial p / \partial x$.
- Spanwise pressure gradient, $\partial p / \partial z$.
- Pressure gradient magnitude, $((\partial p / \partial x)^2 + (\partial p / \partial z)^2)^{1/2}$.
- Total kinetic energy, $u^2 + v^2 + w^2$.
- Turbulence kinetic energy, $u'^2 + v'^2 + w'^2$.
- Entrainment function: $v < 0$ where $|\omega| \approx 0$.
- Phase space functions, P, Q, R .
- Instantaneous dissipation, $\nu u'_{i,j}(u_{i,j}u_{j,i})$.
- Homogeneous dissipation, $\nu u'_{i,j}u'_{j,i}$.
- Circulation in $y - z$ plane, Γ_x .
- Circulation in $x - y$ plane, Γ_z .
- Second invariant of deformation tensor, $u_{i,j}u_{j,i}$.

Vector and integrated functions available in EDDY are:

- Three-dimensional instantaneous velocity vector, \vec{u} .
- Three-dimensional fluctuating velocity vector, \vec{u}' .
- Three-dimensional instantaneous vorticity vector, $\vec{\Omega}$.
- Three-dimensional fluctuating vorticity vector, $\vec{\omega}'$.
- Two-dimensional instantaneous velocity vector in the $x - y$ plane, \overrightarrow{uv} .
- Two-dimensional fluctuating velocity vector in the $x - y$ plane, $\overrightarrow{u'v'}$.
- Two-dimensional fluctuating velocity vector in the $x - z$ plane, $\overrightarrow{u'w'}$.
- Two-dimensional fluctuating velocity vector in the $y - z$ plane, $\overrightarrow{v'w'}$.
- Two-dimensional pressure gradient vector in the $x - z$ plane, $\overrightarrow{\frac{\partial p}{\partial x} \frac{\partial p}{\partial z}}$.
- Two-dimensional instantaneous velocity vector in the $x - y$ plane, as viewed from a moving reference frame with run-time specified convection velocity: $\overrightarrow{(u - U_c)v}$.
- Streamlines.
- Vorticity lines.

7.3.4 GAS

One limitation of EDDY is its inability to simultaneously display more than one quantity. Where this capability was required (the usual case), the display lists for each EDDY function were written to disk in a metafile format consistent with the Ames ARCGRAPH standard. These graphical objects were then accessed and rendered by a program called GAS (Graphics Animation System), which was written by F. Merritt and G. Bancroft of Sterling Software at Ames.

GAS allows the simultaneous display of any number of objects, including surfaces, lines, and vectors. The objects are assembled in 3-space, and hidden surface removal is executed. The result may be interactively manipulated (at least for small scenes) with a mouse, as in EDDY. GAS allows the creation of on-screen animations by saving the transformation matrices of “keyframes” identified by the user, and then interpolating (linear or spline) the matrices over a number of intermediate steps to produce a smooth animation. Each step is displayed on the screen or recorded on film or video (see Sec. 7.4).

Images generated in GAS could be fairly large, using up to 9 Mbytes of display-list memory per scene. Since only about 1/17 of the instantaneous turbulent boundary layer could be loaded into the IRIS at one time, many images were created in segments, and then patched together in hardcopy form or as reduced raster images. Each such “billboard” of the entire computational domain at a single time-step represented up to 135 Mbytes of graphical display-list data.

Both EDDY and GAS screen images could be saved as an RGB file, which is a compressed screen bit-map. These raster images could then be edited and enlarged with PIXEDIT, written by D. Choi at Ames.

7.4 Animations

One of the main objectives of the present study was to investigate the temporal evolution of various structural features, especially the near-wall production processes. Although numerically-simulated turbulence has been available for a decade now, very little has been learned about the details of turbulence dynamics due to the time, effort, and logistical requirements for producing animations of the simulated data.

For this project, the large size of individual graphical realizations generally precluded on-screen animations, so time evolutions were recorded one by one onto 16mm film or videotape. In most cases, the temporal evolution of a segment of simulated flow could be studied only after film/video recording, so film and video animations functioned as a front-line research tool (Level 1 visualization).

Video recording was done from GAS on an Abekus A62 digital video editing system linked to a Silicon Graphics IRIS 4D/GT workstation. This system can record up to 3000 frames of NTSC video on digital random access disk, and can be played back interactively with a trackball (for repetitive viewing of selected

sequences). Sequences were edited digitally on the Abekus and then recorded to 3/4" videotape for post-production. This process was relatively rapid, since Abekus recording is done in real-time; most of the time is consumed in reading the display files from IRIS tape and rendering the images. Long sequences of large datasets required several hours each to record.

Film recording was done with a Dunn 632 film recorder with a 16mm camera, linked to another IRIS 3030 workstation. Movies were made either by generating a separate RGB raster file (≈ 0.5 Mbyte apiece) for each time-step of the animation, or by running GAS with a series of display-list files. This process was generally very slow, requiring up to 45 minutes of production time for each second of projected 16mm film. Considerable effort was expended on automating the animation process for both film and video.

The choice of film or video for the animation sequences was often difficult to make, and the two production processes could rarely be run in parallel. The advantage of film is superior color replication and resolution, and the ability to project on a large screen. Video is more easily edited and duplicated, is less fragile, and is more convenient for distribution purposes. In most cases, animations were recorded on video due to the faster production cycle. Copying from film to video or vice versa did not prove successful in terms of image fidelity.

Four basic types of animations were created during the present study:

- 1) Rotation, pan, and zoom of a static (single time-step) segment of simulation data.
- 2) 2-D plane passing through a static segment of data, with contour lines or "carpet" surface displayed as a function of time.
- 3) 3-D stationary control volume (or 2-D slice) through which flow passes over time.
- 4) Convecting 3-D volume (or 2-D slice) moving with the flow at some downstream convection velocity.

A list of the various animations created during the project is included in Sec. 7.6.

7.5 Stereo Imagery

One of the most fundamental attributes of fluid turbulence is its highly three-dimensional character. In the numerically-simulated boundary layer, visual analysis of several types of complex 3-D surfaces within an instantaneous volume is greatly hindered by the mapping of the 3-D scene onto the 2-D surface of the CRT screen. For this reason, stereoscopic display techniques were developed to allow understanding of the complex topologies and spatial relationship between various structural elements of the flow.

Because of the difficulty in comprehending inherently three-dimensional processes in 2-D, stereo cinematography has also been used for the visualization of marker particles in laboratory turbulent boundary layers, notably by Praturi and

Brodkey (1978). This is the first usage of stereo for numerically simulated turbulence. For the present study, non-stereo viewing of the simulated turbulent flow-field was often overwhelmingly confusing, to the degree that stereo techniques became a virtual necessity for many of the visualizations. Because of its contribution to the end results of this investigation, the background and geometric principals of computer-generated stereo pairs will be described here. Further details are available in Robinson and Hu (1989).

7.5.1 Stereo Imagery

Stereoscopy (or stereopsis) is the phenomenon of simultaneous vision from two non-coincident points in which there is a perception of distance of objects from the viewer. In CFD visualization, the goal is to produce pairs of computer-generated images that mimic the views seen from two eyes. When viewed in stereo (one image to each eye), the image pair conveys depth as well as vertical and horizontal scene information to the viewer.

7.5.2 Stereoscopic Display Systems

In-depth discussions of various stereoscopic display systems can be found in the literature (e.g. Lane, 1982; Hodges and McAllister, 1985). In the present study, a time-multiplexed, liquid-crystal, shutter-based stereo system was used for on-screen visualization of flow structures in the numerical turbulence databases. This system employs electro-optical switching techniques for displaying right and left image pairs sequentially. The image pairs are synchronized with a shutter device worn over the eyes so that each eye sees only the image intended for it. The liquid-crystal shutter consists of front and rear polarizers with a liquid-crystal Pi cell in between. The front and rear polarizers are 90° out of phase and are oriented at 45° with respect to the electrical field applied to the Pi cell. The liquid-crystal Pi cell is used as a half-wave retarder. As a result, light transmitted through the front polarizer is rotated 90° in phase, and can pass through the rear polarizer if enough voltage has been applied. When no voltage is supplied, the assembly acts as a closed shutter. Although the liquid-crystal shutter tends to reduce the total light transmission, this stereoscopic system provides high quality images.

Stereo image pairs are generated in hardcopy form with the graphics workstation and associated film recorder equipment. Common hardcopy types are paper stereo pairs, color 35 mm slides, and 16 mm movies. Paper stereo pairs (such as Fig 7.8) are generally viewed with mechanical stereo viewers. Slides are conveniently viewed through hand held viewers, and may also be projected with two slide projectors onto a single screen. A polarizing filter is used over each projector lens, and the images are overlaid on a lenticular (non-beaded) movie screen. Movies require synchronized projection of both images which can be achieved either by filming both left and right views on the same film frame, or by the use of two separate films.

In the present study, two 16mm movie projectors with synchronized motors were used to display stereo animations of the numerically simulated turbulence. Two linear polarizers which are oriented 90° with respect to each other are mounted in front of each projection lens. Passive glasses with the left and right lenses linearly polarized 90° with respect to each other are used to view the image in stereo.

7.5.3 Depth Cues

Both monocular and binocular depth cues are responsible for the perception of three-dimensional information from computer-generated, two-dimensional images. Shading, perspective, hidden-line and hidden-surface removal, modeling transformation, texture mapping, and motion parallax are examples of monocular depth cues commonly used. Parallax provides the brain's fusion of the slightly different left and right viewpoints to form stereoscopic images. Parallax, accommodation, and convergence (defined below) comprise the most important binocular depth cues. Although stereopsis is possible even without any monocular cues, the interpretation of a three-dimensional scene is greatly enhanced by adding monocular cues and animation to stereo displays.

Parallax, which determines where the images appear to be, is the most important consideration when composing stereoscopic views for projection on a movie screen or CRT display. Parallax is defined as the distance measured between corresponding left and right image points. The corresponding left and right image points are often called conjugate or homologous points. In principle, there are three different types of parallax, namely, zero parallax, positive parallax, and negative parallax, as shown in Figures 7.3, 7.4, and 7.5, respectively.

In the case of zero parallax, the homologous image points coincide and these images appear to be on the plane of the screen. As illustrated in Fig. 7.4, positive parallax will produce images which appear to be behind the CRT screen. Such an image is said to be in CRT space. In case of negative parallax, the image and eye points are crossed over as shown in Fig. 7.5. Graphical objects with negative parallax will appear to be in the viewer space (the space between the viewer and the plane of the screen).

In essence, computer-generated stereoscopic images are simulations of the physical world as observed by the human visual system. Therefore, any display process which departs from the usual perception of the real world should be avoided. For example, it is important to have only horizontal parallax. Vertical parallax will usually cause viewer discomfort, especially in animated sequences. In addition, the horizontal parallax should not greatly exceed the interocular separation, which is approximately 2.5 inches. Excessive horizontal parallax will cause the axes of the viewer's eyes to diverge, which does not normally occur in the real world.

Accommodation (also known as focus) and convergence are other important binocular depth cues. When looking at an object in three-dimensional space, the

eyes are focused (accommodated) as well as converged on the object. When viewing the computer-generated stereoscopic images, the eyes remain focused at the plane of the CRT screen while the eyes converge as if the images are at various distances. To reduce the impact of this departure from habitual accommodation/convergence relationship, it is usually best to keep the value of parallax as low as possible.

7.5.4 Stereoscopic Techniques

The geometrical foundations of the two techniques employed in the current study to generate stereo pairs will be reviewed here. Additional methods are described in Baker (1987) and Hodges et al (1988).

Method A

In the first method (Method A), the left eye image is generated by rotation about the vertical axis with respect to the right eye image. In the following, $[x \ y \ z]$ denotes the Cartesian coordinates of some point P in space. Assuming homogeneous coordinates (see Robinson and Hu, 1989), the transformation for the left eye can be expressed as

$$[x_{ls} \ y_{ls} \ z_{ls} \ w] = [x_r \ y_r \ z_r \ 1] M_l,$$

where M_l is a 4x4 transformation matrix.

As shown in Fig. 7.6, R is the distance from the center of rotation to the eye point, which is at the origin. d is the distance between the eye point and the projection plane. The matrix M_l is composed of a translation along the z axis a distance $-R$, followed by a rotation about y axis, followed by another translation along the z axis a distance R , and finally a perspective projection. Thus, if we let

$$M_1 = \begin{pmatrix} 1 & 0 & 0 & 0 \\ 0 & 1 & 0 & 0 \\ 0 & 0 & 1 & 0 \\ 0 & 0 & -R & 1 \end{pmatrix}$$

= translation along z axis by $-R$

$$M_2 = \begin{pmatrix} \cos\theta & 0 & -\sin\theta & 0 \\ 0 & 1 & 0 & 0 \\ \sin\theta & 0 & \cos\theta & 0 \\ 0 & 0 & 0 & 1 \end{pmatrix}$$

= rotation about y axis by θ

$$M_3 = \begin{pmatrix} 1 & 0 & 0 & 0 \\ 0 & 1 & 0 & 0 \\ 0 & 0 & 1 & 0 \\ 0 & 0 & +R & 1 \end{pmatrix}$$

= translation along z axis by $+R$

$$M_4 = \begin{pmatrix} 1 & 0 & 0 & 0 \\ 0 & 1 & 0 & 0 \\ 0 & 0 & 1 & 1/d \\ 0 & 0 & 0 & 0 \end{pmatrix}$$

= perspective transformation,

then the transformation matrix M_l is

$$M_l = M_1 M_2 M_3 M_4$$

$$= \begin{pmatrix} \cos\theta & 0 & -\sin\theta & -\sin\theta/d \\ 0 & 1 & 0 & 0 \\ \sin\theta & 0 & \cos\theta & \cos\theta/d \\ -R\sin\theta & 0 & -R\cos\theta + R & \frac{R-R\cos\theta}{d} \end{pmatrix}.$$

Since the right eye view is un-rotated, M_r involves only the perspective transformation:

$$M_r = M_4 = \begin{pmatrix} 1 & 0 & 0 & 0 \\ 0 & 1 & 0 & 0 \\ 0 & 0 & 1 & 1/d \\ 0 & 0 & 0 & 0 \end{pmatrix}.$$

Now, since

$$[x_{ls} \ y_{ls} \ z_{ls} \ w] = [x_r \ y_r \ z_r \ 1] M_l,$$

and

$$[x_{rs} \ y_{rs} \ z_{rs} \ w] = [x_r \ y_r \ z_r \ 1] M_r,$$

it can be shown that

$$x_{ls} = \frac{[x_r \cos\theta + z_r \sin\theta - R\sin\theta]}{[-\frac{x_r \sin\theta}{d} + \frac{z_r \cos\theta}{d} + \frac{R(1-\cos\theta)}{d}]}$$

$$y_{ls} = \frac{y_r}{[-\frac{x_r \sin\theta}{d} + \frac{z_r \cos\theta}{d} + \frac{R(1-\cos\theta)}{d}]}$$

$$x_{rs} = \frac{x_r}{z_r/d}$$

$$y_{rs} = \frac{y_r}{z_r/d}$$

The horizontal parallax, H , is equal to $x_{ls} - x_{rs}$. Thus,

$$\begin{aligned} H &= x_{ls} - x_{rs} \\ &= \frac{d(x_r \cos \theta + z_r \sin \theta - R \sin \theta)}{[z_r \cos \theta - x_r \sin \theta + R(1 - \cos \theta)]} - d(x_r/z_r). \end{aligned}$$

Similarly, the vertical parallax, V , is equal to $y_{ls} - y_{rs}$. Thus,

$$\begin{aligned} V &= y_{ls} - y_{rs} \\ &= \frac{dy_r}{[z_r \cos \theta - x_r \sin \theta + R(1 - \cos \theta)]} - d(y_r/z_r) \\ &= \frac{dy_r z_r (1 - \cos \theta) + dy_r x_r \sin \theta - dy_r R (1 - \cos \theta)}{z_r [z_r \cos \theta - x_r \sin \theta + R(1 - \cos \theta)]}. \end{aligned}$$

Note that the rotational method (Method A) will produce a vertical parallax (V) which is usually undesirable in stereoscopic viewing. In practice, the angle of rotation used is between 2 and 7 degrees. For these rotation angles, the vertical parallax is generally small. Although a small amount of vertical parallax may be acceptable in static viewing, it may cause viewer discomfort in animations. Another characteristic of Method A is that the user does not have direct control over the parallax, as shown in the equation. Nevertheless, Method A is a simple and straightforward technique for generating stereoscopic pairs.

Method B

An alternative method (Method B) for generating stereo image pairs involves a lateral perspective shift along the horizontal axis (the x-axis as shown in Fig. 7.7), along with a shift of the resulting images relative to each other.

If we let

$$\begin{aligned} M_5 &= \begin{pmatrix} 1 & 0 & 0 & 0 \\ 0 & 1 & 0 & 0 \\ 0 & 0 & 1 & 0 \\ -e/2 & 0 & 0 & 1 \end{pmatrix} \\ &= \text{translation along x axis by } -e/2 \end{aligned}$$

$$\begin{aligned} M_6 &= \begin{pmatrix} 1 & 0 & 0 & 0 \\ 0 & 1 & 0 & 0 \\ 0 & 0 & 1 & 1/d \\ 0 & 0 & 0 & 0 \end{pmatrix} \\ &= \text{perspective transformation} \end{aligned}$$

$$M_7 = \begin{pmatrix} 1 & 0 & 0 & 0 \\ 0 & 1 & 0 & 0 \\ 0 & 0 & 1 & 0 \\ +e/2 & 0 & 0 & 1 \end{pmatrix}$$

= translation along x axis by $+e/2$,

then the transformation matrix of the perspective projection from the left view point can be expressed as

$$M_l = M_5 M_6 M_7$$

$$= \begin{pmatrix} 1 & 0 & 0 & 0 \\ 0 & 1 & 0 & 0 \\ +e/2d & 0 & 1 & 1/d \\ -e/2 & 0 & 0 & 0 \end{pmatrix}.$$

Similarly, the transformation matrix for the right view is

$$M_r = \begin{pmatrix} 1 & 0 & 0 & 0 \\ 0 & 1 & 0 & 0 \\ -e/2d & 0 & 1 & 1/d \\ +e/2 & 0 & 0 & 0 \end{pmatrix}.$$

After the perspective transformation, it can be shown that

$$x_{ls} = \frac{dx_0}{z_0} - \frac{de}{2z_0} + \frac{e}{2}$$

$$y_{ls} = \frac{dy_0}{z_0}$$

$$x_{rs} = \frac{dx_0}{z_0} + \frac{de}{2z_0} - \frac{e}{2}$$

$$y_{rs} = y_{ls} = \frac{dy_0}{z_0},$$

where $[x_0, y_0, z_0]$ are the coordinates of a point P_0 on the object being displayed.

If the resulting left eye image is displaced along the x-axis a distance S on the projection plane, x_{ls} takes the new value

$$x_{ls} = \frac{dx_0}{z_0} - \frac{de}{2z_0} + \frac{e}{2} + S.$$

In the jargon of computer graphics, S is called the viewport shift.

The horizontal parallax for Method B is computed by

$$H = x_{ls} - x_{rs} = e - \frac{de}{z_0} + S.$$

The vertical parallax for method B is zero:

$$V = y_{ls} - y_{rs} = 0$$

In the preceding equations, e is the interocular distance and is approximately 2.5 inches.

It is clear that Method B offers a way to produce image pairs with zero vertical parallax. Moreover, the viewport shift value S can be set by the user to control the horizontal parallax directly. With this control, one can put the stereo image wherever it looks comfortable to the viewers. An interesting case is when $e = 0$, and S equals a small positive value. The result is a non-stereo image that appears to be in CRT space (behind the surface of the CRT screen) rather than on the screen.

7.5.5 Effects of Varying Stereo Parameters

Using Method B (lateral perspective shift), one can vary the horizontal parallax to optimize the three-dimensional information conveyed to the viewer, while avoiding viewer discomfort. The eye point separation e generates different parallax for image points with different z values (after transformations) while the viewport shift S provides a uniform parallax. Some combination of these two parameters (usually determined through a few trials) will produce desirable stereo pairs. Fig. 7.8 illustrates the effect of different values of e and S . (Note that even black and white, low-resolution images can provide a significant amount of spatial detail if viewed in stereo.)

Figures 7.8a through 7.8c use a constant e value(1.1) while varying the viewport shift. The software generated for the present study produces positive parallax with a positive viewport shift. In Fig. 7.8a, the stereo image is in viewer space (between the eyes and the CRT screen), while in Fig. 7.8b, the image is in the vicinity of the screen. Stereopsis is nearly absent in Fig. 7.8c due to the reduction of parallax. It is also noted that the image in Fig. 7.8c exceeds the viewport due to large viewport shift values. The resultant clipping is undesirable and can cause confusion in depth cues. Therefore, the viewport shift should be chosen to limit clipping of the image.

Figures 7.8d through 7.8f use a constant viewport shift while varying the view point separation. Although the difference of the stereopsis between Fig. 7.8d and Fig. 7.8e is hardly noticeable, it is clear that Fig. 7.8d is in CRT space. In contrast, the image in Fig. 7.8f is well in the viewer space.

Fig. 7.8 demonstrates that the eye point separation and viewport shift determine both the stereopsis and the location of the image in space. It is generally

desirable to keep the image in the vicinity of the screen. In the animation sequences developed in the present study, this was achieved by using viewport shift values of approximately 60, and eye point separation values between 0.85 and 1.10, depending on the scene.

7.5.6 Stereo Summary

Although awkward to include in a bound volume, stereo pairs in the form of slides and polaroids have been used extensively to arrive at some of the conclusions and statistics to presented in later chapters. The technique is especially valuable for illustrating spatial relationships between different structures in the boundary layer. To help evaluate the spatio-temporal evolution of various structures, a number of stereo 16mm movies of the simulated turbulence passing through a stationary control volume were made.

7.6 Listing of Analysis Sets

Several sets of simulation data were stored for specific analysis purposes or animation sequences. The most productive of the analysis sets are listed below. Entries ending in "SET" are one or more slices or volumes of frozen data. Those ending in "SEQ" are sequential sets of data for use in animation sequences. In the table, subset types are numerically identified as follows:

- 1 Two-dimensional slice (384 x 288) in an x - z plane (top-view).
- 2 Two-dimensional slice (384 x 85) in an x - y plane (side-view).
- 3 Three-dimensional subvolume (67 x 55 x 50)
- 4 Other

For the animation sequences, the animation type is identified as:

- 1 Rotation or contour variation of static dataset.
- 2 2-D plane passed through static dataset.
- 3 Flow passing through stationary 3-D control volume.
- 4 Flow in 3-D control volume convecting downstream at U_c .

Name	Sub	Ani	Description
BSEQ	3	4	Volume convecting with vortical structure. $u', v', p', (u'v')_2, (u'v')_4$, and combinations. 41 time-steps.
CSEQ	3	3	Stationary control volume. $u', v', p', (u'v')_2, (u'v')_4, \omega $, TKE, and combinations. 41 time-steps.
DSEQ	1	3	Stationary plane at $y^+ = 15$.

- $u', v', (u'v')_2, (u'v')_4$, and combinations. 41 time-steps.
- FSET 3 - Five subsets surrounding $\pm v'$ pairs in $y^+ = 15$ plane.
 v', p' , and combinations. $t^+ = 96$.
- GSET 1 - Eight x - z planes at $y^+ = 0, 2, 7, 12, 15, 30, 100, 200$,
 $u', v', w', p', \omega_x, \omega_y, \omega'_z$, dissipation, TKE, $u'v', (u'v')_{1,2,3,4}$. $t^+ = 96$.
- HSET 1 - x - z plane at $y^+ = 12$ for $Re_\theta = 670$ and $Re_\theta = 1410$.
 $u', v', (u'v')_2, (u'v')_4$, and combinations. $t^+ = 96$.
- ISSET 1 - x - z plane at wall for underlay of volumes.
 τ'_w, p'_w . $t^+ = 96$.
- KSEQ 3 1 Step through pressure contour levels for single volume.
 $-p'$ surfaces. $t^+ = 96$.
- MSETA3 - Fifteen adjacent subvolumes covering almost entire computational domain.
 Billboards (top-views) of all quantities and combinations, in 3-D. $t^+ = 96$.
- MSETB3 - Same as MSETA, but with $t^+ = 0$.
- MSETC3 - Same as MSETA, but with $t^+ = 192$.
- MSETD3 - Same as MSETA, but with $t^+ = 288$.
- MSETE3 - Same as MSETA, but with $t^+ = 111$.
- NSEQ 2 3 Side-view of flow through x - y plane.
 $p', v', \omega'_z, (u'v')_{1,2,3,4}$, VITA contours. 41 time-steps.
- OSET 4 - Outer turbulent / non-turbulent interface of boundary layer.
 $|\omega| \approx 0$ surface. $t^+ = 96$.
- PSET 3 - Subvolumes with vortical arches identified in MSETA.
 $-p', (u'v')_2, (u'v')_4$ surfaces. $t^+ = 96$.
- QSEQ 1 3 Top-view of wall and $y^+ = 12$ planes.
 $p'_w, (u'v')_{2,4}$ at $y^+ = 12$. 41 time-steps.

- RSEQ 3 3 Near-wall shear layers in 3-D.
 $|\omega|$ surfaces. 41 time-steps.
- RSET 3 - Threshold sensitivity study. Many 3-D contour types.
 $-p', (u'v')_{2,4}$ surfaces, lines at various contour levels. $t^+ = 96$.
- SSEQ 4 1 Rotation of very large set to study vortical structure topology.
 $-p'$ surfaces. $t^+ = 96$.
- TSET 4 - Streamlines in 22 y - z planes for streamwise vortex stats.
Streamlines colored by p' . $t^+ = 90$ to 180 step 9.
- USEQ 4 3 Flow through double-size control volume to study vortex rollup.
 $-u', |\omega|, -p'$ surfaces. 20 time-steps.
- VSET 2 - u', v' vectors in 12 x - y planes for spanwise vortex stats.
Vectors. $t^+ = 90, 99, 108, 117, 126, 135, 144, 153, 162, 171, 180$.
- WSET 2 - Combined color fill and contour lines in x - y planes.
 $u', v', w', p', \omega_x, \omega_y, \omega_z$, dissipation, TKE, $u'v', (u'v')_{1,2,3,4}$. $t^+ = 96$.
- XSET 3 - 3-D Vortical structures from MSETA with bisecting x - y planes.
3-D $-p'$ surfaces, $u', |\omega|$ contours on bisecting plane. $t^+ = 96$.
- YSEQ 4 2 Carpet plot of u for y - z plane passing upstream.
 u carpet plot 3-D surface. 268 quasi-time-steps (positions).
- ZSEQ 4 2 Wall with end and side views to show heights of wall-shear.
 τ'_w, u' , 41 time-steps.

A number of less durable analysis sets were created during the course of the investigation. Several of the sets and sequences listed above (BSEQ, CSEQ, NSEQ, and the MSETs in particular) were used for a variety of different statistical and graphical analyses.

FLOWCHART FOR PRODUCING AN ANIMATION FRAME

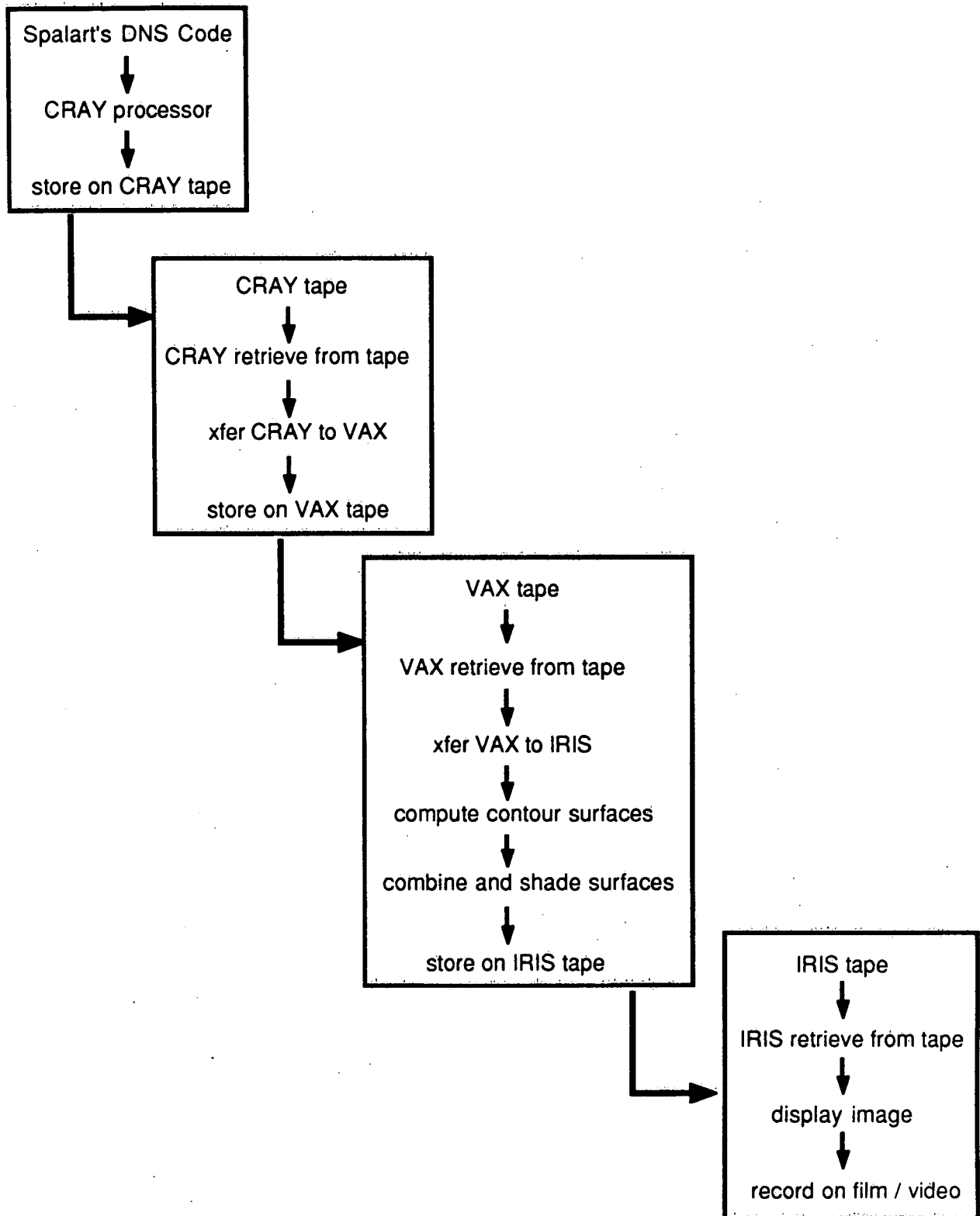


Fig. 7.1 Flowchart of steps required to produce a frame of computer animation.

Visualization Tools

	scalars	vectors
2D	contours	vector projections streamlines particles
2.5D	"carpet" plot	
3D	contour meshes surfaces volumes	vectors streamlines particles

Fig. 7.2 Graphical tools used to visualize various types of turbulence data.

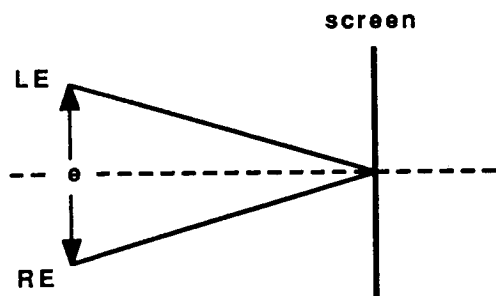


Fig. 7.3 Zero parallax (image appears to be on the screen).

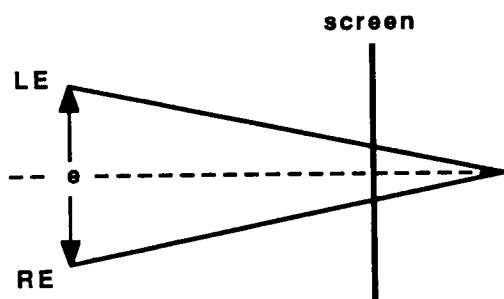


Fig. 7.4 Positive parallax (image appears to be behind the screen).

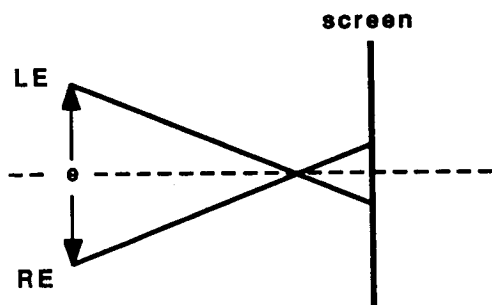


Fig. 7.5 Negative parallax (image appears to be in front of the screen).

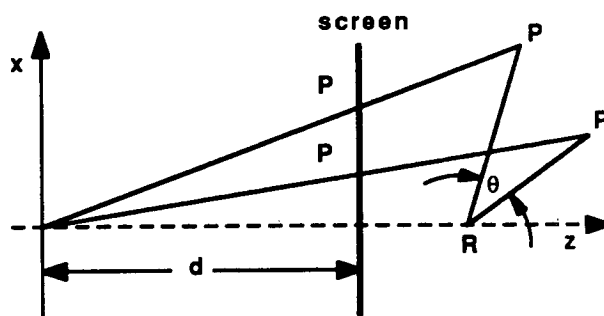


Fig. 7.6 Stereo projection by rotation about the vertical axis (Method A).

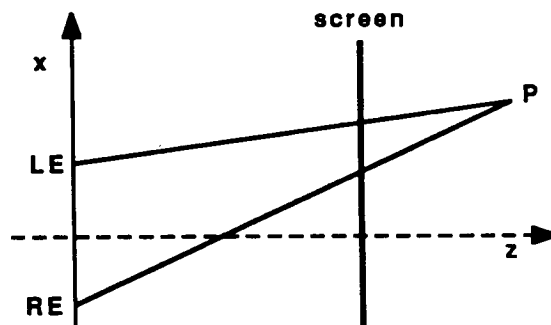


Fig. 7.7 Stereo projection by lateral perspective shift (Method B).

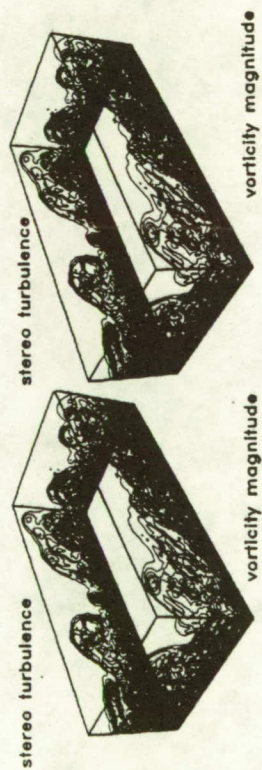


Fig. 6a. Interocular separation $e = 1.1$, viewport displacement $S = 20$.

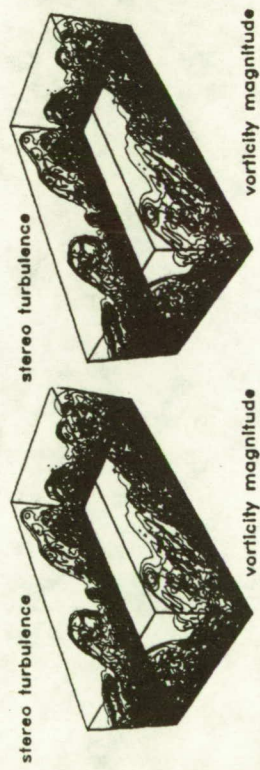


Fig. 6b. $e = 1.1, S = 60$.

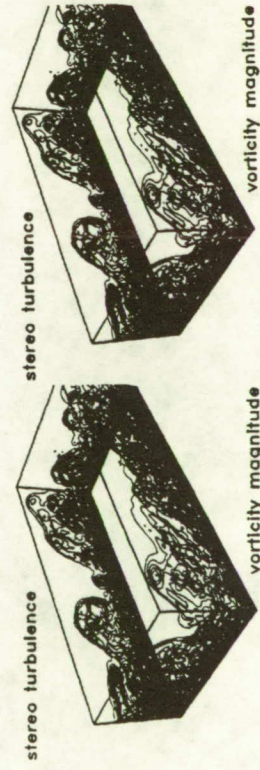


Fig. 6c. $e = 1.1, S = 100$.

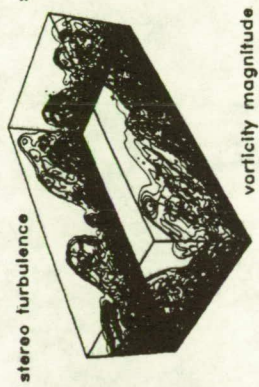


Fig. 6d. $e = 0.6, S = 60$.

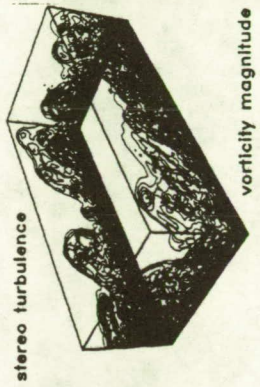


Fig. 6e. $e = 1.0, S = 60$.

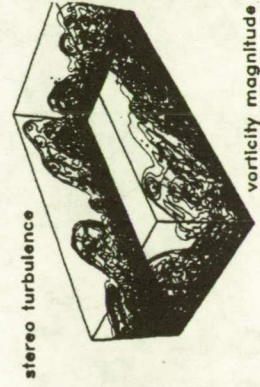


Fig. 6f. $e = 1.4, S = 60$.

Fig. 7.8 Effects of varying stereo parameters (use stereo viewer).

CHAPTER 8 - CHARACTER OF TURBULENCE IN 2-D PLANES

Although an essential characteristic of most turbulent boundary layer structures is their three-dimensionality, it is enlightening to compare various quantities in cross-sections of the instantaneous turbulent flow-field. This is analogous to the results of two-dimensional rakes of sensors in an experimental flow. In this chapter, contour maps of selected turbulence quantities will be discussed for Cartesian-plane slices through the simulated boundary layer, in an effort to summarize the spatial characteristics of the main quantities of interest. The knowledge thus gained will form a basis from which to explore the three-dimensionality of the structural features, which is the focus of the remaining chapters.

8.1 x - z Planes

In this section, contour plots of several quantities in x - z planes at various y^+ values are presented to provide a feel for the spatial character of the different turbulence quantities as a function of distance from the wall.

Although many quantities have been plotted over the course of the study, twelve are chosen as a representative sample for this chapter. The quantities plotted in Figs. 8.1 - 8.13 are u' , v , w , ω_x , ω_y , ω'_z , $u'v'$, $(u'v')_2$, $(u'v')_4$, $(u'v')_1$, $(u'v')_3$, p , turbulence kinetic energy $u'^2 + v'^2 + w'^2$, and instantaneous dissipation $2\nu s'_{ij}s'_{ij}$ (see Sec. 8.1.1.7). For each variable, contour planes are plotted at $y^+ = 7, 15, 30, 100, 194$ (recall that $\delta^+ \approx 300$ for this boundary layer). Approximately 16 contour levels are plotted for each variable; the contour values are given in the respective figure captions. To facilitate comparison, the same contour values are used in all y^+ planes. All positive values are plotted in “warm” colors, ranging from red to yellow to white for increasingly positive contour values. Negative contours are plotted in “cool” colors, ranging from blue to cyan to green for increasingly negative contour values. In the figures, the largest (outside) contour lines correspond to the contour values nearest zero. These will be red for positive, blue for negative. The innermost contour lines correspond to local peaks in the magnitude; white for positive and green for negative. Occasionally, “holes” are seen in the center of concentric contours. This is due to the value of the quantity exceeding the highest (or lowest) assigned contour value.

8.1.1 Same Quantity at Several y^+ Values

In this section, the variation of the twelve selected quantities with y^+ are examined. The area shown in figures 8.1 - 8.13 is a small subsection of the computational domain, measuring 3000 by 400 viscous units in x and z , respectively. In the x -direction, each white grid line is separated by $500 \Delta x^+$. In the z -direction, each white line is separated by $100 \Delta z^+$. Each $x - z$ slice is taken at the same time-step, and is centered at the same $y - z$ location in the computational domain. This allows

estimates of y -direction variation to be made by overlaying the different y^+ planes. Planes for $y^+ = 2$ are not plotted in the figures for this section.

8.1.1.1 u' Contours in $x - z$ Planes

Fig. 8.1 shows instantaneous u' contours in $x - z$ slices of the simulated turbulent boundary layer. In the near-wall region, the expected streaky structure of u -velocity field is clearly evident. As expected from Kim et al's (1971) and Smith and Metzler's (1983) experimental visualizations, the streaky pattern is a dominant feature for $y^+ \leq 30$.

The low-speed regions (streamwise velocity less than the local mean) in the sublayer and buffer region of Fig. 8.1 are elongated and thin, in agreement with experimental observations. (Here and elsewhere in the paper, "local mean" refers to the long-time average over the entire computational $x - z$ plane). Streamwise coherence of single low-speed streaks in the sublayer often exceeds 1500 viscous lengths, with widths ranging from 20 to 80 Δz^+ . The streaky character of the instantaneous low-speed regions is somewhat more pronounced than shown by marked fluid in laboratory flows. This is because markers in low-speed streaks often lift away from the wall during ejections, leaving the remaining near-wall streak unmarked and invisible. However, the current results appear consistent with the wall-temperature data of Hirata and Kasagi (1979) in which continuous visualization at the wall was achieved using liquid crystals.

The high-speed regions in the sublayer (Fig. 8.1) are considerably less elongated than the low-speed regions. Streamwise lengths of high-speed regions rarely reach 1000 Δx^+ , and widths range from 40 to 110 Δz^+ . This difference in "streakiness" is to be expected, since high-speed fluid generally originates from outside the sublayer where the mean velocity gradient is milder and the flow is known to be less streak-like (Smith and Metzler, 1983). Experimental flow visualizations have not shown the character of high-speed regions clearly, since fluid markers introduced near the wall collect in the low-speed regions. Since high-speed regions in the sublayer are less elongated than the low-speed regions, the term "high-speed streak" is not used in the current study.

Another characteristic of low-speed streaks is shown in Fig. 8.2, which is an instantaneous plan-view of the boundary layer at $y^+ = 15$. The colored contours mark regions of significant value of the product $(-u')(w')$ and $(-u')(-w')$. This product may be considered a "streak-skewing" parameter, since it highlights low-speed streaks $(-u')$ that simultaneously exhibit spanwise motion $(+ \text{ or } - w')$. Such regions are potential formation zones for near-wall shear layers, as shown by Alfredsson et al (1988). The correlation may be termed $(u'w')_2$ and $(u'w')_3$, after the quadrants it occupies in the u', w' hodograph plane. The $(u'w')_2$ and $(u'w')_3$ contours in Fig. 8.2 display a vaguely "cross-hatched" pattern, suggestive of possible transverse propagation mechanisms near the wall. Swearingen and Blackwelder

(1987) have drawn parallels between this behavior and spanwise oscillations related to breakdown instabilities in curved-wall flows. A complete explanation for the spanwise motions of the low-speed streaks awaits further investigation.

8.1.1.2 v' Contours in $x - z$ Planes

Contours of v' in the five $x - z$ planes are shown in Fig. 8.3. In the buffer region ($7 \leq y^+ \leq 30$), v' contours exhibit a pronounced streamwise elongation. Continuous streaks of instantaneous vertical motion reach up 600 viscous lengths in x , but the general pattern is of elongated regions significantly shorter than the low-speed streaks at the same y -values. As expected from the peak of $-\overline{u'v'}$ in the buffer region, there is significant spatial correlation between $-u'$ and $+v'$ regions, and between $+u'$ and $-v'$ regions. (Note that the term “elongated” refers to the ratio of length to width rather than to the absolute length. Thus, near-wall v' regions are elongated, even though they are much shorter than the u' regions.)

Less expected is the narrow spanwise extent of significant vertical velocities in the buffer region. Contours of v' are only about $30 \Delta z^+$ wide at $y^+ = 7$, and $50 \Delta z^+$ wide at $y^+ = 30$, which is about half the width of the low-speed streaks at the same y -levels. Thus, wallward fluid in the area where most of the turbulence kinetic energy is produced takes the form of elongated, highly localized, narrow “jets.” This is a significant observation relevant to the question of the transfer of energy from the outer flow to the wall zone. The lack of broad, outer-scale regions of $-v'$ in the buffer layer suggests an indirect (at most) influence of the outer motions on the near-wall turbulence production processes. In addition, the elongated nature and instantaneous correlation between the u' and v' motions near the wall suggest that the same dynamical mechanism is responsible for both the near-wall streaky u' structure and the v' fluctuations and, hence, the Reynolds shear stress.

The $\pm v'$ regions in the buffer region, especially for $y^+ = 7$ and 15, display a strong tendency to occur in side-by-side pairs, which is suggestive of local quasi-streamwise vortices (see also Moin, 1987). This characteristic is explored in some detail within the vortex discussion, Sec. 9.4. In the outer region of the boundary layer, the v' regions broaden considerably and lose their streamwise elongation. Even then, the v' contours are more intermittent and less spread out than the outer-region u' contours.

8.1.1.3 w' Contours in $x - z$ Planes

Contours of w' are plotted in Fig. 8.4. In general, w' exhibits less intermittency and structure (recognizable repeating patterns) than either of the other two velocity components. The w' contours show a mild streamwise elongation for $y^+ \leq 7$, but to a lesser degree than either u' or v' . Contours in the buffer region extend 40 to 100 viscous lengths spanwise, and up to 300 in the streamwise direction. The impact of $-v'$ fluid on the wall would be expected to create near-wall $\pm w'$ motions through re-

direction of the fluid mass. Accordingly, there is a fair degree of correlation between regions of strong w' and v' at $y^+ = 7$, but this is less recognizable at $y^+ \geq 30$.

8.1.1.4 Vorticity Contours

Contours of ω_x, ω_y , and ω'_z are shown in Figs. 8.5, 8.6, and 8.7, respectively. Near the wall, ω'_x should be dominated by its $\partial w'/\partial y$ component, and indeed shows a strong resemblance (Fig. 8.5) to near-wall w' contours (Fig. 8.4). At $y^+ = 30$, ω'_x displays a moderate streamwise elongation, and is thus influenced mainly by its $\partial v'/\partial z$ component, since the w' field at that y -level is not elongated. As pointed out in early LES channel flows by Kim and Moin (1979), the near-wall streamwise vorticity does not display elongated contours with lengths comparable to the low-speed streaks, suggesting that the concept of long streamwise vortices alongside the streaks may be in error. For $y^+ \leq 30$, ω'_x contours are from 20 to 80 viscous lengths wide, and up to 300 in streamwise extent.

The well-defined streaky pattern of the near-wall u' field provides much larger values of $\partial u'/\partial z$ than $\partial w'/\partial x$, so ω'_y contours almost exclusively coincide with the edges of the highly-elongated u' regions for $y^+ \leq 30$. Since the regions of high velocity gradients between the streaks are narrower than the streaks themselves, the ω'_y -pattern is even streakier than the u' -field itself (Fig. 8.6). No additional structural features are implied by this, however.

The contours of ω'_z (Fig. 8.7) are dominated by the streaky u' field near the wall, as expected. The streamwise gradient of v' becomes important by $y^+ = 15$, making the ω'_z contours more spatially intermittent than the u' field for $y^+ \geq 15$.

In the outer region ($y^+ > 30$), all three vorticity contours are of limited extent, low instantaneous magnitude, and devoid of recognizable structure.

8.1.1.5 $u'v'$ Contours in $x - z$ Planes

Contours of $u'v'$ in the $x - z$ planes are plotted in Fig. 8.8. As is necessary for a negative value of $\overline{u'v'}$, most of the contours are negative (blue). The $u'v'$ contours display significant spatial intermittency and pronounced streamwise elongation for $y^+ \leq 30$. By definition, the $u'v'$ contours follow the v' contours closely. To study the $u'v'$ field in more detail, quadrants 2 and 4 are plotted in Fig. 8.9 and 8.10, and quadrants 1 and 3 are shown in Fig. 8.11.

In Fig. 8.9, $(u'v')_2$ motions (ejections) are plotted in blue, cyan, and green, while $(u'v')_4$ motions (sweeps) are drawn in red, yellow, and white. The most striking aspect of the contours of these shear-stress-producing motions is their narrow spanwise extent for $y^+ \leq 30$, which is inherited from both the u' and v' fields. Ejections are more elongated than sweeps because they arise from low-speed streaks, which are more elongated than high-speed regions in the buffer layer. Neither ejections nor sweeps, however, display the extended coherence of the low-speed sublayer streaks. Ejection motions are approximately $30 \Delta z^+$ wide and 100 to 300 Δx^+ long

at $y^+ = 7$, and $50 \Delta z^+$ wide by 150 to 600 Δx^+ long at $y^+ = 30$. The spanwise scale of sweeps is slightly larger than the low-speed streaks and the ejections, but their extent is still less than $80 z^+$ in the buffer region. Thus, sweep motions in the buffer zone are narrow and localized, rather than broad intrushes.

When strong ejections and sweeps are found in close proximity at a given time, they are often laterally associated in a side-by-side pair, following the pattern of the v field. This characteristic was also noted by Moin (1987) in simulated turbulent channel flow, and is evident in Fig. 8.9. Sweeps and ejections rarely follow each other closely in the streamwise direction, contrary to several published structural models. However, slight skewing of the sweep/ejection pair in the $x - z$ plane would cause a fixed probe to detect one followed closely in time by the other. Most single-point conditional sampling schemes do not allow for spanwise variations, so ensemble averages that show sweeps following ejections are to be expected, but are misleading for understanding instantaneous kinematics. The lateral proximity and similar shapes of $(u'v')_2$ and $(u'v')_4$ motions are consistent with the concept that quasi-streamwise vortices in the buffer region are intimately associated with the generation of $-\overline{u'v'}$. This idea is well-supported in the literature (e.g. Moin, 1987) and will be discussed further in Chapters 9, 10, and 11.

A close-up view of $(u'v')_2$ and $(u'v')_4$ motions in the $y^+ = 12$ plane is shown in Fig. 8.10. In the figure, red and yellow regions correspond to ejections, and blue and white regions are sweeps (the reverse scheme as that employed in Fig. 8.9, unfortunately). Instantaneous u', w' vectors are overlaid to illuminate the spanwise velocity field associated with sweeps and ejections. Blue sweep regions are seen to exhibit a diverging flow pattern, consistent with the expectation that wallward fluid is re-directed by the surface. Ejections often occur in regions of converging fluid, similar to a local separation line. These “separating” regions often exhibit pronounced flow convergence on only one side. The strongest spanwise motions appear to occur between spanwise-adjacent sweep/ejection regions, further supporting the existence and importance of quasi-streamwise vortices near the wall.

Contours of the anti-contributors to the Reynolds shear stress, $(u'v')_1$ and $(u'v')_3$ motions are shown in Fig. 8.11. The contour values (see Figure captions) are the same as used for Fig. 8.9. Quadrant 1 contours are blue and quadrant 3 contours are red. For the contour values plotted, the contours have limited extent throughout the boundary layer, with most about 50 viscous lengths wide and 150 long. The contours of $(u'v')_1$ and $(u'v')_3$ are elongated in the buffer region because their constituents are. The contours are highly intermittent for $y^+ > 30$.

8.1.1.6 Pressure Contours in $x - z$ Planes

Contours of static pressure p are plotted in Fig. 8.12. The most striking characteristic of the pressure field is its extent in the wall-normal direction, with nearly identical contours in adjacent $x - z$ -planes. The individual regions of high

and low pressure are conspicuously non-elongated, in agreement with experiment (Emmerling, 1973) and with previous simulations (Grotzbach, 1977; Moin and Kim, 1982). The pressure field throughout the buffer region is essentially equivalent to the wall pressure field, and consists of relatively large-scale fluctuations of 100 to 200 viscous lengths in both x and z . The length-scales of the wall-pressure fluctuations suggest that they are related to outer-scale motions, although the relationship is unclear. This issue is examined in more detail in Chapter 10.

Also noticeable in the near-wall pressure field is the tendency for high-pressure regions (red) to be rounded while low-pressure regions are often more convoluted and branched. Occasional regions of rapidly alternating high and low-pressure may be found (as at $x^+ \approx 450$), as observed experimentally by Thomas and Bull (1983) and by Johansson, Her, and Haritonidis (1987c). These high-amplitude pressure fluctuations may signify regions of dynamically active instabilities, as discussed in Chapter 12.

8.1.1.7 Dissipation Contours in $x - z$ Planes

The mean rate of viscous dissipation of turbulence kinetic energy may be described by a term from the TKE transport equation,

$$\epsilon \equiv 2\nu \overline{s'_{ij}s'_{i,j}} \quad (8.1)$$

where

$$s'_{ij} \equiv \frac{1}{2} \left(\frac{\partial u'_i}{\partial x_j} + \frac{\partial u'_j}{\partial x_i} \right) \quad (8.2)$$

To identify instantaneous locations in the flow in which significant contributions to ϵ are occurring, a fluctuating dissipation is defined as,

$$\epsilon' \equiv 2\nu s'_{ij}s'_{i,j} \quad (8.3)$$

For simplicity, the dissipation scalar was computed as a post-processing operation on the simulation database, using central differences for the spatial gradients. This effectively imposes a spatial filter on the dissipation field. A comparison between a dissipation field computed with first-order central differences and one computed with high-order spectral methods during execution of the simulation code is shown in Fig. 8.13a. The graphical comparison shows that the main effect of “filtering” is to reduce the magnitude of ϵ' , while the contour shapes remain relatively unchanged, other than a “smearing” of large gradients. A spatial filter of the type imposed also imparts a spatial phase shift to the contours. This phase shift amounts to a positional uncertainty in each contour line of at most one grid cell in each direction, which is tolerable for the analysis performed. Since the dissipation

field is studied from a qualitative, visual approach, the filtering effect does not alter any of the conclusions relating to its use. However, as a reminder of the filtered nature of the dissipation field, the subscript “f” will be appended to ϵ' .

Contours of ϵ'_f are plotted in Fig. 8.13b. The instantaneous dissipation function is highly intermittent and small-scale, as classical theory would suggest. The ϵ'_f contours in the buffer region are generally elongated in the streamwise direction, and are approximately 30 viscous lengths wide by 50 to 200 long. The pattern in Fig. 8.13b is strikingly similar to the contours for v' and $(u'v')_{2,4}$. In fact, the most common location for high dissipation in the buffer region is **between** side-by-side regions of $(u'v')_2$ and $(u'v')_4$, which corresponds to the core of the hypothesized quasi-streamwise vortex associated with the ejection/sweep pair. Further exploration of the three-dimensional ϵ'_f field will be made in Chapter 9.

8.1.1.8 Turbulence Kinetic Energy Contours

The instantaneous turbulence kinetic energy per unit volume ($u'^2 + v'^2 + w'^2$) is plotted for the six $x - z$ planes in Fig. 8.14. Since u' is the velocity component with the largest fluctuations, the TKE contours are closely similar to those of u' .

8.1.2 Various Quantities at Same y^+ Values

To facilitate comparison between the twelve quantities plotted in the $x - z$ planes, Figs. 8.16 through 8.21 consist of contours of each quantity plotted for the same data plane, for $y^+ = 2, 7, 15, 30, 100$, and 194. An identification key is provided in Fig. 8.15. The planar subsections are 1000 by 600 viscous lengths in the x and z directions, respectively. Recall that positive values are plotted in red, yellow, and white, while negative values are blue, cyan, and green.

Most of the important comparisons between quantities have been made in the previous section, but these points will be re-iterated:

- (1) For $y^+ \leq 15$, all of the plotted quantities are significantly elongated in the streamwise direction, except for the pressure field and possibly the w' and ω'_x fields.
- (2) $-v'$ motions, and therefore $(u'v')_4$ sweeps, are narrow in the spanwise direction ($\Delta z^+ = 30$ to 50), and are not broad (outer-scale) motions.
- (3) The pressure field fluctuations, especially $+p'$, extend for substantial distances in the wall-normal direction. Wall pressure fluctuations are generally large (100 to 200 viscous lengths), and rounded, with occasional regions of intense, quasi-periodic small-scale fluctuations (see, for example, the the upper right edge of the wall-pressure map in Fig. 10.10.1).
- (4) Instantaneous dissipation contours are small-scale and intermittent throughout the boundary layer. The region between side-by-side sweep/ejection pairs makes significant contributions to the dissipation of TKE.

- (5) Streamwise vorticity contours in the buffer region have an order of magnitude less streamwise coherence than the streaky u' field.

8.2 x - y Planes

Instantaneous side-view ($x - y$) slices through the simulated boundary layer provide an opportunity to qualitatively examine the effect of the mean velocity gradient directly and to display the large outer-scale structures simultaneously with the near-wall inner-scale structures. Side-view planes are commonly visualized in experiments using light-sheets, and the most common multi-sensor technique is the vertical hot-wire rake.

A key for the quantities plotted in Figs. 8.23 and 8.24 is provided in Fig. 8.22. Each of the side-view slices is 1350 viscous units in the streamwise direction by 635 in the wall-normal direction. The mean boundary layer thickness is $\delta^+ \approx 300$, so the figures show the instantaneous deviation of the boundary layer edge about δ and, to some degree, the potential velocity fluctuations beyond the edge of the rotational boundary layer fluid.

The rendering scheme used for the contours in Figs. 8.23 - 8.27 is slightly different than that used for the $x - z$ planes. The scalar values are represented by filled color contours to clearly identify the magnitude, while spatial gradients are made evident by the overlaid black contour lines. Zero values are white, while negative values are shown in cyan, blue, and black, in increasingly negative order. Positive contours range from yellow to red to black, similarly.

The observations described here are based on the study of many $x - y$ planes in addition to those shown as examples in the figures.

8.2.1 u' , v , and w in $x - y$ Planes

Contours for u' , v , and w are plotted in Fig. 8.23 a,b,c. Each of these figures is plotted using the same contour values to allow comparison of the relative fluctuation magnitudes.

The u' contour plot (Fig. 8.23a) displays a number of notable features that are typical of most randomly selected $x - y$ cuts in the simulation database. The u' contours are broad and large-scale in the outer region, generally occurring in streamwise-alternating regions of $+u'$ and $-u'$, with streamwise length-scales usually somewhat greater than wall-normal length-scales, though both are of order δ . Just to the right of center in Fig. 8.23a is an apparent transverse vortex, with $-u'$ (blue) below and $+u'$ (yellow) above the center. The vortex lies at $y^+ \approx 250$ ($y/\delta \approx 0.8$), and has a core diameter of $d^+ \approx 170$. This apparent vortex is evident in the contours of u' , v , ω'_z , p , and TKE.

The most notable feature of the u' field in many side-view planes is the existence of sloping interfaces between $+u'$ and $-u'$ regions. In the outer region, these interfaces often occur on the “backs” of large-scale motions which are capped

by bulges in the outer turbulent/non-turbulent interface. Some of these bulges are observed to span nearly the entire boundary layer. These large-scale shear-layer structures are examined in more detail in Chapter 10.

The near-wall u' -field displays a significantly “structural” character, with narrow, highly sloped fingers of $+u'$ and $-u'$ dominating the region in side-view. The interfaces between high and low-speed fluid form well-defined near-wall shear layers, which are also clearly evident in the ω'_z contours (Fig. 8.23f) and also in contours of the total instantaneous velocity, u . These near-wall shear layers are common below $y^+ \approx 80$; at least four are visible in the example figure. Throughout the layer, “compressive” interfaces ($+u'$ following $-u'$) tend to be sharp and narrow, while “extensive” interfaces tend to be more diffuse and ill-defined (as expected). Compressive interfaces make angles of approximately 10 degrees from the wall in the sublayer and buffer region, increasing to about 25 degrees at $y^+ \approx 50$. Extensive interfaces lie at somewhat steeper angles of 30 to 40 degrees beyond the buffer layer.

Contours for v (Fig. 8.23b) display highly localized fluctuation peaks, with smaller length-scales and fluctuation magnitudes than the u' field. However, in the outer layers, there occasionally exist regions in which there is significant anti-correlation between the u' and v' fields, giving rise to relatively large outer-layer volumes of $-u'v'$. The near-wall v signal does not display the highly organized, sloping nature seen in the u' and ω'_z fields (although there are occasional areas where sloping v structures are discernible). Thus near-wall shear layers are not uniquely associated with significant v motions. However, as will be seen in Chap. 10, near-wall shear layers often exhibit small, localized regions of intense v somewhere along their length. The apparent vortex detected in Fig. 8.23a above is also evident in the v field as an intense doublet of outward and wallward velocity.

The w field (Fig. 8.23c) is also spatially intermittent, but with smaller fluctuation magnitudes than either u' or v . The contours display a sloping nature throughout the boundary layer, more so than v or even u' . The slope of the w patterns in the outer region is slightly greater than for the u' contours: 35 to 60 degrees for w as opposed to 25 to 30 degrees for u' . This difference in slopes may be due to different organizing influences in the u' field and the w field. Sloping structures in u' are generally high/low-speed interfaces which lie at 10 to 30 degrees from the wall, depending on y -location. Sloping w patterns, on the other hand, may be associated with tilted vortical structures, which are commonly presumed to lie at about 45 degrees (Head and Bandyopadhyay, 1981). For example, the $\pm w$ pair seen near the streamwise midpoint of Fig. 8.23c may be associated with a vortex at about 50 degrees to the wall. Perhaps this vortex is related to the transverse vortex just above, forming a curved vortical structure. These ideas are explored further in Chapter 10.

There is also evidence that near the wall, the w field may be associated with the upstream face of near-wall shear layers, where high-speed fluid impacts and flows over and around low-speed fluid, generating transverse motion at the interface. This process may be responsible for the similarity between the near-wall u' and w fields.

Finally, it is expected that significant near-wall w motions will result from sweeps of wallward fluid “splating” on the surface, but this effect is not obvious in single $x - y$ planes.

8.2.2 ω'_x , ω_y , and ω_z in $x - y$ Planes

The velocity and vorticity fields are complementary representations of the same fluid flow. Thus, the vorticity field is not expected to provide different information than would a careful inspection of the velocity field, but may exhibit the various patterns attributed to structural features in a more easily recognizable form.

Contour plots for the three vorticity components contain spurious patterns in the region beyond the boundary layer, which are due to the contour algorithm in the graphics package trying to fit contours to data with very little variation in value.

All three vorticity fields are highly intermittent with small lengths scales, which is to be expected from a gradient field. Contours of ω_x (Fig. 8.23d) exhibit a strongly sloping character, especially near the wall. This behavior is inherited from the w field rather than the v field, which lacks the pronounced sloping patterns. In the wall region, ω_y is due largely to high/low-speed streak interfaces, which are not evident in side-view. There is some evidence of sloping near-wall structures in Fig. 8.23e, due to the w field, but in general, the ω_y structure is not significant from this view. The region identified above as a possible 50 degree vortex appears as a peak in ω_y in the figure.

The contours for ω'_z (Fig. 8.23f) are highly organized in the near-wall region, displaying compact sloping fingers of spanwise vorticity which correspond to the interfaces between $+u'$ and $-u'$ fluid. Contours of ω'_z are the clearest way to identify these near-wall shear layers, although they are also visible in contours of the total (mean plus fluctuating) spanwise vorticity field. A side-view comparison between ω'_z , ω_z , and the total vorticity magnitude, $|\omega|$, is shown in Fig. 8.23g; near-wall shear layers are clearly identifiable in all three plots.

The spanwise vorticity in the near-wall shear layers is generally of the same sign as the mean strain. Near-wall shear layers generally make angles of 10 to 20 degrees with the wall, with the angle becoming less shallow with distance from the wall. The transverse vortex identified in the u' and v' contours of Figs. 8.23a and b is evident in the ω'_z contours as an intense concentration of negative spanwise vorticity.

The magnitude of the instantaneous (mean plus fluctuating) vorticity vector is useful for identifying the outer limits of the turbulent region and for illuminating the distribution of vorticity throughout the boundary layer. Contours of $|\omega|$ are plotted

in Fig. 8.23h for the same data plane as the other side-view figures, but with a different color map. The color sequence for the contours is black, white, yellow, red, magenta, blue, and black as the total vorticity magnitude ranges from zero to its maximum value at the wall. In Fig. 8.23h, large bulges interspersed with deep ($y/\delta \approx 0.2$) irrotational crevasses are visible. These characteristics are in agreement with smoke-flow visualizations of Falco (1977) and conditional sampling results of Blackwelder and Kovasznay (1972), among others. Near the wall, the vorticity is highly localized, rather than spread throughout the wall region. Most of the near-wall vorticity magnitude is packaged into concentrated near-wall shear layers. Small concentrations of $|\omega|$ are found throughout the turbulent region, including within strong vortices, as shown by the contours at the location of the transverse vortex in the center of the figure.

8.2.3 $u'v'$, Ejections, and Sweeps in $x - y$ Planes

Contours of $u'v'$ in the side-view plane (Fig. 8.24a) show $u'v'$ peaks occurring intermittently in space, with a much higher incidence of $-u'v'$ than $+u'v'$, as is necessary for an equilibrium boundary layer. Slight evidence of near-wall sloping structures is visible in the $u'v'$ contours. To examine the $u'v'$ field in more detail, the shear product is split into quadrants and plotted separately.

Contours of $(u'v')_2$ (ejections) are shown in blues in Fig. 8.24b, while $(u'v')_4$ (sweeps) are red and yellow. Ejection and sweep motions are generally localized and are concentrated near the wall, as expected from the $-\overline{u'v'}$ profile. However, ejections and sweeps also occur intermittently in the outer regions, where they are often of larger size than the near-wall variety. In side-view planes, outer-region ejections and sweeps are often observed close together, most often with ejections just upstream of sweeps. This paired configuration is usually associated with a transverse vortex element, as schematically illustrated in Fig. 8.24g. Since transverse vortices generally move downstream at somewhat less than the local mean velocity, the $(u'v')_4$ region on the downstream side of the vortex is usually less intense than the $(u'v')_2$ region upstream.

Examples of transverse vortices with associated ejection/sweep couples are visible near the center and also at the left edge of Fig. 8.24b. Scrutiny of several $x - y$ planes suggests that most of the $(u'v')_2$ contributions to $-\overline{u'v'}$ in the outer region are associated with transverse vortices. No such generalization may be made about $(u'v')_4$ motions, however, and their source in the outer region is unclear from side-view slices. As discussed in Chapter 10, strong outer-region sweeps are generally associated with highly tilted “neck” vortices, which are clearly discernible only in three-dimensional viewing volumes.

Fig. 8.24c shows contours of $(u'v')_1$ (yellow, red) and $(u'v')_3$ (blues). The contributions from these quadrants are small and highly intermittent. A peak in $(u'v')_3$ is observed on the upstream lower side of the transverse vortex near the

center of the figure, in accordance with the kinematics of a transverse vortex in shear flow (Fig. 8.24g).

8.2.4 Pressure, Dissipation, and Turbulence Kinetic Energy in $x - y$ Planes

A side-view of the pressure field is shown in Fig. 8.24d. The contours tend to be large-scale and less intermittent than any of the velocity or vorticity functions. Although pressure structures are generally “tall,” they are rarely perpendicular to the wall. Instead, the pressure contours usually slope slightly downstream at 10 to 20 degrees from the vertical. As mentioned in the discussion of the top-view planes, the positive and negative pressure fluctuation fields possess somewhat different characteristics. In side-view, $+p$ regions are commonly centered on “compressive” $\pm u'$ interfaces. The impact of high-speed fluid upon obstructing lower-speed fluid apparently forms a convecting quasi-stagnation point with high pressure at the interface. This observation is in agreement with several experiments which have discovered high wall-pressure peaks beneath near-wall shear layers (e.g. Dinkelacker and Langeheineken, 1982; Kobashi and Ichijo, 1986; Johansson et al, 1987a). Several examples of high-pressure contours occurring at $\pm u'$ interfaces are visible in the figure. Low pressure regions are commonly centered on vortex cores, such the transverse vortex near the center of Fig. 8.24. This property of the low-pressure field will be exploited to help identify vortices in the next chapter.

Contours of “filtered” instantaneous dissipation ($\epsilon'_f \equiv 2\nu s'_{ij}s'_{ij}$) are plotted in Fig. 8.24e. Due to a disk crash during the analysis, the data plane shown is a different realization than for the rest of Fig. 8.24, so direct comparison cannot be made in this case. In general, ϵ'_f is highly intermittent in space, and is observed to peak within near-wall shear layers (where fluctuating gradients are high), and in the cores of relatively strong vortices (as judged by the associated velocity perturbations). The association between instantaneous dissipation and vortices is further explored in Section 9.2.3.

Turbulence kinetic energy contours (Fig. 8.24e) peak wherever significant velocity perturbations exist, which occur in the side-views within sweeps, ejections, and surrounding vortices.

8.3 $y-z$ Planes

End-view flow visualizations of experimental boundary layers and channels have provided useful observations of near-wall quasi-streamwise vortices, low/high-speed streak interfaces, and ejections (e.g. Smith and Schwartz, 1983). Sample $y - z$ plane slices through the simulated boundary layer are shown in Figs. 8.26 and 8.27, with the various quantities arranged according to Fig. 8.25. The contour values and color mapping are the same as for Figs. 8.23 and 8.24. Note that the dimensions of the end-view plane are considerably smaller than the $x - z$ or $x - y$ planes previously discussed.

As a reference for the contours plotted in Figs. 8.26 and 8.27, the instantaneous v', w' velocity vectors are plotted in the $y - z$ plane in Fig. 8.27c. (The $(u'v')_{1,3}$ contour plot has been omitted).

8.3.1 u' , v , and w in $y - z$ Planes

Fig. 8.26a shows end-view contours of $+u'$ in yellow and red, and $-u'$ in blues. Near the wall, the spanwise-alternating $\pm u'$ pattern of the streaky structure is evident, with an approximate spacing of 100 viscous lengths even for this small sample. Low-speed ($-u'$) fluid is not always confined to the near-wall region, and limited segments of low-speed streaks occasionally extend across the boundary layer. Similarly, high-speed ($+u'$) regions sometimes extend from the outer region to the wall. The $+u'$ and $-u'$ areas shown in the right half of Fig. 8.26a are cross-sections through a low-speed streak and a neighboring high-speed region. A quasi-streamwise vortex is located at the interface, as seen in the same location in Fig. 8.27d. The existence of vortices at the interface of high and low-speed streaks is common (see also Lian, 1987), but not universal. Quasi-streamwise vortices in the near-wall region nearly always have $+u'$ on the downward-rotating side and $-u'$ on the upward-rotating side, but many streak interfaces are devoid of vortices.

The v field (Fig. 8.26b) displays intermittent peaks of relatively limited extent. As noted in the top-views, regions of strong wallward velocity are not wide, outer-scale motions. Instead, the spanwise extent of $-v$ regions typically ranges from 30 to 80 viscous lengths. In the near-wall region, significant v motions are most often associated with quasi-streamwise vortices, as suggested by the $\pm v$ pairs in the top-view slices. In Fig. 8.26b, three vortices are visible near the wall, and each is flanked by regions of significant vertical motion.

Contours of w (Fig. 8.26c) tend to be elongated in the spanwise direction. Near the wall, this behavior may be due to wallward fluid spreading spanwise after arriving at the wall, but this is conjecture only. Quasi-streamwise vortices produce localized regions of spanwise motion above and below the vortex core, as seen in the vortices visible in Figs. 8.26c vs 8.27c.

8.3.2 ω'_x , ω_y , and ω_z in $y - z$ Planes

Streamwise vorticity contours (Fig. 8.26d) in the end-view plane are dominated by quasi-streamwise vortices and by wall-normal gradients of spanwise motions ($\partial w / \partial y$). These two types of ω_x are generally of distinctly different shape, with vortex cores showing rounded contours and $\partial w / \partial y$ occurring in thin regions stretched in the z -direction. A near-wall streamwise vortex often produces a vorticity concentration of one sign in the vortex core, and vorticity of the opposite sign between the vortex and the wall, due to the no-slip constraint on w at the surface. This effect is demonstrated for the vortex in the right side of Fig. 8.26, and is shown schematically in Fig. 8.26g, taken from Kim et al (1987).

As shown in the top-view slices, contours of ω_y are dominated by the high/low-speed streak interfaces; this can also be observed in Fig. 8.26e.

Spanwise vorticity fluctuations (Fig. 8.26f) are clustered near the wall and are due to near-wall shear layers formed at the interface of $+u'$ following $-u'$. At the wall, concentrations of ω'_z are found on the wallward side of low-speed streaks and high-speed regions. Beyond the sublayer, ω'_z concentrations are predominantly negative, as discussed for the side-views, and tend to form narrow arched shapes with spanwise extents similar to that of the u' streaky structure. These patterns are made when a near-wall shear layer is cross-sectioned by the $y - z$ plane, and show the curved nature of the shear layers and their limited spanwise extent. Thus, near-wall shear layers are highly three-dimensional structures.

8.3.3 $u'v'$, Ejections, and Sweeps in $y - z$ Planes

The $u'v'$ field shown in Fig. 8.27a confirms the spatially intermittent character noted in the top and side views. By comparing contours of $(u'v')_2$ and $(u'v')_4$ (Fig. 8.27b) with the velocity vector field below it, the association of quasi-streamwise vortices to the Reynolds shear stress in the wall region is evident. A strong ejection motion is located on the upward-rotating side of the vortex found in the right half of the figure, while a sweep motion is located on the wallward-rotating side. This picture corroborates the suggestion made by the side-by-side sweep/ejection pairs seen in the top-view slices in the buffer region.

A causal relationship between quasi-streamwise vortices and ejection/sweep motions is not established from instantaneous 2-D slices. It may be possible that sweeps or ejections give rise to vortices, but the mechanism is unclear. However, the kinematics of a streamwise vortex in a shear flow **require** the existence of $(u'v')_2$ and $(u'v')_4$ motions alongside the vortex. Thus the importance of streamwise vortices to near-wall turbulence production is reduced to the question of whether such vortices are numerous enough and strong enough to be statistically significant. This issue is addressed in Chapter 10.

8.3.4 Pressure, Dissipation, and Turbulence Kinetic Energy in $y - z$ Planes

In the end-view plane, the pressure field (Fig. 8.27d) shows the vertically elongated, relatively large structures observed in the other two orthogonal planes. Low-pressure contours (blue) effectively isolate regions of rotational motion, due to the low-pressure cores of the vortices. In this view, the source of high-pressure regions is not obvious, but this is expected since side-views showed that high-pressure is most often associated with high streamwise gradients in u' . However, high pressure at the wall is often associated with the impact of high-speed, wallward sweeps.

The contours of instantaneous dissipation (Fig. 8.27e) are strikingly coincident with vortex cores, as can be seen by comparing Figs. 8.27c and 8.27e. As mentioned for the side-view planes, ϵ'_f is also maximized within near-wall shear layers. A cross-section through a shear layer is visible as a thin, wide dissipation peak in Fig. 8.27e.

Turbulence kinetic energy is strongly associated with ejections and sweeps (by definition), and thus quasi-streamwise vortices may be a significant source of TKE in the near-wall region.

8.4 Summary of Observations from 2-D Planes

The study of two-dimensional slices through the numerically simulated turbulent boundary layer has confirmed many experimental results and extended the knowledge of turbulence structure in several categories. Examples of all of the structures listed in Chapter 5 (with the exception of pockets) have been identified using the twelve turbulence quantities selected. The key advantage of the simulated turbulence is the opportunity to compare several quantities in the same plane of frozen data. The knowledge gained from 2-D planes provides a sound footing for the exploration of the three-dimensional nature of the structural features and of their spatial relationships, which is undertaken in the following chapters.

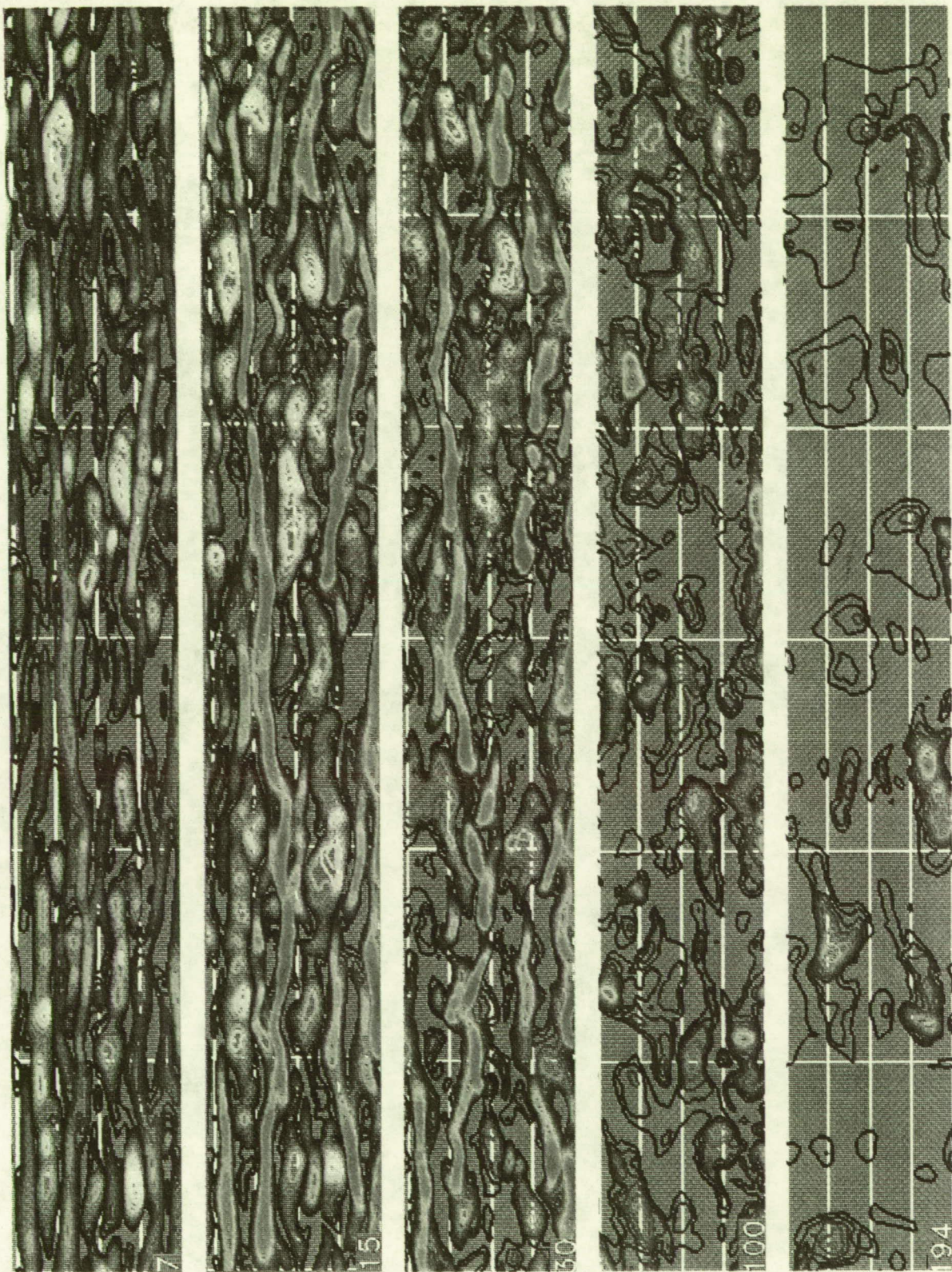


Fig. 8.1 Contours of u' in several x - z planes. Each plot is $3000\Delta x^+$ by $400\Delta z^+$.
Blue to green: $u'^+ = -1.0$ to -7.0 . Red to white: $u'^+ = +1.0$ to $+7.0$.

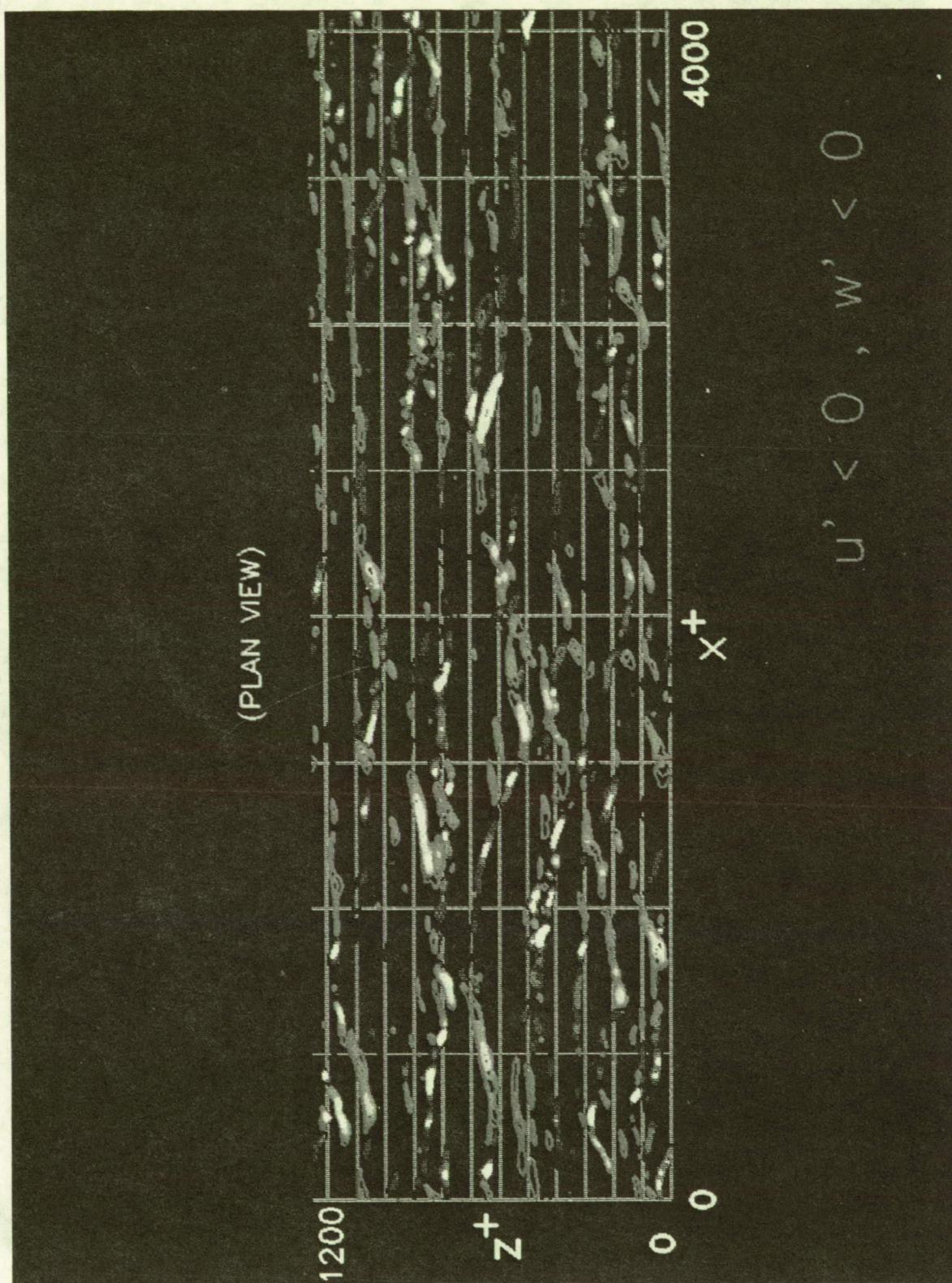


Fig. 8.2 Contours of $(u'w')_2$ and $(u'w')_3$ in an x - z plane at $y^- = 15$.
Green to white: $(u'w')_2/u_\tau^2 = 2.1$ to 14.9 . Red to white: $(u'w')_3/u_\tau^2 = -2.1$ to -14.9 .

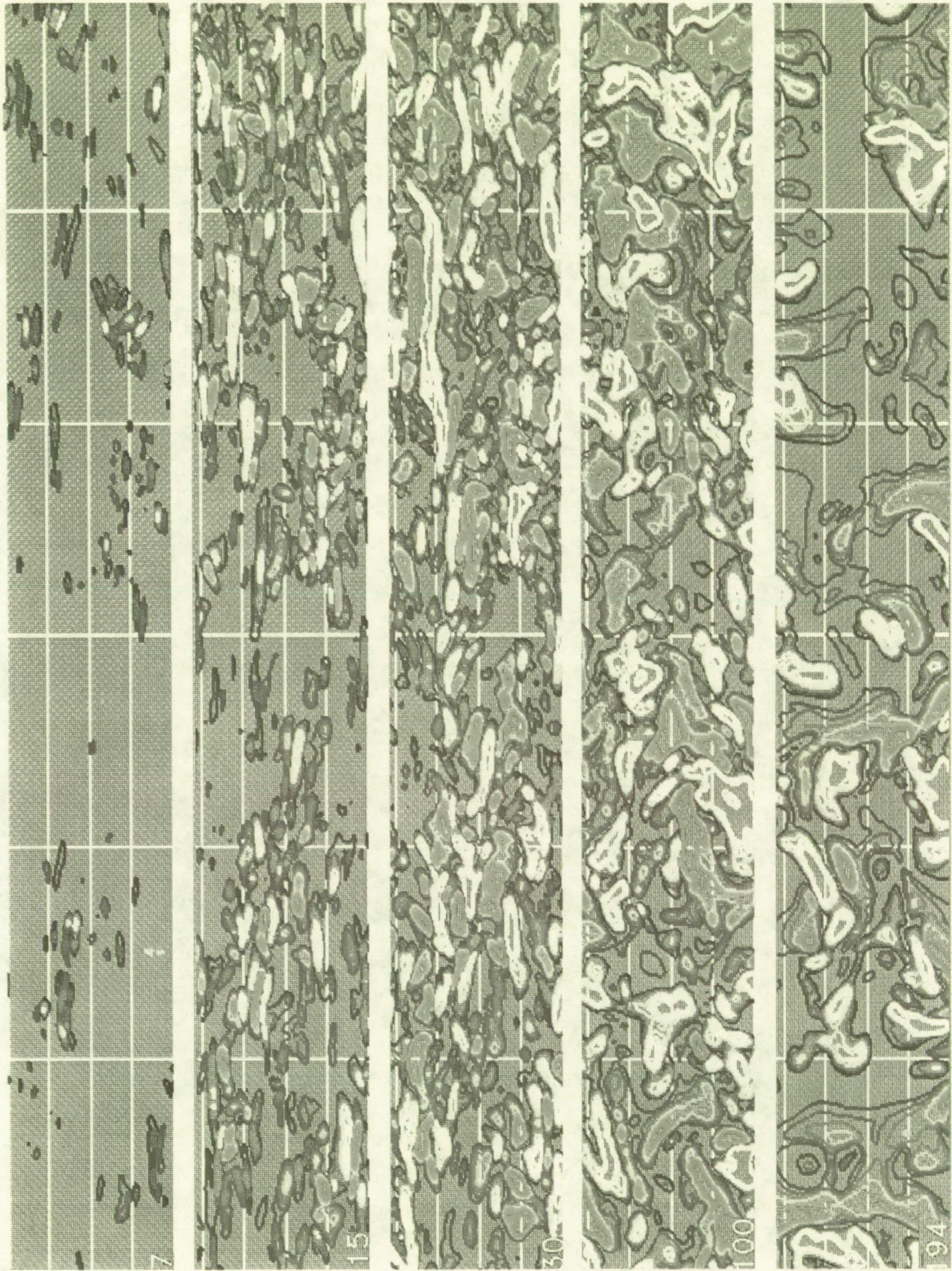


Fig. 8.3 Contours of v in several x - z planes. Each plot is $3000\Delta x^+$ by $400\Delta z^+$. Blue to green: $r^+ = -0.4$ to -1.6 . Red to white: $r^+ = +0.4$ to $+1.6$.

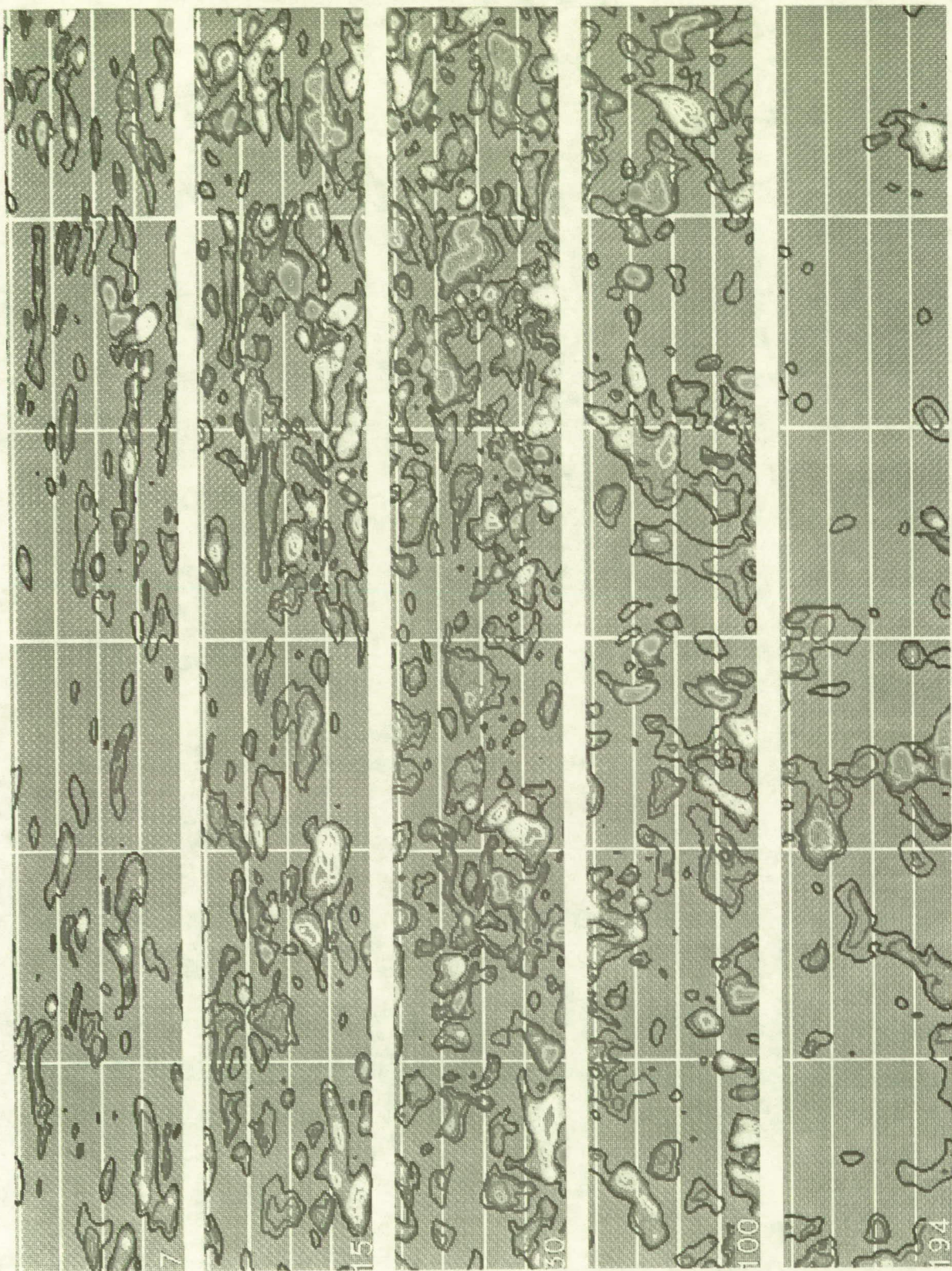


Fig. 8.4 Contours of w in several x - z planes. Each plot is $3000\Delta x^+$ by $400\Delta z^+$. Blue to green: $w^+ = -1.0$ to -4.0 . Red to white: $w^+ = +1.0$ to $+4.0$.

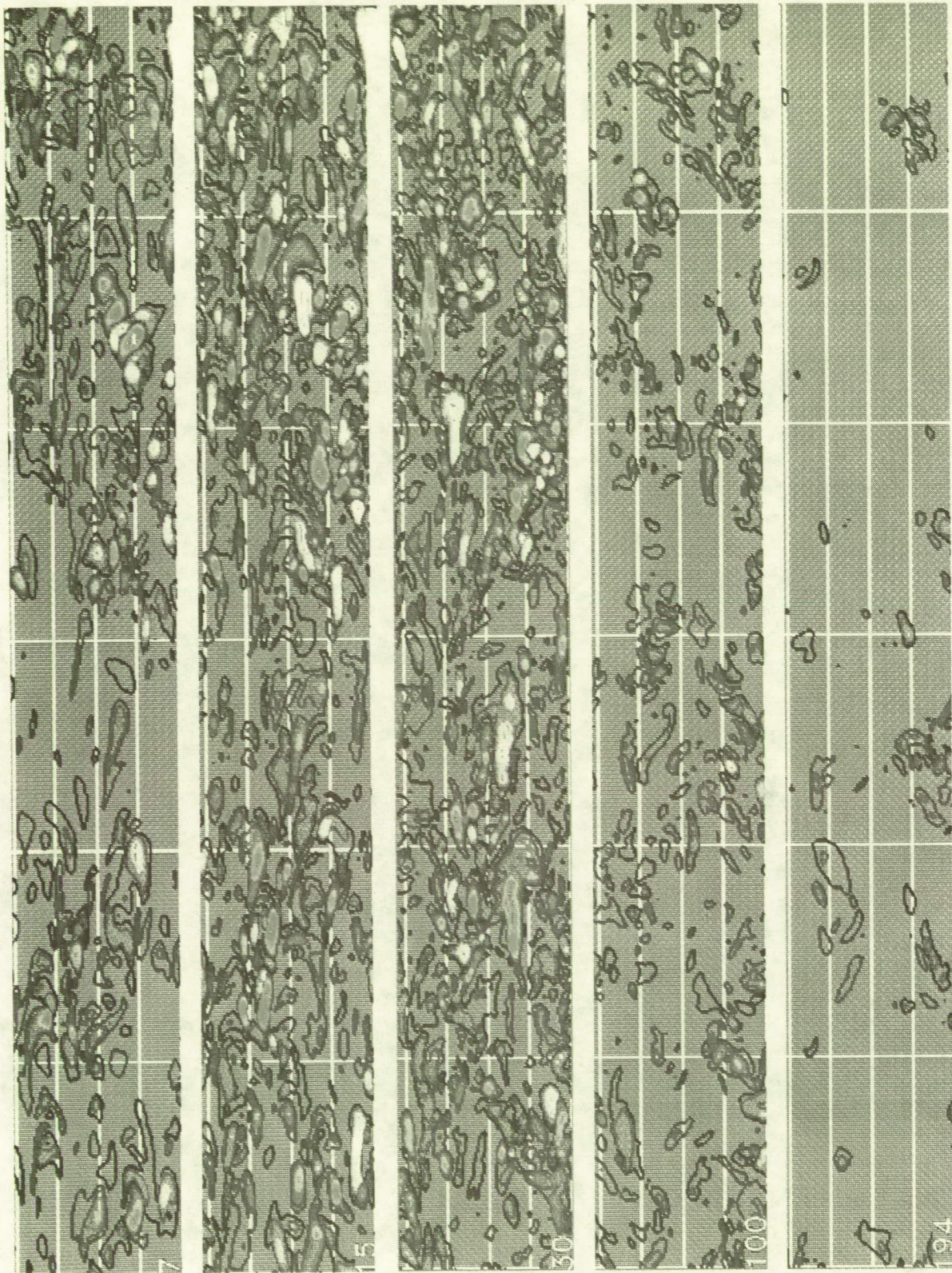


Fig. 8.5 Contours of ω_x in several x - z planes. Each plot is $3000\Delta x^+$ by $400\Delta z^+$.
Blue to green: $\omega_x^+ = -0.1$ to -0.7 . Red to white: $\omega_x^+ = +0.1$ to $+0.7$.

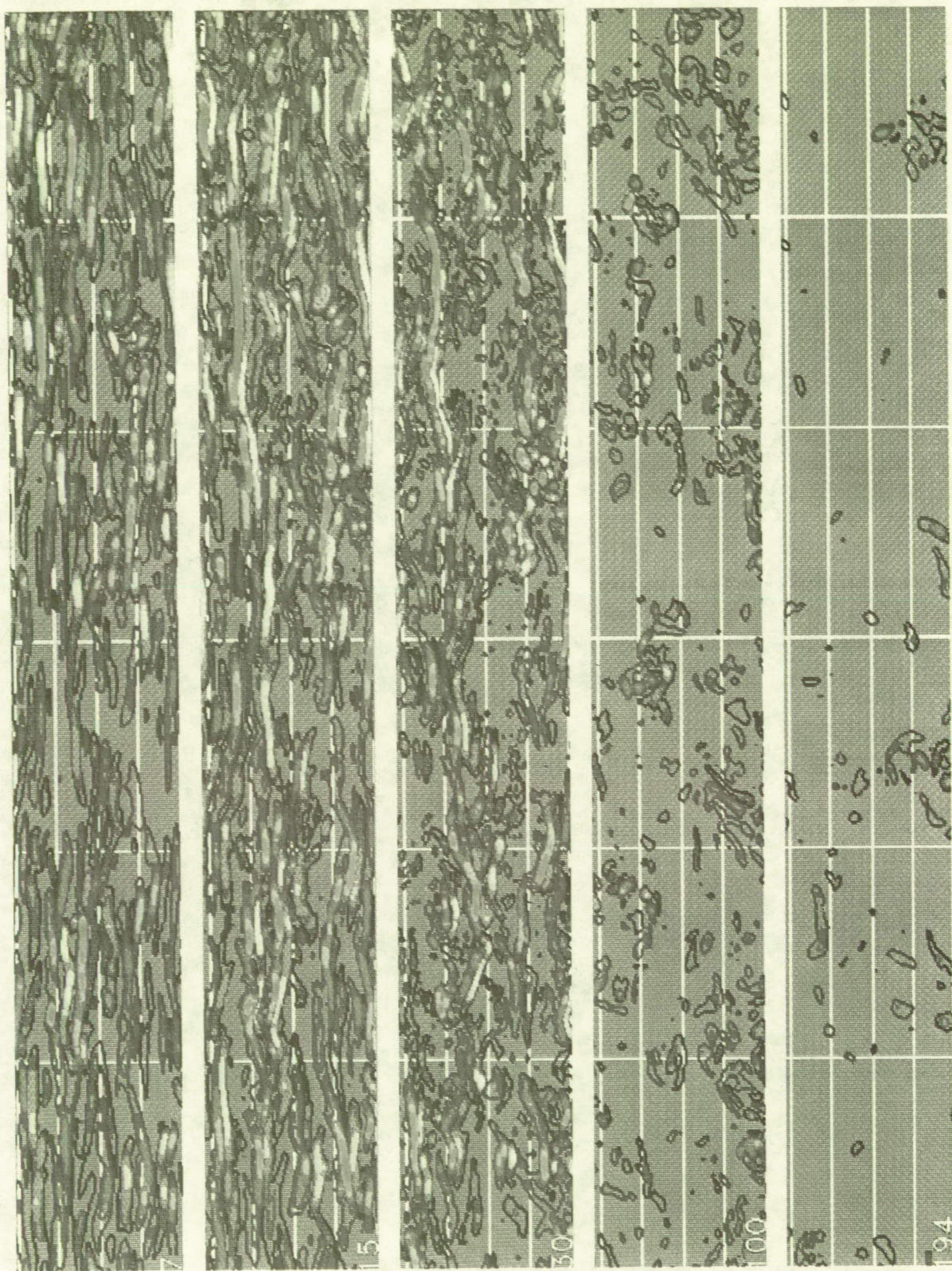


Fig. 8.6 Contours of ω_y in several x - z planes. Each plot is $3000\Delta x^+$ by $400\Delta z^+$.
Blue to green: $\omega_y^+ = -0.1$ to -0.7 . Red to white: $\omega_y^+ = +0.1$ to $+0.7$.

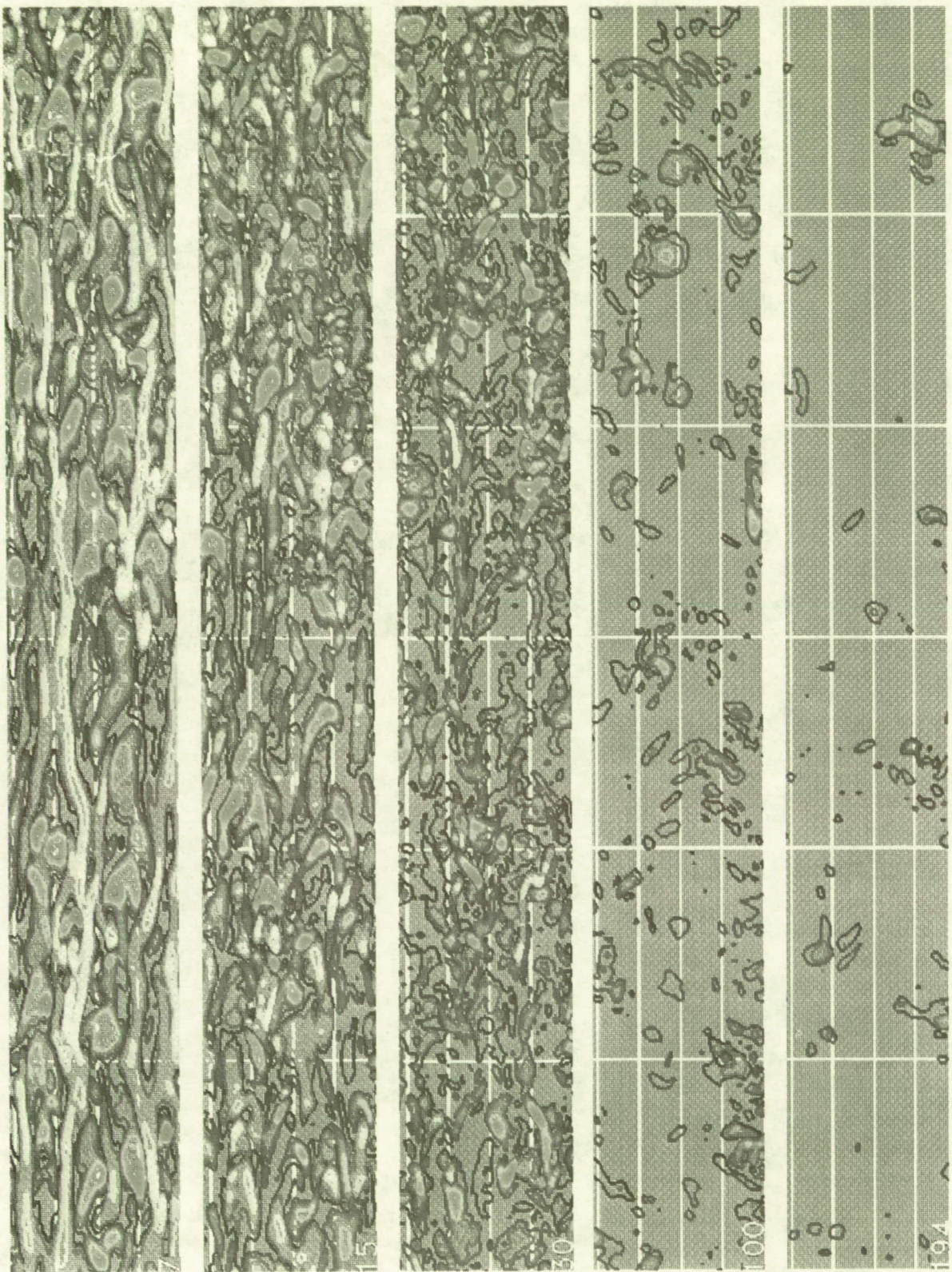


Fig. 8.7 Contours of ω'_z in several x - z planes. Each plot is $3000\Delta x^+$ by $400\Delta z^+$.
Blue to green: $\omega'_z = -0.1$ to -0.7 . Red to white: $\omega'_z = +0.1$ to $+0.7$.

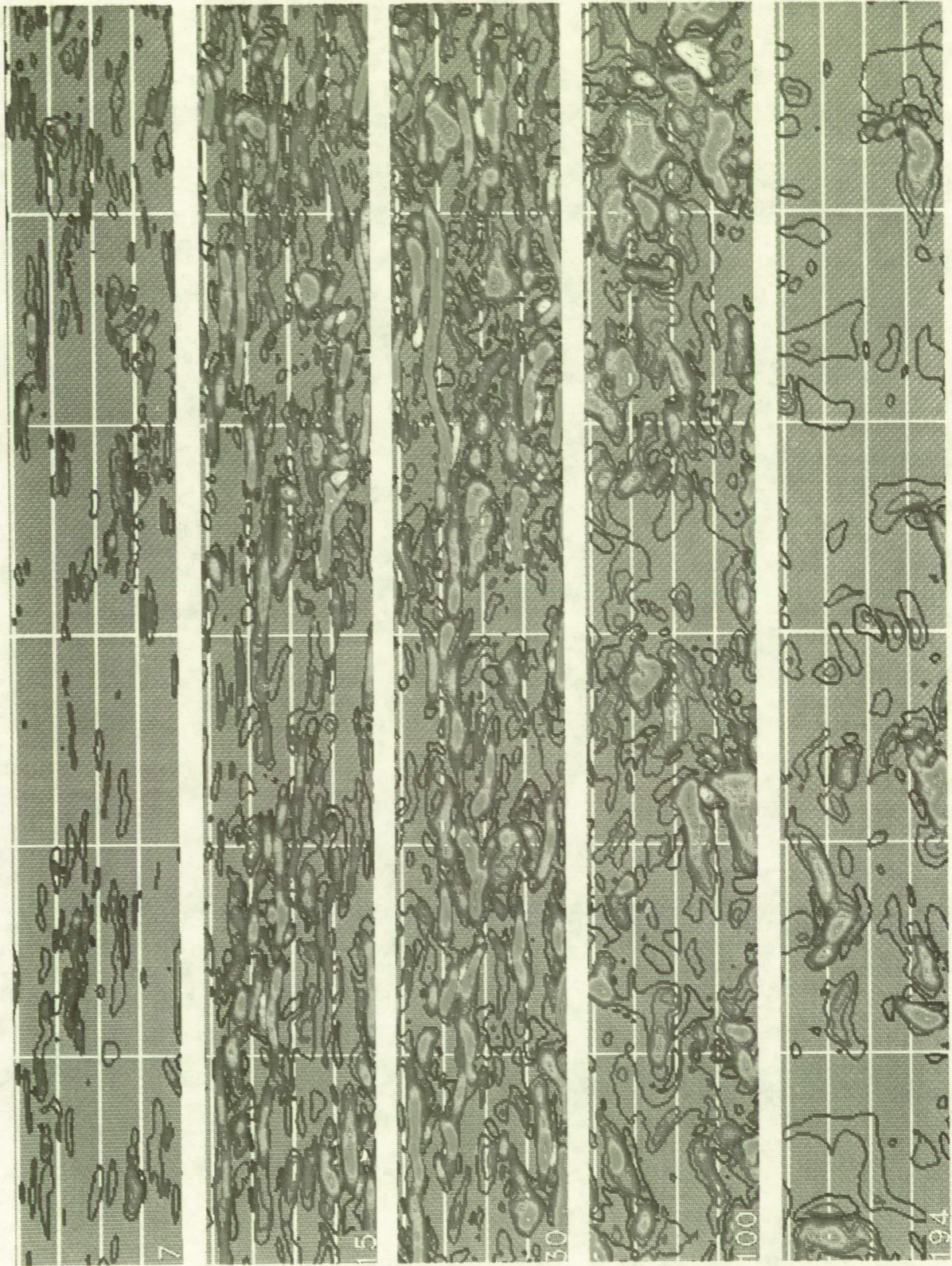


Fig. 8.8 Contours of $u'v'$ in several $x-z$ planes. Each plot is $3000\Delta x^+$ by $400\Delta z^+$.
 Blue to green: $u'v'/u_r^2 = -0.5$ to -7.5 . Red to white: $u'v'/u_r^2 = +0.5$ to $+7.5$.

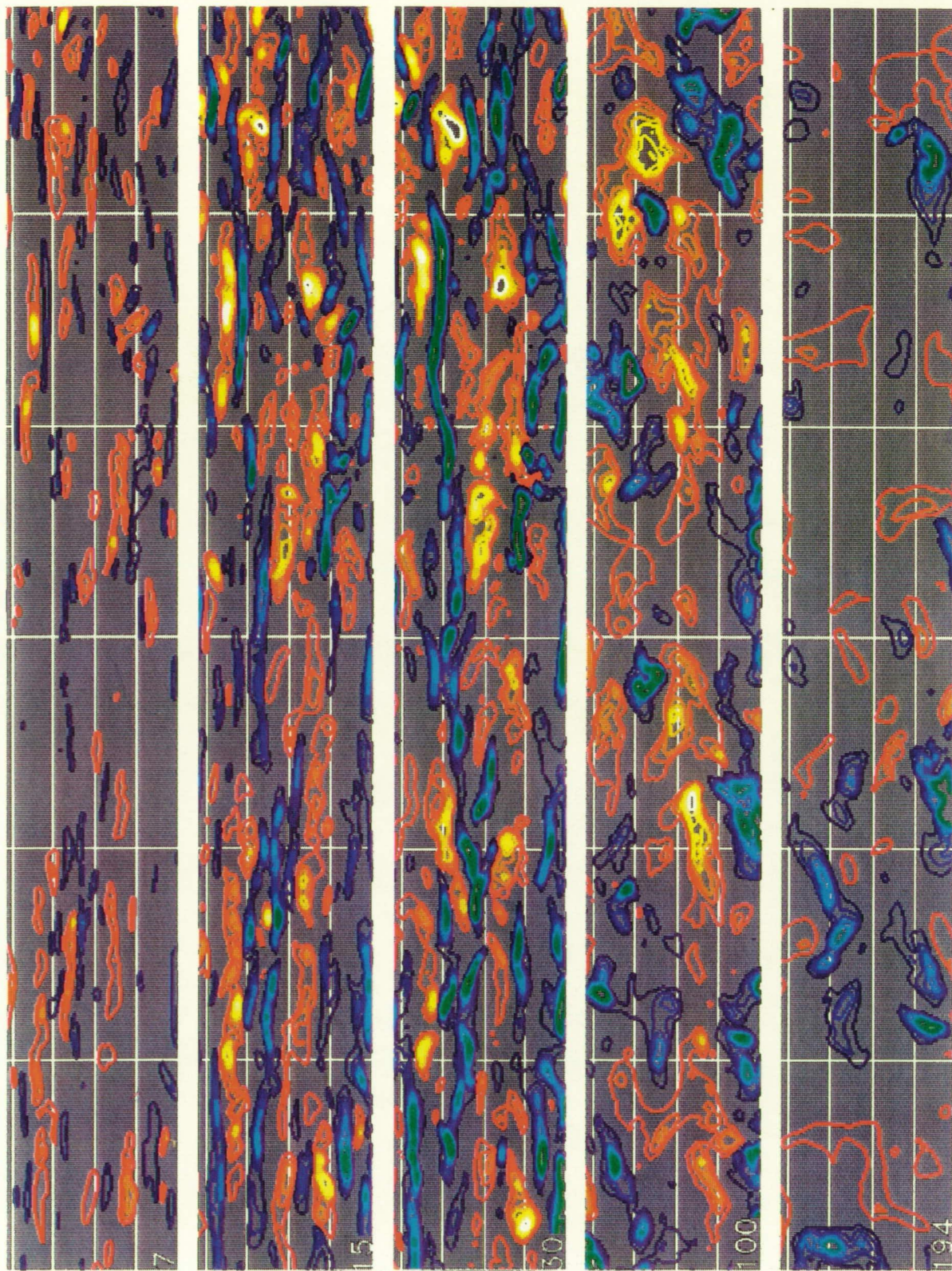


Fig. 8.9 Contours of $(u'v')_2$ and $(u'v')_4$ in several x - z planes. Each plot is $3000\Delta x^+$ by $400\Delta z^+$. Blue to green: $(u'v')_2/u_t^2 = -0.5$ to -7.5 . Red to white: $(u'v')_4/u_t^2 = -0.5$ to -7.5 .

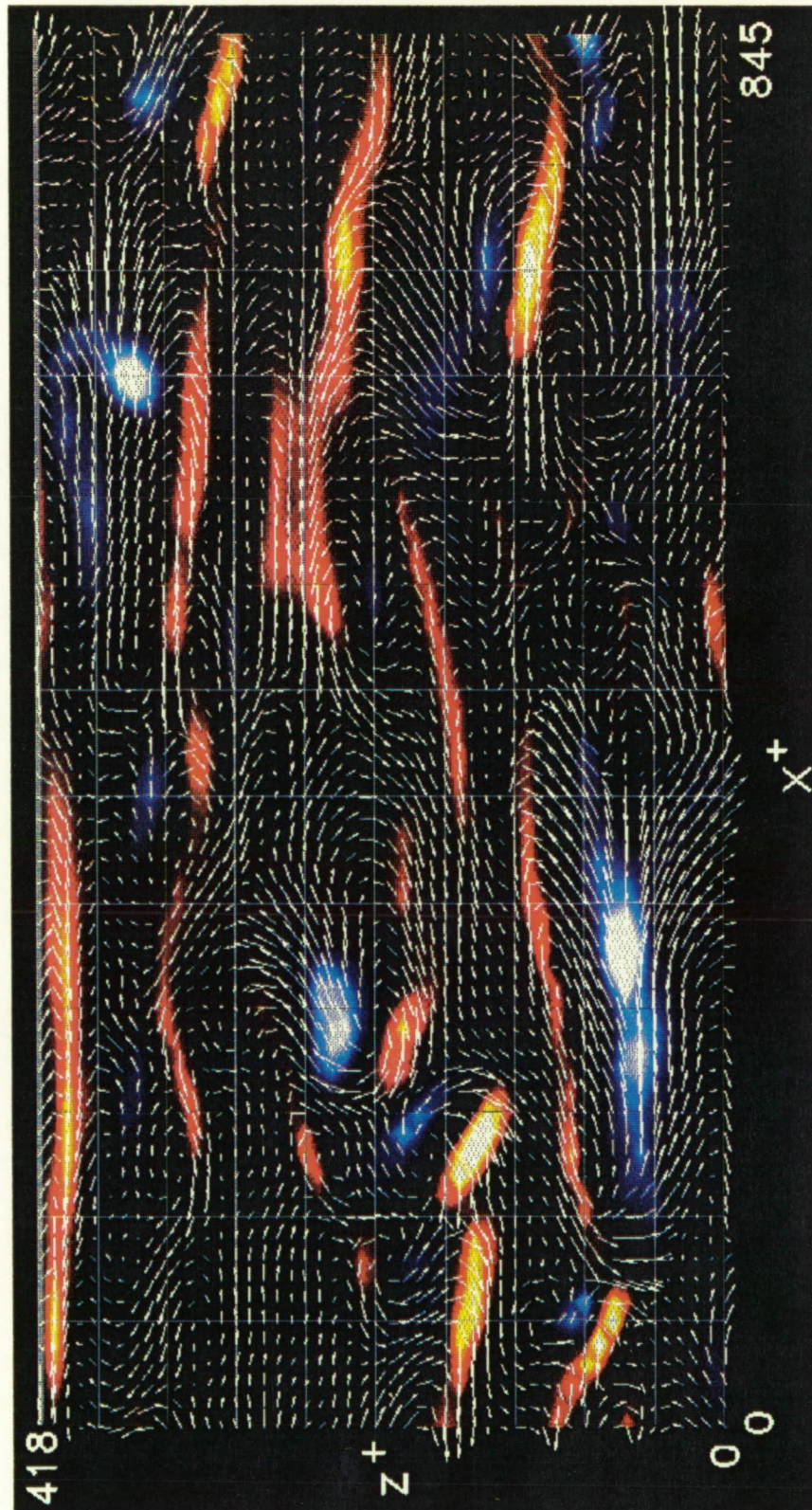


Fig. 8.10 Contours of $(u'v')_2$ and $(u'v')_4$ with u', w' velocity vectors in an x - z plane at $y^+ = 12$. Blue to white: $(u'v')_4/u_\tau^2 = -0.5$ to -6.0 . Red to white: $(u'v')_2/u_\tau^2 = -0.5$ to -6.0 .

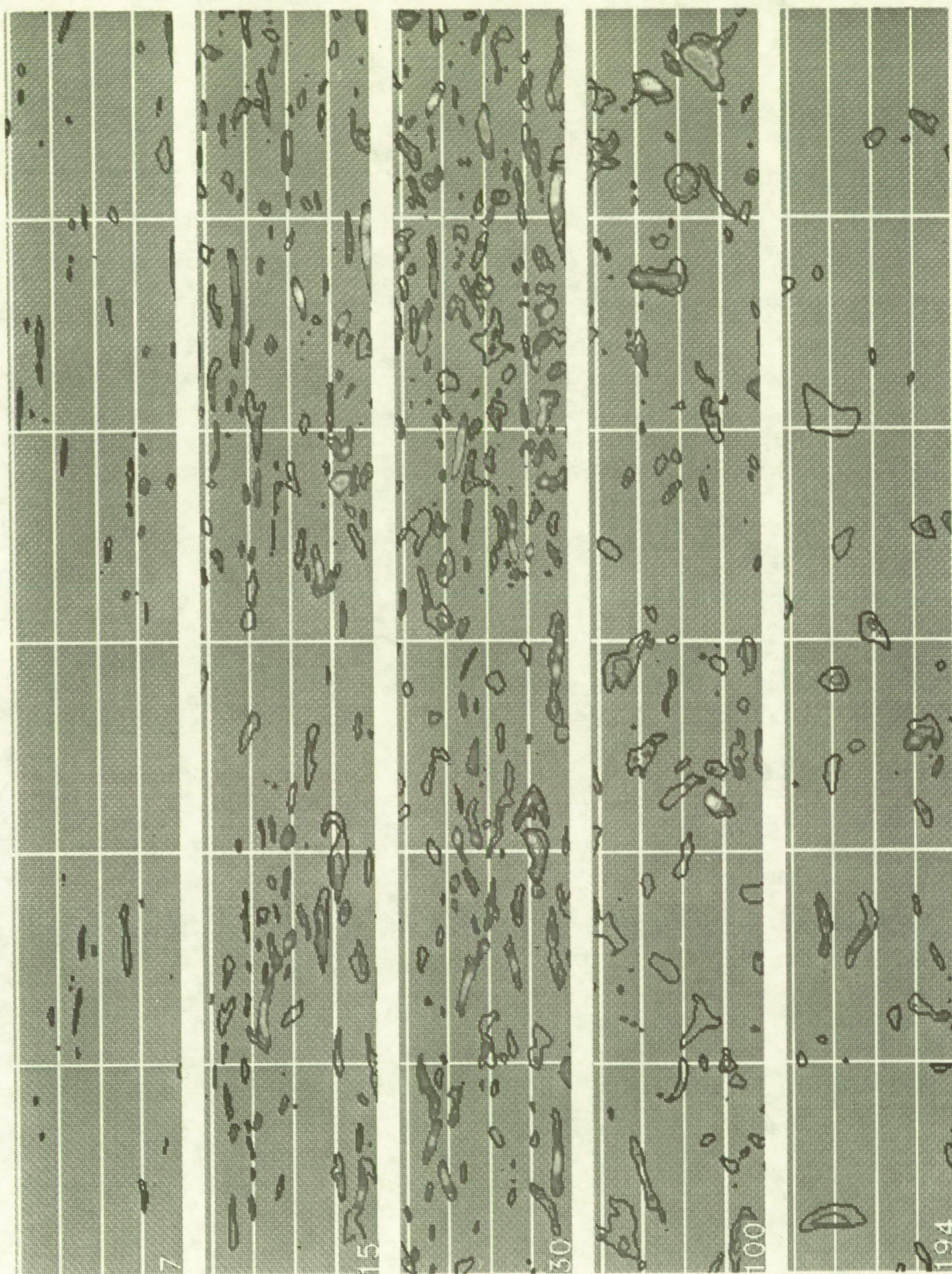


Fig. 8.11 Contours of $(u'v')_1$ and $(u'v')_3$ in several x - z planes. Each plot is $3000\Delta x^+$ by $400\Delta z^+$. Blue to green: $(u'v')_1/u_r^2 = -0.5$ to -7.5 . Red to white: $(u'v')_3/u_r^2 = -0.5$ to -7.5 .

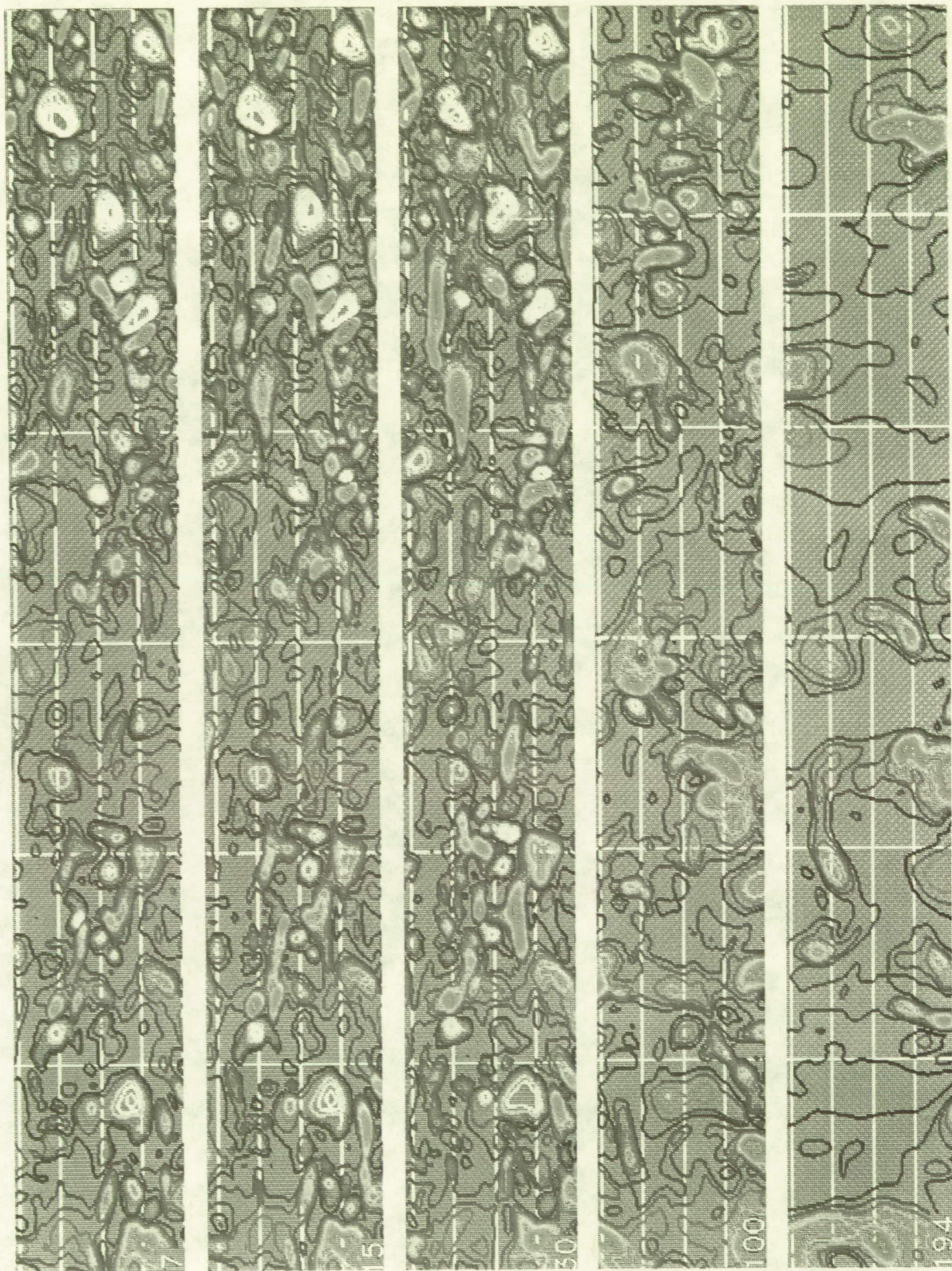


Fig. 8.12 Contours of p in several x - z planes. Each plot is $3000\Delta x^+$ by $400\Delta z^+$. Blue to green: $p^+ = -1.0$ to -8.0 . Red to white: $p^+ = +1.0$ to $+8.0$.

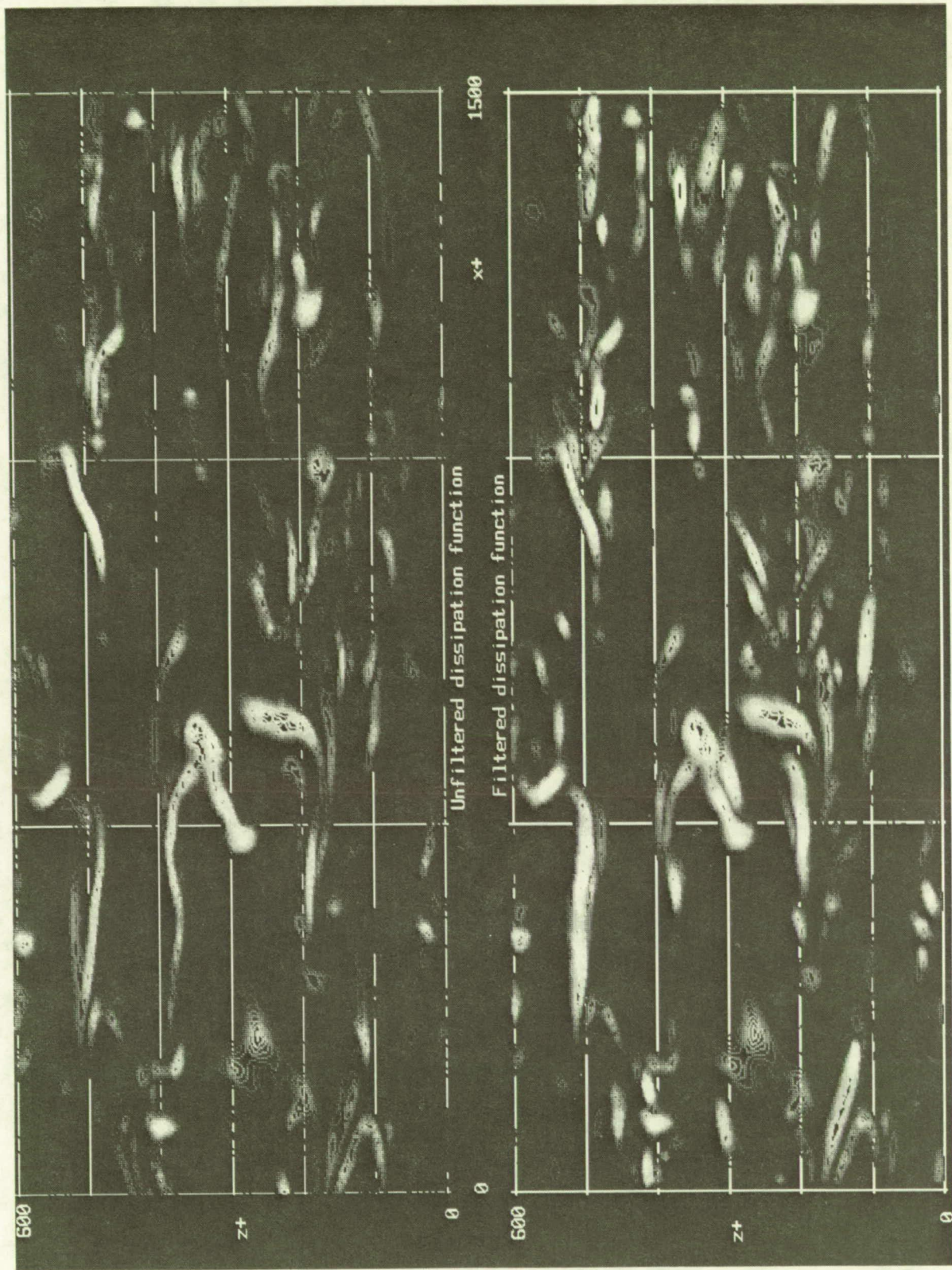


Fig. 8.13a Comparison between filtered (computed with central differences) and unfiltered (computed spectrally) dissipation functions in an x - z plane at $y^+ = 15$.

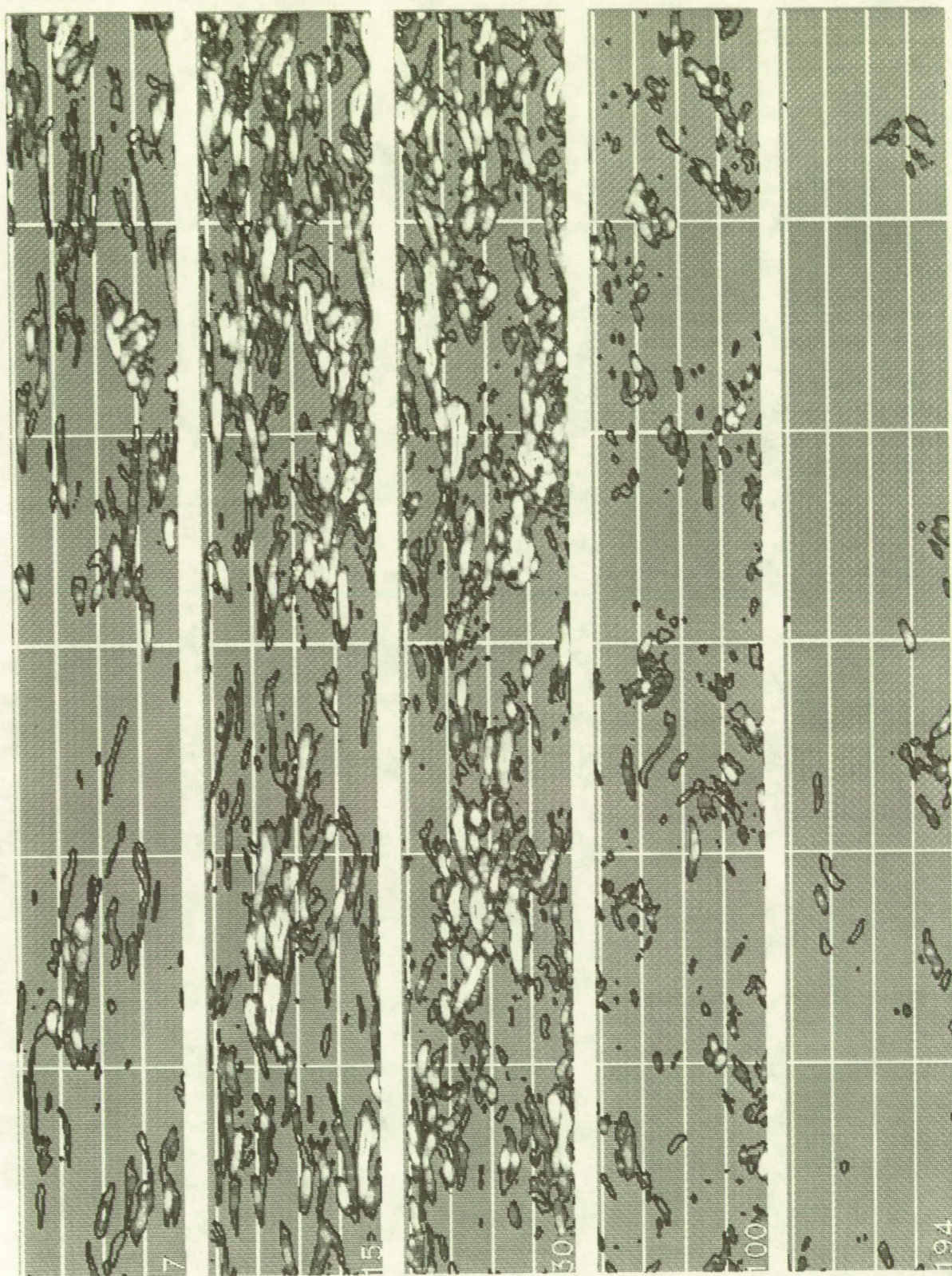


Fig. 8.13b Contours of ϵ_f in several x - z planes. Each plot is $3000\Delta x^+$ by $400\Delta z^+$.
Red to white: $\epsilon_f^\dagger = 0.1$ to 0.8 .

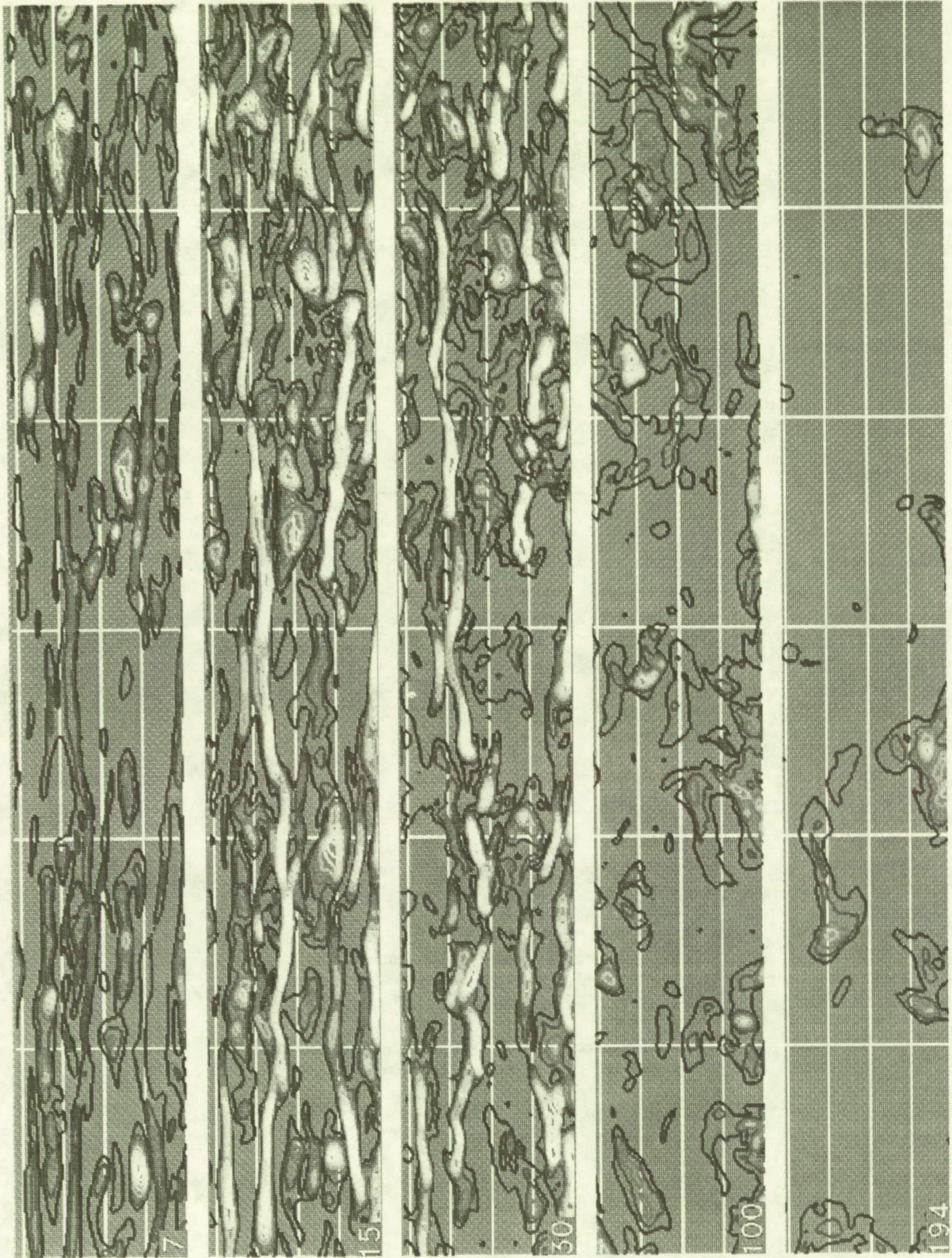
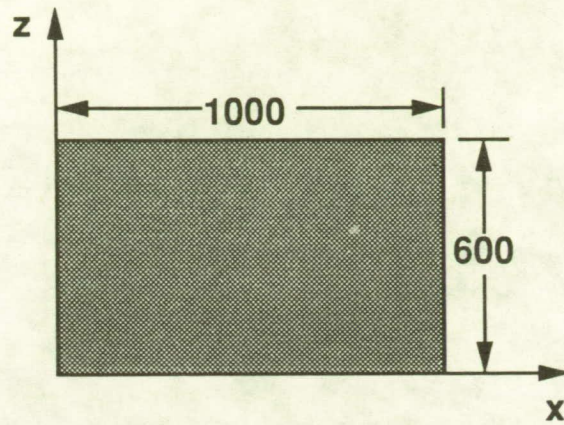


Fig. 8.14 Contours of TKE in several x - z planes. Each plot is $3000\Delta x^+$ by $400\Delta z^+$.
Red to white: $(u'^2 + v'^2 + w'^2)/u_\tau^2 = 5.0$ to 40.0 .



u'	v	w
ω_x	ω_y	ω'_z
p	ϵ'	TKE
$u'v'_{2,4}$	$u'v'_{1,3}$	$u'v'$

Fig. 8.15 Key for Figures 8.16 - 8.21 (Plan-views).

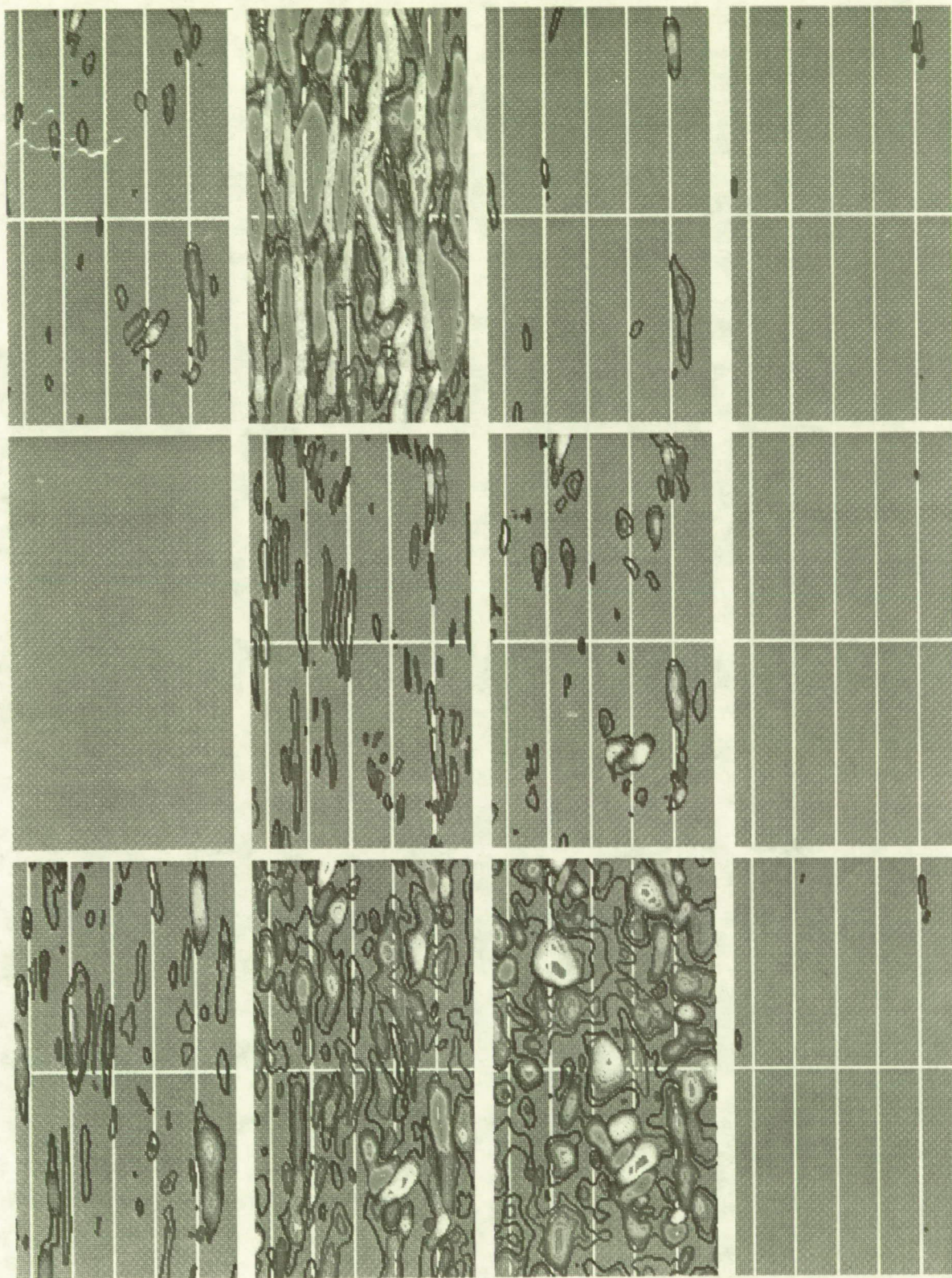


Fig. 8.16 Contours of $u', v, w, \omega_x, \omega_y, \omega_z, p, \epsilon_f, \text{TKE}$, and $u'v'$ in an x - z plane at $y^+ = 2$. See Fig. 8.15 for location key. Each plot is $1000\Delta x^+$ by $600\Delta z^+$. Contour levels are as for Figs. 8.1 - 8.14.

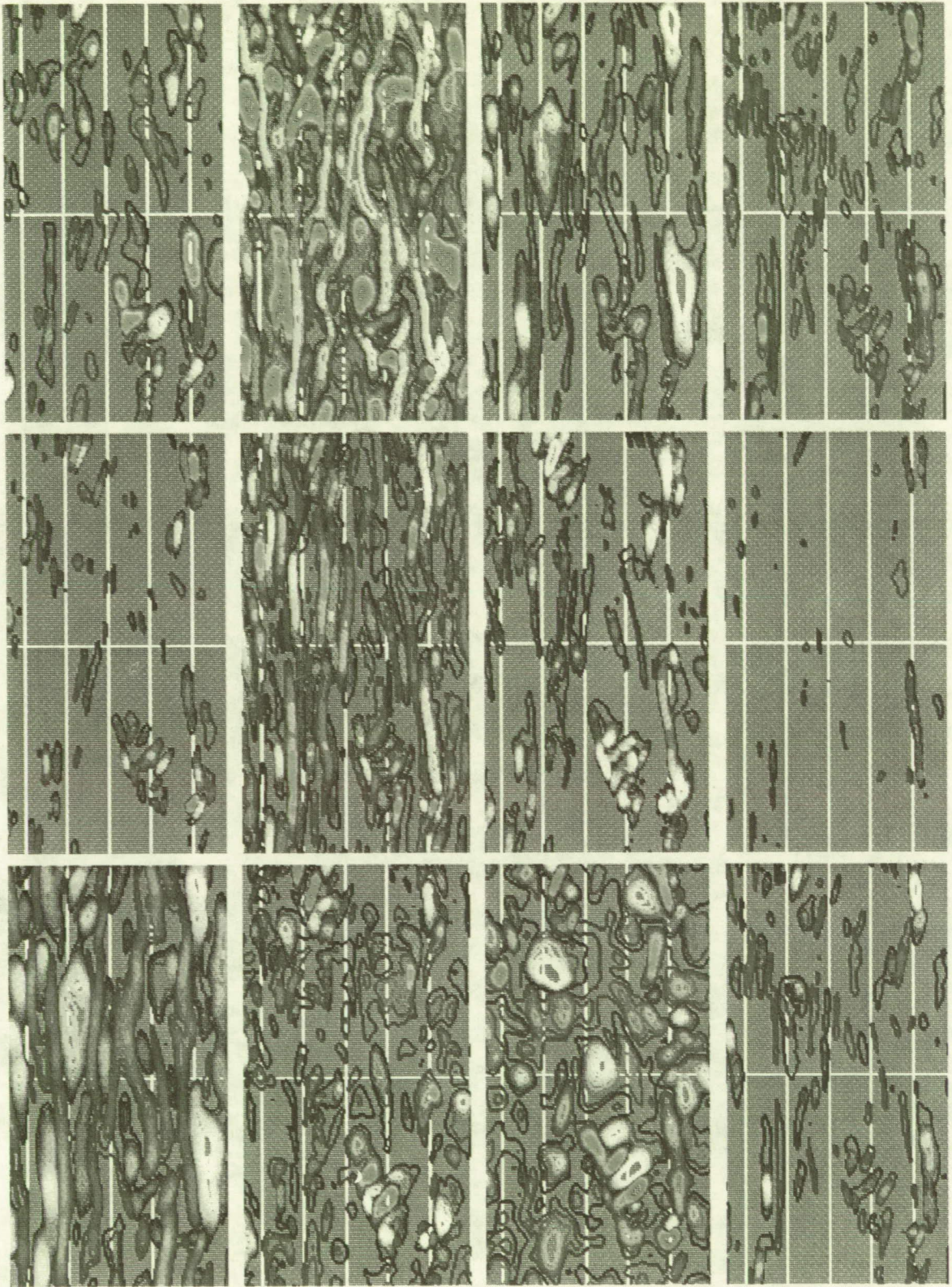


Fig. 8.17 Contours of $u', v, w, \omega_x, \omega_y, \omega_z, p, \epsilon_f$, TKE, and $u'v'$ in an x - z plane at $y^+ = 7$. See Fig. 8.15 for location key. Each plot is $1000\Delta x^+$ by $600\Delta z^+$. Contour levels are as for Figs. 8.1 - 8.14.

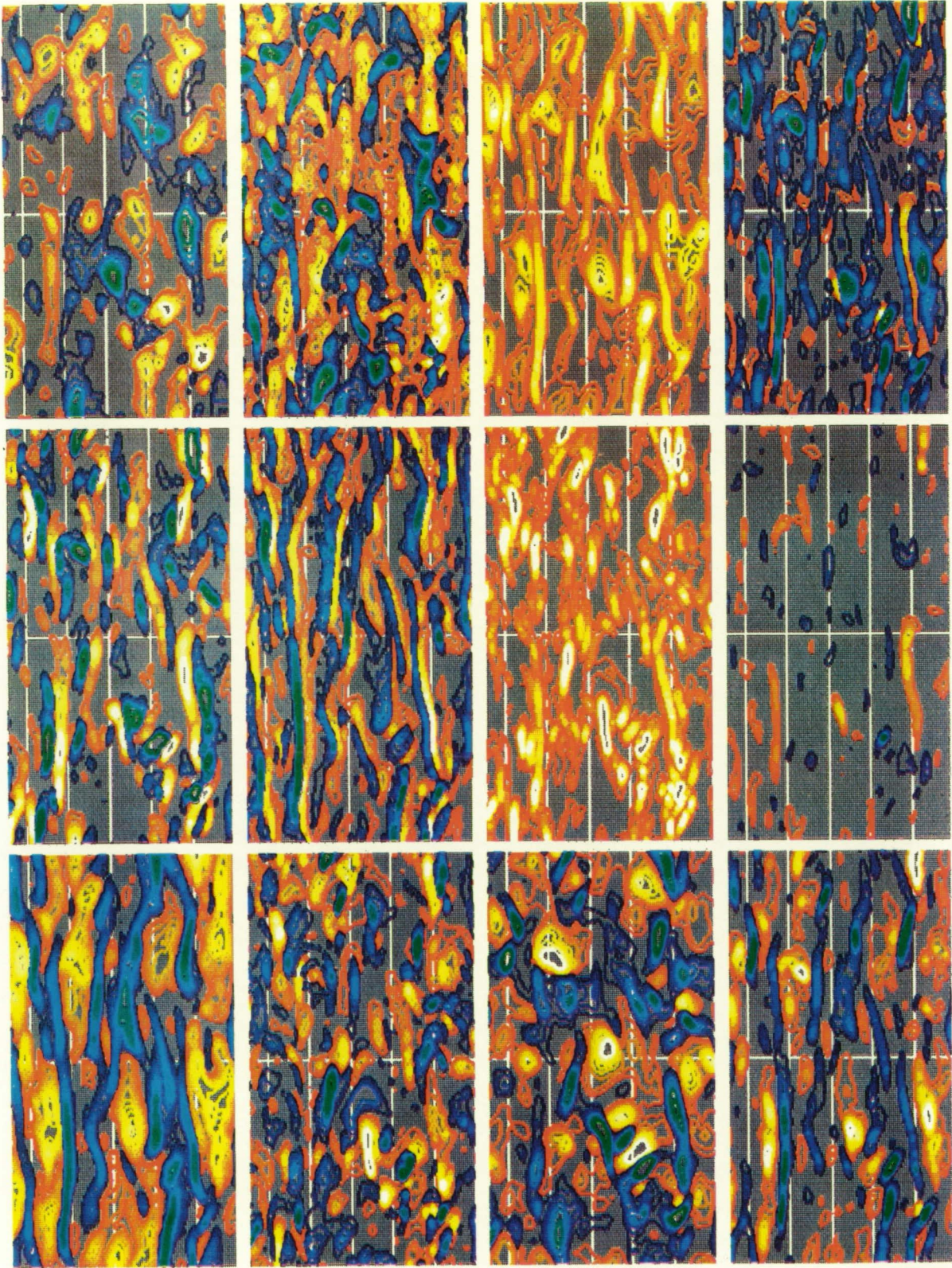


Fig. 8.18 Contours of u' , v , w , ω_x , ω_y , ω_z , p , ϵ_f , TKE, and $u'v'$ in an x - z plane at $y^+ = 15$. See Fig. 8.15 for location key. Each plot is $1000\Delta x^+$ by $600\Delta z^+$. Contour levels are as for Figs. 8.1 - 8.14.

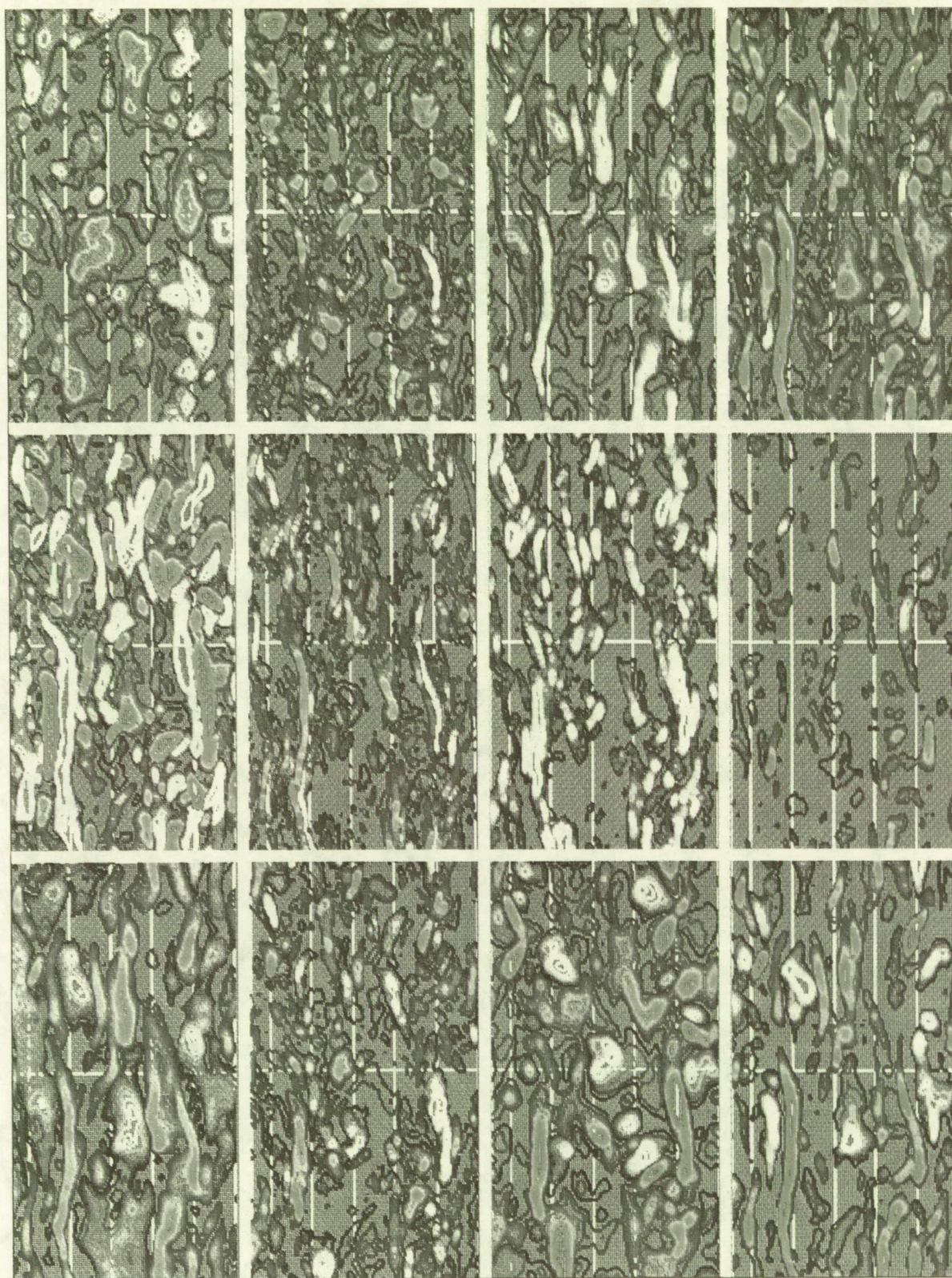


Fig. 8.19 Contours of u' , v , w , ω_x , ω_y , ω_z , p , ϵ_f , TKE, and $u'v'$ in an x - z plane at $y^+ = 30$. See Fig. 8.15 for location key. Each plot is $1000\Delta x^+$ by $600\Delta z^+$. Contour levels are as for Figs. 8.1 - 8.14.

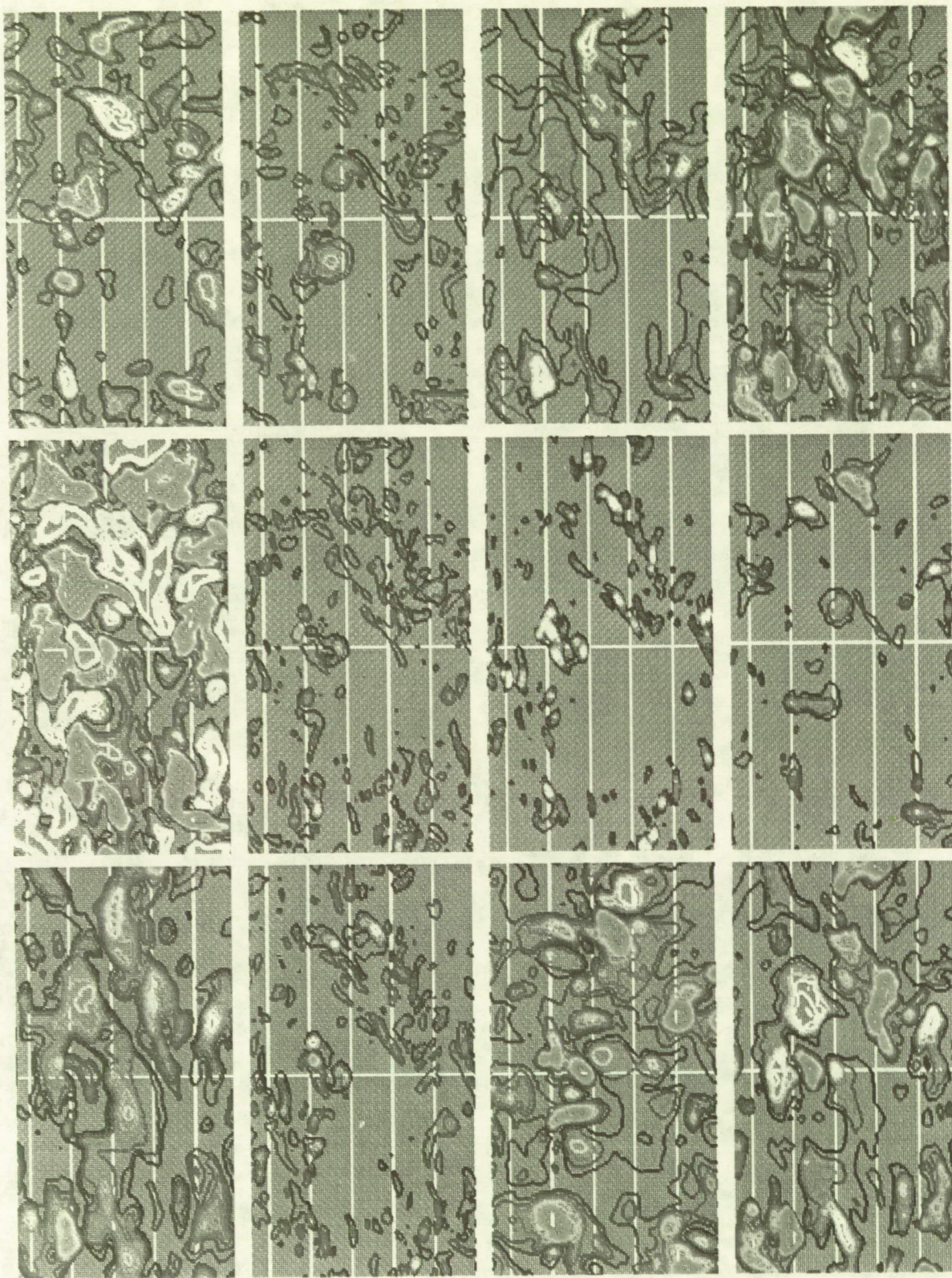


Fig. 8.20 Contours of u' , v , w , ω_x , ω_y , ω_z , p , ϵ_f , TKE, and $u'v'$ in an x - z plane at $y^+ = 100$. See Fig. 8.15 for location key. Each plot is $1000\Delta x^+$ by $600\Delta z^+$. Contour levels are as for Figs. 8.1 - 8.14.

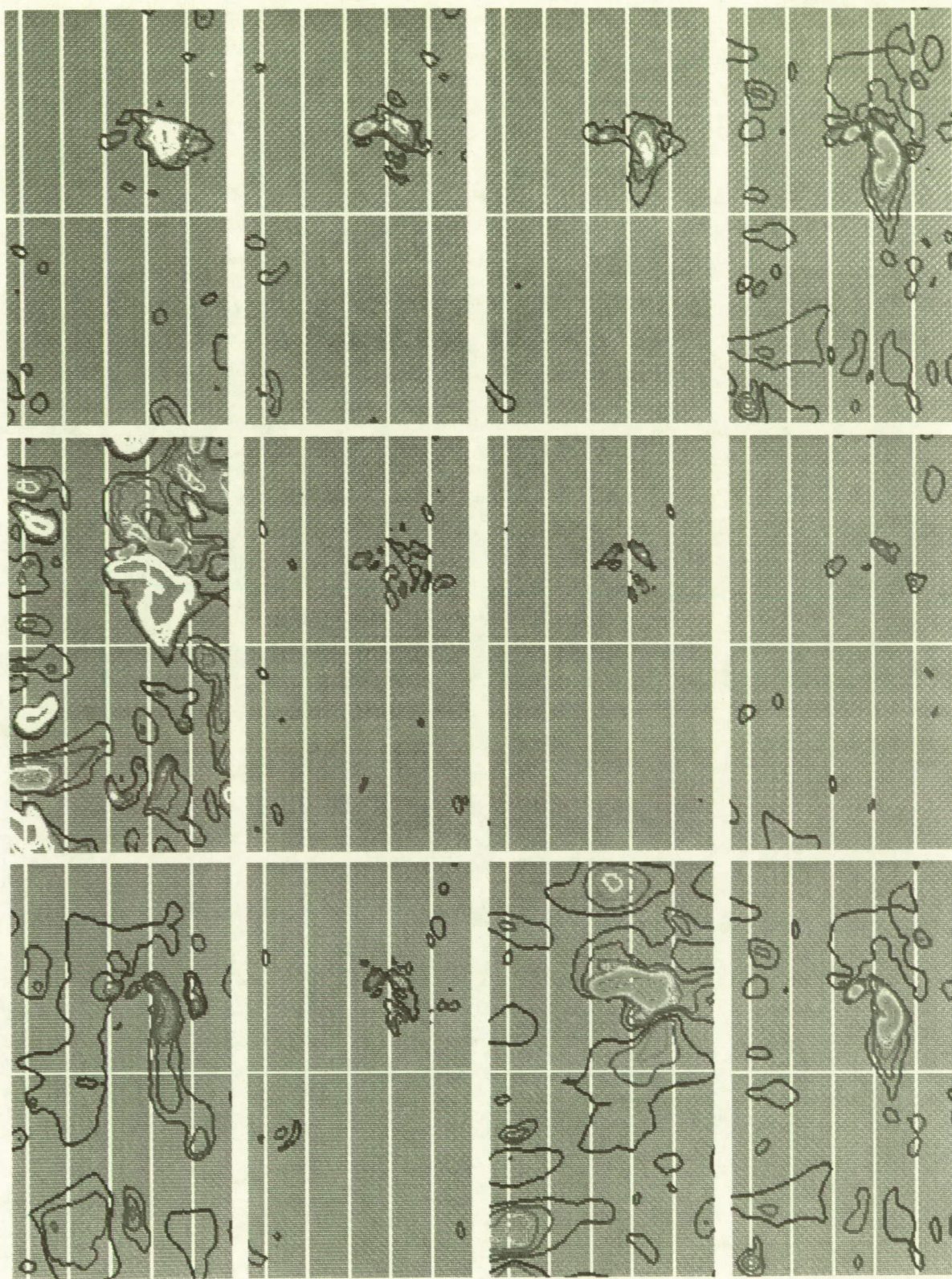
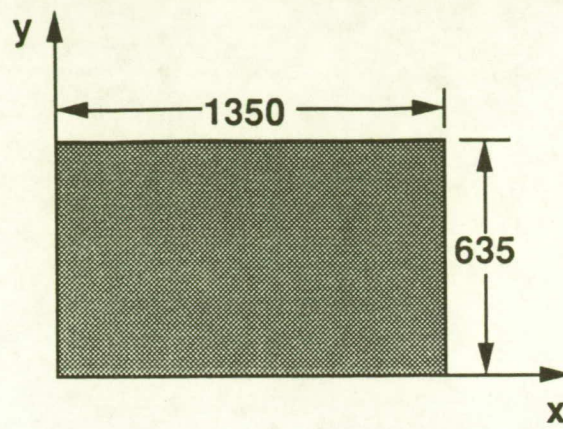


Fig. 8.21 Contours of u' , v , w , ω_x , ω_y , ω'_z , p , ϵ_f , TKE, and $u'v'$ in an x - z plane at $y^+ = 194$. See Fig. 8.15 for location key. Each plot is $1000\Delta x^+$ by $600\Delta z^+$. Contour levels are as for Figs. 8.1 - 8.14.



u'	ω_x
v	ω_y
w	ω'_z

Key for Figs. 8.23 (side-view)

$u'v'$	p
$u'v'^{2,4}$	ϵ'
$u'v'^{1,3}$	TKE

Key for Figs. 8.24 (side-view)

Fig. 8.22 Keys for Figures 8.23 and 8.24 (Side-views).

Fig. 8.22a Contour levels for Figs. 8.23 (a-f), 8.24 (a-f), 8.26 (a-f), and 8.27 (a-f):

Figs. 8.23a and 8.26a: Cyan to black: $u'^+ = -0.1$ to -4.0 . Yellow to black: $u'^+ = +0.1$ to $+4.0$.

Figs. 8.23b and 8.26b: Cyan to black: $v^+ = -0.1$ to -4.0 . Yellow to black: $v^+ = +0.1$ to $+4.0$.

Figs. 8.23c and 8.26c: Cyan to black: $w^+ = -0.1$ to -4.0 . Yellow to black: $w^+ = +0.1$ to $+4.0$.

Figs. 8.23d and 8.26d: Cyan to black: $\omega_x^+ = -0.05$ to -0.5 . Yellow to black: $\omega_x^+ = +0.05$ to $+0.5$.

Figs. 8.23e and 8.26e: Cyan to black: $\omega_y^+ = -0.05$ to -0.5 . Yellow to black: $\omega_y^+ = +0.05$ to $+0.5$.

Figs. 8.23f and 8.26f: Cyan to black: $\omega_z^+ = -0.05$ to -0.5 . Yellow to black: $\omega_z^+ = +0.05$ to $+0.5$.

Figs. 8.24a and 8.27a: Cyan to black: $u'v'/u_\tau^2 = -0.1$ to -10.0 . Yellow to black: $u'v'/u_\tau^2 = +0.1$ to $+10.0$.

Figs. 8.24b and 8.27b: Cyan to black: $(u'v')_2/u_\tau^2 = -0.1$ to -10.0 . Yellow to black: $(u'v')_4/u_\tau^2 = -0.1$ to -10.0 .

Figs. 8.24c: Cyan to black: $(u'v')_1/u_\tau^2 = +0.1$ to $+10.0$. Yellow to black: $(u'v')_3/u_\tau^2 = +0.1$ to $+10.0$.

Figs. 8.24d and 8.27d: Cyan to black: $p^+ = -0.1$ to -14.0 . Yellow to black: $p^+ = +0.1$ to $+14.0$.

Figs. 8.24e and 8.27e: Yellow to black: $\epsilon_f^+ = 0.1$ to 1.5 .

Figs. 8.24f and 8.27f: Yellow to black: $TK E^+ = 1.0$ to 30.0 .

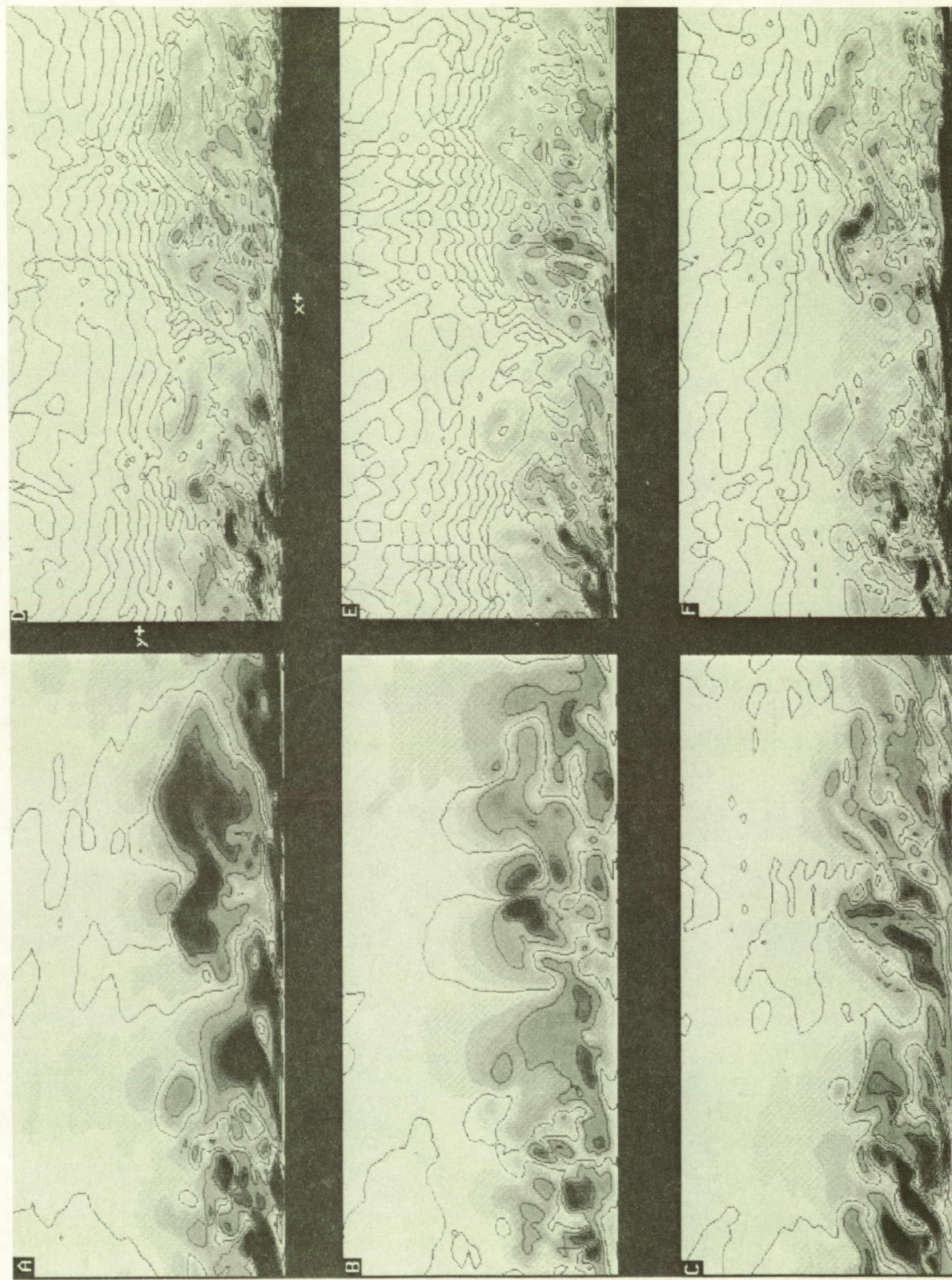


Fig. 8.23 (a-f) Contours of u' , v , w , ω_x , ω_y , and ω'_z in an x - y plane. See Fig. 8.22 for location key. Each plot is $1350\Delta x^+$ by $635\Delta y^+$. Contour levels are listed on Fig. 8.22a.

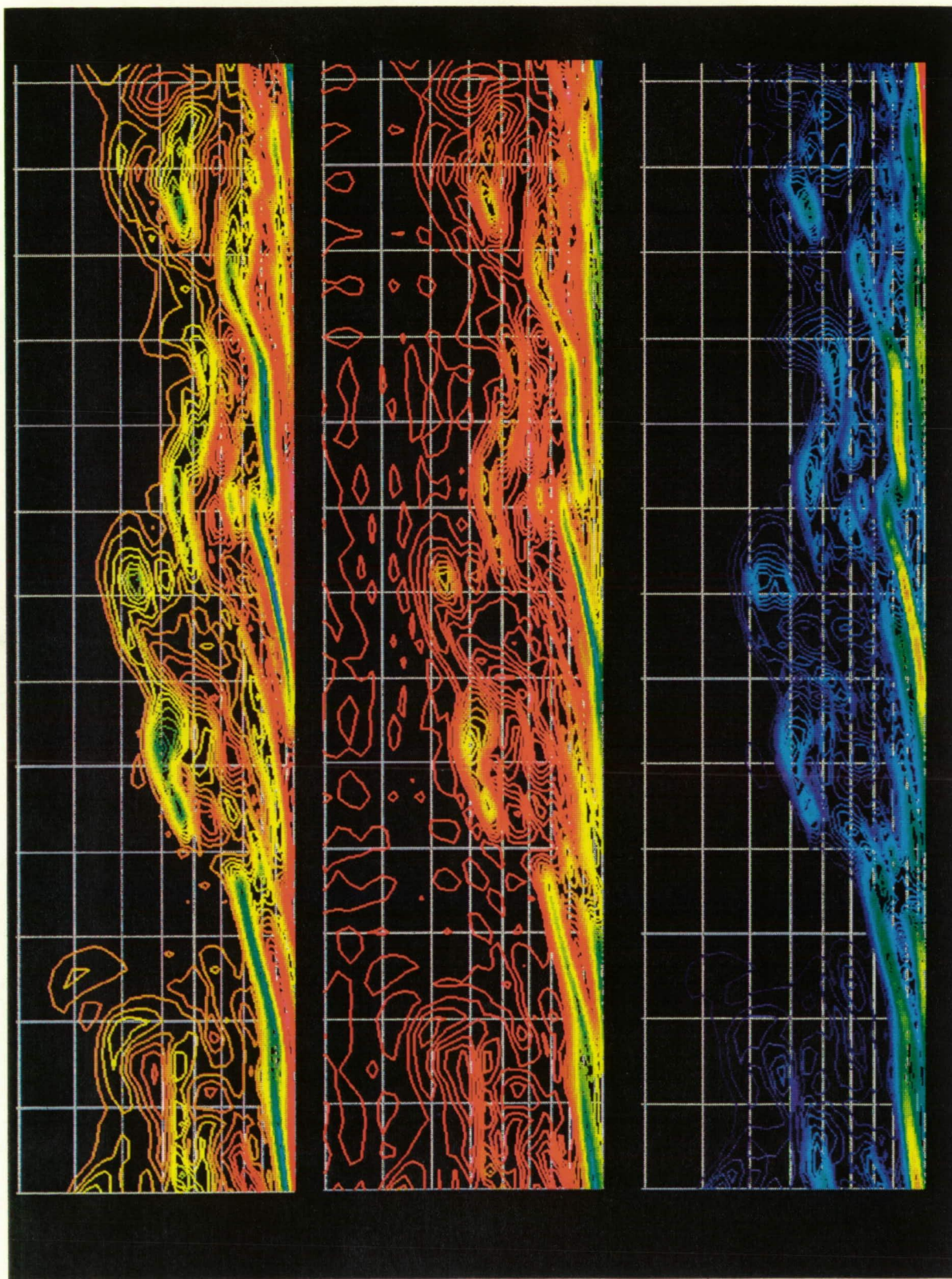


Fig. 8.23g Comparison between ω'_z , ω_z , and vorticity magnitude $|\omega|$ in an x - y plane. All three exhibit near-wall shear layers. Top: blue = $-\omega'_z$; green = 0; red = $+\omega'_z$. Middle: blue = $\omega_z < 0$; red = 0. Bottom: blue = 0; red = $|\omega| > 0$.

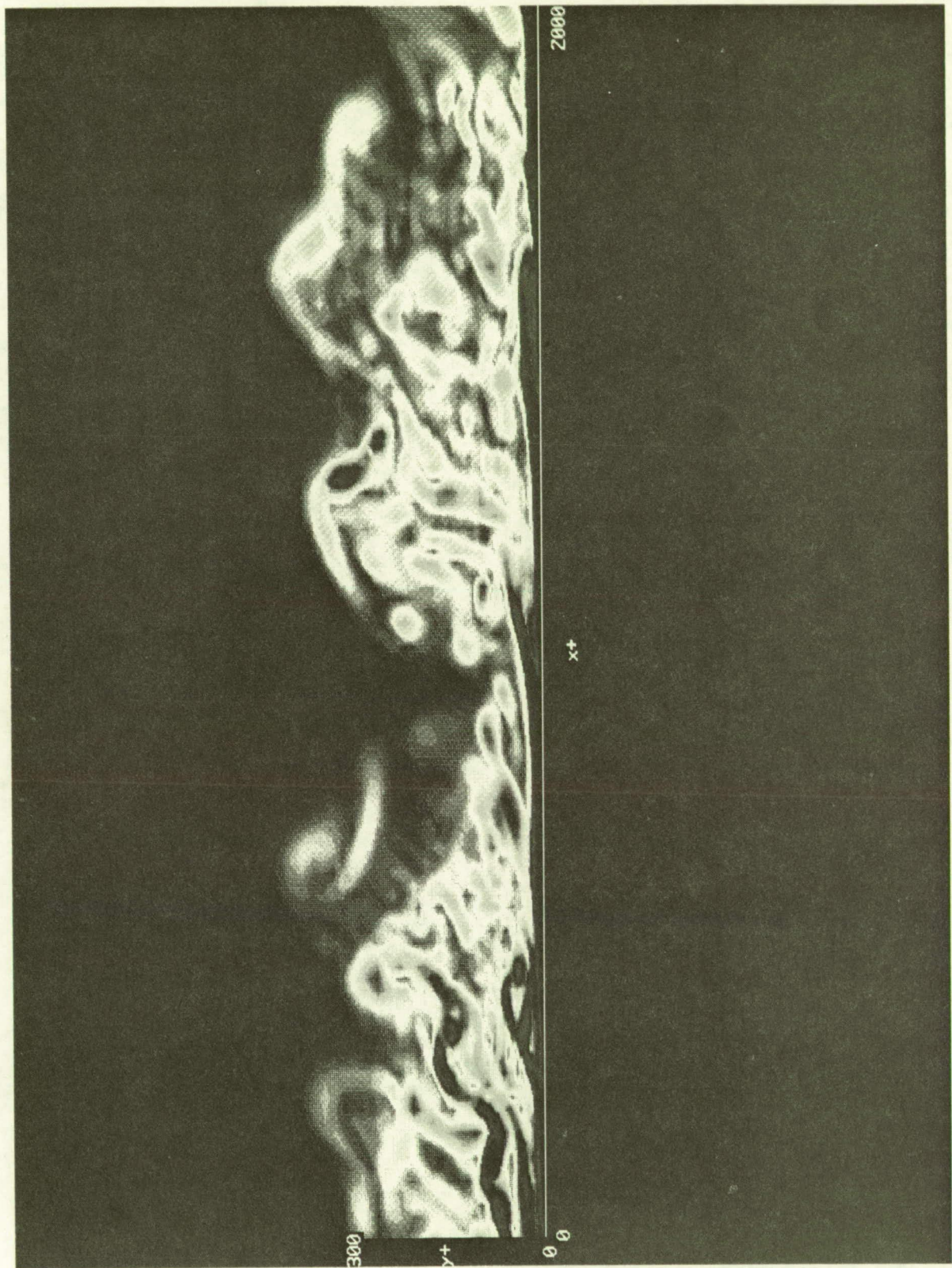


Fig. 8.23h Contours of vorticity magnitude $|\omega|$ in an x - y plane. White to yellow to magenta: $|\omega|^+ = 0.1$ to 1.0.

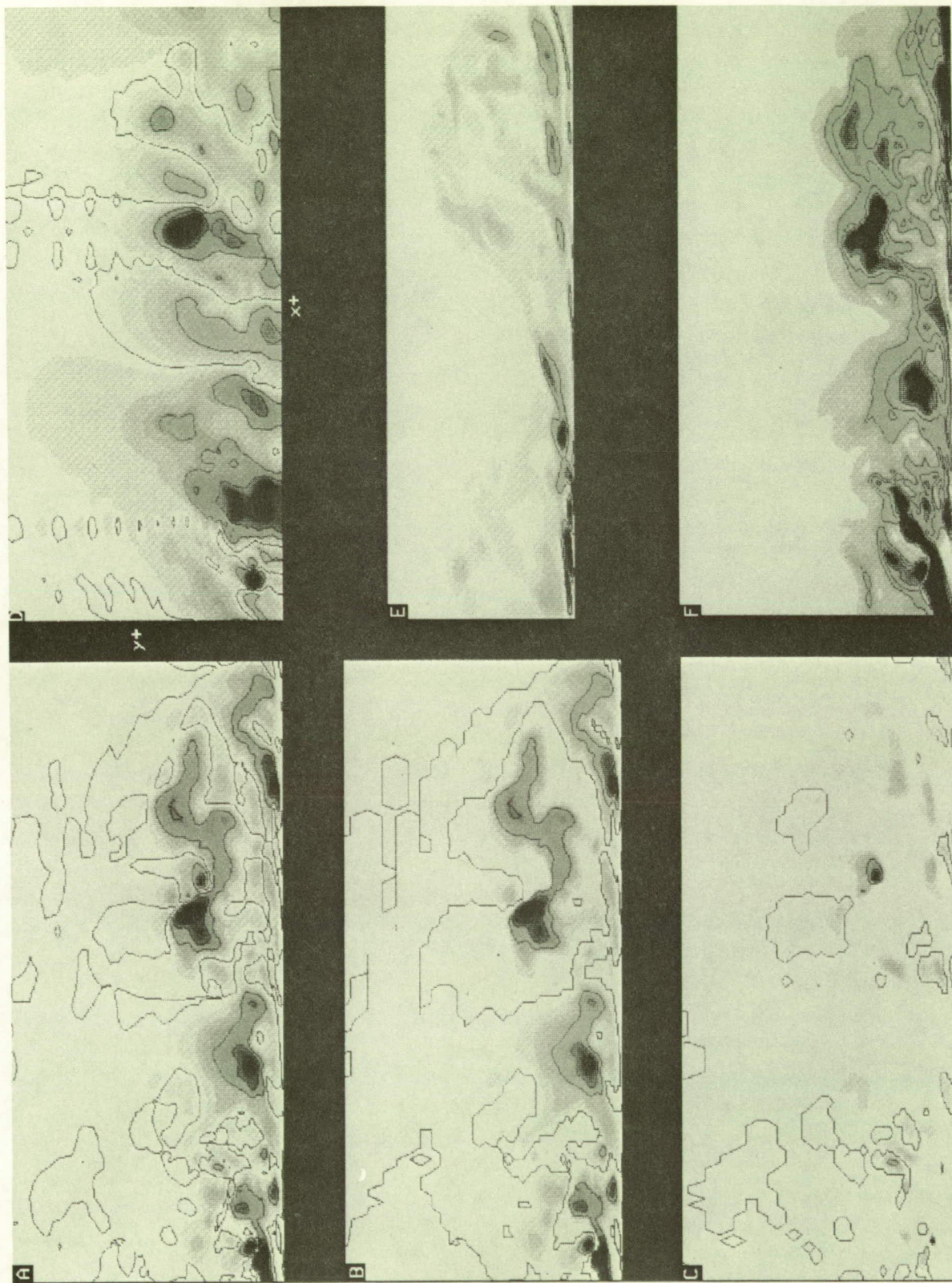


Fig. 8.24 (a-f) Contours of $u'v'$, p , ϵ_f , and TKE in an x - y plane. See Fig. 8.22 for location key. Each plot is $1350\Delta x^+$ by $635\Delta y^+$. Contour levels are listed on Fig. 8.22a.

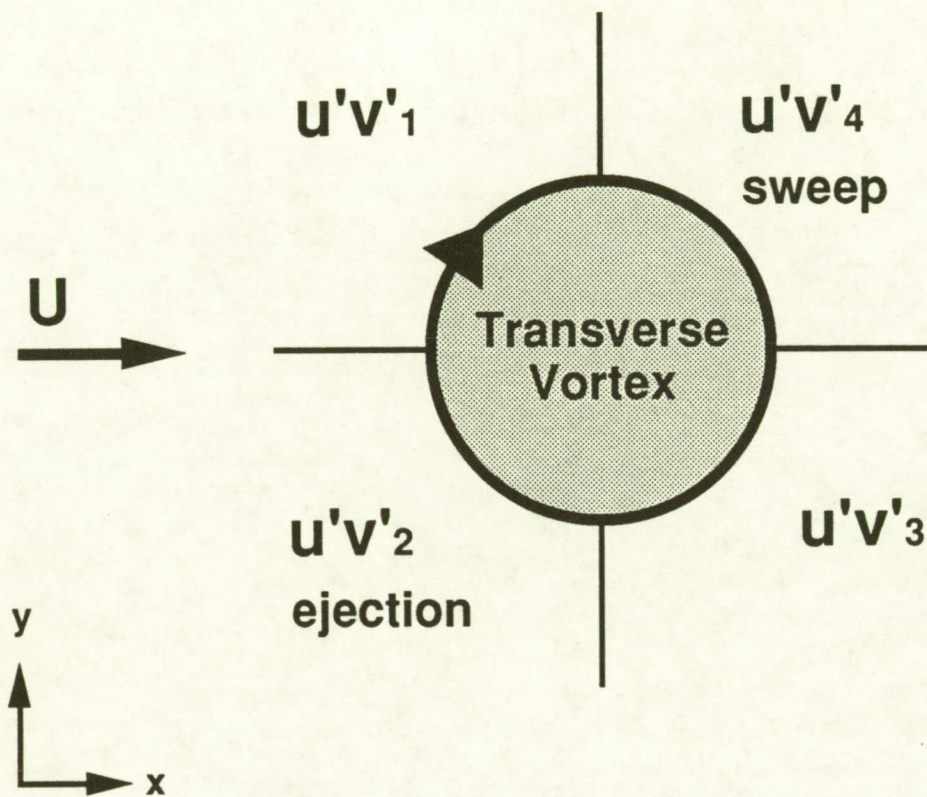
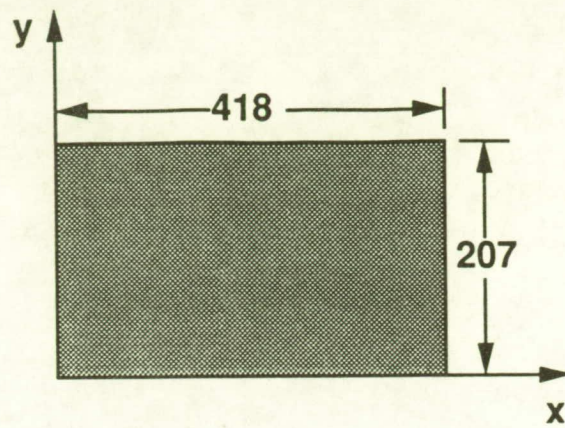


Fig. 8.24g Kinematics of a transverse vortex in x - y plane shear.



u'	ω_x
v	ω_y
w	ω'_z

Key for Fig. 8.26 (end-view)

$u'v'$	p
$u'v'^2_{2,4}$	ε'
v', w' vectors	TKE

Key for Fig. 8.27 (end-view)

Fig. 8.25 Keys for Figures 8.26 and 8.27 (End-views).

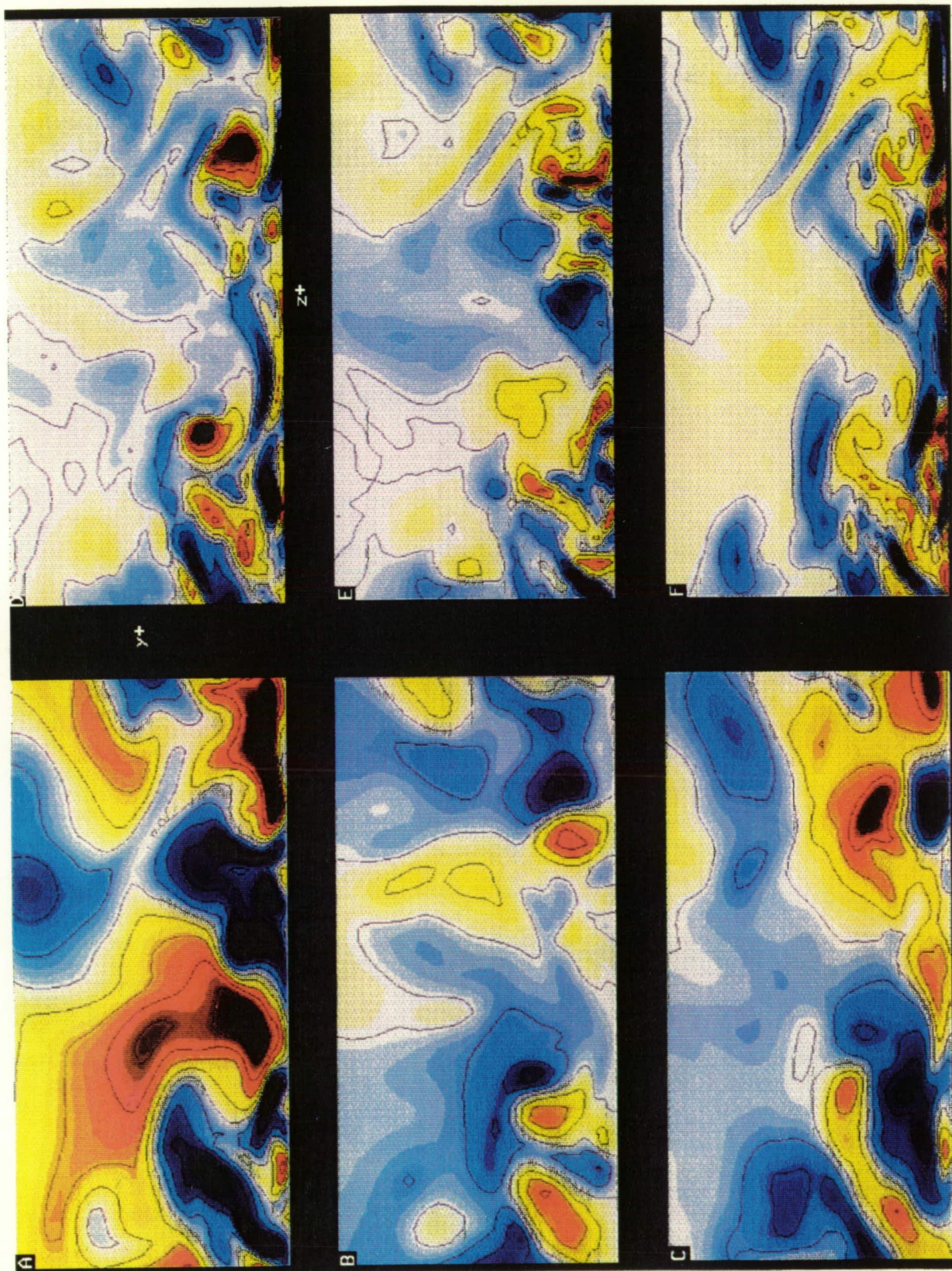


Fig. 8.26 (a-f) Contours of u' , v' , w' , ω_x , ω_y , and ω_z in a y - z plane. See Fig. 8.25 for location key. Each plot is $418\Delta z^+$ by $207\Delta y^+$. Contour levels are listed on Fig. 8.22a.

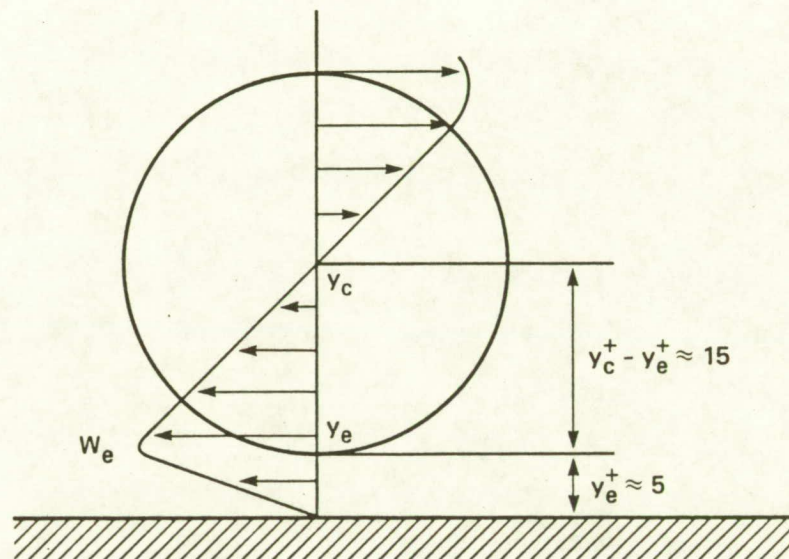


Fig. 8.26g Schematic of near-wall streamwise vortex with resulting high streamwise vorticity at the wall (from Kim, Moin, Moser, 1987).

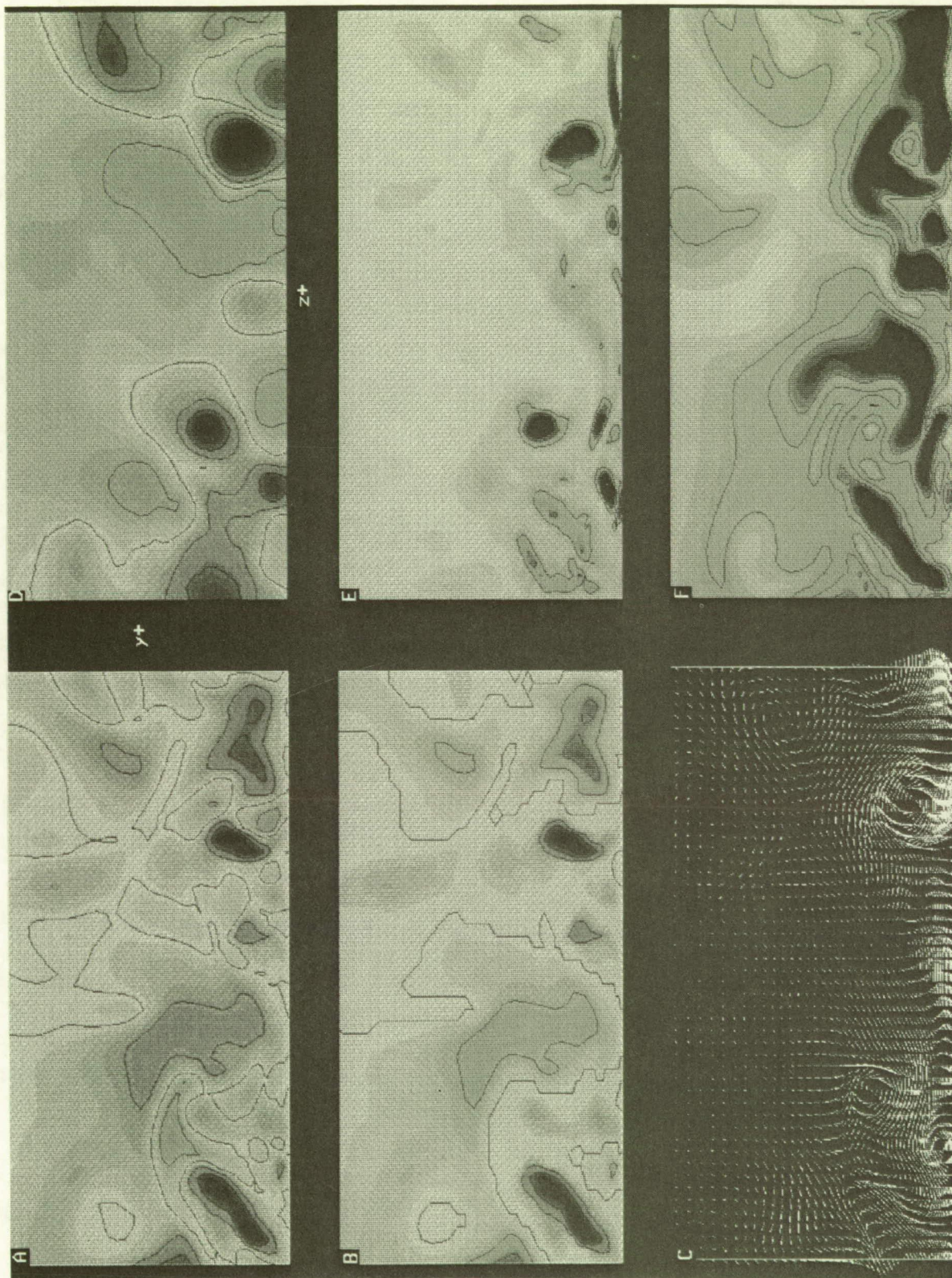


Fig. 8.27 (a-f) Contours of $u'v'$, p , ϵ_f , and TKE in a y - z plane. See Fig. 8.22 for location key. Each plot is $418\Delta z^+$ by $207\Delta y^+$. Contour levels are listed on Fig. 8.22a.

CHAPTER 9 - VORTICES AND THEIR IDENTIFICATION

The concept of vortical motion is intrinsic in the study of coherent structures in turbulent flows. Even in the term “eddy,” we find an implied vortical motion. A significant portion of the boundary layer structure literature is devoted to detection and characterization of vortical elements and structures.

The study of vortices appears to lie at the heart of turbulent boundary layer structure research for several reasons: First, in a boundary layer, any vortex with an orientation other than wall-normal has the potential to function as a “pump” which transports mass and momentum across the mean velocity gradient. Second, the concept of a vortex is invaluable as a conceptual shorthand for a complex class of three-dimensional motions. Given the definition of coherent motion in Sec. 1.5, vortices are among the most coherent of turbulent motions, and tend to be persistent in the absence of destructive instabilities. Finally, strong vortices function as a source for pressure disturbances, by virtue of their low-pressure cores and the high-pressure regions they can induce in the nearby flow.

Because vortical structures may be considered central to the dynamics of boundary layer turbulence (as we shall see in later Chapters), this Chapter will provide a framework for the study of vortical structures in the simulated boundary layer.

9.1 Vortex Definition Issues

One of the hindrances to the study of vortex structures in turbulent boundary layers has been the lack of a rigorous, widely-accepted definition of a vortex for unsteady, viscous flows. For the present effort, the following working definition has been adopted:

A vortex exists when instantaneous streamlines mapped onto a plane normal to the vortex core exhibit a roughly circular or spiral pattern, when viewed from a reference frame moving with the center of the vortex core.

This definition requires an a-priori method for identifying vortex cores, and the process of choosing a reference-frame velocity may be iterative. A number of other vortex definitions exist (e.g. Lugt 1979, Blackwelder and Swearingen 1989) and the issue cannot be considered closed.

The lack of Galilean invariance of the velocity-field flow patterns makes the specific designation of a reference frame velocity necessary (at least in planes which exhibit non-zero time-mean velocity). But to determine the velocity of the vortex core, the vortex itself must have already been identified. This makes the vortex definition itself rather circular. The situation is not hopeless, however, for at least two reasons: 1) Transverse vortices in the boundary layer tend to travel downstream at approximately the local mean velocity, so \bar{U} is usually an excellent first guess for the vortex core velocity; 2) As will be demonstrated in the next section, a number of

scalar fields and Gallilean invariant vector fields are useful for identifying potential vortex cores, which may then be confirmed (or disconfirmed) as vortices by use of the above working definition.

9.1.1 Vortices in the $y - z$ Plane

In the end-view, or $y - z$ plane of the boundary layer, the time-mean velocity is nearly zero, so the above definition based on the instantaneous velocity provides a vortex identification method which is intuitively unambiguous. For example, Fig. 9.1 shows the instantaneous v', w' velocity vectors and the corresponding streamlines for a sample $y - z$ cut through the simulated boundary layer. (Note that these are not streamlines of the three-dimensional flowfield, but rather streamlines integrated through the two-dimensional v', w' velocity field. This qualifier holds for all “streamlines” in 2-D planes mentioned subsequently.) Vortices of a variety of sizes are clearly evident in both views in Fig. 9.1.

Vortices visible in end-plane views need not be (and usually are not) strictly streamwise; they may possess significant spanwise and/or wall-normal components. Thus the term “quasi-streamwise vortex” will be applied to any vortex visible in an instantaneous end-view.

9.1.2 Vortices in the $x - y$ Plane

To demonstrate the effect of reference frame velocity on transverse vortex identification, a series of side-view vector plots in the $x - y$ plane are shown in Fig. 9.2. In the Figure, the same slice of velocity-field data is viewed from a variety of downstream convection velocities. As expected, outer-layer vortices are visible from convection velocities approaching the free-stream velocity, while near-wall vortices are evident from slower reference frames. As mentioned earlier, however, transverse vortices tend to travel downstream at approximately the local mean speed, so a side-view plot (Fig. 9.2) of the perturbation velocity (u', v') vectors illuminates all of the vortices visible from any of the reference frame velocities. Thus, transverse vortices are confirmed in the present study through the use of instantaneous u', v' velocity vectors.

9.1.3 Vortex Propagation Velocities

The issue of vortex definition raises the question of the convection (or propagation) velocity of vortices in a turbulent boundary layer. There is an essential distinction between the apparent velocity of a vortex along its core axis and its velocity perpendicular to the axis.

In the direction normal to the core axis of a vortex, the vortex is convected at essentially the speed of the local particles, according to the Helmholtz' laws of vorticity line movement (Fig. 9.3a). (Viscous diffusion is expected to act on a much longer time-scale than the convective time-scale, so diffusive effects on the vortex

velocity will be small). Thus, a vortex convects with the flow normal to its core, at a speed which may properly be termed its “convection velocity.”

The velocity of a vortex along its core must be considered more carefully. A vortex (as defined by the above working definition) may be thought of as a “bunched” segment of vorticity lines, where the vorticity line density through a cross-section is significantly (although arbitrarily) greater than the local mean. Vorticity lines cannot end within the fluid, but vortices (as defined above) may. While vorticity lines each travel with the fluid particles, the bunched segment that comprises a vortex may move along its core at a velocity quite independent of the fluid speed, through progressive bunching and un-bunching of the vorticity lines. This is analogous to a tubular sleeve sliding along a collection of ropes (Fig. 9.3b). The velocity of a vortex in the direction of its core may therefore be independent of the local fluid velocity, and is thus a “propagation velocity.”

9.1.4 Definitions: Vortical Elements vs. Vortical Structures

It is useful to distinguish between vortical elements and vortical structures. In the present work, a vortical element is defined as a vortex or vortex segment with a single dominant orientation. Examples are “leg,” “neck,” and “head” vortex elements which may occur as portions of a hairpin or half-hairpin vortex (Fig. 9.4). Head elements are transverse vortices, while legs and often necks are “quasi-streamwise” vortices. Leg vortices lie at a shallow angle to the wall; less than approximately 20 degrees. Necks are distinguished by steeper angles of approximately 45 degrees. The difference in angle between legs and necks is arbitrary, but for most of the boundary layer, vortices with intermediate angles of about 30 degrees are relatively uncommon.

A vortex structure is defined as any combination of elements with a common core, generally forming a complex three-dimensional shape. The most commonly discussed vortex structures are hairpins (with extended trailing legs) and horseshoes (without well-defined legs). Horseshoe vortices possess a width/length ratio of approximately unity (as in Theodorsen’s model, see Fig. 11.2) and hairpins are longer in the streamwise direction than they are wide (as in Head and Bandyopadhyay’s high-Reynolds number vortical structures, see Fig. 11.8). This distinction is often unclear or unnecessary, however, and in those cases “hairpin/horseshoe” will be used. Horseshoe-shaped vortical structures will also be referred to as “arches”.

9.2 Detection Methods for Vortices in Simulated Turbulence

Historically, the lack of a definition for vortices in turbulent flow has given rise to a variety of different methods for detecting vortices, most of which involve evaluating the magnitude of a scalar function of the velocity or vorticity field. The numerically simulated turbulence offers the opportunity to evaluate and compare all of these methods against the velocity-field-based definition offered above. The

value of a scalar diagnostic for vortices would be the ability to trace instantaneous vortices through three-dimensional space without having to examine streamlines in cross-cut planes all along the vortex.

During the course of this study, many different vortex identification techniques were explored. The following subset were judged to hold the most promise, and will be compared in the remainder of the chapter.

- 1) Vorticity (magnitude of a particular component, ω_i , or the vorticity vector magnitude, $|\omega|$).
- 2) Vorticity lines (everywhere parallel to the vorticity vector).
- 3) Fluctuating dissipation of turbulence kinetic energy, ϵ' .
- 4) Second invariant of the fluctuating deformation tensor, Π .
- 5) Low static pressure, $-p'$.

Each of these methods is Gallilean invariant, and thus differs fundamentally from the working vortex definition requiring circular instantaneous streamlines. Each method is described below, then evaluated in two and three dimensions.

9.2.1 Vorticity

The most obvious scalar for the identification of vortices is the magnitude of the vorticity component normal to the vortex core. It is also clear, however, that a vortex is not necessary for the presence of vorticity, as a laminar boundary layer demonstrates. Nevertheless, most fluid dynamicists expect a vortex core to be a region of concentrated (that is, greater than the local average) vorticity. The distinction between vorticity and the presence of vortices is one of the key conceptual issues that continue to cloud turbulence structure understanding, and will be addressed at some length in the next section as well as in Chapters 10, 11, and 12.

In the turbulent boundary layer, the use of vorticity magnitude for vortex detection is complicated by the existence of additional, non-vortical, structural features. In the $x - z$ plane near the wall ($y^+ < 40$), the ω_y field is completely dominated by the streaky nature of the u' -field, rendering ω_y virtually useless for identifying near-wall vortices with a wall-normal component (see Fig. 8.6). In the $x - y$ plane, internal shear layers, rather than spanwise vortices, are responsible for most of the concentrations of spanwise vorticity. This is especially true for $y^+ < 80$, as can be seen in (Fig. 8.23). In the $y - z$ plane, other vorticity-producing features are less evident, and the streamwise vorticity is modulated to a large degree by quasi-streamwise vortices. The exception is very near the wall, where spanwise motions and the no-slip condition cause locally large values of $\partial w / \partial y$ (and hence ω_x). However, the correspondence between concentrations of ω_x and quasi-streamwise vortex cores is not always unique, as can be seen by comparing Figs. 8.26d and 8.27c. The outer edge of a vortex often exhibits a vorticity magnitude in excess of the vortex core.

In summary, the vorticity magnitude is useful for boundary layer vortex detection in the $y - z$ plane, but not in the $x - z$ or $x - y$ planes.

9.2.2 Vorticity Lines

The use of vorticity lines (often called vortex lines) in numerically-simulated turbulence has proven useful for detecting vortical structures in the simulation databases (e.g. Moin and Kim, 1985; Kim and Moin, 1986). However, vorticity lines can be misleading unless the distinction between vortex and vorticity is maintained. In the literature of coherent vortical motions, this distinction has not always been made clear. Therefore, as a reminder, this section briefly outlines the causes and implications of horseshoe-shaped vorticity lines in turbulent shear flows. A more thorough discussion of the use of vorticity lines is included in Moin and Kim (1985).

A vorticity line is defined as a line everywhere parallel to the instantaneous vorticity vector, and its location in space is defined by

$$\frac{d\vec{x}}{ds} = \frac{\vec{\omega}}{|\vec{\omega}|} \quad (1)$$

where \vec{x} is the position vector of the vorticity line, s is the distance measured along the vorticity line, and $\vec{\omega}(\vec{x})$ is the vorticity field. In the absence of viscous diffusion, vorticity lines cannot end within the flow, and must travel with the fluid particles.

In a shear flow, it is a kinematical necessity that upright, downstream-leaning, loop-shaped vorticity lines surround a region of fluid which is lifted upwards from the lower speed region into the higher speed flow. Assume a barotropic fluid with conservative body forces, and, for the purpose of demonstration, ignore viscous diffusion effects (which occur over much longer time-scales than those of turbulence production). If we consider outward movement of a low-speed fluid parcel of limited spanwise extent (like a $(u'v')_2$ ejection), initially spanwise vorticity lines will be lifted outward in the region of the upward-moving fluid, and carried downstream by the higher speed flow above. The result is a sloping upright loop in the vorticity lines, without the existence of a vortex. This is illustrated in Fig. 9.5, in which a vorticity line has been integrated through a localized region of lifting, low-speed $(+v', -u')$ fluid within an otherwise two-dimensional, linear shear flow. Similar arguments describe the formation of inverted, upstream-leaning vorticity-line loops for parcels of high-speed, wallward-moving fluid (sweeps).

Vortices consist of “bundles” of vorticity lines, with rotational motion about the bundle axis, so single vorticity lines cannot be construed as vortices. Thus, arrays of “horseshoe”-shaped vorticity lines must always accompany ejections and sweeps, but the association of vortices with these motions is not necessary from a kinematic point of view. To carry the point a bit further, any shear flow with a

mean Reynolds shear stress (and hence $(u'v')_2$ and $(u'v')_4$ motions) must possess horseshoe-shaped vorticity lines, whether or not vortices are present.

When vorticity lines are traced in the vicinity of true vortices, the results can be surprisingly misleading. Consider, for example, a streamwise vortex in a shear flow (a common occurrence in the near-wall region of turbulent boundary layers). Unless the starting point for the integration of equation (1) is chosen almost precisely within the vortex core, the vorticity lines will trace out well-defined upright hairpins on the outward-rotating side of the streamwise vortex, and inverted hairpins on the wallward-rotating side. This is demonstrated in Fig. 9.6a, which shows vorticity lines computed on both sides of a near-wall quasi-streamwise vortex found in the numerically-simulated boundary layer. (Note that even if the starting point for the integration was within the core, the vorticity line will not trace the vortex unless the background vorticity is negligible compared to that of the vortex.) A schematic drawing of vorticity lines with a generic quasi-streamwise vortex is shown in Fig. 9.6b.

These points are not made to denigrate the method of vorticity line tracing, but to raise a warning that horseshoe or hairpin-shaped vorticity lines are vastly more common than similarly shaped vortices. This is a crucial dynamic issue, since isolated vorticity lines play a different role than true vortices with regard to induced motions and propagation of pressure disturbances.

9.2.3 Dissipation

Classical scaling arguments for turbulence ascribe the dissipation of turbulence kinetic energy to the smallest-scale motions in the flow. Since energetic small-scale motions are a product of vortex stretching, it is expected that the cores of stretching vortices are energy dissipation sites. It was shown in Sec. 8.1.1.7 that the regions between side-by-side sweep/ejection pairs in the buffer zone (cores of suggested quasi-streamwise vortices) exhibit high values of dissipation. An instantaneous contribution to the mean dissipation term may be defined as

$$\epsilon' \equiv 2\nu s'_{ij}s'_{ij} \quad (9.1)$$

where

$$s'_{ij} \equiv \frac{1}{2} \left(\frac{\partial u'_i}{\partial x_j} + \frac{\partial u'_j}{\partial x_i} \right) \quad (9.2)$$

Elevated values of ϵ' are to be expected in any strong internal shear layer, as well as within vortex cores, possibly reducing the value of ϵ' as a vortex detection method. In fact, the instantaneous dissipation may be written as

$$\epsilon' = \nu(\omega'_i\omega'_i + u'_{i,j}u'_{j,i}) \quad (9.3)$$

which displays the relationship between ϵ' and the square of the vorticity magnitude, $\omega'_i \omega'_i$. Regions of concentrated vorticity such as vortices and shear layers would therefore both be expected to contribute significantly to the dissipation, depending on the value of $u'_{i,j} u'_{j,i}$.

As discussed in Section 8.1.1.7, the dissipation field is estimated from the simulation velocity and vorticity fields using central differences for the spatial gradients, which effectively “filters” the dissipation field. Although this effect does not alter the qualitative results obtained here (see Fig. 8.13a), the subscript “f” is appended to ϵ' as a reminder.

9.2.4 Second Invariant of the Deformation Tensor

Chong, Perry, and Cantwell (1990), following Perry and Chong (1987) have proposed using the second invariant of the fluctuating deformation tensor to identify regions which exhibit the circular or spiral motion attributed to a vortex. The second invariant is basically the difference between the dissipation rate and the vorticity magnitude:

$$II' \equiv u'_{i,j} u'_{j,i} = 2s'_{ij} s'_{ij} - \omega'_i \omega'_i \quad (9.4)$$

Thus, II' involves a balance between the straining and rotational motions, with $II' < 0$ in the case where $\omega'_i \omega'_i$ dominates. However, as mentioned above, large values of vorticity magnitude do not necessarily denote true rotation with curved streamlines. Note that the fluctuating forms of ϵ and II differ from their instantaneous forms only by $\partial \bar{U} / \partial y$, which is dominated by the gradient in the viscous sublayer. The fluctuating forms are thus employed to focus attention upon the internal turbulent structures rather than on the near-wall mean gradient.

Like the dissipation scalar, II has also been estimated with central differences, and is similarly identified by the “f” subscript.

9.2.5 Low Pressure

Vortex cores are expected to coincide with pressure minima in the boundary layer, as can be seen from an idealized form of the Navier-Stokes equations. In cylindrical coordinates, the radial momentum equation is:

$$\frac{\partial V_r}{\partial t} + (\vec{V} \cdot \vec{\nabla}) V_r - \frac{1}{r} V_\theta^2 = -\frac{1}{\rho} \frac{\partial p}{\partial r} + \nu (\nabla^2 V_r - \frac{V_r}{r^2} - \frac{2}{r^2} \frac{\partial V_\theta}{\partial \theta}) \quad (9.5)$$

where V_r and V_θ are the radial and tangential velocity components, respectively, and r and θ are the radial and tangential coordinate directions.

To focus upon vortical motion which satisfies the definition of Section 9.1, consider a flow with purely circular streamlines in the absence of circumferential variations. For this case, Eqn. 9.5 collapses to the Euler n -equation for flow normal to a curved streamline, even for unsteady and viscous flows:

$$\frac{1}{\rho} \frac{dp}{dr} = \frac{V_\theta^2}{R} \quad (9.6)$$

where r is the local coordinate normal to a streamline, R is the radius of curvature, and V_θ is the local fluid velocity along the streamline. Eqn. 9.6 indicates that pressure decreases in the inward direction, toward the center of streamline curvature. Strong vortices in unsteady, viscous flow are thus expected to possess low-pressure cores, hence the possible utility of the turbulent pressure field as a vortex identification technique.

The circular-streamline flow may also be used to develop a feel for the pressure field within a vortex core. Such a flow is two-dimensional (no axial variation), with only a single component of vorticity, the transport of which is described by:

$$\frac{\partial \omega}{\partial t} = \nu \left(\frac{\partial^2 \omega}{\partial r^2} + \frac{1}{r} \frac{\partial \omega}{\partial r} \right) \quad (9.7)$$

where

$$\omega = \frac{1}{r} \frac{\partial}{\partial r} (r V_\theta) \quad (9.8)$$

For the initial condition of a line vortex of strength Γ_0 , the solution of Eqn. 9.8 is the Oseen distribution of circumferential velocity:

$$V_\theta = \frac{\Gamma_0}{2\pi r} (1 - e^{-r^2/4\nu t}) \quad (9.9)$$

Eqn. 9.9 describes the temporal decay of a line vortex in terms of its circumferential velocity profiles. Although there are no clear characteristic length scales in the unbounded idealized Oseen case, it is useful to normalize Eqn. 9.9 by inner variables, in anticipation of comparison with near-wall vortical structures. The Oseen distribution in wall variables is then:

$$V_\theta^+ = \Gamma_0^+ \frac{1}{r^+} (1 - e^{-r^{+2}/4t^+}) \quad (9.10)$$

where $V_\theta^+ = V_\theta/u_\tau$, $\Gamma_0^+ = \Gamma_0/(2\pi\nu)$, $r^+ = ru_\tau/\nu$, and $t^+ = tu_\tau^2/\nu$. The variation of V_θ with r^+ as a function of t^+ is shown in Fig. 9.7 for two typical values of circulation of a near-wall quasi-streamwise vortex. (See Chapter 11 for vortex circulation results).

An estimate of the pressure distribution through the Oseen vortex may be obtained by integrating Euler's radial equation, Eqn. 9.6:

$$\frac{1}{\rho} \frac{dp}{dr} = \frac{V_\theta^2}{r} \quad (9.6)$$

$$\frac{1}{\rho} \int_r^\infty dp = \int_r^\infty \frac{V_\theta^2}{r} dr \quad (9.11)$$

$$\frac{1}{\rho} (p(\infty) - p(r)) = \int_r^\infty \frac{V_\theta^2}{r} dr \quad (9.12)$$

Substituting the Oseen velocity distribution (Eqn. 9.9) into Eqn. 9.12 gives the radial pressure distribution:

$$\frac{1}{\rho} (p(\infty) - p(r)) = \int_r^\infty \frac{\Gamma_0^2}{4\pi^2 r^3} (1 - e^{-r^2/4\nu t})^2 dr \quad (9.13)$$

Setting the free-stream pressure to zero and non-dimensionalizing by wall variables gives:

$$p^+(r) = - \int_{r^+}^\infty \frac{\Gamma_0^{+2}}{r^{+3}} (1 - e^{-r^{+2}/4t^+})^2 dr^+ \quad (9.14)$$

where $p^+ = p/\rho u_\tau^2$.

The radial Euler equation (Eqn. 9.6) and the Oseen velocity distribution (Eqn. 9.10) are valid for incompressible, viscous, unsteady flows with purely circular streamlines. Therefore, the resulting pressure integral (Eqn. 9.14) should reflect the pressure drop through an idealized vortex in turbulent flow.

The pressure distribution given by numerical integration of Eqn. 9.14 for an initial circulation $\Gamma_0^+ = 20$ is plotted for several times in Fig. 9.8. As the vortex diffuses, the pressure minima within the vortex relaxes toward ambient rapidly, but only within the relatively narrow core region. Even at large values of t^+ however, the Oseen vortex retains a well-defined low-pressure region within its core, supporting the notion of using pressure minima to locate vortices.

Both the vortex definition in Sec. 9.1 and the Oseen model are based upon instantaneously circular (or nearly so) streamlines. Thus a comparison between the Oseen pressure field and that of vortices in the numerical simulation provides a check on the validity of using low-pressure regions to detect vortices which satisfy the definition proposed above.

To check the resemblance of the Oseen model with instantaneous vortices in the simulated boundary layer, a sample quasi-streamwise vortex was chosen for comparison. Fig. 9.9 shows the sample vortex, which is well-defined in the $y-z$ plane. The computed non-dimensional circulation is approximately 75, which is quite high, as will be shown in Chapter 11. The pressure distribution for the DNS vortex was taken along a spanwise line at $y^+ \approx 33$, as shown in Fig. 9.9. The comparative Oseen pressure distribution was computed with Eqn. 9.14, using $\Gamma_0^+ = 75$ and a value of $t^+ = 60$, which was chosen to provide the same minimum

pressure as that found at the center of the DNS vortex. The resulting Oseen pressure distribution agrees well with the DNS distribution, as shown in Fig. 9.10.

The above results have shown that an Oseen vortex model retains a low-pressure core over long diffusing times, and that at least some vortices in the DNS boundary layer resemble Oseen vortices. This suggests that instantaneous vortices within the turbulent boundary layer contain low-pressure cores, in agreement with our original hypothesis. We may generalize to postulate that all boundary layer vortices with sufficient strength to induce significant momentum transport possess low-pressure cores. But if low-pressure regions are to be useful as vortex identifiers, the question that must be addressed is “are all low-pressure regions vortices?” Locally curved streamlines can produce a radial pressure gradient without being circular, and local inviscid, “Bernoulli-type” accelerations are also expected to create low-pressure regions. The following sections will show that although low pressures may arise from a number of sources, virtually all **elongated** low-pressure regions are vortices.

Another important question is why pressure should be more useful than, say, vorticity for detecting vortices that are involved with momentum transport. Vorticity is a “point” quantity, constructed from spatial gradients at a single location. Large vortices with high values of circulation (representing strong “transporters”) often support large velocity gradients spread over broad areas, such that the vorticity magnitude at any point in the vortex is a poor indicator of the total vortex strength.

The pressure, however, is a volume-integrated field quantity which is related to the velocity field through a Poisson equation:

$$p_{,ii} = -u_{i,j}u_{j,i} \quad (9.15)$$

The pressure is a function of the integrated vorticity, Γ (Eqn. 9.14), rather than its point magnitude, so high-circulation vortices are more likely to be identified by low pressure than by high local vorticity. More important, the pressure field is likely to exhibit less intermittent small-scale “noise” than the vorticity field. The pressure field is much less affected by intense, highly localized structural features such as shear layers, which strongly affect the vorticity field and make vortex-hunting with vorticity problematic.

The validity of these arguments will be explored in the next sections, which compare the utility of pressure, vorticity, dissipation, and II' for identifying vortices in the numerical turbulent boundary layer.

9.3 Comparisons in Two Dimensions

For detecting vortices in two-dimensional planes of instantaneous turbulence simulation data, the following techniques are compared:

- perturbation velocity vectors in the 2-D plane
- instantaneous streamlines in the 2-D plane
- the component of vorticity normal to the plane
- the fluctuating pressure field
- instantaneous dissipation of TKE, ϵ'_f
- second invariant of the fluctuating deformation tensor, II_f

In the color contour plots shown in Fig. 9.11 - 9.15, negative quantities are plotted in cyan and blue, positive in yellow and red, and zero (or mean value) in white. Darker colors correspond to higher magnitudes. Numerical keys for the colors are given in each figure caption.

9.3.1 $y - z$ Planes

Vortex detection in the end-view, or $y - z$ plane is relatively unambiguous due to the lack of a significant time-mean velocity. (\bar{V} is non-zero, but negligible). For comparison purposes, a $y - z$ cut-plane has been chosen at random from the simulation database. The plane dimensions are $\Delta z^+ = 418$, $3 < y^+ < 254$ (Figs. 9.11 and 9.12).

At least three well-defined vortices are visible for $y^+ < 80$ in the v', w' vectors in Fig. 9.11. Each vortex displays a circular velocity field, meeting the criterion of the working definition proposed earlier, and is associated with significant v and w motions. These vortices are also evident in the streamlines integrated through the v, w field, along with a number of additional vortices. This comparison points out an intrinsic difficulty with integrated streamlines: all vortices are made visible, but many are too weak to be significant in the sense of transport potential. It is difficult to ascertain the relative strength of vortices from streamline patterns, but fairly simple to do so from the vectors.

Streamwise vorticity contours are overlaid with streamlines in Fig. 9.11. The vorticity does an excellent job of identifying each of the “strong” vortices visible in the vector field. However, ω_x is also concentrated in local $\partial w / \partial y$ shear layers, making it difficult to differentiate between vortices and shear layers without the aid of streamline or vector plots.

The fluctuating pressure field is also overlaid with instantaneous streamlines in Fig. 9.11. As expected from Section 9.2.5, strong vortices are marked by low pressure ($-p'$), weak vortices are not, and convergence or “eddy interaction” zones are marked by high pressure ($+p'$). The striking aspect of the pressure contour plot (in Fig. 9.11 as well as in the many other $y - z$ planes studied) is the lack of intermittent noise; virtually every minimum and maximum in the pressure field can be correlated with a well-defined flow-pattern in the vectors or streamlines. The low-noise quality of the pressure field makes it a promising candidate for “blind” identification of vortices, without the need for overlaid vector fields. This would allow computer searching of the simulation database for vortex cores, rather than

relying entirely on subjective human judgement to identify vortices.

From Sections 8.1.1.7 and 9.2.3, we expect the magnitude of the instantaneous dissipation, ϵ' , to peak within the cores of stretching vortices and within strong internal shear layers. Confirmation of this expectation has already been shown in Figs. 8.24 and 8.27, and is also supported by the ϵ'_f contours in Fig. 9.12. Here, the intense vortices visible in the vector plot each exhibit concentrations of ϵ'_f . The $\partial w/\partial y$ shear layers which cluttered the ω_x plot do not affect the dissipation function significantly, but the stronger $\partial u'/\partial y$ shear layers do, and a cross section of one of these can be seen at the bottom right of the ϵ'_f plot. In general, ϵ'_f contours show a greater correlation with intense vortices than ω_x contours, and closely resemble the $-p'$ contours. However, the conclusion that ϵ'_f is useful for vortex detection turns out to hold true only in near-wall regions of $y - z$ planes, as will be shown in the next sections.

Contours of the second invariant of $\partial u'_i/\partial x_j$ in the $y - z$ plane are nearly identical to those of ϵ'_f , as seen in Fig. 9.12. For the vortices in the sample data-plane, the dissipation outweighs the vorticity magnitude, resulting in a positive value of II_f .

To confirm that the vortices being hunted are indeed contributors to turbulence production, the second and fourth quadrants of $u'v'$ are also plotted in Fig. 9.12. Yellow and red contours correspond to $(u'v')_2$ and cyan and blue contours are $(u'v')_4$. The strong vortex near the wall at the right of Fig. 9.12 is associated with very high local peaks in $u'v'$. Other strong vortices are similarly associated with contributions to the Reynolds shear stress, justifying the attention being paid to vortices and their detection. Further exploration of the role of quasi-streamwise vortices in turbulence production is found in Chapters 10 and 11.

To summarize vortex detection methods in the $y - z$ plane, v, w vectors clearly display the strong vortices, while streamlines show all the vortices, without regard to their strength. Streamwise vorticity is concentrated in vortices, but also in shear layers. Low pressure regions exhibit an excellent and nearly unique correspondence with strong vortices, and do not reflect internal shear layers. Dissipation and II_f are also well-correlated with vortex cores, with only minor spurious peaks due to shear layers.

9.3.2 $x - y$ Planes

In side-view planes, vortices can be visualized with u', v' vectors, assuming that vortices move at approximately the local mean velocity. This method becomes ambiguous in the near-wall region due to the high mean gradient, but is fairly accurate otherwise, as discussed in Section 9.1.2. An example is shown in Fig. 9.13, in which u', v' vectors are plotted in an $x - y$ cut through the simulated boundary layer. A large transverse vortex is visible in the vector pattern at $y^+ \approx 200$, as are smaller vortices at $y^+ \approx 60$ and 25. Note that the magnitude of $-u'$ below the large

outer vortex exceeds that of $+u'$ above it, suggesting that the vortex is convecting at slightly less than the value of \bar{U} at its center.

Contours of fluctuating spanwise vorticity plotted in Fig. 9.13 exhibit ω'_z peaks at the locations of the vortices sighted in the velocity vector field, but also show intense vorticity concentrations along the numerous $\partial u'/\partial y$ shear layers. (As shown in Fig. 8.23g, near-wall shear layers are also clearly visible in contours of ω_z and $|\omega|$.) Consideration of many side-view planes has shown that in the outer region of the boundary layer ($y/\delta > 0.5$), strong ω'_z peaks are commonly associated with transverse vortex cores. Nearer the wall, shear layers dominate the vorticity field, making independent transverse vortex detection with ω'_z almost impossible.

In side-view planes as well as end-view planes, the pressure-field is a good identifier of transverse vortices, as shown by the distinct pressure minima at vortex locations in Fig. 9.13. In the figure, a strong low-pressure region without association with a transverse vortex occurs beneath the large outer vortex. In this case, examination of the three-dimensional data volume found that a quasi-streamwise vortex at that location was responsible for the pressure minimum. The pressure field can be misleading when considered in two-dimensional slices, unlike directional quantities such as the vorticity component normal to the plane.

The magnitude of the instantaneous dissipation was reasonably successful at identifying quasi-streamwise vortices in $y - z$ planes, but is considerable less useful for identifying transverse vortices in $x - y$ planes, as can be seen in Fig. 9.14. In the figure, the near-wall transverse vortex shows a high value of ϵ'_f , but the outer vortices do not. This may be because high dissipation rates are expected within rapidly stretching vortices, which occur in the severe gradient near the wall. Outer-region vortices are less likely to undergo rapid stretching, and so dissipate less TKE.

The second invariant, II_f , again resembles ϵ'_f in the side-view planes, but exhibits a slightly negative magnitude in the core of outer-region vortices. These vortices contain vorticity, as seen in Fig. 9.13, but little dissipation, giving II_f a negative value (Eqn. 9.4). However, the II_f -field, as well as the ϵ'_f -field is too dominated by shear-layers to be reliable for transverse vortex identification.

Contours of $(u'v')_2$ and $(u'v')_4$ are also shown in figure 9.14. The outer-region transverse vortex visible in the u', v' vectors is associated with a very large and intense ejection, in accordance with the kinematics sketched in Fig. 8.24g. Detection of such large outer-region vortices is more difficult than the near-wall quasi-streamwise vortices, but is clearly important for insight into turbulence production mechanisms.

9.4 Comparisons in Three Dimensions

The reason for pursuing methods of identifying vortices with scalar magnitudes rather than vector or streamline plots is to allow marking the three-dimensional

shape of vortices, and then to follow their evolution in time. This is clearly not possible with individual planar vector plots. To plot a scalar quantity in three dimensions, a contour value must first be chosen. In a plane, this “threshold” corresponds to a contour line; in a volume, it becomes a three-dimensional contour surface, with higher magnitudes inside the surface and lower outside (or vise-versa).

For three-dimensional vortices, $-p'$, ϵ'_f , all three components of vorticity, plus the fluctuating vorticity magnitude will be compared. To test the performance of each scalar in three dimensions, a contour value for each is first chosen from a $y-z$ plane intersecting a quasi-streamwise vortex. Planar contours and the selected threshold value are shown for each of the scalars in Fig. 9.15. The threshold values have been chosen to roughly encircle the sample quasi-streamwise vortex. The relationship between the sample 2-D vortex and the computational subvolume through which it is to be traced is shown in Fig. 9.16.

Three-dimensional contour surfaces in the subvolume for each of the scalars are shown in Fig. 9.17. The low-pressure surface displays a striking series of loops and hooks, as well as a long quasi-streamwise segment. Low-pressure contours in this and many other subvolumes are generally elongated, and elongated low-pressure regions consist of vortices for every case checked. The low-pressure field is significantly less noisy than the other scalars plotted in the figures. Because of the strong resemblance of the low-pressure structure to various hairpin-vortex models, the vortex elements in this example are labeled according to Fig. 9.4.

A separate surface for each component of the fluctuating vorticity is plotted in Fig. 9.17. The sublayer and buffer layer regions ($y^+ < 25$) have been removed to avoid obscuration of the major structures by the highly complex near-wall vorticity field. The structure of the vorticity field is perhaps better visualized by the magnitude of the fluctuating vorticity vector, for which an iso-value surface is shown in Fig. 9.17. The major features visible in the low-pressure surface are discernable in the $|\omega'|$ surface, but they would not be identified without the pressure plot as a reference. In fact, vorticity surfaces were plotted without particular success for some months before the utility of low-pressure surfaces were realized.

Surfaces of constant dissipation rate are also plotted for the subvolume in Fig. 9.17. Near the wall, quasi-streamwise vortices are visible as high-dissipation regions, as are near-wall shear layers. Dissipation in the outer region is generally below the magnitude of the contour level chosen. In general, the three-dimensional vortical structure so evident in the pressure field is not reflected by either the II_f -field (not shown) or by the ϵ'_f -field.

The three-dimensional shape of the $-p'$ surface in Fig. 9.17 deserves further scrutiny. The most pressing issue is to confirm whether the elongated low-pressure regions are indeed vortices according to our working definition. In Fig. 9.18, the low-pressure regions are intersected by a number of $y-z$ planes, in which instantaneous

v, w vectors are plotted in Fig. 9.19. The results show that the low-pressure region encloses a true vortex in every case. The picture of Fig. 9.18 changes with different choices of contour level, but the general geometry of the elongated low-pressure regions is only weakly sensitive to contour level. This is because strong vortices tend to possess a rapid radial pressure gradient (Fig. 9.15 and Eqn. 9.6). Sensitivity of the low-pressure surfaces to variations in contour level is discussed further in Chapter 10.

Not all low-pressure regions are vortices, but the examination of at least 150 cases, in addition to much additional indirect evidence has convinced the author that virtually all **elongated** low-pressure regions consist of relatively strong vortices. Combinations of low pressure and high $|\omega'|$ have also been tried to unravel some of the non-elongated low-pressure regions. Since these regions are often not identifiable vortices, the vorticity is concentrated in shear layers that surround the region, and the combination of $|\omega'|$ and $-p'$ does not usually lead to new insight.

For comparison, a set of vorticity lines initiated from section D of the long vortex leg in Fig. 9.18 is plotted in Fig. 9.20. Colors are used only to identify the starting locations of the vorticity lines. Although the lines of integration through the vorticity field are somewhat tangled, both vortical loops are made visible. It is difficult to detect new vortical structures with vorticity lines, for the reasons outlined in Section 9.2.2. However, if started from a section through a known vortex, vorticity lines provide a useful diagnostic of the spatial extent of that vortex.

9.5 Summary of Vortex Detection Methods

In the near-wall region, low-pressure, instantaneous dissipation rate, and streamwise vorticity are each fairly successful at detecting quasi-streamwise vortices, with their relative reliability given by the order listed. In the outer region, vorticity is much better than dissipation, although low pressure is better yet. In general, however, the vorticity field is too contaminated with noise from internal shear layers to be consistently effective for locating vortices. For three dimensional vortical structures throughout the boundary layer, elongated low-pressure regions display a high degree of correspondence to vortices of significant circulation intensity. For this reason, elongated low-pressure surfaces will be used in the remainder of the chapters to identify, examine, and categorize instantaneous vortices.

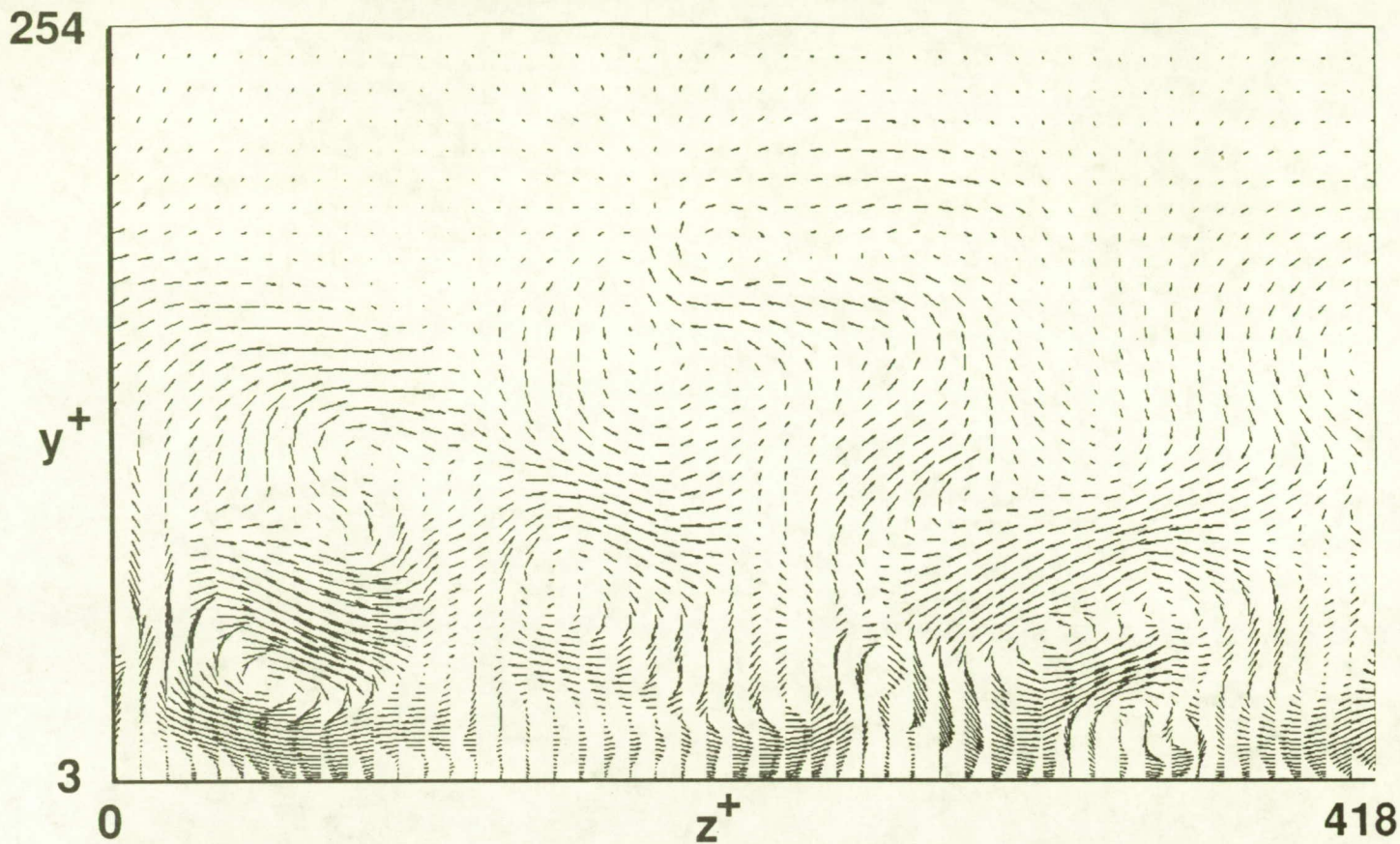


Fig. 9.1a Example of instantaneous v', w' vectors in a y - z plane.

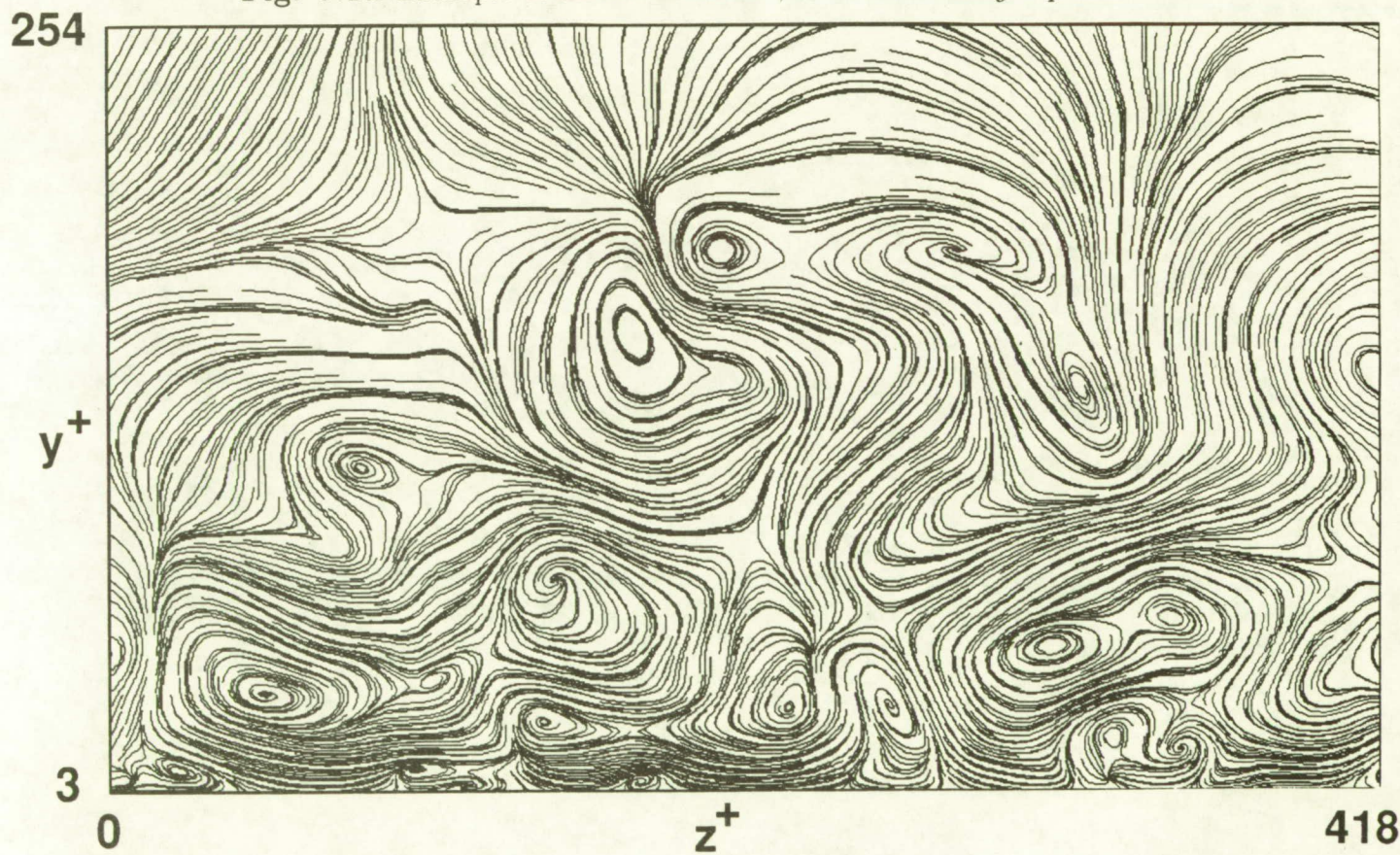


Fig. 9.1b Two-dimensional streamlines integrated through the instantaneous velocity field of Fig. 9.1a.

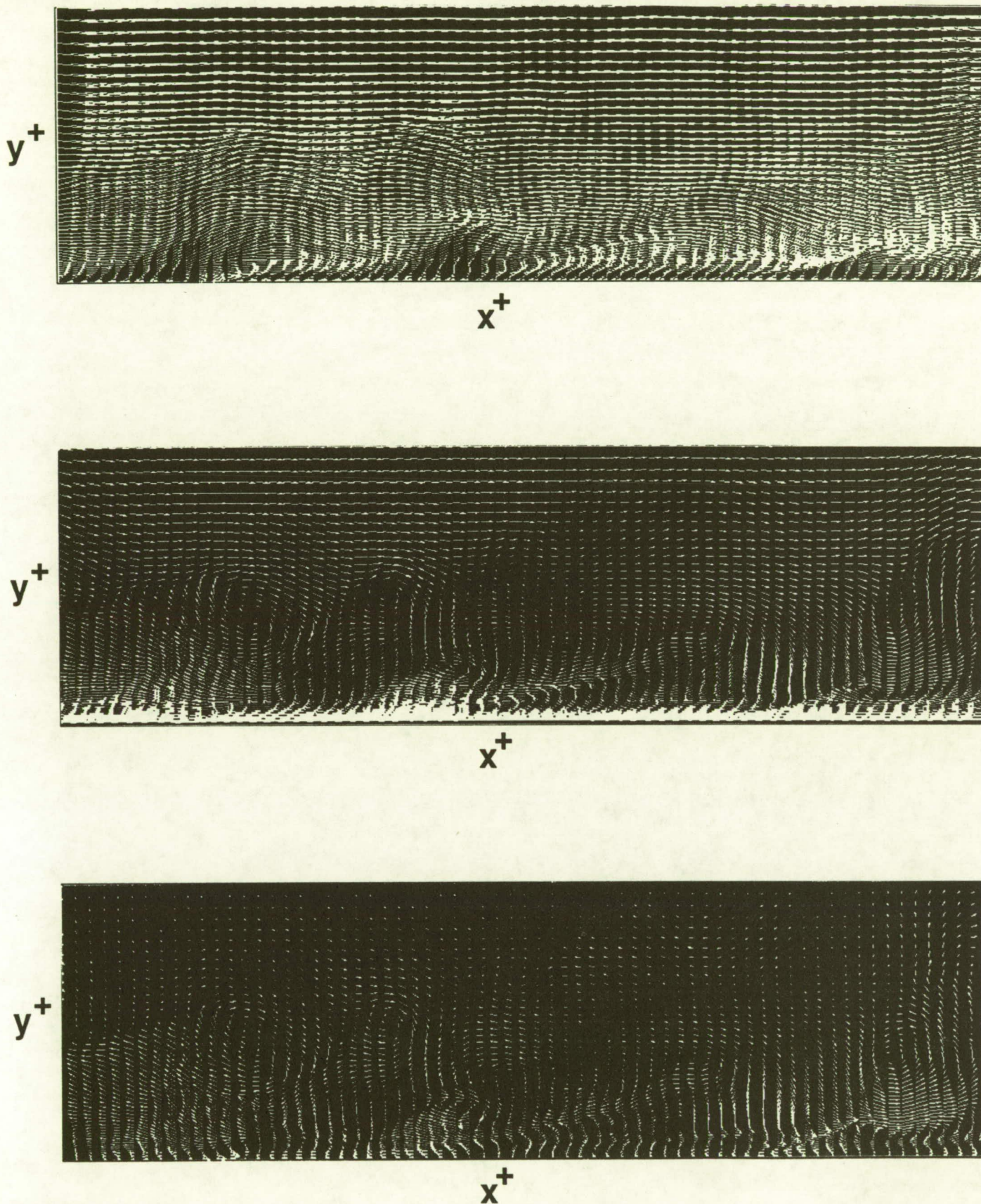


Fig. 9.2 Effect of reference-frame convection velocity on instantaneous x - y plane vector field. Top: $U_{conv} = 6u_\tau \approx 0.3U_e$. Middle: $U_{conv} = 16u_\tau \approx 0.8U_e$. Bottom: u', v' vectors; $U_{conv} = \bar{U}(y)$.

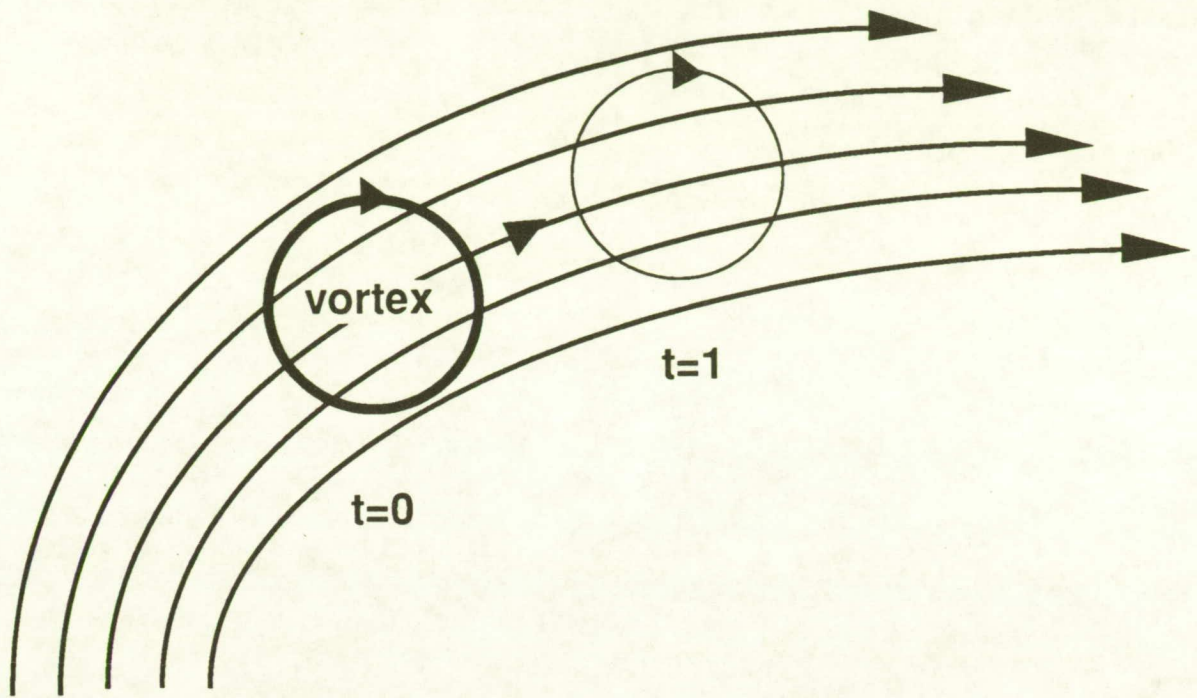


Fig. 9.3a Convection of a vortex in a direction normal to its core axis.

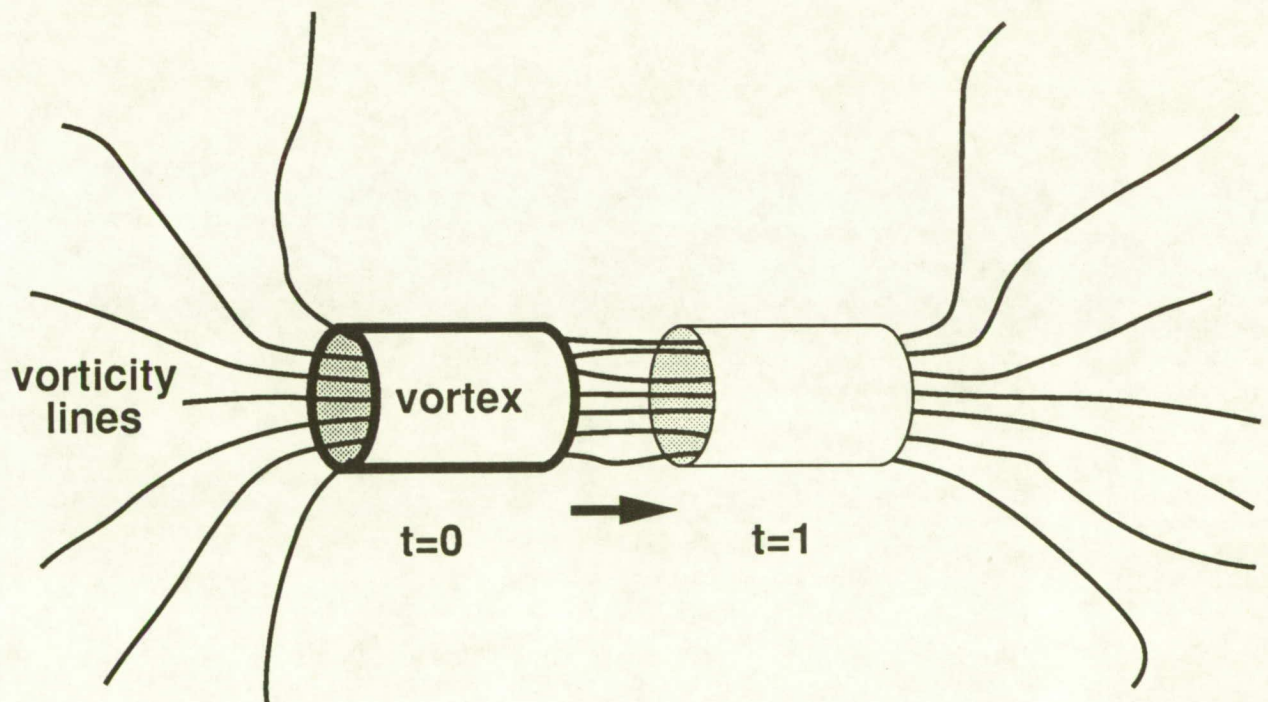


Fig. 9.3b Propagation of a vortex along its core axis.

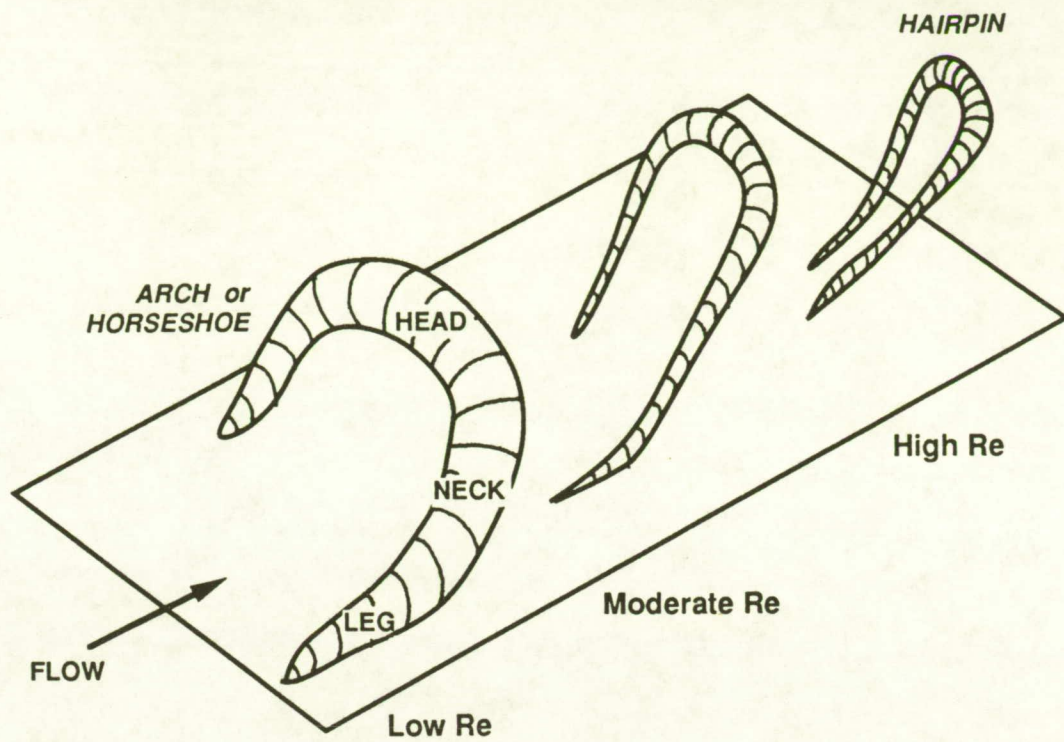


Fig. 9.4 Schematic diagrams of vortical structures and associated terminology. One-sided arches and hairpins are also possible and are more common than symmetrical loops at low Reynolds numbers.

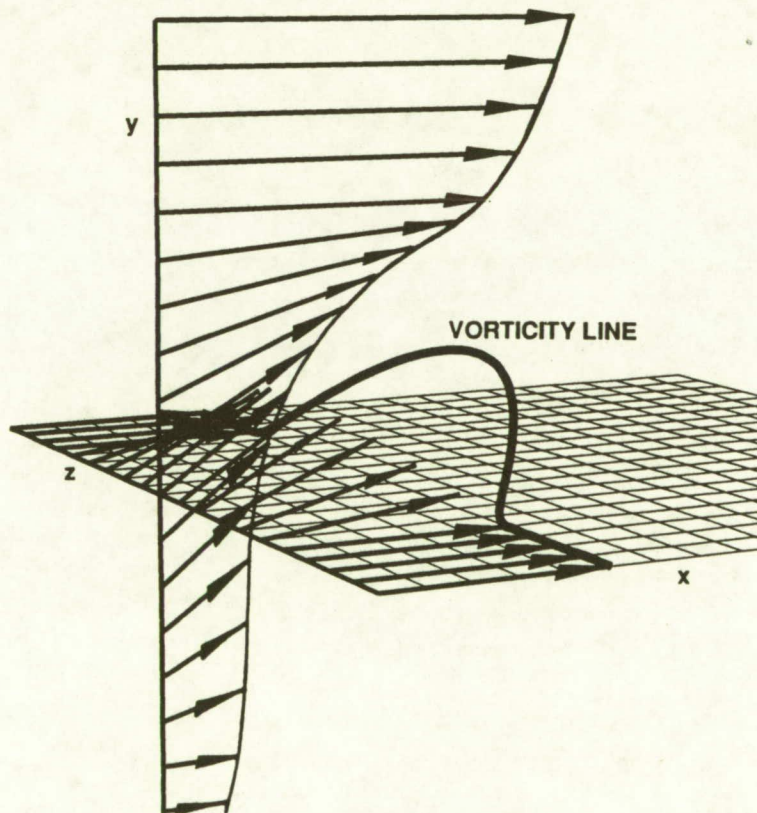


Fig. 9.5 Vorticity line computed for a localized region of lifting, low-speed fluid ($-u'$, $+v'$) within an otherwise two-dimensional, linear shear flow.

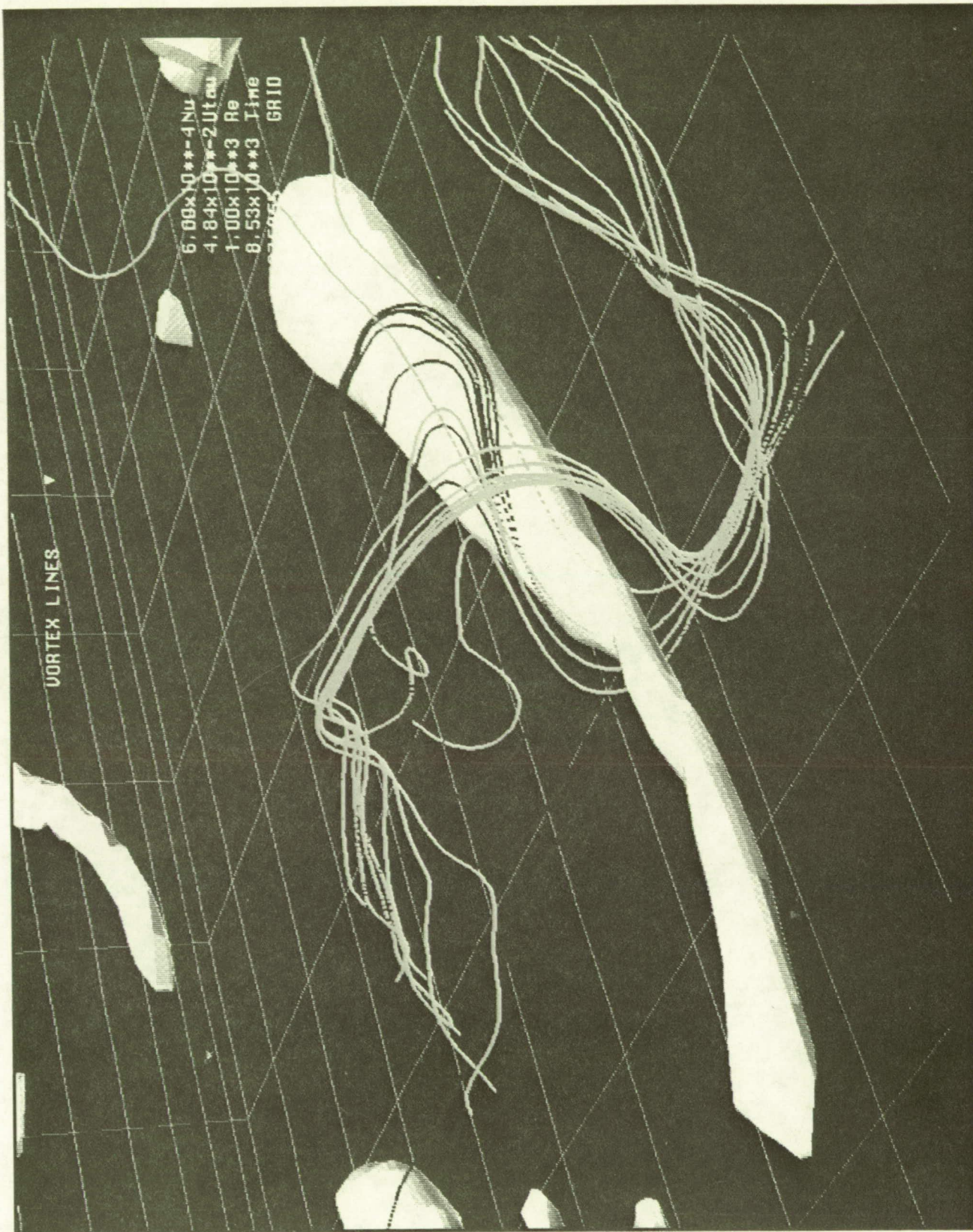


Fig. 9.6a Vorticity lines traced from either side of a quasi-streamwise vortex in the simulated boundary layer. White: low-pressure vortex core. Yellow: vorticity line initiated from right-hand side of vortex. Red: vorticity line initiated from left-hand side of vortex.

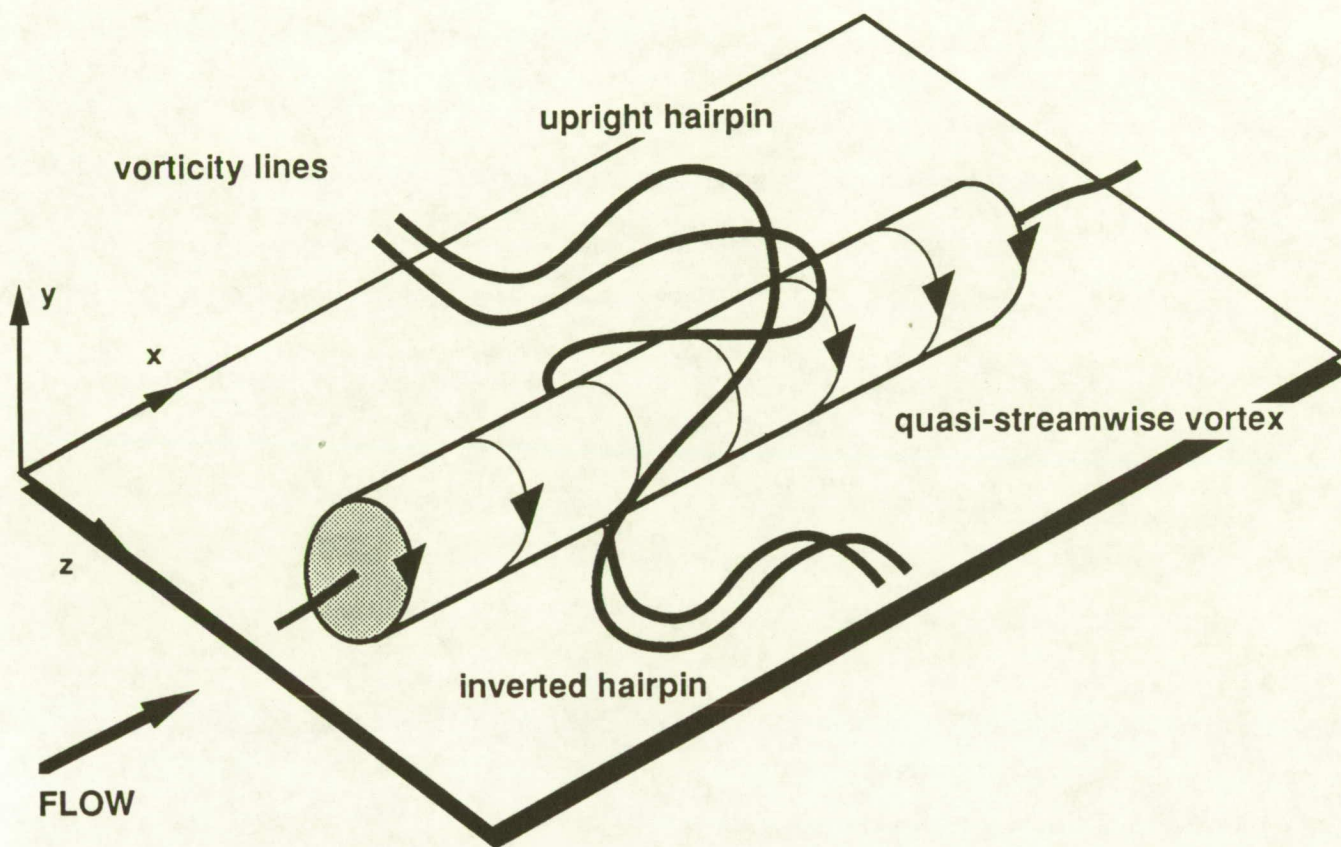


Fig. 9.6b Vorticity lines traced from either side of a quasi-streamwise vortex in a boundary layer, showing upright and inverted hairpin shapes.

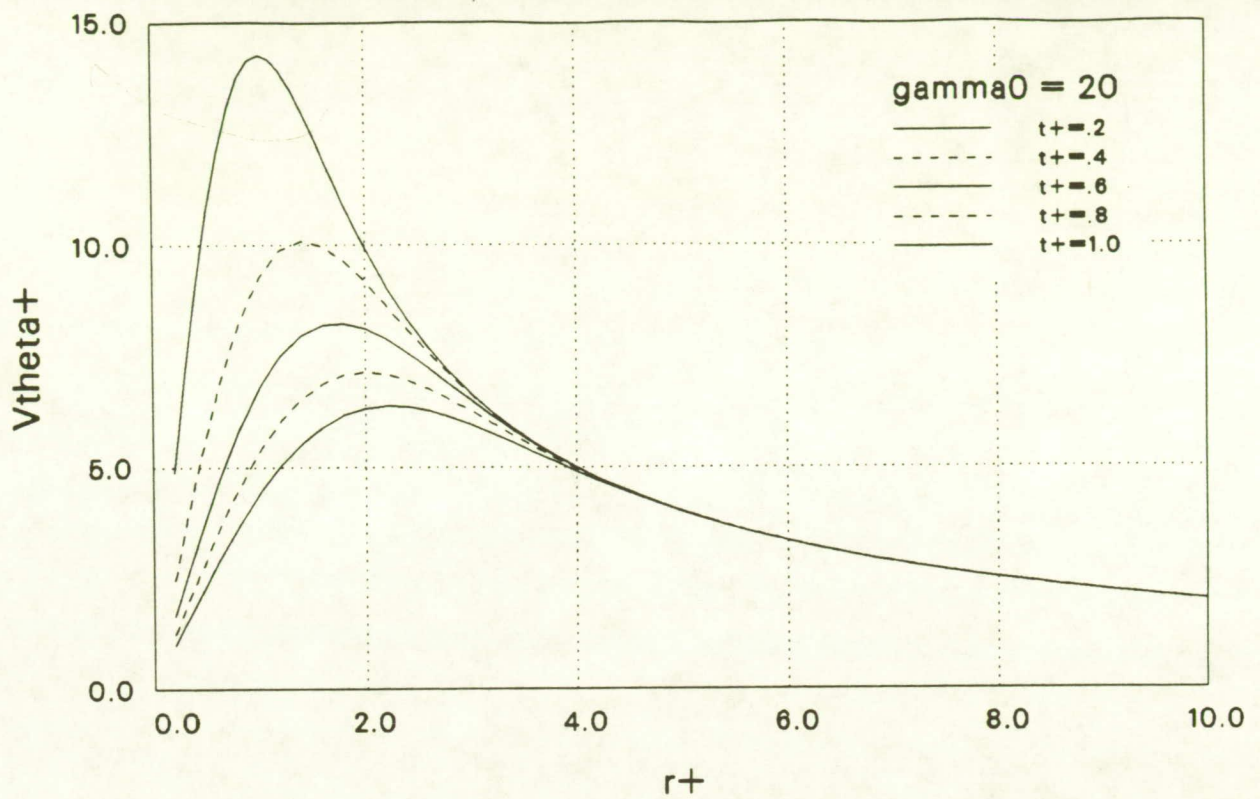


Fig. 9.7a Radial distribution of circumferential velocity V_{θ} for a temporally diffusing Oseen vortex (eqn. 9.10). Initial circulation: $\Gamma_0^+ = 20$.

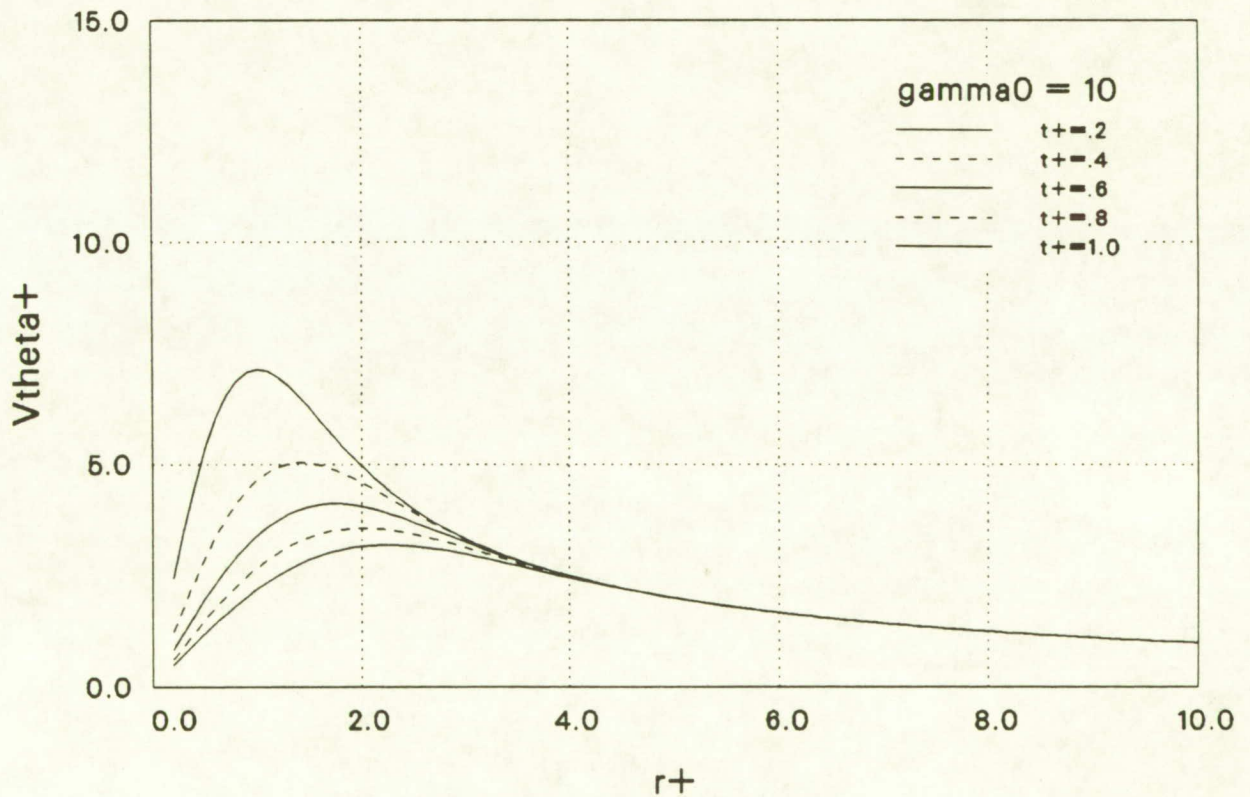


Fig. 9.7b Radial distribution of circumferential velocity V_{θ} for a temporally diffusing Oseen vortex (eqn. 9.10). Initial circulation: $\Gamma_0^+ = 10$.

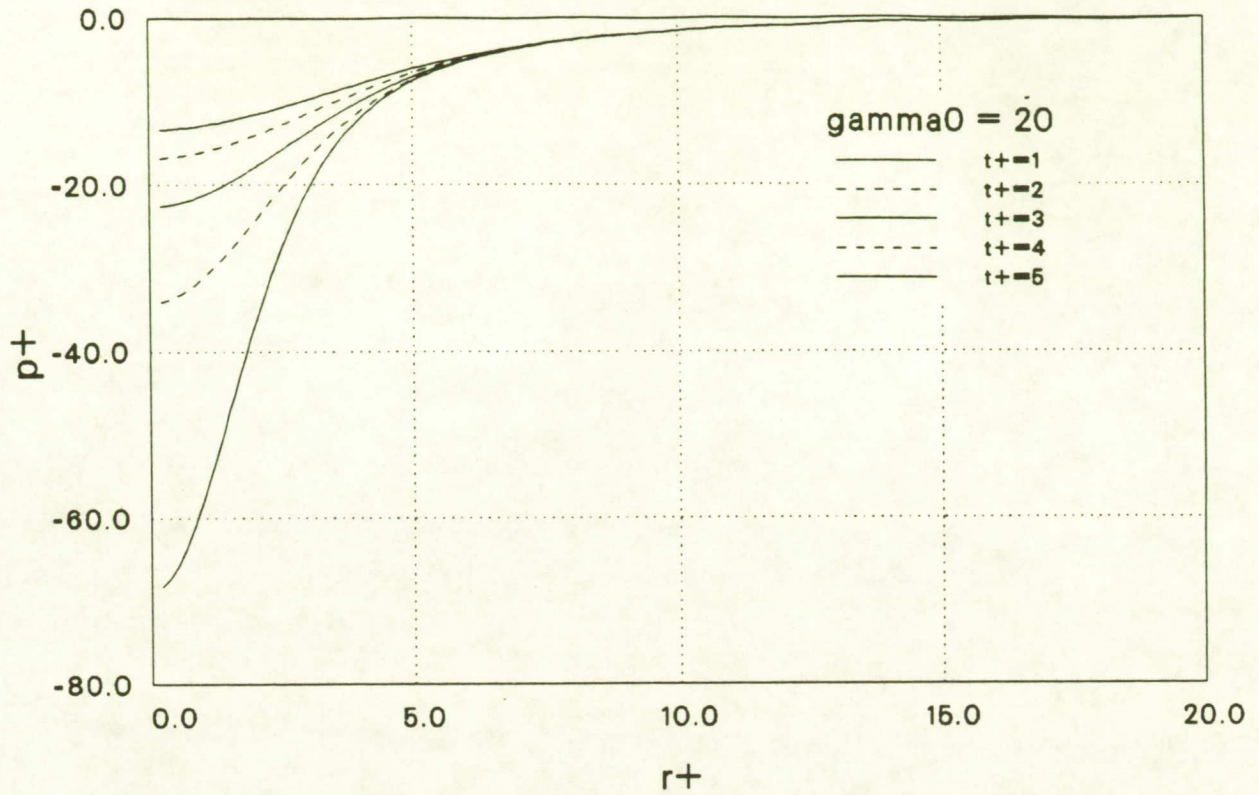


Fig. 9.8 Radial pressure distribution for a temporally diffusing Oseen vortex (eqn. 9.14). Initial circulation: $\Gamma_0^+ = 20$.

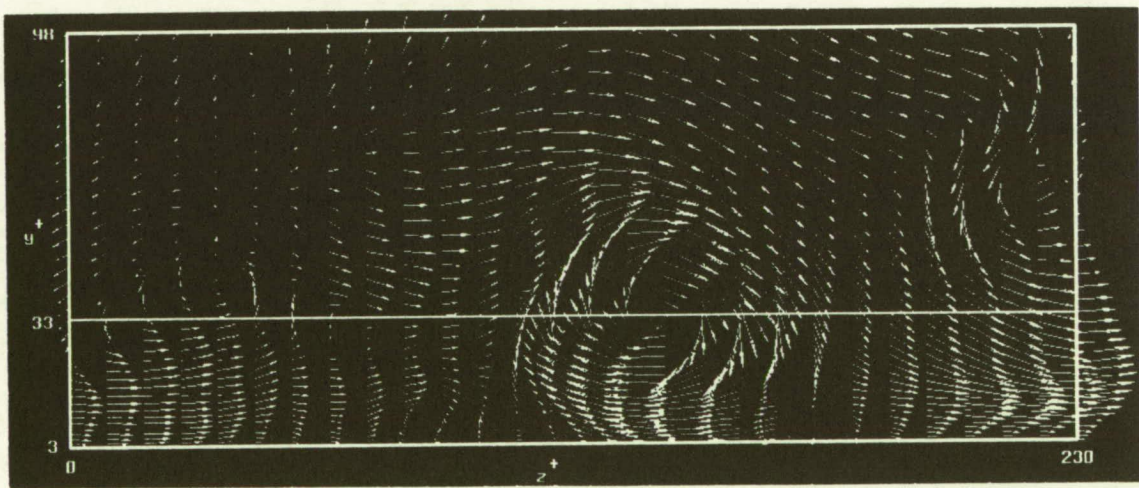


Fig. 9.9 Sample quasi-streamwise vortex in the numerical simulation, identified by v', w' vectors in the y - z plane. Pressure distribution along horizontal line at $y^+ = 33$ is plotted in Fig. 9.10. Measured circulation of this vortex: $\Gamma^+ \approx 75$.

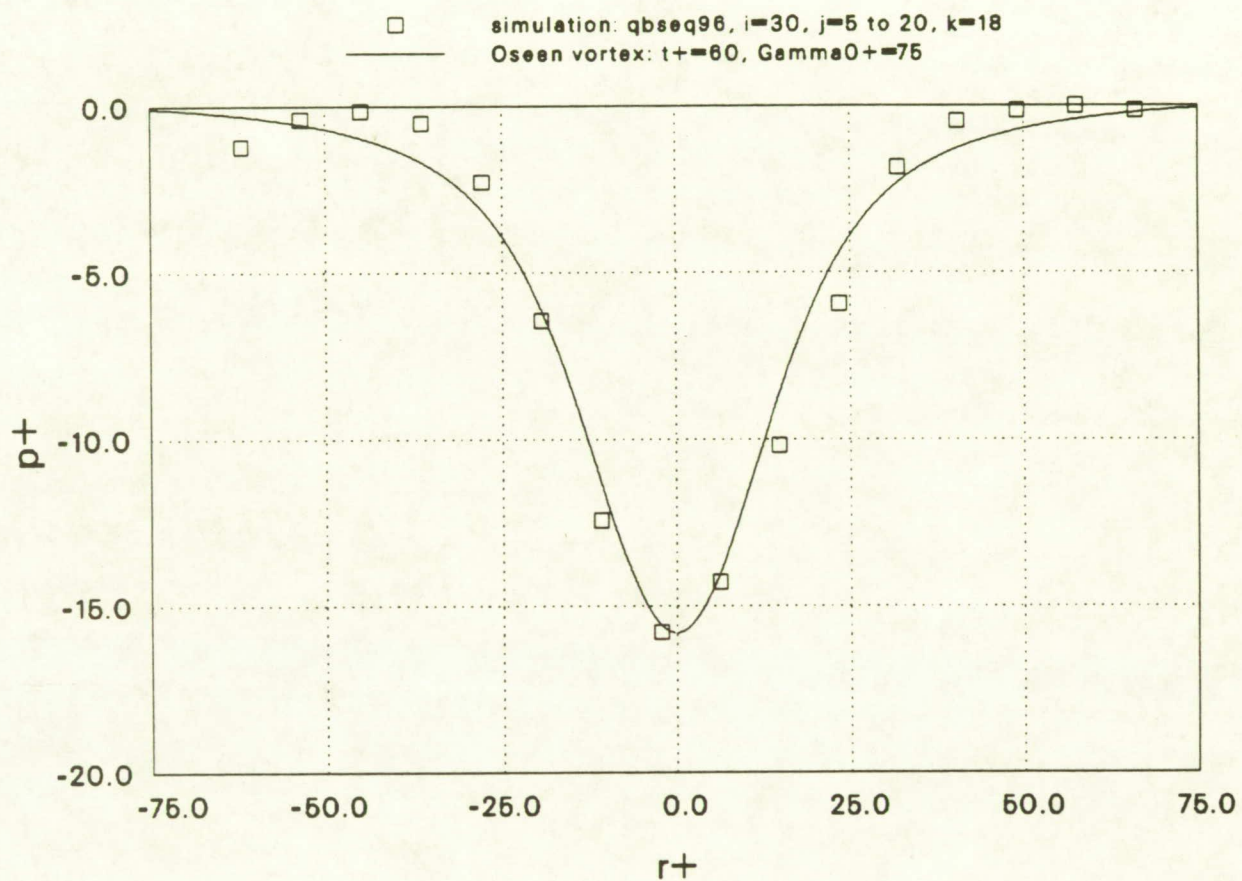


Fig. 9.10 Radial pressure distribution for sample vortex of Fig. 9.9, and for matched Oseen vortex ($\Gamma_0^+ = 75, t^+ = 60$).

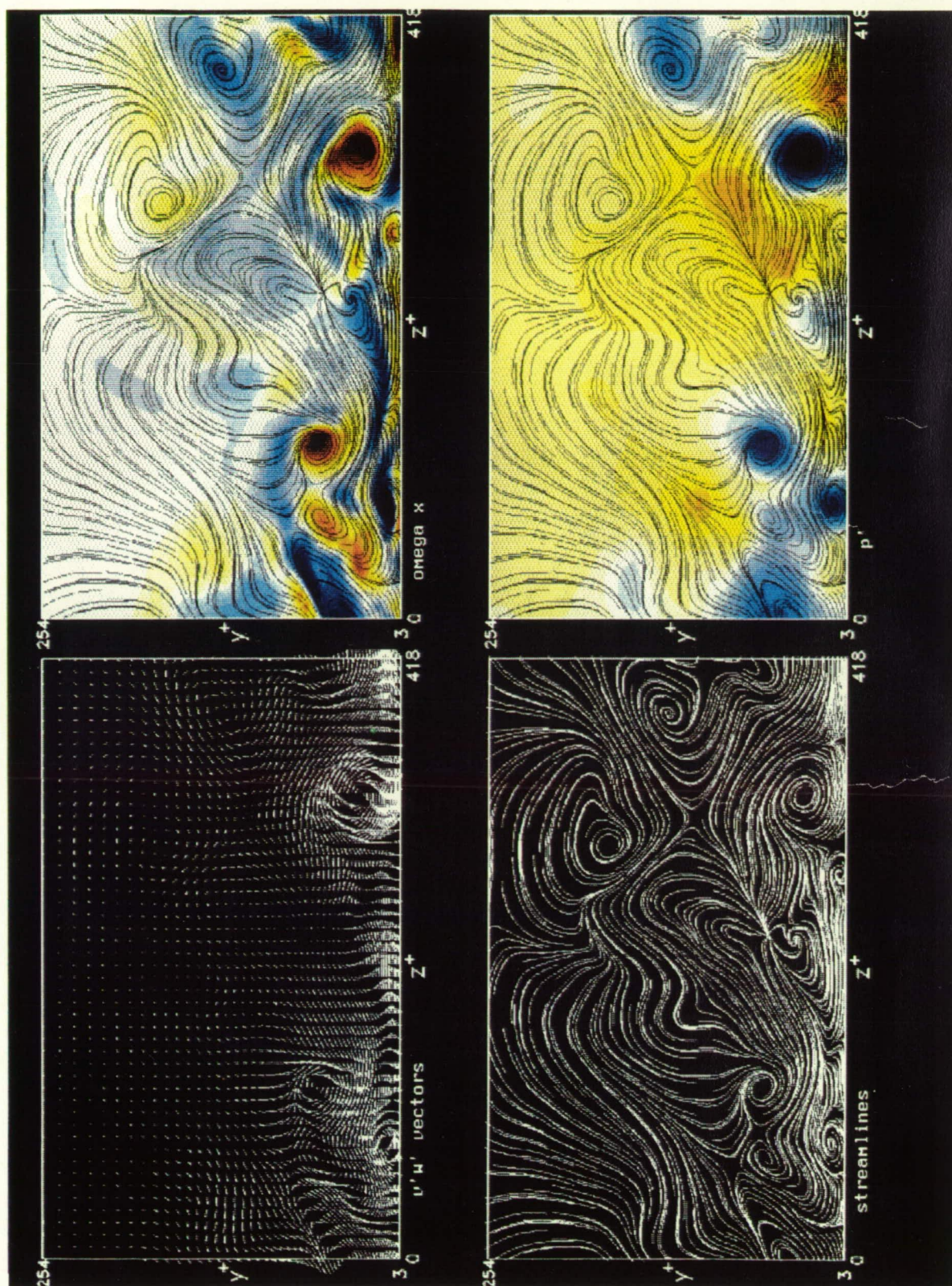


Fig. 9.11 Comparison of various vortex-detection methods in an instantaneous end-view plane. Upper left : v', w' velocity vectors. Lower left : streamlines computed through the 2-D v', w' field. Upper right: streamwise vorticity; yellow to red = $+\omega_z$; cyan to blue = $-\omega_z$. Lower right: fluctuating pressure; yellow to red = $+p'$; cyan to blue = $-p'$.

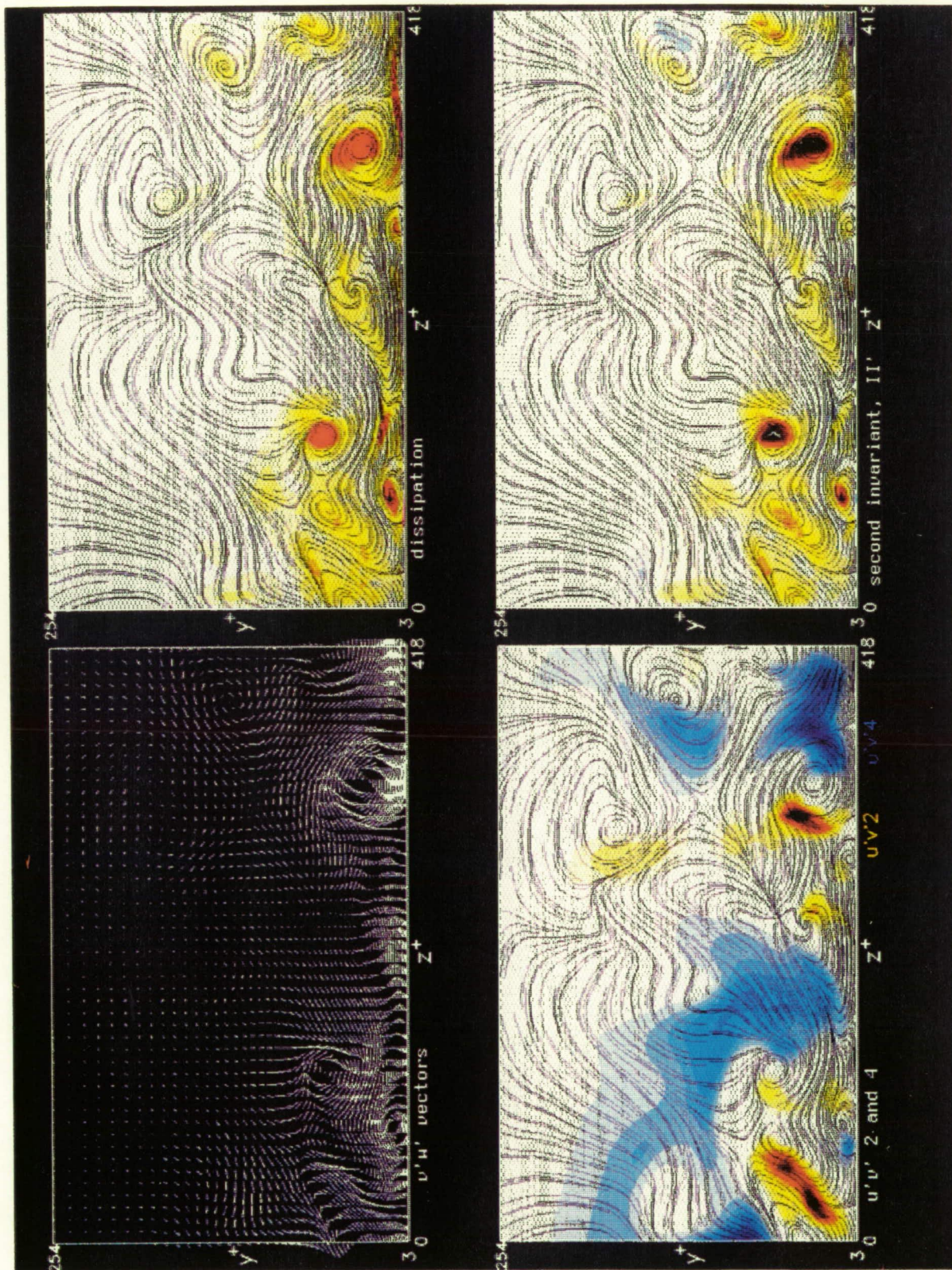


Fig. 9.12 Comparison of various vortex-detection methods in an instantaneous end-view plane (continued). Upper left : v', w' velocity vectors. Lower left : ejections and sweeps; yellow to red = $(u'v')_2$; cyan to blue = $(u'v')_4$. Upper right: dissipation function; yellow to red = $+\epsilon'_f$. Lower right: fluctuating component of second invariant; yellow to red = $+\Pi'$.

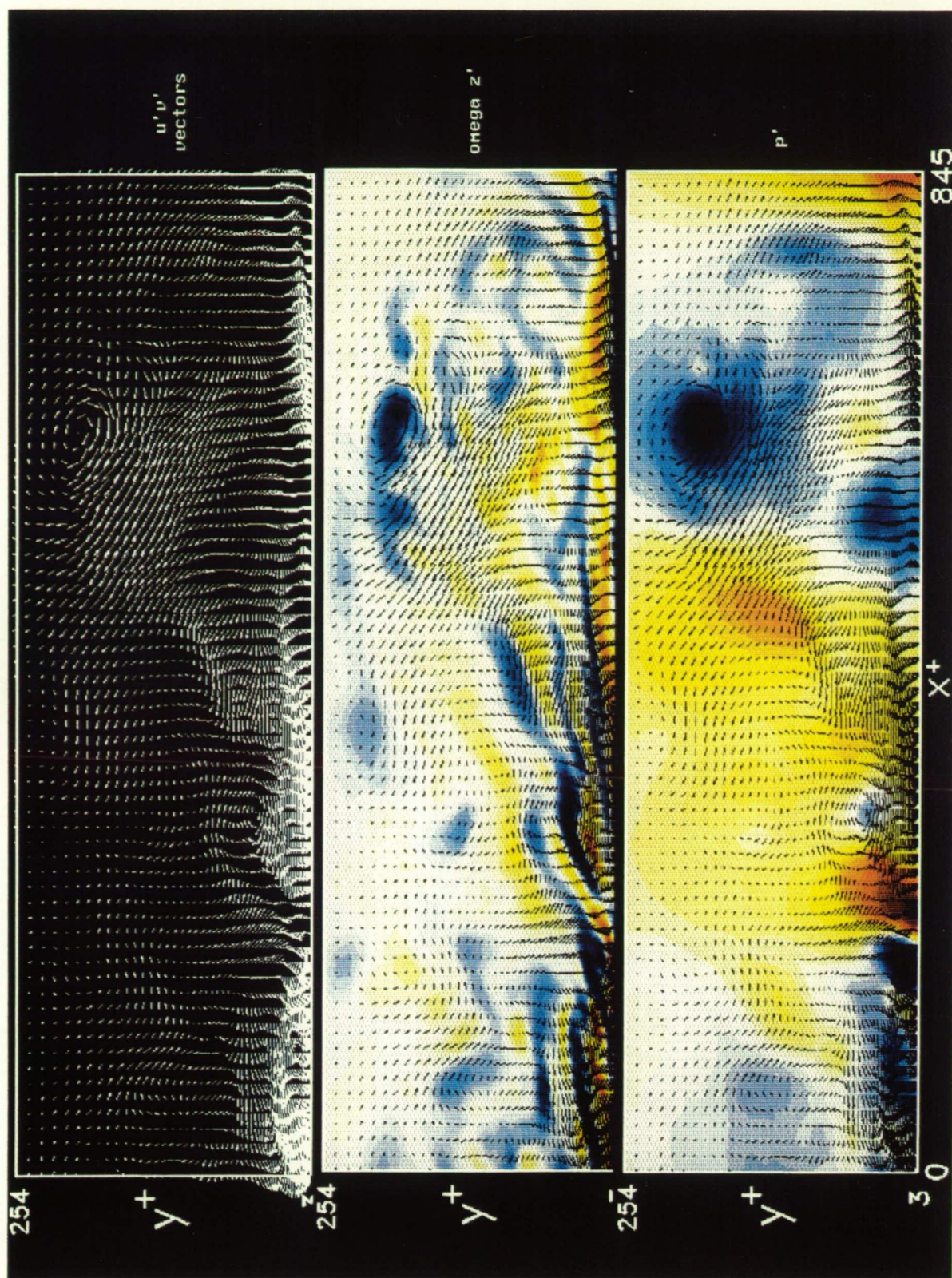


Fig. 9.13 Comparison of various vortex-detection methods in an instantaneous side-view plane. Top : u', v' velocity vectors. Middle: fluctuating spanwise vorticity; yellow to red = $+\omega_z'$; cyan to blue = $-\omega_z'$. Bottom: fluctuating pressure; yellow to red = $+p'$; cyan to blue = $-p'$.

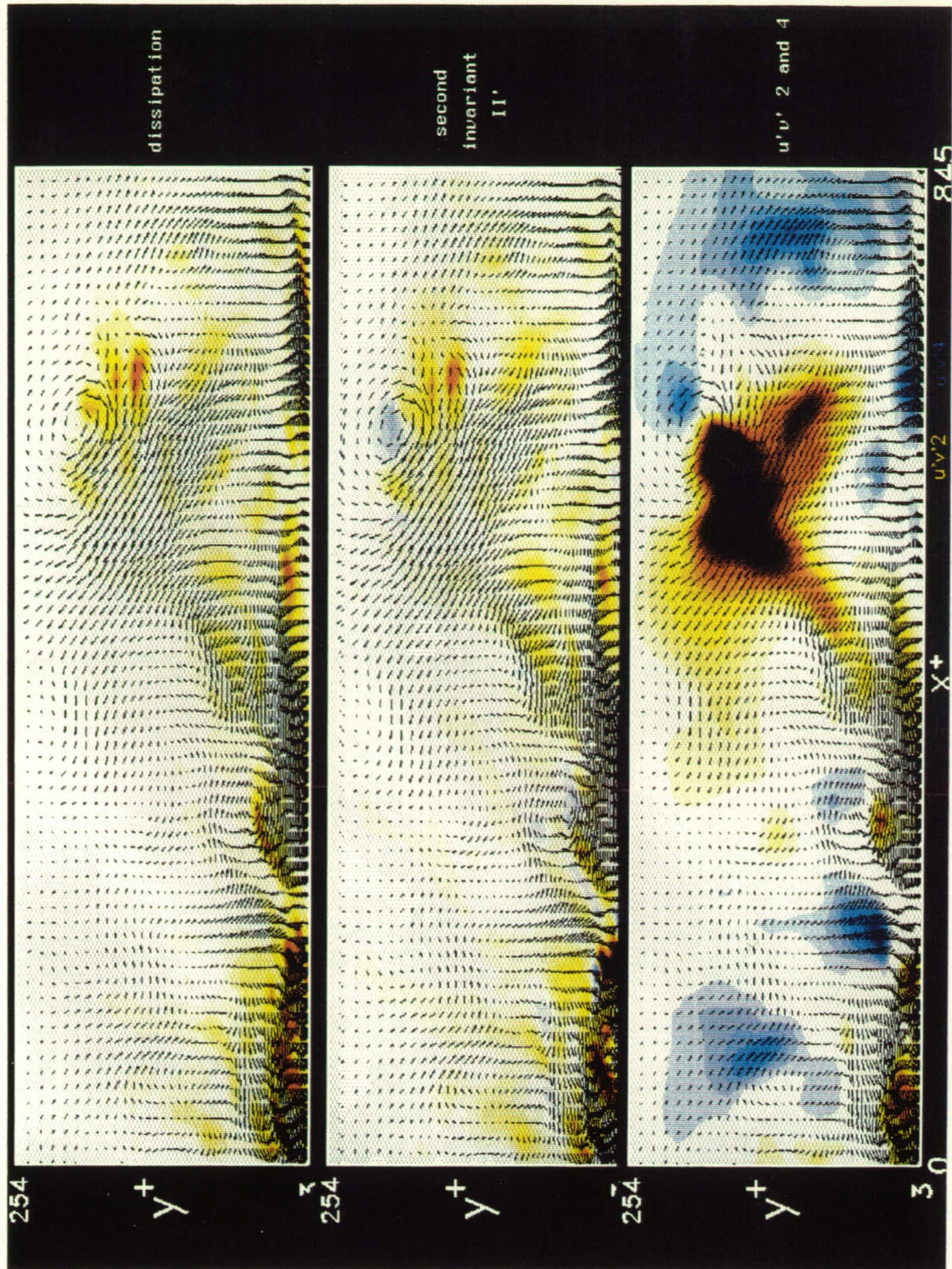


Fig. 9.14 Comparison of various vortex-detection methods in an instantaneous side-view plane (continued). Top: dissipation function; yellow to red = $+\epsilon'_f$. Middle: fluctuating component of second invariant; yellow to red = $+II'$. Bottom: ejections and sweeps; yellow to red = $(u'v')_2$; cyan to blue = $(u'v')_4$.

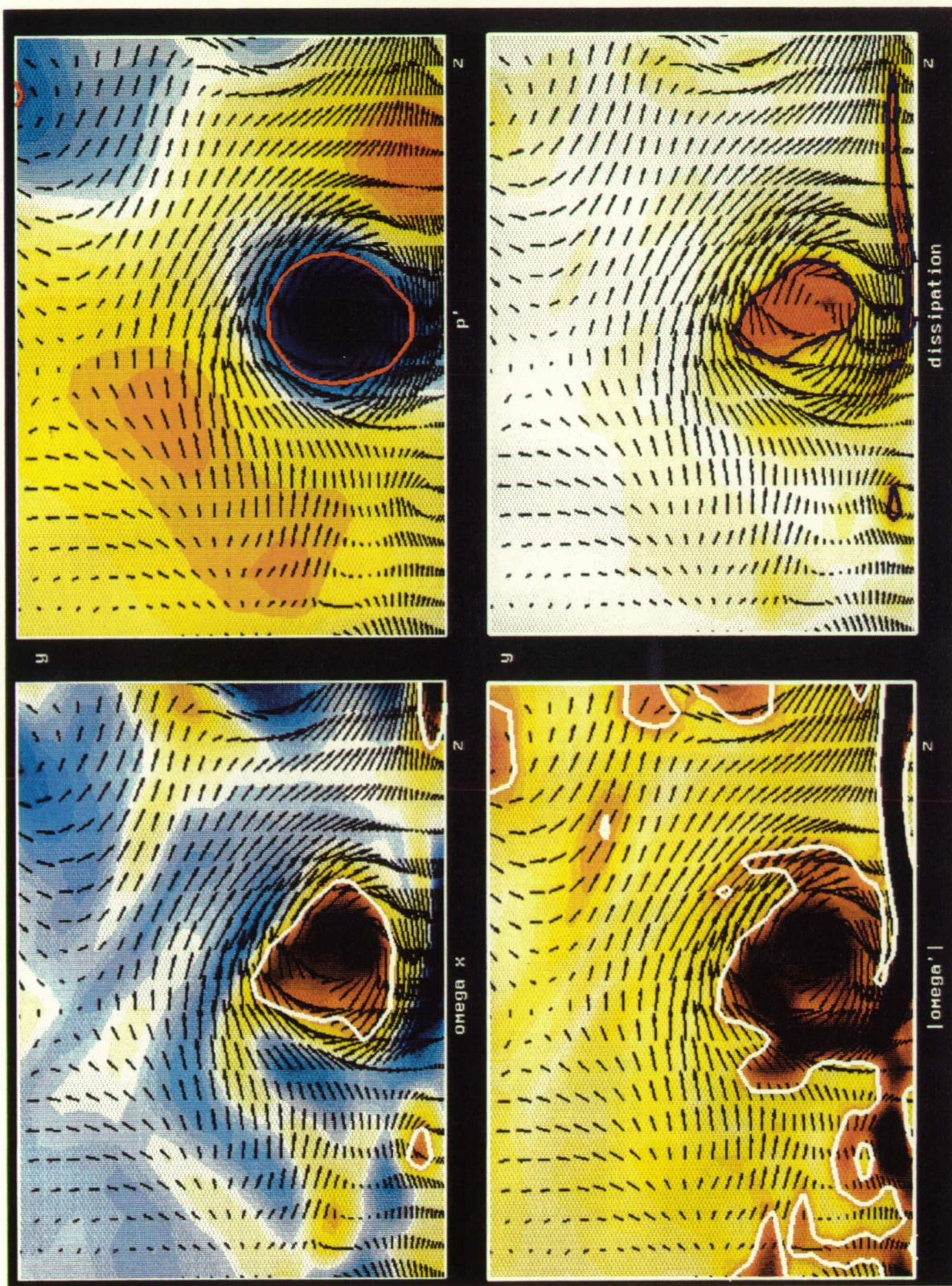


Fig. 9.15 Comparison of various vortex-detection methods for a sample quasi-streamwise vortex. Upper left : streamwise vorticity; yellow to red = $+\omega_x$; cyan to blue = $-\omega_x$. Lower left : vorticity magnitude; yellow to red = $+\omega_x$. Upper right: fluctuating pressure; yellow to red = $+p'$; cyan to blue = $-p'$. Lower right: dissipation function; yellow to red = $+\epsilon'_f$.

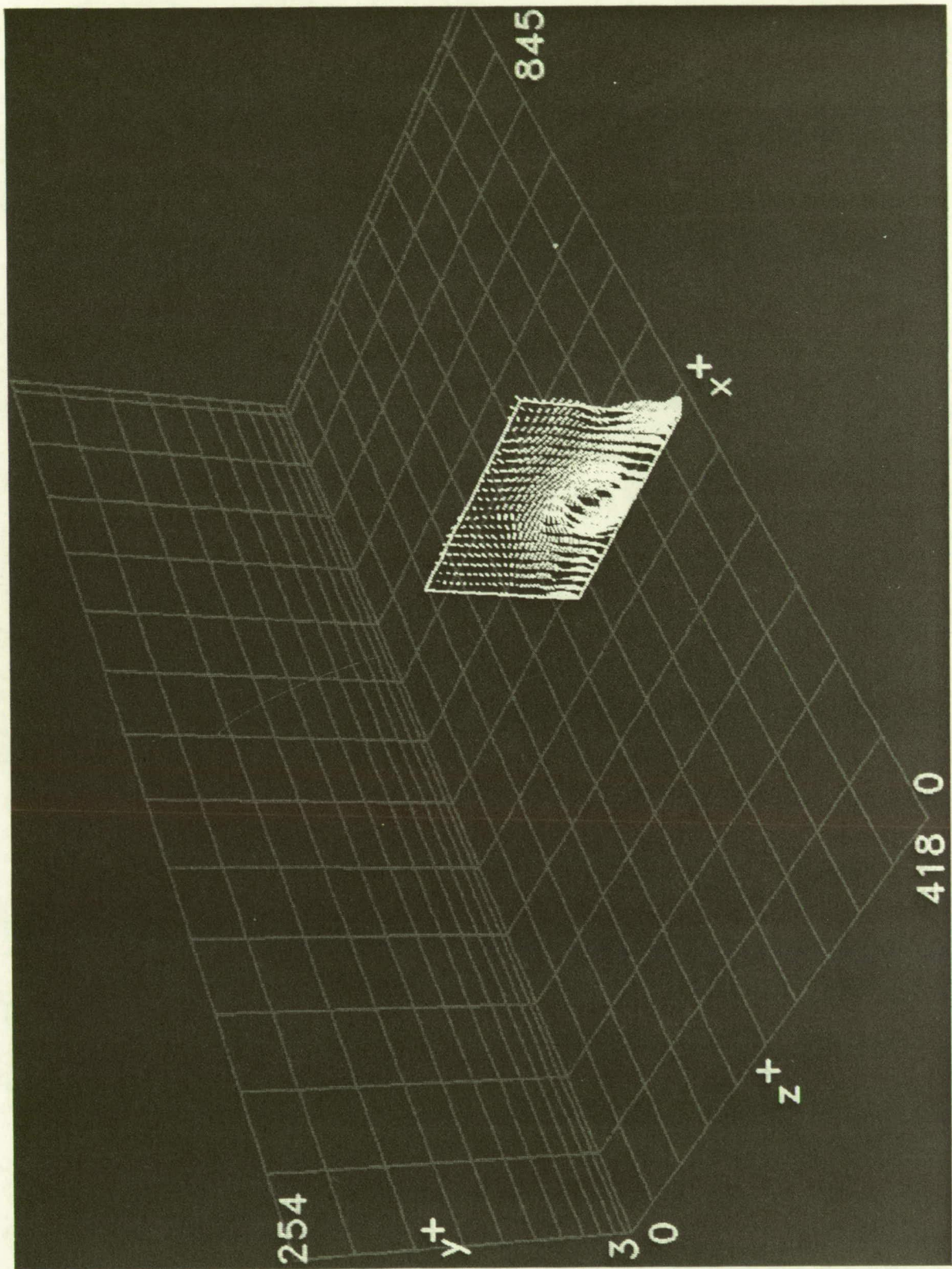


Fig. 9.16 Spatial location in subvolume S of y - z -cut through the sample quasi-streamwise vortex shown in Fig. 9.15.

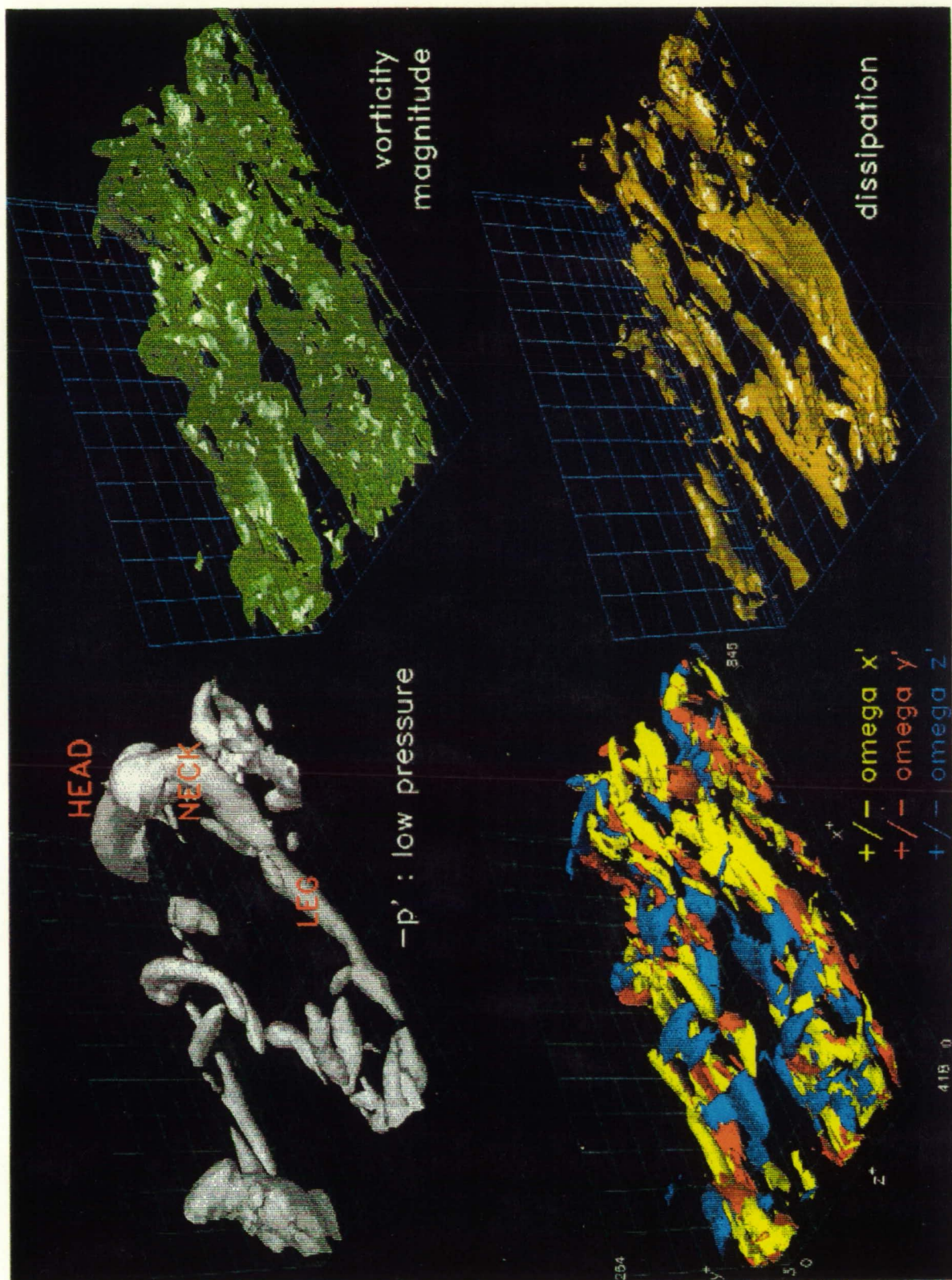


Fig. 9.17 Comparison of various vortex-detection methods for three-dimensional vortical structures in subvolume S . Upper left : fluctuating pressure; surface contour for $p^{++} = -4.2$. Lower left : fluctuating vorticity components; surface contours for $\omega'^{++} = 0.3$. Upper right : fluctuating vorticity magnitude; surface contours for $|\omega'^{++}| = 0.3$. Lower right: dissipation function; surface contours for $\epsilon_f'^{++} = 0.45$.

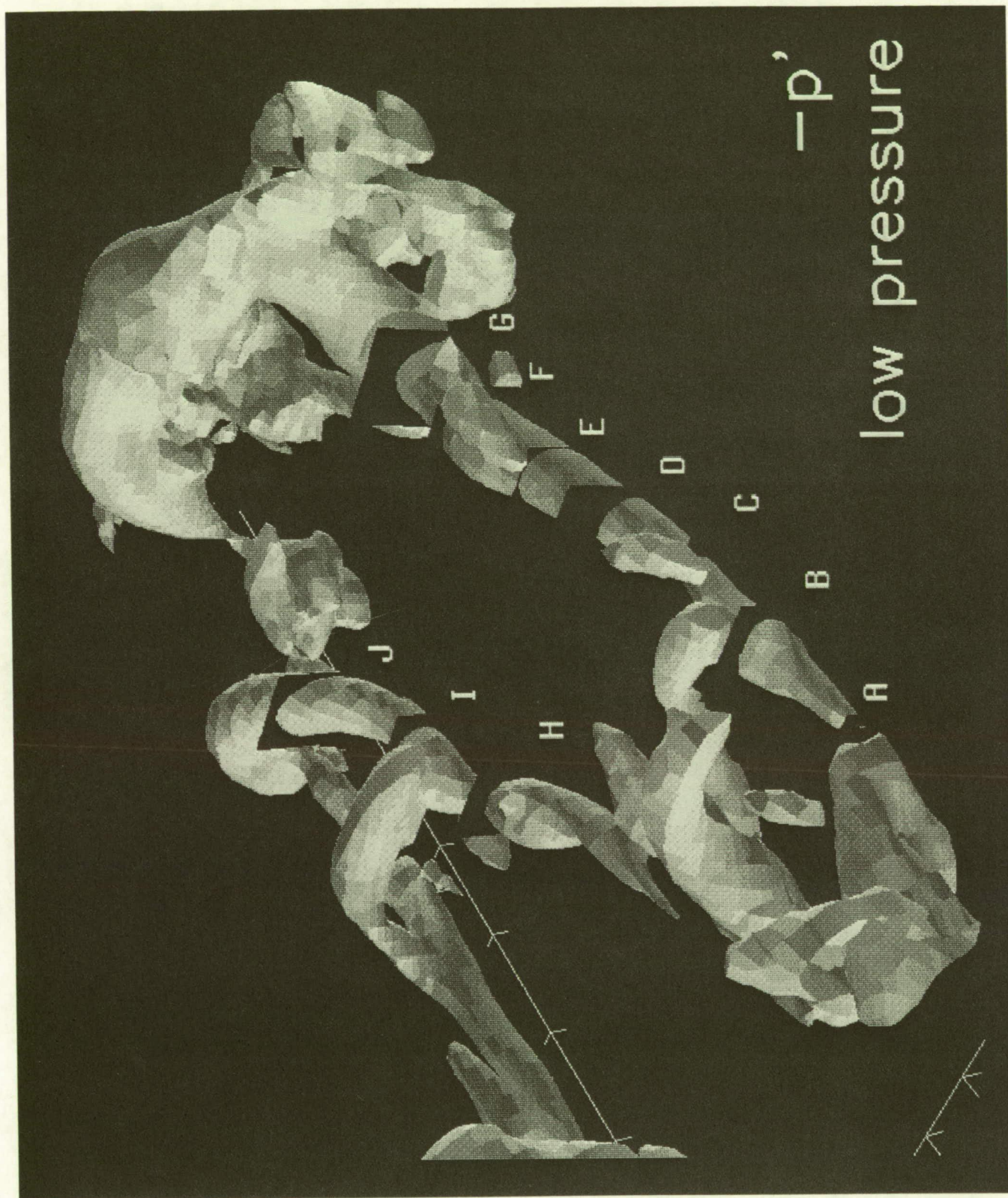


Fig. 9.18 Sample y - z cut-planes through elongated low-pressure regions.

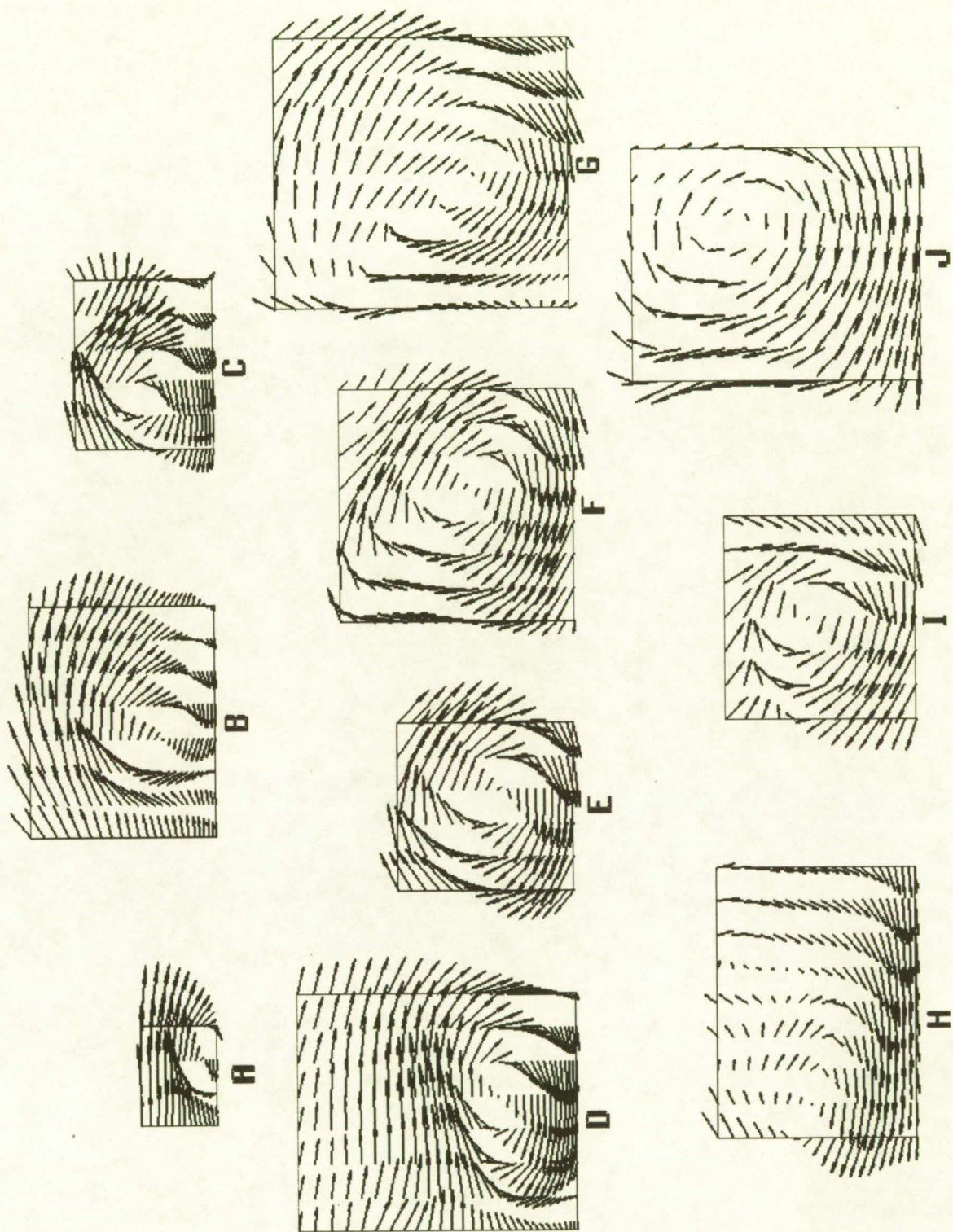


Fig. 9.19 Instantaneous v', w' velocity vectors in each $y-z$ cut-plane shown in Fig. 9.18 show that elongated low-pressure regions coincide with vortex cores.

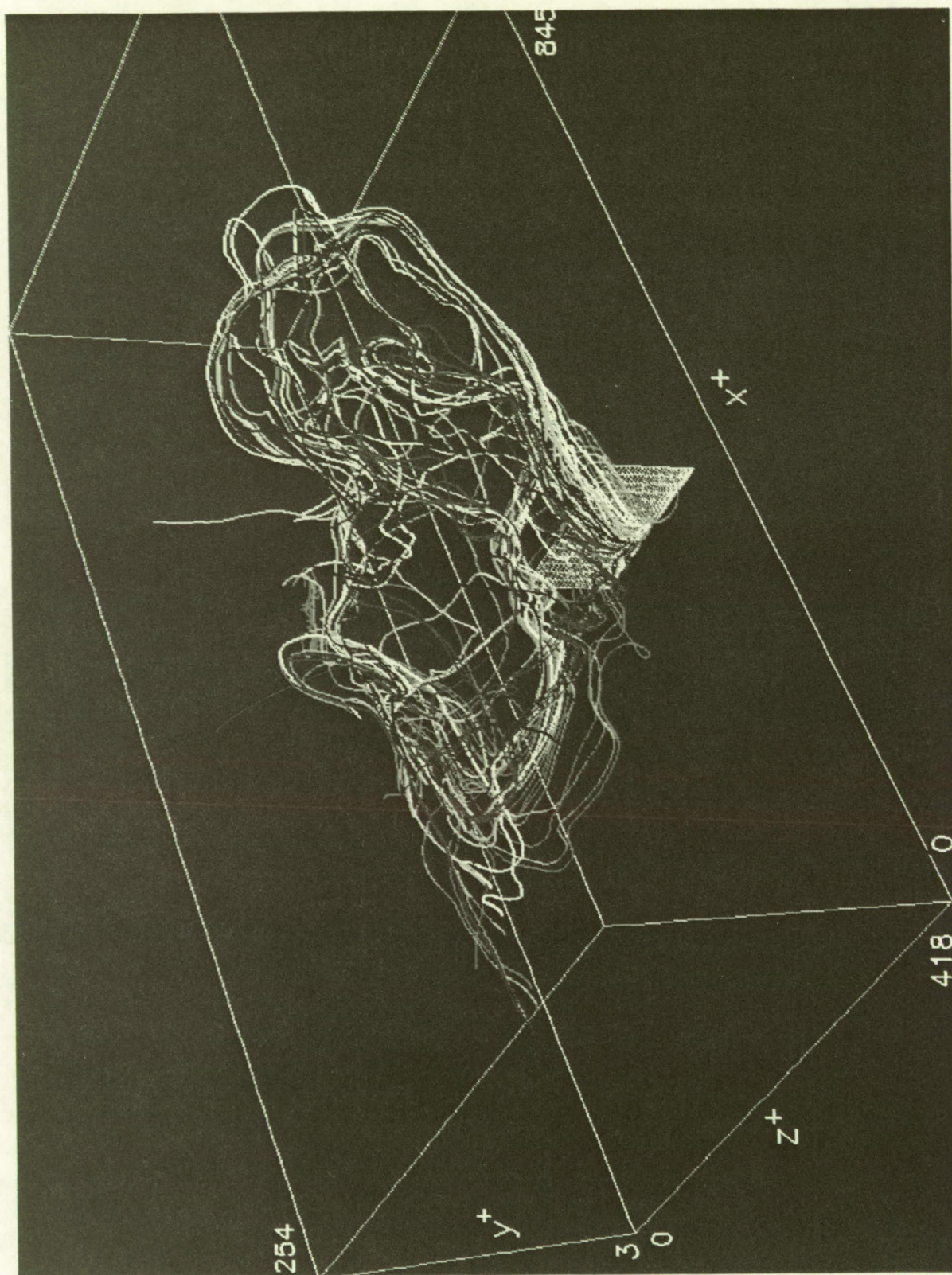


Fig. 9.20 Vorticity lines integrated from starting points within the sample quasi-streamwise vortex shown in Fig. 9.16.

CHAPTER 10 - SPATIAL/TEMPORAL RELATIONSHIPS BETWEEN STRUCTURES

The objective of this chapter is to describe the instantaneous three-dimensional character of the structural features enumerated in Chapter 5, and to show examples of the spatial kinematic relationships between several of the structures. Selected temporal evolutions will be discussed, but only briefly, since the videotapes produced during this work are far more efficient at conveying the information than written descriptions. Most of the observations discussed have been made with the aid of stereo images, of which hundreds have been generated during the study. For reference, the types of coherent motions investigated are:

- Wall low-speed streaks
- Ejections, $(u'v')_2$, including lifting low-speed streaks
- Sweeps, $(u'v')_4$, including intrushes
- Vortical elements and structures
- Near-wall shear layers
- Near-wall pockets
- Bulges and large-scale motions (LSM's)
- Backs (of LSM's)

Descriptions and historical backgrounds for each of these structures is given in Chapter 5.

There is some overlap between this chapter and Chapter 8, but the focus of the two chapters is different enough to warrant some repetition. Chapter 8 presented the contour patterns in 2-D cut-planes while this chapter emphasizes coherent motions in three dimensions.

The conclusions stated in this chapter are the result of studying many segments of numerical data. Many of these observations are illustrated here, however, with a single subvolume of the computational domain, to be referred to as subvolume S. The dimensions of this subvolume are shown in Fig. 6.6. One or more examples of each type of structure exist in subvolume S, making it relatively simple to demonstrate various spatial relationships. In many cases, the example shown in the subvolume is augmented with an overhead "billboard" view of most of the entire computational domain. These "billboards" serve two functions: (1) they provide confirmation of the generality of the conclusions illustrated with subvolume S, and (2) they provide a feel for the variation of features from one realization to the next. The latter is especially important since such variations are large and are important for understanding the kinematics of turbulence structure and the problems associated with its measurement. The contour levels used for the figures are generally recorded in the figure captions rather than in the text.

10.1 Instantaneous Streamwise Velocity Profiles

As a preamble to the study of instantaneous turbulent structures, it is instructive to note the nature of the instantaneous streamwise velocity profile. This may be done in the form of a three-dimensional velocity surface, whose displacement from the vertical axis reflects the magnitude of the local streamwise velocity (Fig. 10.1.1). The video animation from which these figures are taken vividly demonstrates the constant and significant departures from the familiar mean boundary layer $\bar{U}(y)$ profile. The spanwise variations in $U(y, z, t)$ are especially obvious. Although many features are discernible in the time evolution of the velocity sheet, the most important conclusion is that the mean profile essentially never occurs instantaneously.

10.2 Sublayer Streaky Structure

Fig. 10.2.1 shows an instantaneous plan view of the $x - z$ plane at $y^+ \approx 3$ in the simulated turbulent boundary layer. The red low-speed regions (streamwise velocity less than the local mean) are elongated and thin, in agreement with many experimental observations. (Here and elsewhere in the paper, “local mean” refers to the spatial average over the entire computational $x - z$ plane at constant y^+ , for at least five time steps.) Streamwise coherence of single low-speed streaks often exceeds 1500 viscous lengths, with widths ranging from 20 to 80 Δz^+ . The streaky character of the instantaneous low-speed regions is somewhat more pronounced than that of marked fluid in laboratory flows (Fig 5.1) because markers in low-speed streaks lift away from the wall during ejections, leaving the remaining near-wall streak unmarked and invisible. However, the current results appear consistent with the wall-temperature data of Hirata and Kasagi (1979) in which continuous visualization at the wall was achieved using liquid crystals. The spanwise width and spacing of the low-speed streaks are in agreement with the experimental results of Schraub (see Kline et al, 1967).

The high-speed regions in the sublayer (blue in Fig. 10.2.1) are considerably less elongated, and are also somewhat wider than the low-speed regions. Streamwise lengths of high-speed regions seldom exceed 600 x^+ , and widths range from 40 to 110 Δz^+ . This difference in “streakiness” is to be expected, since high-speed fluid generally originates from outside the sublayer where the mean velocity gradient is lower and the flow is known to be less streak-like. Experimental flow visualizations have not shown this character of high-speed regions clearly, however, since fluid markers introduced near the wall collect in the low-speed regions. Since high-speed regions in the sublayer are less elongated than the low-speed regions, the term “high-speed region” is preferable to “high-speed streak.”

The wall-normal extent of near-wall low and high-speed regions are made visible by the addition of side and end-view planes to the $y^+ = 3$ plane (Fig. 10.2.2).

In the video from which this image is taken, cross-sections of sublayer low-speed streaks commonly display an upwelling “mushroom” shape, in close agreement with experimental end-view visualizations of Smith and Metzler (1983). Low-speed fluid is occasionally seen in the end-plane to extend far out into the boundary layer (as in Fig. 10.2.2), suggestive of outward ejections of fluid from the wall region. Somewhat surprisingly, high-speed regions are usually fairly local, extending only a limited distance from the wall. On the whole, deep intrusions of high-speed fluid from the outer region to the wall (inrushes) are less common than similarly extensive outward excursions of low-speed fluid. Ejections and sweeps are discussed further in Sec. 10.6.

The three-dimensional extent of an instantaneous low-speed region in subvolume S is shown by iso-value surface contours for $u' = -3u_\tau$ in Fig. 10.2.3. Portions of at least two elongated low-speed streaks are visible near the wall, as are significant regions of locally low-speed fluid away from the wall. In the example shown, the low-speed region extends to $y^+ \approx 200$. Near the wall, low-speed regions often exhibit a slight longitudinal twist, suggesting the presence of quasi-streamwise vortices. This implication is explored in Section 10.6. Neighboring near-wall low-speed streaks are occasionally connected by a spanwise “bridge” of low-speed fluid which is not elongated in the x direction.

10.3 Ejections and Sweeps

The quadrant technique has been used to define and identify ejections and sweeps. The quadrant method involves splitting the instantaneous product of u' and v' into four categories according to the quadrant occupied in the $u'v'$ hodograph (Fig. 5.1). Since its introduction by Wallace et al (1972) and by Willmarth and Lu (1972), the quadrant method has been widely used to assign structural significance to motions that contribute to the boundary layer closure term, the Reynolds shear stress. Recall that under this definition, sweeps and ejections may occur anywhere in the boundary layer.

It is important to distinguish between the Reynolds shear stress, which is defined only as an average, and the instantaneous value of $u'v'$. To facilitate this distinction, the term “shear product” will occasionally be used to refer to the instantaneous value of $u'v'$ at a location in space.

A plan-view of significant ejection (red) and sweep (blue) motions in the $y^+ = 15$ plane is shown in Fig. 10.3.1. The white lines within the colored contours outline particularly strong ejections and sweeps, for which $-u'v' \leq -4u_\tau^2$ (or $-u'v' \leq -2.7u'_{rms}v'_{rms}$.) As expected from experimental results and from previous simulations, the contours of strong quadrant 2 and 4 motions are highly intermittent in space; neither displays the extended streamwise coherence of the low-speed regions. However, quadrant 2 motions are elongated in the x -direction, due to the

streaky nature of its $-u'$ constituent. The spanwise scale of sweeps is slightly larger than the low-speed streaks and the ejections, but their extent is still less than $80 z^+$. As noted in Chapter 8, strong ejections and sweeps are often laterally associated, in a side-by-side pair. Each pair is associated with a single quasi-streamwise vortex, as will be shown in Section 10.6.

Two long-standing theories concerning near-wall ejections and sweeps are not supported by the contours in Fig. 10.3.1.

First, sweeps are rarely situated directly upstream of ejections, although single-point u' VITA detections combined with $u'v'$ quadrant analysis have often suggested otherwise. This is because a slightly skewed sweep/ejection pair convecting past a stationary probe would be interpreted as a sweep following an ejection (or vice versa) in the probe signal. The prevalent use of the more common "positive" near-wall VITA events (temporal u' accelerations) by experimentalists filters out all but the cases in which ejections ($-u'$) occur downstream from sweeps ($+u'$). Thus, single-point conditional sampling results have led to conceptual models which describe sweeps arriving at the wall from the outer region and "kicking off" ejections in front of them. The picture gleaned from the simulated turbulence is entirely different, and resolves the apparent inconsistency between probe results which ascribe ejections to near-wall vortices (e.g. Bakewell and Lumley, 1967; Guezennec, 1985) and those which find sweeps directly upstream of ejections (e.g. Praturi and Brodkey, 1978).

The second point which differs from some classical experimental results is that sweep motions in the buffer zone of the simulated boundary layer are narrow and localized, rather than broad inrushes. This observation is contrary to the accepted concept of bursting in the early seventies, in which near-wall ejection activity is wiped away by the arrival of a δ -scale sweep of high-speed fluid from upstream (e.g. Corino and Brodkey, 1969; Praturi and Brodkey, 1978). The narrow character of the $+u'$ regions and the corresponding $(u'v')_4$ regions in the buffer zone imply that most near-wall sweeps are locally produced, and that direct mass transfer from the outer flow is relatively uncommon (see Section 10.16). This evidence also supports the concept of near-wall vortical structures acting as fluid transport pumps. (Note, however, that high-speed fluid with little or no wallward component often exists upstream of an ejection. This "gusting" motion is sometimes called a "sweep" in the literature, but does not constitute a significant $(u'v')_4$ contribution to the Reynolds stress.)

Fig. 10.3.2 shows the three-dimensional nature of $(u'v')_2$ and $(u'v')_4$ regions in the instantaneous subvolume S for several contour levels. This and many other realizations show that strong ejections occur with two types of instantaneous spatial character: 1) thin and elongated in the buffer and lower log regions, and 2) broader and more globule-shaped in the outer log and wake regions. The relatively large scales (diameters up to 200 viscous lengths) of some of the outer-region ejections is

rather unexpected. Since ejections near the wall originate from low-speed streaks by definition, their character is expected to be at least somewhat elongated. Ejections are not observed to extend over the entire streamwise length of a streak, however. Only portions of the low-speed regions extend out of the sublayer.

At any given time, strong sweeps occupy less volume in the simulated boundary layer than equally strong ejections. This result agrees with the probe-based statistics of Wallace et al (1972), Willmarth and Lu (1972), and others, who have shown ejections to dominate the contributions to the Reynolds shear stress outside the buffer region.

An overhead view of $u'v' = -4u_\tau$ contour surfaces in the entire computational domain (Fig. 10.3.3) confirms the spatially intermittent nature of shear stress production, the streamwise elongation of ejections but not sweeps, and the greater population of ejections. Stereo viewing confirms that the spanwise extent of the ejection regions is roughly dependent on distance from the wall, but that sweeps are relatively narrow throughout the boundary layer.

10.4 Low-speed Streaks with Ejections and Sweeps

Fig. 10.4.1 is a plan-view of an $x - z$ plane in the simulated boundary layer at $y^+ \approx 15$. Ejections and sweeps are shown for the same contour levels as listed above. Low-speed streaks are identified by contours of streamwise velocity $3u_\tau$ below the local mean. Strong ejections are seen to occur only on low-speed streaks, as they must by definition (both are regions of $-u'$). The simulated boundary layer supports Corino and Brodkey's (1969) and Bogard and Tiederman's (1986) finding that several ejections may arise from a single low-speed streak, although the number of ejections per streak is dependent upon the contour levels chosen for $-u'$ and $(u'v')_2$. (The contour value for $(u'v')_2$ in Fig. 10.4.1 corresponds to a value of approximately 2.6, when normalized by the product of u'_{rms} and v'_{rms} at $y^+ = 15$). Strong ejections seem to originate from the central portion of streaks more commonly than from either end.

10.5 Vortical Elements and Structures

It was noted in Section 10.3 as well as in Chapter 8 that vertical motions in the sublayer (and thus, sweeps and ejections) commonly occur in side-by-side pairs, suggesting the presence of quasi-streamwise vortices. (Such vortices have been discussed extensively in the literature, which is reviewed in Chapter 11). The lateral pairing of near-wall vertical motions is clearly shown in figure 10.5.1a, in which instantaneous contours of v' are plotted in the $y^+ = 12$ plane.

A view of wall-normal fluctuations in the $y^+ = 15$ plane is shown in Fig. 10.5.1b, in which only regions of significant $+/-v'$ magnitude are plotted. Hand-counting of v' regions in several such plots showed that 78% (of a sample of 225)

of $+v'$ motions have at least one $-v'$ motion to the side. Triplets of alternating positive and negative v' accounted for only 3% of the total, while 22% of the $+v'$ regions was not paired with a neighbor. Two types of v' triplets are possible (Types A and B in Fig. 10.5.1c). Type A conforms to the notion of a side-by-side counter-rotating vortex pair, while type B is more likely to be associated with the surface impact of wallward fluid. Of the triplets identified in the $y^+ = 15$ planes, only 21% were of type A, the remainder being type B.

It is possible that a quasi-streamwise vortex pair would have one leg at a different y -plane than the other, and would thus be undetectable in a plot such as Fig. 10.5.1b. However, inspection of the v' -field in adjacent x - z planes failed to produce any additional clearly identifiable vortex pairs.

The above results lead to the conclusion that most vertical motions in the region of maximum turbulence production are associated with vortical motions, and that most vortices occur singly, rather than in pairs.

The spanwise dimensions of significant wallward motions are limited to less than approximately 70 viscous lengths. The spanwise separation between $+/-v'$ pairs ranges from 40 to 70 viscous lengths. Another measure of the prevalence of v' pairs and of their mean separation is a two point correlation in the $x - z$ plane at $y^+ = 15$ (Fig. 10.5.1d). The $R_{v,v}(x, z)$ pattern shows a clear anti-correlation trend in the spanwise direction, with a distance between peaks of about 38 viscous lengths, which would correspond to the mean core diameter of the quasi-streamwise vortices which apparently dominate the near-wall region. This result agrees well with the vortex-diameter distribution shown in Fig. 11.20.

The streamwise extent of strong v' pairs in the buffer zone ranges from 50 to 250 viscous lengths, depending on the contour value chosen; however, this is not indicative of the streamwise dimensions of near-wall quasi-streamwise vortices. Since Fig. 10.5.1b depicts a plane of data at constant y , a vortex with an inclination angle to the wall would be intersected in a limited region by the plane. An estimate of the angle may be obtained from the length-to-width ratio of the v' pairs, as shown in Fig. 10.5.1e. With an average length of 190 viscous lengths for the well-defined pairs, and a span of 38 units from the two-point correlation, the mean vortex inclination angle at $y^+ = 15$ is roughly 11.5 degrees.

The instantaneous pressure field is used to investigate the three-dimensional structure of vortices embedded in the simulated boundary layer, as outlined in Chapter 9. Extensive checking has shown that elongated low-pressure regions exhibit an almost unique correspondence to the cores of relatively strong vortices. Fig. 10.5.2 shows low-pressure surface contours in subvolume S for three contour values. The inner contour is rendered as a solid surface, and corresponds to $p' = -4\rho u_\tau^2$.

A number of important observations may be made concerning the shape of the elongated low-pressure regions (which were shown in Chapter 9 to be vortices)

in Fig. 10.5.2. The most striking aspect of the major vortical structures is their looped shape. The large loop is more of a hook, with a single long trailing leg. The head of the large hook measures about 250 spanwise viscous lengths, or about 0.8δ , and lies at about $y^+ = 200$. A neck extends toward the wall at approximately 45 degrees, joining a leg of almost 400 viscous units in length. The far side of the hook includes a weak neck, but no leg. A smaller, similarly one-sided loop is visible on the far side of the subvolume. Just upstream of the smaller vortical arch is a small transverse region of low pressure, which appears to be a newly formed secondary vortex, possibly rolled up on the low-speed fluid lifted by the action of the downstream vortical arch in the manner described by Acarlar and Smith (1987b). The formation of this particular secondary vortex is clearly visible in time evolutions of the simulation (see Fig. 10.6.8b).

The loop-like vortical structures in Fig. 10.5.2 are strongly suggestive of the hairpin or horseshoe vortices discussed in many previous papers, beginning with Theodorsen (1952). The main difference between the example shown and the common conceptual vortex models is the distinct lack of symmetry of the structures in the simulated boundary layer. To judge the effects of contour level on the vortex structure geometry, four different low-pressure contour surfaces for subvolume S are shown in Fig. 10.5.3. In general, varying the contour level over a limited range affects the diameter and, in some cases, the topological connectivity of the low-pressure regions, but does not significantly alter the overall form of the vortical structures. This is due to the fairly rapid radial pressure gradient found within the cores of turbulent vortices. A video that steps through 100 pressure contour levels in subvolume S confirms this finding.

To establish the variation in three-dimensional vortex geometries beyond subvolume S, $p' = -4\rho u_\tau^2$ contour surfaces are plotted for most of the computational domain in Fig. 10.5.4. (The contour variation studies described in Chapter 9 suggested $-4\rho u_\tau^2$ as a good isobar value for illuminating the strong vortical structures.) To the author's knowledge, Fig. 10.5.4 represents the first time all of the significant vortical structures have been visualized in an instantaneous three-dimensional segment of turbulent boundary layer. The variety of shapes and topologies in Fig. 10.5.4 is such that no single configuration may be termed dominant. A number of features show up repeatedly, however, and these may be grouped into the broad categories of arches (one or two-sided), hairpins (one or two-sided), quasi-streamwise vortices (legs), and unidentifiable bundles.

Although the shapes of the vortical structures are somewhat dependent upon the pressure contour level used to find them, an approximate census of the members of each shape category is still educational. The following counts were made by examining stereo pairs of the entire computational domain at two widely separated time-steps. The sample included approximately 200 structures:

Two-sided hairpins: 2 %

One-sided hairpins: 7 %

Two-sided arches: 30 %

One-sided arches: 11 %

Quasi-streamwise: 30 %

Unidentified: 20 %

The distinction between arches and quasi-streamwise vortices is least sensitive to variations in pressure contour level, so the only conclusions that should be drawn are that both arches and quasi-streamwise vortices are common in the boundary layer, each accounting for about a third of the visible low-pressure regions, or about 40% of the vortical structures (assuming non-elongated low-pressure regions are not vortices). Stereo viewing shows that, as expected, arches reside away from the wall and quasi-streamwise vortices are generally found near the wall. Two additional approaches for identifying and categorizing turbulent vortical structures are currently under development and will be reported separately.

To summarize the character of vortical structures in the simulated boundary layer: Arch- or horseshoe-like vortical structures (head/neck) combinations are common, but long leg vortices are not. The legs that do exist can be quite long in the streamwise direction, reaching up to at least $\Delta x^+ = 400$. True hairpin vortices, with two trailing legs, are very rare. Many vortical structures are strongly asymmetric. Hook-like shapes, as in Fig. 10.5.2, appear relatively often. In some cases, the missing neck can be identified on an asymmetric hook-like vortical structure when the contour level of the isobaric surfaces is varied. Vortical arches occur in a variety of sizes, and their heads are found at y -locations ranging from the outer edge of the buffer region to the edge of the boundary layer. Arches generally extend as far in the wall-normal direction as in the spanwise direction. The spanwise extent of vortical arches ranges from 50 to 350 viscous lengths in the simulated layer. The above conclusions hold true over a range of $-p'$ contour values. Additional statistics on the spatial character of vortical structures in the boundary layer are presented in Chapter 11.

10.6 Vortical Structures with Low-Speed Streaks, Ejections, Sweeps

Plan views of low-pressure surfaces ($p' = -4\rho u_\tau^2$) and low-speed surfaces ($u' = -3u_\tau$) are shown for two widely separated times of the simulated boundary layer in Fig. 10.6.1. Immediately obvious is the spatial relationship between low-speed streaks and vortical structures. In the sublayer, buffer, and log zones, low-speed regions often exist without the presence of vortical structures, but vortices are almost always found in close proximity with low-speed regions. The association is even stronger in the wake region, where most low-speed regions are adjacent to vortices. A relatively common configuration in the low-pressure/low-speed field is

that of a small ($\Delta z^+ < 80$) near-wall arch straddling a low-speed streak. This brings to mind several models of vortex-birth in the boundary layer (e.g. Acarlar and Smith, 1987b), in which the high shear region formed atop a low speed streak “rolls up” into a transverse vortex element or arch-shaped vortex. Time-evolutions of the simulated boundary layer solutions suggest that this local instability mechanism is in fact a major means of vortex generation in turbulent (as well as in laminar) boundary layers. Apparent newborn vortical arches usually extend between 30 and 80 viscous units from the wall, with a similar spanwise extent. These dimensions are in close agreement with near-wall low-speed streak widths.

Low-speed streaks in the near-wall region extend for much longer distances in the streamwise direction than do any quasi-streamwise vortices. Thus, although there is clearly a relationship between vortices and low-speed streaks, the streaks are not bounded by long streamwise vortices on each side. This observation confirms the simulated channel-flow findings of Moin and Kim (1985).

Since the cause of low-speed streaks is still uncertain, it is worth investigating further the spatial relationship observed between streaks and vortices in Fig. 10.6.2. The interface between near-wall low- and high-speed regions (called “streak interface”) has been observed experimentally to exhibit a vortical nature in end-view planes (Smith and Metzler, 1983; Kasagi et al, 1986; Lian, 1987). This observation may also be made in the simulated turbulence, as demonstrated in Fig. 10.6.2. A close up of a vortical streak interface is shown in Fig. 10.6.3.

When a quasi-streamwise vortex extends into the near-wall region (and most of them do), the vortex is almost invariably flanked laterally by a low-speed and a high-speed region, which is the kinematic expectation. However, not all streak interfaces have vortices (although they generate significant wall-normal vorticity), which is consistent with the observed lack of streamwise vortices as long as streaks. The impression gained from the study of many static and evolving segments of the simulation database is that streaks may be left behind by single (not pairs of) quasi-streamwise vortices being convected overtop and through the viscous near-wall layer at a speed higher than than sublayer mean velocity. These vortices lift low-speed fluid along their upward-rotating sides. Strong vortices induce low-speed fluid rapidly outward in an ejection, but the more plentiful weaker quasi-streamwise vortices just collect enough fluid to leave low-speed streaks behind in their wakes. The streaks apparently do not require continuous pumping to maintain their coherence, but persist as elongated low-speed regions with a gradual outward movement until disturbed by another event. As discussed in connection with the v' field, the emphasis here is on single quasi-streamwise vortices, rather than counter-rotating pairs. This scenario is in general agreement with that of Smith (1984), Moin (1987), and others, but requires further investigation before becoming acceptable as an explanation for streak formation.

An example of the three-dimensional spatial relationship between vortical structures, low-speed regions, and ejection motions is shown for subvolume S in Fig. 10.6.4. Contour surfaces are shown for $u' = -3u_\tau$ (yellow), $p' = -4\rho u_\tau^2$ (white), and $(u'v')_2 = -4u_\tau^2$ (red). The figure shows low-speed fluid concentrated below and upstream of the vortical heads, and alongside the trailing vortex leg. The regions where low-speed fluid possesses a significant outward velocity component are marked in red as $(u'v')_2$ ejections. Most of the lifting low-speed fluid in the subvolume are in close proximity to the vortical structures. The large-scale, outer-region ejections discussed in Fig. 10.3.2 are now seen in Fig. 10.6.4 to be located just below and upstream of the vortical heads, and on the inboard side of necks, where the inductive influence of the head and neck are combined.

The association between vortical structures and significant contributions to the Reynolds shear stress in subvolume S is demonstrated in Figs. 10.6.5. and 10.6.6. The instantaneous spatial association of both sweeps and ejections with the vortical structures is striking.

Strong ejection regions ($(u'v')_2 \leq -4\rho u_\tau^2$ in Fig. 10.6.5) generally occur in two locations: (1) Alongside quasi-streamwise leg vortices, on the inboard (towards the head) side of the leg. This is the upward-rotating side of the vortex, so the picture is kinematically consistent. (2) Underneath and upstream of head vortices. Ejections in location 2 are significantly farther from the wall than those in location 1. Both the head and neck seem to contribute to strong outward induction of low-speed fluid in location 2.

Fig. 10.6.6 clearly demonstrates that a counter-rotating pair of streamwise vortices, as proposed by Offen and Kline (1975) and Smith (1984) is not necessary to induce strong ejections from the near-wall region. Strong ejections are associated with single quasi-streamwise leg vortices in several locations in the figure, in agreement with Pearson and Abernathy's (1984) numerical studies of vortices in viscous shear layers, and with the ensemble-averaged simulation results of Guezennec et al (1989).

The kinematics of $(u'v')_4$ sweep motions in the boundary layer has been much less well understood than that of ejections, due mostly to the relative ease of marking ejections in the near-wall region. In the present results, sweeps are also found to be closely related to the existence of vortical structures. Strong sweeps are also observed mainly in two locations: (1) On the outboard, wallward-rotating side of a quasi-streamwise leg vortex and (2) on the outboard side (away from the head) of a neck vortex. In both locations, vortex induction directs fluid from outer high-speed regions toward the wall, contributing to the Reynolds shear stress in the process. Since quasi-streamwise vortices are more numerous in the wall region, near-wall sweeps are generally associated with these vortices, while sweeps beyond the log layer are usually associated with neck vortices. The downstream sides of transverse,

or head, vortices also contribute to $(u'v')_4$, but to a small degree because of the de-focussing of the induction field caused by the arch-like curvature of the head. Also, as mentioned in Section 8.2.3, transverse vortices in the outer region tend to convect at speeds lower than the local mean, so the magnitude of $-u'$ below the head is generally greater than that of $+u'$ above the head. This effect also reduces the contribution to $(u'v')_4$ by transverse vortices.

To generalize the impressions given by Fig. 10.6.5, a plan view of the computational domain is shown in Fig. 10.6.7. The spatial association of the low-pressure vortical structures with strong $(-u'v' \leq -6u_\tau^2)$ ejections and sweeps is nearly unique. That is, almost every region of intense $(u'v')_2$ and of intense $(u'v')_4$ lies adjacent to a vortical structure identified by elongated low-pressure contours. The figure also re-emphasizes that the vortical structures in the boundary layer do not occur as forests of hairpins, or rings, or any other single, repeated shape; instead, vortices exist in a wide variety of shapes and sizes.

Among the least understood aspects of boundary layer coherent motions are the evolution characteristics of vortical structures. With the aid of the pressure field as a vortex identifier, the numerical simulation may be used to full advantage to investigate this topic.

To observe the temporal development of the main vortical structure in sub-volume S (Fig. 10.6.5), a sliding subvolume was convected downstream with the structure (Fig. 10.6.8a) for 41 time-steps, each with $\Delta t^+ = 3$. The convection velocity of the head of the vortical structure was found to be quite constant at approximately $17u_\tau$ ($\approx 0.85U_e$). This velocity is lower than that of the local mean of $19.5u_\tau$, which exists at the location of the head, $y^+ \approx 200$. The convection velocity of the subvolume was matched to that of the vortex head.

The temporal evolution of the structures in the convecting subvolume is shown in Fig. 10.6.8b, with every third step shown, so $\Delta t^+ = 9$ for the figure. The time step shown in Fig. 10.6.5 corresponds to step 12 in Fig. 10.6.8b. The large vortical loop structure in the subvolume is visible for the duration of the time-sequence, spanning a Δt^+ of 120 and travelling approximately 2000 viscous units downstream, indicating a very persistent structure. Near-wall structures are considerably more fleeting, especially quasi-streamwise leg vortices.

A summary of the main observations gleaned from the time sequences is listed here, and the reader is referred to the appropriate video for more detail:

- Large vortical arches or hooks are long-lived, but trailing legs sometimes grow from descending necks (apparently by streamwise stretching - see steps 8 through 14), break away or dissipate, and then occasionally re-grow from the same outer parent structure. Near-wall legs are relatively dynamic, but can extend up to 500 viscous lengths in x (step 14) in rare cases.
- Secondary transverse vortices sometimes appear spanning the low-speed fluid

upstream of a small near-wall arch, but the more common case is for a secondary vortex to grow straddling the low-speed fluid lifted by a single quasi-streamwise vortex.

- Large (δ -scale) vortical arches occasionally bifurcate in the center of the head, with one side disappearing while the other side survives and seems to reform the arch.
- At all times, significant sweeps and ejections are closely related to vortical structures, with the kinematic associations as described for Fig. 10.6.5. The longevity of the large vortical arch in the convecting subvolume results in a large $(u'v')_2$ region which travels downstream for at least 200 viscous units.

When watching the animated time sequences, it is important to note that long-lived, convecting regions of $-u'v'$ are not isolated masses of marked fluid, but are instead convecting “pumping” locations. Throughout the lifetime of a $-u'v'$ region, fluid is being constantly “ejected” or “swept” through it. As a result, an ejection event that seems short from the viewpoint of a stationary probe may actually be relatively long-lived in time, and may be convected a fairly long distance downstream during its lifetime.

Broader interpretations of the observations from time-sequences will be given in Chapter 12 and further details will be reported separately.

Let us return momentarily to the contribution of near-wall quasi-streamwise vortices to the Reynolds shear stress. Fig. 10.6.9 is another view of the significant $-u'v'$ regions in the $y^+ = 15$ plane, with a number of side-by-side sweep/ejection pairs visible. To determine whether these doublets are actually indicative of streamwise vortical motion, cross-plane cuts have been taken through the data at the locations indicated in the figure. Green bars (A-E) mark cuts through sweep/ejection pairs. For comparison, yellow bars (F-I) identify cuts through ejections without a visible neighboring sweep, and cyan bars (J-M) mark cuts through non-paired sweeps.

Cross-flow vectors colored by $u'v'$ quadrant and magnitude are plotted for each section in Figs. 10.6.10-12. For cuts across sweep/ejection pairs (A-E), Fig. 10.6.10 shows that a quasi-streamwise vortex is the cause in every case. This result holds true for every pair similarly dissected (approximately 50). About half of the non-paired $(u'v')_2$ motions are also associated with vortices, although usually of a larger scale than for the pairs. The remainder of the isolated ejections are due either to out-of-plane vortex induction by transverse vortices, or to the collision of converging spanwise streams (as in F). Isolated near-wall sweeps are also commonly associated with streamwise vortical motion (J and M), but also occur due to deep intrusions arriving from the outer region via induction by vortical necks.

A rough estimate of the percentage of buffer-region $\overline{u'v'}$ due to quasi-streamwise vortices can be made as follows: In Section 10.5, it was shown that for the $y^+ = 15$ plane, 78% of v' fluctuations larger than $0.8u_\tau$ are found in pairs or triplets, (with

very few triplets). Conditional averages in the plane show that these regions account for 37% of the total $\overline{u'v'}$ at $y^+ = 15$. The remaining 63% of $\overline{u'v'}$ is therefore due to single, or non-paired v' -regions.

Assuming all v' pairs or triplets are due to quasi-streamwise vortices, then these vortices are related to 37% of $\overline{u'v'}$ at $y^+ = 15$. As discussed above, most (about 60%) of the single v' or $-u'v'$ regions are also found to be associated with quasi streamwise vortices, which then account for 0.6×0.63 , or 38% of $\overline{u'v'}$. Summing up, we estimate that $37\% + 38\% = 75\%$ of $\overline{u'v'}$ at $y^+ = 15$ is due to the presence of quasi-streamwise vortices in the near-wall region.

This 75% value is consistent with the percentage of the Reynolds shear stress which is self-maintained by inner-region motions, as deduced from entirely different types of data by Kline and Robinson (1989a). The balance of the shear stress production is related to direct influence by motions in the outer layer (see Sections 10.16, 10.20).

To summarize the spatio/temporal relationships between vortices and ejections and sweeps, it may be said that most of the strong contributions to $-\overline{u'v'}$ occur directly adjacent to a vortical structure of some kind. In addition, most vortices identified as elongated low-pressure regions are directly adjacent to ejection and/or sweep contributions to $-\overline{u'v'}$. This nearly unique relationship implies that vortices comprise an essential and possibly central element of turbulence production and momentum transfer in the boundary layer.

10.7 Near-Wall Shear Layers (NWSL's)

In the current study of the simulated boundary layer, the sublayer and buffer region are found to be densely populated with near-wall shear layers. Shear layers can be found in any randomly selected $x - y$ slice through the data, and are most common below $y^+ = 80$. The spacing between shear layers in x is irregular, but the typical streamwise distance between sequential NWSL's is between 100 to 500 viscous lengths.

Several examples of near-wall shear layers in the simulation are shown using two different graphical methods in Figs. 10.7.1 and 10.7.2. The structures are nearly parallel to the wall in the sublayer, and lie at an increasing but shallow (< 20 degrees) angles to the wall as y^+ increases. The spanwise dimension of near-wall shear layers ranges from 30 to 60 viscous lengths, implying that highly three-dimensional motions are involved in their formation. The three-dimensional character of NWSL's is illustrated by contour surfaces of constant $|\omega|$ in Fig. 10.7.2, which is a frame taken from a stereo 16mm movie. Time-sequences show that NWSL's typically survive long enough to travel several hundred viscous units downstream, in agreement with Johansson et al's (1987) findings.

Near-wall shear layers exist on the upstream edge of kinked sections (and occasionally on the end) of a low-speed streak as an unavoidable consequence of surrounding higher-speed fluid impacting the low-speed streak. When a portion of a streak lifts in an ejection, an intense, lifted shear layer forms along the upstream face of the ejection. The formation of this intense shear layer does not require significant values of either $-v'$ or $+u'$ in the fluid above the lifting streak. The severe near-wall mean velocity gradient is sufficient to provide upstream fluid with significantly higher x -momentum than the ejection. In these cases, NWSL's are closely related to turbulence production, though not necessarily in a causal sense. Moreover, the instantaneous streamwise velocity profiles through lifted shear layers are inflectional, suggesting the possibility of local dynamic instability, as discussed by a number of earlier authors.

A second type of "flattened" shear layer is formed when high-speed fluid presses against the wall, creating locally high wall-shear stress. Flattened near-wall shear layers are not expected to be dynamically significant, however, since they produce a vorticity concentration at the wall, rather than in the flow-field.

10.8 Near-Wall Shear Layers with Vortices, Ejections and High-Pressure

A new observation made in the current study is that some of the near-wall shear layers roll up into transverse vortices. Transverse roll-up of internal shear layers has previously been observed for $y^+ > 200$ in visual experiments by Nychas et al (1973), and this has also been observed in the simulated turbulence, but the current results suggest that shear layers are more common near the wall than far from it, and that transverse rollup occurs more commonly below $y^+ = 80$.

Figs. 10.8.1 through 10.8.4 show an example of near-wall shear layer roll-up. The y -scale in Figs. 10.8.1, 10.8.3, and 10.8.4 has been enlarged by a factor of two to help identify the sloping near-wall structures. In Fig. 10.8.1, the shear layer is visualized with contours of spanwise vorticity, with pressure and $(u'v')_2$ contours superimposed. Although the vorticity is high everywhere along the shear layer, a low-pressure region is seen to exist only at the outer tip; this low-pressure zone marks the core of a transverse vortex, as confirmed by the instantaneous vector field in Fig. 10.8.2, which has been plotted in a reference frame moving downstream with the shear layer tip at its measured propagation velocity of $15u_\tau$.

A region of strong $(u'v')_2$ motion is associated with the transverse roll-up of the shear layer in Fig. 10.8.1, but is not present along the remainder of the shear layer. The study of several similar cases shows that NWSL's are not directly associated with strong $u'v'$ peaks until they roll up into transverse vortex elements. At any given time, near-wall shear layers are statistically associated with only a small percentage of the shear stress production for $y^+ < 80$, but all shear layers may be **dynamically** significant due to their potential for rolling up into vortices which in

turn generate strong ejections. Although a sufficient sample for statistical distributions has not yet been obtained for NWSL roll-ups, it appears that rollup occurs mainly in the rather narrow band of $30 \leq y^+ \leq 80$, which corresponds roughly with the logarithmic layer in the simulated boundary layer of the present study. This implies that near-wall shear layers are not major direct producers of $-u'v'$ in the buffer zone, where turbulence production peaks, but that shear-layer instability leading to vortex formation may contribute significantly to $-\overline{u'v'}$ in the log region. Perhaps the major dynamical importance of near-wall shear layers is their role as vortex generators, rather than as direct producers of $-u'v'$.

An alternative view of the role of near-wall shear layers is presented by Alfredsson et al (1988), who point out that the production term $\overline{u'v'}\partial\overline{U}/\partial y$ requires both high shear and high $\overline{u'v'}$. Alfredsson et al show that the ensemble-averaged production term is enhanced by near-wall shear layers, and so they make direct contributions to near-wall turbulence production, whether or not they roll up into vortices. The point being made in the current work is that direct, instantaneous cross-gradient momentum transport is achieved more effectively by the transverse vortices that may grow from near-wall shear layers, than by the shear layers themselves.

One of the best-known attributes of near-wall shear layers, that of a coincident high-pressure region, is shown by the green contours in Fig. 10.8.1. High pressure accompanies shear layers regardless of whether they roll up, and occurs due to the re-direction of high-speed fluid impacting the upstream face of lower-speed fluid, creating a local quasi-stagnation zone. This inviscid phenomena has been reported widely in both experiments and numerical simulations (Chapters 2 and 3).

The time evolution of the NWSL of Fig. 10.8.2 is shown with side-view ω_z contours in Fig. 10.8.3. The main shear layer of Fig. 10.8.2 can be seen at $x^+ \approx 100$ in step 7 of the time series. In the sequence, the shear layer is seen to develop a vorticity concentration (the transverse vortex) near its mid-point, which becomes the dominant feature of the shear layer. In this example, the vortex head eventually separates from the shear layer, and moves downstream with a slight wallward component of motion. In most other cases, the vortex moves outward after appearing.

Selected stages of sequence in Fig. 10.8.3 are shown in Fig. 10.8.4, along with pressure and $(u'v')_2$ contours. The figure confirms that high pressure is associated with the near-wall shear layer at all times, but significant ejection motion does not occur until vortical motion appears, as indicated by the concentrated low-pressure peak at the "head."

Current work is underway to provide statistical characterization of the rollup of near-wall shear layers. This will include frequency of occurrence and time-scales of rollups, relationship between shear layer intensity and resulting vortex strength, and quantitative contribution of shear layers to $-\overline{u'v'}$, with and without rollups.

A different kind of association between vortices and near-wall shear layers is shown in Fig. 10.8.5, in which a shear layer is seen formed atop a region of low-speed fluid apparently lifted by a quasi-streamwise vortex. The shear layer shown in blue is the same as in Figs. 10.8.1 and 10.8.2; the low-speed fluid is on the wallward side of the shear layer. The band of blue contours along the wall in Fig. 10.8.5 reflects the high vorticity caused by the no-slip condition at the wall. This scenario is similar to that described by Stuart (1975) for transitional boundary layers, and suggests a method by which streamwise vortices may give rise to transverse vortices. If these newly-formed near-wall transverse vortices grow outward and into arch or hairpin shapes, a mechanism for “single-vortex” regeneration of vortex structures is seen. Vortex regeneration remains poorly understood, but is discussed further in Chapter 12. An end-plane cut through the near-wall shear layer and the quasi-streamwise vortex (Fig. 10.8.6) shows the geometrical relationship between the vortex-induced lifted fluid and the high-vorticity shear layer. Of particular importance is the transverse extent of the shear layer, which is similar to the diameter of the quasi-streamwise vortex. (Although near-wall shear layers are identified here using ω'_z contours, similar results are obtained with ω_z , as was shown in Fig. 8.23g).

10.9 Vortical Structures with High-Pressure Regions

Fig. 10.9.1 shows contour surfaces for $p' = +3\rho u_\tau^2$ in subvolume S, along with the low-pressure surfaces of the vortical structures. High-pressure regions in the turbulent boundary layer tend to be rounded, as opposed to the elongated low-pressure regions. High-pressure occurs where high-speed fluid impacts low-speed fluid, causing the high-speed fluid to flow around the obstruction and creating a convecting high-pressure quasi-stagnation point in the impact zone.

This “eddy interaction” frequently occurs in two locations. The first location is some distance upstream of the head portions of arch-like vortical structures, where the low-speed fluid left behind by the rotation of the head and neck vortices is rear-ended by the following high-speed fluid. This is visible upstream of both vortical loop structures in Fig. 10.9.1, and also upstream of the secondary vortex associated with the smaller loop. The second common location for high-pressure zones is below sweeps, when high-speed fluid moves wallward into the realm of slower flow. This usually occurs on the downward-rotating side of neck vortices, as discussed in Section 10.6.

In a plan-view of the boundary layer (Fig. 10.9.2), high-pressure zones are seen to exist almost exclusively at the upstream edges of low-speed regions, and commonly a short distance upstream of vortical structures. High-speed fluid impacting the rear of lifted low-speed streaks appears to be a major cause of positive wall pressure fluctuations, as discussed in Section 10.11.

10.10 Wall-Pressure Fluctuations

Contours of instantaneous wall-pressure fluctuations are shown for the simulated boundary layer in Fig. 10.10.1. The patterns differ dramatically from the elongated streamwise velocity field at $y^+ = 3$, which is shown for comparison. The contour shapes are in good qualitative agreement with experimental results (Dinkelacker et al, 1977) and with previous simulations (Grotzbach and Schumann, 1979; Rogallo and Moin, 1984). High-pressure regions tend to be rounded in shape while low-pressure regions are more often finger-like. High- and low-pressure regions appear roughly similar in dimensions, with most regions ranging from 50 to 200 wall units in both directions. However, occasional high- and low-pressure regions with extents of over 400 viscous lengths (1.3δ) occur, suggesting outer-flow sources. In animated time evolutions, lifetimes of the individual pressure fluctuations scale with their spatial extents (larger regions persist longer), as would be expected, and in agreement with experimental results (Willmarth, 1975b).

For dynamical issues, it is pressure **gradients** rather than pressure magnitudes that provide fluctuating forces within the boundary layer. As measure of this potential influence, the magnitude of the two-dimensional instantaneous wall-pressure gradient, $((\partial p/\partial x)^2 + (\partial p/\partial z)^2)^{1/2}$, is compared with the wall-pressure fluctuations in Fig. 10.10.2. (The pressure gradients were estimated by central differencing. As with the dissipation function in Sec. 8.1.1.7, the spatial filtering introduced by low-order differencing does not affect the qualitative conclusions being drawn here.) The pressure gradient pattern displays a distinct braided pattern overall, with elongated individual peak regions measuring 30 to 80 viscous lengths across. As expected, significant wall-pressure gradients occur below the edges of near-wall vortices, and at the boundaries of regions of high wall-pressure.

10.11 Wall-Pressure Fluctuations with Vortices, Ejections, Sweeps

The practical importance of wall-pressure fluctuations, especially in underwater vehicle noise generation, has motivated a substantial research effort into the connections between turbulence generation mechanisms in the boundary layer and the underlying wall-pressure fluctuations. In Fig. 10.11.1, strong $(-u'v' \leq -4u_\tau^2)$ ejections and sweeps at $y^+ = 12$ are overlaid upon the wall-pressure field. As expected from the difference in contour patterns, the correlation between the two fields is not strong or immediately obvious. Some relationships may be observed, however:

- High-pressure regions are sometimes found beneath strong sublayer sweeps, consistent with the notion of wallward fluid impacting the surface. This, however, is less common than the high-pressure generated at the quasi-stagnation point on an internal shear layer (Section 10.9, Fig. 10.11.5).

- The location beneath side-by-side sweep/ejection pairs usually exhibits low wall-pressure, which is consistent with the notion of a quasi-streamwise vortex causing the sweep/ejection pair (Sec. 10.6). Apparently the low pressure in the cores of these near-wall vortices is also detectable as pressure minima at the wall.
- Compact regions of high-amplitude wall-pressure peaks of alternating sign occasionally occur, generally accompanied by significant $-u'v'$ in the buffer zone. These regions resemble the “wave packets” of wall-pressure fluctuations investigated by Schewe (1983) and Johansson et al (1987c). However, analysis of the three-dimensional velocity field surrounding such regions suggest that they are a site of multiple shear-induced vortex rollups atop a low-speed streak. Thus, regions of intense, high-frequency wall-pressure fluctuations may more accurately be described as the pressure patterns associated with convecting near-wall eddy structures rather than as coherent pressure waves, which would propagate at the sonic velocity.

The wall-pressure gradient magnitude field is compared with sweep and ejection contours at $y^+ = 15$ in Fig. 10.11.2. Although broad regions of activity in the $-u'v'$ field are reflected in the wall pressure gradient, the correlation appears to be weak.

A comparison between the pressure fluctuations within the boundary layer and the wall-pressure beneath it is shown in Fig. 10.11.3. In general, high-pressure regions within the flow are well-correlated with high wall-pressure peaks, in agreement with the observation (Sec. 8.2.4) that the pressure field (especially the high-pressure component) is elongated in the wall-normal direction.

Since low-pressure regions in the flow-field tend to be elongated rather than rotund, they do not always extend to the wall, making the correlation between the field and the wall weaker for low-pressure regions than for high. However, strong near-wall vortical structures affect the wall directly via the low-pressure fields surrounding their cores. Quasi-streamwise vortices are the most common form of near-wall vortex (Chapter 11), and are therefore expected to exert a greater influence on the wall pressure than other vortex geometries.

The relationship of the low-pressure regions in subvolume S to the wall-pressure field is depicted in Fig. 10.11.4. The wall-pressure is rendered as a carpet map, with high-pressure appearing as magenta peaks, and low-pressure in the blue valleys. Although considerably more enlightening in stereo, the figure shows a low-pressure trough beneath the extended vortex leg, and high-pressure peaks beneath sweeps and eddy-collision zones.

The effect of near-wall shear layers on the wall-pressure is demonstrated in Fig. 10.11.5. In the figure, a well-defined near-wall shear layer exhibits a high-pressure region along the high/low-speed interface, and this high-pressure is seen to extend to the wall. This association between near-wall shear layers and high-pressure regions

has been documented in numerous previous experimental (e.g. Brown and Thomas, 1977) and numerical investigations (e.g. Johansson et al, 1987b).

To summarize the wall-pressure results, high wall-pressure peaks are generally due to “eddy interactions” (including near-wall shear layers) in the flow directly above. The length-scale of the high-pressure zones corresponds approximately to the distance from the wall to the pressure source. Low-pressure peaks at the wall are often due to near-wall vortices, and tend to be somewhat elongated or “fingered” as a result. Because of the integrated nature of the pressure field, several stacked layers of vortical structure can combine to produce a spidery low-pressure signal at the wall. High-amplitude, small-scale wave-like groups of pressure pulses appear to be related to the rollup of new vortices from intense shear layers near the wall. Statistics supporting these conclusions are being collected for later dissemination.

10.12 Pockets

When distributed markers are introduced into the sublayer of a turbulent boundary layer or channel, roughly circular regions devoid of marked fluid appear in the plan view. These have been named pockets (Falco, 1980a), and they give the visual impression of being a “footprint” of some outer structure that induces fluid toward the wall. Kim et al (1987) have shown that pockets become visible in numerically simulated channel flow only with distributed fluid markers, not with simulated bubble-lines. This observation confirms a similar experimental finding of Falco. However, time evolution of the marked flow field is necessary to detect pockets with distributed markers. In the current analysis of the simulated boundary layer, we have endeavored to detect pockets in instantaneous flow fields, without the addition of simulated flow markers.

If pockets are associated with wallward-moving fluid in the sublayer, the instantaneous streamlines in the $x - z$ plane would be expected to diverge in the pocket region. Fig. 10.12.1 shows instantaneous streamlines computed in the $y^+ = 2$ plane of the simulated boundary layer. Regions of abrupt spanwise divergence of the streamlines are evident in the figure. The spanwise dimensions of these regions range from 50 to 100 viscous lengths, in agreement with pocket dimensions reported by Falco (1983). Regions of converging streamlines may be likened to “detachment” lines in a separating flow, and regions of diverging streamlines to “reattachment” lines.

10.13 Pockets with Sweeps and Wall-Pressure Fluctuations

Spanwise divergence of instantaneous streamlines in the sublayer is, by virtue of continuity and the streaky nature of the streamwise velocity in the sublayer, most likely to be associated with wallward velocity. Wallward fluid in the sublayer arrives from regions with relatively higher streamwise velocity, so diverging instantaneous streamlines are generally expected to be associated with $(u'v')_4$ motions, or sweeps.

Since sweeps are observed to be commonly associated with vortices in the simulated boundary layer, pockets are likely to be the footprint of fluid swept toward the wall by vortical structures. This idea is nominally consistent with Falco's (1980a) ideas concerning pocket formation, although the form and motion of the responsible vortex remains in question. No ring vortices were observed during this numerical investigation, although all other features of Falco's conceptual model (large-scale motions, δ -scale shear layers, near-wall sweeps and pockets, etc.) were observed.

Fig. 10.13.1 shows instantaneous streamlines at $y^+ = 2$ together with contours of instantaneous wall pressure. As expected, local regions of high pressure coincide with spanwise divergence of the streamlines (wallward motion) and low pressure regions occur along lines of converging streamlines (outward motion). Thus, pockets may be interpreted as evidence of local wallward motions with regions of high pressure at the wall.

10.14 Bulges in the Outer Interface and Large-Scale Motions (LSM's)

Corrsin and Kistler (1954), Kovasnay et al (1970), and others have shown that the instantaneous outer interface between the turbulent boundary layer and the potential free stream consists of large-scale bulges, separated by deep, narrow incursions of free-stream flow into the layer. In the simulated boundary layer, the instantaneous edge of the rotational flow can be identified by contours of low total vorticity magnitude, $|\omega|$, as shown in Figs. 10.14.1 through 10.14.3. The outer surface of the boundary layer exhibits the expected broad outward bulges and narrow irrotational incursions. The interface bulges extend from 0.8 to 3δ in the streamwise direction, and from 0.7 to 1.3δ in the spanwise direction. Each bulge contains a parcel of fluid which will be referred to generically as a "large-scale motion." Bulges and their associated LSM's are seen in side-view and end-view cross sections in Figs. 10.14.1 and 10.14.2, respectively. Simultaneous side and end-views are assembled in Fig. 10.14.3, which is taken from a movie of the time evolution of the boundary layer vorticity magnitude.

In this low Reynolds number boundary layer, the narrow intruding folds of outer irrotational flow often reach as low as $y/\delta \approx 0.25$, implying an occasional direct interaction between the free-stream and the wall region. (See also Section 10.20). This is the type of motion that outer-region Large-Eddy Breakup Devices would be expected to impede, thereby reducing the mean wall shear stress by disallowing the local high shear contributions by these "inrushes" from the free stream. Possible causes of inrushes are discussed in Section 10.16.

Although the potential chasms between bulges clearly affect the near-wall region, they do not occur with sufficient spatial frequency to play a major role. Moreover, the effective spatial frequency of chasms will diminish with increasing Reynolds number, since δ^+ scales as $Re_\theta^{0.7}$, and bulges scale with δ^+ . Even at $Re_\theta = 670$, significant inrushes from the outer flow to the wall region occur only about once

for every δ by δ square of area in the $x - z$ plane. Since $\delta^+ \approx 300$, intrushes occur in the wall region approximately every 300 viscous units in each direction, which is considerably greater than the turbulence production intervals visible in, for example, Fig. 10.3.1. The length scale separation between the inner and outer scales increases with Reynolds number, so intrushes from the free-stream to the wall are expected to be a minor factor in near-wall turbulence production for high-Reynolds number boundary layers (at least for flows with negligible free-stream fluctuations).

10.15 Vortical Structures and Dissipation

The instantaneous dissipation function ϵ'_f was evaluated in Chapter 9 as a detector for strong vortical structures. This approach derived from classical arguments that rapidly stretching vortices should be significant energy dissipation sites. The conclusion was that ϵ'_f is useful for detecting 2-D vortices in the end-view ($y - z$) plane, but that low-pressure is much more successful for identifying strong three-dimensional vortical structures. In this section we focus on the kinematic (and probably dynamic) association between vortical structures and the dissipation field, rather than on vortex detection.

Contours of ϵ'_f are overlaid on the low-pressure vortical structures of subvolume S in Fig. 10.15.1. To avoid cluttering the picture with numerous near-wall shear layers, only the region $y^+ > 30$ is shown. As found in Chapter 9, ϵ'_f is concentrated in near-wall quasi-streamwise vortices, which are presumably being rapidly stretched by the streamwise velocity gradient. Outer-region vortices, which are mostly transverse and are subjected to much less strain, show only weak dissipation regions. The tendency for ϵ'_f to coincide with streamwise, but not transverse vortices is clearly evident in a top-view of a $1600\Delta x^+$ by $1250\Delta z^+$ segment of the computational domain in Fig. 10.15.2.

The significant implication of this ϵ'_f organization is that near-wall, stretching vortices tend to dissipate rapidly and thus have brief lifetimes. Outer-region transverse vortices dissipate much more slowly and persist for much longer time-scales. Both of these inferences are strongly implied by the time-sequence animations discussed in Sec. 10.6, in which near-wall quasi-streamwise vortices appear and disintegrate rapidly, while large, transverse vortices in the outer region live long enough to convect downstream for most of the computational domain. Experimental results that large-scale sloping shear layers can be tracked for significant streamwise distances suggest a relationship between such "backs" and outer-region transverse vortices, which is explored in Sec. 10.18.

10.16 Vortical Structures and Entrainment

Side-view experimental flow visualizations have resulted in a general picture of entrainment of irrotational flow into a turbulent boundary as a lateral folding

and engulfment of the potential fluid between bulges (e.g. Bevilaqua and Lykoudis, 1977). To learn more about entrainment in the simulated boundary layer, vertical flows within regions with very low vorticity magnitude were plotted. Fig. 10.16.1 illustrates the conclusions of this study with the flow in subvolume S. Two cross-planes bisecting the head of the main vortical structure were chosen, and $+/-v'$ was plotted for $|\omega|^+ < 0.025$ in both planes. The orange and blue regions denote wallward and outward irrotational flow, respectively. In the side-view, confirmation of the classical picture of entrainment is obtained. Potential flow is being drawn into the boundary layer on the downstream, wallward-rotating side of the outer-region vortical head. The end-view shows irrotational fluid also being drawn down the side of the vortical loop, apparently as a result of induction by the necks. This gives a highly three-dimensional picture of entrainment, which can be visualized as high-speed fluid passing over and around the slower outer-region vortical arches, while the tilted neck elements induce free-stream into the turbulent layer. Portions of this mechanism were described by Falco (1983), from results of combined flow-visualizations and hot-wire measurements.

The importance of vortical structures to the entrainment process is evident in a top view of the simulated boundary layer, shown in Fig. 10.16.2. Approximately 85% of the high-entrainment regions (yellow) are closely associated with vortical structures. Although entrainment does occur on the downstream side of vortical arches, it appears that the greater share of entrainment is accomplished by "lateral inflows" due to tilted neck vortices. This observation implies that the statistically most important entrainment mechanism in turbulent boundary layers is not a passive, two-dimensional folding of the outer interface, but active wallward pumping by tilted vortical elements, in a fundamentally three-dimensional process.

10.17 Backs

Delta-scale, sloping structures with strong local values of $\partial u'/\partial x$ have been investigated by a number of groups using multi-sensor temperature and velocity probes (e.g. Brown and Thomas, 1977; Chen and Blackwelder, 1978; Subramanian et al, 1982). Space-time correlations and conditional sampling procedures have given from 12 to 30 degrees for the outer-region angle between the wall and these large structures. Because these structures are commonly associated with the upstream side of the large-scale motions discussed above (Kovasznay et al, 1970), they will be referred to as "backs" (though they have also been described as "fronts" by some authors).

It appears appropriate to differentiate between "backs" (which also have transverse vorticity) and near-wall shear layers. Backs are tall (delta-scale) near-discontinuities in u of limited (10-40 viscous lengths) streamwise thickness, and with spacing in the streamwise direction of the order of the boundary layer thickness. In

contrast, near-wall shear layers have dimensions on the scale of the near-wall layer, and exist mostly below $y^+ = 80$. It is not yet clear if the size and spacing of these shear-layer structures are distributed smoothly from small to large, or if there is a bimodal distribution, confirming two different types of structure. Recent statistical analyses of simulated turbulence by Moin et al (1987) have shown some evidence of a “two-layer” structural makeup of a low Reynolds number channel. Experimental ensemble averages have not generally separated the data into two structures because the commonly used single-point VITA technique is unable to distinguish between near-wall structures and δ -scale structures. Also, the scale separation between the two structures would be most pronounced at high Reynolds numbers, where probe sensors are usually too long to independently detect the small-scale structures near the wall.

Following Brown and Thomas (1977), Fig. 10.17.1 shows instantaneous velocity vectors in an $x - y$ plane moving at $0.8U_e$ in the simulated boundary layer. A back structure is clearly evident as a large-scale, sloping shear layer with transverse vorticity. This instantaneous picture is strikingly similar to Brown and Thomas’ ensemble-averaged velocity field in the vicinity of backs. Fig. 10.17.2 shows the instantaneous transverse vorticity associated with the same cut through the back as in Fig. 10.17.1. The $+u' / -u'$ interface that forms a back is highly convoluted and curved, rather than nearly two-dimensional. The shape of a vorticity contour surface along a back is too complicated for useful viewing without stereo images.

Some backs extend all the way to the sublayer, as noted by Brown and Thomas (1977), and Robinson (1982). For these cases, the distinction between back and near-wall shear layer is unnecessary. However, side-views such as Fig. 10.14.1 show many more NWSL’s than backs, so the differentiation between inner and outer region structures appears valid and useful.

10.18 Backs with Vortical Structures

Several researchers have reported on outer-flow vortical structures that are inclined to the wall downstream at approximately 45 degrees (e.g., Head and Bandyopadhyay, 1981; Kim and Moin, 1986). Hot-wire rake studies have consistently given from 12 to 30 degrees for the slope of the backs of large-scale motions in the outer region (Brown and Thomas, 1977; Rajagopalan and Antonia, 1979; Robinson, 1982). Bandyopadhyay (1980) attempted to resolve this discrepancy by speculating that the shallow-angle backs are composed of the heads of arrays of 45 degree hairpin vortices.

For the current study, an example of the spatial relationship between a back and the hook-like vortical structure in subvolume S is shown in Fig. 10.18.1. In this example, the back, which is sloped at about 30 degrees, is located upstream of the 45 degree vortical structure. Apparently, the low-speed fluid being left behind

by the action of the vortex is crowded from behind by the faster upstream flow. The interface between the upstream fluid and the low-speed remnants of vortex induction forms the velocity discontinuity which is the back. In this scenario, the back is generated without need for the row of hairpin vortices suggested by Bandyopadhyay. The relationship between backs and large-scale vortical arches shown in Fig. 10.18.1 has been found to hold true for several other examples. To generalize, all backs identified in a spot-check of the simulated boundary layer (approximately 12 samples) lie upstream of a hook or arch-like vortical structure with its head in the outer region.

Note that the generality of the descriptions of the large scale motions in low Reynolds number simulations may be limited in view of Murlis et al's (1982) finding that the outer structure depends on viscosity up to $Re_\theta \approx 5000$.

10.19 Wall-Shear Fluctuations

Wall-shear fluctuations are related to the viscous drag and integrated heat transfer coefficient of a boundary layer, and so are of considerable practical interest. Regions of high and low wall shear stress at the boundary of the simulated layer (computed from $\partial u / \partial y$ at $y^+ = 0.03$) are shown in Fig. 10.19.1. The streaky structure is evident, but so are previously unnoticed groups of small-scale, quasi-periodic fluctuations in the regions of low wall-shear. The streamwise wavelength of the oscillations ranges from 30 to 70 viscous lengths, and the pattern continues for up to 8 cycles in some cases. Periodic variations in the wall-shear signal were also discovered by Brown and Thomas (1977), but in regions of **higher** than average shear. The discrepancy between these findings are being explored by filtering the wall-shear field in a manner similar to that used by Brown and Thomas.

10.20 Wall Shear Fluctuations with Vortical Structures and LSMs

Vortical structures in the simulated flow are shown in Fig. 10.20.1, along with u' contours at $y^+ = 3$, which are used to approximate the wall-shear stress field. Correlation between the two fields are not immediately obvious, but careful viewing in stereo shows that the near-wall portions of vortices generally affect the wall-shear field noticeably. In particular, wallward sweeps adjacent to near-wall quasi-streamwise vortices are reflected in locally high values of wall shear below and to the side of the vortex.

The outer-flow bulges and associated large-scale motions are seen in Fig. 10.20.2 to have little relation to the wall-shear fluctuations, although, as described in Section 10.14, occasional wallward inflows from the outer region produce narrow regions of unusually high wall shear stress. The transverse extent of the inflows scale approximately with the diameter of the tilted vortex responsible for the motion. As

a result, inflows are narrow ($\Delta z^+ < 100$) even though they are direct transfers of fluid from the outer region.

10.21 Summary

The results presented in this chapter have related virtually all of the important coherent motions in the boundary layer to vortical elements and structures. In particular, ejection and sweep motions, which are the constituents of the Reynolds shear stress and maintain turbulence mixing, are strikingly closely associated with vortical structures. For $y^+ < 30$, quasi-streamwise vortices dominate the turbulence production process. Since most of the turbulence kinetic energy for the entire boundary layer is produced in this region, it appears that quasi-streamwise vortices are the central motion in boundary layer turbulence production. In the region $30 < y^+ < 80$ (which includes the log layer for the current simulation) quasi-streamwise vortices are joined by newly-formed vortical arches which may roll up from intense shear layers. For $y^+ > 80$, both turbulence production (ejections and sweeps) and entrainment appear to be governed by large-scale vortical arches and hooks. Both heads and necks play important roles in the outer region.

Because of the apparent central role of vortical structures and elements, the next chapter will review the pertinent literature and present population, size, and strength statistics for both quasi-streamwise and transverse vortices in the simulated boundary layer.

Instantaneous Velocity Profile: $u(y,z,t)$



Fig. 10.1.1 Instantaneous streamwise velocity profile in two spatial dimensions; $u(x,z)$, for $3 < y^+ < 258$.
Blue: $u \approx 0$. Magenta: $u \approx U_e$.

Sublayer Streaky Structure



Fig. 10.1.1.2 Streaky structure in the u' -field at $y^+ = 3$.
Red to yellow: $u'^+ = -1.0$ to -4.0 . Blue to white: $u'^+ = +1.0$ to $+4.0$.

Fluctuating Streamwise Velocity u'

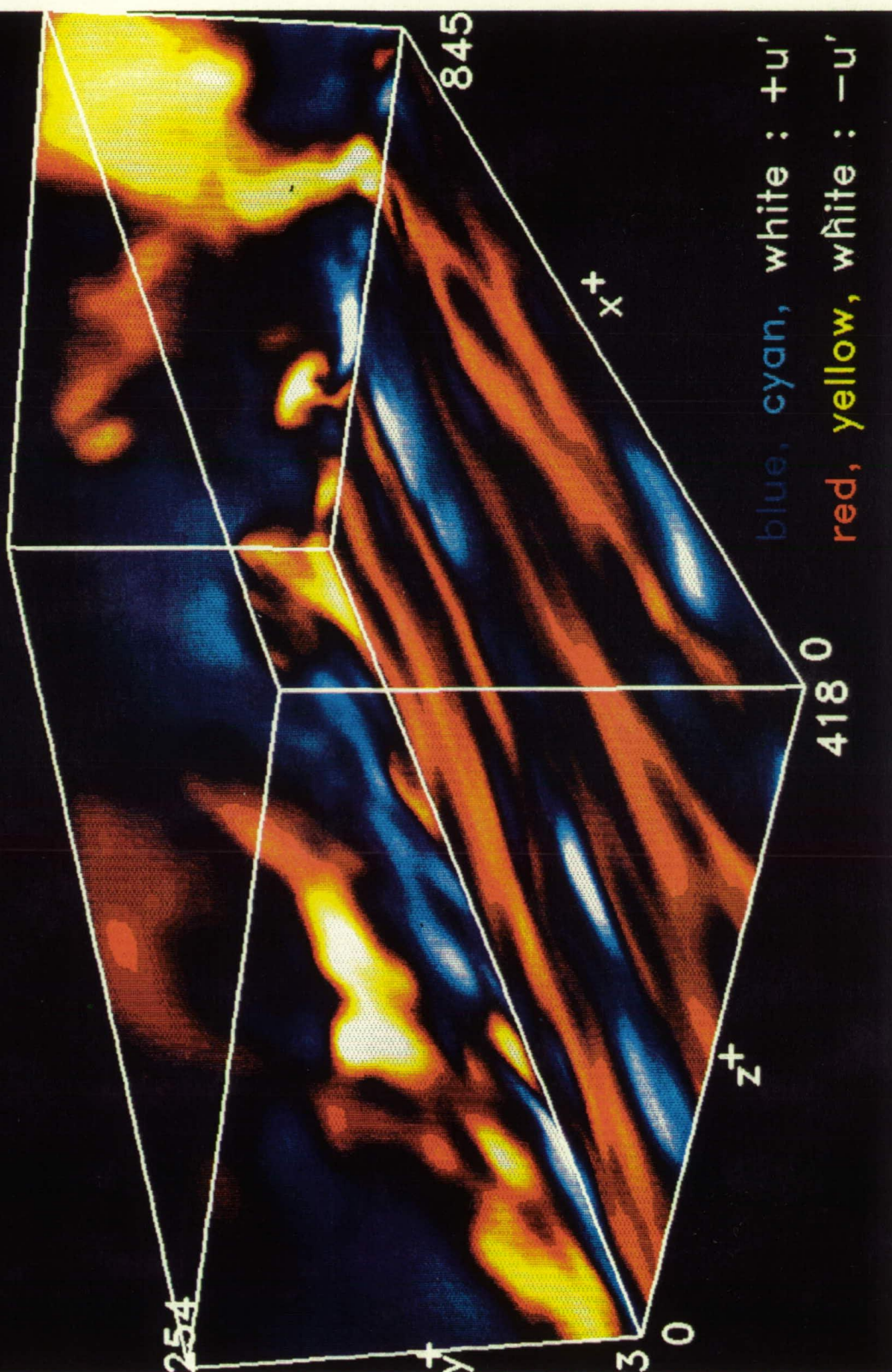


Fig. 10.2.2 u' contours on three sides of a sample computational subvolume. Red to white : low-speed fluid ($u' < 0$). Blue to white: high-speed fluid ($u' > 0$).

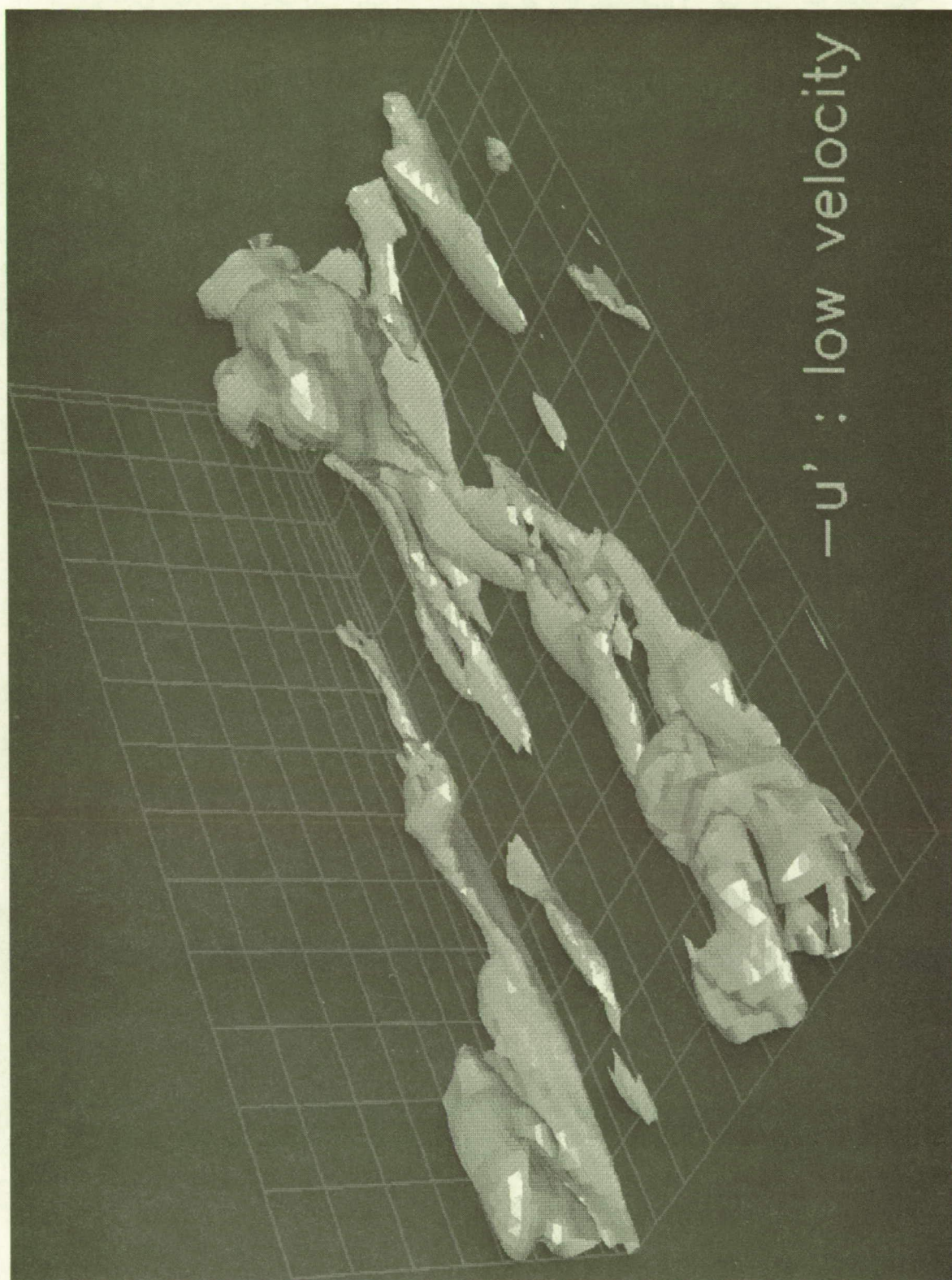


Fig. 10.2.3 Example of instantaneous 3-D $-u'$ contour surface in sample subvolume S .
Yellow: low-speed fluid, $u'^+ = -3.0$.

Ejections and Sweeps at $y^+ = 15$



Fig. 10.3.1 Sweeps and ejections in the $y^+ = 15$ plane.

Red: ejections, $(u'v')_2/u_\tau^2 = -1.0$ to -10.0 . Blue: sweeps, $(u'v')_4/u_\tau^2 = -1.0$ to -10.0 . White contour lines: $u'v'/u_\tau^2 = -4.0$.

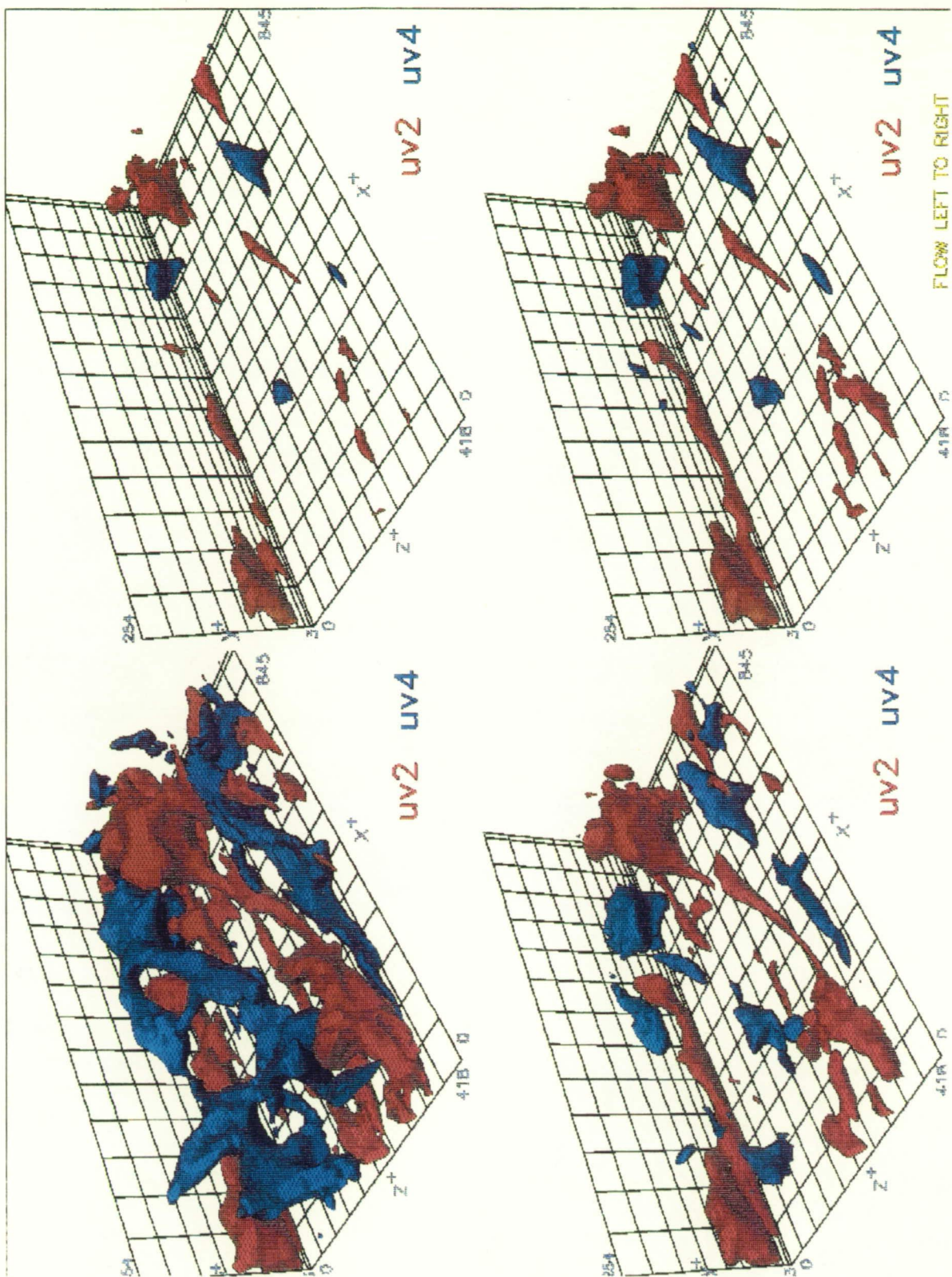


Fig. 10.3.2 Effect of contour-level variation on $(u'v')_2$ and $(u'v')_4$ contour surfaces. Red: ejections. Blue: sweeps. Upper left: $u'v'/u_\tau^2 = -2.0$. Lower left: $u'v'/u_\tau^2 = -4.0$. Upper right: $u'v'/u_\tau^2 = -6.0$. Upper right: $u'v'/u_\tau^2 = -8.0$.

Ejections and Sweeps

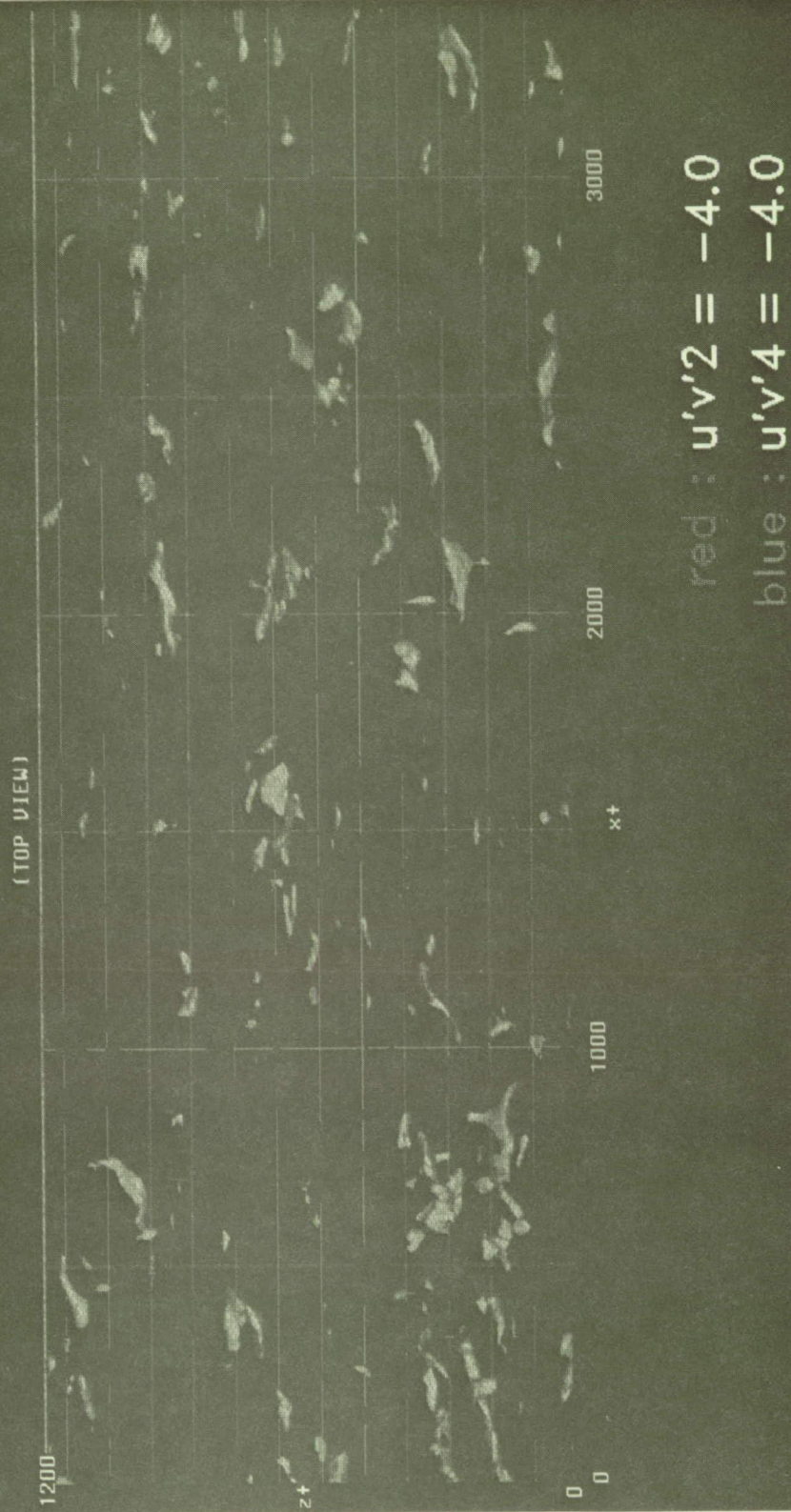
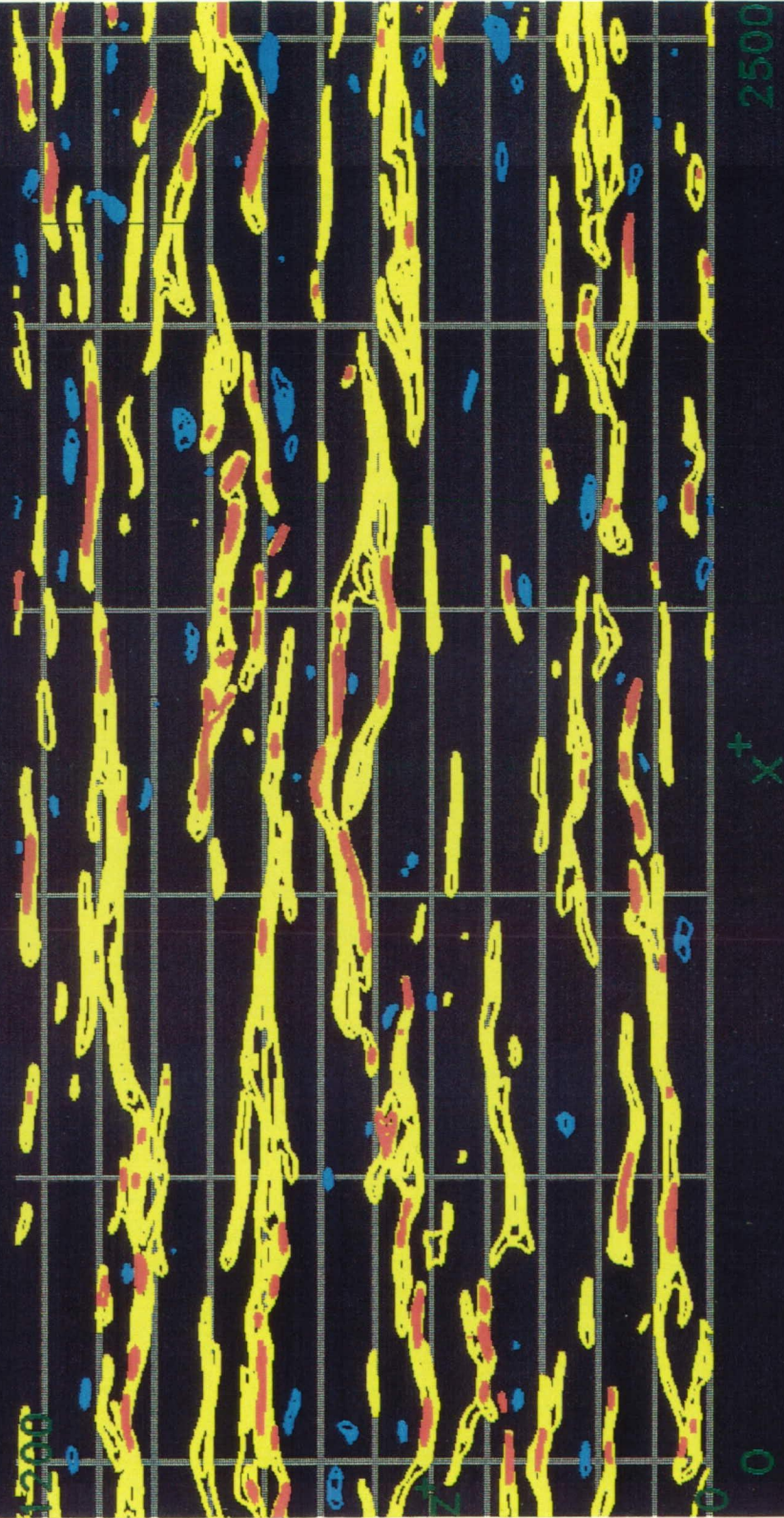


Fig. 10.3.3 3-D contour surfaces of $(u'v')_2$ and $(u'v')_4$.
 Red: ejections, $(u'v')_2/u_\tau^2 = -4.0$. Blue: sweeps, $(u'v')_4/u_\tau^2 = -4.0$.

Low-Speed Streaks, Ejections, and Sweeps

$y^+ = 15$

(PLAN VIEW)



$-u'$ $u'v'2$ $u'v'4$

Fig. 10.4.1 Low-speed streaks, ejections, and sweeps in the $y^+ = 15$ plane.

Yellow: low-speed fluid, $u'^+ \leq -3.0$. Red: ejections, $(u'v')_2/u_\tau^2 \leq -4.2$. Blue: sweeps, $(u'v')_4/u_\tau^2 \leq -4.2$.



Fig. 10.5.1a Wall-normal velocity fluctuations in the $y^+ = 12$ plane.
 Yellow: $v'^+ = +0.2$ to $+2.0$. Magenta: $v'^+ = -0.2$ to -2.0 .

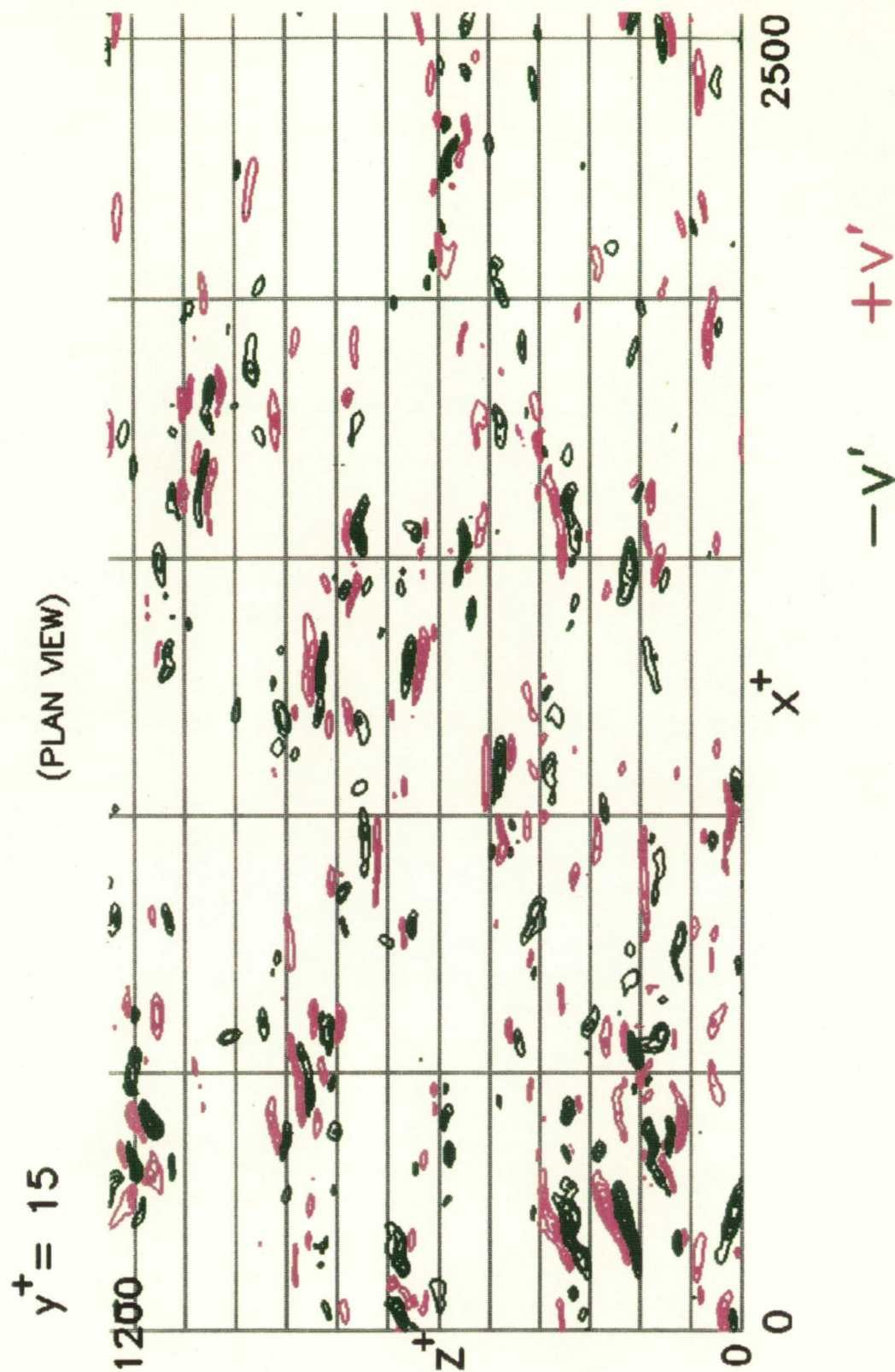
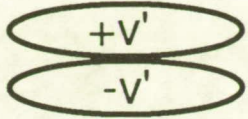
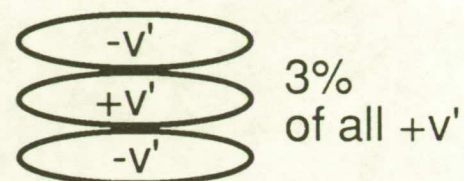
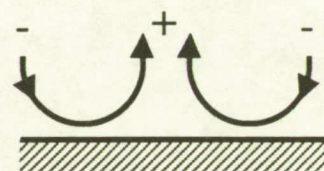
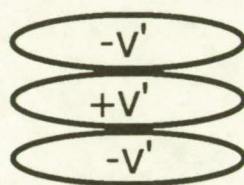


Fig. 10.5.1b Wall-normal velocity fluctuations in the $y^+ = 15$ plane.
Green: $v'^+ = -1.0$. Magenta: $v'^+ = +1.0$.

- pair / triplet population:  75% of all $+v'$

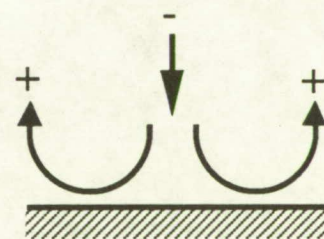
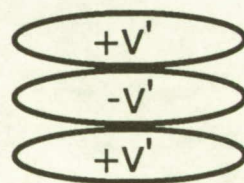


- triplets:



CASE A

21% of triplets



CASE B

79% of triplets

Fig. 10.5.1c Summary of $v' \geq u_\tau$ regions at $y^+ = 15$. Pairs (suggesting single quasi-streamwise vortices) are common, while triplets (suggesting vortex pairs) are rare. Most triplets do not correspond to ejection-producing vortex pairs.

spanwise separation \approx vortex diameter $\approx 35^+$

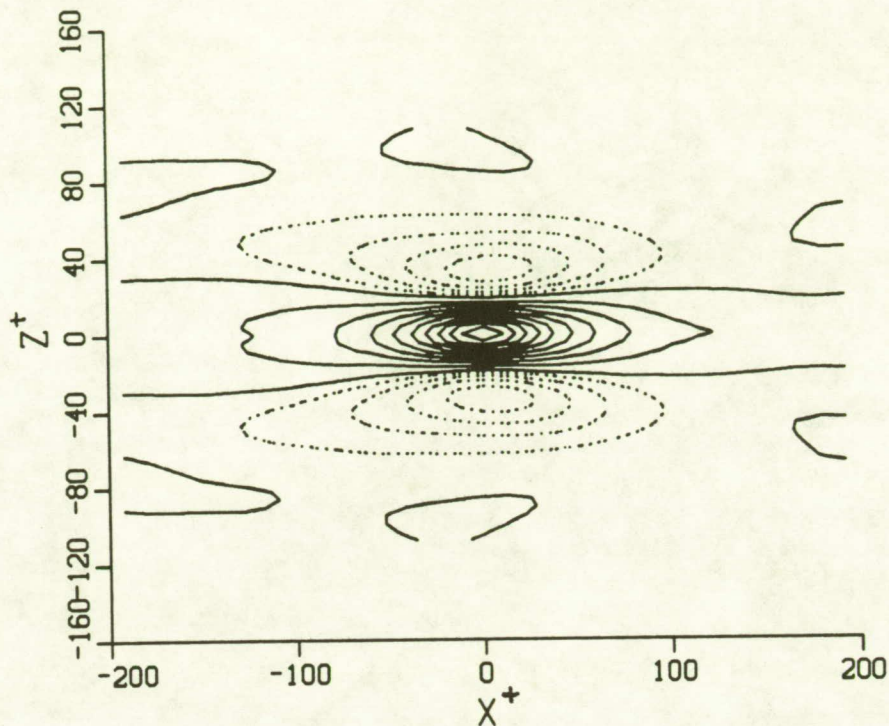
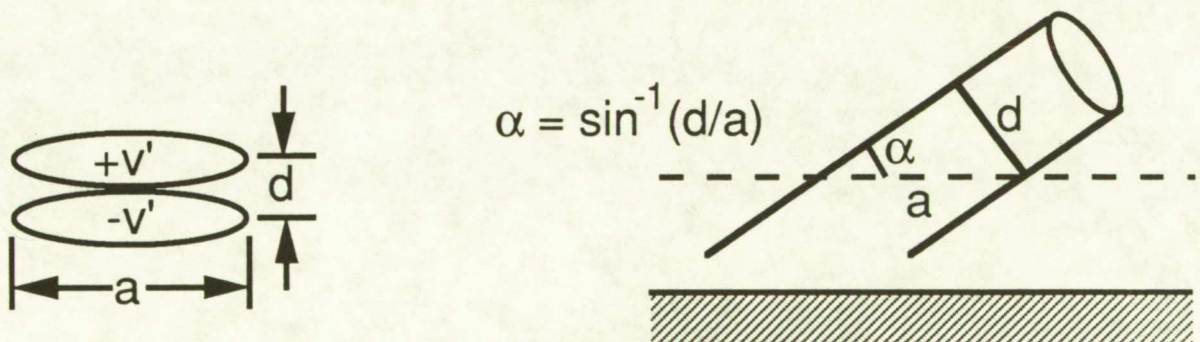


Fig. 10.5.1d Two-point correlation contours for v' in the $y^+ = 15$ plane ($R_{vv}(x, z)$). Results suggest quasi-streamwise vortices with a mean diameter of 38 viscous lengths.



inclination angle $\approx 11^\circ$

Fig. 10.5.1e Estimation of an average inclination angle for near-wall quasi-streamwise vortices.

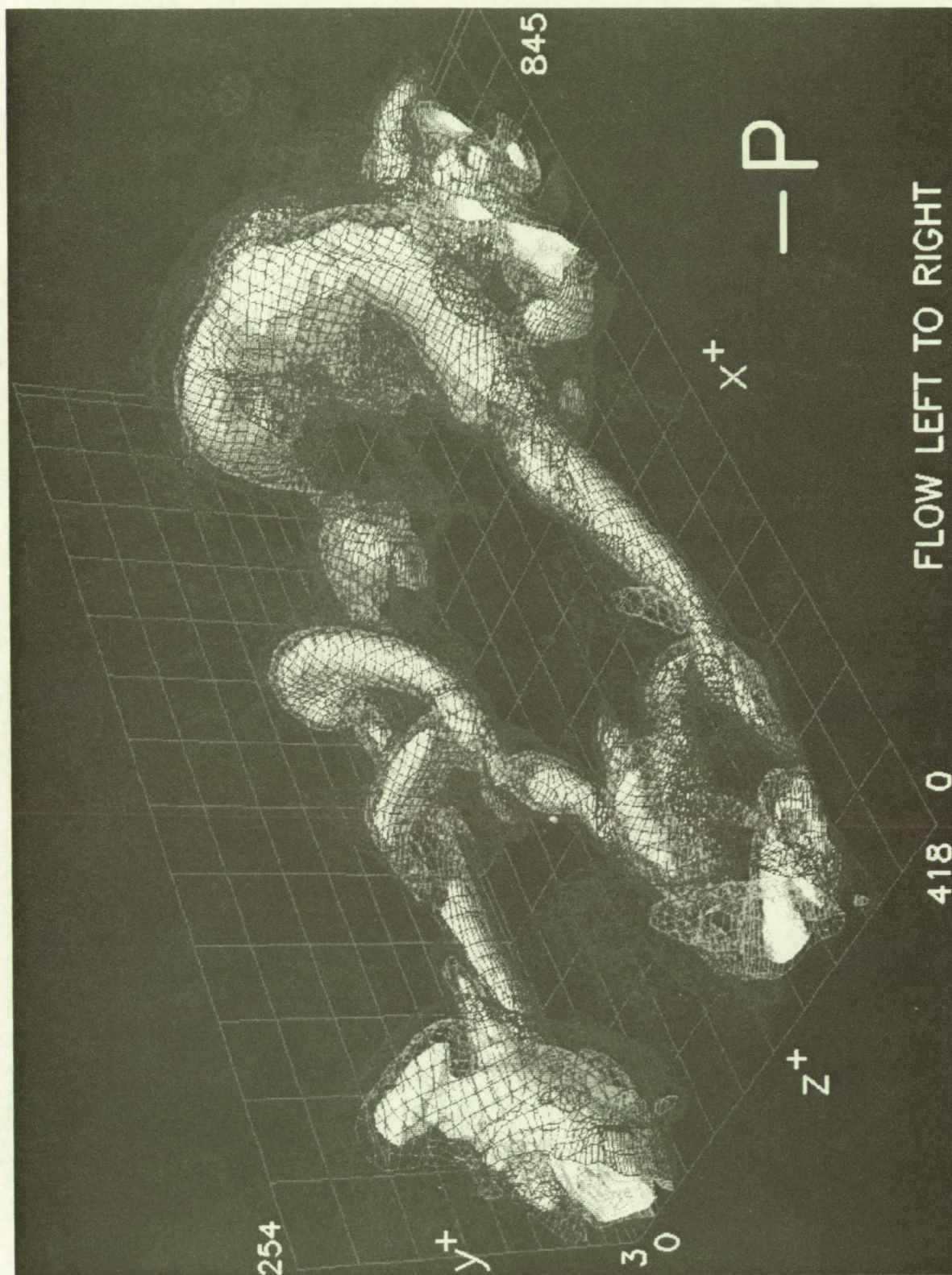


Fig. 10.5.2 3-D contour surfaces of low pressure in sample subvolume S .
 Blue net surface: $p'^{++} = -2.0$. Cyan net surface: $p'^{++} = -4.0$. White solid surface: $p'^{++} = -6.0$.

Pressure Contour Level Variation

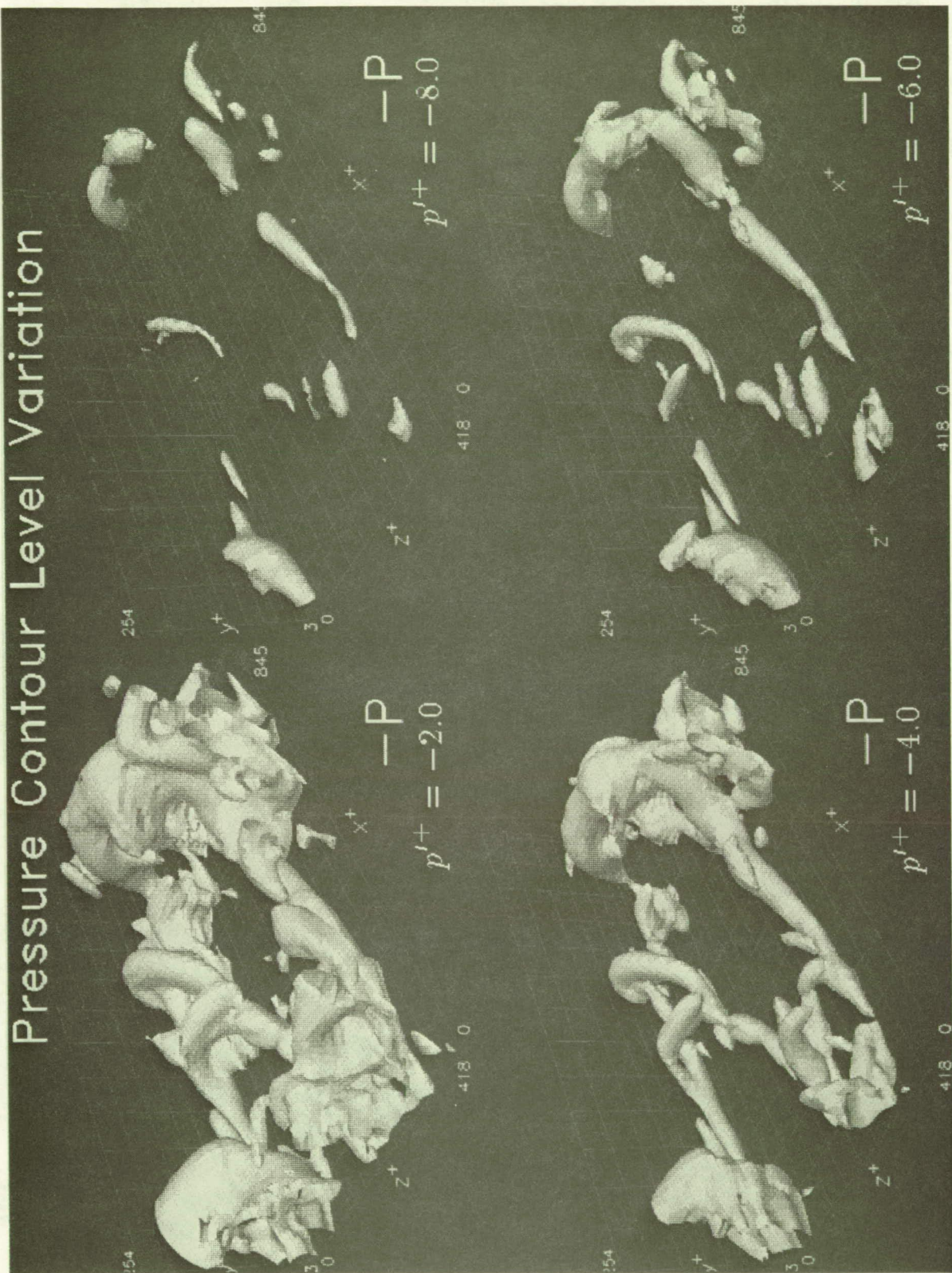


Fig. 10.5.3 Effect of contour-level variation on low-pressure contour surfaces in sample subvolume S . Upper left: $p'^{+} = -2.0$. Lower left: $p'^{+} = -4.0$. Lower right: $p'^{+} = -6.0$. Upper right: $p'^{+} = -8.0$.

Vortical Structures (Elongated $-p'$ Regions)

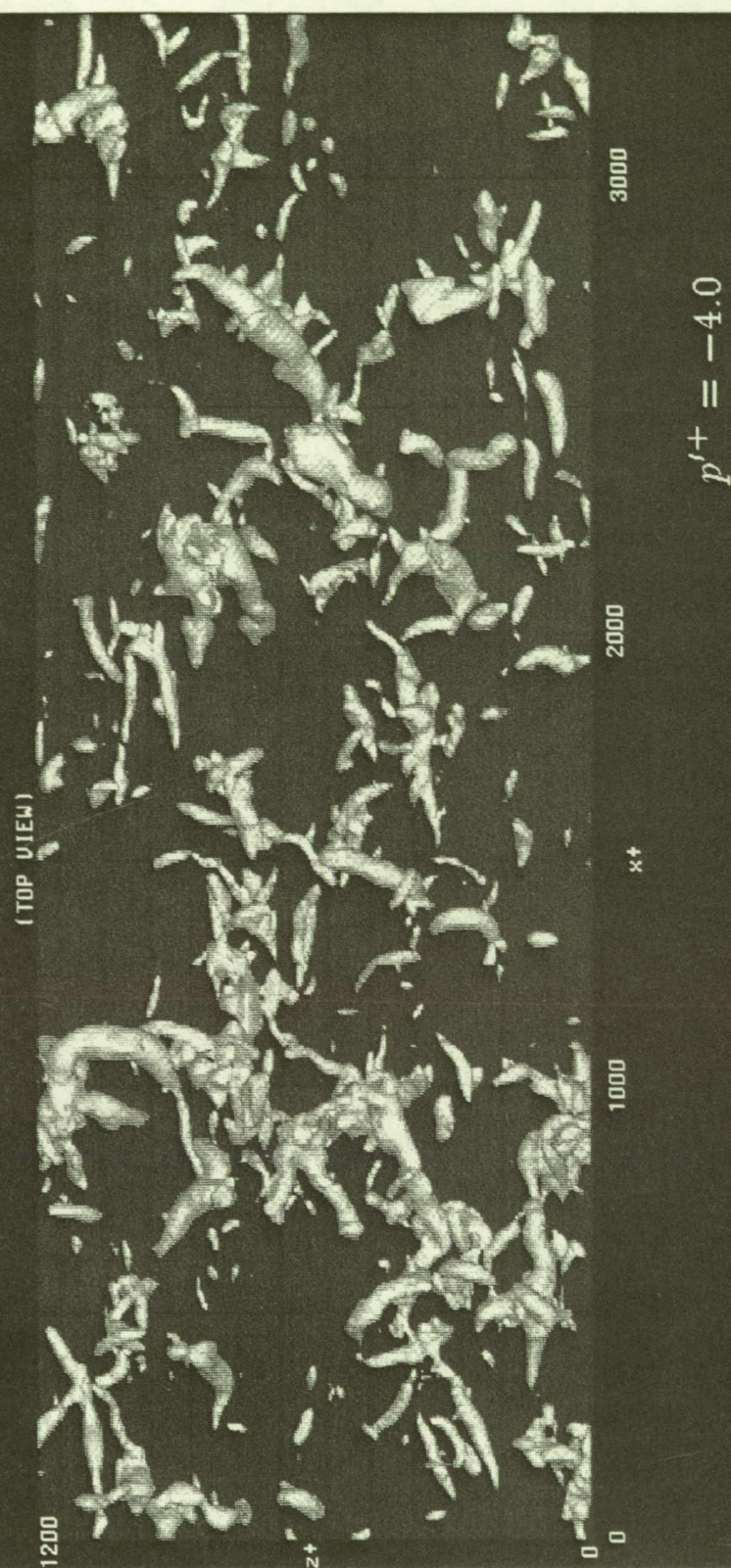


Fig. 10.5.4 3-D contour surfaces of low pressure. White: $p'^+ = -4.0$.

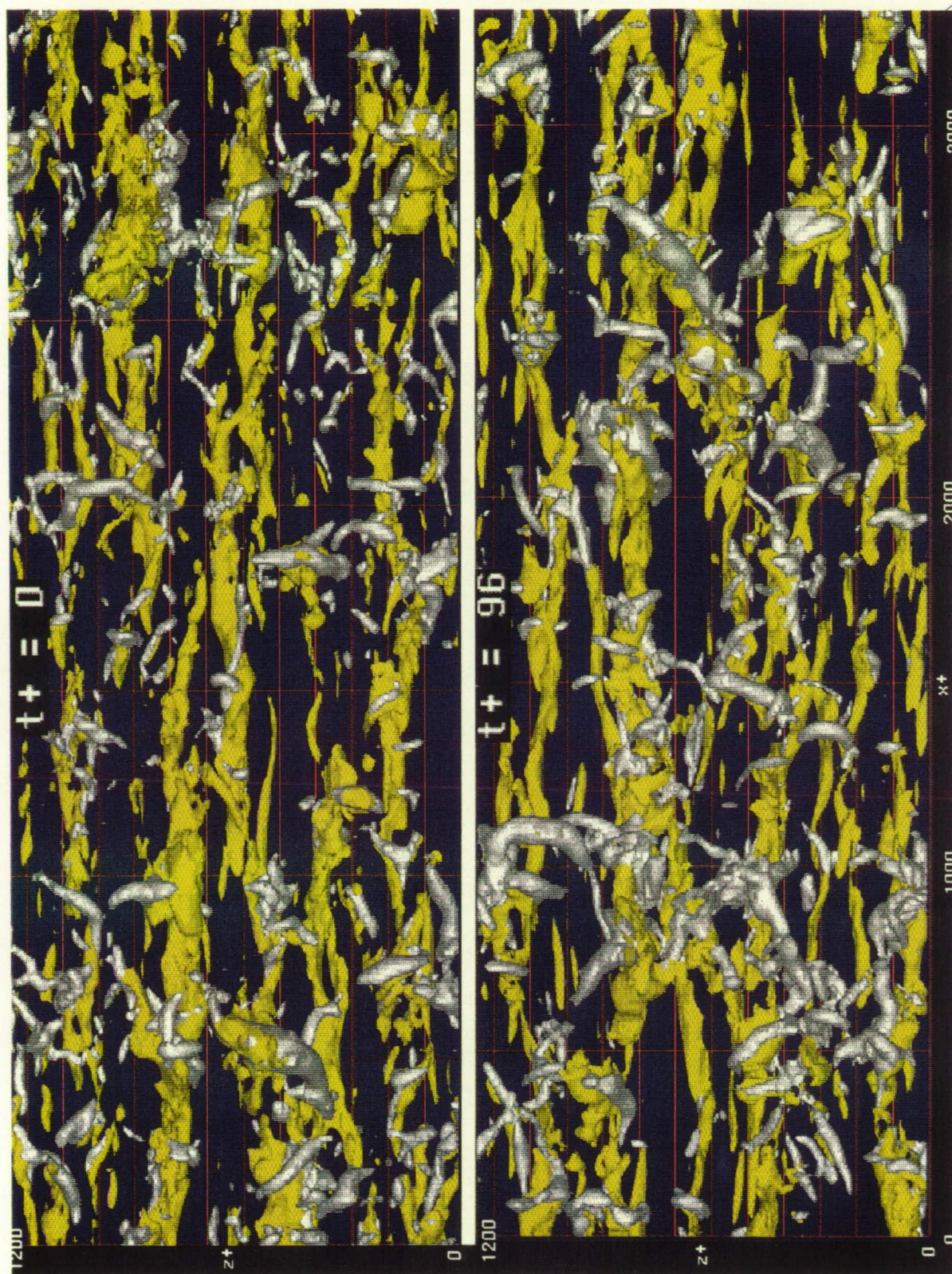


Fig. 10.6.1 3-D contour surfaces of $-u'$ and low pressure at two widely different time-steps. Yellow: low-speed fluid, $u'^+ = -3.0$. White: low-pressure regions, $p'^+ = -4.0$.

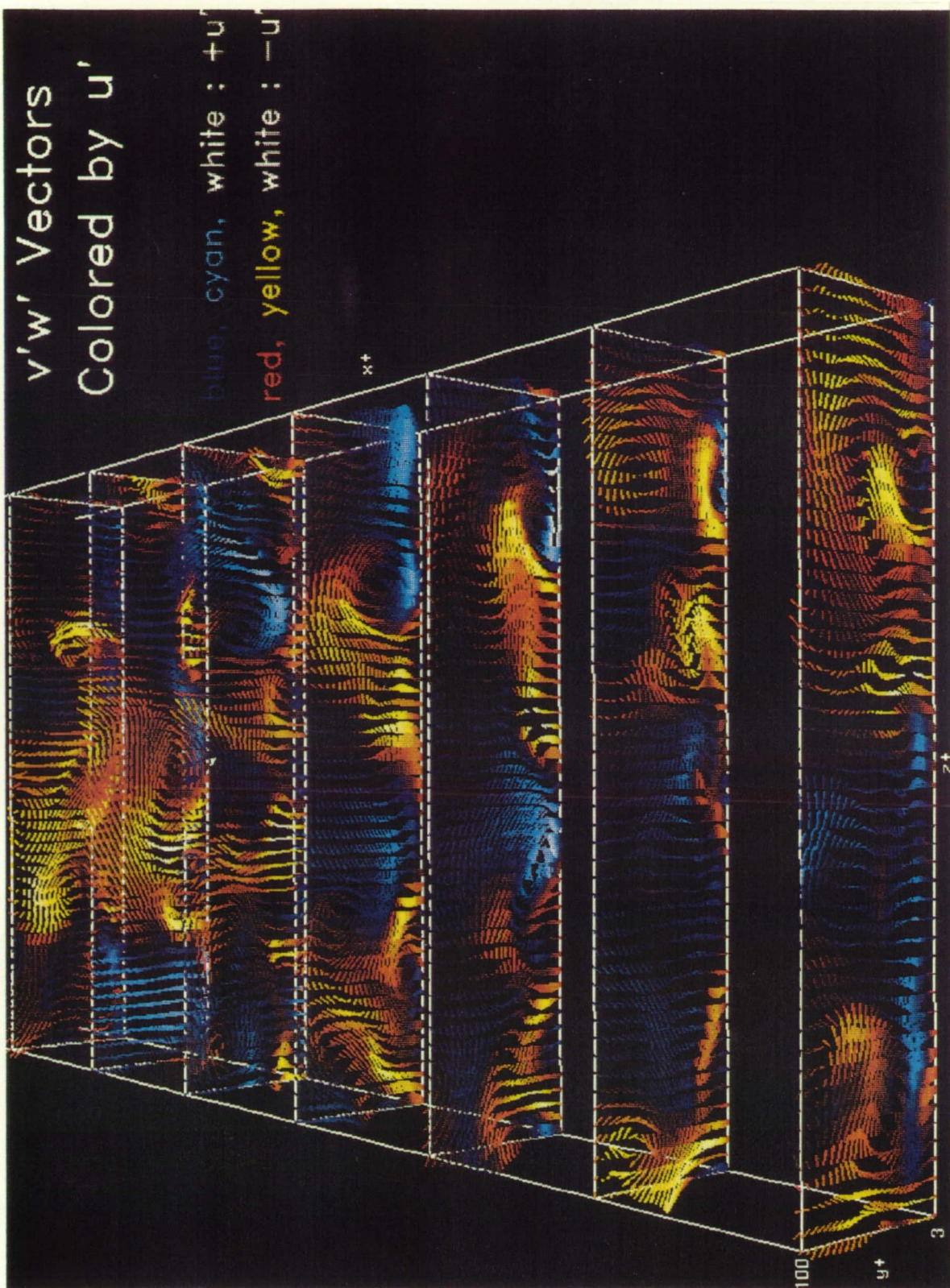


Fig. 10.6.2 Vortical nature of high/low-speed interfaces, shown by instantaneous v' , w' vectors colored according to the magnitude of u' . (Mean flow is from bottom to top; Δx^+ between planes ≈ 140 .) Red to yellow: low-speed, $u' < 0$. Blue to white: high-speed, $u' > 0$.

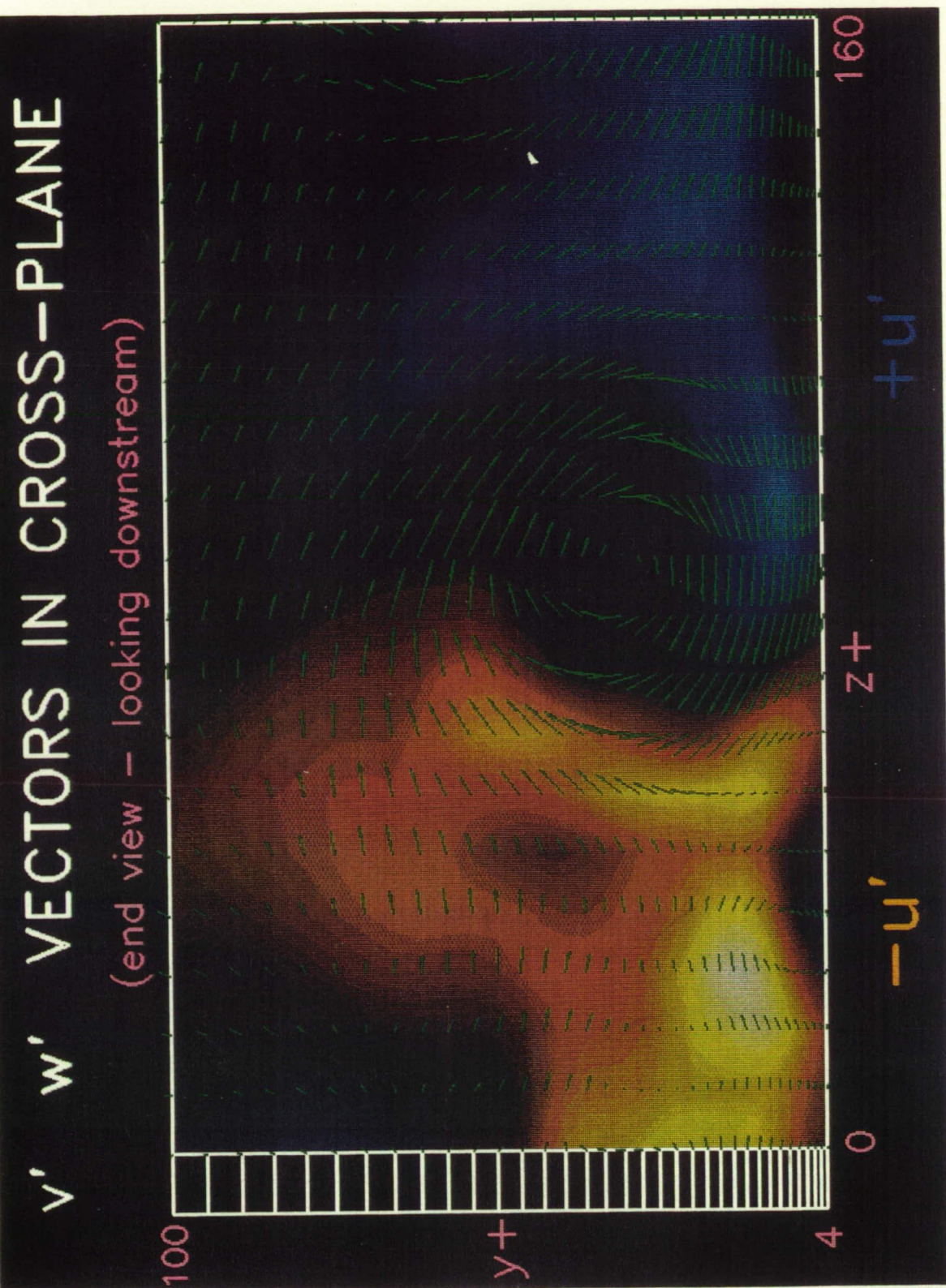


Fig. 10.6.3 End-view cut through a high/low-speed streak interface. Red to yellow: low-speed fluid, $u'^+ < 0$. Blue to cyan: high-speed fluid, $u'^+ > 0$. Green: instantaneous v' , w' vectors.

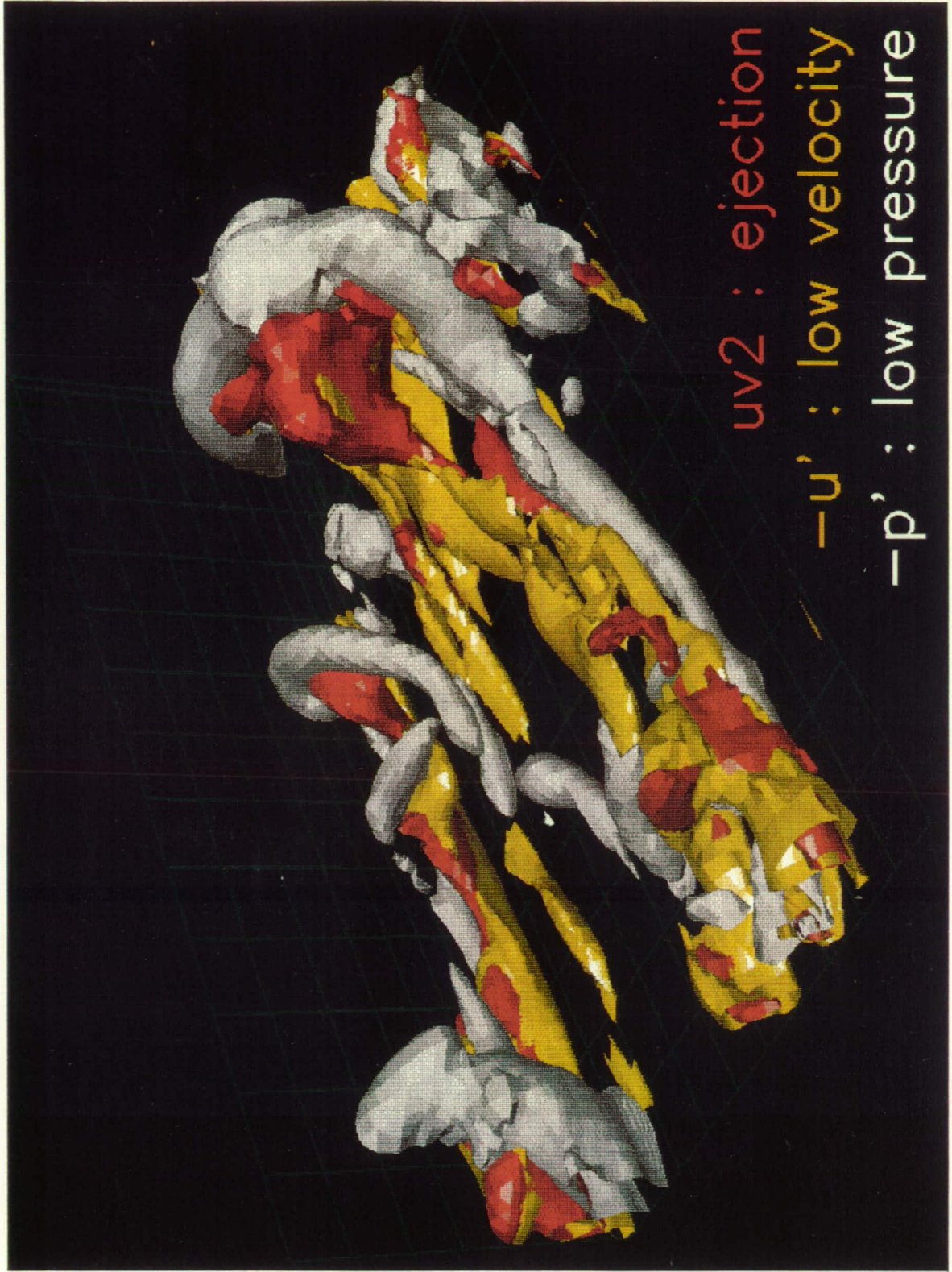


Fig. 10.6.4 3-D surface contours of low pressure, low streamwise velocity, and ejections in sample subvolume S. White: low pressure, $p'^+ = -4.2$. Yellow: low-speed fluid, $u'^+ = -3.0$. Red: ejection, $(u'v')_2/u_r^2 = -4.2$.

Vortical Structures, Ejections, and Sweeps

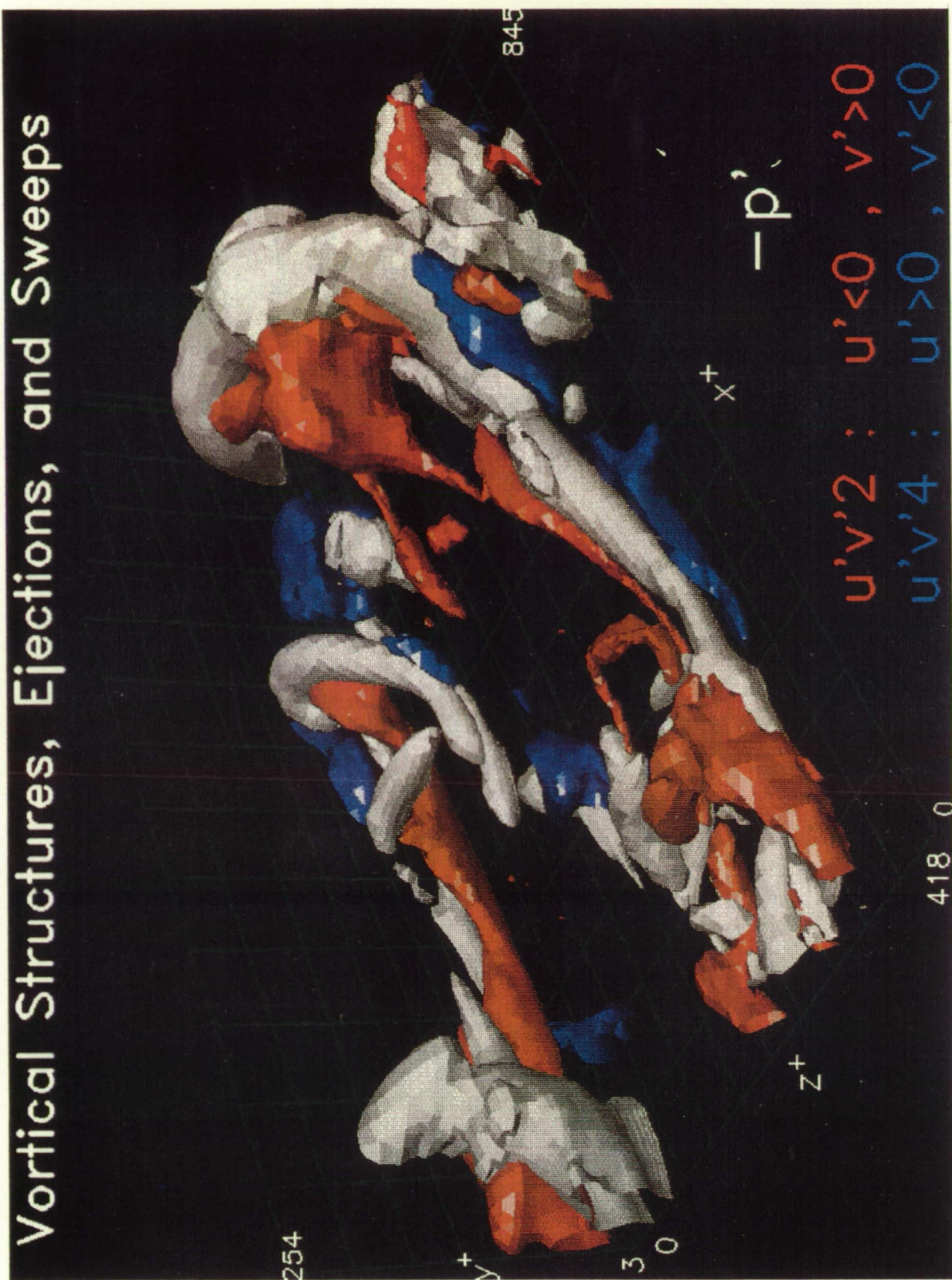


Fig. 10.6.5 3-D surface contours of low pressure, ejections, and sweeps in sample subvolume S. (Oblique view). White: low pressure, $p^+ = -4.2$. Red: ejection, $(u'v')_2/u_r^2 = -4.2$. Blue: sweep, $(u'v')_4/u_r^2 = -4.2$.

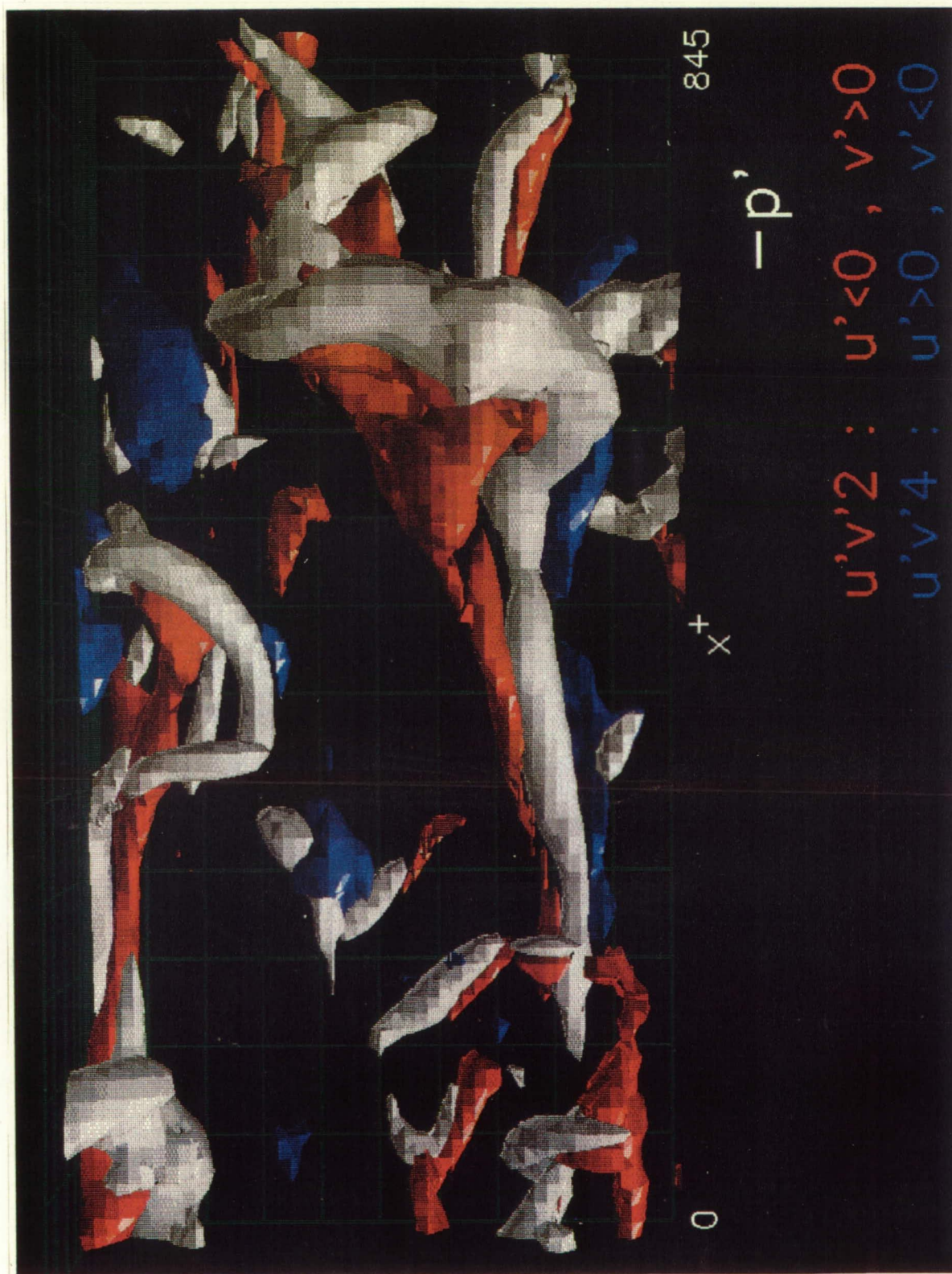


Fig. 10.6.6 3-D surface contours of low pressure, ejections, and sweeps in sample subvolume S. (Top view).
 White: low pressure, $p'^+ = -4.2$. Red: ejection, $(u'v')_2/u_\tau^2 = -4.2$. Blue: sweep, $(u'v')_4/u_\tau^2 = -4.2$.

Vortical Structures, Ejections, and Sweeps

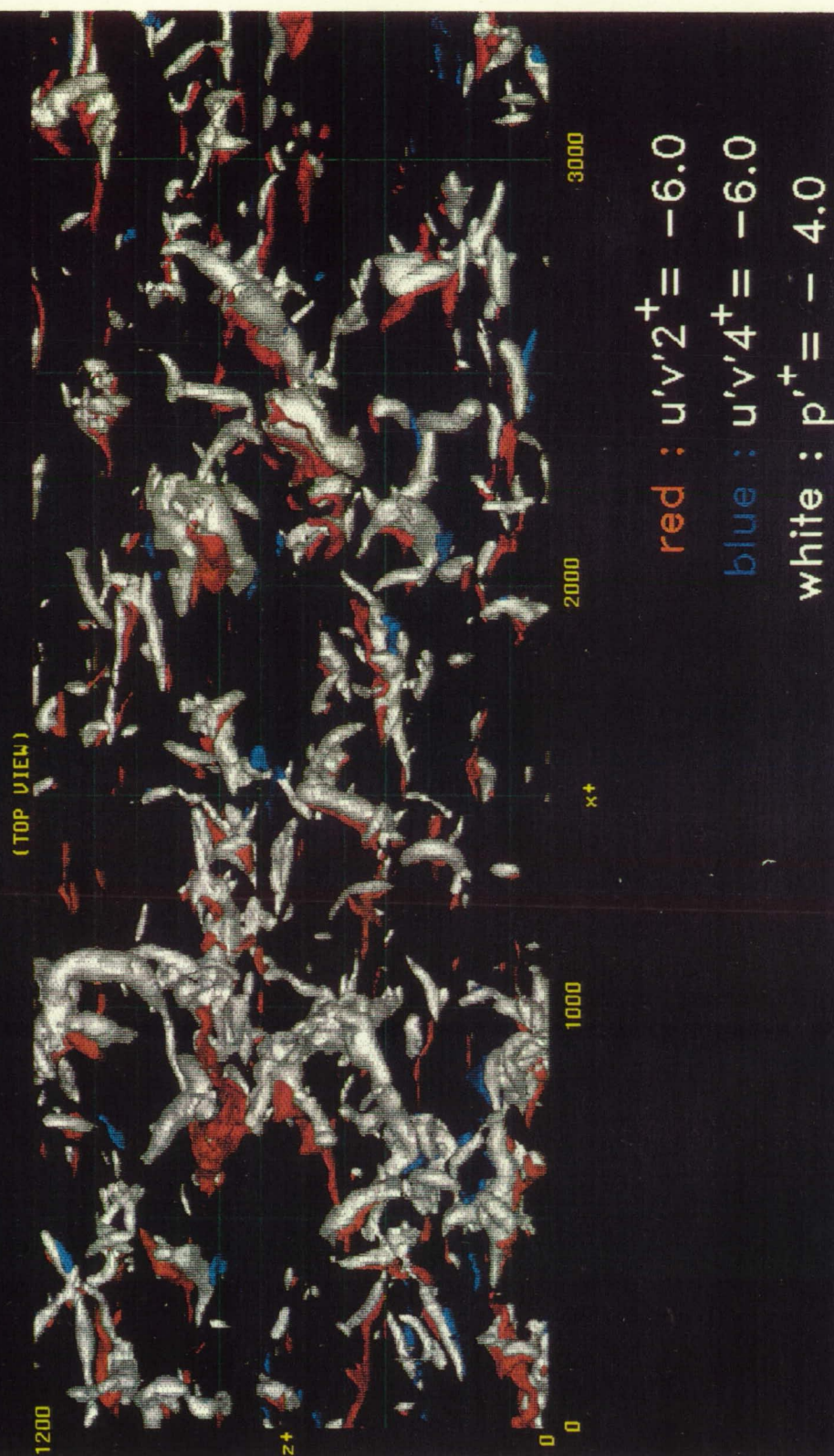
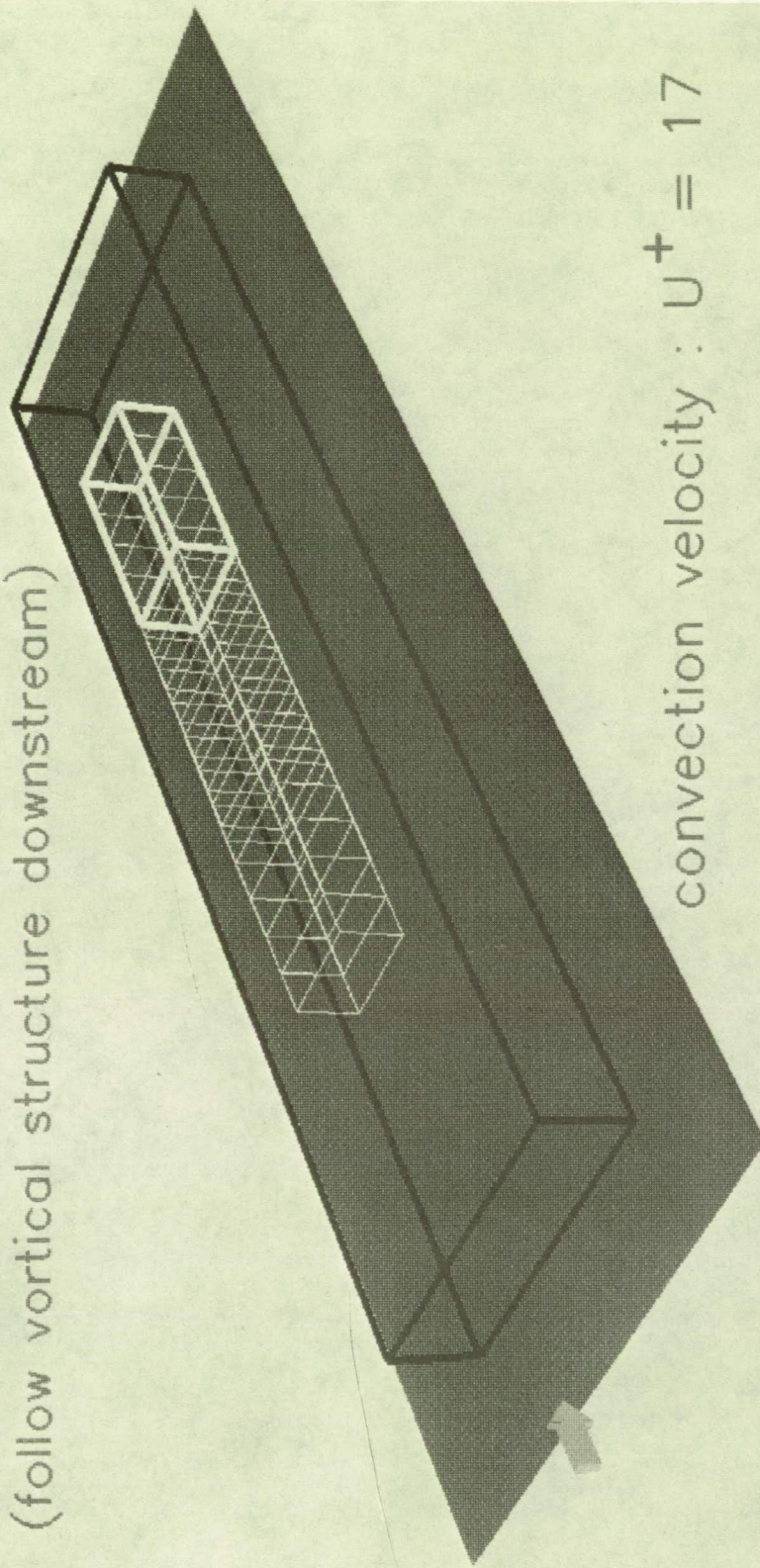


Fig. 10.6.7 3-D surface contours of low pressure, ejections, and sweeps. (Top view).
White: low pressure, $p'^+ = -4.0$. Red: ejection, $(u'v')_2/u_\tau^2 = -6.0$. Blue: sweep, $(u'v')_4/u_\tau^2 = -6.0$.

CONNECTING VIEWING VOLUME

(follow vortical structure downstream)



convection velocity : $U^+ = 17$

follow for 41 time steps

delta $t^+ = 3$

Fig. 10.6.8a Connecting viewing volume used to observe spatial/temporal evolution of large vortical arch.

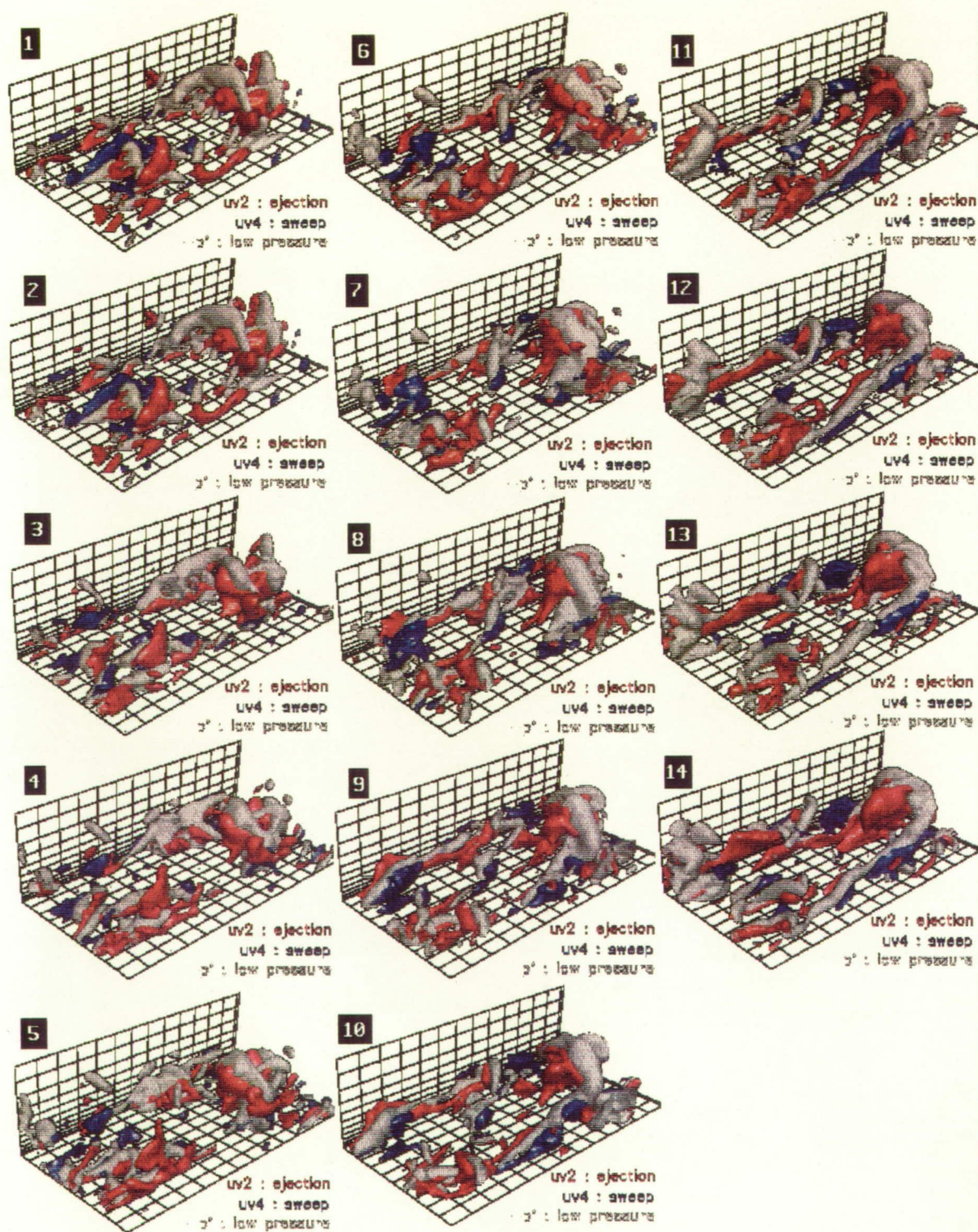


Fig. 10.6.8b Time-sequence showing the evolution of vortical structures (white) and associated ejection (red) and sweep (blue) regions, as seen from a convecting reference frame ($U_c = 17u_\tau$). Time between each step is $\Delta t^+ = 9$. (See Fig. 10.6.5 for contour values).



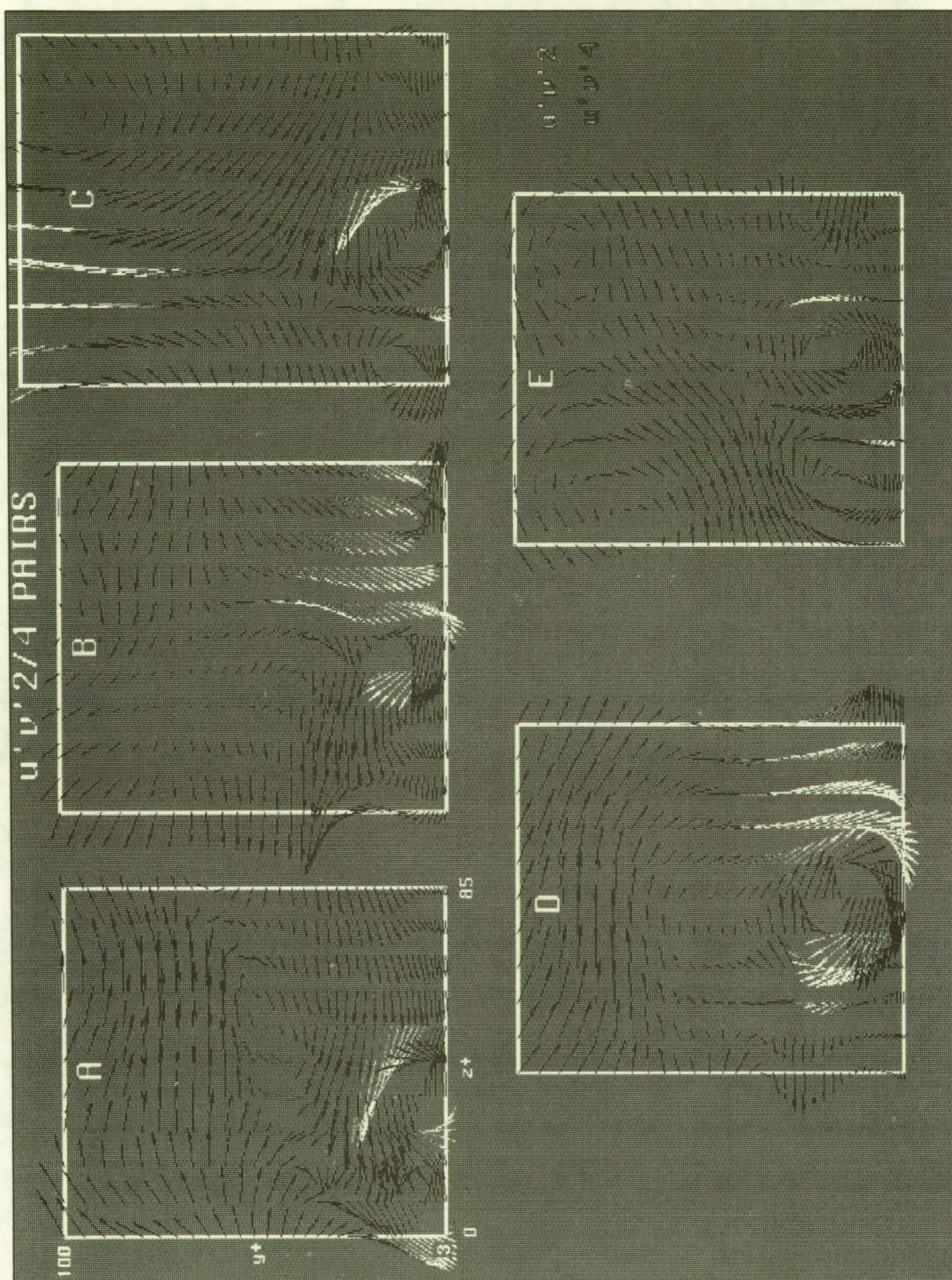


Fig. 10.6.10 v', w' velocity vectors in y - z cut-planes A-E through sweep/ejection pairs from Fig. 8.6.9. Vectors are colored according to $u'v'$ quadrant. Red to yellow to white = $(u'v')_2$. Blue to cyan to white = $(u'v')_4$.

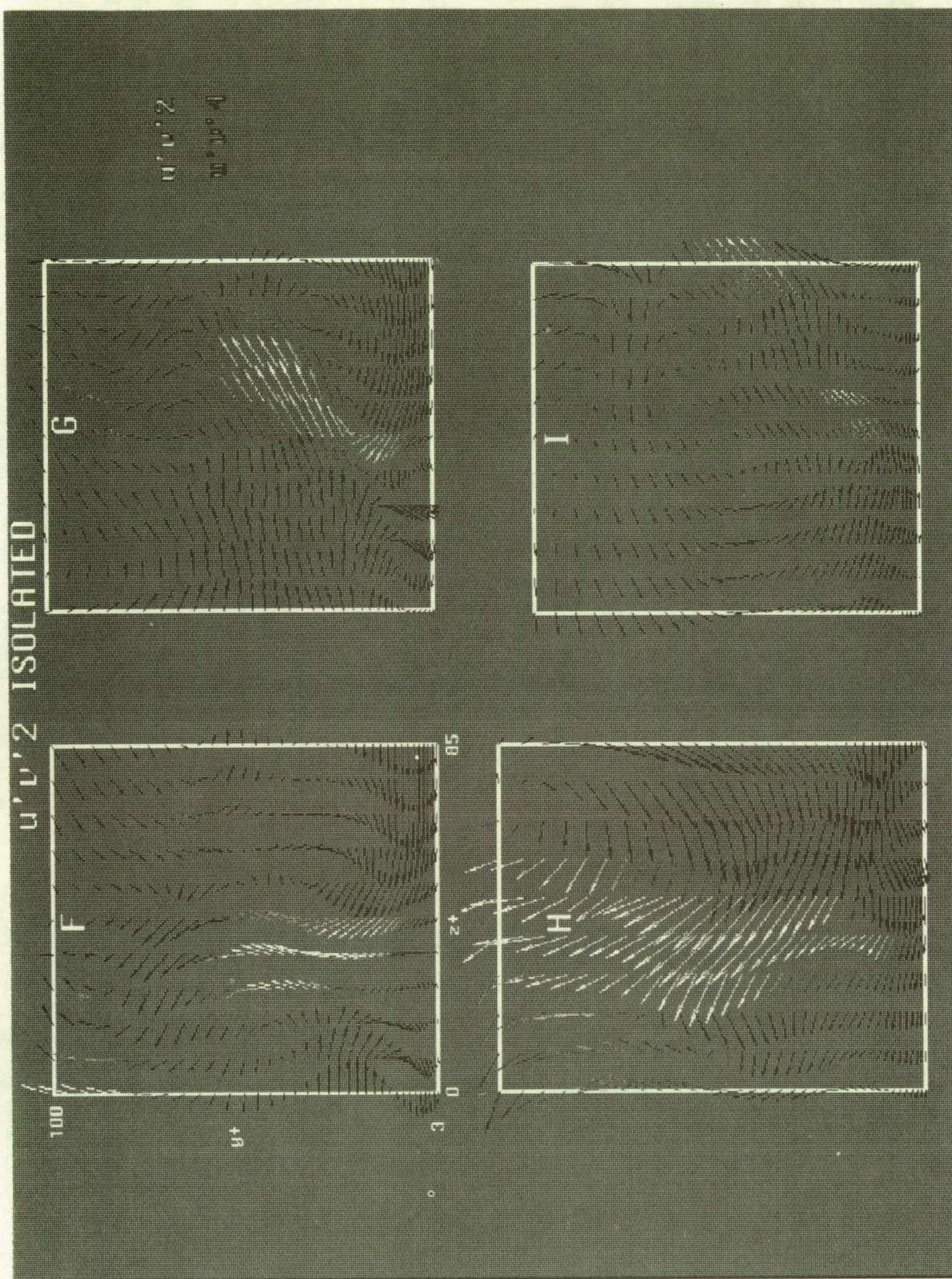
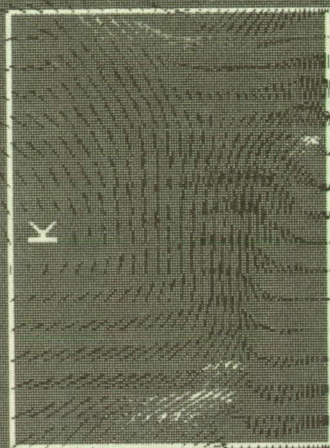
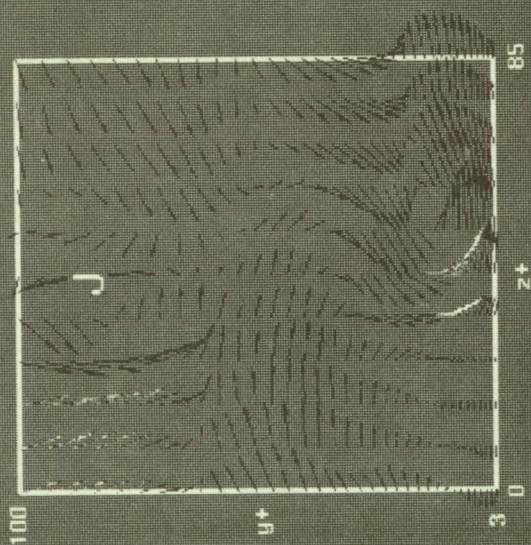


Fig. 10.6.11 v', w' velocity vectors in y - z cut-planes F-I through un-paired ejections from Fig. 8.6.9. Vectors are colored according to $u'v'$ quadrant. Red to yellow to white $= (u'v')_2$. Blue to cyan to white $= (u'v')_4$.

$u'v'4$ ISOLATED



$u'v'2$
 $u'v'4$

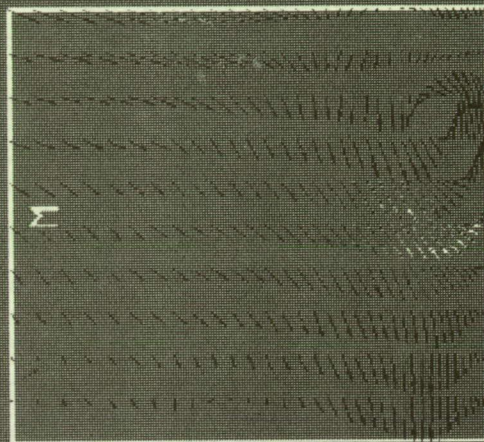
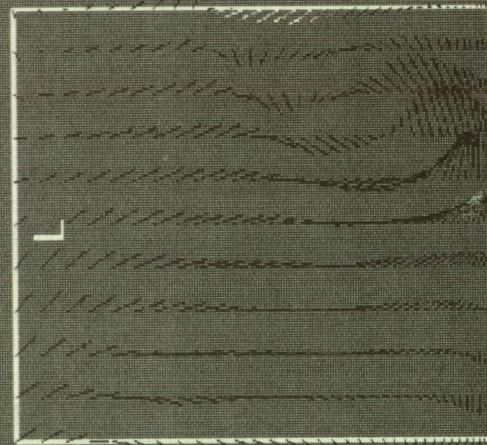


Fig. 10.6.12 v', w' velocity vectors in $y-z$ cut-planes J-M through un-paired sweeps from Fig. 8.6.9. Vectors are colored according to $u'v'$ quadrant. Red to yellow to white = $(u'v')_2$. Blue to cyan to white = $(u'v')_4$.

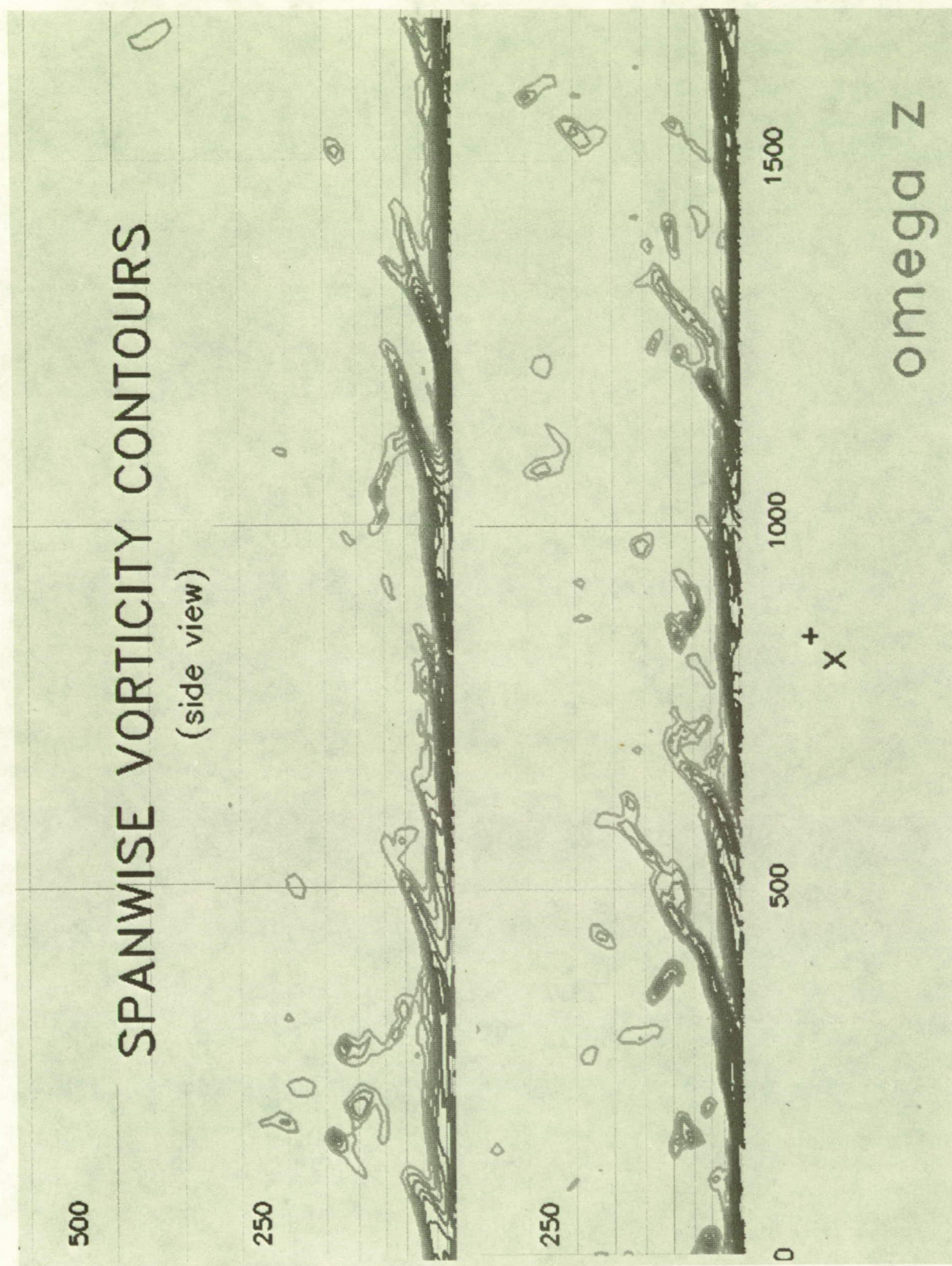


Fig. 10.7.1 Near-wall shear layers identified in two sample x - y planes by contours of spanwise vorticity, ω_z .

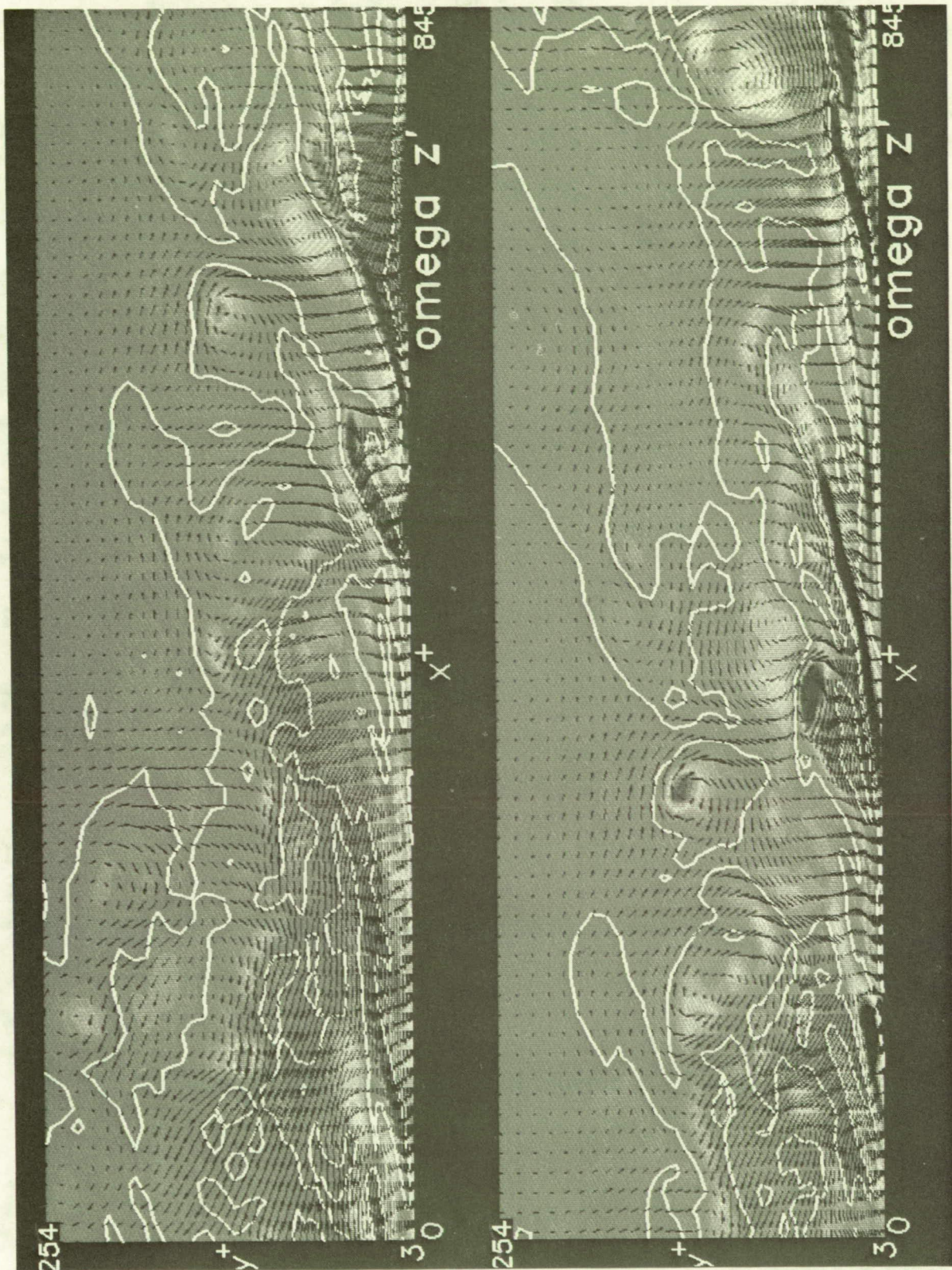


Fig. 10.7.1a Near-wall shear layers identified in two sample x - y planes by contours of fluctuating spanwise vorticity, ω'_z , with overlaid u' , v' velocity vectors. Yellow to red: $\omega'_z > 0$. Cyan to blue: $\omega'_z < 0$. Green: $\omega'_z \approx 0$ (or $\omega_z = \overline{\omega_z}$).

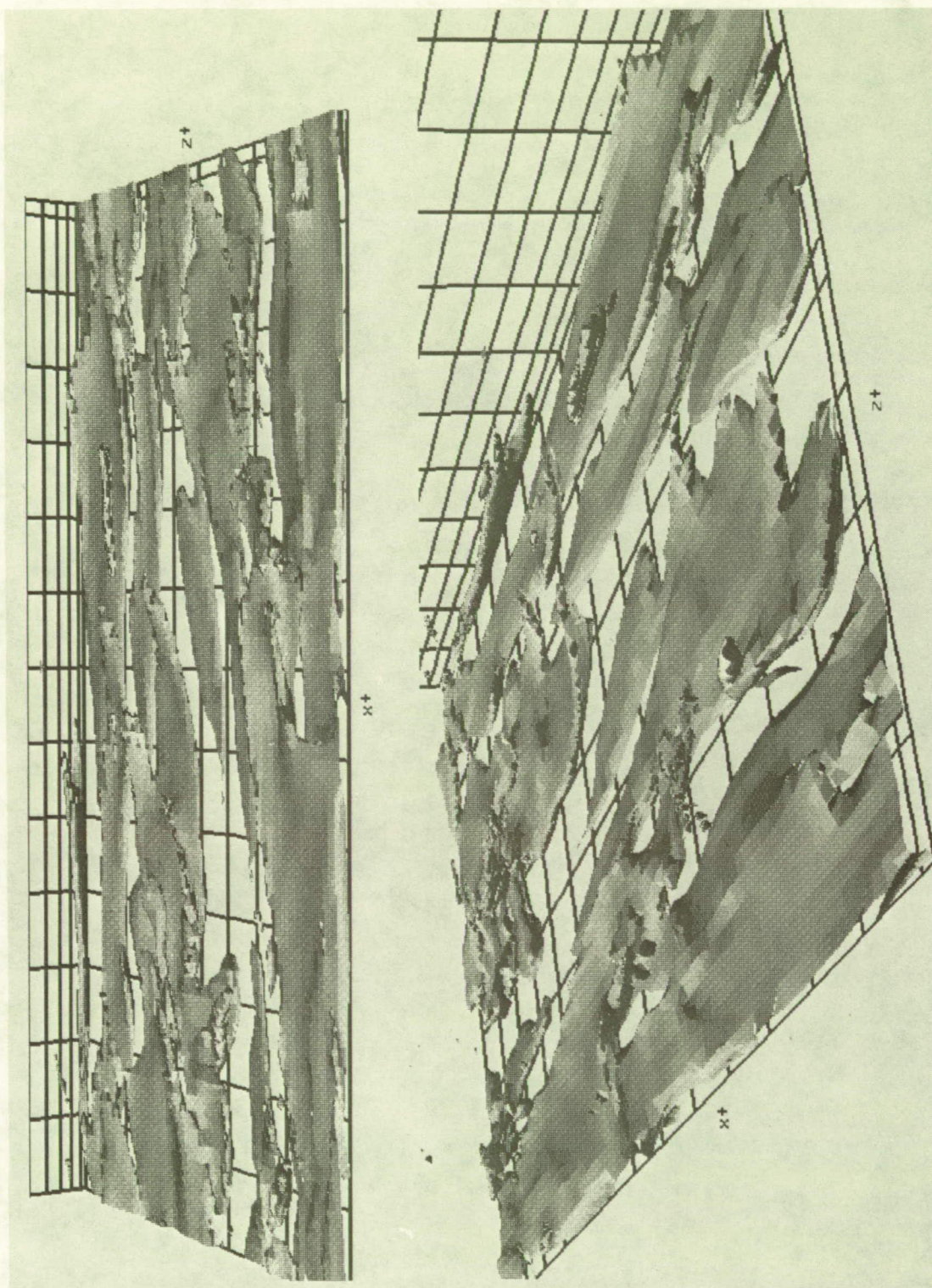


Fig. 10.7.2 Three-dimensional views of near-wall shear layers identified by surface contours of vorticity magnitude, $|\omega^+| = 0.8$.

PRESSURE, $u'v'^2$, VORTICITY CONTOURS

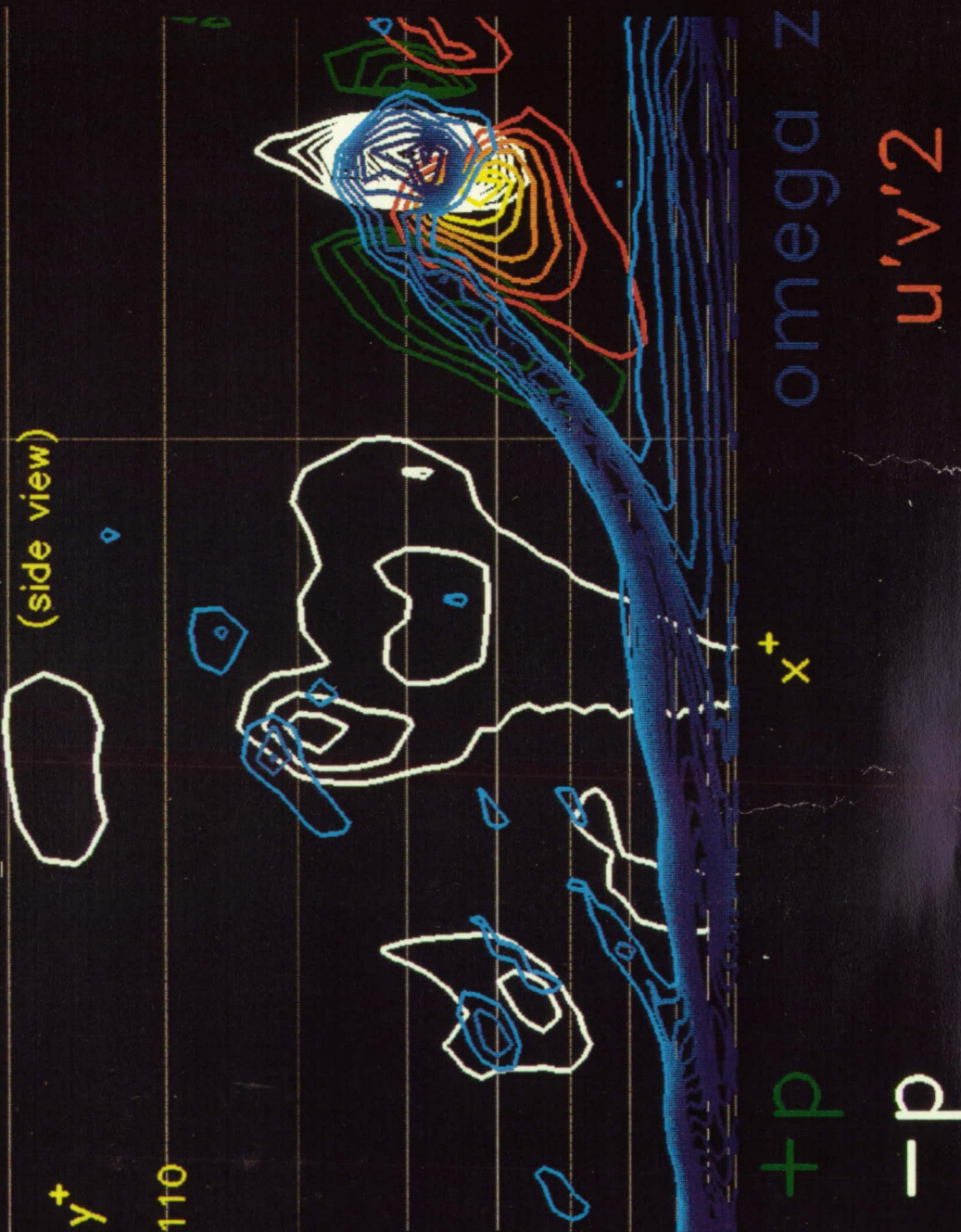


Fig. 10.8.1 Example of a near-wall shear layer (blue) with associated low-pressure (white), high-pressure (green), and ejection (red to yellow) regions. (The y -scale has been expanded by a factor of two).

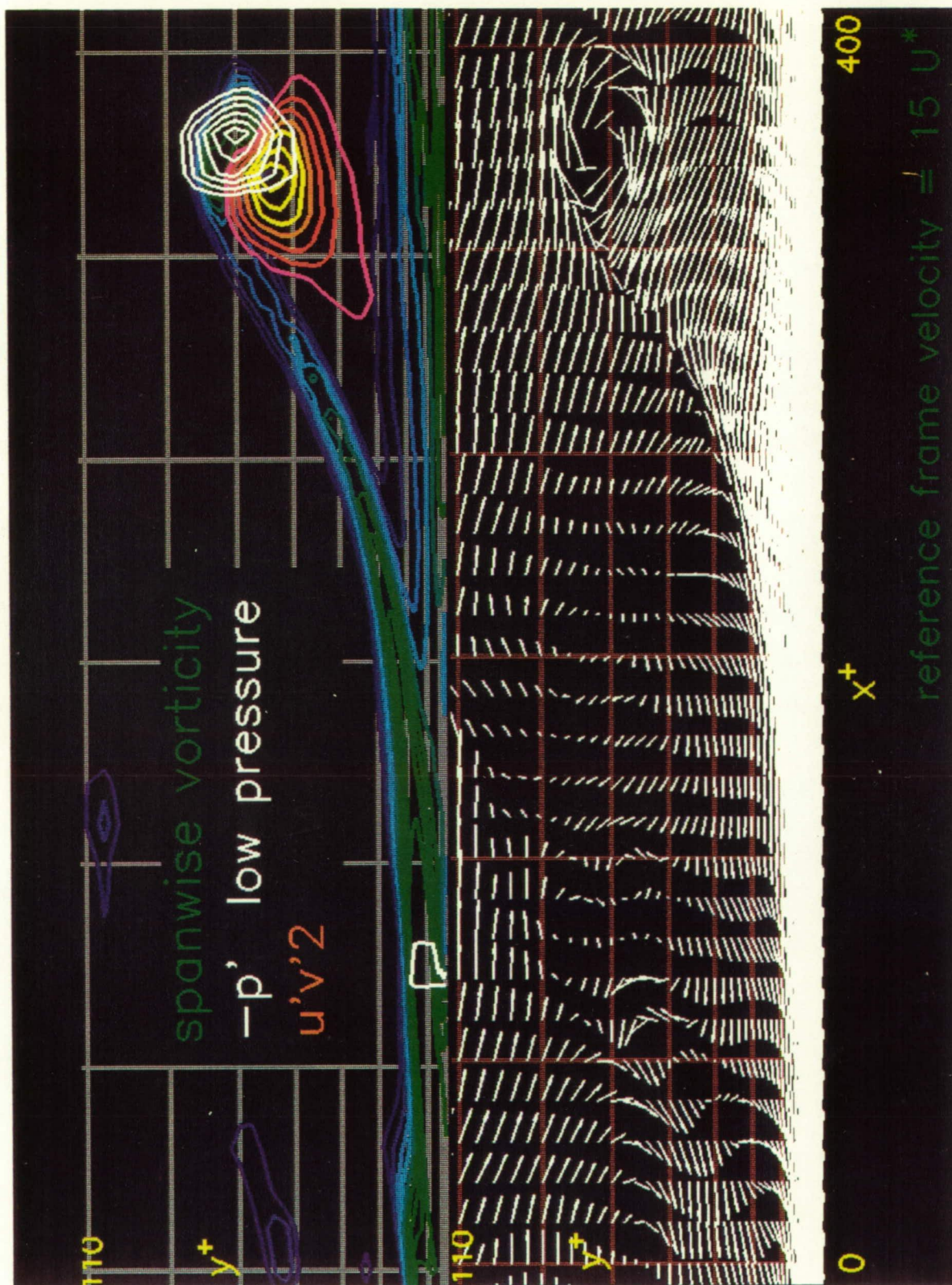


Fig. 10.8.2 Top: Near-wall shear layer (blue to green) with a low-pressure transverse vortex at the shear-layer tip (white), and associated ejection (red to yellow) regions. Bottom: Same NWSL from convecting reference frame.

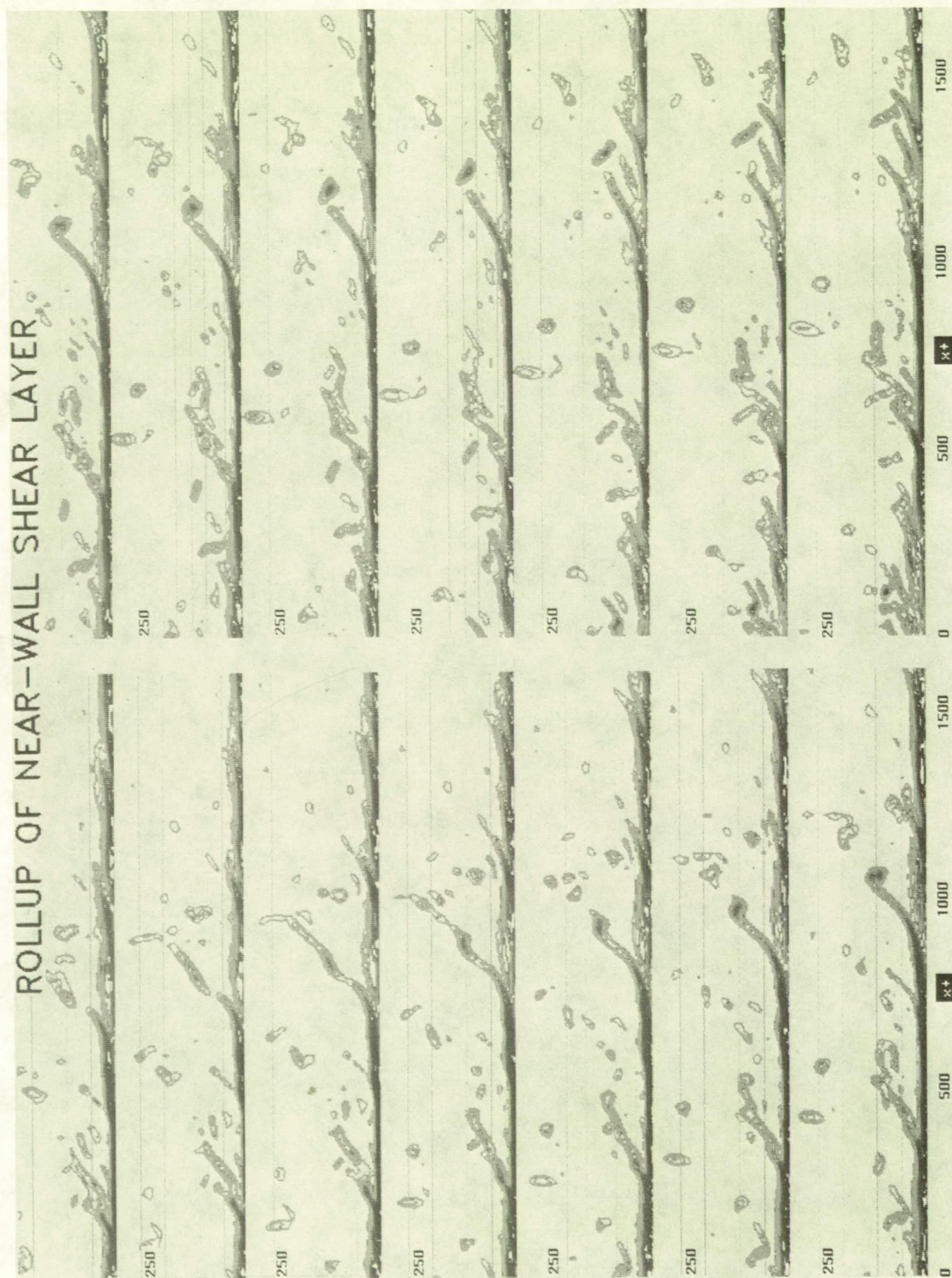


Fig. 10.8.3 Time-sequence showing rollup of a near-wall shear layer, identified by contours of spanwise vorticity. Time between each step is $\Delta t^+ = 3$. (The y -scale has been expanded by a factor of two).



Fig. 10.8.4 Time-sequence showing selected stages of rollup of a near-wall shear layer, identified by contours of spanwise vorticity. Time between each step is $\Delta t^+ = 9$, starting from top. (The y -scale has been expanded by a factor of two).

Quasi-Streamwise Vortex and Near-wall Shear Layer

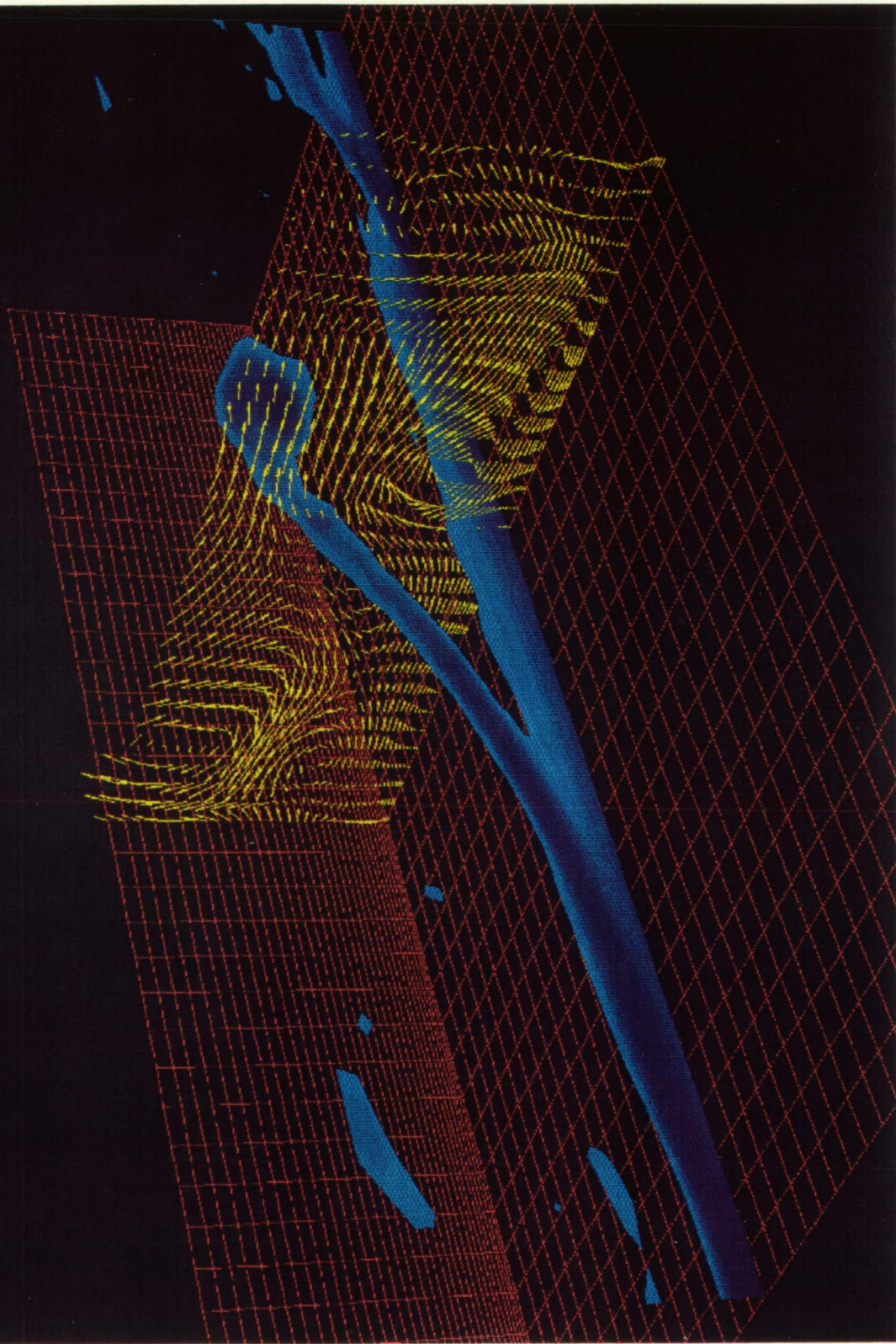


Fig. 10.8.5 Near-wall shear layer (blue ω'_z contours in the x - y plane) and quasi-streamwise vortex (yellow v', w' velocity vectors in the y - z plane).

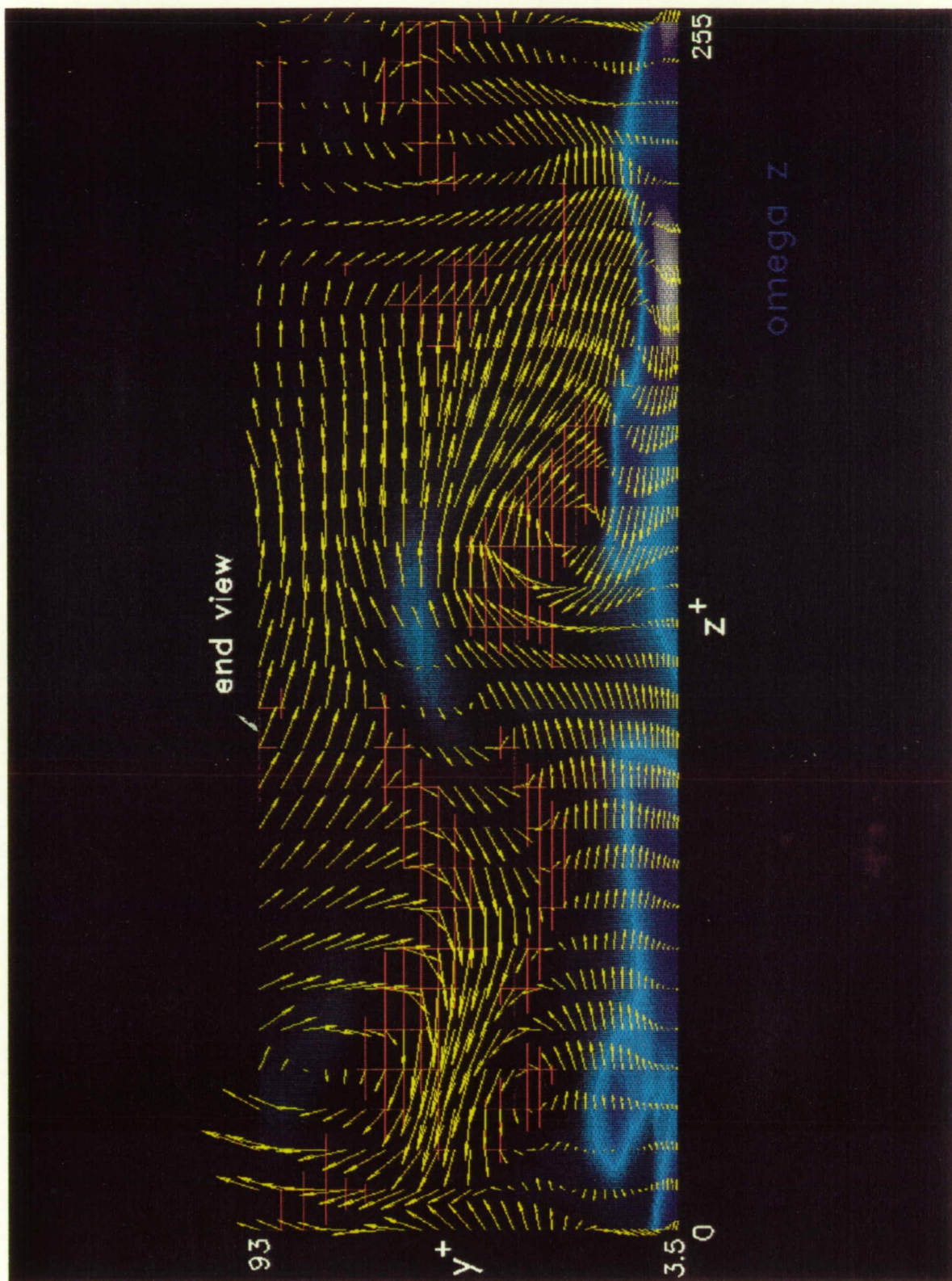


Fig. 10.8.6 y - z plane cut through a near-wall shear layer (blue ω'_z contours), showing associated quasi-streamwise vortex (yellow v', w' velocity vectors).

Vortical Structures and High-Pressure Regions

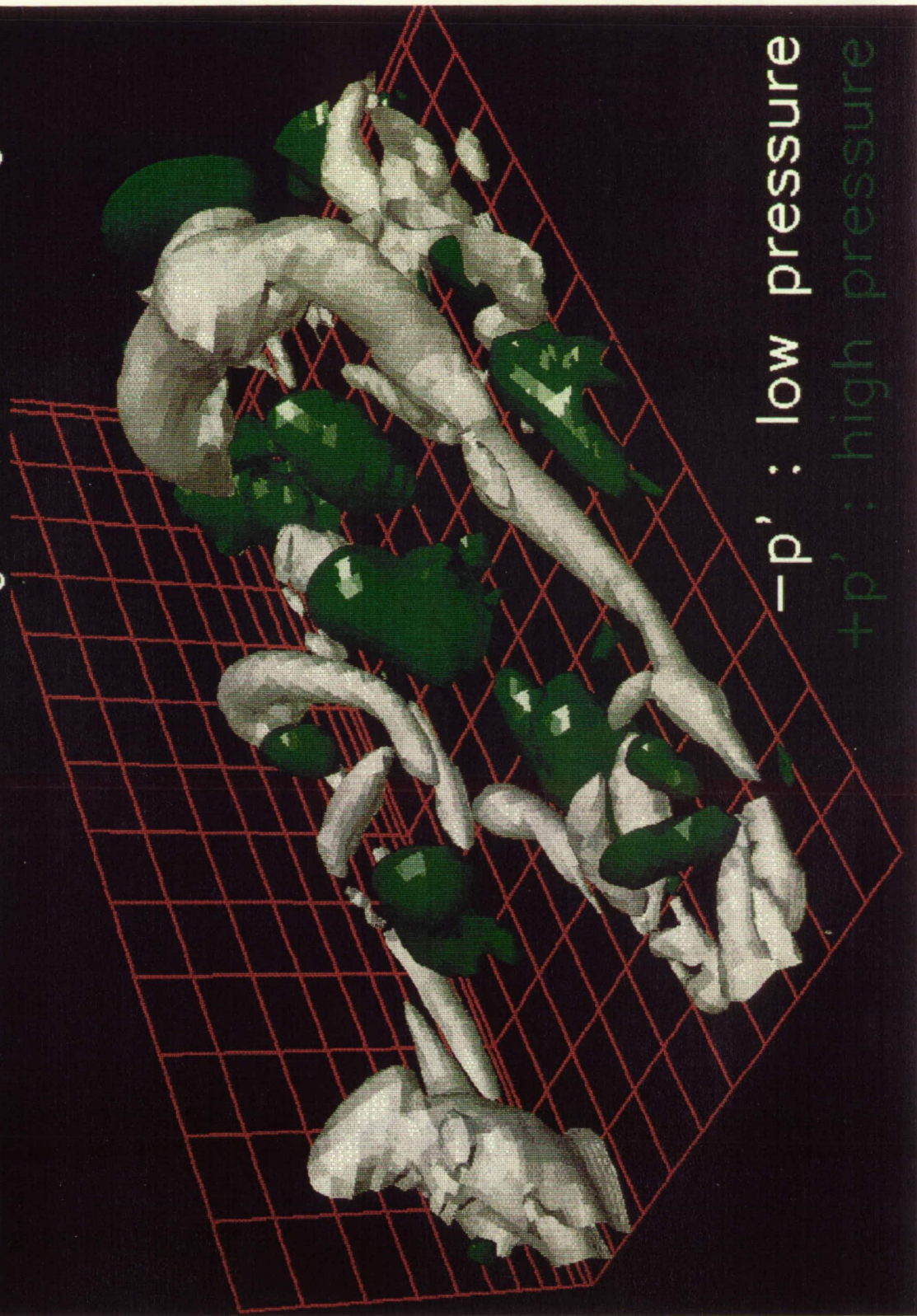


Fig. 10.9.1 3-D surface contours of low and high pressure in sample subvolume S .
White: low pressure, $p'^+ = -4.2$. Green: high pressure, $p'^+ = +4.2$.

Vortical Structures and High-Pressure Regions

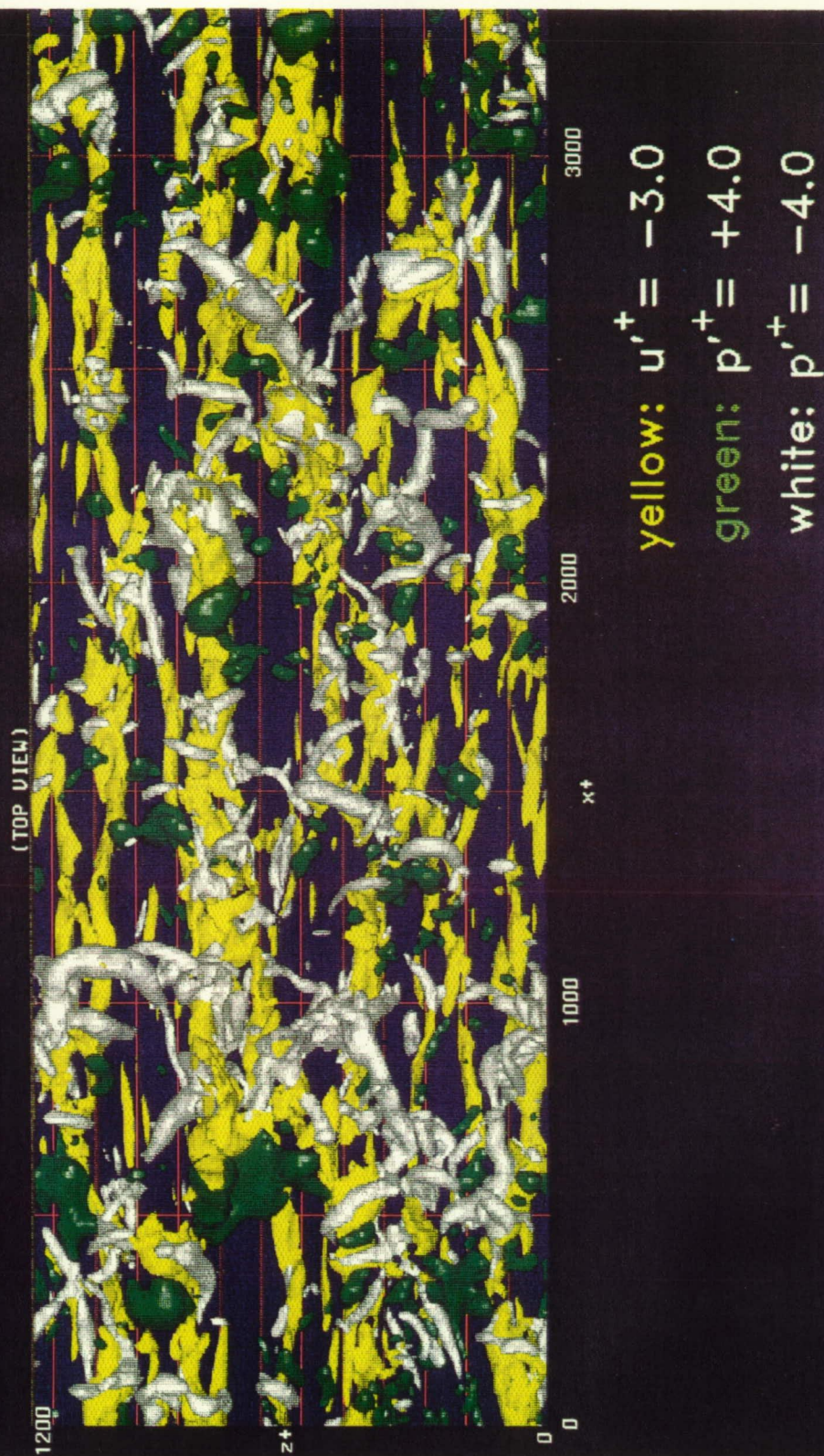


Fig. 10.9.2 3-D contour surfaces of low pressure, high pressure, and low streamwise velocity. White: low pressure, $p'^+ = -4.0$. Green: high pressure, $p'^+ = +4.0$. Yellow: low-speed, $u'^+ = -3.0$.

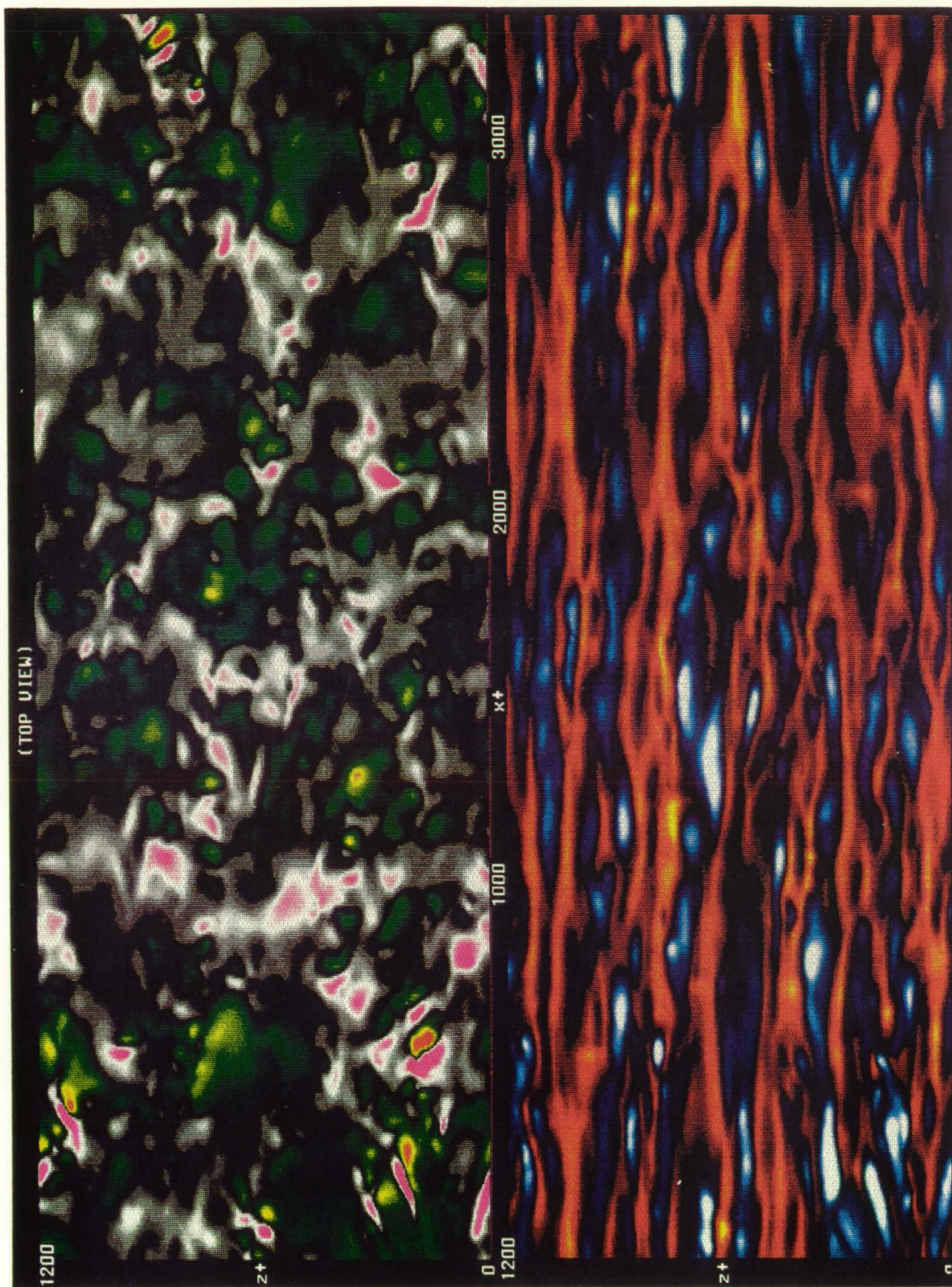


Fig. 10.10.1 Comparison between instantaneous wall-pressure field (top) and streaky structure in the u' -field at $y^+ = 3$ (bottom).

Green to yellow: $p_w'^+ = +1.0$ to $+12.0$. White to magenta: $p_w'^+ = -1.0$ to -12.0 .

Red to yellow: $u'^+ = -1.0$ to -4.0 . Blue to white: $u'^+ = +1.0$ to $+4.0$.

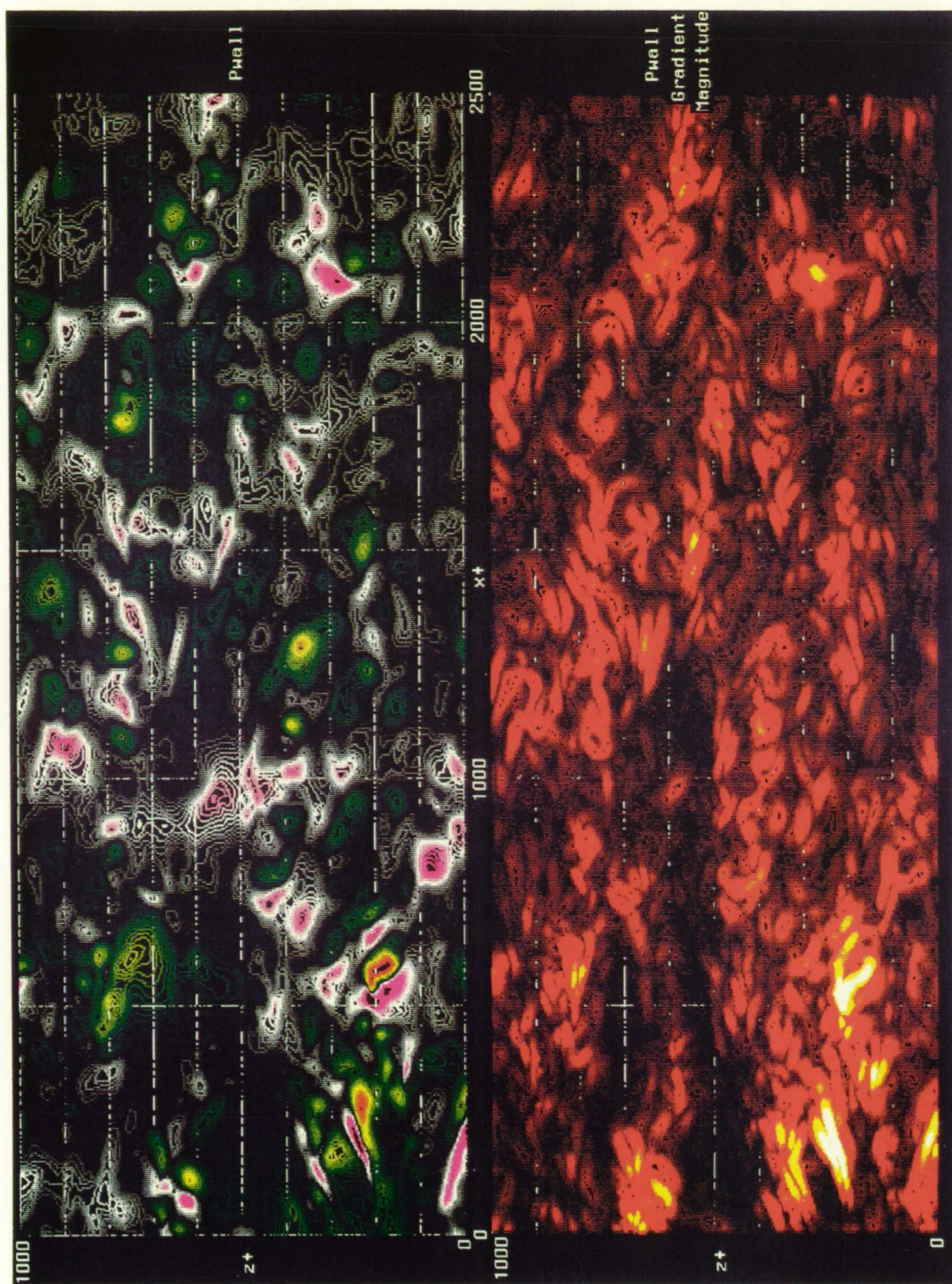


Fig. 10.10.2 Comparison between instantaneous wall-pressure field (top) and magnitude of horizontal component of wall-pressure gradient vector (bottom).
 Green to yellow: $p_w^{'+} = +1.0$ to $+12.0$. White to magenta: $p_w^{'+} = -1.0$ to -12.0 . Red to white: $((\partial p / \partial x)^2 + (\partial p / \partial z)^2)^{1/2+} = 0$ to 1.0 .

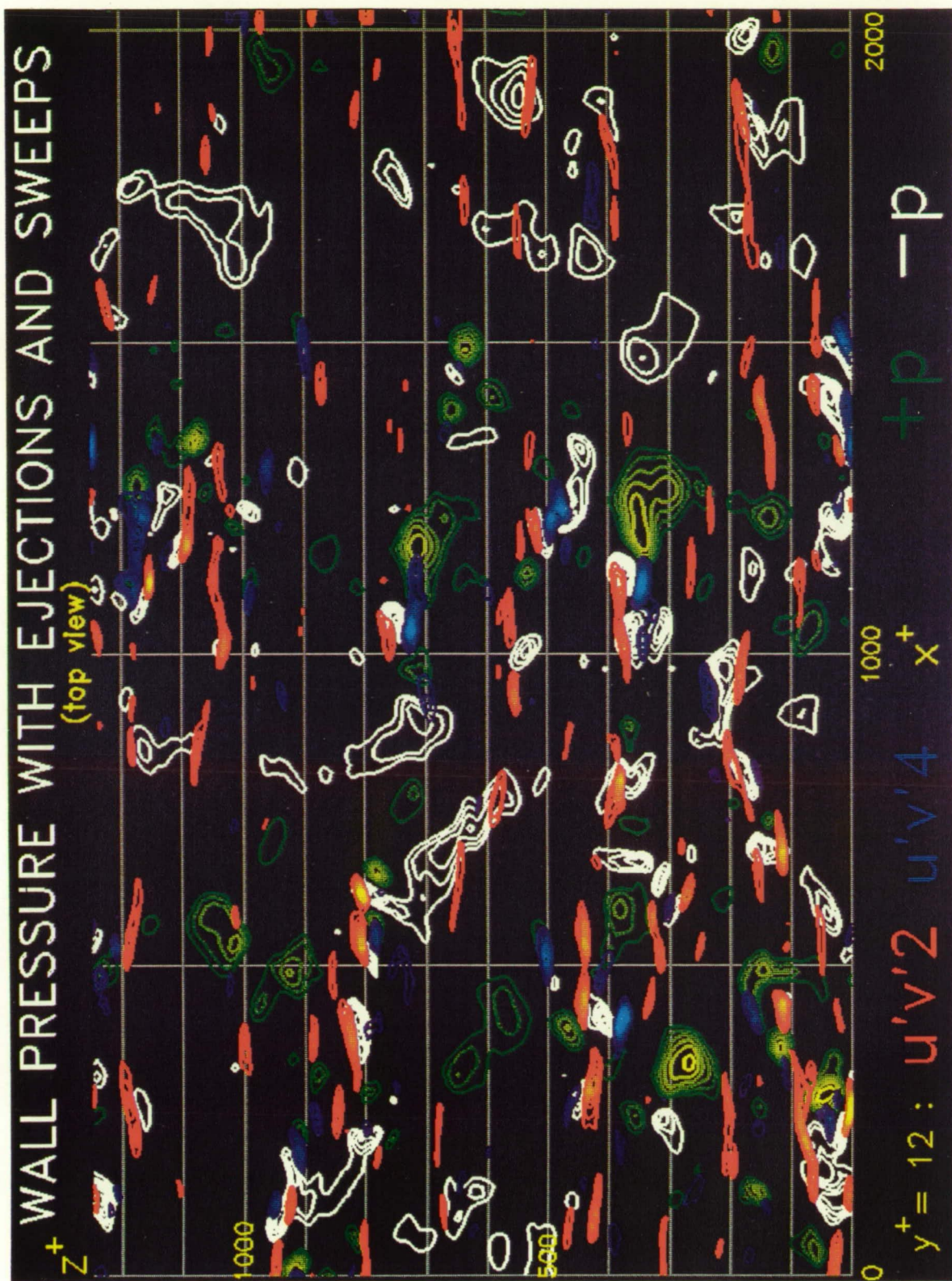


Fig. 10.11.1 Wall-pressure fluctuations (green and white) with ejections (red) and sweeps (blue) at $y^+ = 12$. Green to yellow: high p_w . White to magenta: low p_w . Red to yellow: $(u'v')_2/u_\tau^2 \leq -4.0$. Blue to cyan: $(u'v')_4/u_\tau^2 \leq -4.0$.

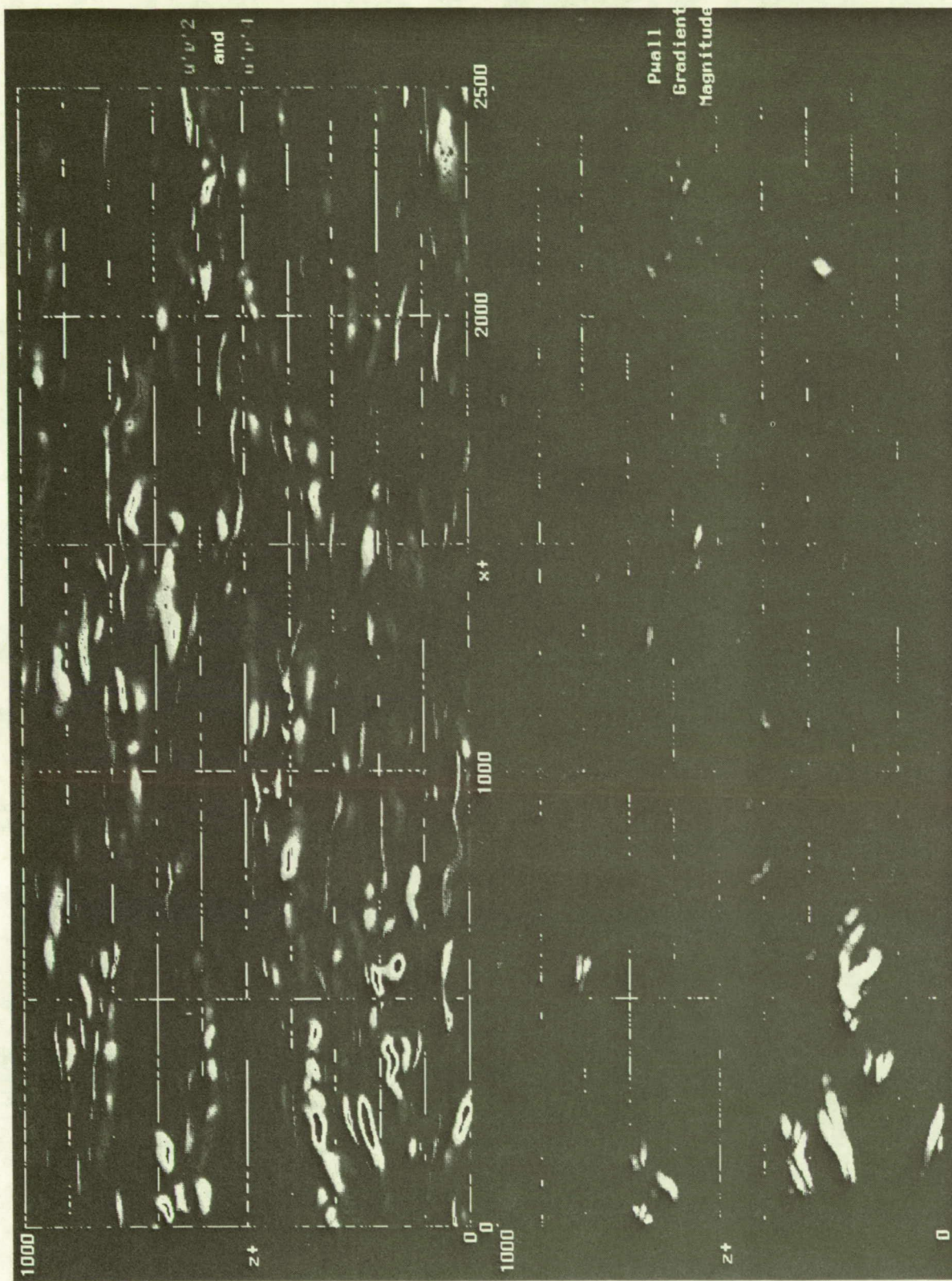


Fig. 10.11.2 Comparison between ejections and sweeps at $y^+ = 15$ (top) and magnitude of horizontal component of wall-pressure gradient vector (bottom).

Red to yellow: $(u'v')_2/u_r^2 = -1.0$ to -6.0 . Blue to cyan: $(u'v')_4/u_r^2 = -1.0$ to -6.0 . Red to white: $((\partial p/\partial x)^2 + (\partial p/\partial z)^2)^{1/2+} = 0$ to 1.0 .



Fig. 10.11.3 Comparison between 3-D contour surfaces of low and high pressure (top), and wall-pressure fluctuations (bottom).
 White (top): low pressure, $p'^{+} = -4.0$. Green (top): high pressure, $p'^{+} = +4.0$. White to magenta (bottom): $p'_{w}^{+} = -1.0$ to -12.0 . Green to yellow (bottom): $p'_{w}^{+} = +1.0$ to $+12.0$.

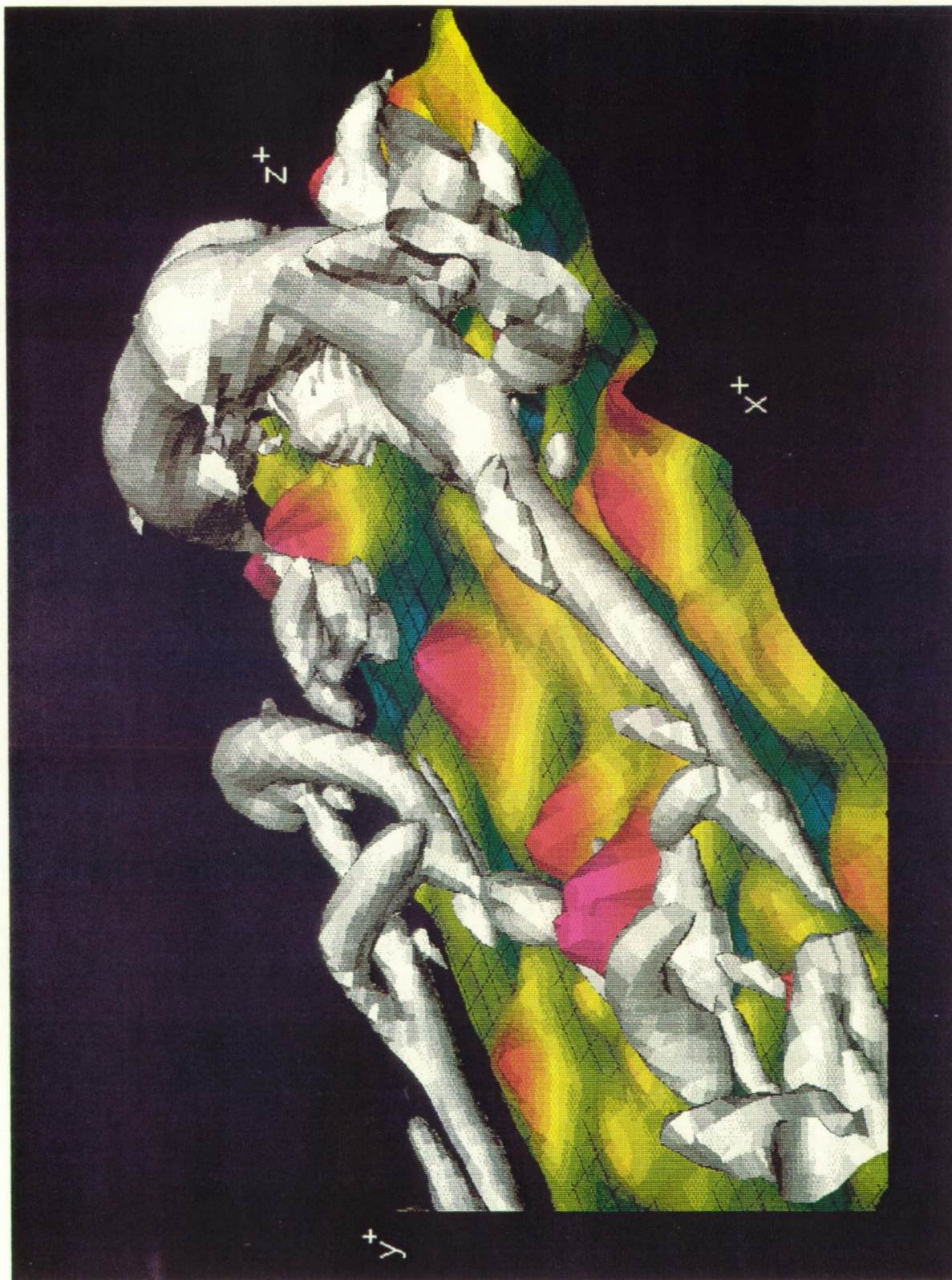


Fig. 10.11.4 Comparison between 3-D contour surfaces of low-pressure and wall-pressure fluctuations in sample subvolume S . White: low pressure, $p'^+ = -4.2$. Yellow to magenta: high p_w . Cyan to blue: low p_w .

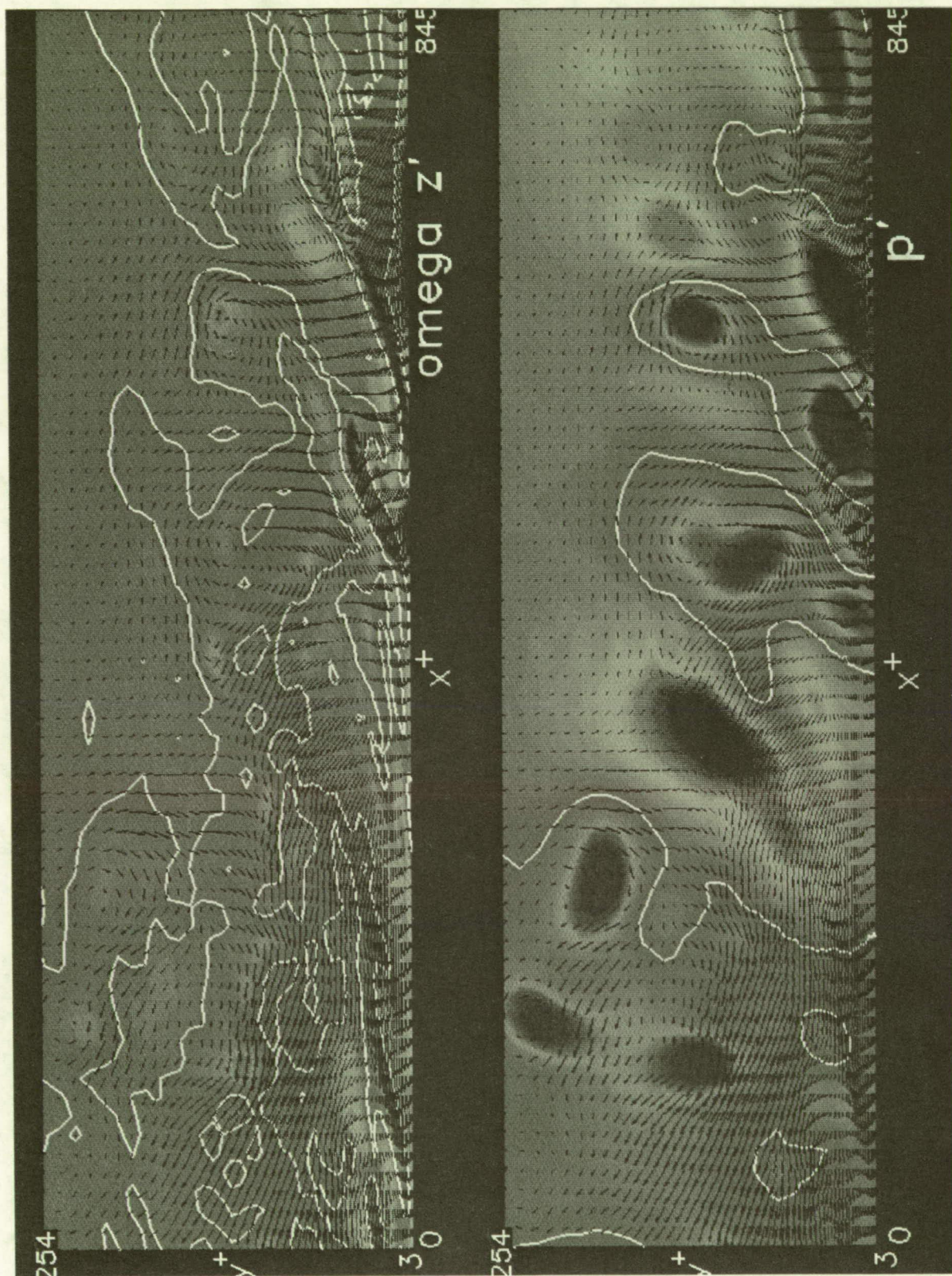


Fig. 10.11.5 Near-wall shear layer (top) with associated instantaneous pressure field (bottom). Blue to yellow to red (top): $\omega_z^+ = -0.2$ to -1.5 . Green to magenta (bottom): $p^+ = 0$ to $+10.0$. Green to Blue (bottom): $p^+ = 0$ to -10.0 .

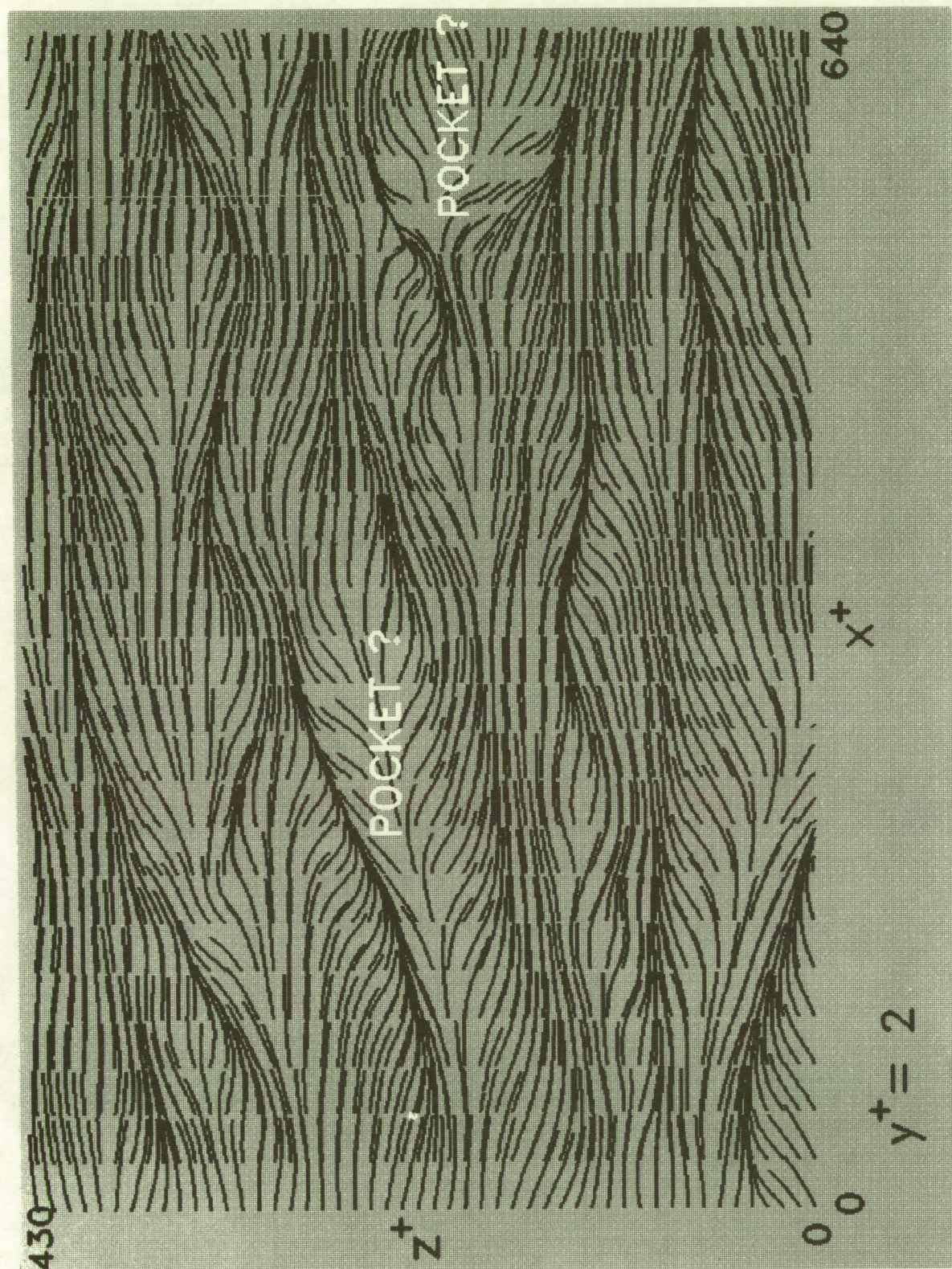


Fig. 10.12.1 Instantaneous streamlines mapped onto an x - z plane at $y^+ = 2$.

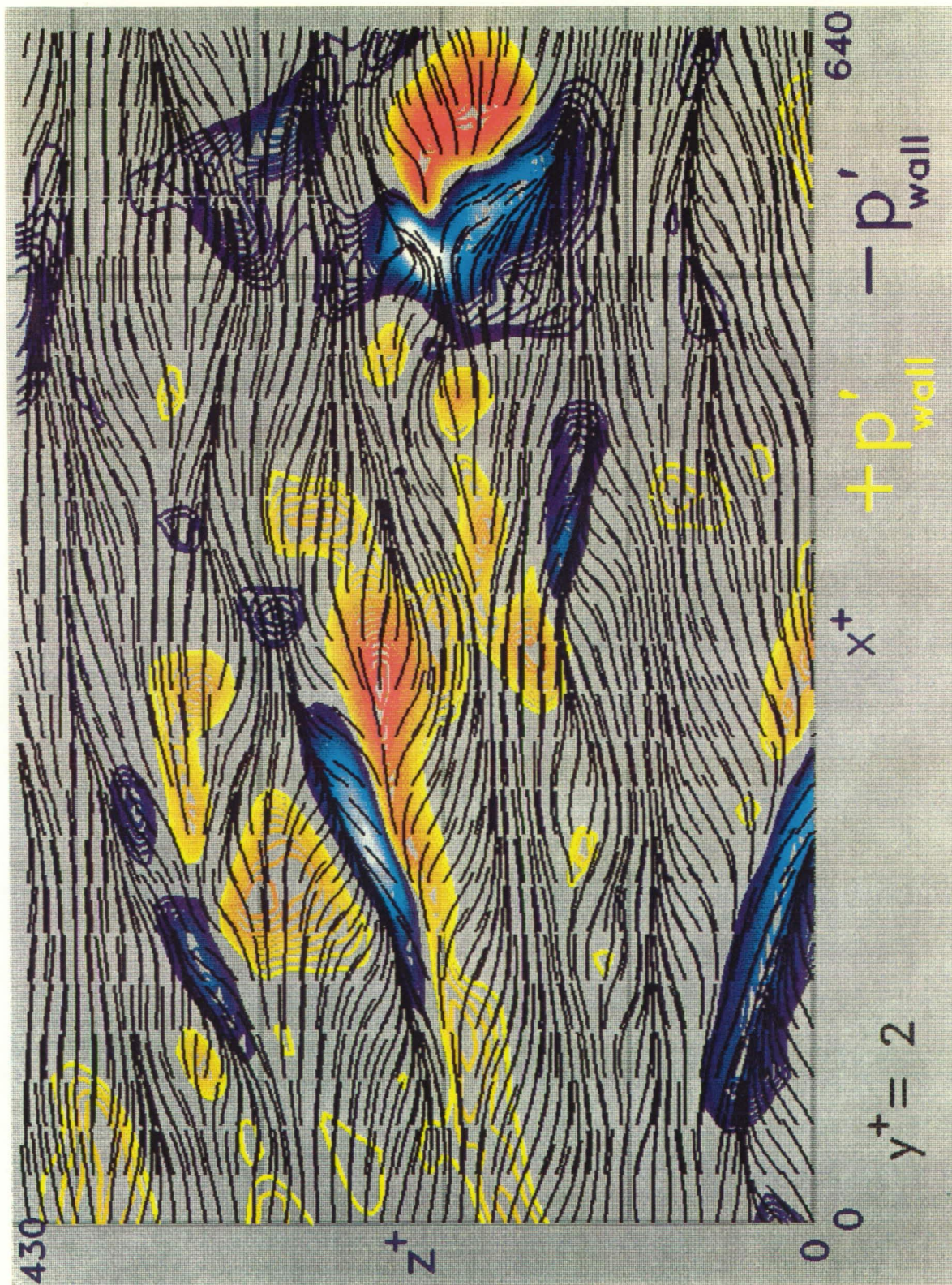


Fig. 10.13.1 Instantaneous streamlines mapped onto an x - z plane at $y^+ = 2$, overlaid with contours of wall-pressure. Yellow to red: $p_w^+ = +3.0$ to $+25.0$. Blue to white: $p_w^+ = -3.0$ to -25.0 .

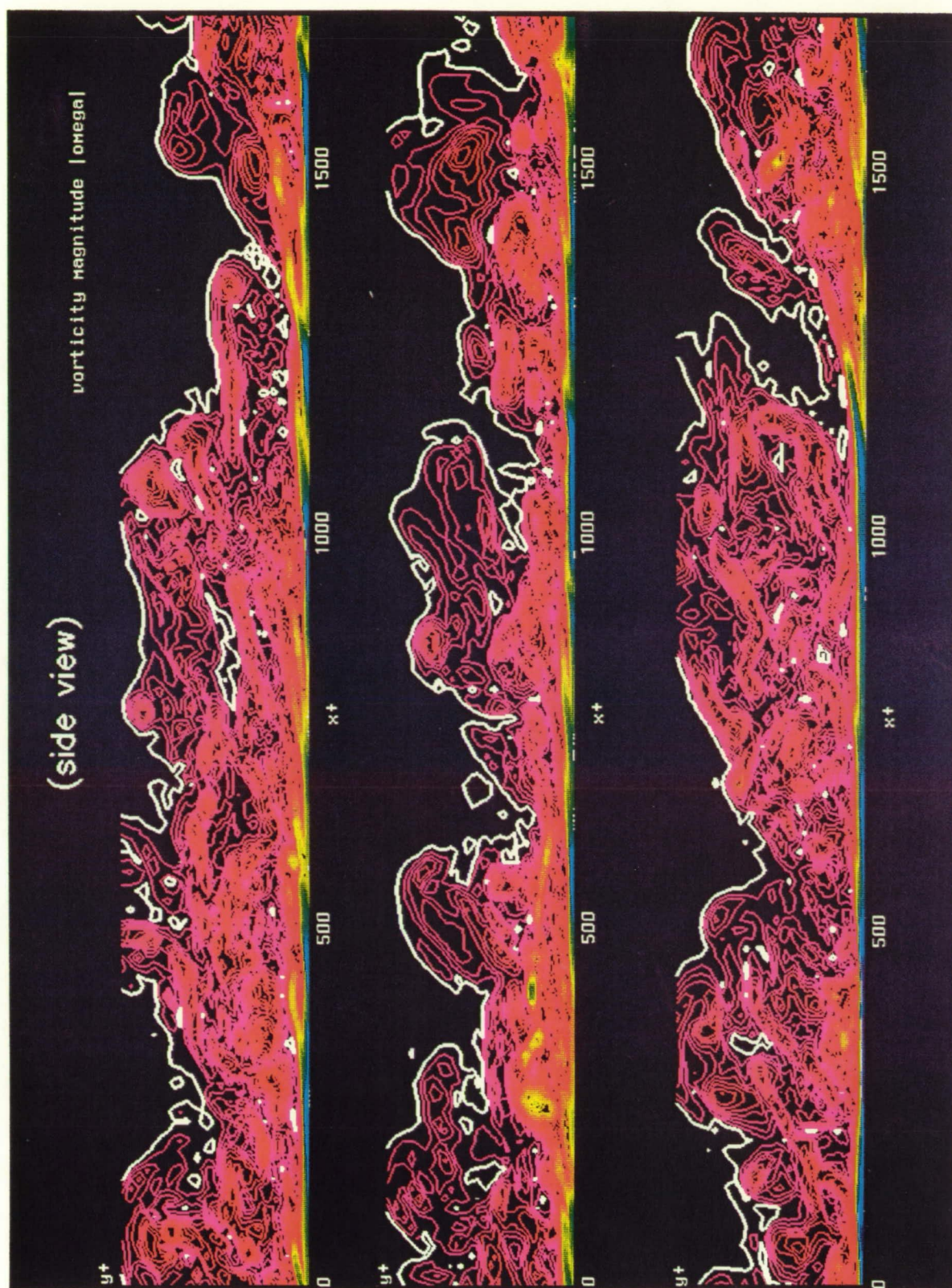


Fig. 10.14.1 Side-view contours of vorticity magnitude, showing bulges in the outer interface and near-wall shear layers. Magenta to yellow to blue: $|\omega|^+ = 0.05$ to 2.5. White: $|\omega|^+ = 0.025$.

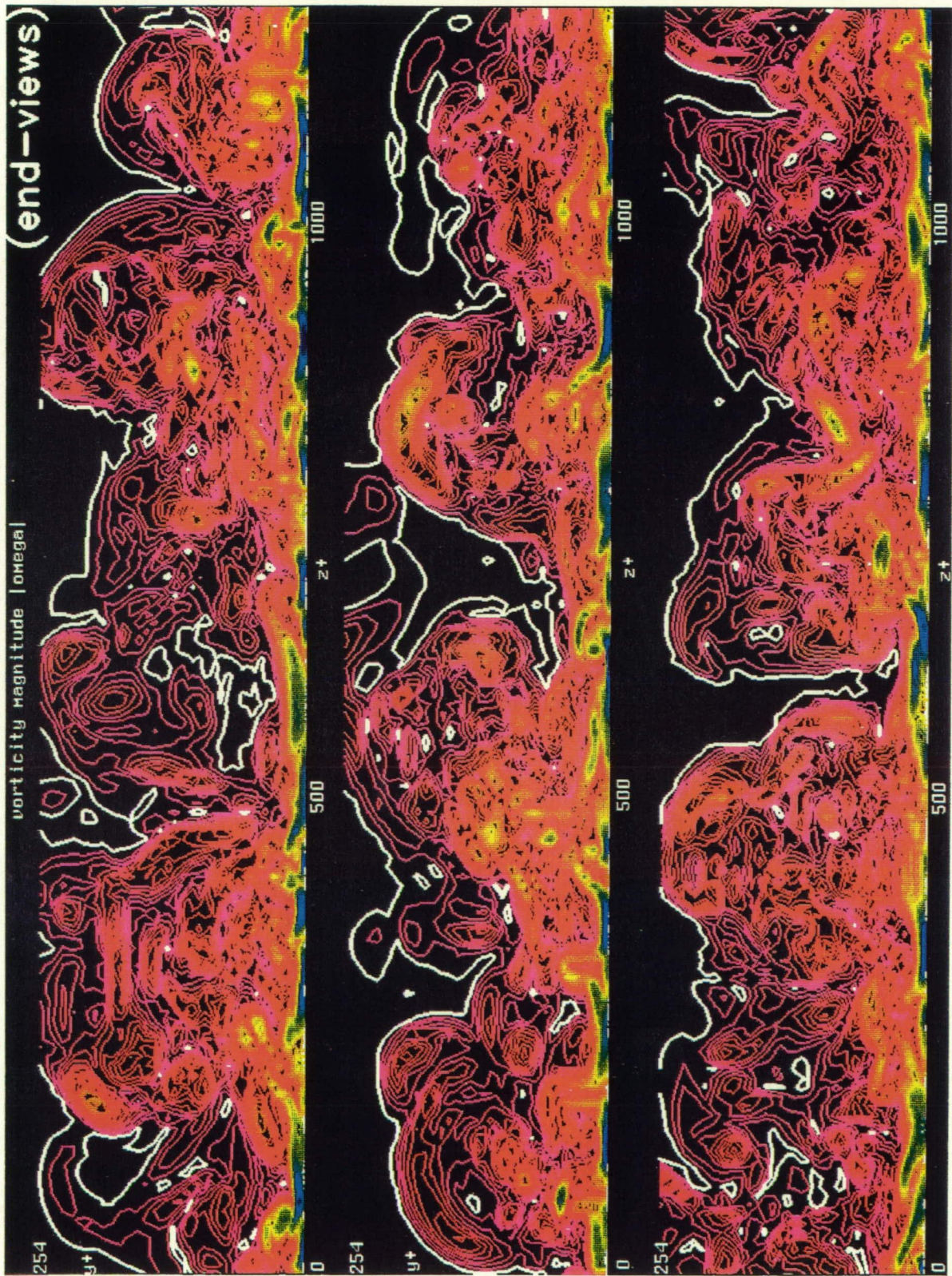


Fig. 10.14.2 End-view contours of vorticity magnitude, showing bulges in the outer interface and cuts through near-wall shear layers. Magenta to yellow to blue: $|\omega|^+ = 0.05$ to 2.5 . White: $|\omega|^+ = 0.025$.

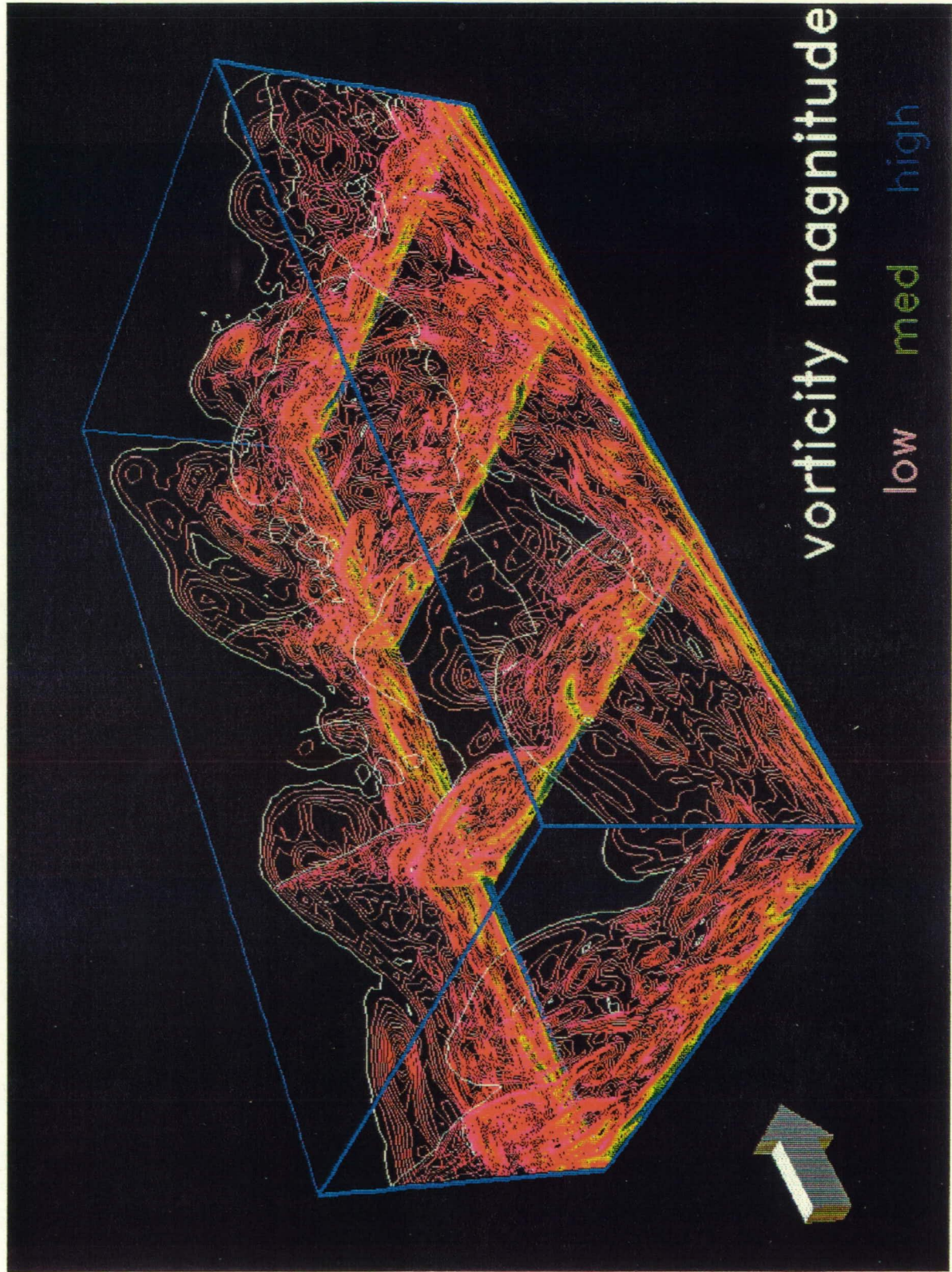


Fig. 10.14.3 Contours of vorticity magnitude, illustrating the three-dimensional character of bulges in the outer interface. Magenta to yellow to blue: $|\omega|^+ = 0.05$ to 2.5. White: $|\omega|^+ = 0.025$.

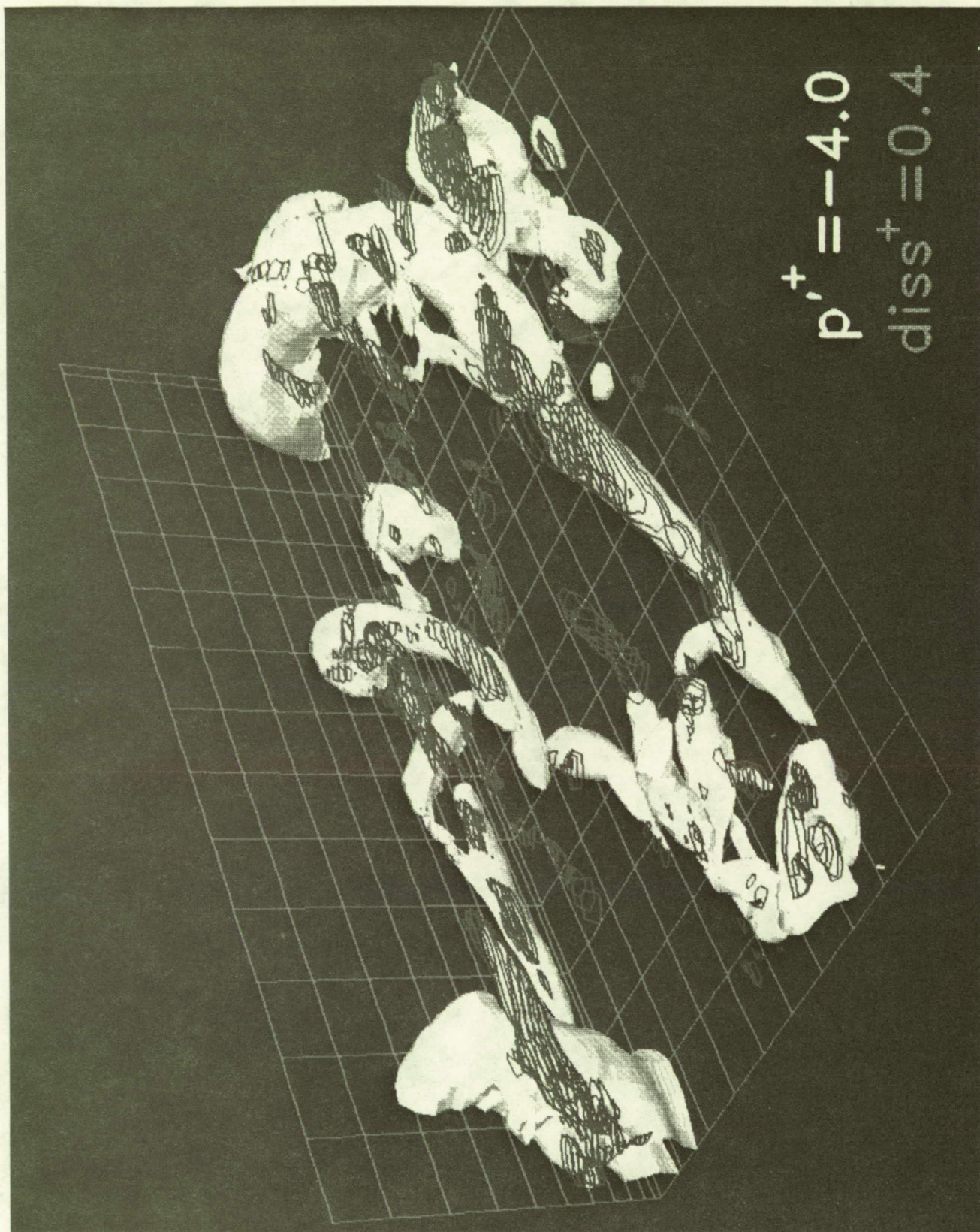


Fig. 10.15.1 Contours of instantaneous dissipation function ϵ'_f overlaid on low-pressure vortical structures in subvolume S. White: low pressure, $p'^+ = -4.2$. Magenta: $\epsilon'_f{}^+ = 0.4$ (shown only for $y^+ > 30$).

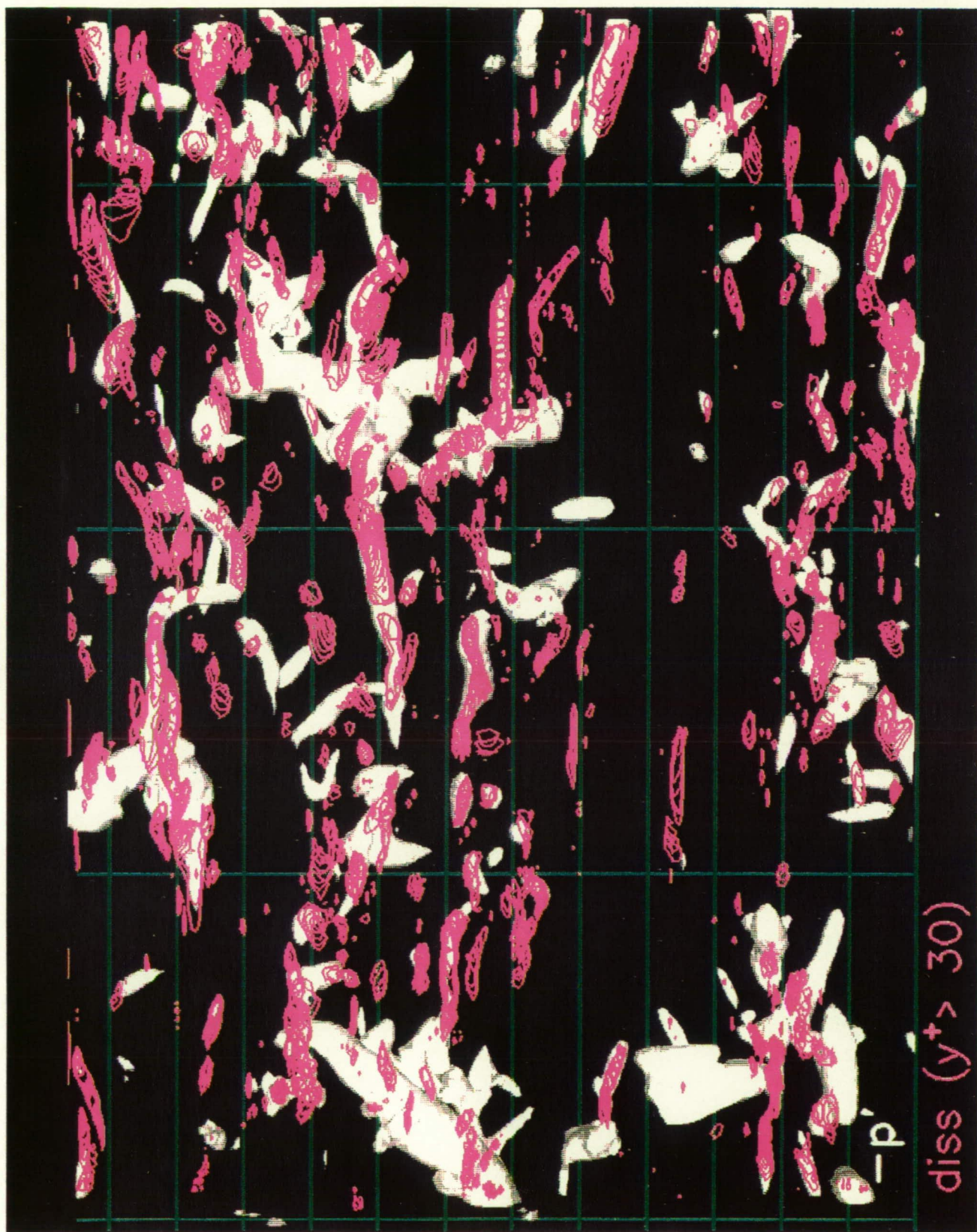
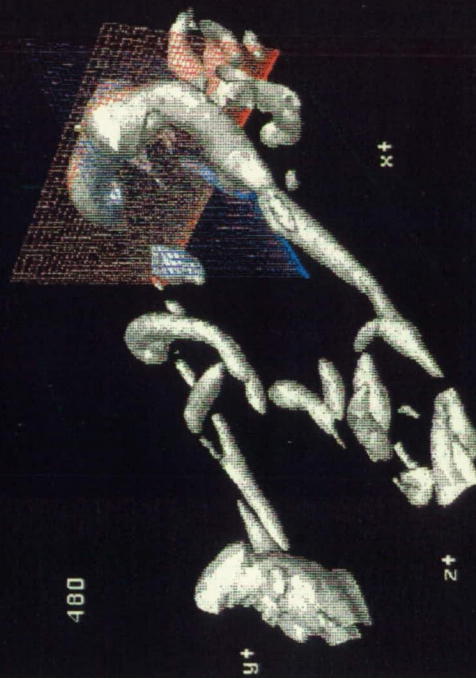


Fig. 10.15.2 Contours of instantaneous dissipation function ϵ'_f overlaid on low-pressure vortical structures. White: low pressure, $p'^+ = -4.2$. Magenta: $\epsilon'_+ = 0.4$ (shown only for $y^+ > 30$).

Vortical Structures and Entrainment



$$p^{'+} = -4.0$$

$$v' \text{ where } |\omega|^{'+} \leq 0.025$$

blue, cyan, white : $+v'$

red, yellow, white : $-v'$

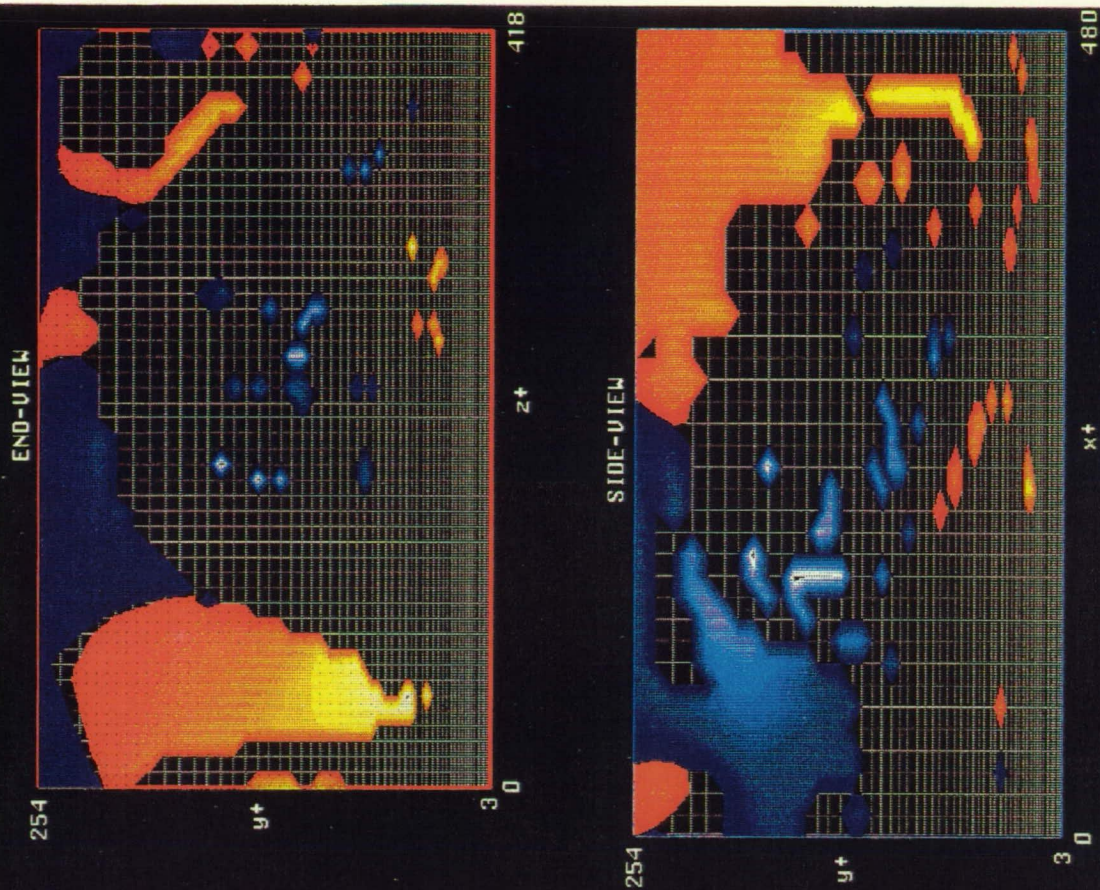
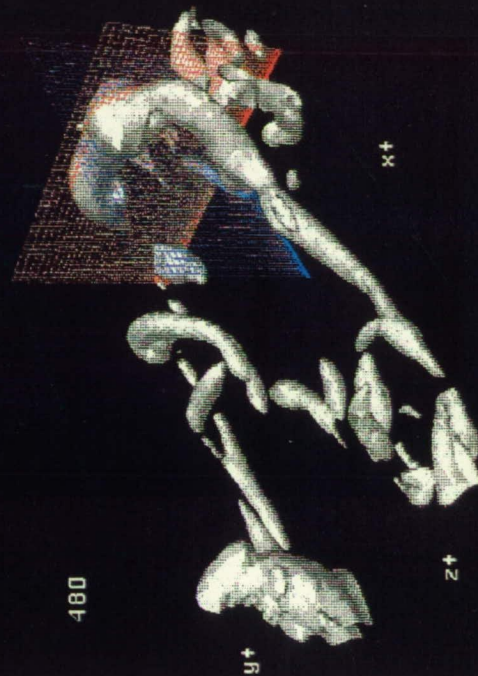


Fig. 10.16.1 Entrainment associated with a large vortical structure in sample subvolume S . Contours show magnitude of wall-normal motion of nearly irrotational fluid.

Red to yellow: wallward ($-v$) motion where $|\omega|^{'+} \leq 0.025$. Blue to white: outward ($+v$) motion where $|\omega|^{'+} \leq 0.025$.

Vortical Structures and Entrainment



$$p'^+ = -4.0$$

$$v' \text{ where } |\omega|^+ \leq 0.025$$

blue, cyan, white : $+v'$
red, yellow, white : $-v'$

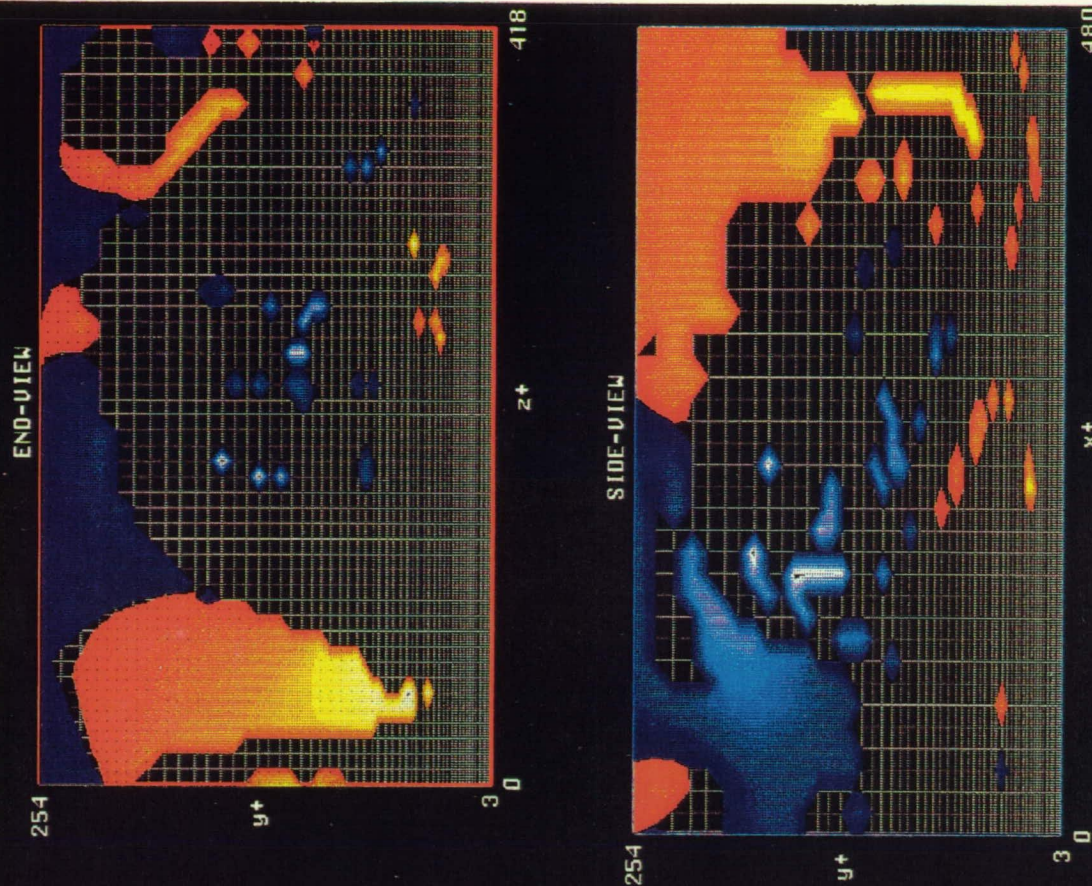
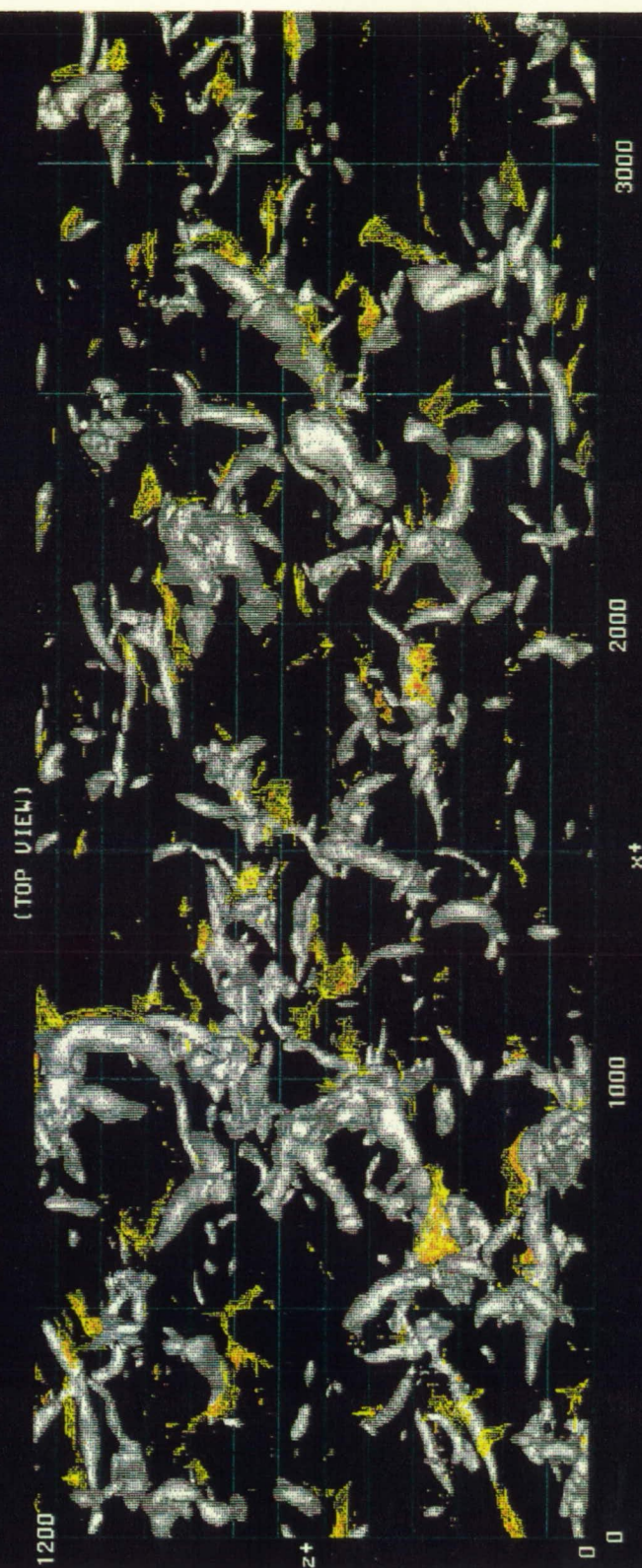


Fig. 10.16.1 Entrainment associated with a large vortical structure in sample subvolume S . Contours show magnitude of wall-normal motion of nearly irrotational fluid.

Red to yellow: wallward ($-v$) motion where $|\omega|^+ \leq 0.025$. Blue to white: outward ($+v$) motion where $|\omega|^+ \leq 0.025$.

Vortical Structures and Entrainment



$$p'^+ = -4.0$$

$$-v' \text{ where } |\omega|^+ \leq 0.025$$

Fig. 10.16.2 Entrainment motions with 3-D contour surfaces of low-pressure. Yellow: wallward $(-v)$ motion where $|\omega|^+ \leq 0.025$. White: low pressure, $p'^+ = -4.0$.

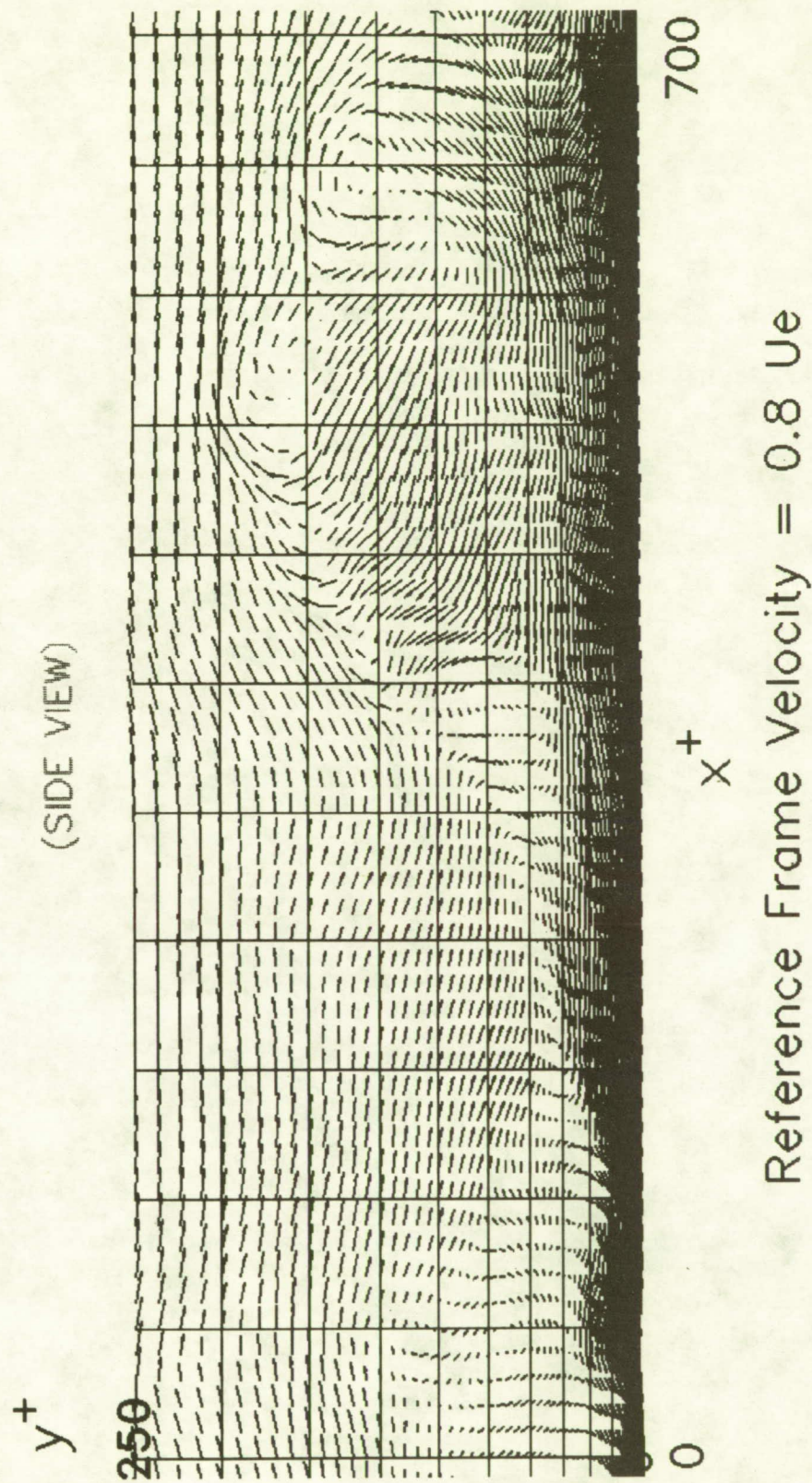


Fig. 10.17.1 Instantaneous u' , v' velocity vectors in an x - y plane moving downstream at $0.8U_e$.

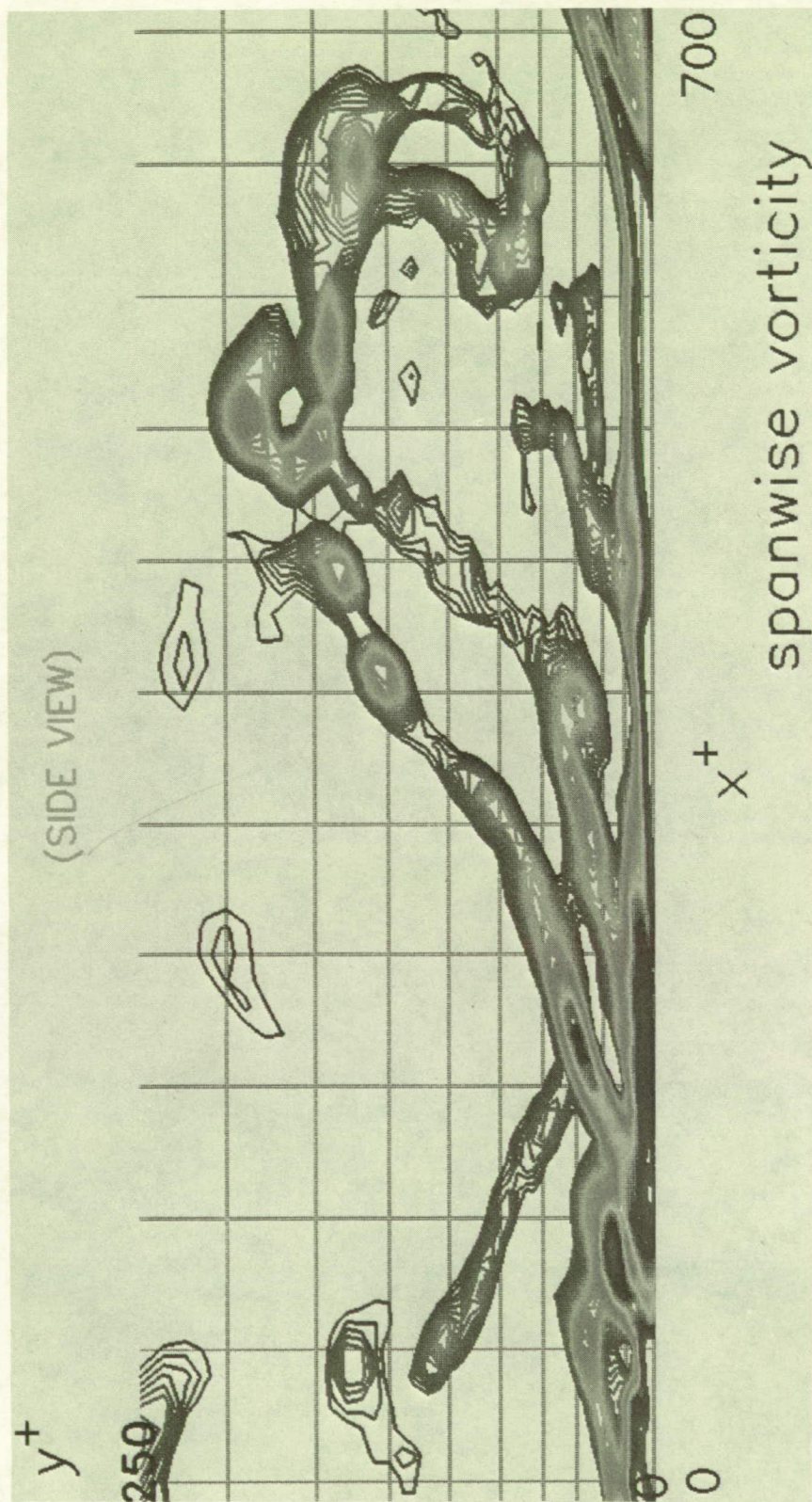


Fig. 10.17.2 Contours of transverse vorticity in the same x - y plane as shown in Fig. 10.17.1. Blue to yellow to magenta: $\omega_z^+ = -0.2$ to -3.0 .

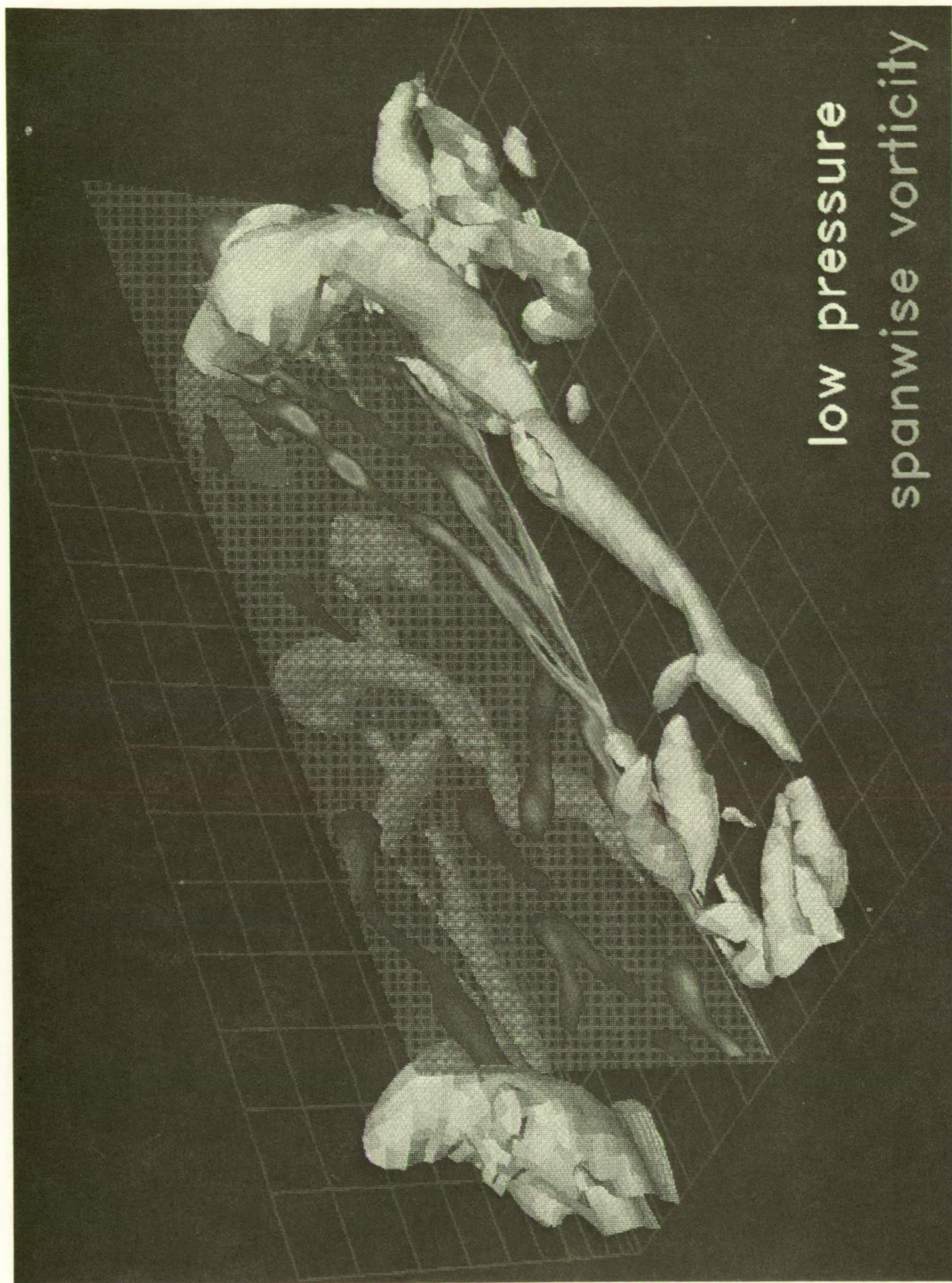
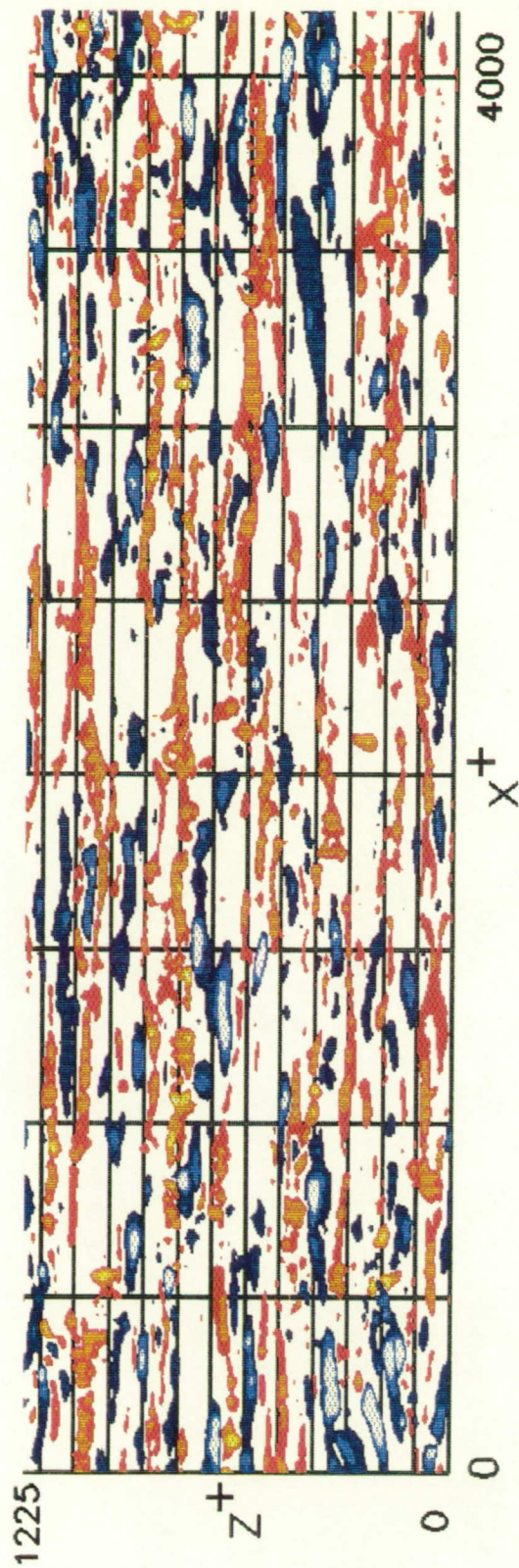


Fig. 10.18.1 "Back" or upstream interface of a large-scale motion, shown in an x - y plane with 3-D contour surfaces of low pressure.

Blue to yellow to magenta: $\omega_z^+ = -0.2$ to -3.0 . White: low pressure, $p'^+ = -4.2$.

INSTANTANEOUS WALL-SHEAR FLUCTUATIONS

(PLAN VIEW)



high wall-shear regions
low wall-shear regions

Fig. 10.19.1 Instantaneous wall-shear fluctuations.
Red to yellow: high shear, $+\tau'_w$. Blue to cyan: low shear, $-\tau'_w$.

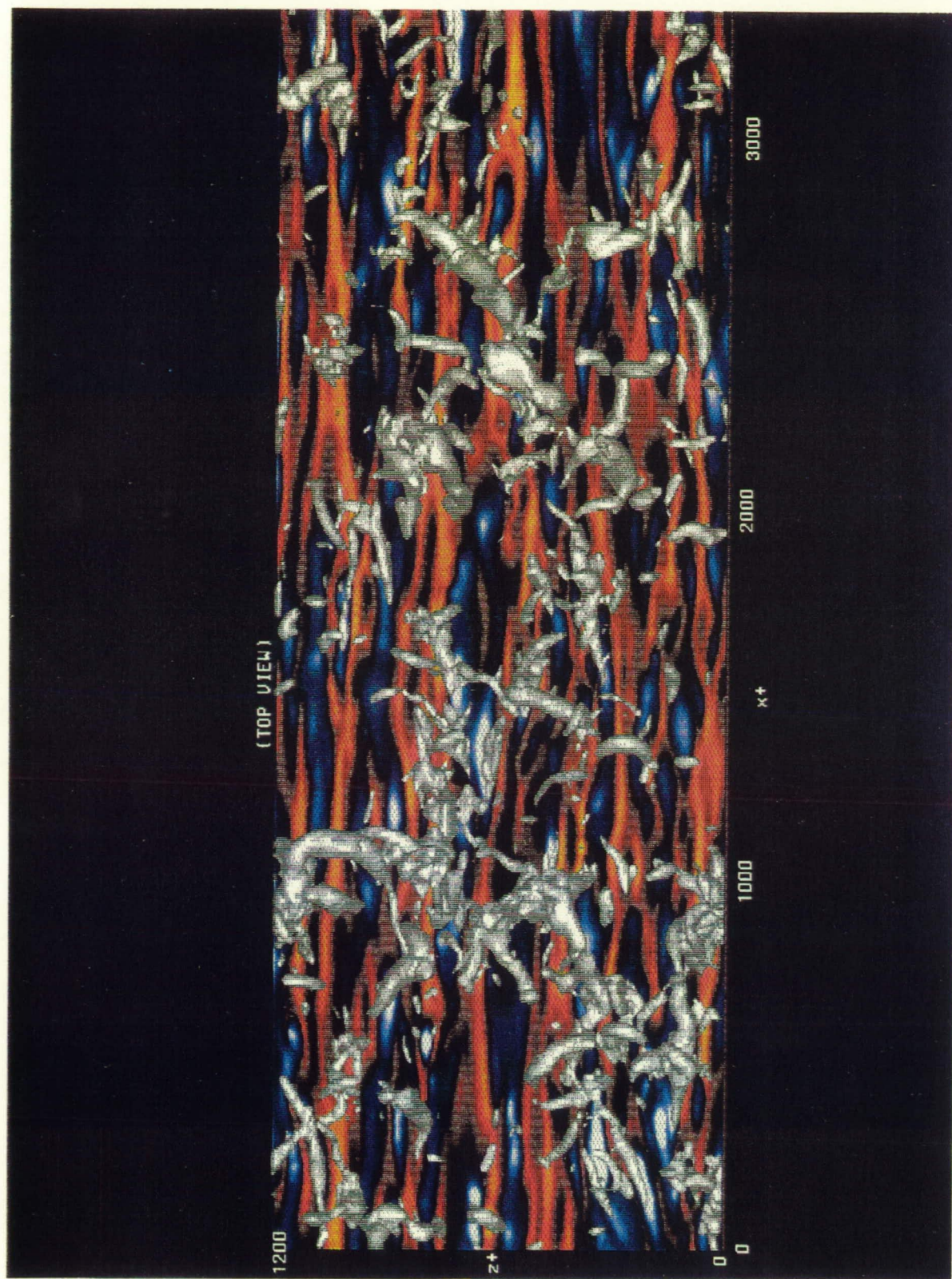


Fig. 10.20.1 Wall-shear patterns approximated by u' field at $y^+ = 3$, with 3-D contour surfaces of low pressure. White: low pressure, $p'^+ = -4.0$. Red to yellow: $u'^+ = -1.0$ to -4.0 . Blue to white: $u'^+ = +1.0$ to $+4.0$.

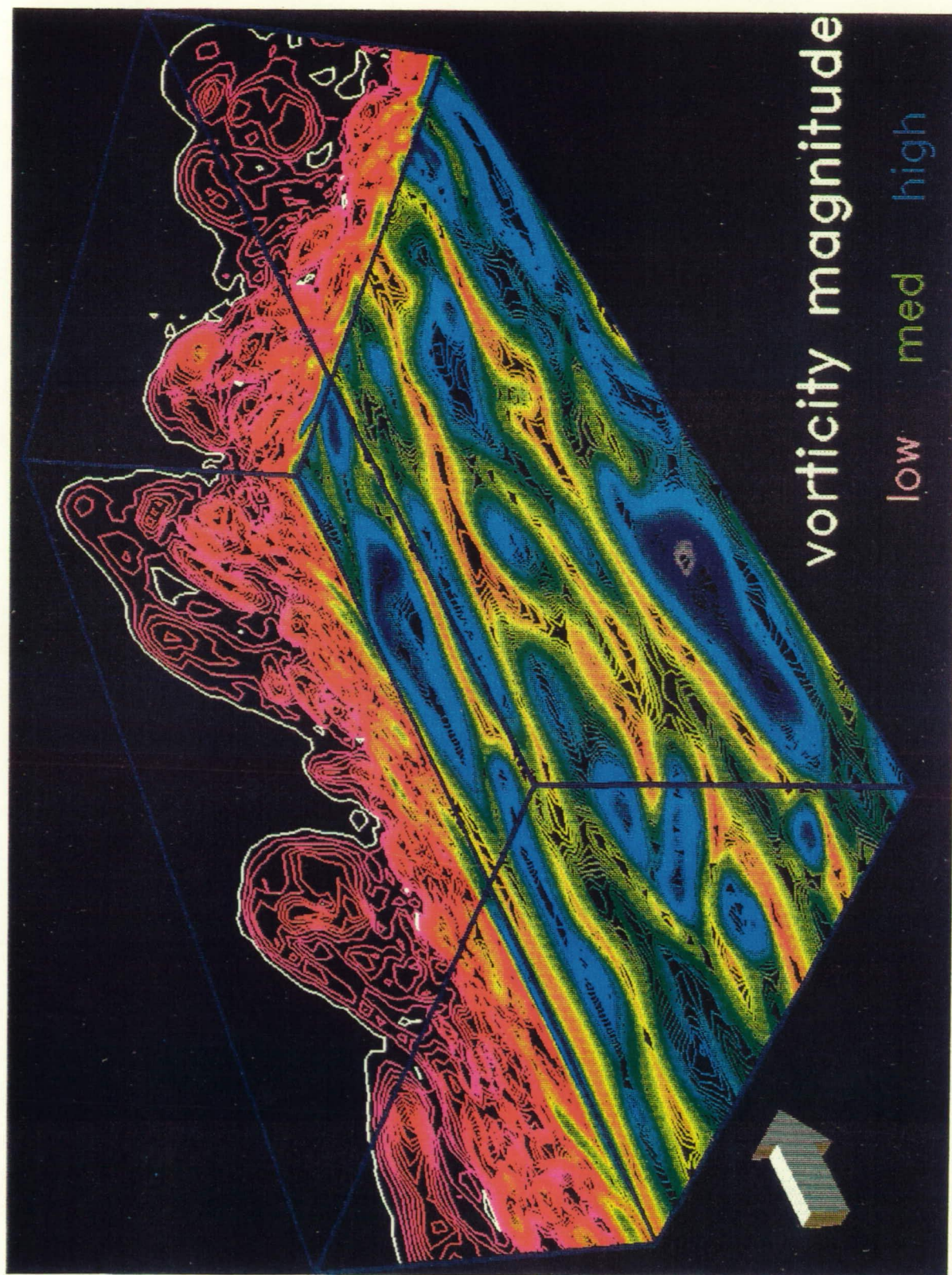


Fig. 10.20.2 Contours of vorticity magnitude, showing bulges in the outer interface, near-wall shear layers, and the sublayer streaky structure. Magenta to yellow to blue: $|\omega|^+ = 0.05$ to 2.5. White: $|\omega|^+ = 0.025$.

CHAPTER 11 - VORTICAL ELEMENTS AND STRUCTURES IN THE TURBULENT BOUNDARY LAYER

The previous three chapters of results from the numerically simulated boundary layer have shown that vortical motion is related in some way to virtually all types of coherent motions in the flow, suggesting that a deeper look into vortical motions is justified. The objective of this chapter is to review the experimental and computational evidence for vortical structures in turbulent boundary layers, and then to add to the knowledge base with distributions of vortex size, location, and strength from the simulated boundary layer.

There is a considerable overlap between Chapter 2 and the literature review presented in this chapter. However, the references in this chapter pertain solely to vortical structures and are sorted according to vortex type, providing the reader with a focussed subset of the broad-based historical review of Chapter 2, so some redundancy seems tolerable.

11.1 Experimental and Computational Evidence for Quasi-Streamwise Vortices

Vortices with a major streamwise (x) component are generally identified in experimental and computational results with single cross-stream (y - z) planes of marked fluid or computed velocity vectors. This method may not allow for differentiation between purely streamwise vortices and those tilted with respect to the wall. Thus, much of the data reviewed in this section could apply to both leg and neck vortices (in the nomenclature of Fig. 11.1), so the vortex elements are referred to here as "quasi-streamwise." Both purely streamwise and tilted quasi-streamwise vortices are capable of momentum transport across the velocity gradient, but the vortex dynamics are obviously affected by the orientation, since the wall-normal velocity gradient provides rapid stretching of the tilted vortices only.

Table 11.1 lists some of the many articles that make reference to quasi-streamwise vortices in turbulent boundary layers, either by flow-visualization in the $y - z$ plane, by probe measurement, or by numerical simulation. The A-F categorization shows that about half of the results are from visual studies, and half include quantitative data. Some studies provide both types of data by employing particle or bubble displacement techniques. Nearly a third of the references include some kind of simplified predictive model for near-wall streamwise vortices in the turbulent boundary layer.

Quasi-streamwise vortices were observed early in the history of turbulent structure research. Kim et al (1971) noted the common appearance of quasi-streamwise vortices in conjunction with the oscillation phase of the turbulence-generating bursting process. Grass (1971) also observed quasi-streamwise vortices, generally during

near-wall "inrush" and "ejection" events. Clark and Markland (1971) made careful observations of relatively long quasi-streamwise vortices (often counter-rotating pairs) with a 3 to 7 degree upward tilt in the wall region of a turbulent water channel.

Perhaps the most extensive direct information concerning quasi-streamwise vortices has come from the end-view hydrogen-bubble visualization studies of Smith and Schwartz (1983) and Kasagi, Hirata, and Nishino (1986). These studies confirmed the common occurrence of quasi-streamwise vortices in the near-wall region, including frequent observation of counter-rotating pairs. In the simultaneous top and end views by Smith and Schwartz, counter-rotating vortex pairs in the near-wall region were always associated in space and time with low-speed streak formation. Further recent results by Kasagi (1989) suggest that solitary quasi-streamwise vortices are more common than vortex pairs in the near-wall region, and that the vortical structures are not as long as the near-wall low-speed streaks.

Additional visual evidence of the existence and character of quasi-streamwise vortices can be found in Kastrinakis et al (1978) (who re-analyzed the film of Corino and Brodkey, 1969), Praturi and Brodkey (1978), and Lian (1987). Probe-based (or quantitative flow-visualization) results from which vortex behavior is inferred are presented in Willmarth and Lu (1972), Blackwelder and Eckelmann (1979), , Utami and Ueno (1987), Kreplin and Eckelmann (1979), and Nakagawa and Nezu (1981).

The apparent association between near-wall quasi-streamwise vortices and both the generation of low-speed streaks and turbulence production has motivated a number of streamwise vortex models with at least some predictive abilities. These include Bakewell and Lumley's (1967) proper orthogonal decomposition of experimental data, which showed that most of the near-wall Reynolds shear stress and turbulence kinetic energy could be represented by a dominant eddy structure which consisted of a streamwise vortex pair. These results were confirmed and extended by Herzog (1986), and more recently by Aubrey et al (1988), who used much more detailed experimental data. Additional streamwise vortex models have been proposed and developed over the years by a number of groups. Representative references of recent results are Hanratty (1988), Ersoy and Walker (1986), Pearson and Abernathy (1984), and Jang et al (1986).

Recent numerical simulations of turbulence have been used extensively to study the nature of embedded vortices in simulated channel flows and boundary layers. Although most of the attention has been given to three-dimensional vortex structures, quasi-streamwise vortices have been found in both instantaneous realizations and in conditionally-averaged results from the simulations.

Kim (1983) used VITA-type conditional averages to educe tilted streamwise vortex pairs in the near-wall region of a Large-Eddy Simulation (LES) of a fully

developed turbulent channel flow. Kim's average near-wall vortices were considerably shorter than the low-speed streaks in the simulation. In an extensive study of the vorticity field of an LES channel flow, Kim and Moin (1985, 1986) only rarely observed quasi-streamwise vortices (bundles of largely streamwise vortex lines). The vortices that were detected were of generally limited longitudinal extent ($\Delta x^+ < 100$), in agreement with Kim's (1983) earlier conclusions from the same data.

In the results of a direct simulation of a channel flow, Moin (1987) observed that, unlike the u' field near the wall, the v' and w' contours do not show significant streamwise elongation and that the regions of large v' tend to occur in side-by-side inward/outward pairs, suggesting quasi-streamwise vortices. Moin found these vortices occurred most commonly singly, rather than in counter-rotating pairs of equal strength, in contrast to conditionally averaged results (e.g. Blackwelder and Eckelmann, 1979; Herzog, 1986; Kim, 1983; Moin, 1984). Moser and Moin (1984), and Guezennec et al (1989) have also concluded that single quasi-streamwise vortices are statistically more common than equal-strength pairs in direct numerical simulations of turbulence.

Moin's (1987) quasi-streamwise vortices were only 100 to 200 viscous units long, but retained their coherence while travelling several channel half-widths downstream. Moin reported regions of high $u'v'$ adjacent to every observed quasi-streamwise vortex in the wall region, and concluded that relatively short, single vortices are the fundamental structures associated with regions of high turbulence production.

Statistical decompositions of the simulated turbulence velocity fields have provided additional insight into the nature and statistical significance of quasi-streamwise vortices (e.g. Moin, Adrian, and Kim, 1987; Moin and Moser, 1989).

Given the available evidence, there is no doubt that quasi-streamwise vortices exist in numbers sufficient to play an active role in near-wall turbulence dynamics. There is reasonable agreement in the literature on the size and location of quasi-streamwise vortices: diameters from $15\nu/u_\tau$ to $50\nu/u_\tau$, with centers occurring predominantly between $y^+ = 20$ and $y^+ = 70$. Although early papers proposed quasi-streamwise vortex extents on the order of the streak lengths ($\approx 1000\Delta x^+$), there now appears to be a consensus that quasi-streamwise vortices are about an order of magnitude shorter than the longest sublayer streaks. Quasi-streamwise vortices are generally considered to occur both singly and in counter-rotating pairs, and, in the near-wall region, to tilt upwards from the wall at a shallow (3 to 7 degree) angle. In the outer region, vortices more commonly make angles of approximately 45 degrees with the wall, which corresponds to the direction of maximum vorticity production due to stretching by the mean gradient. There is almost no information available in the literature on the strength (circulation) of quasi-streamwise vortices

in turbulent boundary layers.

The formation mechanisms and evolution of the quasi-streamwise vortices are poorly understood. The most popular theory is that they are the trailing, stretching legs of hairpin vortices. However, Falco (1982, 1983) suggests that quasi-streamwise vortices are created from the passage of a ring vortex eddy over the sublayer. It has also been proposed that quasi-streamwise vortices arise due to local flow curvature and an accompanying Görtler instability (Brown and Thomas, 1977). Acarlar and Smith (1987) propose yet another means by which quasi-streamwise vortices may be generated (see Fig. 11.12). None of these theories are fundamentally contradictory, and in fact multiple formation mechanisms of quasi-streamwise vortices seems probable.

11.2 Experimental and Computational Evidence for Spanwise Vortices

In the spanwise (x - y side-view plane) of a turbulent channel or boundary layer, the detection of a vortex in the velocity field is obviously dependent upon the motion of the observer's reference frame. The mean velocity gradient combined with the turbulent unsteadiness make experimental detection of transverse vortices in the boundary layer difficult and often ambiguous. Cautions against potentially deceptive illusions created by reference frame choice and streaklines in unsteady flows have been published by Hama (1962) and again recently by Kurosaka and Sundaram (1986).

As a result of these experimental difficulties, relatively few references discuss transverse vortices specifically, although they are usually an element of three-dimensional vortex structures. Some of the exceptions are listed in Table 11.2. For the present purposes, the table does not include the many papers on the large, relatively weakly rotational δ -scale motions, such as those described in, for example, Kovasnay et al (1970), Brown and Thomas (1977), and Antonia et al (1988).

Most of the evidence for strong local transverse vortical motion is from side-view flow-visualization studies such as Kim et al (1971), Clark and Markland (1971), Nychas et al (1973), Praturi and Brodkey (1978), Lian (1986), and Smith and Lu (1988). Probe-based data which imply transverse vortices are included in Nakagawa and Nezu (1981).

The most common reference to transverse vortices is in regard to near-wall hydrodynamic instability (e.g. Einstein and Li, 1956; Kline et al, 1967; Black, 1968; Smith, 1984), in which a local instability occurs at the shear-layer interface of high and low-speed fluid, resulting in a transverse vortex rollup.

Perhaps the earliest extensive description of transverse vortices is included in Clark and Markland (1971), who found them to be the predominant vortex element in the $y^+ > 70$ region. Clark and Markland observed that the streamwise lifetime of transverse vortices increases as distance from the wall increases, and that the diameter grows but the spin-rate slows during the vortex lifetime.

Kim et al (1971) found that transverse vortical motion occasionally appeared during the oscillatory phases of what they defined as the near-wall bursting process, but not as commonly as streamwise vortical motion or "wavy" motion.

Nychas et al (1973) described large-scale transverse vortices (of both rotational signs) that appeared to roll up at the shear-layer interface of high and low-speed fluid for $y^+ > 70$. These vortices were suggested to be the cause of the outer interface bulges described by Blackwelder and Kovasznay (1972), and others. In addition, a close spatial association was observed between the passage of transverse vortices and the occurrence of near-wall ejections of low-speed fluid. Outer-region transverse vortices were therefore suggested by Nychas et al to be the key structural element which connects the near-wall activity with the outer-flow large eddies.

Nychas et al's results were extended by Praturi and Brodkey (1978), who observed inflows of free-stream potential fluid (entrainment) in the vicinity of the large outer-flow transverse vortices. Contrary to the earlier speculations of several groups, it was stated by Praturi and Brodkey that large-scale bulges in the outer turbulent/non-turbulent interface are not caused by unusually high-momentum ejections of fluid from the near-wall region, but instead by the outer-region transverse vortical motions.

The presence of transverse vortices at the interface of high- and low-speed fluid in the outer-layer was also emphasized by Nakagawa and Nezu (1981). Formation of transverse vortices for $y^+ < 100$ was described by Robinson et al (1988) as a rollup of near-wall shear layers consisting of locally concentrated spanwise vorticity.

Smith and Lu (1988) applied digital image processing techniques to detect hydrogen-bubble patterns in side-views of a turbulent boundary layer, using pattern-recognition templates obtained from bubble patterns surrounding artificially-generated hairpin vortices in a laminar boundary layer. The resulting distribution of detected vortex patterns is skewed toward the wall, with a peak in the distribution centered at $y^+ \approx 40$. As will be seen in Sec. 11.5, quasi-streamwise vortices in the simulated boundary layer display a distribution similar to Smith and Lu's, but transverse vortices are relatively rare in the near-wall region. This suggests that Smith and Lu's technique, even though based on side-views, is identifying structures associated more with quasi-streamwise than transverse vortices. It is difficult to draw any conclusions from this comparison concerning the existence of hairpin vortices.

It is fairly well-established that transverse vortices are common in the outer region of turbulent boundary layers, and less so in the near-wall region. Statistics of size, location, and strength are lacking, however. It remains unclear from the literature whether the common mode is for transverse vortices to form locally in the outer region (Nychas et al, 1973) or in the buffer region and then migrate outward (Smith, 1984).

11.3 Hairpin/Horseshoe Vortex Conceptual Models

Horseshoe or hairpin-shaped vortical structures dominate the proposed conceptual models for boundary layer turbulence. Notable alternative (but not necessarily conflicting) concepts are the inclined roller-eddy model of Townsend (1976) (see also Guezennec, 1986), and the vortex ring models of Falco (1983, 1988) and of Kobashi and Ichijo (1986). (See Table 11.3). In the interest of brevity, only the horseshoe/hairpin models are reviewed here. Earlier reviews of hairpin vortex models have also been published by Wallace (1982, 1985).

Theodorsen (1952) proposed the first hairpin vortex model for boundary-layer turbulence (Fig. 11.2). In the model, vortical “tornadoes” form astride near-wall regions of low-velocity fluid, and grow outward with heads inclined downstream at 45 degrees, and with spanwise dimensions proportional to the distance from the wall. The streamwise distance travelled by a mature vortex structure was postulated as approximately equal to the distance from its head to the wall. This vortical model was proposed as the fundamental structure of turbulent boundary layers, being responsible for both the production and dissipation of turbulence energy. It is notable that extended quasi-streamwise vortex elements (legs) did not play a major role in Theodorsen’s model. A useful synopsis of Theodorsen’s paper is given in Head and Bandyopadhyay (1981).

Willmarth and Tu (1967) devised a model for the average eddy structure of the near-wall region, based on correlation measurements between wall-pressure and near-wall velocity fluctuations (Fig. 11.3). The model describes the deformation of initially two-dimensional transverse vorticity lines into three-dimensional hairpin shapes sloped downstream at about 10 degrees from the wall, with the dominant element being vorticity lines with a streamwise component. Although Willmarth and Tu (1967) proposed their hairpin vortex-line model for the near-wall region only, Willmarth and Lu (1972) suggested that near-wall hairpin vortices may evolve to a larger scale, producing the intermittent bulges in the outer edge of the boundary layer and providing an outward interaction mechanism between the inner and outer regions.

Black (1968) used a simple instability argument to propose a flow model based upon horseshoe vortices which are “shed” from a near-wall instability. In their early formation stages, the vortex structures were described as closed loops, or rings (Fig. 11.5a). As the outer portions of the vortex evolve outward and downstream, the wallward transverse element of the original ring is left behind to decay in the viscous sublayer, leaving a horseshoe-shaped vortex. The heads of these discrete vortices move outward from the wall, thereby stretching the trailing legs and inclining the horseshoe vortex. The vortex structures induce an inviscid outflow of low-speed fluid from within the vortex loop, creating motions which are seen as sharp, intermittent spikes of Reynolds shear stress by a stationary probe. Instead of individual

horseshoe vortices, Black proposed a structure comprised of several horseshoe elements in various stages of growth, which share a common front-like trajectory in space. The vortex structure is maintained for much longer periods than the lifetime of the component vortex elements by the continuous creation of new elements which replace the older members (Fig. 11.5b).

Both Hinze (1975) (Fig. 11.6) and Offen and Kline (1975) (Fig. 11.7) attempted to synthesize the then-known coherent elements of near-wall turbulence production with a horseshoe-shaped vortex model. Hinze related the induced fluid motion surrounding the vortex loop to the experimentally observed bursting process. In Hinze's model, fluid lifted between the legs of the vortex loop gives rise to a locally unstable shear layer, which then violently breaks down (bursts), apparently destroying the parent vortex structure in the process. Offen and Kline (building on earlier speculations by Kline et al, 1967) related the three kinds of oscillatory motion observed during the near-wall bursting process by Kim et al (1971) to the passage of a horseshoe vortex. Offen and Kline also discussed pairing of aligned vortex structures and violent interaction of non-aligned vortices.

Experimental support for the many available hairpin vortex models came from Head and Bandyopadhyay (1981), who published photographs of smoke-filled turbulent boundary layers in which loop-shaped forms at 45° to the wall were visible. By conducting visualization studies over a range of Reynolds numbers ($500 < Re_\theta < 17500$), Head and Bandyopadhyay drew a distinction between the wide, arch-shaped forms visible at low Reynolds numbers and agglomerations of elongated hairpin-shaped structures at high Reynolds numbers (Fig. 11.8). Although the authors (and many others since) have interpreted these smoke-filled loops as vortices, quantifiable evidence of their existence and statistical/dynamical relevance remains to be obtained.

An attempt to construct a predictive tool based on experimentally-postulated hairpin vortex models was made by Perry and Chong (1982). Perry et al (1986) extended Perry and Chong's (1982) model in which the boundary layer is represented by a forest of Λ -shaped vortices, which were introduced as a candidate form for Townsend's (1976) "attached-eddy" hypothesis. Biot-Savart calculations of a geometrical hierarchy of such vortices gave promising reproductions of the mean profile, Reynolds shear-stress, turbulence intensities, and spectra for a turbulent boundary layer, lending credibility to the idea of vortical loops as the dynamically dominant boundary layer structure. (Another type of hairpin-vortex predictive model is proposed by Kasagi 1989). Recently, Perry et al (1989) have extended the attached eddy hypothesis to formulate a rudimentary closure scheme for the prediction of turbulent boundary layers with streamwise pressure gradients. Perry et al's models are discussed in more detail in Chapter 2.

Falco (1982) observed the formation of short-lived, near-wall hairpin vortices

on the downstream edge of sublayer “pocket” modules, which are created from the impact of relatively high-speed fluid upon the sublayer. These hairpin vortex structures were found to be associated with outward ejections of low-speed fluid, in agreement with the hypotheses of Kline et al (1967), and others.

Wallace (1982; updated in 1985) collected the evidence for hairpin/horseshoe vortices in boundary layers and constructed a schematic vortex model which included quantitative dimensions (Fig. 11.10). To explain the birth of the horseshoe vortices, Wallace uses the Navier-Stokes equations at the wall to show that local wall-pressure gradients are equivalent to an outward diffusion of vorticity from the wall. Although this process would result in a warping of near-wall vorticity sheets, it remains unclear how the perturbed vorticity field gives rise to true vortices (as defined in Sec. 9.1).

Smith (1984) proposed a vortex model of the near-wall boundary layer which related nested arrays of hairpin vortices to the bursting process, and to low-speed streak formation, near-wall shear layers, ejections, and sweeps (Fig. 11.11). These vortices are postulated by Acarlar and Smith (1987 a,b) to form as a result of shear-layer instabilities on the top and sides of low-speed streaks, and a single hairpin may spawn other secondary offspring vortices in its wake. The major feature of Smith’s model is the existence of paired quasi-streamwise legs trailing upstream from a hairpin vortex structure. These stretching legs form counter-rotating vortices which collect low-speed fluid into persistent elongated streaks and pump near-wall fluid outward in ejections. The conceptual model developed in the current study (Chapter 12) is similar to Smith’s model, but with an important difference in the spanwise symmetry of the vortex structures. In the simulated boundary layer, it is observed that a single quasi-streamwise vortex is sufficient to induce ejections, create streaks, and regenerate new vortical structures, and that symmetric and/or nested hairpins are rare. Nevertheless, Smith’s model functions as a useful idealization of the instantaneous physics.

By the time numerical simulation of turbulent flow became feasible in the late 1970’s, many conceptual boundary layer models involving hairpin/horseshoe vortices had been proposed, but they were supported by only a minimal experimental database of mostly circumstantial evidence. This led Moin and Kim (1985) to search for and characterize hairpin vortices in their Large-Eddy and Direct simulations of turbulent channel flow.

Moin and Kim (1985) showed that for the outer region of the simulated channel-flow, vorticity vectors tend to be inclined at about 45 degrees to the wall. Three-dimensional vorticity lines were commonly found in horseshoe shapes, though usually asymmetric (Fig. 11.13). These horseshoe-shaped structures appeared to coalesce from deformed vortex sheets, and generally did not exhibit elongated streamwise legs. From these results, Moin and Kim concluded that 45 degree, hairpin-

shaped **vortices** are statistically relevant features of turbulent channel flow structure.

Continuing their investigation of numerical channel-flow, Kim and Moin (1986) applied variants of the VITA and $u'v'$ quadrant-splitting technique to investigate associations between hairpin/horseshoe vortical structures and outer-region ($y^+ \geq 100$) turbulence-producing events. As may have been expected from Fig. 9.5, upright horseshoe-shaped vorticity lines were found to be associated with ejection ($(u'v')_2$) motions, while inverted horseshoes were found in conjunction with sweep ($(u'v')_4$) motions. Quasi-streamwise vortices were rarely found in the outer region, and those identified were generally of limited ($\Delta x^+ < 100$) streamwise extent.

A number of additional hairpin/horseshoe vortex conceptual models are proposed in the literature, including Fiedler (1986) (Fig. 11.14), Utami and Ueno (1987) (Fig. 11.15), Adrian (1989) (Fig. 11.16), and Kasagi (1989) (Fig. 11.17). Many of these models are similar in their depiction of a looped vortical structure, but most models do not account for the existence of all the structural features enumerated in Chapter 5. Also, not all models are described in terms of dynamic relationships among coherent motions, and a wide variety of concepts exists among those models that do address dynamics. It is not possible to conclusively accept or reject any of the above models based on currently available data.

11.4 Literature Summary

The existence of vortical elements in turbulent boundary layers is well established. However, experimental and even computational detections of horseshoe/hairpin vortical structures are outnumbered by the theoretical arguments for their existence. Most critically, the role of vortical structures as a dynamical element of boundary-layer turbulence is mostly hypothesis. Quasi-streamwise vortices are the most thoroughly documented of the vortex elements, but distributions of the diameters, distance from the wall, strength, and population of all types of boundary-layer vortices are scarce.

11.5 Vortices in the Numerically Simulated Boundary Layer

In accordance with the working definition of a vortex stated in Chapter 9, vortices in the end-view ($y - z$) and side-view ($x - y$) planes have been identified by plots of instantaneous streamlines or vectors. For quasi-streamwise vortices, streamlines were plotted in 25 $y - z$ planes with dimensions $\Delta z^+ = 418$ by $\Delta y^+ = 250$. For spanwise vortices instantaneous vectors constructed with the fluctuating velocity (u', v') components were found to display all vortices identifiable from a reference frame moving at any streamwise velocity between 0 and U_e . (This suggests that transverse vortices travel downstream at velocities not too different from the local mean velocity.) Dimensions of the 15 $x - y$ -plane views used for the transverse vortex counting were $\Delta x^+ = 845$ by $\Delta y^+ = 250$. All data-planes were chosen at

widely different and unrelated spatial and/or temporal locations in the simulation database. Examples of the $y - z$ and $x - y$ planes are given in Fig. 11.18, in which vortices are clearly visible in the streamlines, but less obvious in the vectors.

For each vortex visually identified in the plots, the diameter, distance from the wall, core area, and approximate circulation was recorded. For the streamlines in the end-view planes, the diameter was estimated by measuring the extent of the bounding streamline of a group of closed concentric streamlines, and the area was estimated as the area of a circle with that diameter. Transverse vortices were more difficult to identify in the side-view vector plots, although strong (high circulation) vortices with significant perturbation velocities tended to be fairly obvious. For this reason, there may be a bias towards stronger transverse vortices in the data presented below, and this effect is accentuated near the wall. Though tedious, hand-counting of the “visual vortices” was considered preferable to more sophisticated, but less reliable vortex identification methods, at least for a first set of control data.

11.5.1 Quasi-Streamwise Vortex Results

Statistics were computed for a sample of 229 quasi-streamwise vortices identified visually in the simulated boundary layer. Recall that vortices visible in end-plane ($y - z$) views need not be (and usually are not) strictly streamwise but may possess significant spanwise and/or wall-normal components, and are thus referred to as “quasi-streamwise.”

The distribution of distances of the vortex centers to the wall is shown in Fig. 11.19. In agreement with experimental results, quasi-streamwise vortices are more commonly found in the wall region, with 72% of the total occurring for $y^+ < 100$. The diameter distribution in Fig. 11.20 shows that 73% of the visual quasi-streamwise vortices have diameters between 10 and 40 viscous lengths, and 90% between 10 and 60 viscous lengths. The average diameter of the quasi-streamwise vortices in the sample is 34 viscous lengths.

The variation of quasi-streamwise vortex diameters with distance from the wall is plotted in Fig. 11.21. Larger vortices generally reside further from the wall, but the data is broadly scattered between the $d^+ = 2y^+$ line and the lower bound of $d^+ \approx 10$.

Since visual identification of vortices cannot easily determine their potential as significant momentum transport “pumps,” the circulation of each visual vortex was also computed. Following Pearson and Abernathy (1984), the circulation is described in terms of a vortex Reynolds number defined as

$$R_V \equiv \Gamma / 2\pi\nu, \quad (2)$$

where Γ is the circulation computed by integrating the streamwise vorticity ω_x over the vortex area. As a reference value for evaluating the strengths of vortices, the

vortex Reynolds number of a δ by δ box in the $x - y$ plane may be computed. For the numerically simulated boundary layer, this reference circulation is

$$R_{V\delta} = \frac{U_e \delta}{2\pi\nu} \approx 955. \quad (3)$$

Since Γ is computed as an area integral, very large vortices are likely to contain high values of circulation. To estimate the intensity of the vortices, the vortex Reynolds number R_V may be divided by the area of the vortex, non-dimensionalized by viscous units. Using the δ by δ box, a reference intensity for the simulated boundary layer is ≈ 0.011 , which may be taken as a mean circulation intensity for the boundary layer.

The vortex Reynolds number and intensity distributions for visually-identified quasi-streamwise vortices are shown in Figs. 11.22 and 11.23, respectively. The average value of R_V is 22, but the distribution has a long tail toward much higher values. However, the intensity distribution (Fig. 11.23) shows that about 90% of the quasi-streamwise vortices have a higher intensity than the boundary layer reference value of 0.011. The most intense quasi-streamwise vortices have intensity values up to nearly 10 times the reference value, and nearly all of the very intense vortices occur for $y^+ < 75$. Vortices with higher intensities than the average circulation intensity in the boundary layer may be expected to have sufficient strength to induce significant momentum transport through induction.

11.5.2 Spanwise Vortex Results

The sample used for transverse vortex statistics was 85 “visual vortices.” From the wall-distance distribution in Fig. 11.24, it is seen that transverse vortices tend to be located outside the near-wall region, with over 80% of the population occurring for $80 < y^+ < 180$, in a boundary layer with $\delta^+ \approx 300$. The broad, outer-region distribution of transverse vortices differs significantly from the near-wall preference of quasi-streamwise vortices (Fig. 11.19).

Transverse vortices also tend to exhibit larger diameters than quasi-streamwise vortices. The distribution in Fig. 11.25 shows 74% of transverse vortex diameters measuring between 30 and 70 viscous lengths, with an average value of 51. The variation of transverse vortex diameter with distance from the wall (Fig. 11.26) exhibits wide scatter, but the data is fit reasonably well by a $d^+ = \kappa y^+$ line, where $\kappa = 0.41$ is the Karman constant. This apparent agreement with the boundary-layer mixing-length distribution is not surprising, and suggests that transverse vortices do indeed play a statistically significant role in determining the average statistics within a turbulent boundary layer. Note, however, that the $d^+ = \kappa y^+$ line fits the data far beyond the range where the mixing length is linearly dependent on distance from the wall ($y \leq 0.1\delta$). A larger sample of transverse vortices is needed to properly ascertain the statistical significance of their presence.

Since transverse vortices are embedded in a mean velocity gradient, their circulation was computed with the fluctuating component ($\omega'_z(x, y) = \omega(x, y) - \bar{\omega}(y)$) of spanwise vorticity. This approach may be criticized on the grounds that the transverse vortices may themselves be the mean vorticity, but it was desired to compare the circulation intensities between quasi-streamwise and transverse vortices.

The distribution of vortex Reynolds number (Fig. 11.27) shows that transverse vortices tend to have higher circulation values than quasi-streamwise vortices (comparing again to the boundary-layer reference value of 955), which is to be expected given their generally larger diameter. The R_V distribution peaks at about 30 for transverse vortices, and at about 12 for streamwise. About 17% of the transverse vortices were found to have positive values of circulation, i.e. containing lower total circulation than the local mean, which is negative.

The circulation intensity (R_V/A^+) distribution for transverse vortices is plotted in Fig. 11.28. Transverse vortices are significantly less intense than quasi-streamwise vortices, with the peak in the distribution appearing at just above the reference intensity value of 0.011. However, occasional intense transverse vortices do occur and are generally found below $y^+ = 75$, as in the case of quasi-streamwise vortices.

If circulation intensity is assumed to determine the potential of a vortex for producing contributions to $-\overline{u'v'}$, the clustering of high-intensity quasi-streamwise vortices near the wall, and the distribution of low-intensity transverse vortices in the outer flow are consistent with the shape of the turbulence production ($-\overline{u'v'} \frac{\partial \bar{U}}{\partial y}$) profile in a boundary layer.

To improve the size of the samples used to construct the distributions shown in Figs. 11.19 through 11.28, a new method for locating vortices in the simulation using software detection criteria is being developed, and will be reported on separately.

11.6 Summary

From the brief literature review presented, the following general conclusions may be drawn regarding vortices as coherent motions in turbulent boundary layers:

- The major vortex elements (quasi-streamwise “legs,” transverse “heads,” and “necks”) all exist within the boundary layer. However, vortex structures of a wide variety of shapes also apparently exist, and the evidence for the prevalence of particular forms (horseshoes, hairpins, rings, etc.) is not yet conclusive.
- The buffer and log regions are dominated by quasi-streamwise vortices with an outward tilt (distributions of tilt angles have been collected and will be published elsewhere). These vortices appear to be kinematically associated with $(u'v')_2$ and $(u'v')_4$ motions, and are probably related to the near-wall streaky structure, although the specific cause-and-effect relationships for the latter remain unclear. Spanwise and 45-degree vortices are more commonly found in the outer region ($y^+ > 100$). These vortices have a consistent kinematical re-

lation to a large fraction of the Reynolds stress production outside the buffer zone, as seen in Chapter 10.

- Horseshoe/hairpin vortex models are consistent with many forms of experimental data, but actual evidence of such vortical structures existing in turbulent boundary layers is limited. As a result, much of the kinematic and dynamic behavior of horseshoe/hairpin vortices is postulated or inferred indirectly from measurable statistics.

Statistical analysis of instantaneous vortices in the numerically simulated boundary layer has added the following new information:

- Transverse vortices are found most commonly in the wake region, quasi-streamwise vortices most commonly in the buffer region, and the overlap of the distributions corresponds roughly with the logarithmic region.
- Transverse vortices are less common, but larger than quasi-streamwise vortices. Most transverse vortices are 30 to 70 viscous lengths in diameter, while most quasi-streamwise vortex diameters range from 10 to 40 viscous lengths. In both cases, vortices nearer the wall are smaller.
- For transverse vortices, the variation of vortex diameter with distance from the wall is similar to the mixing-length distribution.
- Quasi-streamwise vortices possess up to 10 times the mean circulation intensity of the boundary layer, and nearly all show higher intensities than the reference value. Transverse vortices are significantly less intense than quasi-streamwise vortices. For both types of vortex, those nearer the wall tend to exhibit higher circulation intensities.

The findings in Chapters 8, 9, and 10 have implied that vortical structures are the central elements of the coherent motion responsible for turbulence production in boundary layers. Experimental support for this conclusion is broad, although largely indirect due to the difficulty of detecting vortices in the laboratory. There is little counter-evidence in the literature to refute the central role of vortices, but the major geometrical forms and the dynamics of their growth and interaction remain controversial. Chapter 10 has shown that vortices occur with a wide variety of geometries, so that to focus on a single shape could lead to misleading, or at least incomplete results.

Since only a limited class of flows may currently be simulated numerically, there is an obvious need for the development of more robust experimental methods for vortex identification in turbulent flows. Recent advances in multi-sensor hot-wire anemometry (Antonia et al, 1988), scanning two-component laser-doppler anemometry (Williams and Economou, 1987), particle-displacement imagery (Landreth et al, 1988), and digital image pattern recognition (Corke, 1984; Smith and Lu, 1988) may lead to methods by which the conclusions of the current study are extended to more practical flows.

Categories:

- A: Conceptual model (description of physics only)
- B: Analytical model (predictive in some sense)
- C: Probe data evidence (quantitative)
- D: Visual evidence (qualitative)
- E: Laminar boundary layer simulation
- F: Numerical simulation (LES or DNS)

Table 11.1: Quasi-Streamwise Vortex References

Authors	Year	Category
Bakewell and Lumley	1967	B,C
Kline et al	1967	D
Kim et al	1971	C,D
Grass	1971	D
Clark and Markland	1971	D
Willmarth and Lu	1972	C
Brown and Thomas	1977	A,C
Kastrinakis et al	1978	C,D
Praturi and Brodkey	1978	D
Kreplin and Eckelmann	1979	C
Blackwelder & Eckelmann	1979	A,C
Nakagawa and Nezu	1981	A,C
Falco	1982	A,D
Falco	1983	A,D
Smith and Schwartz	1983	D
Kim	1983	C,F
Pearson and Abernathy	1984	B
Moin	1984	B,C,F
Moin and Kim	1985	C,F
Herzog	1986	B,C
Jang et al	1986	B
Kasagi et al	1986	B,C,D
Kim and Moin	1986	C,F
Ersoy and Walker	1986	B
Swearingen & Blackwelder	1987	C,D,E
Acarlar and Smith	1987	A,D
Lian	1987	D
Utami and Ueno	1987	C
Moin	1987	C,F
Moin, Adrian, Kim	1987	C,F
Aubrey et al	1988	B,C
Hanratty	1988	B
Kasagi	1988	B,C,D
Guezennec et al	1989	C,F
Robinson et al	1989	D,F

Table 11.2: Spanwise Vortex References

Authors	Year	Category
Clark and Markland	1971	D
Kim et al	1971	C,D
Nychas et al	1973	D
Praturi and Brodkey	1978	D
Nakagawa and Nezu	1981	A,C
Lian	1987	D
Smith and Lu	1988	C,D
Robinson et al	1988	D,F
Robinson et al	1989	D,F

Table 11.3: Vortex Structure References

Authors	Year	Category
Theodorsen	1952	A
Willmarth and Tu	1967	A,C
Kline et al	1967	A,C,D
Black	1968	A,B
Hinze	1975	A
Offen and Kline	1975	A
Townsend	1976	A,B
Smith	1978	A,D
Head & Bandyopadhyay	1981	A,D
Wallace	1982	A
Perry and Chong	1982	B
Falco	1982	A,D
Falco	1983	A,C,D
Smith and Metzler	1983	A,C
Smith	1984	A
Wallace	1985	A
Moin and Kim	1985	C,F
Kim and Moin	1986	C,F
Guezennec	1986	A,C
Kobashi and Ichijo	1986	A,C
Fiedler	1986	A
Perry et al	1986	B
Acarlar and Smith	1987	A,C,D,E
Utami and Ueno	1987	A,C
Chu and Falco	1988	A,D,E
Smith and Lu	1988	C,D
Kasagi	1988	A,B,C
Robinson et al	1988	D,F
Robinson et al	1989	D,F

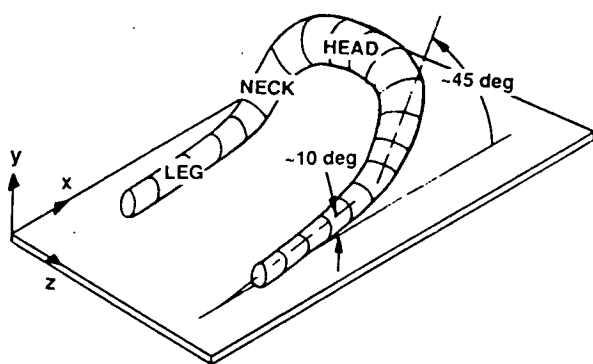


Fig. 11.1. Nomenclature for schematic hairpin vortex.

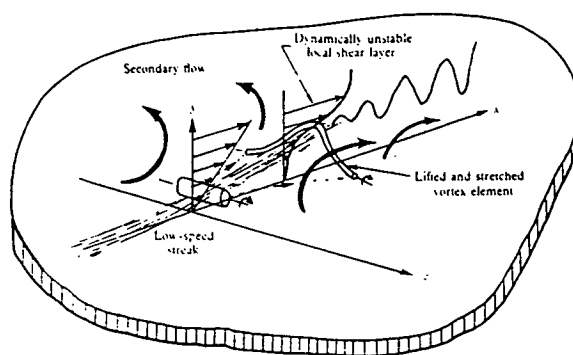


Fig. 11.4. Kline et al (1967). "The mechanics of streak breakup."

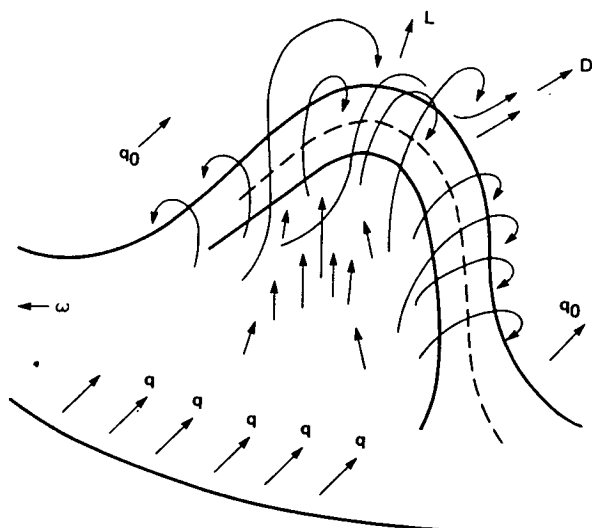


Fig. 11.2. Theodorsen (1952). "Primary structure of wallbound turbulence."

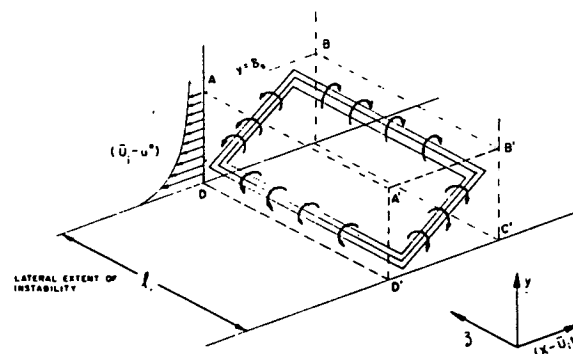


Fig. 11.5a. Black (1968). "Generation of ring-vortices by instability in actual shear layer."

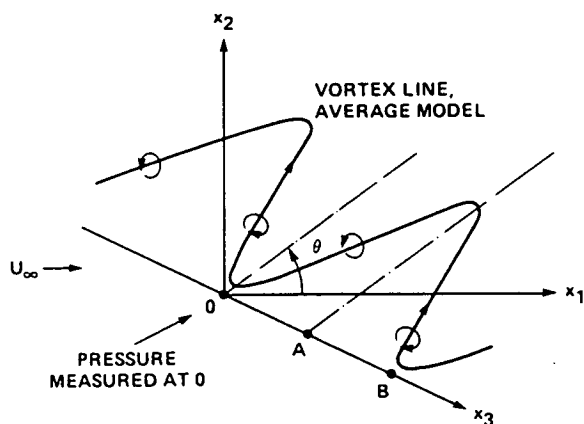


Fig. 11.3. Willmarth and Tu (1967). "Structure of an average model of vortex line near the wall..."

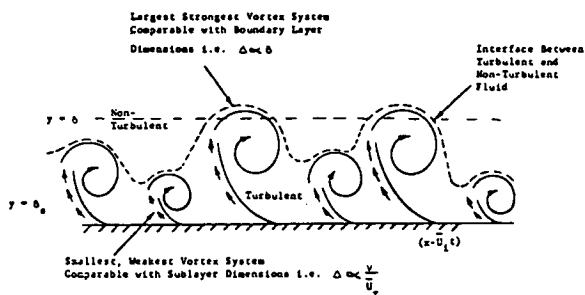


Fig. 11.5b. Black (1968). "Intermittency explained by random variation in strength of consecutive vortex systems."

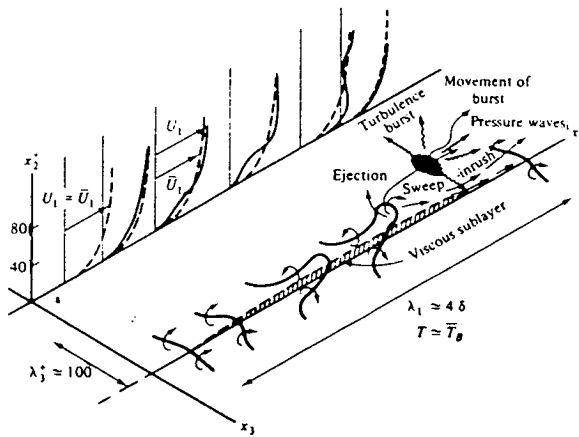


Fig. 11.6. Hinze (1975). "Conceptual model of the turbulence near the wall during a cyclic process, with average spacings λ_1 and λ_2 ."

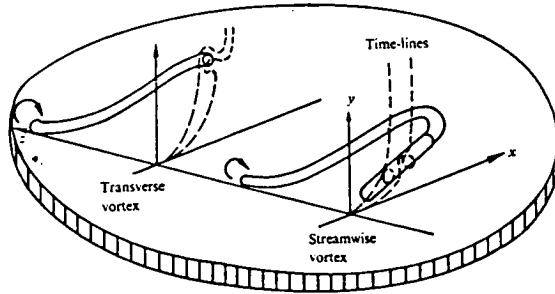


Fig. 11.7. Offen and Kline (1975). "Time-line patterns at different locations of a lifted and stretched vortex element."

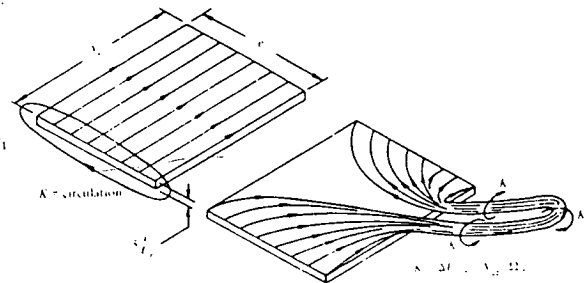


Fig. 11.9a. Perry and Chong (1982). "Carpet of vorticity being wrapped into vortex (schematic)."

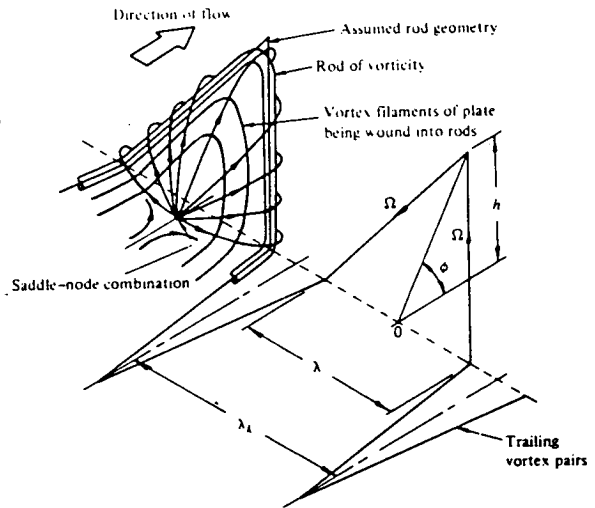


Fig. 11.9b. Perry and Chong (1982). "Λ-vortex configuration".

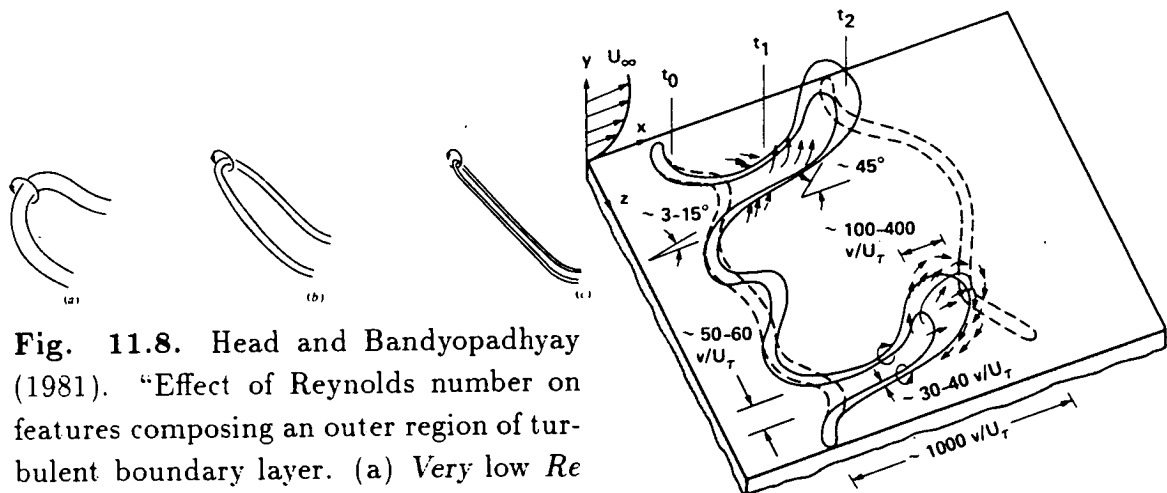


Fig. 11.8. Head and Bandyopadhyay (1981). "Effect of Reynolds number on features composing an outer region of turbulent boundary layer. (a) Very low Re (loops); (b) low-moderate Re (elongated loops or horseshoes); (c) moderate-high Re (elongated hairpins or vortex pairs)."

Fig. 11.10. Wallace (1982, 1985). "Conceptual model of hairpin vortices from warped sheets of vorticity."

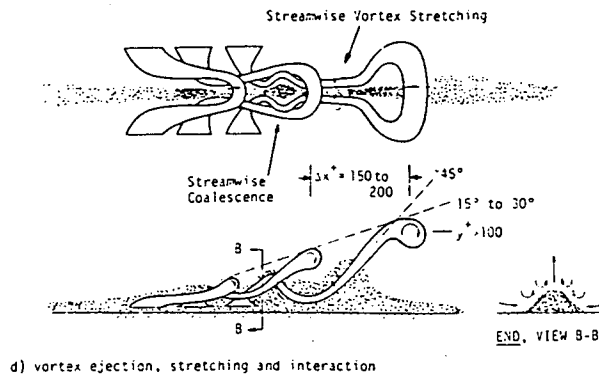


Fig. 11.11. Smith (1984). "Illustration of the breakdown and formation of hairpin vortices during a streak bursting process. Low-speed streak regions indicated by shading."

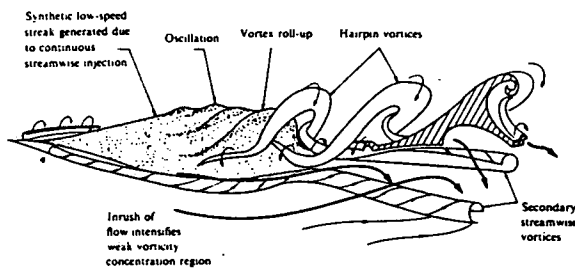


Fig. 11.12. Acarlar and Smith (1987b). "Schematic of breakup of a synthetic low-speed streak generating hairpin vortices. Secondary streamwise vortical structures are generated owing to inrush of fluid."

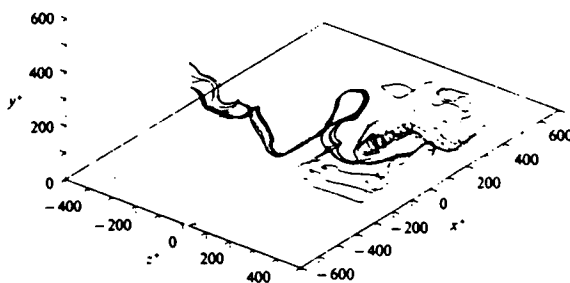


Fig. 11.13. Kim and Moin (1986). "Vortex lines showing an instantaneous structure detected by QD-2."

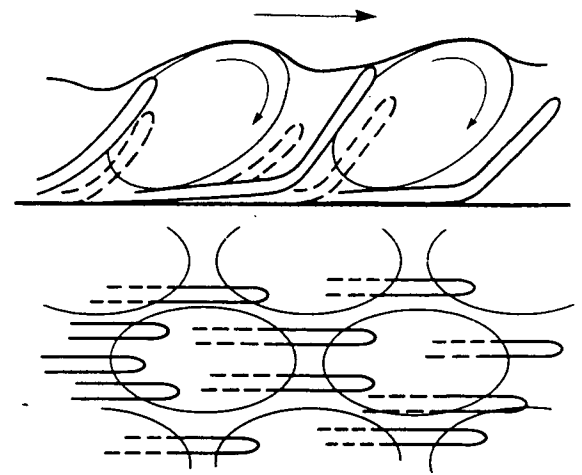


Fig. 11.14. Fiedler (1986). "Boundary layer structure."

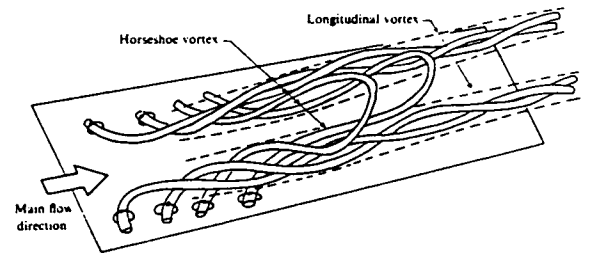


Fig. 11.15. Utami and Ueno (1987). "Conceptual model representing the overall structure of turbulence in the wall region in the fully developed stage. Solid lines denote vortex tubes."

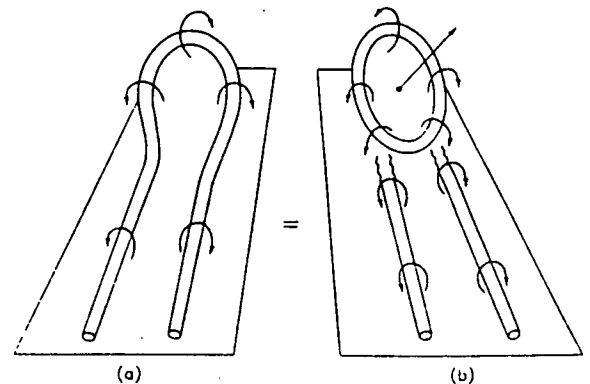


Fig. 11.16. Adrian (1988). "(a) Hairpin vortex close to the wall, (b) decomposition of a wall hairpin into a vortex ring plus mean shear plus two streamwise vortices."

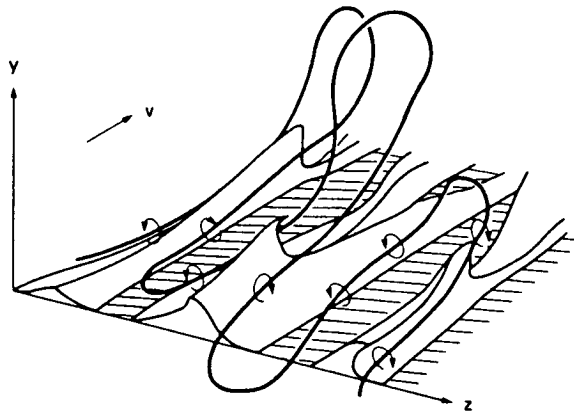


Fig. 11.17. Kasagi (1988). "Conceptual model of the wall-layer structure."

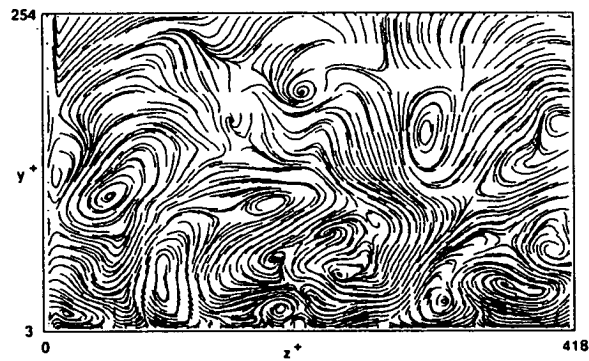


Fig. 11.18a. Example from Spalart's (1988) numerically simulated boundary layer: instantaneous streamlines in an end-view ($y - z$) plane.

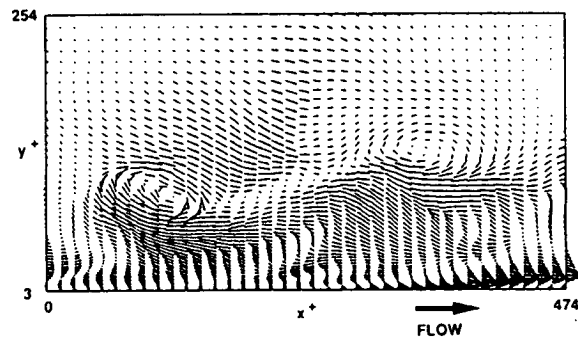


Fig. 11.18b. Example from Spalart's (1988) numerically simulated boundary

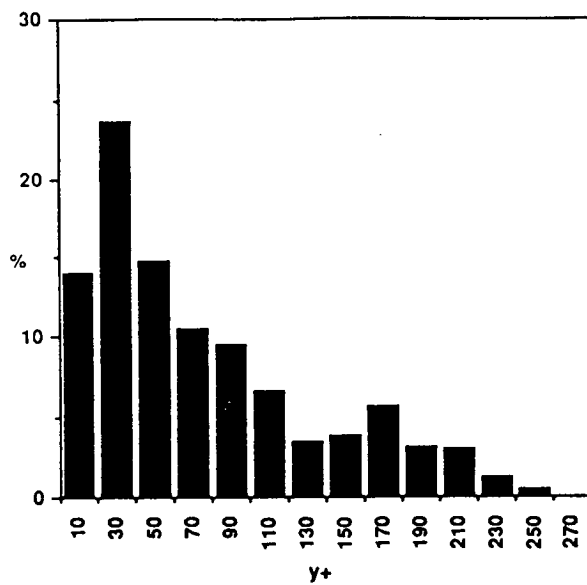


Fig. 11.19. Distribution of distances from the wall for visually-identified quasi-streamwise vortices.

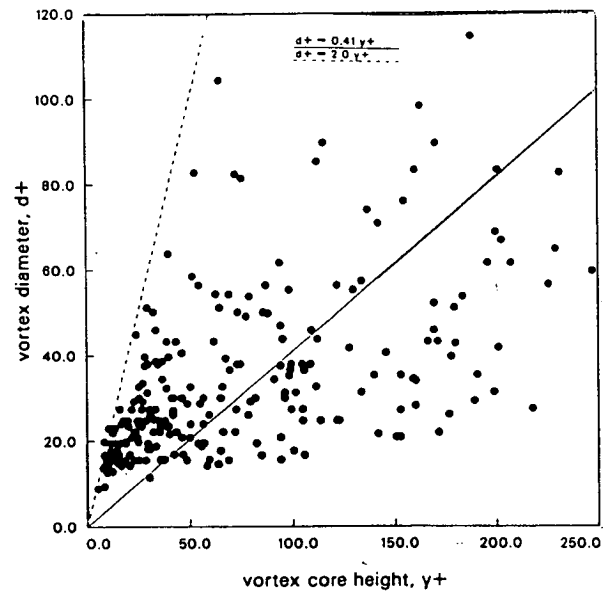


Fig. 11.21. Variation of vortex diameter with distance from the wall for visually-identified quasi-streamwise vortices.

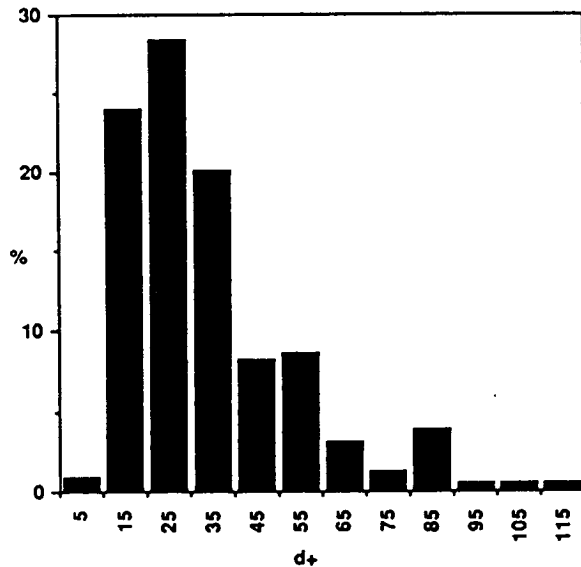


Fig. 11.20. Distribution of vortex diameters for visually-identified quasi-streamwise vortices.

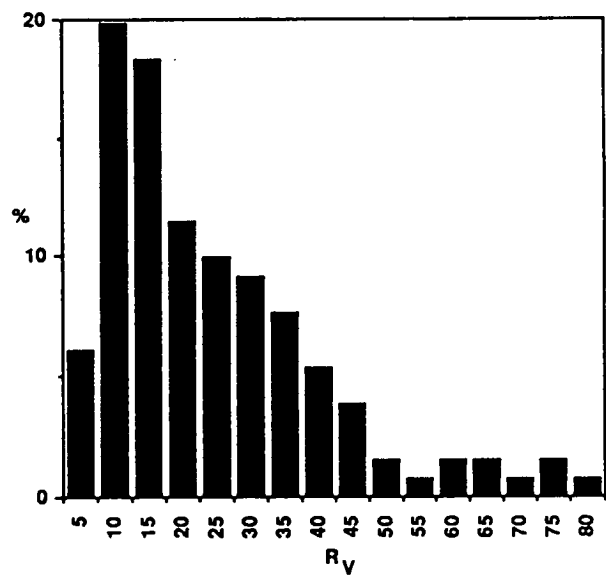


Fig. 11.22. Distribution of vortex Reynolds number R_v (circulation) for visually-identified quasi-streamwise vortices.

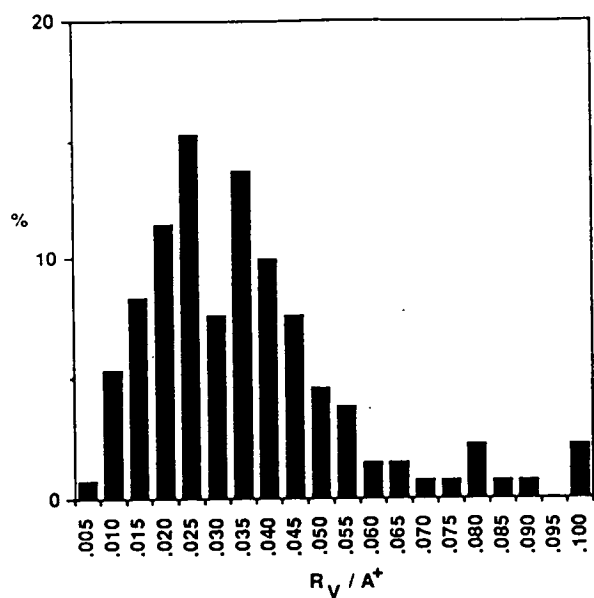


Fig. 11.23. Distribution of vortex intensity (R_V/A^+) for visually-identified quasi-streamwise vortices.

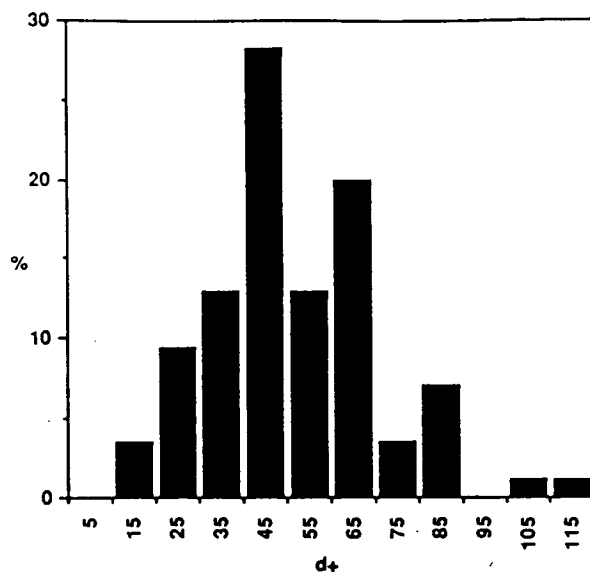


Fig. 11.25. Distribution of vortex diameters for visually-identified **transverse vortices**.

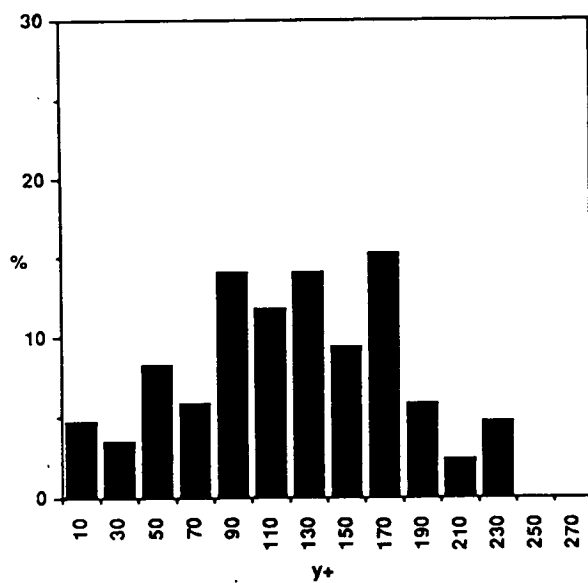


Fig. 11.24. Distribution of distances from the wall for visually-identified **transverse vortices**.

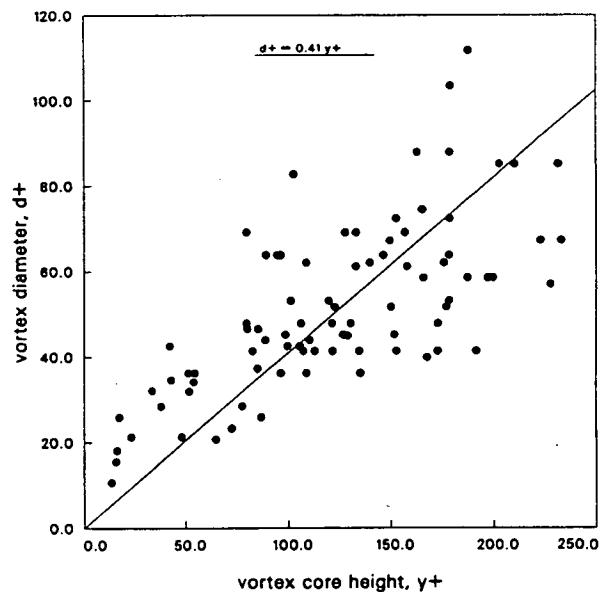


Fig. 11.26. Variation of vortex diameter with distance from the wall for visually-identified **transverse vortices**.

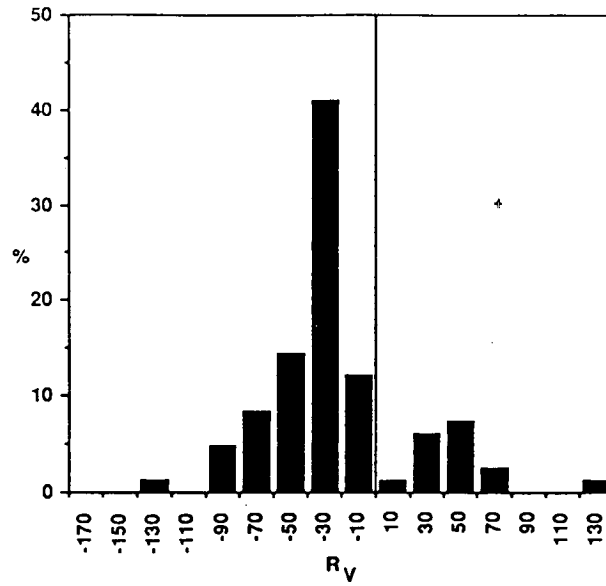


Fig. 11.27. Distribution of vortex Reynolds number R_V (circulation) for visually-identified **transverse vortices**.

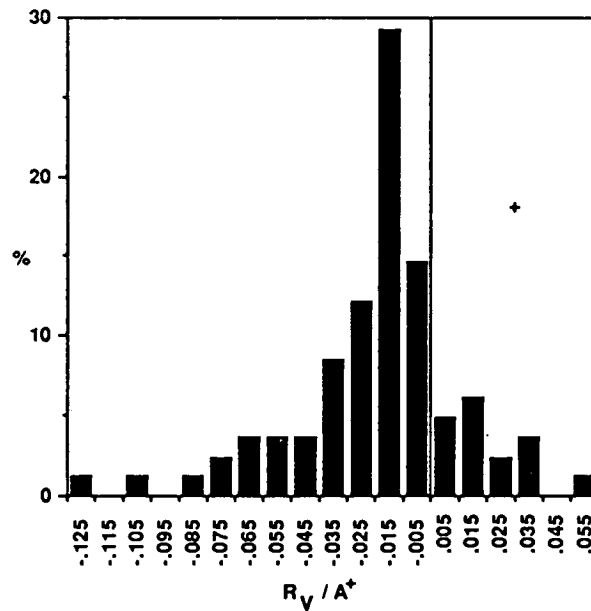


Fig. 11.28. Distribution of vortex intensity (R_V / A^+) for visually-identified **transverse vortices**.

CHAPTER 12 - CONCLUSIONS

The previous chapters have presented the results of utilizing a direct numerical simulation to investigate the character and inter-relationships between the known types of coherent motions in turbulent boundary layers. The major conclusions of this effort are as follows:

- 1) Vortical structures may be considered central to the process of turbulence production by coherent motions in the boundary layer. A unified picture of coherent structure is impossible without vortical structures serving as the framework and the “glue” that binds together the many disparate structural elements. With knowledge of this framework, most of the structural results available in the literature may be fit together to form a consistent picture with surprisingly little disagreement.
- 2) No single form of vortical structure may be considered representative of the wide variety of shapes taken by vortices in the boundary layer. Quasi-streamwise vortices, transverse vortices, one and two-sided arches, and one and two-sided hairpins all exist, and occur with frequencies that depend on distance from the wall. However, asymmetric vortical structures are the most common, while complete, symmetric hairpin vortices are rare compared to other shapes.
- 3) Throughout the boundary layer, $(u'v')_2$ and $(u'v')_4$ contributions to the Reynolds shear stress are strongly associated with vortical structures. Nearly all strong ejections and sweeps are found adjacent to vortical structures and virtually all vortical structures with significant circulation are adjacent to $(u'v')_2$ and/or $(u'v')_4$ motions. Because of this association, ejections are considerable more intermittent in space than in time, which leads to a different view of the “bursting” process than that commonly accepted.
- 4) Previously poorly understood sweep and inrush motions have been found to exhibit spanwise length scales similar to the diameters of the vortices they are usually associated with, and are not broad, δ -scale motions. The role of $(u'v')_4$ motions in entrainment, communication between the outer and inner regions, and contribution to $-\overline{u'v'}$ has been clarified by the current results.
- 5) Low-pressure regions in the boundary layer are strongly associated with the cores of strong vortices, and the cores of near-wall vortices can produce significant low-pressure regions at the wall. High-pressure regions are generally formed when high-speed fluid impacts the upstream side of low-speed fluid, creating a convecting, quasi-stagnation point. Most high-pressure regions at the wall are confirmed to arise from this mechanism, which is manifested as a highly sloped near-wall shear layer. Local regions of intense quasi-periodic wall-pressure fluctuations are often associated with the multiple rollup of transverse vortices atop a wall low-speed streak.

These conclusions are valid for the numerically simulated, $Re_\theta = 670$ canonical

boundary layer of Spalart (1988), and may in some aspects be limited to low Reynolds number boundary layers.

This final chapter will generalize the kinematic relationships between structures, characterize the major boundary layer zones in terms of the dominant vortical structures, and present preliminary speculations concerning the dynamics of vortices and turbulence generation. Sections 12.2 and 12.3 fulfill one of the major objectives of the work by outlining the elements of a kinematic model of boundary layer structure, which has been developed by utilizing new results from the DNS boundary layer to blend together the consistent and best-documented aspects of several previously published conceptual models.

12.1 Conclusions Regarding the Key Controversies

The most controversial issues in the field of boundary layer structure have long been:

- 1) The bursting process
- 2) Near-wall streak formation
- 3) Mass and momentum transfer from the inner to the outer layers
- 4) Mass and momentum transfer from the outer to the inner layers
- 5) The existence and role of hairpin/horseshoe/ring vortices

The information gained from the simulated boundary layer in each of these categories is reviewed below.

12.1.1 The Bursting Process

“Bursting” is the term popularly used since Runstadler et al (1963) to refer to the production of turbulence in the boundary layer via violent outward eruptions of near-wall fluid. This concept is commonly invoked in the literature of turbulence physics, but the definition and usage of the term “bursting” has long been a source of confusion and mis-communication. The meaning of the term has evolved over the years, but in an accumulative sense, such that several meanings are now ascribed to “bursting,” without universal agreement as to the proper one. A partial history of usage is as follows:

- Violent breakup of a low-speed streak after lifting (Runstadler et al 1963, Kline et al 1967).
- Three-stage process of low-speed streak lift-up, oscillation, and breakup (Kim et al 1971, Blackwelder 1989).
- Shear-layer interface sandwiched between an upstream, high-speed “sweep” and a downstream, low-speed “ejection” (numerous authors, early seventies - present).
- Occurrence of a single-point event found by a specified detection criterion, usually VITA or Quadrant (numerous authors, mid-seventies - present).

- One or more $(u'v')_2$ ejections emanating from a single low-speed streak (Bogard and Tiederman 1986, Talmon et al 1986).

In addition to these definitions of bursting, there are many hypothesized **causes** of the bursting process, most of which involve a vortical structure of some type (see Robinson 1989). The non-unique meanings associated with the term have prompted me to exclude “bursting” from the taxonomy of Chapter 5 in favor of more tightly defined structural elements of the turbulence-production processes. Together, these better-defined elements describe the various various events which have been called “bursting” in clearer ways.

Most definitions of the bursting process describe a highly intermittent, explosive event, which is an intuitively satisfying concept for the production of turbulent motion. However, a significantly different picture emerges from the study of numerically simulated turbulence. In this alternate scenario, the manner in which turbulence is produced in the near-wall region is not actually “burst”-like, and appears to be much more intermittent in space than in time. In other words, turbulence production regions (ejections and sweeps) in the buffer layer appear spotty in the instantaneous $x - z$ plane, but persist for significant temporal durations as they move downstream. The passage of such a production region past a stationary probe or aggregation of fluid marker would produce sudden velocity excursions at the measurement station over a limited time, without making clear the passage of an associated vortical structure.

The simulation results show clearly that the low Reynolds-number near-wall turbulence maintenance process is dominated by tilted quasi-streamwise vortices, with diameter and strength distributions as given in Chapter 11. Thus, it is concluded from the current study that *the low Reynolds-number bursting process as seen from a stationary location is interpreted as the passage of a relatively long-lived, single, quasi-streamwise vortex, which ejects low-speed fluid away from the wall by vortex induction.* (See also Kim and Moin 1986, Kim 1987, and Guezennec et al 1989). Near-wall arches and transverse vortices also generate strong ejection motions, but are outnumbered by quasi-streamwise vortices in the buffer region, where the bursting process is observed to originate.

There is so far little quantitative evidence to support this alternative view of bursting, although descriptive reference to vortex passage is made by Black (1968), Clark and Markland (1971), Kim et al (1971), Acarlar and Smith (1987b), and others. Explicit experimental agreement is available from Nakagawa and Nezu (1981), who state in their conclusions that “the bursting motion is a kind of large-scale eddy structure, and its coherent structure is fairly inclined downstream toward the wall. It is convected downstream with a longer lifetime than the bursting passing-period...”. Confirming results for long-lived production regions in numerical channel flow are provided by Alfredsson et al (1988).

In summary, there are currently two general concepts in use for the term “bursting:” 1) A violent, temporally intermittent eruption of fluid away from the wall. A form of local instability is often implied in this case; 2) A localized ejection of fluid from the wall, caused by the passage of one or more tilted, quasi-streamwise vortices, which persist for considerably longer time-scales than do the observed ejection motions. Since both concepts usually involve vortical structures, the main difference between the two is the degree of temporal intermittency, and whether or not an instability is involved. The results of the current study strongly support the second of these concepts.

12.1.2 Wall-Streak Formation

The formation mechanism(s) for the sublayer streaky structure requires additional clarification. This and previous numerical simulation studies have shown convincingly that long pairs of streamwise counter-rotating vortices do not flank low-speed streaks (e.g. Kim and Moin, 1979), but several alternative theories are available. From the current investigation, the most likely scenario is that of **single** quasi-streamwise vortical elements convecting downstream, leaving near-wall low-speed fluid trailing from the upward-rotating side of the vortices, and high-speed fluid on the opposite side (see Fig. 12.1). Since the streamwise velocity gradient is steepest near the wall, lifting low-speed regions would undergo more severe shearing action than high-speed regions arriving from further out, which would result in low-speed streaks being longer than high-speed regions. This streak-formation hypothesis is consistent with all of the evidence available from the current simulation. (Lee et al, 1987, show that a streaky structure also exists in highly sheared homogeneous turbulence, without the existence of quasi-streamwise vortices, so the vortices in the boundary layer may serve to exacerbate a condition which already tends to exist.)

There is little evidence to support the necessity of vortex pairs for streak formation, and significant evidence which refutes the idea. Also, it appears from time-evolutions of the DNS boundary layer that the formation of small arch-shaped vortices atop low-speed streaks helps maintain some streaks by “extruding” the low-speed fluid through the arch as it travels downstream (Fig. 12.14). These remarks regarding streak formation are largely inferences from the observed behavior, and cannot be classified as strong conclusions.

12.1.3 Outward Interactions

One of the oldest of turbulence structure controversies concerns the importance, direction, and form of communication between the inner and outer regions in a boundary layer. As shown in Kline and Robinson (1989a), the sum of inward and outward interactions is expected to play a relatively minor role in boundary layer physics, but the question remains as to how the interactions take place.

For the case of near-wall activity affecting the outer layer (outward interaction), communication occurs at two different rates: 1) A rapid transfer of momentum from the wall to the outer region through unusually energetic buffer region ejections. This has experimentally been shown to occur for at least low Reynolds number flows (e.g. Kim et al, 1971), but has not been investigated in the current study; 2) The relatively gradual outward migration of transverse head vortices (and associated necks, if present). This motion has been observed in the present study, and is supported by a number of flow-visualization experiments (e.g. Praturi and Brodkey, 1978; Head and Bandyopadhyay, 1981).

Although the relative importance between the two types of outward interactions can not be ascertained from the present results, the second type is likely to influence the outer layer more actively, since outward migration of vortices apparently supplies the wake region with the vortical structures which are ultimately responsible for entrainment. (See also Section 12.4.3.)

12.1.4 Inward Interactions

From the study of the DNS boundary layer, it appears that the outer region affects the near-wall region mainly through vortex-induced intrushes and sweeps. Intrushes are narrow in the spanwise direction, and the frequency with which they extend from the edge of the boundary layer to the wall is likely to decrease with increasing Reynolds Number. The notion of δ -scale, sloping shear layers passing over the wall region and “setting off” turbulence production events (e.g. Corino and Brodkey, 1969; Brown and Thomas, 1977) is not supported by the current results. Scaling arguments also work against this theory, as near-wall regions of high $-u'v'$ are more closely-spaced than δ in both x and z . Although the evidence for direct outer-to-inner region interaction is strong for the low Re simulated boundary layer, the inner region is clearly capable of maintaining turbulent flow by itself. As discussed by Kline and Robinson (1989a), the outer region can be expected to play a role in approximately 20% to 30% of the turbulence production in the buffer region.

12.1.5 Hairpin, Horseshoe, and Ring Vortices

The attractive concept of arrays of hairpin vortices (e.g. Head and Bandyopadhyay, 1981) filling the boundary layer is not well-supported by the current investigation, at least at these very low Reynolds numbers. As demonstrated in Fig. 10.6.4, vortical structures in the DNS flow come in a wide variety of forms. Nevertheless, arch-like vortices are common, though generally asymmetric, and the horseshoe shape is likely to provide a useful model for the log and wake-region statistics (e.g. Perry et al, 1986). For dynamical considerations, however, the symmetric hairpin/horseshoe geometry is probably inappropriate, as occurrences of paired counter-rotating legs are rare in the present flow, and spanwise interaction

scales are more often related to single vortex legs and necks (see Section 12.4.5). Using the vortex detection methods outlined in Chapter 9, no ring-shaped vortices were identified in the numerically simulated boundary layer. The lack of vortex rings may be due in part to inadequate resolution in the computational grid; however, the structure that does exist provides turbulence statistics which match experiments to a fine level of detail.

12.2 Kinematic Relationships Between Vortices and Other Structures

The current study of the numerically simulated turbulent boundary layer began with examination of all eight structure classes listed in Chapter 5. As the results given in Chapters 8-10 were accumulated, the emphasis gradually shifted toward vortical structures because of their pervasive presence in the vicinity of nearly all structures of interest. Eventually it became clear that each type of coherent motion was related to vortical structures in kinematically consistent ways, leading to the major conclusion that vortical motions are central to the sequence of events responsible for turbulence production throughout the boundary layer. Investigation of individual realizations, rather than traditional statistical analysis, led to the conclusion that several statistically relevant vortical forms exist, instead of just one. Analysis of single realizations and of time-sequences also showed that the production and dissipation of turbulence kinetic energy are generally related to vortical structures in more than one way and apparently involve non-unique dynamical mechanisms. This result may help explain the lack of apparent convergence in many aspects of probe-based turbulence structure studies.

To generalize the findings of the present work, the kinematic relationships between vortical structures and each of the remaining classes of coherent motion are described in schematic form below. A few of the points cross into the realm of dynamics, but kinematics and dynamics are often logically inseparable. For conciseness, the points are made in bullet format.

INNER ZONE: BUFFER and LOG REGIONS

12.2.1 Inner-Region Vortices and Low-Speed Streaks

- Low-speed streaks may be left behind by single near-wall quasi-streamwise vortices (counter-rotating pairs are rare and not necessary) (Fig. 12.1).
- The initial widths of low and high-speed streaks are similar to the quasi-streamwise vortex diameter (Fig. 12.1).
- Vortical arches can “roll up” upon lifted low-speed streaks through local shear-layer instability (Figs. 12.14, 12.15).
- Young vortical arches can re-form low-speed streaks after vortex formation (Fig. 12.14).
- A cyclic relationship exists between streaks and vortices: vortices create and maintain streaks, lifted streaks give rise to new vortices (Fig. 12.19).

12.2.2 Inner-Region Vortices and Ejections/Sweeps

- Ejections occur alongside single tilted quasi-streamwise vortices, with occasional contributions by counter-rotating pairs (Fig. 12.2).
- Sweeps occur primarily alongside single tilted quasi-streamwise vortices (Fig. 12.2).

12.2.3 Inner-Region Vortices and Near-Wall Shear Layers

- Near-wall shear layers are created when relatively high-speed fluid impacts low-speed fluid lifted by a quasi-streamwise vortex (Fig. 12.3).
- Near-wall shear layers are also created when relatively high-speed fluid impacts the kinked side of a low-speed streak, as per Alfredsson et al (1988) (Fig. 12.3).
- Near-wall shear layers may roll up into transverse vortices or arches (Fig. 12.15).

12.2.4 Inner-Region Vortices and Near-Wall Pressure Field

- High-pressure quasi-stagnation points occur at the shear-layer interface between low-speed fluid lifted by quasi-streamwise vortex and the upstream high-speed fluid (Fig. 12.4).
- The pressure at the wall directly beneath a near-wall vortex is reduced by the low-pressure vortex core. Wall-pressure is increased in the region where fluid is induced toward the wall by the vortex. (Fig. 12.4).

12.2.5 Inner-Region Vortices and Pockets

- Sublayer pockets are found beneath wallward flow alongside the downward-rotating side of near-wall quasi-streamwise vortices and near-wall necks (Fig. 12.5).
- One or two weak streamwise vortices may arise due to redirection of wallward fluid found alongside trailing edges of pockets (Fig. 12.5).
- Pocket look-alikes can occur in the lower log layer between two vortical arches with small streamwise separation (Fig. 12.6).

12.2.6 Inner-Region Vortices and Dissipation

- Near-wall dissipation occurs mainly in the cores of rapidly stretching quasi-streamwise vortices, and in the high velocity gradients associated with near-wall shear layers. (Fig. 12.7)

OUTER ZONE: LOG and WAKE REGIONS

12.2.7 Outer-Region Vortices and Ejections/Sweeps

- Ejections occur upstream and below one or two-sided vortical arches (arches are head/neck combinations) (Fig. 12.8).
- Strong sweeps occur primarily on the outboard side of tilted necks; weak sweeps often occur on the downstream side of heads (Fig. 12.8).

12.2.8 Outer-Region Vortices and LSMs, Bulges, Backs

- The back (angle ≈ 30 degrees) of large-scale motion is found at interface between low-speed fluid left behind by an outer-region vortical arch (one or two-sided) and the following higher-speed fluid. The back is highly contorted and three-dimensional, and may reach to the wall (Fig. 12.9).
- New outer-layer transverse vortices sometimes roll up on backs through an apparent shear-layer instability (Fig. 12.9).
- A three-dimensional bulge in the turbulent/non-turbulent interface occurs above a large-scale transverse vortex (or head). However, not all bulges have large vortices within them; bulges may form from upwelling fluid and in any case may retain their shape after the causal mechanism has dispersed (Fig. 12.9).

12.2.9 Outer-Region Vortices and Inrushes/Entrainment

- Irrotational flow is entrained on downstream side of heads (Fig. 12.10).
- Irrotational flow is also entrained alongside necks of vortical arches; inflows sometimes reach to wall region for low Re flows (Fig. 12.10).

12.2.10 Outer-Region Vortices and Pressure Field

- High-pressure quasi-stagnation points occur at the interface between low-speed fluid left behind by vortical arch and upstream high-speed fluid (Fig. 12.11).
- High-pressure quasi-stagnation points occur at the interface between high-speed fluid alongside a neck and pre-existing low-speed fluid below the sweep (Fig. 12.11).

12.2.11 Outer-Region Vortices and Dissipation

- Dissipation is high in the stretching necks of arch-shaped vortices, but low in the transverse heads, where vortex-stretching is weak. As an apparent result, transverse vortices persist for much longer times (and are convected farther downstream) than neck and leg vortex elements, which are stretching and dissipating rapidly (Fig. 12.12).

12.3 Kinematic Characterization of the Boundary Layer via Vortical Models

In the average sense, a basic physical aspect of an equilibrium boundary layer is the existence of different scaling laws for the inner and outer regions. Both laws hold in an overlap (log) region. For physical realizability, a conceptual model of turbulence structure must reflect the duality of scale by varying its character for each region of the boundary layer. Thus, the kinematic model described below is constructed differently for the buffer, logarithmic, and wake regions. Since the various classes of coherent motion may be associated with vortical structures in the manner described in the previous section, the boundary layer may be represented

in its simplest conceptual form by arrays of vortical structures. All of the zones are illustrated in Fig. 12.13.

12.3.1 Buffer Region

In the conceptual model, the buffer region is dominated by single, quasi-streamwise vortices with a mean upward tilt ranging from 5 degrees at $y^+ = 15$ to approximately 15 degrees at $y^+ = 30$. Mean diameters increase with distance from the wall; location, diameter, and circulation distributions are as given in Chapter 11. Since there is not a unique association between near-wall quasi-streamwise vortices and low-speed streaks, the mean spanwise spacing between vortices should be greater than the mean spanwise streak spacing of 100 viscous lengths.

12.3.2 Logarithmic Region

The log layer is the overlap zone between the wall and outer regions, so it is appropriate that two types of vortical structure co-exist in the log layer. In the model, both quasi-streamwise vortices and vortical arches (one and two-sided) are present, as shown by the overlap of the location distributions in Chapter 11. Quasi-streamwise and transverse vortices may often be connected, but for a purely kinematic model this is unimportant (but of critical importance for a dynamic model). Quasi-streamwise vortices occur at mean angles ranging from 15 to 30 degrees, with distributions as given in Chapter 11. The transverse span of arches approximates the width of the low-speed streaks at the bottom of the log layer, and the span grows as an approximately linear function of distance from the wall for other locations in the log zone. The diameter and circulation of arches are approximated by the distributions for transverse vortices given in Chapter 11. The relative population of quasi-streamwise vortices vs. vortical arches varies with increasing y^+ until only arches exist at the start of the wake zone.

12.3.3 Wake Region

The wake region is populated by one and two-side vortical arches, with necks that descend at 45 degree angles to the wall plane. Diameter and circulation distributions are as given for transverse vortices in Chapter 11. The transverse scale of vortical head elements is approximately equal to its distance from the wall. Spacing in x and z is on the order of δ .

12.4 Dynamical Speculations: Vortical Structure Formation and Evolution

The formation and, to some degree, the evolution of vortical structures in the boundary layer are dynamical issues, and so may only be speculated upon from the current passive observations. Therefore, the hypotheses below are not so much conclusions of the present investigation as they are a starting point for a true dynamical study of vortical motions. Nevertheless, time sequences of the

DNS boundary layer have provided completely new opportunities for the study of turbulent structure evolution, and the interpretations represent some novel and provocative ideas for further study.

12.4.1 Near-Wall Arch Formation

Although instabilities in the 3-D, unsteady, viscous world of the turbulent boundary layer are poorly understood, it is a nearly universally-accepted speculation that transverse or arch-shaped vortical structures form (“roll up”) on the tops and/or sides of near-wall low-speed streaks due to the inflectional (and presumably unstable) velocity profile associated with the sharp velocity gradient at the interface of the streak and the surrounding high-speed fluid (Figs. 12.14 and 12.15).

Evidence of this rollup process has been observed to occur frequently in animations of the DNS boundary layer, and small arches tightly straddling low-speed streaks are fairly common in frozen-time samples.

12.4.2 Near-Wall Quasi-Streamwise Vortex Formation

Considering the importance of quasi-streamwise vortices to the production of turbulence kinetic energy in the buffer region (Section 12.2, 12.3), the question of how quasi-streamwise vortices are formed is of major relevance to the understanding of boundary layer dynamics. Three different possibilities have emerged from the present work; two are adaptations of ideas from the literature and one (#2 below) is apparently new (Fig. 12.16):

- 1) A vortical arch forms on a low-speed streak, with a well-developed leg extending into the lower buffer zone across a high streamwise velocity gradient. As the arch (or hook) convects downstream, the leg is rapidly stretched by the velocity gradient into a tilted quasi-streamwise vortex of significant circulation. Viscous dissipation due to the intense stretching eventually destroys the vortex.
- 2) A neck descends from a “mature” vortical arch or hook into low-momentum near-wall fluid. As the parent arch convects downstream, the descending neck is rapidly stretched into an elongated vortex leg, which eventually dissipates or breaks off. The process may be repeated over and over, with any number of quasi-streamwise vortices being spawned by a single long-lived arch or hook in the outer layers.
- 3) Fluid impacting the wall is redirected to the sides, rolling into one or two near-wall streamwise vortices. This is basically the concept of the “pocket vortex” described by Falco (1983) (see also Fig. 12.5).

Evidence of each of these processes, especially #2, have been detected in the DNS boundary layer, but it is unclear at present which is statistically dominant. It would appear that #'s 1 and 2 are most important dynamically, since they involve rapid vortex stretching while #3 does not. As implied schematically in Fig. 12.5, the

“pocket vortices” produced by mechanism #3 appear to be weaker than the parent quasi-streamwise vortex element.

12.4.3 Outward Growth of Arches

The outward growth of arch-like vortical structures is usually attributed to inviscid circulation lift acting on the fluid particles within the head element ($L = -\rho U\Gamma$). For a transverse vortex with rotation in the direction of the mean shear, outward lift requires a streamwise relative velocity or, equivalently, the vortex must be moving downstream at less than the local mean speed. This is likely to be the usual case since, if a transverse vortex forms on a low-speed streak near the wall, it is surrounded by higher-speed fluid which provides the initial outward impulse. Thereafter, the vortex is moving into increasingly higher-speed fluid so the lift vector is always away from the wall. Note that the outward velocity of the vortex will diminish as $\partial u/\partial y$ decreases with y .

In time-sequences of the simulated boundary layer, transverse vortices are observed to migrate outward gradually. A few vortices move wallward, and these may be the rare cases in which the vortex finds itself moving faster than the local flow, reversing the sign on its lift vector. Also, some transverse vortices, rotate in the direction opposite to the mean shear, and these would presumably migrate wallward.

12.4.4 Outer Region Transverse Vortex Formation

It is commonly presumed that transverse vortices in the outer region get there from the wall region by the outward migration described in the previous section. However, Nychas et al (1973), followed by Praturi and Brodkey (1978), described the apparent rollup of relatively large-scale transverse vortices along outer-region shear layers. This implies a more dynamic outer region, and one that may be able to maintain its turbulence in the absence of wall region activity. However, it is known that the outer region quickly perishes upon suppression of the near-wall turbulence (Uzkan and Reynolds, 1967). Outer-region rollups are evident in some of the time-sequences of the simulated boundary layer, but they are infrequent compared to the observed rollup of near-wall shear layers. Outer-region rollups tend to occur along the backs of large-scale motions in the outer region, where high-speed fluid slides up the trailing face of a wedge of low-speed fluid (Fig. 12.17). This scenario is somewhat different from that of Nychas et al (1973), but is in agreement with flow visualizations by Falco (1977).

12.4.5 Vortex Regeneration Patterns

Smith (1984) has proposed a mechanism by which hairpin vortices generate similar offspring from secondary vortices which roll up along the low-speed fluid lifted between the legs of the parent hairpin (Fig. 12.18a). This process has been observed to occur behind near-wall vortical arches in the numerically simulated

flow; an example is the smaller vortex loop and its offspring in Fig. 10.6.8b (in the center of the picture, near the back grid).

Another, more common, regeneration mode has been observed in the present study, however. In this mode, low-speed fluid lifted by a **single** vortex leg gives rise to a secondary vortex through a presumed shear-layer instability (Fig. 12.18b). The important difference between the two vortex regeneration mechanisms is the spanwise scale of the offspring vortices. In Smith's mechanism, the transverse scale of the secondary vortex is determined by the distance between the legs of the parent vortex, as shown in Fig. 12.18a. In the new process, a counter-rotating pair of legs is not required, and the transverse scale of the secondary vortex is set by the diameter of the original quasi-streamwise vortex, resulting in a completely different regeneration pattern (Fig. 12.18b). The second of these mechanisms is considerably more common in the simulated boundary layer. While Smith's mode occurs only for small parent arches, the new mode seems to occur from isolated, newly-formed legs as well as from stretched "descenders" from mature arches or hooks.

12.4.6 Summary: Vortex Evolution

The main conclusion of this study is that the self-maintaining cycle of turbulence production in a boundary layer is driven by (or perhaps equal to) the formation and regeneration of embedded vortical structures. The hypotheses of the previous sections concerning the dynamics of these vortices are summarized in Fig. 12.19. In the figure, a mature vortical arch (generally one-sided or at least lopsided) gives rise to a trailing quasi-streamwise vortex. As discussed in Sec. 12.4.2, this is only one of several mechanisms by which quasi-streamwise vortices may be formed. Regardless of how they arise, quasi-streamwise vortex elements collect and lift low-speed near-wall fluid, leaving behind a persistent low-speed streak. Relatively high-speed fluid scrubbing the vortex-lifted low-speed fluid creates a shear layer which rolls up into a new vortical arch (again possibly lopsided) through an instability mechanism presumed to be similar to that of an inviscid, steady shear layer. The new arch grows outward by agglomeration and/or self-induction and circulation lift, and the cycle can repeat itself. Transverse vortex elements (such as heads of arches) do not undergo severe stretching and thus their dissipation level is much lower than the rapidly-stretched quasi-streamwise vortices near the wall. As a result, transverse elements are far more persistent than the very dynamic quasi-streamwise vortices.

The schematic shown in Fig. 12.19 is highly idealized; the mechanisms proposed operate in a highly turbulent environment which no doubt influences their dynamics. Also, the model is intended to describe only the low Reynolds number canonical boundary layer, although several of its features may be more universal. It is of particular importance to note that many aspects of boundary-layer structure dynamics occur in more than one way. This non-uniqueness may limit the effectiveness of some turbulence control methodologies, and certainly complicates matters

when trying to distinguish cause from effect.

12.5 Future Research Issues

The conceptual kinematic model presented in this chapter is primarily a combined product of a number of models that have gone before, but with several of the conceptual gaps filled by study of the DNS boundary layer. The model is reminiscent of Smith's (1984) model, but without the symmetry of counter-rotating leg vortices and closely-nested hairpins. Townsend's (1976) single roller eddy is certainly consistent with many aspects of the present model, and the outer-region concepts are basically inherited from Kovasnay et al (1970), Brown and Thomas (1977), Falco (1979), and others. Elements of Praturi and Brodkey (1978), Offen and Kline (1975), Head and Bandyopadhyay (1981), and several others' models are included. The objective of developing a combined model by using the DNS database to fill the gaps left in the literature appears to have been met, at least for a kinematic concept. With the perspective provided by extended study of both the literature as a whole and of the numerical boundary layer, many perceived disagreements in the community are now recognizable as different statements of the same phenomena, or as referring to disparate parts of the complex whole. From this new perspective, there is an unexpected degree of consensus and convergence in the body of turbulent structure knowledge.

For canonical boundary layers, progress in the past decade has been rapid and gratifyingly convergent when compared to the widely disparate conclusions drawn in the earlier years. However, major open issues remain; these research needs can be organized into five categories:

- 1) Kinematics: Further characterize vortical structures and internal shear-layers, including their relationships to turbulence production and dissipation, temporal longevity, rates of growth and decay, strength, topologies and shapes, passage frequencies, and typical space-time trajectories. Also strengthen knowledge of feed-back between wall-pressure fluctuations and near-wall events.
- 2) Dynamics: Vortex and shear-layer formation dynamics, growth mechanisms, interaction modes, and their sensitivity to Reynolds number variations. Increased understanding of unsteady, three-dimensional shear-layer instabilities. More complete understanding of inward and outward interactions, and their Reynolds-number dependencies. Clarify scaling laws for near-wall production events. Better understanding of near-wall streak formation and reasons for constant mean transverse spacing.
- 3) Links between numerical simulations and experiments: Simulate experimental techniques such as flow visualization, particle-tracking, and hot-wire probes in numerical turbulence. Use simulation results to develop experimental methods for detecting and quantifying vortices in laboratory flows. Use simulations

to develop event detection and control schemes for turbulence modification in the laboratory. Extend numerical results to higher Reynolds numbers with experiments.

- 4) Non-canonical boundary layers: Effects of pressure gradients, compressibility, density stratification, wall roughness, three-dimensionality, non-equilibrium, unsteadiness, free-stream turbulence, and combinations of the above.
- 5) Links to modelling: Provide physical insight for Reynolds-averaged modelling efforts. Eventual development of “structural/statistical” model for predictive use.

The unsolved dynamical issues are clearly the most important in terms of “understanding” boundary-layer coherent motions; the key dynamics questions may be identified as: 1) vortex formation and evolution; and 2) interaction between coherent motions in the inner and outer regions of the boundary layer. (Cantwell, 1989 provides an additional viewpoint concerning future research directions in turbulent boundary layer structure.)

12.6 Final Discussion

Most of the causative coherent motions in the canonical turbulent boundary layer may be characterized as either vortices or shear layers. Kinematical combinations and dynamical relationships between these two fundamental classes of structure comprise the foundation physics of the momentum-transport and mixing properties of the boundary layer. Observations show that shear layers may give birth to vortices and vortical structures may create shear layers, but there are apparently non-unique formation mechanisms for each. To gain the depth of understanding required to improve practical modelling and control methodologies will require focussed study of these basic three-dimensional structural features, which in turn requires improved experimental/numerical techniques for their detection.

Several decades of intense academic study have provided an extensive knowledge-base of the simple canonical case. The immediate need is to learn to utilize this store of information in the context of boundary-layer modelling and control methodologies, with the eventual goal of practical application to engineering problems involving real-world, non-canonical boundary layers.

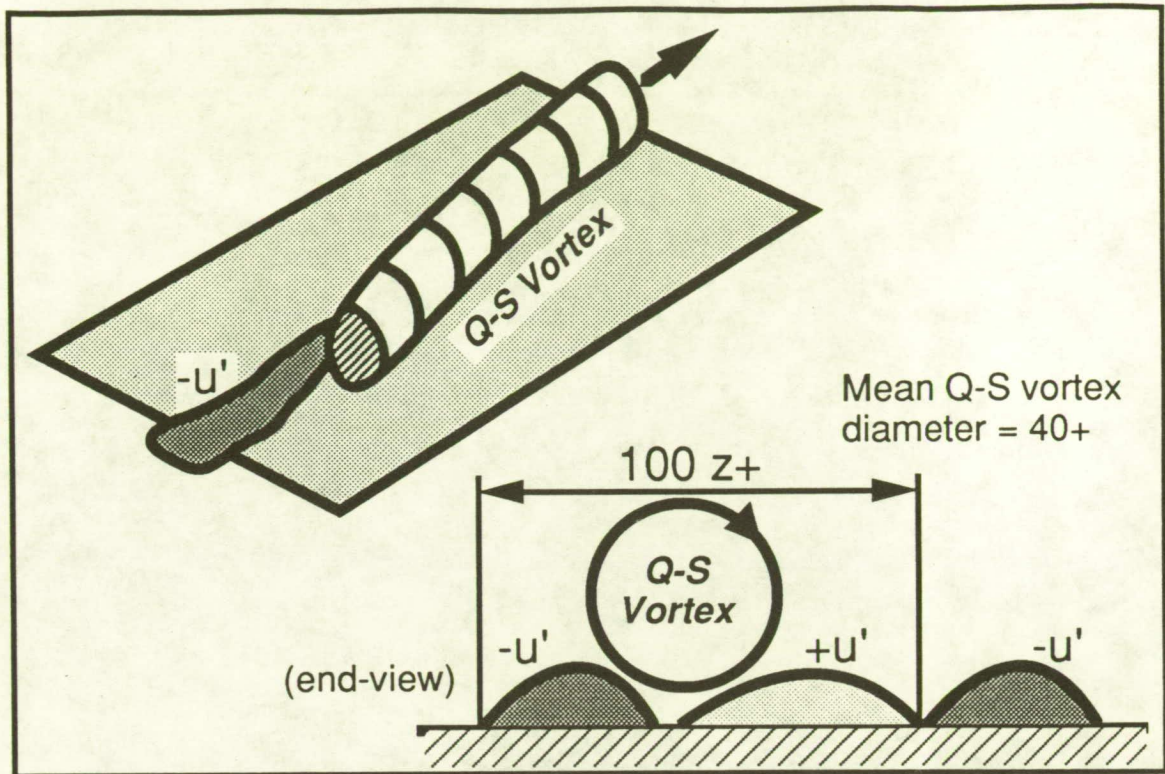


Fig. 12.1 Relationship between near-wall quasi-streamwise vortices and low-speed streaks in the sublayer and buffer layer.

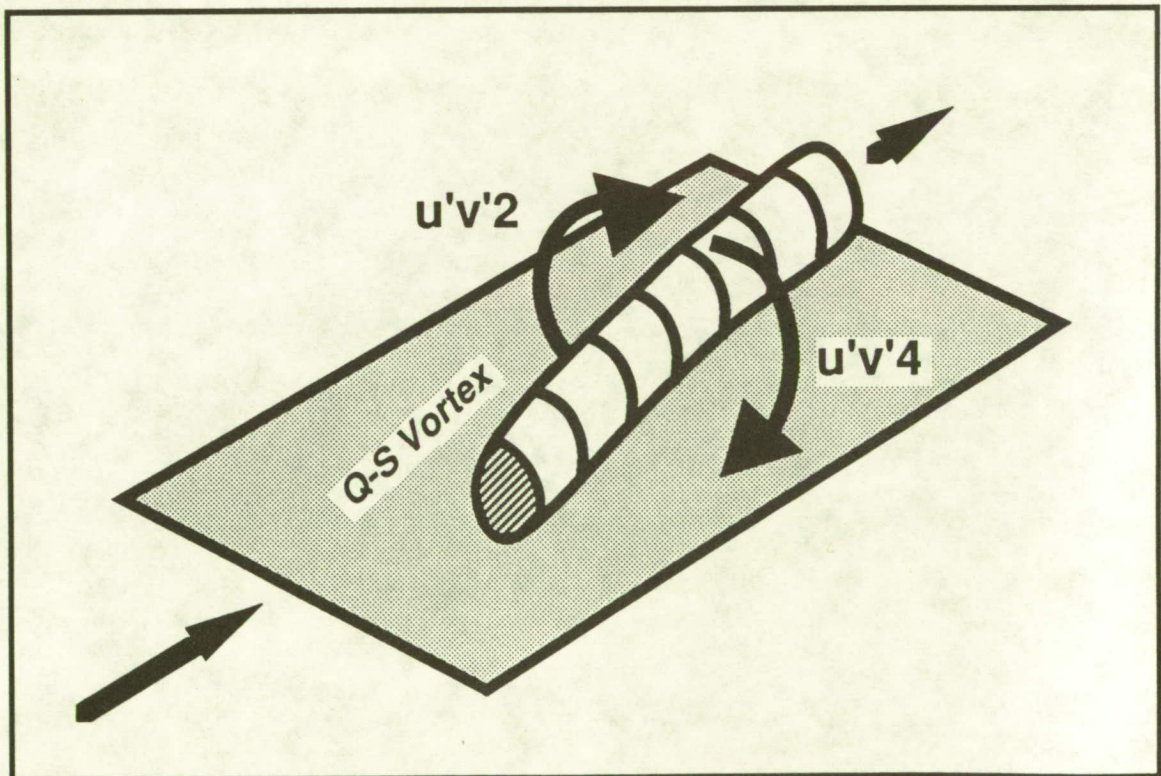


Fig. 12.2 Generation of both ejections and sweeps by a single near-wall quasi-streamwise vortex. Single vortices are less efficient than counter-rotating pairs, but are nonetheless effective transport pumps and are more common than pairs.

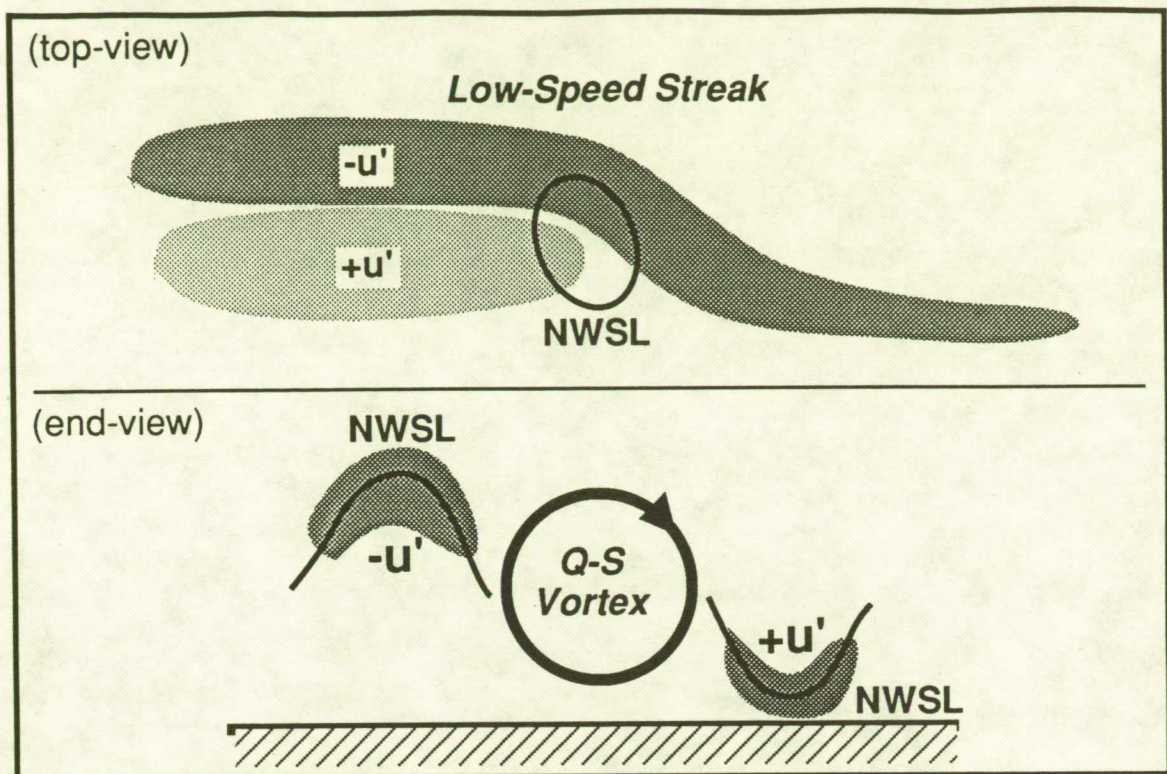


Fig. 12.3 Formation mechanisms for near-wall shear layers. Top: shear layer forms at kink in a low-speed streak (Alfredsson et al, 1988). Bottom: shear layer forms atop low-speed fluid lifted by a quasi-streamwise vortex.

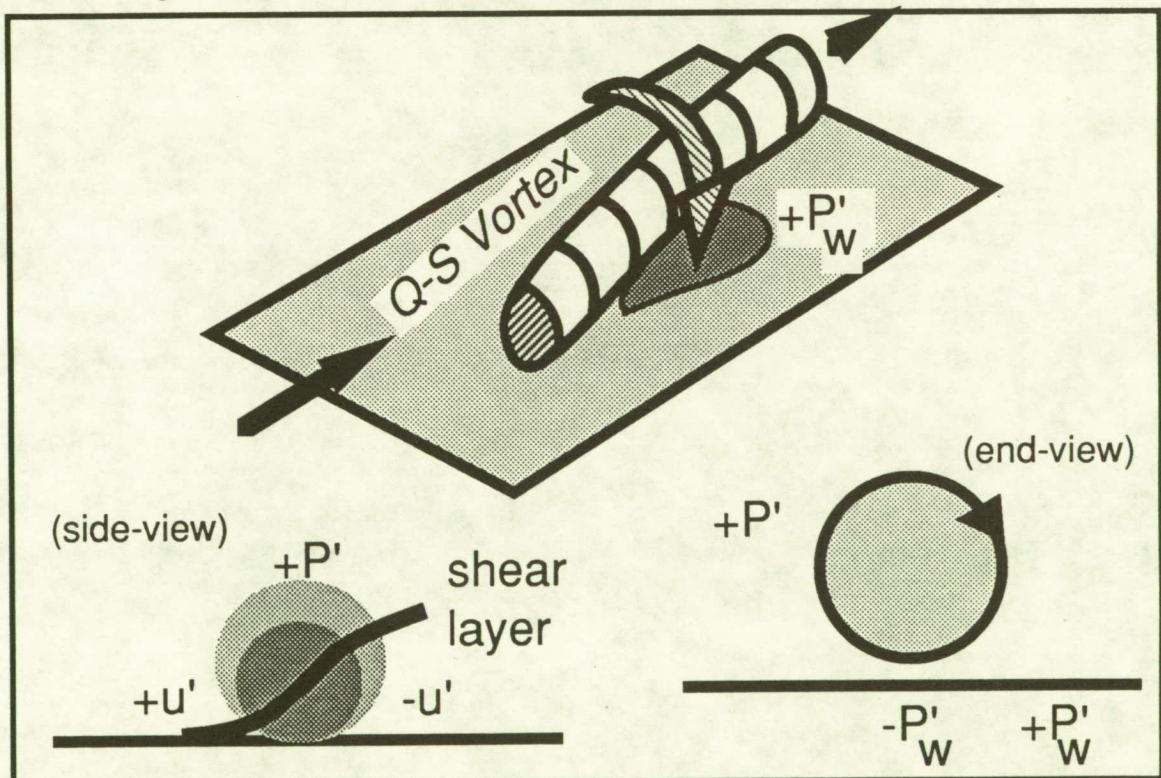


Fig. 12.4 Associations between near-wall quasi-streamwise vortices and the near-wall pressure field. Vortex cores are low pressure, high-speed/low-speed interaction zones are high-pressure. Both of these can affect the wall pressure.

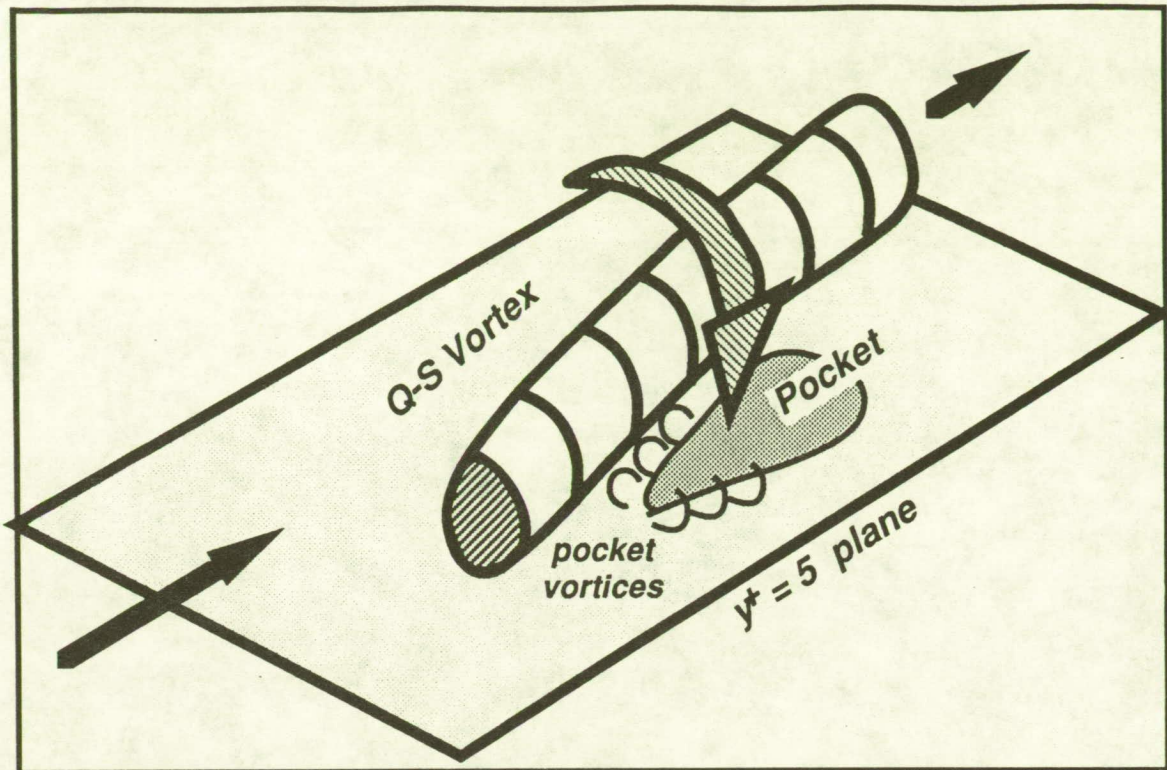


Fig. 12.5 Creation of a sublayer pocket by fluid induced toward the wall by a quasi-streamwise vortex. Secondary “pocket vortices” may form on the upstream edges of the pocket.

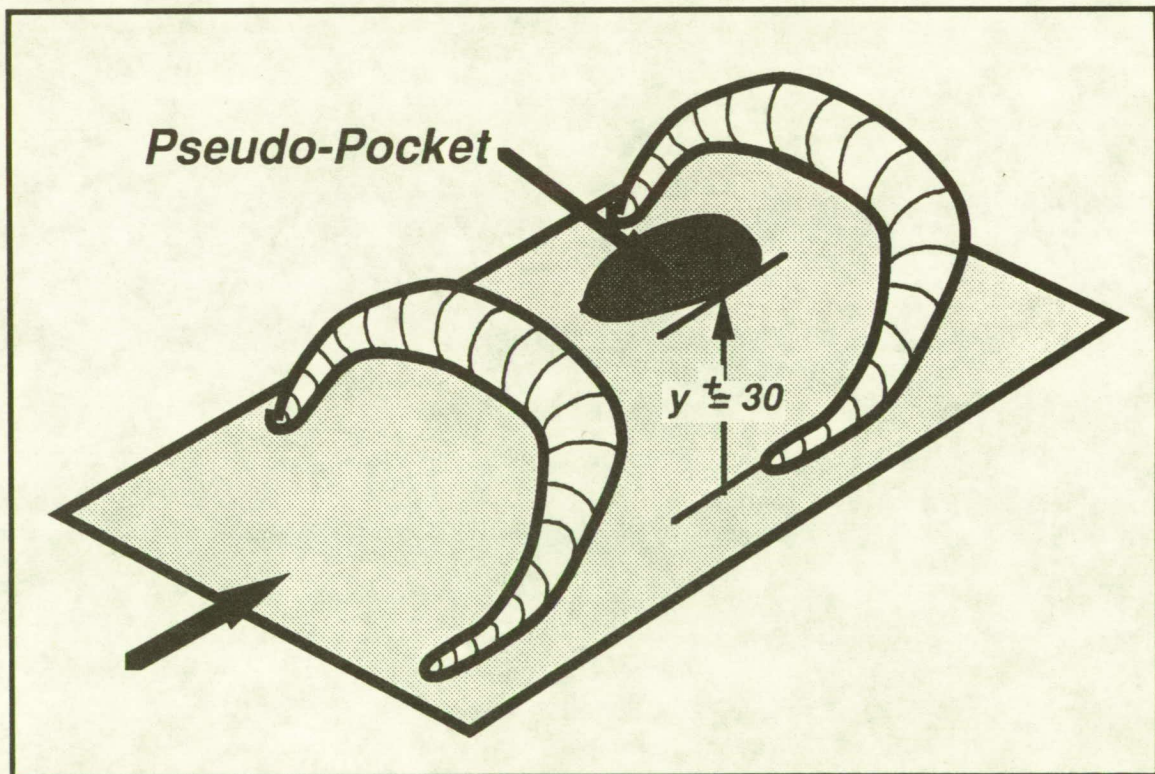


Fig. 12.6 Pocket-shaped regions can also be formed well outside the sublayer by the mutual action of two hairpin vortices, which draw marked fluid away from the region between the vortices (see also Acarlar and Smith, 1987).

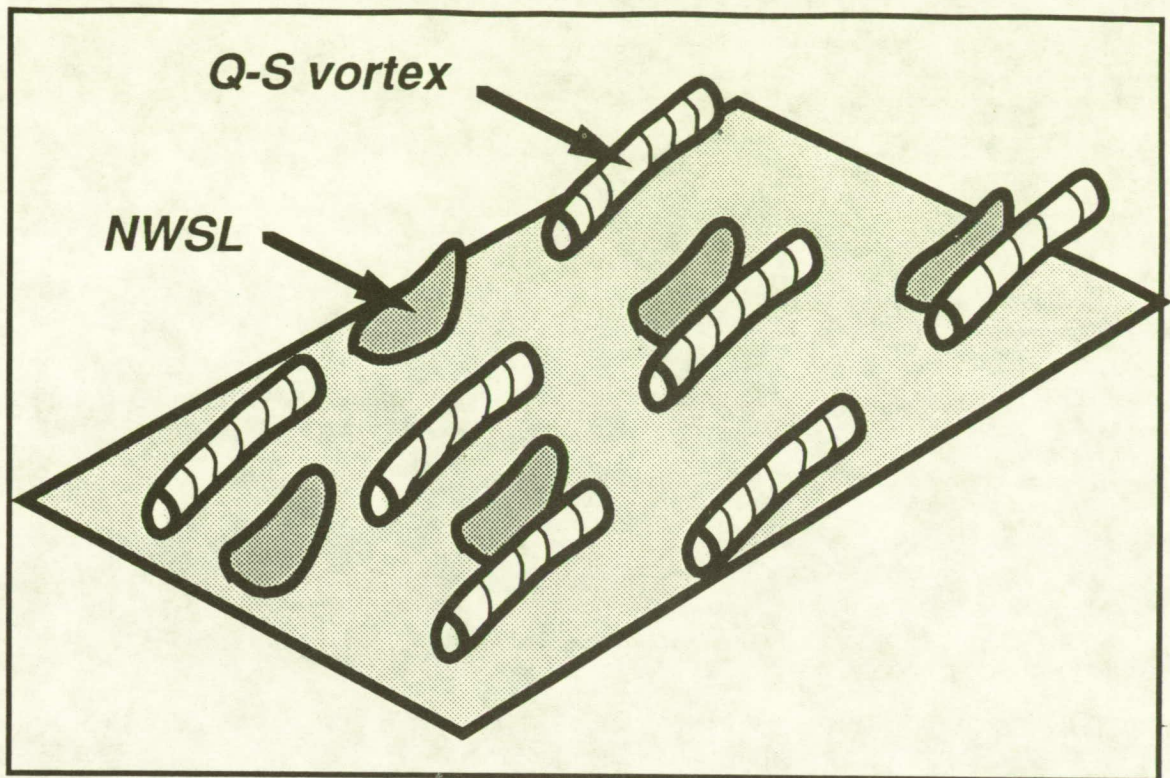


Fig. 12.7 Dissipation in the near-wall region is concentrated in near-wall shear layers and stretching quasi-streamwise vortices.

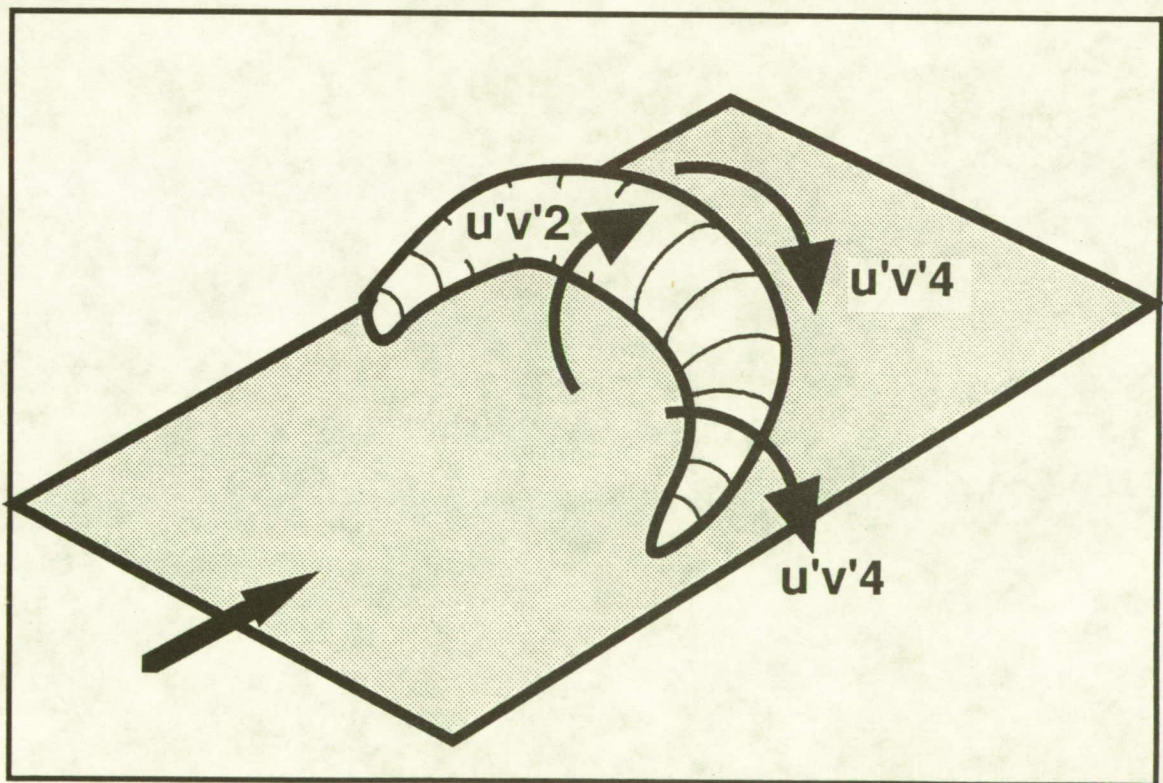


Fig. 12.8 Ejections and sweeps in the outer region are associated with one or two-sided arch-like vortical structures.

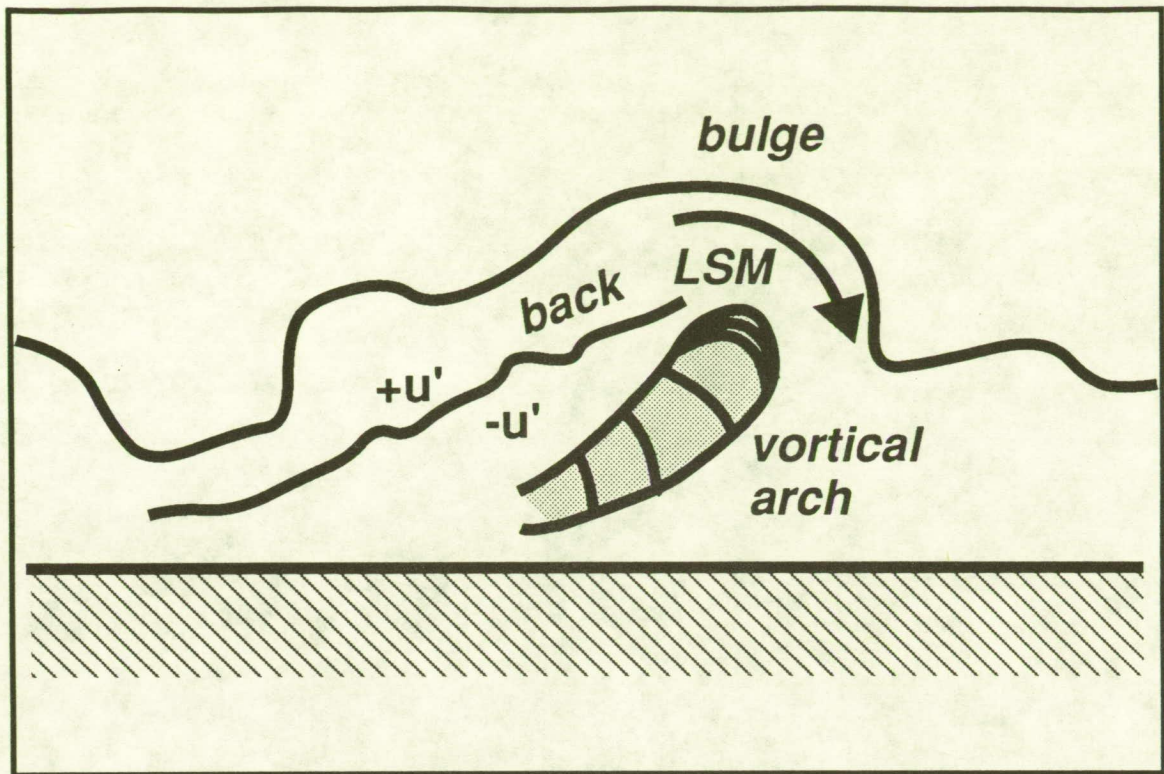


Fig. 12.9 Association between large-scale vortical arches and bulges in the instantaneous edge of the boundary layer. The “back” of the large-scale motion (LSM) is a shear-layer interface between high and low-speed fluid.

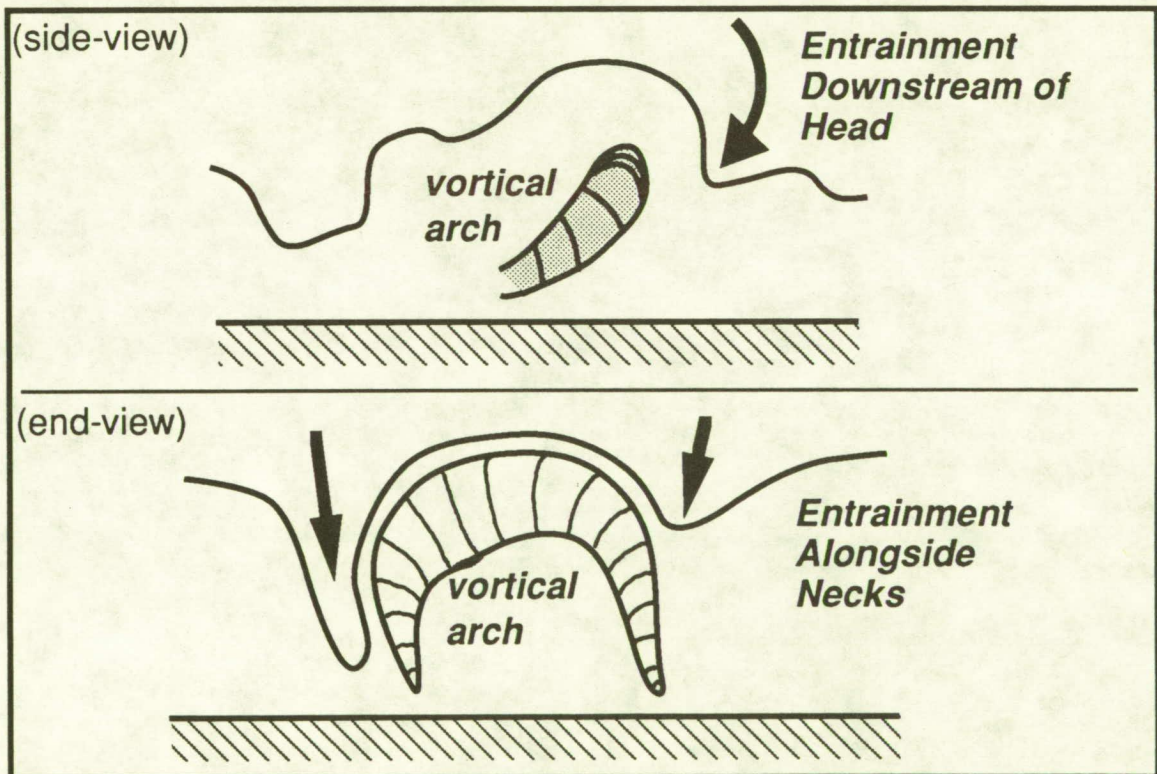


Fig. 12.10 Entrainment may occur downstream of a transverse vortex element and/or alongside the necks of an outer-region vortical arch.

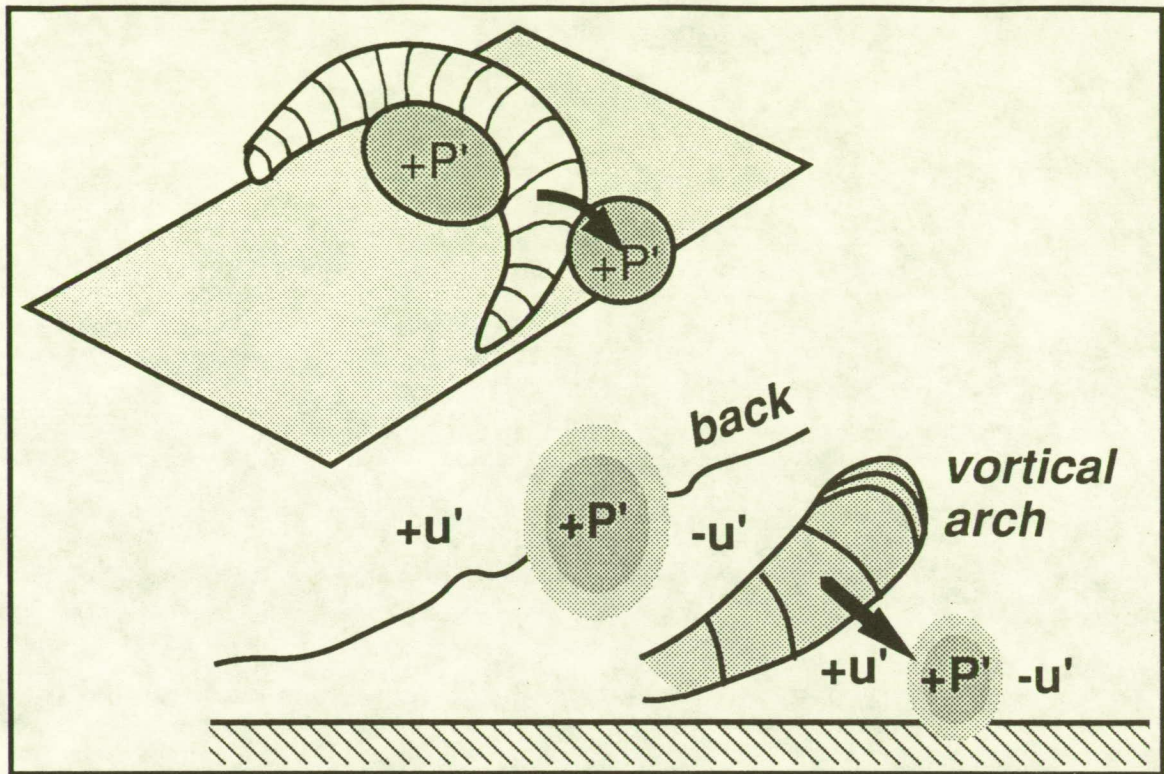


Fig. 12.11 Outer-region vortical structures influence the pressure field: vortex cores are low pressure; high-speed/low-speed interaction zones are high-pressure.

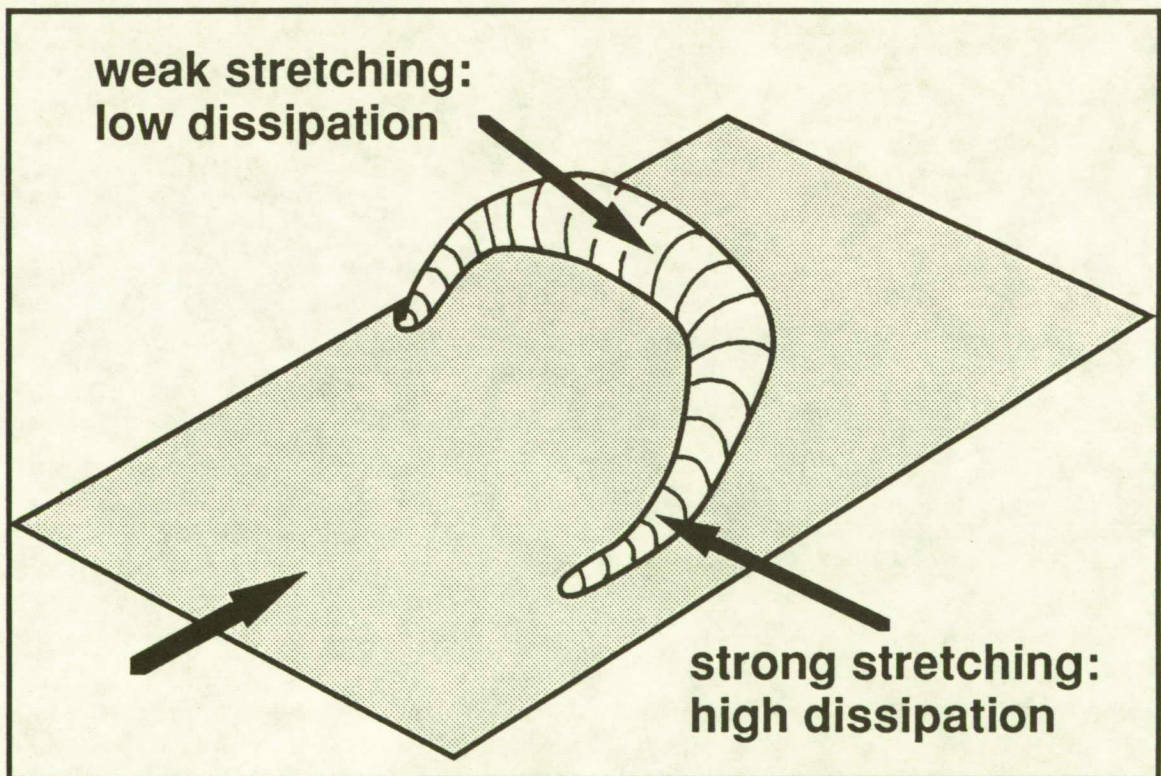


Fig. 12.12 Dissipation is low in the transverse heads of outer-region vortical structures, but high in the stretching neck elements.

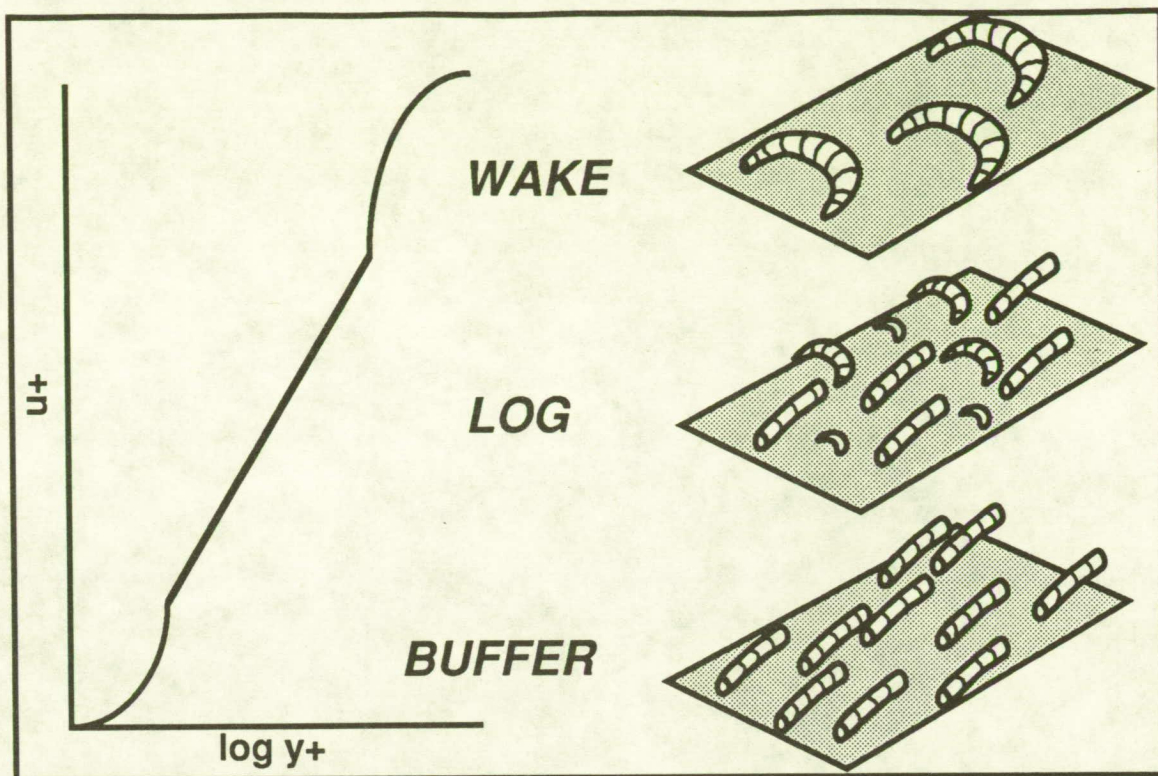


Fig. 12.13 Idealized schematic of vortical structure populations in the different regions of the canonical boundary layer.

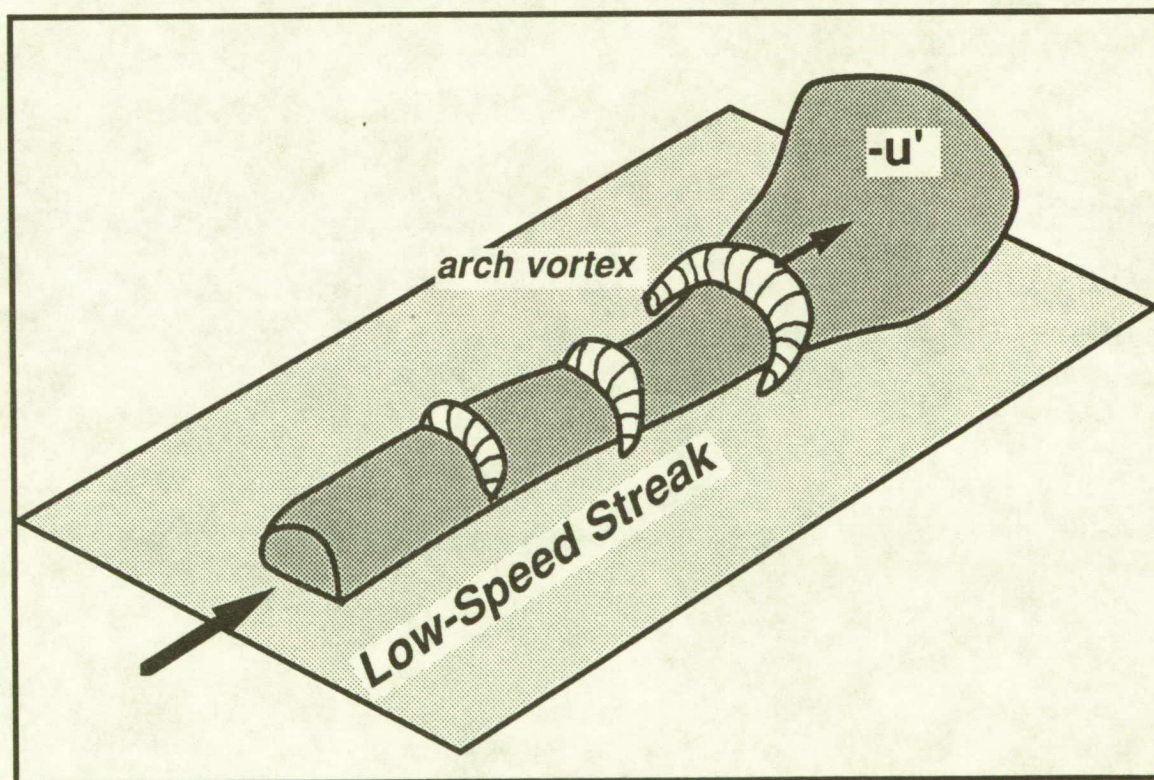


Fig. 12.14 Formation of near-wall vortical arches astride a low-speed streak. Once formed, an arch may re-form the streak, enhancing its longevity.

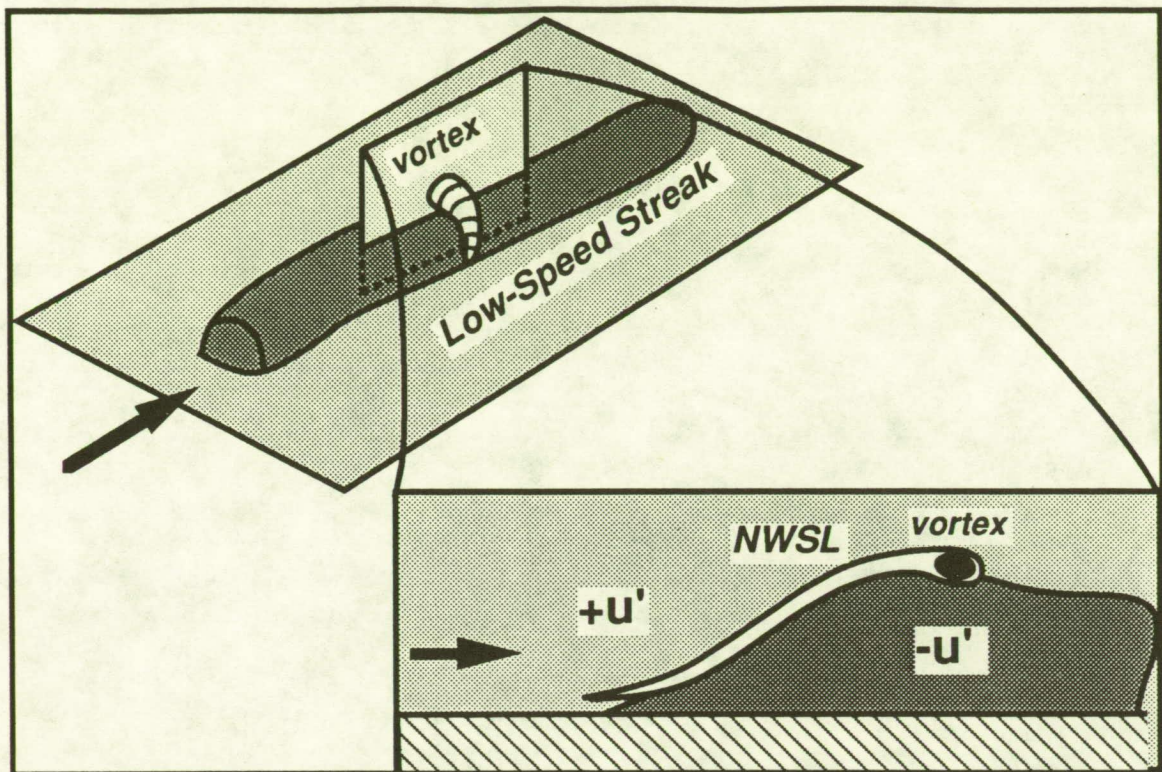


Fig. 12.15 Rollup of a near-wall shear layer formed at the interface between high and low-speed fluid.

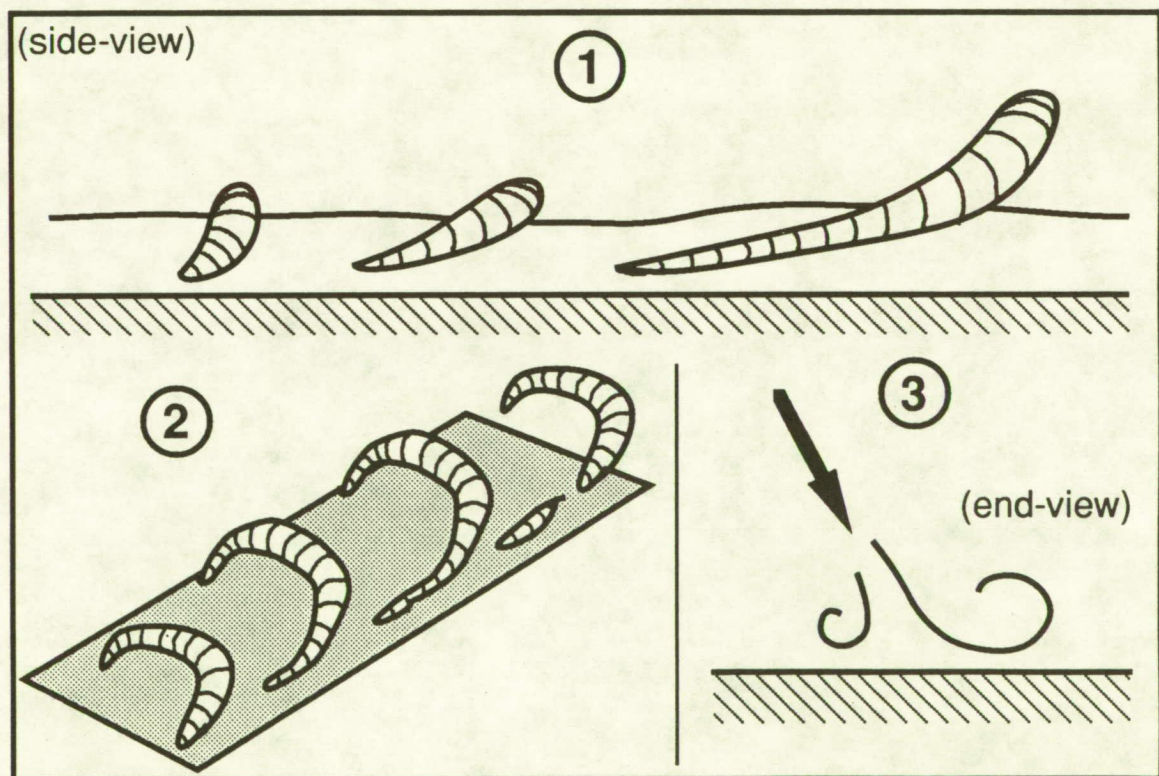


Fig. 12.16 Possible formation mechanisms for near-wall quasi-streamwise vortices. 1) stretched leg of a new vortical arch; 2) decender from the neck of a mature vortical structure; 3) re-direction of wallward fluid by continuity ("splat").

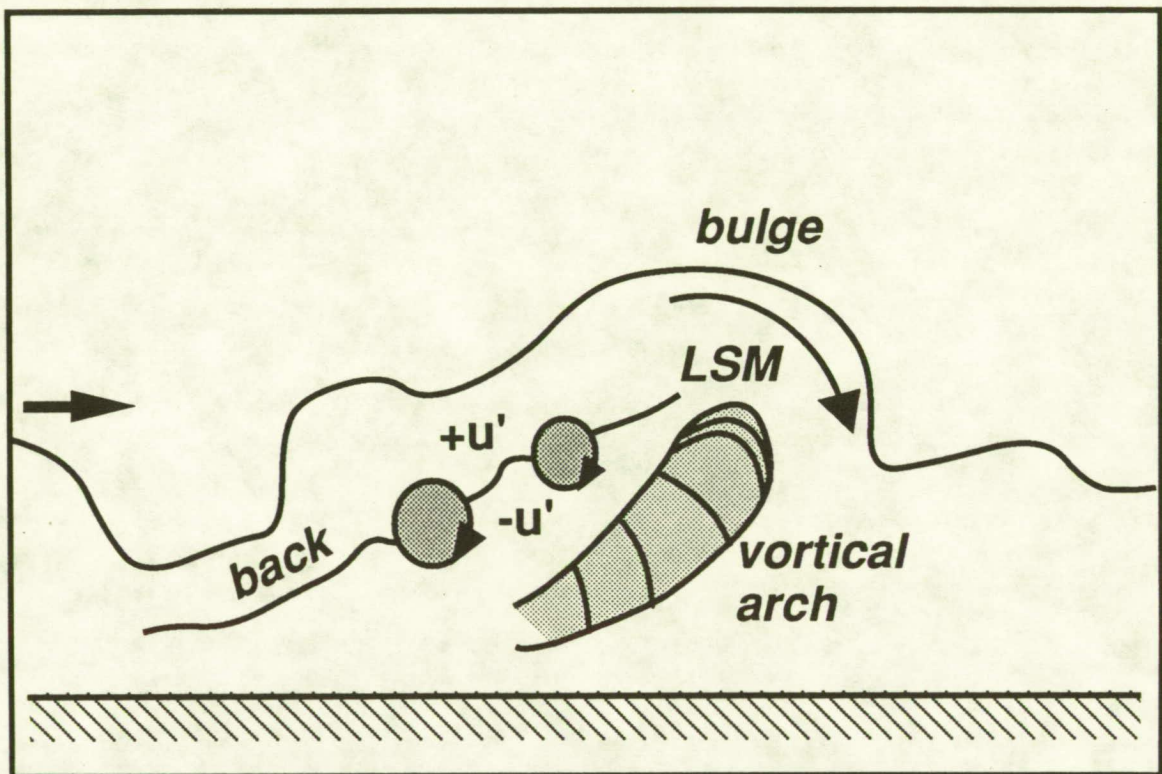


Fig. 12.17 Possible formation mechanism of outer-region transverse vortices: rollup of shear-layer "back" of a large-scale motion associated with a vortical arch.

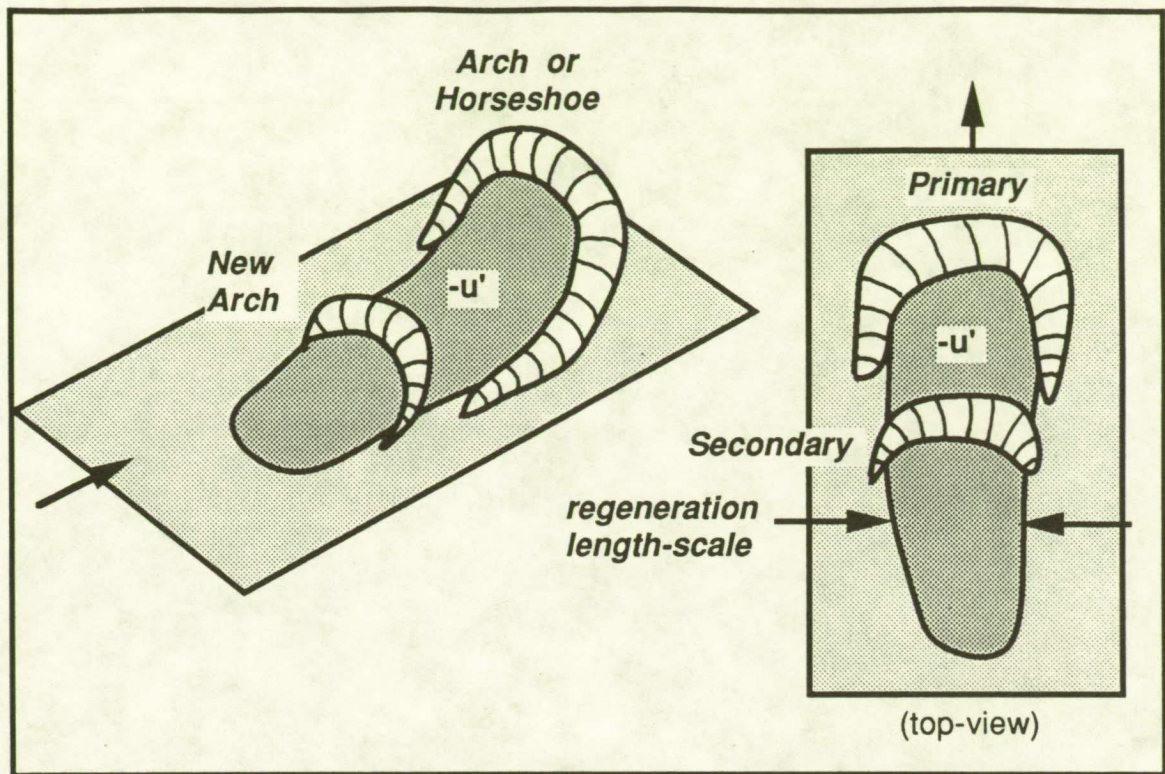


Fig. 12.18a Symmetric regeneration of vortical arches or hairpins (Snith, 1984). Observed for small vortical structures found in the near-wall region.

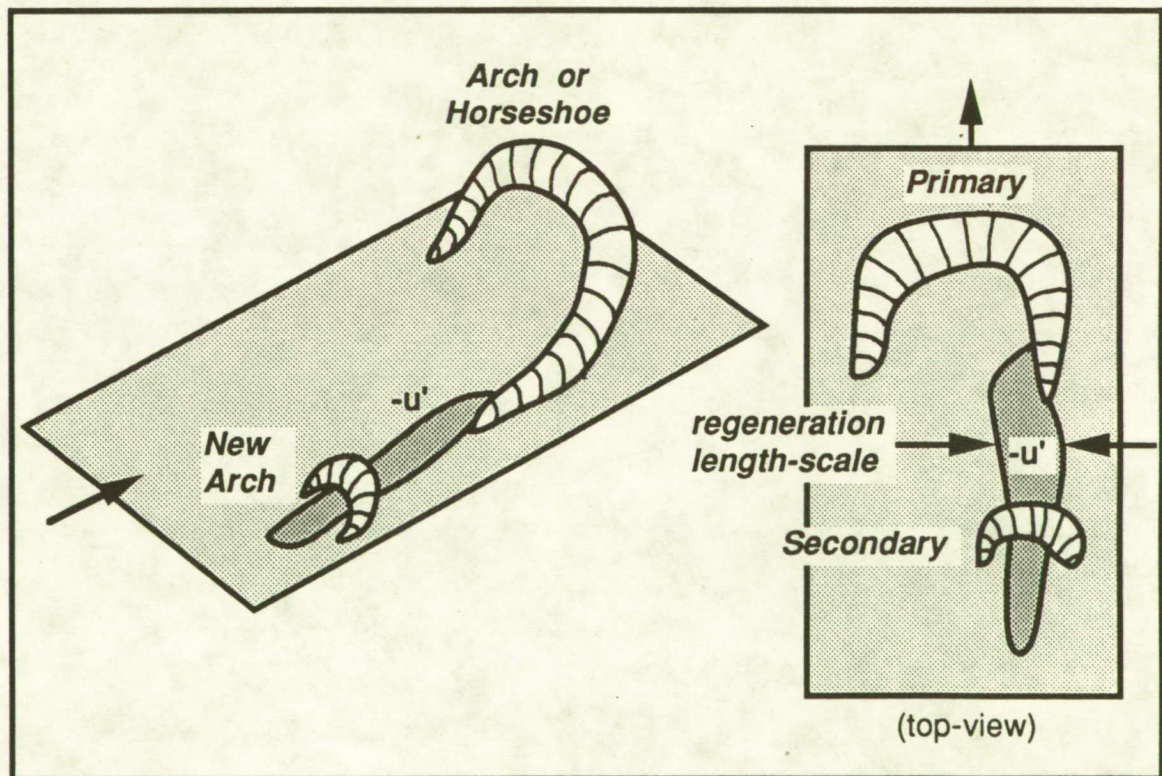


Fig. 12.18b One-sided regeneration of vortical arches. May occur repeatedly with mature, outer-region vortical structures as well as with younger, smaller, near-wall arches.

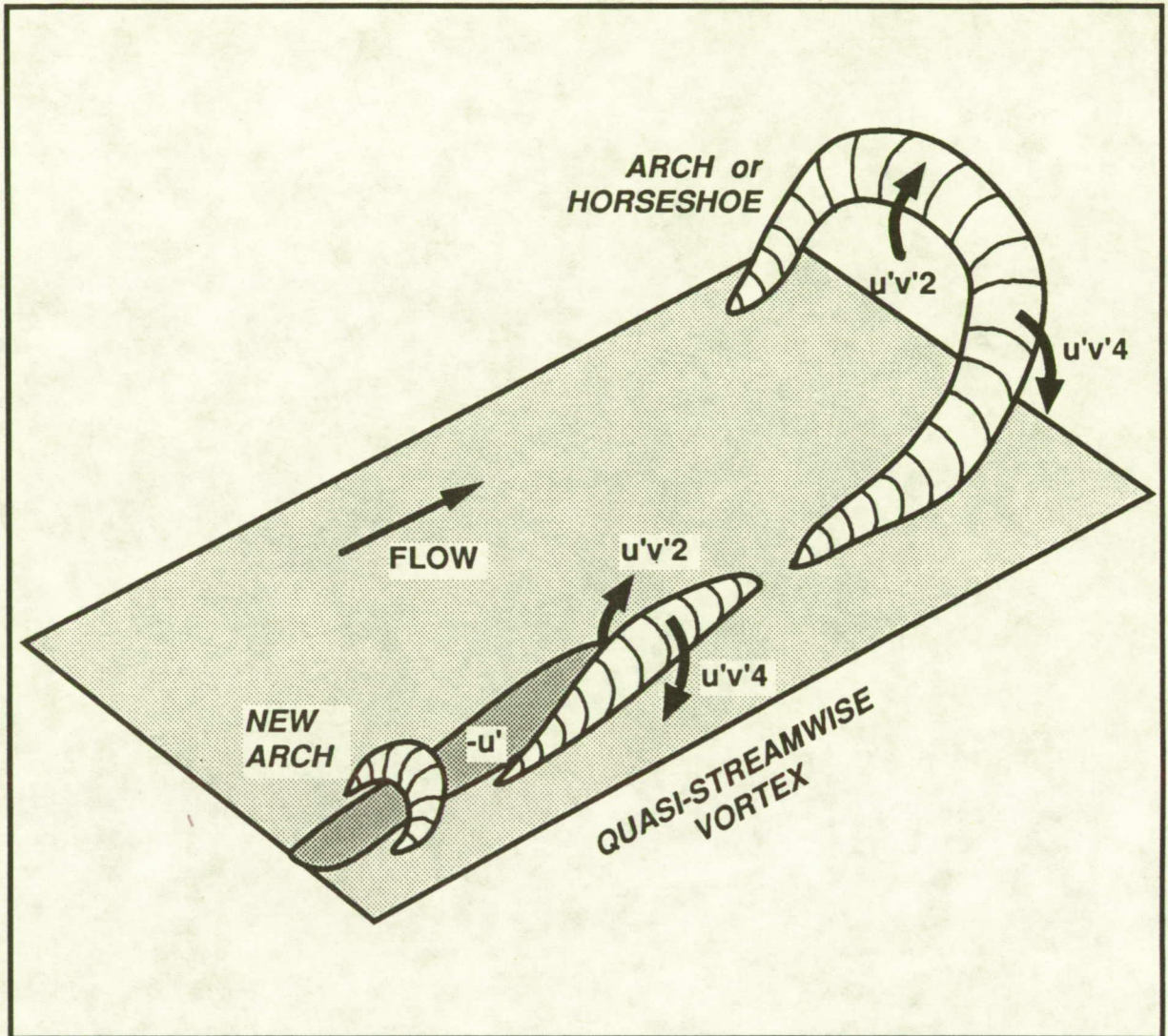


Fig. 12.19 Summary schematic of vortex regeneration and the association between vortical structures and Reynolds stress production in both the inner and outer regions of a low Re boundary layer.

REFERENCES

- Acarlar, M.S. and Smith, C.R. 1987a. A Study of Hairpin Vortices in a Laminar Boundary Layer. Part I: Hairpin Vortices Generated by a Hemisphere Protuberance, *J. Fluid Mech.*, Vol. 175.
- Acarlar, M.S. and Smith, C.R. 1987b. A Study of Hairpin Vortices in a Laminar Boundary Layer. Part II: Hairpin Vortices Generated by Fluid Injection. *J. Fluid Mech.* Vol. 175.
- Adrian, R.J., Moin, P. and Moser, R.D. 1987. Stochastic Estimation of Conditional Eddies in Turbulent Channel Flow. *Proc. 1987 Summer Program of the Center for Turbulence Research*, CTR-S87.
- Alfredsson, P.H. and Johansson, A.V. 1984. Time Scales in Turbulent Channel Flow. *Phys. Fluids* Vol. 27.
- Alfredsson, P.H., Johansson, A.V., and Kim, J. 1988. Turbulence Production Near Walls: the Role of Flow Structures with Spanwise Asymmetry. *Proc. 1988 Summer Program of the Center for Turbulence Research*, CTR-S88.
- Antonia, R.A. 1972. Conditionally Sampled Measurements Near the Outer Edge of a Turbulent Boundary Layer. *J. Fluid Mech.* vol. 56.
- Antonia, R.A. 1981. Conditional Sampling in Turbulence Measurement. *Ann. Rev. Fluid Mech.* Vol. 13.
- Antonia, R.A., Browne, L.W.B., and Bisset, D.K. 1989. Effect of Reynolds Number on the Organised Motion in a Turbulent Boundary Layer. *Near Wall Turbulence: 1988 Zaric Memorial Conference*, Hemisphere.
- Baker, J. 1987. Generating Images for a Time-Multiplexed Stereoscopic Computer Graphics System. *True 3D Imaging Techniques and Display Technologies*, Proc. SPIE 761.
- Bakewell, H.P. and Lumley, J.L. 1967. Viscous Sublayer and Adjacent Wall Region in Turbulent Pipe Flow. *Phys. Fluids* Vol. 10, No. 9.
- Bandyopadhyay, P. 1980. Large Structure with a Characteristic Upstream Interface in Turbulent Boundary Layers. *Phys. Fluids* vol. 23, no. 11.
- Barlow, R.S. and Johnston, J.P. 1985. Structure of Turbulent Boundary Layers on a Concave Surface. *Rept. MD-47*, Dept. Mech. Eng., Stanford Univ.
- Bevilaqua, P.M. and Lykoudis, P.S. 1977. Some Observations on the Mechanism of Entrainment. *AIAA J.* Vol. 15, No. 8.
- Black, T.J. 1968. An Analytical Study of the Measured Wall Pressure Field Under Supersonic Turbulent Boundary Layers. *NASA CR-888*.

- Blackwelder, R.F. and Kovasznay, L.S.G. 1972. Time Scales and Correlations in a Turbulent Boundary Layer. *Phys. Fluids* Vol. 15, No. 9.
- Blackwelder, R.F. and Kaplan, R.E. 1976. On the Wall Structure of the Turbulent Boundary Layer. *J. Fluid Mech.* Vol. 76.
- Blackwelder, R.F. and Eckelmann, H. 1979. Streamwise Vortices Associated with the Bursting Phenomenon. *J. Fluid Mech.* Vol. 94.
- Blackwelder, R.F. and Haritonidis, J.H. 1983. The Bursting Frequency in Turbulent Boundary Layers. *J. Fluid Mech.* Vol. 132.
- Blackwelder, R.F. 1988. Coherent Structures Associated with Turbulent Transport. *Transport Phenomena in Turbulent Flows*, Hemisphere.
- Blackwelder, R.F. 1989. Some Ideas on the Control of Near-Wall Eddies. *AIAA Paper 89-1009*.
- Blackwelder, R.F. and Swearingen, J.D. 1989. The Role of Inflectional Velocity Profiles in Wall-Bounded Flows. *Near Wall Turbulence: 1988 Zaric Memorial Conference*, Hemisphere.
- Bogard, D.G. and Tiederman, W.G. 1986. Burst Detection with Single-Point Velocity Measurements. *J. Fluid Mech.* Vol. 162.
- indentBogard, D.G. and Tiederman, W.G. 1987. Characteristics of Ejections in Turbulent Channel Flow. *J. Fluid Mech.* 179.
- Bradshaw, P. 1967. *J. Fluid Mech.* Vol. 30.
- Brodkey, R.S., Wallace, J.M., and Eckelmann, H. 1974. Some Properties of Truncated Signals in Bounded Shear Flows. *J. Fluid Mech.* Vol. 63, Pt. 2.
- Brown, G.L. and Thomas, A.S.W. 1977. Large Structure in a Turbulent Boundary Layer. *Phys. Fluids Suppl.* Vol. 20, No. 10.
- Bull, M.K. 1967. Wall-Pressure Fluctuations Associated with Subsonic Turbulent Boundary Layer Flow. *J. Fluid Mech.* Vol. 28.
- Burton, T.E. 1974. The Connection Between Intermittent Turbulent Activity near the Wall of a Turbulent Boundary Layer with Pressure Fluctuations at the Wall. *Tech. Rept. No. 70208-10*, Massachusetts Institute of Technology, Cambridge, Mass.
- Cantwell, B.J. 1981. Organized Motion in Turbulent Flows. *Ann. Rev. Fluid Mech.* Vol. 13.
- Cantwell, B.J. 1989. Future Directions in Turbulence Research and the Role of Organized Motion. *Whither Turbulence Workshop*, Cornell University.
- Chen, C-H. P. and Blackwelder, R.F. 1978. Large-Scale Motion in a Turbulent Boundary Layer: A Study Using Temperature Contamination. *J. Fluid Mech.* Vol. 89.

- Chong, M.S., Perry, A.E., and Cantwell, B.J. 1990. A General Classification of Three-Dimensional Flow Fields. To appear, *Phys. Fluids A*.
- Clark, J.A. and Markland, E. 1971. Flow Visualization in Turbulent Boundary Layers. *J. Hydr. Div. ASCE* Vol 97.
- Corcos, G.M. 1962. *Univ. Cal. Inst. of Eng. Res. Rept.*, Series 183, no. 1.
- Corcos, G.M. 1964. The Structure of the Turbulent Pressure Field in Boundary-Layer Flows. *J. Fluid Mech.* Vol. 18.
- Corino, E.R. and Brodkey, R.S. 1969. A Visual Investigation of the Wall Region in Turbulent Flow. *J. Fluid Mech.* Vol. 37, Pt. 1.
- Corrsin, S. 1943. Investigation of Flow in an Axially Symmetric Heated Jet of Air. *NACA Adv. Conf. Rep.* 3123.
- Corrsin, S. and Kistler, A.L. 1954. The Free-Stream Boundaries of Turbulent Flows. *NACA TN* 3133.
- Corrsin, S. 1957. *Publication 515*, Nat'l Academy of Sciences.
- Dinkelacker, A., Hessel, M., Meier, G.E.A., and Schewe, G. 1977. Investigation of Pressure Fluctuations Beneath a Turbulent Boundary Layer by means of an Optical Method. *Phys. Fluids Suppl.* Vol. 20., No. 10.
- Dinkelacker, A. and Langeheineken, T. 1983. Relations Between Wall Pressure Fluctuations and Velocity Fluctuations in Turbulent Flow. *Proc. IUTAM Symp.*, Marseille, Springer.
- Dinkelacker, A. and Sieber, M. 1987. Coherent Structures in Turbulent Pipe Flow. *Advances in Turbulence*, Springer-Verlag, p. 391.
- Einstein H.A. and Li, H. 1956. The Viscous Sublayer Along a Smooth Boundary. *J. Eng. Mech.*, A.S.C.E., Vol. 82, No. EM 2.
- Emmerling, R., Meier, G.E.A., and Dinkelacker, A. 1973. Investigation of the Instantaneous Structure of the Wall Pressure under a Turbulent Boundary Layer. *AGARD Conf. Proc. No. 131*, Brussels, Belgium.
- Ersoy, S. and Walker, J.D.A. 1986. The Boundary Layer due to a Three-Dimensional Vortex Loop, *AIAA J.*, vol. 24.
- Falco, R.E. 1977. Coherent Motions in the Outer Region of Turbulent Boundary Layers. *Phys. Fluids Suppl.* Vol. 20, No. 10.
- Falco, R.E. 1980a. Combined Simultaneous Flow Visualization/Hot-Wire Anemometry for the Study of Turbulent Flows. *Trans. ASME* Vol. 102.
- Falco, R.E. 1980b. The Production of Turbulence Near a Wall. *AIAA Paper* 80-1356.
- Falco, R.E. 1982. A Synthesis and Model of Wall Region Turbulence Structure, *Structure of Turbulence, Heat, and Mass Transfer*, p. 124, Hemisphere.

- Falco, R.E. 1983. New Results, a Review and Synthesis of the Mechanism of Turbulence Production in Boundary Layers and its Modification. *AIAA 83-0377*.
- Favre, A.J., Gaviglio, J.J., and Dumas, R. 1957. Space-Time Double Correlations and Spectra in a Turbulent Boundary Layer. *J. Fluid Mech.*, Vol. 2.
- Fiedler, H. and Head, M.R. 1966. Intermittency Measurements in the Turbulent Boundary Layer. *J. Fluid Mech.*, vol. 25.
- Fiedler, H.E. 1986. Coherent Structures. *Advances in Turbulence*, Springer-Verlag.
- Gartshore, I.S. 1966. *J. Fluid Mech.*, vol. 24, part 1.
- Grant, H.L. 1958. The Large Eddies of Turbulent Motion. *J. Fluid Mech.*, Vol. 4.
- Grass, A.J. 1971. Structural Features of Turbulent Flow over Smooth and Rough Boundaries. *J. Fluid Mech.* Vol. 50.
- Grotzbach, G. 1978. Convective Velocities of Wall Pressure Fluctuations in a Turbulent Channel Flow Deduced from a Computer-Generated Movie. *Lect. Notes in Physics* 76, vol. 2, Springer-Verlag.
- Grotzbach, G. and Schumann, U. 1979. Direct Numerical Simulation of Turbulent Velocity-, Pressure-, and Temperature-Fields in Channel Flows. *Turbulent Shear Flows I*, Springer.
- Guezennec, Y. 1985. Documentation of Large Coherent Structures Associated with Wall Events. Ph.D. Dissertation, Illinois Institute of Technology, Chicago, Illinois.
- Guezennec, Y., Piomelli, U., and Kim, J. 1989. On the Shape and Dynamics of Wall Structures in Turbulent Channel Flow. *Phys. Fluids* Vol. A1.
- Gupta, A.K., Laufer, J., and Kaplan, R.E. 1971. Spatial Structure in the Viscous Sublayer. *J. Fluid Mech.* Vol. 50, Pt. 3.
- Hama, F.R. 1962. Progressive Deformation of a Curved Vortex Filament by its own Induction, *Phys. Fluids*, vol. 5.
- Head, M.R. and Bandyopadhyay, P. 1981. New Aspects of Turbulent Boundary Layer Structure. *J. Fluid Mech.* Vol. 107.
- Hedley, T.B. and Keffer, J.F. 1974. Some Turbulent/Non-Turbulent Properties of the Outer Intermittent Region of a Boundary Layer. *J. Fluid Mech.* Vol. 64, Part 4.
- Herzog, S. 1986. The Large-Scale Structure in the Near-Wall Region of Turbulent Pipe Flow. Thesis, Cornell University.
- Hinze, J.O. 1975. *Turbulence*. McGraw-Hill.
- Hirata, M. and Kasagi, N. 1979. Studies of Large-Eddy Structures in Turbulent Shear Flows with the Aid of Flow Visualization Techniques. *Studies in Heat Transfer*, Ed. J.P. Hartnett et al, Hemisphere.

- Hussain, A.K.M.F. 1986. Coherent Structures and Turbulence. *J. Fluid Mech.* Vol. 173.
- Jang, P.S., Benney, D.J., Gran, R.L. 1986. On the Origin of Streamwise Vortices in a Turbulent Boundary Layer. *J. Fluid Mech.* Vol. 169.
- Jimenez, J., Moin, P., Moser, R.D., and Keefe, L.R. 1987. Ejection Mechanisms in the Sublayer of a Turbulent Channel. *Proc. 1987 Summer Program of the Center for Turbulence Research, CTR-S87.*
- Johansson, A.V. and Alfredsson, P.H. 1982. On the Structure of Turbulent Channel Flow. *J. Fluid Mech.* Vol. 122.
- Johansson, A.V., Alfredsson, P.H., and Eckelmann, H. 1987a. On the Evolution of Shear-Layer Structures in Near-Wall Turbulence. *Advances in Turbulence*, Springer-Verlag.
- Johansson, A.V., Alfredsson, P.H., and Kim, J. 1987b. Shear-Layer Structures in Near-Wall Turbulence. *Proc. 1987 Summer Program of the Center for Turbulence Research, CTR-S87.*
- Johansson, A.V., Her, A.V., and Haritonidis, J.H. 1987c. On the Generation of High Amplitude Pressure Peaks in Turbulent Boundary Layers and Spots. *J. Fluid Mech.* Vol. 175.
- Karlsson, R.I. and Johansson, T.G. 1987. LDV Measurements of Velocity Fluctuations in a Turbulent Boundary Layer. *Laser Anemometry in Fluid Mechanics III*, Eds. R.J. Adrian et al.
- Kasagi, N., Hirata, M., and Nishino, K. 1986. Streamwise Pseudo-Vortical Structures and Associated Vorticity in the Near-Wall Region of a Wall-Bounded Turbulent Shear Flow. *Exp. Fluids*, Vol. 4.
- Kasagi, N. 1989. Structural Study of Near-Wall Turbulence and its Heat Transfer Mechanism. *Near Wall Turbulence: 1988 Zaric Memorial Conference*, Hemisphere.
- Kastrinakis, E.G., Wallace, J.M., Willmarth, W.W., Ghorashi, B., and Brodkey, R.S. 1978. On the Mechanism of Bounded Turbulent Shear Flows, *Lecture Notes in Physics* 75, Springer-Verlag.
- Kim, H.T., Kline, S.J., and Reynolds, W.C. 1971. The Production of Turbulence Near a Smooth Wall in a Turbulent Boundary Layer. *J. Fluid Mech.* Vol. 50, Pt 1.
- Kim, J. and Moin, P. 1979. Large-Eddy Simulation of Turbulent Channel Flow. *NASA TM 78619*. Also in *AGARD Symp. on Turbulent Boundary Layer*, 1979.
- Kim, J. 1983. On the Structure of Wall-Bounded Turbulent Flows. *Phys. Fluids* Vol. 26.

- Kim, J. 1985. Turbulence Structures Associated with the Bursting Event. *Phys. Fluids* Vol. 28.
- Kim, J. and Moin, P. 1986. Flow Structures Responsible for the Bursting Process. *Bull. APS*, vol. 31, no. 10.
- Kim, J. and Moin, P. 1986. The Structure of the Vorticity Field in Turbulent Channel Flow. Part 2: Study of Ensemble-Averaged Fields, *J. Fluid Mech.*, vol. 162.
- Kim, J., Moin, P., and Moser, R.D. 1987. Turbulence Statistics in Fully-Developed Channel Flow at Low Reynolds Number. *J. Fluid Mech.* Vol. 177.
- Kim, J. 1987. Evolution of a Vortical Structure Associated with the Bursting Event in a Channel Flow. *Turbulent Shear Flows* 5, Springer-Verlag.
- Kim, J. 1987. Overview of Research by the Turbulence Structure Group. *Proc. 1987 Summer Program of the Center for Turbulence Research*, CTR-S87.
- Kim, J. and Spalart, P.R. 1987. Scaling of the Bursting Frequency in Turbulent Boundary Layers at Low Reynolds Numbers. *Phys. Fluids* Vol. 30.
- Klebanoff, P.S. 1954. Characteristics of Turbulence in a Boundary Layer with Zero Pressure Gradient. *NACA TN-3178*.
- Kline, S.J. and Runstadler, P.W. 1959. Some Preliminary Results of Visual Studies of the Flow Model of the Wall Layers of the Turbulent Boundary Layer. *Trans. ASME, Ser. E*, Vol. 2.
- Kline, S.J., Reynolds, W.C., Schraub, F.A., Runstadler, P.W. 1967. The Structure of Turbulent Boundary Layers. *J. Fluid Mech.* Vol. 30.
- Kline, S.J. and Robinson, S.K. 1989a. Quasi-Coherent Structures in the Turbulent Boundary Layer: Part I: Status Report on a Community-Wide Summary of the Data. *Near Wall Turbulence: 1988 Zaric Memorial Conference*, Hemisphere.
- Kline, S.J. and Robinson, S.K. 1989b. Turbulent Boundary Layer Structure: Progress, Status, and Challenges. *2nd IUTAM Symposium on Structure of Turbulence and Drag Reduction*, Zurich, Switzerland.
- Kobashi, Y. and Ichijo, M. 1986. Wall Pressure and its Relation to Turbulent Structure of a Boundary Layer. *Exp. Fluids* Vol. 4.
- Kobashi, Y. and Ichijo, M. 1989. Relation Between Wall Pressure and Turbulent Structure Near Wall Turbulence: 1988 Zaric Memorial Conference, Hemisphere.
- Kovasznay, L.S.G. 1970. The Turbulent Boundary Layer. *Ann. Rev. Fluid Mech.* Vol. 2.
- Kovasznay, L.S.G., Kibens, V., and Blackwelder, R.F. 1970. Large-Scale Motion in the Intermittent Region of a Turbulent Boundary Layer. *J. Fluid Mech.* Vol. 41, Pt. 2.

- Kreplin, H.-P. and Eckelmann, H. 1979. Propagation of Perturbations in the Viscous Sublayer and Adjacent Wall Region. *J. Fluid Mech.* Vol. 95, Pt. 2.
- Lane, B. 1982. Stereoscopic Displays. *Processing and Display of Three-Dimensional Data, Proc. SPIE* 367.
- Hodges, L.F. and McAllister, D.F. 1985. Stereo and Alternating-Pair Techniques for Display of Computer-Generated Images. *IEEE Computer Graphics and Applications*, Sept., 1985.
- Hodges, L.F., Love, S., Johnson, P., and McAllister, D.F., Sher, L.D., and Noble, L. 1988. Stereoscopic and Multiplanar Computer Graphics. *Course Notes no. 21*, ACM SIGGRAPH 1988.
- Laufer, J. 1953. The Structure of Turbulence in a Fully Developed Pipe. *NACA TN* 2954.
- Laufer, J. 1975. New Trends in Experimental Research. *Ann. Rev. Fluid Mech.* Vol. 7.
- Lee, M.J., Kim, J., and Moin, P. 1987. Turbulence Structure at High Shear Rate. *6th Symposium on Turbulent Shear Flows*, Toulouse, France.
- Lian, Q.X. 1987. Coherent Structures of Turbulent Boundary Layer in Flows with Adverse Pressure Gradient, in *Sino-U.S. Joint Fundamental Experimental Aerodynamics Symposium*, Hampton, VA.
- Lighthill, M.J. 1963. In *Laminar Boundary Layers*, Clarendon Press, Oxford, p. 99.
- Lu, S.S. and Willmarth, W.W. 1973. Measurements of the Structure of the Reynolds Stress in a Turbulent Boundary Layer. *J. Fluid Mech.* Vol. 60.
- Luchik, T.S. and Tiederman, W.G. 1987. Timescale and Structure of Ejections and Bursts in Turbulent Channel Flows. *J. Fluid Mech.* Vol. 174.
- Lugt, H.J. 1979. The Dilemma of Defining a Vortex. *Recent Developments in Theoretical and Experimental Fluid Mechanics*, Springer.
- Lumley, J.L. 1981. Coherent Structures in Turbulence. *Transition and Turbulence*, ed. R.E. Meyer, Academic.
- Moin, P., Reynolds, W.C., and Ferziger, J.H. 1978. Large-Eddy Simulation of Incompressible Turbulent Channel Flow. *Rept. TF-12*, Dept. Mech. Eng., Stanford Univ.
- Moin, P. 1984. Probing Turbulence via Large Eddy Simulation. *AIAA Paper* 84-0174.
- Moin, P. and Kim, J. 1985. The Structure of the Vorticity Field in Turbulent Channel Flow. Part 1: Analysis of Instantaneous Fields and Statistical Correlations. *J. Fluid Mech.* Vol. 155.
- Moin, P., Leonard, A., and Kim, J. 1986. Evolution of a Curved Vortex Filament into a Vortex Ring, *Phys. Fluids*, vol. 29, no. 4.

- Moin, P. 1987. Analysis of Turbulence Data Generated by Numerical Simulations. *AIAA Paper 87-0194*.
- Moin, P., Adrian, R.J., and Kim, J. 1987. Stochastic Estimation of Conditional Eddies in Turbulent Channel Flow. *6th Symposium on Turbulent Shear Flows*, Toulouse, France.
- Moin, P. and Moser, R.D. 1989. Characteristic-Eddy Decomposition of Turbulence in a Channel. *J. Fluid Mech.* Vol. 200.
- Murlis, J., Tsai, H.M., and Bradshaw, P. 1982. The Structure of Turbulent Boundary Layers at Low Reynolds Numbers. *J. Fluid Mech.* Vol. 122.
- Nakagawa, H. and Nezu, I. 1981. Structure of Space-Time Correlations of Bursting Phenomena in an Open-Channel Flow. *J. Fluid Mech.* Vol. 104.
- Narasimha, R. and Kailas, S.V. 1987. Energy Events in the Atmospheric Boundary Layer. *Tech. Memo. DU 8701*, Nat'l Aero. Lab., India.
- Nychas, S.G., Hershey, H.C., and Brodkey, R.S. 1973. A Visual Study of Turbulent Shear Flow. *J. Fluid Mech.* Vol. 61.
- Offen, G.R. and Kline, S.J. 1974. Combined Dye-Streak and Hydrogen-Bubble Visual Observations of a Turbulent Boundary Layer. *J. Fluid Mech.* Vol. 62, Pt. 2.
- Offen, G.R. and Kline, S.J. 1975. A Proposed Model of the Bursting Process in Turbulent Boundary Layers. *J. Fluid Mech.* Vol. 70, Pt. 2.
- Pearson, C.F. and Abernathy, F.H. 1984. Evolution of the Flow Field Associated with a Streamwise Diffusing Vortex, *J. Fluid Mech.*, vol. 146.
- Perry, A.E. and Chong, M.S. 1982. On the Mechanism of Wall Turbulence. *J. Fluid Mech.* Vol. 119.
- Perry, A.E., Henbest, S., and Chong, M.S. 1986. A Theoretical and Experimental Study of Wall Turbulence. *J. Fluid Mech.* Vol. 165.
- Perry, A.E. and Chong, M.S. 1987. *Ann. Rev. Fluid Mech.* Vol. 19.
- Perry, A.E., Li, J.D., Henbest, S., and Marusic, I. 1989. The Attached Eddy Hypothesis in Wall Turbulence. *Near Wall Turbulence: 1988 Zaric Memorial Conference*, Hemisphere.
- Praturi, A.K. and Brodkey, R.S. 1978. A Stereoscopic Visual Study of Coherent Structures in Turbulent Shear Flow. *J. Fluid Mech.* Vol. 89, Pt. 2.
- Randolph, M., Eckelmann, H., and Nychas, S.G. 1989. On the Relation Between Sweeps and Streamwise Vortices. *Advances in Turbulence 2*, Springer-Verlag.
- Reynolds, W.C. 1989. The Potential and Limitations of Direct and Large Eddy Simulations. *Whither Turbulence Workshop*, Cornell University.

- Reiss, L.P. and Hanratty, T.J. 1963. An Experimental Study of the Unsteady Nature of the Viscous Sublayer. *AIChE J.* Vol. 9 No. 2.
- Repik, Y.U. and Sosedko, Y.P. 1980. Investigation of the Space-Time Flow Pattern in the Wall Region of a Turbulent Boundary Layer. *Fl. Mech. - Soviet Research*, vol. 9, no. 2.
- Robinson, S.K. 1982. An Experimental Search for Near-Wall Boundary Conditions for Large-Eddy Simulation. *AIAA Paper 82-0963*.
- Robinson, S.K. 1986. Instantaneous Velocity Profile Measurements in a Turbulent Boundary Layer. *Chem. Eng. Commun.* vol.43.
- Robinson, S.K. 1986. Space-Time Correlation Measurements in a Compressible Turbulent Boundary Layer. *AIAA Paper 86-1130*.
- Robinson, S.K., Kline, S.J., and Spalart, P.R. 1988. Spatial Character and Time Evolution of Coherent Structures in a Numerically Simulated Boundary Layer. *AIAA Paper 88-3577*.
- Robinson, S.K., Kline, S.J., and Spalart, P.R. 1989. A Review of Quasi-Coherent Structures in a Numerically Simulated Turbulent Boundary Layer. *NASA TM-102191*.
- Robinson, S.K. 1989. A Review of Vortex Structures and Associated Coherent Motions in Turbulent Boundary Layers. *2nd IUTAM Symposium on Structure of Turbulence and Drag Reduction*, Zurich, Switzerland.
- Robinson, S.K. and Hu, K.C. 1989. Stereo Image Visualization of Numerically Simulated Turbulence. *AIAA Paper 89-0141*.
- Rogallo, R.S. and Moin, P. 1984. Numerical Simulation of Turbulent Flows. *Ann. Rev. Fluid Mech.* Vol. 16.
- Ruetnik, J.R. 1954. *Rept. I-19*, The Johns Hopkins Univ.
- Runstadler, P.G., Kline, S.J., and Reynolds, W.C. 1963. An Experimental Investigation of Flow Structure of the Turbulent Boundary Layer. *Mech. Engrg. Dept. Rept. MD-8*.
- Saffman, P.G. 1978. Problems and Progress in the Theory of Turbulence. *Structure and Mechanisms of Turbulence II*, Springer-Verlag.
- Sandborn, V.A. 1959. Measurements of Intermittency of Turbulent Motion in a Boundary Layer. *J. Fluid Mech.* Vol. 6.
- Schewe, G. 1983. On the Structure and Resolution of Wall-Pressure Fluctuations Associated with Turbulent Boundary-Layer Flow. *J. Fluid Mech.* Vol. 134.
- Schraub, F.A. and Kline, S.J. 1965. A Study of the Structure of the Turbulent Boundary Layer with and Without Longitudinal Pressure Gradient. *Rept. MD-12*, Dept. Mech. Eng., Stanford Univ.

- Smith, C.R. and Abbott, D.E., 1978. *Coherent Structure of Turbulent Boundary Layers*, AFOSR/Lehigh University Workshop.
- Smith, C.R. and Metzler, S.P. 1983. The Characteristics of Low-Speed Streaks in the Near-Wall Region of a Turbulent Boundary Layer. *J. Fluid Mech.* Vol. 129.
- Smith, C.R. and Schwartz, S.P. 1983. Observation of Streamwise Rotation in the Near-Wall Region of a Turbulent Boundary Layer. *Phys. Fluids* Vol. 26.
- Smith, C.R. 1984. A Synthesized Model of the Near-Wall Behavior in Turbulent Boundary Layers. in *Proc. of 8th Symp. on Turbulence*, University of Missouri-Rolla.
- Spalart, P.R. and Leonard, A. 1985. Direct Numerical Simulation of Equilibrium Turbulent Boundary Layers. *5th Symposium on Turbulent Shear Flows*, Ithaca, New York.
- Spalart, P.R. 1986. Direct Simulation of a Turbulent Boundary Layer up to $Re_\theta = 1410$. *TM 89407 NASA*.
- Spalart, P.R. 1988. Direct Simulation of a Turbulent Boundary Layer up to $Re_\theta = 1410$. *J. Fluid Mech.* Vol. 187.
- Spina, E.F. and Smits, A.J. 1987. Organized Structures in a Compressible, Turbulent Boundary Layer. *J. Fluid Mech.* Vol. 182.
- Stuart, J.T. 1965. The Production of Intense Shear Layers by Vortex Stretching and Convection. *AGARD Rept.* 514.
- Subramanian, C.S., Rajagopalan, S., Antonia, R.A., Chambers, A.J. 1982. Comparison of Conditional Sampling Techniques in a Turbulent Boundary Layer. *J. Fluid Mech.* Vol. 123.
- Swearingen, J.D. and Blackwelder, R.F. 1987. The Growth and Breakdown of Streamwise Vortices in the Presence of a Wall, *J. Fluid Mech.*, vol. 182.
- Talmon, A.M., Kunen, J.M.G, and Ooms, G. 1986. Simultaneous Flow Visualization and Reynolds-Stress Measurement in a Turbulent Boundary Layer. *J. Fluid Mech.* Vol. 163.
- Theodorsen, T. 1952. Mechanism of Turbulence. In *Proc. 2nd Midwestern Conf. on Fluid Mech.*, Ohio State University, Columbus, Ohio.
- Thomas, A.S.W. and Bull, M.K. 1983. On the Role of Wall-Pressure Fluctuations in Deterministic Motions in the Turbulent Boundary Layer. *J. Fluid Mech.* Vol. 128.
- Townsend, A.A. 1951. The Structure of the Turbulent Boundary Layer. *Proc. Cambridge Phil. Soc.*, Vol. 47, Pt. 2.
- Townsend, A.A. 1956. *The Structure of Turbulent Shear Flow*. Cambridge University Press. 1st ed.

- Townsend, A.A. 1970. Entrainment and the Structure of Turbulent Shear Flow. *J. Fluid Mech.* Vol. 41.
- Townsend, A.A. 1976. *The Structure of Turbulent Shear Flow*. Cambridge University Press. 2nd ed.
- Tritton, D.J. 1967. Some New Correlation Measurements in a Turbulent Boundary Layer. *J. Fluid Mech.* Vol. 28.
- Utami, T. and Ueno, T. 1987. Experimental Study on the Coherent Structure of Turbulent Open-Channel Flow Using Visualization and Picture Processing. *J. Fluid Mech.* Vol. 174.
- Uzkan, T. and Reynolds, W.C. 1967. a Shear-Free Turbulent Boundary Layer. *J. Fluid Mech.* Vol. 28.
- Wallace, J.M., Eckelmann, H., and Brodkey, R.S. 1972. The Wall Region in Turbulent Shear Flow. *J. Fluid Mech.* Vol. 54, Pt. 1.
- Wallace, J.M. 1982. On the Structure of Bounded Turbulent Shear Flow: A Personal View. In *Developments in Theoretical and Applied Mechanics*, XI, University of Alabama, Huntsville.
- Wallace, J.M. 1985. The Vortical Structure of Bounded Turbulent Shear Flow. In *Lecture Notes in Physics* 235, Springer-Verlag.
- Wei, T. and Willmarth, W.W. 1987. Reynolds Number Effects on the Structure of Turbulent Channel Flow. *J. Fluid Mech.* Vol. 179.
- Willmarth, W.W. and Woolridge, C.E. 1962. Measurements of the Fluctuating Pressure at the Wall Beneath a Thick Turbulent Boundary Layer. *J. Fluid Mech.* Vol. 14.
- Willmarth, W.W. and Tu, B.J. 1967. Structure of Turbulence in the Boundary Layer Near the Wall. *Phys. Fluids* Vol. 10, p. S134.
- Willmarth, W.W. and Lu, S.S. 1972. Structure of the Reynolds Stress Near the Wall. *J. Fluid Mech.* Vol. 55.
- Willmarth, W.W. 1975a. Structure of Turbulence in Boundary Layers. *Advances in Applied Mechanics*, Vol. 15.
- Willmarth, W.W. 1975b. Pressure Fluctuations Beneath Turbulent Boundary Layers. *Ann. Rev. Fluid Mech.* Vol. 7.

Report Documentation Page

1. Report No. NASA TM-103859		2. Government Accession No.		3. Recipient's Catalog No.	
4. Title and Subtitle The Kinematics of Turbulent Boundary Layer Structure				5. Report Date April 1991	
				6. Performing Organization Code	
7. Author(s) Stephen Kern Robinson				8. Performing Organization Report No. A-91123	
				10. Work Unit No.	
9. Performing Organization Name and Address Ames Research Center Moffett Field, CA 94035-1000				11. Contract or Grant No.	
				13. Type of Report and Period Covered Technical Memorandum	
12. Sponsoring Agency Name and Address National Aeronautics and Space Administration Washington, DC 20546-0001				14. Sponsoring Agency Code	
15. Supplementary Notes Point of Contact: Stephen Kern Robinson, Langley Research Center, MS 163, Hampton, VA 23665-5225, (804) 864-5541/5547 or FTS 928-5541/5547 Research was performed and report was prepared while author was located at Ames Research Center.					
16. Abstract <p>The long history of research into the internal structure of turbulent boundary layers has not provided a unified picture of the physics responsible for turbulence production and dissipation. The goals of the present research are to 1) define the current state of boundary layer structure knowledge, and 2) utilize direct numerical simulation results to help close the unresolved issues identified in Part A and to unify the fragmented knowledge of the various coherent motions into a consistent kinematic model of boundary layer structure.</p> <p>The results of the current study show that all classes of coherent motion in the low Reynolds number turbulent boundary layer may be related to vortical structures, but that no single form of vortex is representative of the wide variety of vortical structures observed. In particular, ejection and sweep motions, as well as entrainment from the free-stream are shown to have strong spatial and temporal relationships with vortical structures. Distributions of vortex size, location, and intensity show that quasi-streamwise vortices dominate the buffer region, while transverse vortices and vortical arches dominate the wake region. Both types of vortical structure are common in the log region.</p> <p>The inter-relationships between the various structures and the population distributions of vortices are combined into a conceptual kinematic model for the boundary layer. Aspects of vortical structure dynamics are also postulated, based on time-sequence animations of the numerically simulated flow.</p>					
17. Key Words (Suggested by Author(s)) Boundary layer Turbulent Coherent structures			18. Distribution Statement Unclassified-Unlimited Subject Category - 34		
19. Security Classif. (of this report) Unclassified		20. Security Classif. (of this page) Unclassified		22. Price A21	
				21. No. of Pages 490	